Probing femtosecond and attosecond electronic and chiral dynamics : high-order harmonic generation, XUV free induction decay, photoelectron spectroscopy and Coulomb explosion

Samuel Beaulieu

▶ **To cite this version:**

Samuel Beaulieu. Probing femtosecond and attosecond electronic and chiral dynamics : high-order harmonic generation, XUV free induction decay, photoelectron spectroscopy and Coulomb explosion. Other [cond-mat.other]. Université de Bordeaux; Institut national de la recherche scientifique (Québec, province), 2018. English. NNT : 2018BORD0063 . tel-01939703

HAL Id: tel-01939703
https://theses.hal.science/tel-01939703

Submitted on 4 Dec 2018

HAL is a multi-disciplinary open access archive for the deposit and dissemination of scientific research documents, whether they are published or not. The documents may come from teaching and research institutions in France or abroad, or from public or private research centers.

L'archive ouverte pluridisciplinaire **HAL**, est destinée au dépôt et à la diffusion de documents scientifiques de niveau recherche, publiés ou non, émanant des établissements d'enseignement et de recherche français ou étrangers, des laboratoires publics ou privés.

THÈSE EN COTUTELLE PRÉSENTÉE

POUR OBTENIR LE GRADE DE

DOCTEUR DE

L'UNIVERSITÉ DE BORDEAUX

ET L'INSTITUT DE LA RECHERCHE SCIENTIFIQUE

ÉCOLE DOCTORALE UBX

SPÉCIALITÉ *Lasers*, *Matière et Nanosciences*

INRS-EMT

SPÉCIALITÉ *Sciences de l'énergie et des matériaux*

Par Samuel BEAULIEU

Probing Femtosecond and Attosecond Electronic and Chiral Dynamics

High-Order Harmonic Generation, XUV Free Induction Decay, Photoelectron Spectroscopy and Coulomb Explosion.

Sous la direction de Yann MAIRESSE
et de François LEGARE

Soutenue 23 mai 2018

Membres du jury :

Mme HUET, Thérèse	Professeure	Université de Lille	Présidente
M. POISSON, Lionel	Directeur de recherche	CNRS	Rapporteur
M. NISOLI, Mauro	Professeur	Politecnico Milano	Rapporteur
M. CORKUM, Paul	Professeur	Université d'Ottawa	Examinateur
Mme L'HUILLIER, Anne	Professeur	Université de Lund	Examinateur
M. MARSI, Marino	Professeur	Université d'Orsay	Examinateur

Titre :Mesure de dynamiques électroniques et chirales à l'échelle femtoseconde et attoseconde

Résumé :

Ce manuscrit de thèse s'articule autour de l'étude de l'interaction entre des impulsions lumineuses ultrabrèves et des atomes ainsi que des molécules polyatomiques et chirales en phase gazeuse. En utilisant des techniques développées en physique attoseconde ainsi qu'en femtochimie, notre objectif général est de parvenir à une meilleure compréhension des dynamiques ultrarapides photoinduites dans la matière. Pour ce faire, nous avons développé des sources de lumière à ultrabrèves dans le proche infrarouge et l'infrarouge moyen, qui ont été utilisées pour construire une source de rayons X dans la fenêtre de l'eau, basée sur la génération d'harmoniques d'ordre élevé (GHOE), ainsi que pour l'étude de nouveaux canaux de GHOE impliquant des états hautement excités (Rydberg). Cette dernière étude a démontré une émission harmonique via l'ionisation depuis des états de Rydberg et la recombinaison radiative sur l'état fondamental, attirant ainsi notre intérêt pour le rôle des états de Rydberg en physique des champs forts. Cela nous a conduit à étudier la décroissance libre de l'induction XUV de paquets d'ondes électroniques comme une nouvelle technique de spectroscopie 2D. De plus, nous avons découvert que l'interaction entre un laser intense et un atome préparé dans une superposition cohérente d'états électroniques peut conduire à la génération de lignes hyper-Raman concomitantes avec la GHOE standard. Ce mécanisme avait été prédit lors des premiers calculs théoriques de GHOE, mais n'avait jamais été démontré expérimentalement. Par la suite, nous nous sommes intéressé à l'étude de systèmes moléculaires, dans lesquelles une excitation électronique induite par la lumière peut déclencher des dynamiques nucléaires. Nous avons étudié la photoisomérisation non-adiabatique de l'acétylène cationique en vinylidène cationique ainsi que le contrôle cohérent de la localisation électronique lors de la photodissociation de H_2^+. La simplicité de ces systèmes moléculaires a permis la comparaison des résultats expérimentaux avec des calculs théoriques de pointe, révélant l'importance du couplage entre les degrés de liberté nucléaires et électroniques lors de dynamiques moléculaires photoinduites.

Un autre pilier majeur de cette thèse est l'étude de l'ionisation de molécules chirales avec des impulsions chirales. On sait depuis les années 70 que l'ionisation d'un ensemble de molécules chirales aléatoirement orientées, en utilisant une impulsion polarisée circulairement, conduit à une forte asymétrie avant-arrière dans le nombre de photoélectrons émis, selon l'axe de propagation de la lumière (Dichroisme Circulaire de Photoélectron, DCPE). Avant cette thèse, le DCPE a été largement étudié à l'aide du rayonnement synchrotron (ionisation à un photon) et a récemment été démontré avec des lasers femtoseconde, via des schémas d'ionisation multiphotonique. Dans cette thèse, nous avons montré que le DCPE est un effet universel, c'est-à-dire qu'il émerge dans tous les régimes d'ionisation: l'ionisation à un photon, l'ionisation à multiphonique, l'ionisation au-dessus du seuil ainsi que l'ionisation par effet tunnel. Ensuite, nous avons démontré que la combinaison d'approches standard de femtochimie et du DCPE peuvent être utilisées pour suivre des dynamique de molécules chirales photoexcitées. En utilisant des approches expérimentales similaires, avec des séquences d'impulsions ayant des états de polarisation contre-intuitifs, nous avons démontré un nouvel effet chiroptique, appelé Dichroïsme Circulaire de Photoexcitation (DCPX), qui est décrit par un courant électronique directionnel et chirosensible, lorsque plusieurs niveaux sont

peuplées de manière cohérente avec de la lumière chirale. Enfin, nous avons introduit une perspective temporelle à la photoionisation chirale en mesurant l'asymétrie avant-arrière des retards de photoionisation dans les molécules chirales photoionisées par des impulsions lumineuses chirales.

Mots clés : Chiralité, Photoionisation, Champ fort, GHOE, Lasers, Etats excités, Cohérence

Title : Probing Femtosecond and Attosecond Electronic and Chiral Dynamics

Abstract :

This thesis manuscript is articulated around the investigation of the interaction between ultrashort light pulses and gas-phase atoms, polyatomic and chiral molecules. Using the toolboxes developed in attosecond and strong-field physics as well as in femtochemistry, our general goal is to reach a better understanding of subtle effects underlying ultrafast light-induced dynamics in matter. To do so, we developed cutting-edge near-infrared and mid-infrared few-cycle light sources, which were used to build a water-window soft-X-ray source based on high-order harmonic generation (HHG), as well as to study new HHG channels involving highly-excited (Rydberg) states. The latter study revealed a delayed HHG emission from the ionization of Rydberg states and radiative recombination onto the electronic ground state, triggering our interest in the role of Rydberg states in strong-field physics. This led us to investigate the laser-induced XUV Free Induced Decay from electronic wavepackets as a new background-free 2D spectroscopic technique. Moreover, we have found out that strong-field interaction with a well prepared coherent superposition of electronic states led to the generation of hyper-Raman lines concomitant with standard high-order harmonics. These spectral features were predicted in the early-days theoretical calculations of HHG but had never been reported experimentally.

After these experiments in rare gas atoms, we moved to molecular targets, in which light-induced electronic excitation can trigger nuclear dynamics. Using simple benchmark molecules, we have studied dynamics involving the participation of both nuclear and electronic degrees of freedom: first, we studied the ultrafast non-adiabatic photoisomerization of the acetylene cation into vinylidene cation, and second, we investigated the coherent control of electron localization during molecular photodissociation of H_2^+. The simplicity of these molecular targets enabled the comparison of the experimental results with state-of-the-art theoretical calculations, revealing the importance of the coupling between nuclear and electronic degrees of freedom in photoinduced molecular dynamics.

The other major pillar of this thesis is the study of ionization of chiral molecules using chiral light pulses. It has been known since the 70s that the ionization from an ensemble of randomly oriented chiral molecules, using circularly polarized light pulse, leads to a strong forward-backward asymmetry in the number of emitted photoelectrons, along the light propagation axis (Photoelectron Circular Dichroism, PECD). Prior to this thesis, PECD was widely studied at synchrotron facilities (single-photon ionization) and had recently been demonstrated using table-top lasers in resonant-enhanced multiphoton ionization schemes. In this thesis, we have shown that PECD is a universal effect, i.e. that it emerges in all ionization

regimes, from single photon ionization, to few-photon ionization, to above-threshold ionization, up to the tunneling ionization regime. This bridges the gap between chiral photoionization and strong-field physics. Next, we have shown how the combination of standard femtochemistry approaches and PECD can be used to follow the dynamics of photoexcited chiral molecules using time-resolved PECD. Using similar experimental approaches, but by using pulse sequences with counter-intuitive polarization states, we have demonstrated a novel electric dipolar chiroptical effect, called Photoexcitation Circular Dichroism (PXCD), which emerges as a directional and chirosensitive electron current when multiple excited bound states of chiral molecules are coherently populated with chiral light. Last, we introduced a time-domain perspective on chiral photoionization by measuring the forward-backward asymmetry of photoionization delays in chiral molecules photoionized by chiral light pulses. Our work thus carried chiral-sensitive studies down to the femtosecond and attosecond ranges.

Keywords : Chirality, Photoionization, Strong-field, HHG, Excited states, Coherence

Centre Lasers Intenses et Applications, UMR5107, 43, rue Pierre Noailles - 33400 *Talence*

Unité de recherche

[Intitulé, n° de l'unité et adresse de l'unité de recherche]

Copyright © 2018 Samuel Beaulieu

PUBLISHED BY UNIVERSITY OF BORDEAUX AND INRS

Manuscript edited in LaTeXusing a template by Mathias Legrand (le- grand.mathias@gmail.com), and modify by Vel (vel@latextemplates.com). Most of figures are produced using Matlab and Inkscape. Others are taken from cited references.
Printed in August 2018

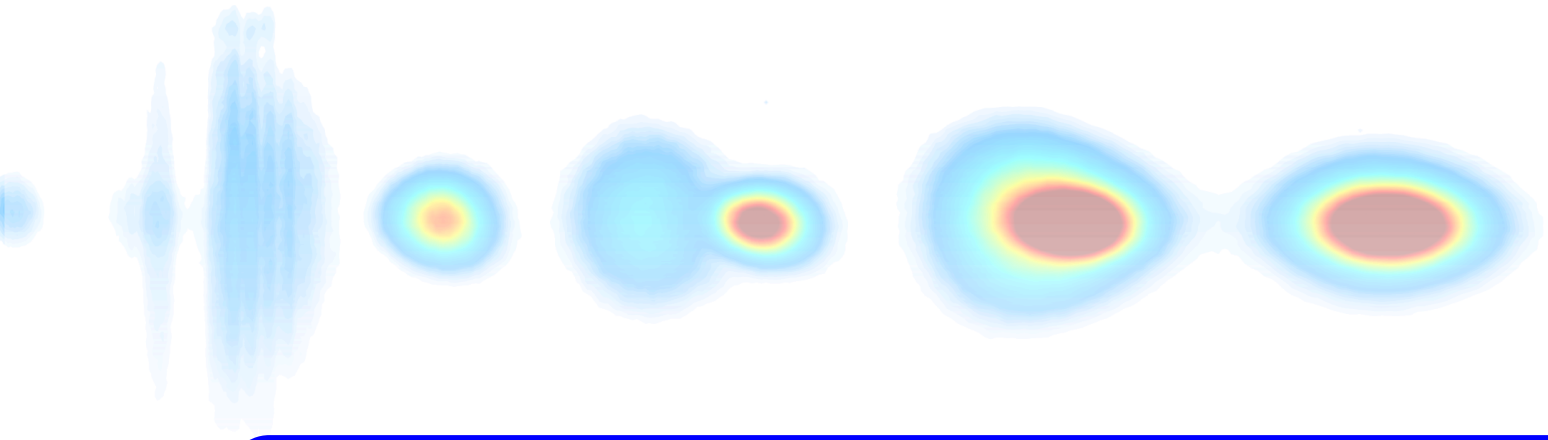

Contents

0.1 List of publications

List of publications in peer-reviewed journals (april 2018):

[21] A. Comby, S. Beaulieu, E. Constant, D. Descamps, S. Petit and Y. Mairesse, *Absolute gas density profiling in high-order harmonic generation*, Optics express **26**, 6001-6009 (2018)

[20] S. Camp, S. Beaulieu, K. J. Schafer and M. B. Gaarde, *Resonantly-initiated quantum trajectories and their role in the generation of near-threshold harmonics*, Journal of Physics B: Atomic, Molecular and Optical Physics **51**, 064001 (2018)

[19] S. Beaulieu, A. Comby, D. Descamps, B. Fabre, G. A. Garcia, R. Géneaux, A.G. Harvey, F. Légaré, Z. Masin, L. Nahon, A.F. Ordonez, S. Petit, B. Pons, Y. Mairesse, O. Smirnova and V. Blanchet, *Photoexcitation circular dichroism in chiral molecules*, Nature Physics **1** (2018)

[18] S. Beaulieu, A. Comby, A. Clergerie, J. Caillat, D. Descamps, N. Dudovich, B. Fabre, R. Géneaux, F. Légaré, S. Petit, B. Pons, G. Porat, T. Ruchon, R. Taïeb, V. Blanchet and Y. Mairesse, *Attosecond-resolved photoionization of chiral molecules*, Science **358**, 1288 (2017)

[17] B. Basdevant, A.-A. Guilbault, S. Beaulieu, A. J. Des Lauriers and C. Y. Legault, *Iodine (III)-mediated synthesis of chiral -substituted ketones: recent advances and mechanistic insights*, Pure and Applied Chemistry **89**, 781-789 (2017)

[16] R. Géneaux, C. Chappuis, T. Auguste, S. Beaulieu, T. T. Gorman, F. Lepetit, L. F. DiMauro and T. Ruchon, *Radial index of Laguerre-Gaussian modes in high-order-harmonic generation*, Physical Review A **95**, 051801(R) (2017)

[15] S. Beaulieu, E. Bloch, L. Barreau, A. Comby, D. Descamps, R. Géneaux, F. Légaré, S. Petit and Y. Mairesse, *Phase-resolved two-dimensional spectroscopy of electronic wavepackets by laser-induced XUV free induction decay*, Physical Review A **95**, 041401(R) (2017)

[14] S. Beaulieu, A. Comby, B. Fabre, D. Descamps, A. Ferré, G.A. Garcia, R. Géneaux, F. Légaré, L. Nahon, S. Petit, T. Ruchon, B. Pons, V. Blanchet and Y. Mairesse, *Probing ultrafast dynamics of chiral molecules using time-resolved photoelectron circular dichroism*, Faraday Discussions **194**, 325-348 (2016)

[13] A. Comby, S. Beaulieu, M. Boggio-Pasqua, D. Descamps, F. Légaré, L. Nahon, S. Petit, B. Pons, B. Fabre, Y. Mairesse and V. Blanchet, *Relaxation Dynamics in Photoexcited Chiral Molecules Studied by Time-Resolved Photoelectron Circular Dichroism: Toward Chiral Femtochemistry*, The Journal of Physical Chemistry Letters **7** (22), 4514-4519 (2016)

[12] S. Beaulieu, A. Ferré, R. Géneaux, R. Canonge, D. Descamps, B. Fabre, N. Fedorov, F. Légaré, S. Petit, T. Ruchon, V. Blanchet, Y. Mairesse and B. Pons, *Universality of photoelectron circular dichroism in the photoionization of chiral molecules*, New Journal of Physics **18**, 102002 (2016)

[11] S. Beaulieu, S. Camp, D. Descamps, A. Comby, V. Wanie, S. Petit, F. Légaré, K. J. Schafer, M.B. Gaarde, F. Catoire and Y. Mairesse, *Role of Excited States In High-order Harmonic Generation*, Physical Review Letters **117**, 203001 (2016)

[10] L. Nahon, L. Nag, G.A. Garcia, I. Myrgorodska, U. Meierhenrich, S. Beaulieu, V. Wanie, V. Blanchet, R. Géneaux and I. Powis, *Determination of accurate electron chiral asymmetries in fenchone and camphor in the VUV range: sensitivity to isomerism and enantiomeric purity*, Physical Chemistry Chemical Physics **18**, 12696-12706 (2016)

[9] V. Wanie, H. Ibrahim, S. Beaulieu, N. Thiré, B. E. Schmidt, Y. Deng, A. S. Alnaser, I. V. Litvinyuk, X.-M. Tong and F. Légaré, *Coherent control of* H_2/D_2 *dissociative ionization by a mid-*

infrared two-color laser field, Journal of Physics B: Atomic, Molecular and Optical Physics **49**, 025601 (2015)

[8] V. Cardin, N. Thiré, S. Beaulieu, V. Wanie, F. Légaré and B. E. Schmidt, *0.42 TW 2-cycle pulses at 1.8 µm via hollow-core fiber compression*, Applied Physics Letters **107**, 181101 (2015)

[7] S. Beaulieu and C. Y. Legault, *Mechanistic Insights on the Iodine (III) - Mediated αOxidation of Ketones*, Chemistry-A European Journal **21**, 11206-11211 (2015)

[6] N. Thiré, S. Beaulieu, V. Cardin, A. Laramée, V. Wanie, B. E. Schmidt and F. Légaré, *10 mJ 5-cycle pulses at 1.8 µm through optical parametric amplification*, Applied Physics Letters **106**, 091110 (2015)

[5] B. Wales, E. Bisson, R. Karimi, S. Beaulieu, A. Ramadhan, M. Giguere, Z. Long, W.-K. Liu, J.-C. Kieffer, F. Légaré and J. Sanderson, *Coulomb imaging of the concerted and stepwise break up processes of OCS ions in intense femtosecond laser radiation*, Journal of Electron Spectroscopy and Related Phenomena **195**, 332-336 (2014)

[4] H. Ibrahim, B. Wales, S. Beaulieu, B. E. Schmidt, N. Thiré, E. P. Fowe, E. Bisson, C. T. Hebeisen, V. Wanie, M. Giguere, J.-C. Kieffer, M. Spanner, A. D. Bandrauk, J. Sanderson, M. S. Schuurman and F. Légaré, *Tabletop imaging of structural evolutions in chemical reactions demonstrated for the acetylene cation*, Nature communications **5**, 4422 (2014)

[3] B. Wales, R. Karimi, E. Bisson, S. Beaulieu, M. Giguere, T. Motojima, R. Anderson, J. Matsumoto, J.-C. Kieffer, F. Légaré, H. Shiromaru and J. Sanderson, *Comparing Coulomb explosion dynamics of multiply charged triatomic molecules after ionization by highly charged ion impact and few cycle femtosecond laser pulses*, Physica Scripta **T156**, 014068 (2013)

[2] R. Karimi, E. Bisson, B. Wales, S. Beaulieu, M. Giguere, Z. Long, W.-K. Liu, J.-C. Kieffer, F. Légaré and J. Sanderson, N_2O *ionization and dissociation dynamics in intense femtosecond laser radiation, probed by systematic pulse length variation from 7 to 500 fs*, The Journal of Chemical Physics **138**, 204311 (2013)

[1] P.-A. Champagne, J. Pomarole, M.-E. Therien, Y. Benhassine, S. Beaulieu, C. Y. Legault and J.-F. Paquin, *Enabling Nucleophilic Substitution Reactions of Activated Alkyl Fluorides through Hydrogen Bonding*, Organic Letters **15**, 2210-2213 (2013)

0.2 Acknowledgement/Remerciement

First of all, I would like to acknowledge the members of my thesis committee, Paul Corkum, Thérèse Huet, Anne L'Huillier, Marino Marsi, Mauro Nisoli and Lionel Poisson, for carefully reading the manuscript and participating to stimulating and exciting discussions during and after the defence.

Now, for the rest of the acknowledgements, let me switch to French.

J'aimerais chaleureusement remercier mes deux co-directeurs de thèse, François Légaré et Yann Mairesse. François, quelle rencontre déterminante lors de ce fameux colloque de chimie de l'Université de Sherbrooke en 2009. Merci d'avoir fait confiance à un jeune de première année du baccalauréat en chimie pour faire un stage dans ton labo. Merci de m'avoir toujours appuyé au maximum. Merci de m'avoir appris à m'amuser en faisant de la science, ainsi que m'avoir introduit à une myriade de scientifiques de la communauté de physique attoseconde. Tu as clairement eu un impact majeur et positif dans mon parcours scientifique. Yann, quoi dire. D'abord, merci infiniment pour l'accueil à Bordeaux. Le partage de la découverte de la ville à vélo, des concerts dans les caves malpropres de Bordeaux et des cafés du dimanche ont fait en sorte que je me suis rapidement senti à la maison. De plus, quelle belle expérience de bosser avec toi. J'ai énormément appris durant ces quatres années. Tu as été une ressource infinie d'idées et de solutions. Merci pour la grande liberté de penser et d'action que tu m'as offerte. Tes qualités scientifiques n'ont d'égale que tes qualités humaines.

Lors de cette thèse en co-tutelle, j'ai eu la chance de côtoyer et d'être influencé par des collègues géniaux, autant au Québec qu'en France. Tout d'abord, du côté québécois, j'aimerais remercier Heide Ibrahim, qui a été la première à m'apprendre les rudiments des lasers femto ainsi que leur interaction avec des molécules. Ce fût un plaisir de travailler avec toi. Nico, Dr Thiré, j'ai eu énormément de plaisir à tes cotés, autant au labo qu'ailleurs. Tu es maintenant beaucoup plus que mon post-doc (colloque de l'UdeS $\sim$ 2013). Merci pour les 1600 km de route pour assister à la soutenance, ça m'a touché. Wanie, nos parcours se suivent depuis longtemps et c'est une bonne chose. Toujours un bonheur de te côtoyer, sur différents continents et dans toutes circonstances. J'espère que ça va continuer. Merci à toutes les autres personnes qui ont contribué à mon développement ainsi qu'à l'ambiance sympatique au labo: Bruno, Philippe, Antoine, Vincent Cardin, Vincent Gruson, Mina, Carol, Léo, Eric, ainsi que plusieurs autres. Merci au staff administratif de l'INRS pour leur gentillesse ainsi que leur efficacité.

Pour ce qui est du CELIA, j'aimerais d'abord remercier Valérie Blanchet. Ta fougue, ton authenticité ainsi que ton amour évident et contagieux pour la science ont clairement eu une influence positive sur ces années passées au CELIA. Ce fût vraiment un plaisir. Merci aux théoriciens du groupe hamoniques et applications avec qui j'ai pu travailler: Fabrice, toujours un plaisir de discuter de science (et autres) avec toi. Baptiste, homme d'une gentillesse infini. Je garderai de bon souvenirs de Toulouse en ta compagnie. Bernard, merci pour tous ces calculs et échanges scientifiques (ainsi que non-scientifique). On aura bien rigolé. Merci aux autres membres du groupe harmoniques, pour l'ambiance agréable et tout le reste: Constance, Eric C., Eric M., Henri, Hervé, Kevin et Patrick. Merci à Dominique et Stéphane, premièrement pour avoir fourni de super photons pour tous nos manips, sans vous, la productivité aurait été nettement moindre. Merci pour votre regard toujours critique et constructif sur les résultats produits avec Aurore. Merci à Céline, Emmanuelle, Sonia et Sophie pour avoir été d'une grande aide et d'une grande patience avec moi, québécois qui ne connaissait pas trop les subtilités de l'administration française. Merci aux autres thésard avec qui j'ai bossé. Alex, j'ai vraiment passé de super moments en ta compagnie, autant à Bordeaux, dans le Périgord ainsi que lors de votre

visite au Québec. Etienne, ce fût un plaisir de bosser avec toi, ainsi que de partager l'appart (ainsi que la découverte des commerces avoisinant) avec toi. Enfin, merci tout spécial à El Comby. Mon aventure Bordelaise aurait été plus fade sans toi. Autant au labo, qu'à vélo, qu'au El Sitio, ta présence fût toujours autant rafraichissante qu'agréable. Merci pour ton énergie et ton enthousiasme.

Merci aux théoriciens 'extérieurs' avec qui j'ai eu la chance de collaborer étroitement durant ma thèse: Micheal Schuurman et Michael Spanner du NRC, Andre D. Bandrauk et Emmanuel P. Fowe de l'Université de Sherbrooke, Seth Camp, Mette Gaarde et Ken Shafer du LSU, Vasily Strelkov du RAS Moscow ainsi qu'Andres Ordonez, Alvaro Jimenez-Galan, Misha Ivanov et Olga Smirnova du MBI.

Merci à Thierry Ruchon et Romain Géneaux de m'avoir accueilli dans votre labo pour les manips sur les HHG-OAM ainsi que la découverte de la Butte-aux-Cailles, à Paris. Ce fut une super expérience.

Merci à Richard "clé de 13" Taïeb ainsi que Jérémie Caillat pour le stage de théoricien d'une semaine dans votre labo. Honnêtement ce fût vraiment une semaine géniale.

Merci à Laurent Nahon et Gustavo Garcia pour le beamtime sur DESIRS, ainsi que la collaboration "PECD".

Merci aux prof de Sherbrooke pour l'éveil scientifique. Merci particulier à Pat, Claude Y., Serge et Armand.

Merci à Sam Palato. Pour reprendre tes mots, pour les échanges scientifiques dans un contexte scientifique, scientifiques dans un contexte non-scientifique ainsi que non-scientifiques dans un contexte scientifique. Parler de science avec toi est clairement une de mes activitées favorites.

Merci à la promo 46 de chimie de l'UdeS. Je garde de super souvenirs de ces années. Merci particulier à Kim, pour l'enseignement de l'assiduité dans les études. Ce fût fort utile.

Merci à la famille Baslé-Grinsell: Betty, Marco, Tom, Sarah, ainsi que la famille étendue. Votre accueil ainsi que tous ces beaux moments passés avec vous à Nantes, Bordeaux, Angrie, Montréal et Paris ont grandement contribués à mon intégration dans ce pays. Merci pour tous.

Merci à mes chums de Sainte-Julie/Montréal. Je ne vous nommerai pas, vous vous reconnaissez. L'évolution à vos côtés depuis fort longtemps m'a réellement fait grandir. J'ai passé d'innombrable super moments avec vous. Merci pour les conversations des fois intelligentes, des fois moins. C'est génial d'avoir une telle bande d'amis.

Merci à mes parents et ma soeur. Vous m'avez toujours encouragés, tout en me laissant la liberté de faire mes choix. Merci pour l'éducation et les valeurs que vous m'avez transmisses. Je ne pourrais pas avoir espéré mieux. Désolé pour la distance. Ca rend simplement les moments passés avec vous unique et plus intenses. Merci infiniment pour tout.

En terminant, merci, stylo de l'UdeS. Tu m'as permis de rencontrer un être extraordinaire. Alix, comment fais-tu pour transformer chaque moment anodin en fête? Je ne croyais pas que cette utopie serait réalité un jour. Merci pour tous ces merveilleux moments passés, présents et futurs. Love.

0.3 Introduction générale

0.3.1 Photos et films

«Une image vaut mille mots» est un idiome faisant référence au fait que, parfois, une seule image peut être plus informative qu'une description exhaustive d'un objet ou d'une situation. Même si «une image vaut mille mots», elle ne donne aucune information sur l'évolution temporelle du décor: elle ne fournit aucune information sur ce qui s'est passé avant, et/ou après le moment exact où la photo a été prise. Pour capturer l'évolution dynamique du décor, il faudrait échanger son appareil photo contre un caméscope. Un caméscope typique prend un cliché tous les $\sim$ 33 millisecondes (ms) et les fait défiler les uns après les autres. Puisque le système visuel humain traite de 10 à 12 images par seconde, ces séries d'images (30 images par seconde) sont perçues par les humains comme un mouvement fluide. De plus, parce que «le tout est plus que la somme de ses parties» (Aristote), cette succession d'images nous donne des informations sur l'évolution dynamique du décor et, souvent, fournit une relation causale entre chaque image enregistrée les unes après les autres. Un caméscope permet ainsi d'augmenter la dimensionnalité de l'information capturée, et nous offre la possibilité de comprendre l'évolution du décor.

Avec un temps d'exposition de $\sim$ 33 ms, une caméra peut prendre un cliché net d'un objet se déplaçant à une vitesse maximum d'environ 50 km/h. Tous objets ayant une vitesse supérieure à cette limite apparaîtront brouillés sur la photographie. Pour figer le mouvement d'un objet se déplaçant à une vitesse supérieure, par exemple un guépard en pleine vitesse de pointe (> 110 km/h), une caméra offrant un temps d'exposition aussi court que 0.25 ms (1/4000 s) doit être utilisée. Des caméras permettant un temps d'exposition aussi court que 0.0625 ms (1/16000 s) sont aujourd'hui commercialement disponible et accessible au grand public. Elles permettent, par exemple, de figer le mouvement des ailes d'un colibri, qui, en plein vol, bas des ailes plus de 80 fois par seconde.

Un autre exemple de technique permettant de figer le mouvement d'objets en mouvement très rapide se base sur une stratégie différente: l'illumination de la scène pendant un très bref instant. Un exemple de ce type de technique est la stroboscopie. La stroboscopie utilise un dispositif, qui peut être mécanique ou électronique, permettant de générer une séquence de flashs lumineux brefs et intenses. Cette technique permet d'utiliser une caméra à grand temps d'exposition, tout en préservant une résolution temporelle qui est proportionnelle au temps d'illumination de la scène. Un des exemples historiques de l'utilisation de cette technique est l'étude de la dynamique des fluides à l'aide de la stroboscopie par le professeur du MIT (Massachusetts Institut of Technology) Harold Eugene Edgerton, aussi connu sous le nom de *Papa Flash*. On doit la fameuse photographie «Milk Drop Coronet», *i.e.* la couronne de lait, à Edgerton et sa technique de photographie stroboscopique, utilisant un éclairage transitoire du décor.

Durant cette thèse, nous nous intéresserons à l'étude du comportement dynamique ultrarapide des atomes et des molécules, sur des échelles de temps extremement brèves. Par analogie avec les exemples ci-dessus, les molécules constituertont le décor dynamique d'intérêt, que nous éclairerons avec des flashs de lumière ultrabrefs. Ces flashs seront ainsi capables de figer la scène, qui sera capturée par divers types de détecteurs, qui jouront le rôle du caméscope.

0.3.2 Spectroscopie statique et information dynamique

L'étude de l'absorption et de l'émission de lumière par la matière (spectroscopie) est à l'origine des fondements de la mécanique quantique. Elle révèle en effet que les atomes et les molécules absorbent ou émettent du rayonnement électromagnétique à des énergies

bien définies. Ceci est une conséquence de la nature discrète de leurs états quantiques (états propres). Chaque atome ou molécule possède un ensemble unique d'états propres, dont les énergies peuvent être déterminées en mesurant le spectre d'absorption ou d'émission. La spectroscopie d'absoption et d'émission sont utilisées dans une myriade de différents domaines scientifiques. Par exemple, la composition chimique des étoiles et d'autres entités astronomiques peut être déterminées en mesurant le spectre d'absoption ou d'émission de ces corps. Cette technique, nommé *spectroscopie astomonique*, a été introduit par Joseph von Fraunhofer au début du XIXe siècle, lorsqu'il découvrit des raies d'émission bien précises dans le spectre du Soleil, permettant d'identifier sa composition chimique.

L'absorption de lumière par une molécule peut initier divers types de phénomènes dynamiques, selon la longueur d'onde du rayonnement utilisée. Par exemple, un rayonnement de faible énergie (grande longeur d'onde, *e.g.* micro-onde) induira préférentiellement des mouvements de rotation des molécules. Lorsque l'énergie du rayonnement augmente (*e.g* gamme spectrale infrarouge), l'absorption de photon peut faire vibrer les liaisons interatomiques au sein de la molécule. Enfin, si le rayonnement atteint la gamme de l'utraviolet, il peut exciter les électrons de la molécule.

Dans cette thèse, nous nous intéressons à l'étude de la physique atomique et moléculaire d'un point de vue dynamique (résolu en temps). Les objets que nous devons caractériser nécessitant une description quantique, il nous faudrait dans l'idéal mesurer l'évolution temporelle de sa fonction d'onde $\Psi(t)$. Nous avons vu en introduction que la mesure de dynamiques nécessitait a priori des dispositifs expérimentaux adéquats, jouant le rôle de caméra ultrarapide. Cependant il est tout de même possible d'extraire de précieuses informations sur la dynamique d'atomes ou de molécules depuis leur spectre d'absorption. En effet, le domaine temporel et le domaine spectral sont intimement liés. On peut passer de l'un à l'autre par une simple transformation mathématique, *i.e.* la transformée de Fourier. Les informations spectrales extraites des mesures spectroscopiques peuvent donc être utilisées pour obtenir une certaine quantité d'informations dynamiques sur les molécules étudiées. L'une des relations fondamentales dérivées de la description théorique de la spectroscopie relie le spectre d'absorption ($\sigma(E_\Omega)$) à la fonction d'onde dépendante du temps $\Psi(t)$,

$$\sigma(E_\Omega) \propto \int_{-\infty}^{+\infty} \langle \Psi_0 | \Psi(t) \rangle e^{iE(\Omega)t/\hbar} dt \tag{1}$$

où $\hbar$ est la constante de Planck réduite, et Ψ_0 est la fonction d'onde initiale. Nous voyons dans cette équation que le spectre d'absorption dépend de l'évolution temporelle de la fonction d'onde. Plus précisément, il dépend de l'intégrale de recouvrement entre la fonction d'onde dépendante du temps évaluée à l'instant t ($\Psi(t)$) et la fonction d'onde initiale (Ψ_0), que l'on appelle la fonction d'autocorrélation dépendante du temps $S(t)$, où $S(t) = \langle \Psi_0 | \Psi(t) \rangle$. Nous illustrons à présent le lien entre informations spectrales et dynamiques à partir de deux cas simples.

Le schéma présenté à la Fig. 2 illustre la relation entre le spectre d'absorption et la fonction d'autocorrélation. Les formes des surfaces d'énergie potentielle des états impliqués dans la transition dictent la dynamique de la molécule excitée. Par exemple, le peuplement d'un état excité lié ou d'un état purement dissociatif conduira à des fonctions d'autocorrélation dépendante du temps très différentes, et donc à des spectres d'absorption très différents. Sur la Fig. 2 (a), l'absorption de la lumière mène à l'excitation d'une molécule qui est initialement dans son état fondamental Ψ_0 vers un état excité lié, sur lequel la fonction d'onde dépendant du temps $\Psi(t)$ évolue. Sur la Fig. 2 (b), la fonction

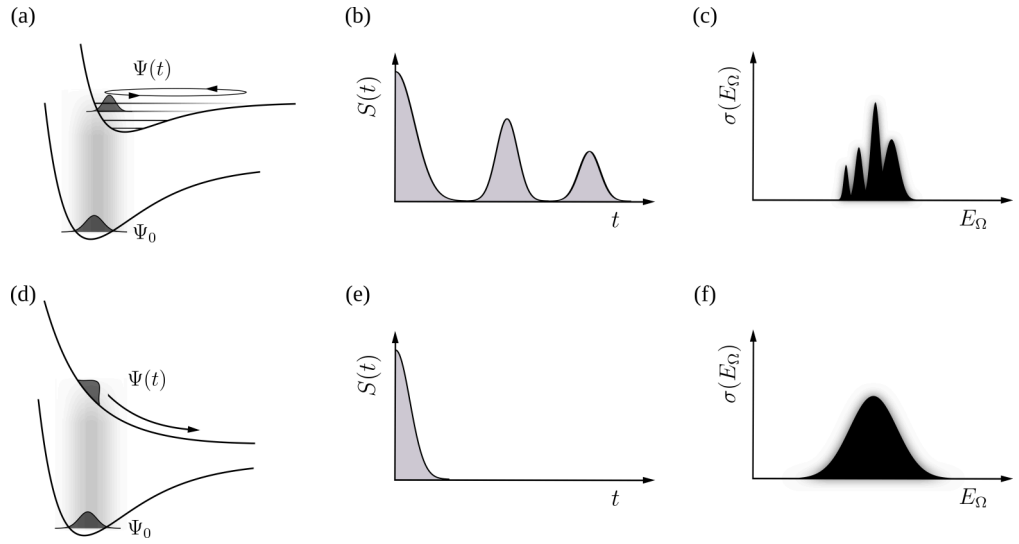

Figure 1: Schéma de la correspondance entre les surfaces d'énergies potentielles (SEP) d'un système arbitraire, qui est photoexcité de l'état fondamental vers un état excité, la fonction d'autocorrélation associée $S(t)$ à cette dynamique, et le spectre d'absorption $\sigma(E_\Omega)$ associé. En (a) et (d), la zone grise ombragée représente la région de Franck-Condon.

d'autocorrélation $S(t)$ correspondante subit d'abord une décroissance rapide, puisque $\Psi(t)$ s'éloigne de la région de Franck-Condon, conduisant à une diminution de son recouvrement avec Ψ_0 (la région de Franck-Condon est une région sur la surface d'énergie potentielle de l'état final qui est accessible via une transition verticale depuis l'état initial, voir Fig. 2). Chaque fois que $\Psi(t)$ revient dans la région Franck-Condon, son recouvrement avec Ψ_0 augmente à nouveau. Le spectre d'absorption associé à cette dynamique, qui est la transformée de Fourier de la fonction d'autocorrélation $S(t)$, est représenté sur la Fig. 2 (c). Sur la Fig. 2 (d), l'absorption de la lumière mène à l'excitation d'une molécule vers un état excité dissociatif. La fonction d'autocorrélation associée ($S(t)$) subit une décroissance rapide irréversible: la fonction d'onde ne revient jamais dans la région de Franck-Condon, en raison du caractère dissociatif de la SEP, ce qui mène à un large pic sans structure dans le spectre d'absorption (Fig. 2 (f)).

Le spectre d'absorption étant l'observable la plus commune dans la plupart des techniques spectroscopiques optiques, il est possible, avec une connaissance de base des propriétés de la transformée de Fourier, de retrouver des caractérstiques der la dynamique moléculaire qui s'est produite après l'absorption de lumière. Les amplitudes, les largeurs et les formes de raies spectrales qui décrivent le spectre d'absorption statique encodent quantité d'informations sur la dynamique moléculaire photoinduite. Relier le spectre d'absorption moléculaire à l'évolution temporelle sur des états excités, en ayant souvent recours à l'aide de calculs de chimie quantique, a été (et est toujours) un terrain de jeu fascinant pour les physiciens moléculaires.

Néanmoins, la fonction d'autocorrélation dépendante du temps n'encode pas la totalité de la dynamique se déroulant sur les états excités. En effet, puisqu'elle est définie comme l'intégrale de recouvrement avec la fonction d'onde initiale, elle n'est sensible qu'à la dynamique se produisant au voisinage de celle ci, appelée la région de Franck-Condon. Il est donc assez frustrant de n'avoir accès qu'à une petite fraction de la dynamique, *i.e.* de regarder la dynamique avec les «lunettes filtrantes» de la région de Franck-Condon. Est-il possible d'enlever ces «lunettes» et de sonder entièrement la dynamique moléculaire, depuis la région de Franck-Condon, en passant par les états de transitions, pour finir sur

différents canaux de fragmentation? Comme nous le verrons ci-dessous, ceci est le but de la spectroscopie résolue en temps, dont le développement a permis un changement de paradigme en spectroscopie et a permis aux physiciens d'acquérir une compréhension plus profonde de la dynamique d'états excitées moléculaires.

0.3.3 Spectroscopie résolue en temps

L'un des premiers exemples publié dans la littérature de techniques spectroscopiques résolues en temps est la «photolyse flash». L'idée originale consiste à exciter des molécules en utilisant une impulsion de lumière intense et brève, à l'aide des lampes flash (étape «pompe»), et à enregistrer le spectre d'absorption des molécules excitées, après un bref intervalle de temps (étape «sonde»). Ce type de schéma est appelé «expérience pompe-sonde». En utilisant cette technique, les scientifiques ont réussi à mesurer, pour la première fois, le spectre d'absorption d'espèces moléculaires ayant de très courtes durées de vies et à fournir la première démonstration expérimentale de l'existence de radicaux libres, en profitant de la résolution temporelle milliseconde de la technique [Porter 1950]. Manfred Eigen, Ronald George Wreyford Norrish et George Porter ont mis au point cette technique de photolyse flash dans les années 1940, ce qui les a menés à partager le prix Nobel de chimie de 1967.

Une étape importante a été franchie avec la découverte du laser dans les années 1960 [Maiman 1960]. Peu de temps après, les scientifiques ont commencé à maîtriser cette nouvelle technologie et ont été en mesure de fournir des impulsions lumineuses cohérentes et extrêmement brèves. Dans les années 1980, des durées d'impulsion laser atteignant la centaine de femtoseconde (1 fs = 10^{-15} s) étaient disponibles. L'utilisation d'impulsions femtoseconde (en configuration pompe-sonde) a ouvert un nouveau champ de recherche appelé «femtochimie». La femtochimie permet de sonder le mouvement des noyaux, de la région de Franck-Condon vers les états de transitions, jusqu'à la formation de produits de photodissociation, avec une résolution temporelle femtoseconde (pour une revue, voir [Zewail 2000]). La femtochimie a révolutionné la façon dont les scientifiques perçoivent la cinétique d'une transformation photochimique, en permettant une visualisation directe du mouvement nucléaire et des géométries des états de transition, ce qui était totalement impossible en utilisant des techniques spectroscopiques conventionnelles. L'importance de la femtochimie a été reconnue par la communauté scientifique, conduisant au prix Nobel de chimie 1999 attribué à Ahmed Zewail.

Le désir d'étudier des dynamiques de plus en plus rapides nécessite la génération d'impulsions lumineuses de plus en plus brèves. Suite au succès de la femtochimie, il y a eu un fort intérêt à atteindre le domaine attoseconde, qui est l'échelle de temps typique du mouvement des électrons dans la matière. La durée d'impulsion la plus brève que l'on peut génerer est typiquement un cycle optique de la fréquence centrale du spectre. Pour les lasers infrarouges conventionnels (environ 800 nm), cette limite est de l'ordre de $\sim$ 2-3 fs. Cette limitation empêche de générer des impulsions sub-femtoseconde avec cette technologie, ce qui limite la résolution temporelle ultime pouvant être obtenue, en utilisant des schémas pompe-sonde, à quelques femtosecondes. Produire des impulsions plus brèves nécessite de diminuer la période d'oscillation de la lumière, *i.e.* d'augmenter l'énergie des photons. De la fin des années 1980 jusqu'au début des années 2000, les scientifiques ont réalisé d'importants progrès jusqu'à produire [Ferray et al. 1988; McPherson et al. 1987] et caractériser [Hentschel et al. 2001; Paul et al. 2001] des impulsions de durée attoseconde (1 as = 10^{-18} s) . La technologie clé qui a permis ces avancées spectaculaires est un mécanisme de conversion de fréquence extrêmement non-linéaire et non-perturbatif dans les gaz, appelé 'génération d'harmoniques d'ordre

élevé' (GHOE).

Depuis sa naissance en 2001, le domaine de la science attoseconde a connu des développements impressionnants (pour une revue, voir [Krausz et al. 2009]). De nos jours, des impulsions de durées inférieures à 50 attoseconde sont produites [Gaumnitz et al. 2017]. Les impulsions attosecondes ont été utilisées pour étudier la dynamique d'ionisation ultrarapide d'atomes [Klünder et al. 2011; Schultze et al. 2010], de molécules [Calegari et al. 2014; Haessler et al. 2009; Huppert et al. 2016; Neidel et al. 2013] et de solides [Cavalieri et al. 2007; Schultze et al. 2014], mesurant l'instant auquel les électrons sont éjectés de la cible ou révélant la dynamique du trou créé lors de l'ionisation. Il a été également démontré que des schémas de mesures innovants, utilisant le processus de génération d'harmoniques d'ordre élevé pour sonder le milieu générateur, fournissent des informations structurelles et dynamiques, avec des résolutions temporelles de l'ordre que quelques dizaines d'attosecondes et des résolutions spatiales de l'ordre de l'Ångström [Haessler et al. 2011; Itatani et al. 2004; Marangos 2016].

0.3.4 Objectifs de cette thèse

Malgré les progrès impressionnants de la spectroscopie ultrarapide au cours des 20 dernières années, plusieurs défis importants étaient toujours à relever, lors du commencement de cette thèse. Les travaux présentés dans ce manuscrit ont visé à résoudre quelques-uns de ces défis. Le manuscrit de thèse est divisé en six chapitres:

Chapitre 1: Sources lasers pour la physique en champs forts et la physique attoseconde

Le premier défi que nous avons cherché à relever est d'ordre plutôt technique: *le développement de sources lumineuses de pointe*, qui est un élément extrêmement important concernant le progrès de la science attoseconde. Réduire la durée des impulsions, augmenter leur intensité crête, mais aussi, comme nous le verrons, augmenter la longueur d'onde du laser, ouvrent de nouvelles perspectives pour les expériences en physique attoseconde/champs forts. Nous avons développé deux sources d'impulsions laser dites de «quelques cycles optiques», l'une à ALLS et l'autre au CELIA. La source à ALLS est basée sur un amplificateur paramétrique optique à haute énergie (dans l'infrarouge moyen) [Thiré et al. 2015], suivi d'une compression des impulsions jusqu'au régime de «quelques cycles optiques», en utilisant la propagation non-linéaire dans une fibre creuse remplie de gaz rare [Cardin et al. 2015]. La source au CELIA utilise cette technique pour compresser des impulsions de 800 nm.

Chapitre 2: Nouveaux degrés de liberté en génération harmoniques d'ordre élevé

Le premier résultat démontré suite à nos développements de sources lasers de pointes est la possibilité de produire des impulsions attosecondes intenses à très haute énergie de photon. Nous avons développé une ligne de lumière produisant des photons couvrant entièrement la gamme spectrale de la fenêtre de l'eau (285 eV - 530 eV). Avec cette source, nous avons démontré des mesures monocoups de spectre d'absorption, au niveau de la raie d'absorption K du carbone (285 eV). D'un point de vue plus fondamental, nous avons utilisé des impulsions de «quelques cycles optiques» pour étudier la réponse en champ fort d'un système simple - l'atome d'argon. Ces expériences peuvent être considérées comme un deuxième défi: *parvenir à une meilleure compréhension de l'interaction de la matière soumise à des champs laser intenses*. Cette stratégie nous a permis de découvrir de nombreux

nouveaux effets liés à l'excitation des états de Rydberg par le champ laser intense: GHOE par l'ionisation à partir des états de Rydberg et la recombinaison sur l'état fondamental [Beaulieu et al. 2016a], la décroissance libre de l'induction dans l'XUV [Beaulieu et al. 2017a], et la génération de lignes Hyper-Raman, de façon concomitante avec la GHOE standard. Dans ces expériences, la simplicité et la connaissance spectroscopique antérieure du système (Argon), et l'utilisation d'impulsions lumineuses de pointe, nous ont permis de révéler et de comprendre des effets complexes et parfois inattendus, lors de l'interaction champ fort - argon. Enfin, nous avons complexifié l'interaction lumière-matière en introduisant du moment angulaire orbital dans le champ laser infrarouge, afin d'étudier son transfert vers le rayonnement harmonique.

Chapitre 3: Dynamique nucléaire et électronique de molécules simples

L'un des Graal de la spectroscopie ultrarapide est de *mesurer la dynamique impliquant un couplage entre les degrés de libertés nucléaire et électronique*. Suivant notre précédente stratégie d'étudier des systèmes simples, nous avons choisi d'étudié la photoisomérisation de l'acétylène cationique ($[HC=CH]^+$) en vinylidène cationique ($[C=CH_2]^+$). Cette réaction unimoléculaire est possible grâce à une intersection conique qui permet le passage du paquet d'ondes, du premier état électroniquement excité de l'acétylène cationique vers l'état électronique fondamental du vinylidène cationique. La simplicité de cette petite molécule polyatomique (C_2H_2) a permis de comparer les résultats expérimentaux avec des calculs théoriques quantitatifs de pointe [Ibrahim et al. 2014]. Ensuite, nous avons utilisé la molécule la plus simple du monde (H_2^+) pour étudier le contrôle cohérent de la localisation électronique lors de la photodissociation moléculaire [Wanie et al. 2016], en utilisant des impulsions infrarouges à deux couleurs. La comparaison des résultats expérimentaux avec des calculs impliquant la résolution de l'équation de Schördinger dépendante du temps (TDSE) a révélé que le traitement complètement indépendant des degrés de libertés nucléaire et électronique était insuffisant pour simuler la dynamique de la localisation électronique, même dans un système moléculaire aussi simple.

Chapitre 4: Dichroïsme circulaire de photoélectrons statique

Après avoir étudié des molécules simples, nous nous sommes intéressés aux molécules chirales. Les molécules chirales ne sont pas superposables à leur image dans un miroir. La chiralité est une propriété géométrique qui s'applique pas seulement aux molécules: par exemple, certaines particules subatomiques ainsi que certaines entités astrophysiques, comme les galaxies, sont aussi chirales. A l'échelle humaine, nos mains sont l'un des exemples les plus célèbres d'objets chiraux. On peut se rendre compte de l'importance de la chiralité en essayant de mettre une main droite dans un gant conçu pour une main gauche. En effet, l'interaction entre deux objets chiraux permet de discriminer si un objet chiral est «gauche» ou «droite». Cela peut avoir des conséquences énormes au niveau moléculaire: puisque notre corps est composé de beaucoup de molécules chirales, les activités biochimiques de deux images miroirs ('énantiomères') peuvent être radicalement différentes dans notre corps.

L'identification de la chiralité moléculaire nécessite l'interaction avec un autre objet chiral. La lumière est chirale lorsqu'elle est polarisée circulairement, et l'interaction entre les photons polarisés circulairement et les molécules chirales est la technique la plus largement utilisée pour la discrimination de la chiralité moléculaire. Comme nous l'avons vu précédemment, l'observable typique en spectroscopie est le spectre d'absorption $\sigma(E_\Omega)$.

Le spectre d'absorption d'une molécule chirale, n'est pas strictement identique lorsqu'il est mesuré avec de la lumière polarisée circulairement gauche ou droite (E^G_Ω ou E^D_Ω) : $\sigma(E^G_\Omega) - \sigma(E^D_\Omega) \neq 0$. Cette différence dans l'absorption de la lumière polarisée circulairement gauche ou droite est appelée «dichroïsme circulaire» (DC). L'origine du DC provient de l'interférence entre des transitions dipolaires électrique et magnétique (ou quadrupolaire électrique) et est typiquement si faible ($\sim$ millième de %) qu'il n'est pas possible d'utiliser cette technique pour étudier la chiralité dans les milieux dilués, tels que dans un ensemble de molécules chirales en phase gazeuse.

Récemment, un changement de paradigme s'est produit dans le domaine de l'interaction lumière-molécules chirales. Il a été réalisé que l'ionisation de molécules chirales à l'aide de lumière circulairement polarisée permettait d'augmenter la dimensionnalité des mesures, en enregistrant la distribution angulaire des photoélectrons (DAP). Les scientifiques ont prédit [Ritchie 1976] et mesuré [Böwering et al. 2001] une asymétrie gigantesque (typiquement 1-20%) dans le nombre d'électrons éjectés vers l'avant ou vers l'arrière d'un échantillon de molécules chirales aléatoirement alignées, par rapport à l'axe de propagation de la lumière. Cette éjection asymétrique d'électrons à partir de molécules chirales est appelée dichroïsme circulaire de photoélectrons (DCPE) et est un effet purement dipolaire électrique. Sa sensibilité en fait l'une des sondes les plus attrayantes de la chiralité moléculaire dans les milieux gazeux.

Historiquement, les expériences de DCPE ont été menées en utilisant le rayonnement synchrotron (ionisation à un photon) [Böwering et al. 2001]. Récemment, quelques expériences pionnières ont démontré que le DCPE existait aussi lors de l'ionisation résonante à quelques photons (Resonant Enhanced Multiphoton Ionization, REMPI) [Lehmann et al. 2013; Lux et al. 2012]. Provenant de la communauté de la physique en champs forts, nous nous sommes naturellement posés la question suivante: *Le DCPE est-il un effet universel dans la photoionisation de molécules chirales par la lumière polarisée circulairement?*. Nous avons testé la sensibilité du PECD au régime d'ionisation: ionisation à un seul photon, résonante à quelques photons (REMPI), au-dessus du seuil (Above Threshold ionization), jusqu'au régime de l'ionisation tunnel. Nous avons conclu que DCPE était universel, *i.e.* qu'il est inhérent à la photoionisation de molécules chirales par de la lumière chirale, émergeant dans *tous* les régimes d'ionisation [Beaulieu et al. 2016b].

Chapitre 5: Dynamique ultrarapide des molécules chirales

Avant le début de cette thèse, le DCPE était considéré comme une sonde *statique* de la chiralité moléculaire. L'un des principaux objectifs de cette thèse était donc de *combler le fossé entre le DCPE et la spectroscopie ultrarapide*, permettant d'aborder des questions importantes liées à la transformation dynamique de la matière chirale. Pour atteindre cet objectif, nous avons abordé le problème sous différents angles. Dans un premier temps, nous avons introduit et démontré le concept de DCPE résolu en temps, qui est l'analogue chiral à l'approche de la femtochimie «à la Zewail», pour l'étude de la dynamique en *temps-réel* de molécules chirales [Beaulieu et al. 2016c; Comby et al. 2016]. Notre approche de DCPE pompe-sonde femtoseconde nous a permis de découvrir accidentellement un nouveau phénomène chiroptique, que nous avons appelé DCPX (dichroïsme circulaire de photoexcitation), et qui est décrit comme un courant d'électrons directionnel et chirosensible, qui apparaît lorsque plusieurs états liés sont peuplés de manière cohérente avec de la lumière chirale [Beaulieu et al. 2018b].

Chapitre 6: Photoionisation de molécules chirales résolue à l'échelle attoseconde

Le dichroïsme circulaire de photoélectrons émerge de la dynamique de diffusion des électrons quittant le potentiel moléculaire chiral. L'une des principaux résultats des développements en métrologie attoseconde ces dernières années est la mesure de délais attosecondes entre des électrons quittant un atome ou une molécule, lors de la photoionisation. Nous nous sommes donc demandé si nous pouvions *mesurer des délais de photoionisation chirale*, c'est-à-dire suivre directement la dynamique de photoionisation attoseconde sous-jacente au DCPE. Nous sommes parvenus à mesurer une asymétrie avant-arrière dans les délais de photoionisation des molécules chirales photoionisées par une impulsion de lumière chirale. Cette mesure a permis d'apporter une perspective temporelle sur la formation de paquet d'ondes électroniques asymétrique vers l'avant et vers l'arrière, assurant une jonction entre les domaines de l'étude des molécules chirales et la science attoseconde [Beaulieu et al. 2017b].

Contexte de la thèse: cotutelle France-Québec

Cette thèse s'inscrit dans le cadre d'une cotutelle internationale entre le laboratoire CELIA, à Bordeaux, en France, où j'ai travaillé dans l'équipe Harmoniques et Applications et l'INRS-EMT, à Montréal, au Canada, où j'ai travaillé dans le groupe du Pr François Légaré. Le groupe Harmoniques et Applications est constitué de 10 chercheurs permanents (5 en expérimental et 5 en théorie), ainsi que typiquement quelque doctorants. Plusieurs travaux présentés dans cette thèse ont été menées en étroite collaboration avec d'autres membres de l'équipe: Bernard Pons (théorie), Baptiste Fabre (théorie), Fabrice Catoire (théorie), Valérie Blanchet (expériences) ainsi que les autres doctorants du groupe, Alex Clergerie (théorie, 2015-2018), Antoine Comby (expériences, 2016-2019) et Etienne Bloch (expériences, 2017-2020). Le groupe du Pr Légaré est typiquement constitué d'une dizaine d'étudiants de M. Sc. et Ph.D. ainsi que 4-5 stagiaires postdoctoraux. J'ai passé environ 50 % des 4 ans de ma thèse à Bordeaux et 50 % à Montréal.

Les travaux portant sur la dynamique moléculaire sondée par Explosion Comlombienne, ainsi que sur le développement d'OPA haute énergie et d'une source de rayons X mous de table dans la fenêtre de l'eau ont étés réalisé à l'INRS. Ces expériences ont été principalement réalisés en début de thèse, mais l'analyse et la rédaction d'articles se sont prolongés sur toute la durée de la thèse. La post-compression d'impulsions lasers (IR et mid-IR) à l'aide de fibre creuse tendue a d'abord été développé dans le laboratoire du Pr Légaré, durant ma maîtrise (mon master, pour les Français) ainsi que lors du début de ma thèse. J'ai ensuite importé cette technique au CELIA, dans le cadre de ma cotutelle et d'un partenariat avec une spin-off qui a émergé du développement de ces fibres (few-cycle inc.). Les expériences concernant la décroissance libre de l'induction dans l'XUV, la génération de lignes Hyper-Raman, la génération d'harmoniques d'ordre élèves depuis des états excités, ainsi que toutes les expériences concernant la photoionisation de molécules chirales (universalité du PECD, dichroïsme circulaire de photoexcitation, PECD résolu en temps, délai attoseconde lors de la photoemission, etc..) ont été effectuées à Bordeaux.

0.4 General introduction

0.4.1 Pictures and movies

“A picture is worth a thousand words" is an idiom referring to the fact that sometimes, a single image can be more informative than an exhaustive description of an object or a situation. Taking a picture of a given scenery freezes it forever on a photographic film or on digital memory, depending on which kind of technology is used to take the picture. Even if “a picture is worth a thousand words", it does not give any information about the time-evolution of the scenery: it does not provide any information about what happened before, and after the exact moment at which the picture was taken. To capture the dynamical evolution of the scenery, one would need to trade the camera for a video recorder. A typical video recorder takes picture every ~ 33 millisecond and stacks them back to back. Because human visual system process 10 to 12 images per second, these series of pictures (30 frames per second) are perceived by humans as smooth motion. Moreover, because “the whole is more than the sum of its parts" (Aristotle), movies give us information about the dynamical evolution of the scenery, and often, provide a causal relationship between each frame recorded back to back. Trading a camera for a video recorder thus allow us to increase the dimensionality of the captured information, and gives us the chance to understand the behavior and the evolution of the scenery.

With an exposure time of ~ 33 ms, a camera can take snapshots of an object moving at a maximum speed of about 50 km/h. All objects moving at speed above this threshold will appear blurred on the photograph. To freeze the motion of an object moving at higher speeds, for example, a cheetah running at full speed (> 110 km/h), a camera with an exposure time as short as 0.25 ms (1/4000 s) must be used. Cameras with an exposure time as short as 0.0625 ms (1/16000 s) are now commercially available and accessible to the general public. They allow, for example, to freeze the motion of the wings of a hummingbird, which, in flight, flaps its wings more than 80 times per second.

Another example of a technique used for freezing the motion of very fast moving objects is based on a different approach: the illumination of the scenery for a very short time. An example of this type of technique is stroboscopy. Stroboscopy uses devices, which can either be mechanical or electronic, to generate a sequence of brief and intense light flashes. This technique makes it possible to use a camera with a high exposure time while preserving a temporal resolution that is given by the illumination time of the scenery. One of the historical examples of the use of this technique is the study of fluid dynamics using stroboscopy, pioneered by MIT (Massachusetts Institute of Technology) professor Harold Eugene Edgerton, also known as *Papa Flash*. One owes the famous photography "Milk Drop Coronet" to Edgerton and his technique of stroboscopic photography, using a transient lighting of the scenery.

In this thesis, we will aim at investigating the ultrafast dynamical behavior of atoms and molecules, which occurs on very short time scales. By analogy with the examples above, the molecules constitute the dynamic scenery of interest, which we will illuminate with ultrashort flashes of light. These flashes will enable us to freeze the scenery, which will be captured by various types of detectors playing the role of the video recorder.

0.4.2 Static spectroscopy and dynamical information

The investigation of light absorption and emission from matter (spectroscopy) is at the origin of the foundation of quantum mechanics. Spectroscopy reveals that atoms and molecules absorb or emit electromagnetic radiation at well-defined energies. This is a consequence of the discrete nature of their quantum states (eigenstates). Each atom or molecule possess a unique set of eigenstates, whose energies can be accessed by

measuring its absorption or emission spectrum. Absorption spectroscopy is used in a myriad of different scientific fields. For example, the chemical composition of stars and other astronomical bodies can be determined by measuring their absorption or emission spectrum. This technique, named *Astronomical Spectroscopy*, was introduced by Joseph von Fraunhofer at the beginning of the 19th century, when he discovered very precise emission lines in the Sun's spectrum, allowing him to identify its chemical composition.

The absorption of light by a molecule can initiate various types of dynamical phenomena, depending on the wavelength of the absorbed light. For example, a low energy radiation (long wavelength, *e.g.* microwave) will preferentially induce rotational motions of the molecules. As the energy of the radiation increases (*e.g* infrared spectral range), photon absorption can initiate vibrational motion within the molecule. Finally, if the radiation reaches the ultraviolet spectral range, it can excite the electrons within the molecule.

In this thesis, we are interested in studying atomic and molecular physics from a dynamical (time-resolved) perspective. Since the objects that we have to characterize (atoms and molecules) need a quantum mechanical description, we would ideally have to measure the time evolution of their wavefunction $\Psi(t)$. We have seen in the introduction that the measurement of ultrafast dynamics required adequate and cutting-edge experimental devices, playing the role of an ultrafast camera. However, it is still possible to extract valuable information about the dynamics of atoms or molecules from their static absorption spectrum. Indeed, the time domain and the spectral domain are intimately linked. We can go from one to the other by a simple mathematical transformation, *i.e* the Fourier transform. The spectral information extracted from spectroscopic measurements can, therefore, be used to obtain a certain amount of dynamical information on the photoexcited molecules. One of the fundamental relationships derived from the theoretical description of spectroscopy links the absorption spectrum ($\sigma(E_\Omega)$) to the time-dependent wavefunction $\Psi(t)$,

$$\sigma(E_\Omega) \propto \int_{-\infty}^{+\infty} \langle \Psi_0 | \Psi(t) \rangle e^{iE(\Omega)t/\hbar} dt \tag{2}$$

where $\hbar$ is the reduced Planck constant, and Ψ_0 is the initial wavefunction. We notice in this equation that the absorption spectrum depends on the temporal evolution of the wavefunction. Specifically, it depends on the overlap integral between the time-dependent wavefunction evaluated at time t ($\Psi(t)$) and the initial wave function (Ψ_0), which is called the time-dependent autocorrelation function $S(t)$, where $S(t) = \langle \Psi_0 | \Psi(t) \rangle$. We will now illustrate the link between spectroscopic and dynamical information, from two simple cases.

The scheme presented in Fig. 2 illustrates the relationship between the absorption spectrum and the autocorrelation function. The shape of the potential energy surfaces of states involved in the radiative transition dictates the dynamics of the excited molecule. For example, populating a bound or a purely dissociative excited state will lead to very different time-dependent autocorrelation functions, and thus, to very different absorption spectra. In Fig. 2 (a), the absorption of light promotes a molecule which is initially in its ground state Ψ_0 to an excited bound state, on which the time-dependent wavefunction $\Psi(t)$ evolves. In Fig. 2 (b), the associated autocorrelation function $S(t)$ undergoes a fast decay at early times, since $\Psi(t)$ moves away from the Franck-Condon region, leading to a decrease of the overlap with Ψ_0 (Franck–Condon region is a region of the final potential energy surface which is accessible by a vertical transition from the initial state, as illustrated in Fig. 2). Every time the $\Psi(t)$ moves back to the inner turning point, the overlap with Ψ_0 increase again. In Fig. 2 (c), we show the associated energy-resolved

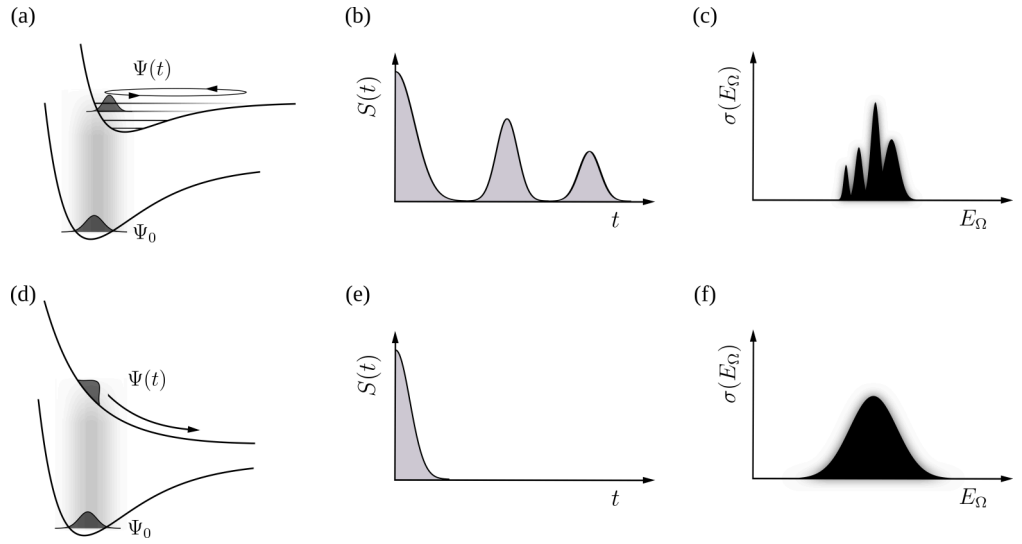

Figure 2: Scheme of the correspondence between the potential energy surface (PES) landscape of a prototypical system, that is photoexcited from the ground to an excited state, the associated autocorrelation function $S(t)$, and the associated total energy-dependent absorption spectrum $\sigma(E_\Omega)$. In (a) and (d), the shaded gray area represents the Franck-Condon region.

absorption spectrum, which is the Fourier transform of the autocorrelation function $S(t)$ and which encodes the vibrational structures (and Franck-Condon factors). In Fig. 2 (d), the absorption of light promotes a molecule which is initially in its ground state Ψ_0 to an excited dissociative state. In Fig. 2 (e), the associated autocorrelation function $S(t)$ undergoes a fast decay at early times and never increase again: the wavefunction never comes back to the Franck-Condon region, because of the dissociative nature of the PES, leading to a structureless broad peak in the absorption spectrum (Fig. 2 (f)).

Since the absorption spectrum is the measured observable in most standard spectroscopic techniques, it is possible, with basic knowledge of the properties of the Fourier transform, to retrieve the molecular dynamics which occurred in the Franck-Condon region, after absorption of light. The spectral amplitudes, linewidths, and lineshapes underlying the static energy-dependent absorption spectrum of a molecule thus encode amazingly rich amount of information about its photoinduced dynamics. Linking the molecular absorption spectrum to its time-dependent evolution onto excited states, often helped by quantum chemical calculation, has been (and is still) a fascinating playground for molecular physicists.

Nevertheless, the time-dependent autocorrelation function does not encode the entire excited state dynamics. Indeed, since it is by definition given by the overlap integral with the initial wavefunction, it is only sensitive to the dynamics occurring in the vicinity of the Franck-Condon region. It is thus quite frustrating to have only access to a small window of the dynamics, *i.e.* to look at the dynamics with the 'filtering goggles' of the Franck-Condon region. Is it possible to remove these goggle and to probe the full time-dependent molecular dynamics, as it evolves from the Franck-Condon region, through the transition state, and possibly towards different fragmentation channels? As we will see below, this is the aim of time-resolved spectroscopy, whose development has enabled a paradigm shift in spectroscopy and has lead physicists to gain a much deeper understanding of the full excited state dynamics in molecules.

0.4.3 Time-resolved spectroscopy

One of the first examples published in the literature of time-resolved spectroscopic techniques is 'flash photolysis'. The original idea consists of exciting molecules using a strong and brief light pulse, fired by flash lamps ('pump' step), and to record the absorption spectrum of the excited molecules within a short time interval ('probe' step). This kind of scheme is called a 'pump-probe' experiment. Using this technique, scientists have succeeded in measuring, for the first time, absorption spectra of short-lived molecular species and providing the first experimental evidence of the existence of free radicals, by taking advantage of the millisecond temporal resolution of the technique (see, for example, [Porter 1950]). This was the first step beyond the Franck-Condon region dynamical study of photochemical processes. This flash photolysis technique was pioneered in the 1940s by Manfred Eigen, Ronald George Wreyford Norrish, and George Porter, and led them to share the 1967 Nobel Prize in Chemistry.

In the 1960s, the optical laser was discovered [Maiman 1960]. Soon after, scientists started to master this new technology and were able to deliver extremely short coherent bursts of light. In the 1980s, laser pulse durations down to the femtosecond (1 fs = 10^{-15} s) range were available. Using femtosecond pulses in pump-probe configurations opened a new research field called 'femtochemistry'. Femtochemistry enables to probe the motion of nuclei within the entire excited state dynamical space, from the Franck-Condon to the transition state region, down to the formation of photodissociation products, with a femtosecond time resolution (for a review, see [Zewail 2000]). Femtochemistry has revolutionized the way scientists think about the kinetics of a photochemical transformation, by enabling direct visualization of nuclear motion and transition state geometries, something which was completely impossible using conventional frequency-domain spectroscopic techniques. The importance of femtochemistry was recognized by the scientific community, leading to the 1999 Nobel Prize in Chemistry attributed to Ahmed Zewail.

The investigation of faster and faster dynamics calls for the generation of shorter and shorter light pulses. Following the success of femtochemistry, there was a strong motivation to reach the attosecond domain, which is the typical timescale of electronic motion in matter.

The shortest pulse duration that one can achieve is typically one optical cycle of the carrier frequency of the spectrum. For conventional infrared lasers (around 800 nm central frequency), this limit is on the order of $\sim$ 2-3 fs. This limitation prevents to generate sub-femtosecond pulses with conventional infrared lasers, thus clamping the ultimate temporal resolution achievable using standard pump-probe schemes to few-femtosecond. Producing shorter pulses require decreasing the period of the light, *i.e.* increasing the photon energy. From the late 1980s to the early 2000s, scientists worked hard to produce [Ferray et al. 1988; McPherson et al. 1987] and characterize [Hentschel et al. 2001; Paul et al. 2001] pulses of attosecond duration (1 as = 10^{-18} s). The key technology that enabled these spectacular progress was a newly discovered mechanism of extreme non-linear and non-perturbative frequency upconversion in gases, called High-order Harmonic Generation (HHG).

Since its birth in 2001, the field of attosecond science has known impressive developments (for a review, see [Krausz et al. 2009]). Attosecond pulses below 50 as can nowadays be produced [Gaumnitz et al. 2017], with good control of the spectral phase. These pulses have been used to investigate the ultrafast ionization dynamics of atoms [Klünder et al. 2011; Schultze et al. 2010], molecules [Calegari et al. 2014; Haessler et al. 2009; Huppert et al. 2016; Neidel et al. 2013] and solids [Cavalieri et al. 2007; Schultze et al. 2014], revealing the time at which the electrons are ejected or tracking the dynamics of

the remaining hole. Innovative measurements schemes, using the high-order harmonic generation process to probe the generating medium, have also been demonstrated to provide structural and dynamical information with attosecond temporal and Ångström spatial resolutions [Haessler et al. 2011; Itatani et al. 2004; Marangos 2016].

0.4.4 Presentation and aims of this thesis

Despite the impressive progress of ultrafast time-resolved spectroscopy in the past 20 years, several important challenges remained at the beginning of this thesis. The work presented here aimed at solving a few of them. The thesis is divided into six chapters:

Chapter 1: Drivers for strong-field and attosecond physics

The first challenge we aimed at solving is a technical one: *the development of cutting-edge light sources*, which is an extremely important element of progress in attosecond science. Reducing the pulse duration, increasing the laser intensity, but also as we will see, increasing the laser wavelength, open new perspectives for attosecond and strong-field experiments. We thus developed two sources of intense few-cycle laser pulses, one at ALLS and one at CELIA. The ALLS source is based on a high-energy mid-IR optical parametric amplifier [Thiré et al. 2015], followed by a compression of laser pulses down to the few-cycle regime using non-linear propagation is gas-filled hollow-core fiber [Cardin et al. 2015]. The CELIA source directly uses the latter technique to compress 800 nm pulses.

Chapter 2: Novel degrees of freedom in high-order harmonic generation

The first outcome of our source development is the possibility to produce intense attosecond pulses at high photon energy. We developed a beamline producing light until the so-called water window spectral range and demonstrated single-shot absorption measurement at the carbon K-edge. From a more fundamental point of view, we used few-cycle pulses to investigate the strong-field response of a well-characterized system – argon atoms. This can be considered as a second challenge: *reaching a better understanding of strong-field light matter interaction*. This strategy led us to unravel many novel effects related to the excitation of Rydberg states by the strong laser field: HHG emission by ionization from Rydberg states and recombination to the ground state [Beaulieu et al. 2016a], the background-free laser-induced XUV Free-Induction Decay [Beaulieu et al. 2017a], and the generation of Hyper-Raman Lines concomitant with standard high harmonics. In these experiments, the simplicity and the prior spectroscopic knowledge of the system (Argon), associated to the cutting-edge nature of the light source, enabled us to reveal and understand complex and sometimes unexpected effects. Last, we complexified the light-matter interaction by introducing orbital angular momentum in the strong laser field to investigate its transfer to the high-harmonic radiation.

Chapter 3: Nuclear and electronic dynamics in simple molecules

One of the grails of ultrafast time-resolved spectroscopy is to *measure dynamics involving a coupling between the nuclear and electronic degrees of freedom*. Following our strategy of studying simple systems first, we investigated the photoisomerization of the acetylene cation ($[HC=CH]^+$) into vinylidene cation ($[C=CH_2]^+$). This reaction is possible thanks to a conical intersection which allows the passage of the wavepacket from an electronically excited cationic state of acetylene to the ground electronic state of cationic vinylidene. The

simplicity of this small polyatomic molecule (C_2H_2) has allowed the comparison of the experimental results with quantitative state-of-the-art theoretical calculations, enabling tackling the complex coupled nuclear and electronic dynamics [Ibrahim et al. 2014]. Next, we used the world's simplest molecule (H_2^+) to study the coherent control of the electron localization during molecular photodissociation [Wanie et al. 2016], using phase-locked two-color mid-IR pulses. The comparison of experimental results with time-dependent Schrödinger equation (TDSE) calculations revealed that treating the nuclear and electronic degree of freedom completely independently was insufficient to simulate the electron localization dynamics, even in such a small and simple molecular system.

Chapter 4: Static photoelectron circular dichroism

After investigating simple molecules, we turned our attention to chiral molecules. Chiral molecules are not superimposable to their mirror image. Chirality is a geometrical property that applies not only to molecules: from sub-atomic particles to astrophysical entities like galaxies. On the human scale, our hands are one of the most famous examples of chiral objects. One can experience the effect of chirality by trying to put a right hand into a left-handed glove. Indeed, the interaction between two chiral objects allows discriminating between their different handedness. This can have tremendous consequences at the molecular level: since our body is composed of a lot of chiral molecules with well-defined handedness, the biochemical activities of two mirror-images ('enantiomers') can be drastically different, when released in our body.

The identification of molecular handedness requires the interaction with another chiral object. Light is chiral when it is circularly polarized, and the interaction between circularly polarized photons and chiral molecules is the most widely used technique for molecular handedness discrimination. As introduced earlier, the standard observable in spectroscopy is the total energy-resolved absorption $\sigma(E_\Omega)$. The absorption spectrum of a chiral molecule using left- or right- circularly polarized light (E_Ω^L or E_Ω^R) is not strictly identical ($\sigma(E_\Omega^L) - \sigma(E_\Omega^R) \neq 0$). This difference in the absorption of left- or right- circularly polarized light is called Circular Dichroism (CD). This CD originates from the interference between electric and magnetic dipole (or electric quadrupolar) transitions and is typically so weak ($\sim$ thousandth of %) that it not possible to use this technique to study chirality in dilute media, such as gas phase chiral molecular ensemble.

Not so long ago, a paradigm shift occurred in the field of chiral light-matter interaction. It was realized that photoionizing chiral molecules using chiral light allows one to increase the dimensionality of the measurement, by recording the photoelectron angular distribution (PAD). Scientists predicted [Ritchie 1976] and measured [Böwering et al. 2001] a gigantic asymmetry (typically 1-20 %) in the number of electrons ejected forward or backward a sample of randomly oriented chiral molecules, with respect to the light propagation axis. This asymmetric ejection of electrons from chiral molecules is called Photoelectron Circular Dichroism (PECD), and is a pure electric dipolar effect. Its sensitivity makes it one of the most attractive probes of molecular chirality in gas-phase media.

Historically, PECD experiments were conducted using synchrotron radiation (single-photon ionization) [Böwering et al. 2001]. More recently, a few pioneering experiments demonstrated that PECD also emerged in resonant-enhanced few-photon ionization using table-top UV pulses [Lehmann et al. 2013; Lux et al. 2012]. Coming from a strong-field and attosecond science background, we asked ourselves: *Is photoelectron circular dichroism a universal effect in the photoionization of chiral molecules by circularly polarized light?* . We tested

the sensitivity of PECD to the ionization regime, from single-photon, resonant-enhanced multiphoton ionization, above-threshold ionization up to the tunneling regime. We concluded that PECD is universal, *i.e.* that its inherent to photoionization of chiral molecules using chiral light, emerging in *all* ionization regimes [Beaulieu et al. 2016b].

Chapter 5: Ultrafast dynamics of chiral molecules

Before the beginning of this Ph.D. thesis, PECD was considered as a *static* probe of molecular chirality. One of the main goals of this thesis was thus *to bridge the gap between PECD, which enables fundamental studies of molecules with peculiar symmetry properties, and ultrafast spectroscopy, which allows addressing important questions related to the dynamical transformation of matter*. To reach that goal, we tackled the problem from different perspectives. First, we introduced and demonstrated the concept of time-resolved PECD (TR-PECD), which is a chiral analog of the '*à la* Zewail' femtochemistry approach, to study the *real-time* dynamics of chiral molecules and the influence of these dynamics from the point of view of the 'PECD' chiroptical observable [Beaulieu et al. 2016c; Comby et al. 2016]. Our femtosecond pump-probe PECD approach led us to *accidentally* discover a new chiroptical phenomenon, which we called PXCD, and which emerges as a directional and chirosensitive electron current when multiple excited bound states of chiral molecules are coherently populated with chiral light [Beaulieu et al. 2018b].

Chapter 6: Attosecond-resolved photoionization of chiral molecules

Photoelectron circular dichroism emerges from the scattering dynamics of the outgoing electrons in the chiral potential. One of the main achievements of attosecond metrology in the past few years is the measurement of the ionization delays associated with photoionization. We thus wondered if we could *measure chiral photoionization delays*, i.e. directly track the attosecond photoionization dynamics underlying PECD. Using state-of-the-art attosecond metrology, we measured a forward-backward asymmetry in photoionization delays from chiral molecules photoionized by chiral light pulse. It allowed bringing time-domain perspectives on the forward-backward asymmetric build-up photoelectron wavepacket, bridging the gap between chirality and attosecond science [Beaulieu et al. 2017b].

Context of the thesis: "Cotutelle" France-Québec

This thesis was an international cotutelle between the CELIA laboratory, in Bordeaux, France, where I worked in the Harmonics and Applications team and the INRS-EMT, in Montreal, Canada, where I worked in the group of Prof. François Légaré. The Harmonics et Applications group is made of 10 permanent researchers (5 experimentalists and 5 theoreticians) and few Ph.D. students. Several aspects presented in this thesis were conducted in close collaboration with other members of this team: Bernard Pons (theory), Baptiste Fabre (theory), Fabrice Catoire (theory), Valérie Blanchet (experiments) as well as with other Ph.D. students of the group: Alex Clergerie (theory, 2015-2018), Antoine Comby (experiments, 2016-2019) and Etienne Bloch (experiments, 2017-2020). Prof. Légaré's group is typically composed of about ten graduate students (M.Sc. and Ph.D.) as well as 4-5 postdoctoral fellows. I spent about 50 % of the 4 years of my thesis in Bordeaux and 50 % in Montréal.

The studies on molecular dynamics probed by Coulomb Explosion, as well as on the development of a high energy OPA and an HHG-based table-top water-window soft-X-ray

source were carried out at INRS. These experiments were mainly done at the beginning of the thesis, but the analysis and the writing of papers were prolonged throughout the entire duration of the thesis. The post-compression of laser pulses (IR and mid-IR) using stretched hollow-core fiber was first developed in the laboratory of Prof. Légaré, during my master's degree as well as during the beginning of my Ph.D. I imported this technique to CELIA laboratory, as part of my cotutelle and a partnership with a spin-off that emerged from the development of these stretched hollow-core fibers (few-cycle inc.). Experiments on XUV Free-Induction Decay, the generation of Hyper-Raman lines, HHG from excited states, as well as all the experiments concerning the photoionization of chiral molecules (universality of PECD, time-resolved PECD, PXCD, attosecond-resolved photoionization, etc.) were carried out in Bordeaux.

1. Drivers for Strong-Field and Attosecond Physics

1.1 The quest for intense ultrashort Mid-IR pulses

1.1.1 The birth of strong-field and attosecond physics

The demonstration of the first working laser in the 1960s by Maiman [Maiman 1960] has triggered the discovery of a new class of optical phenomena: nonlinear optics. Indeed, only one year after the discovery of the ruby laser ($\lambda = 694.3$ nm), Franken *et al.* demonstrated the phenomenon of nonlinear frequency up-conversion [Franken et al. 1961]. When laser pulses of a duration of few milliseconds and spectrally centered around 694.3 nm were focused into a crystalline birefringent quartz crystal at a peak intensity of few 10^7 W/cm^2, the second harmonic (347.2 nm) of the fundamental laser frequency was observed. This phenomenon, called Second Harmonic Generation (SHG), is one of the simplest nonlinear optical processes and can be fully described using first-order perturbation theory.

Later on, scientists started to master the art of designing new materials and new architectures to build powerful lasers at different central wavelengths. Our goal here is not to make a complete overview of the different ultrafast laser technologies, but to give a few examples of the different laser systems that were used for few key experiments that led to the foundations of strong-field and attosecond physics.

One of the main experimental findings at the origin of strong-field physics is without any doubt the first observation of Above-Threshold Ionization (ATI) peaks in the photo-electron spectrum of Xenon, when irradiated with strong second harmonic of a Nd:glass laser, by the CEA-Saclay group, in 1979 [Agostini et al. 1979]. By focusing strong 532 nm pulses into a gas-jet of Xenon, Agostini *et al.* observed a second photoelectron peak above the six-photon ionization threshold. In order to be able to trigger this highly nonlinear process, the intensity of the laser pulses needed to be close to 10^{13} W/cm^2. To reach such intensities, joule-class Nd: glass laser, with pulse duration on the order of ~ 10 ns were used. Almost 10 years later, after further improving the Nd:glass lasers performance by shortening the pulse duration down to few tens of picoseconds, the CEA-Saclay group reported on an extremely nonlinear frequency up-conversion in rare gas, from the IR to the XUV range [Ferray et al. 1988]. A similar phenomenon was observed almost at the

same time in Chicago, using a KrF excimer laser [McPherson et al. 1987]. The spectrum observed in the Saclay experiment was a frequency comb made of odd harmonics of the driving laser, up to the 33rd order. The extremely nonlinear phenomenon of High-order harmonic generation (HHG) was discovered. This very brief overview shows how much laser technology is important to scientific advances. It opens new regimes for laser-matter interaction, triggering new experimental discoveries, which initiate new theoretical developments.

Indeed, unlike other low-order nonlinear processes, such as second- or third-harmonic generation, HHG could not be explained by means of perturbation theory. To explain the emission mechanism and the characteristics of the XUV high-harmonic frequency comb, researchers developed nonperturbative models, which have set the foundations of the field of 'Recollision physics' [Corkum 1993; Kuchiev 1987; Schafer et al. 1993]. The physics underlying the high-harmonic generation process was found to be indeed remarkably simple since the process can be understood as a semi-classical three-step model: 1) the strong laser field bends the Coulomb potential of the atom, which allows an electron to be tunnel-ionized from the ground state. 2) The free electron is accelerated by the strong laser field and gains kinetic energy. 3) Last, when the sign of the oscillating electric field reverses, the electron is driven back to the vicinity of its parent ion and can finally radiatively recombine onto the ground state, leading to the emission of extreme ultraviolet (XUV) photons. In 1993, the semi-classical three-step model introduced by Paul Corkum succeeded to explain, among other characteristics of the XUV radiation, the origin of the scaling law of the HHG cut-off (E_{co}) with the driving laser wavelength and intensity: the maximum photon energy of the generated harmonics is $E_{co} \sim I_p + 3.2U_p$, where I_p is the ionization potential of the atom, U_p is the ponderomotive energy of the freed electron ($U_p \propto I\lambda^2$, I is the laser peak intensity and λ is the driving laser central wavelengths. This relationship was previously empirically extracted from TSDE calculations by Krause *et al.* [Krause et al. 1992], and now had a physical interpretation: the maximum photon energy is determined by the maximum kinetic energy that the electron can gain.

Even if the spectral characterization of high-order harmonics was first performed in the late 80's, one had to wait until the beginning of the 21st century to have an experimental measurement of their temporal profiles [Paul et al. 2001]. Indeed, Paul *et al.* experimentally demonstrated that the high-order harmonics emerge in the time-domain as a train of short attosecond bursts [Paul et al. 2001]. This discovery marks the birth of the field of attosecond science. Since then, scientists have been working hard to generate always shorter attosecond pulses. The general requirement for generating the shortest light pulses is to produce the largest possible spectral bandwidth, at the highest possible central frequency, *with all the spectral components in phase*. Up to date, the shortest light pulse ever reported is a 43 as pulses, which is made of a $\sim$ 100 eV bandwidth XUV supercontinuum extending up to photon energy of 180 eV. Such a spectrum has been synthesized by driving HHG in Neon using sub-2 cycles mid-IR pulses [Gaumnitz et al. 2017].

1.1.2 Scaling of high-order harmonic generation

The necessity to increase the high-order harmonic cutoff energy calls for new developments in ultrashort laser technology. First, let us consider the simple scaling law which has been derived using the semi-classical three-step model: $E_{co} \propto I_p + 3.2U_p$, where $U_p \propto I\lambda^2$. At first sight, a simple strategy to reach high photon energy is to increase the laser intensity, since the ponderomotive energy scales linearly with this physical quantity. However, there is a threshold intensity beyond which one cannot efficiently generate high harmonics. This intensity is called *saturation intensity* (I_{sat}), and is related to the depletion of the

ground electronic state by strong-field ionization. This depletion lowers the recombination probability in the last step of the generating process. Furthermore, if the ground state is fully depleted, HHG cannot occur because no electron can tunnel out anymore. The saturation intensity is usually between $10^{14} - 10^{15}$ W/cm^2, depending on the ionization potential of the target, the driving laser wavelength, but also the pulse duration, since the ground state depletion accumulates over the whole laser pulse. For example, if one uses a long and intense driving laser pulse, the ground state can be fully depleted before the peak of the pulse. This leads to efficient XUV emission only on the rising edge of the pulse, and to a low cut-off energy since the HHG occurs at an intensity weaker than the pulse peak intensity. The solution to this issue is to drive HHG with few-cycle laser pulses, where the ionization and radiative recombination (XUV emission) are strongly confined within the most intense part of the laser pulse envelope. It is then possible to produce efficient emission of high energy XUV photons, in the form of a single or a train of few attosecond duration.

A second important ingredient to control the properties of the HHG emission is the laser wavelength. The ponderomotive potential and high-harmonic cut-off scale quadratically with the driving laser wavelength. It was recently shown that driving HHG using 6-cycles, 3.9 μm, 10 mJ pulses can lead to the emission of broad spectrum extending up to 1600 eV [Popmintchev et al. 2012]. Going towards longer driving wavelength is thus obviously the key solution to extend the HHG cut-off, and to possibly generate shorter attosecond pulses. However, there is also a major drawback when driving HHG with long-wavelength laser pulses. The electron which is accelerated in the second step of the HHG mechanism can, in fact, be described as an (almost) free electron wavepacket, which spreads due to quantum mechanical diffusion. The longer the electron wavepacket travels in the continuum, the more it spreads, and the lower is its overlap with the localized bound electronic wavefunction during the radiative recombination step. When using longer driving wavelength, the travel time and travel distance of the electron wavepacket in the continuum are longer/larger, resulting in a decay of the recombination probability. While the HHG cut-off energy scale as λ^2 [Krause et al. 1992] [Corkum 1993], the HHG yield has been shown to have an even more dramatic wavelength scaling of $\sim \lambda^{-6}$ [Shiner et al. 2009]. Therefore, increasing the driving laser wavelength leads to a trade-off between the generation of high-energy photons and the conversion efficiency.

The description of HHG given above only takes into account the single atom response to strong driving laser pulses. However, macroscopic effects also need to be taken into account, to ensure an efficient build-up of the HHG signal (for nice reviews about macroscopic aspects of HHG, see [Gaarde et al. 2008] and [Heyl et al. 2017]). Indeed, in order to have a macroscopic (measurable) HHG signal, the XUV emission needs to be phase-matched. Since the XUV emission is temporally locked with the driving laser, this means that the XUV and the driving laser must travel in phase in the generating medium. This is the so-called phase-matching condition. Many parameters, such as the laser intensity and wavelength, the focusing geometry, the ionization fraction, the atomic dipole phase and the gas density are playing fundamental roles in the phase-matching of the harmonic emission. As we will see later, in the chapter dedicated to HHG, the optimal pressure that leads to the phase-matched emission of high-order harmonics quickly increases with the driving wavelength. This macroscopic consideration will somehow partially compensate for the detrimental single-atom scaling of HHG efficiency with increasing driving laser wavelength.

In conclusion, in order to generate ultrashort and high photon energy XUV pulses, one needs to drive HHG with intense, few-cycle and long wavelength laser pulses. In the next

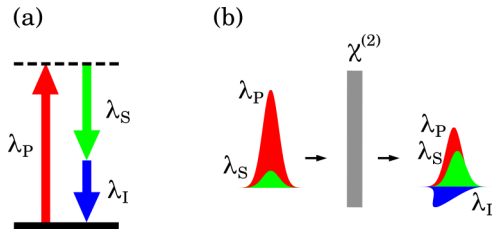

Figure 1.1: Schematic of the Optical Parametric Amplification (OPA) process. (a) In the energy domain, OPA can be seen as energy transfer from the pump beam to the signal beam. Due to energy conservation, a third optical beam called Idler is generated during the nonlinear parametric interaction within the crystal. (b) Scheme of the different laser pulses before and after the parametric amplification process. The relative amplitudes of the pulses are not at scale. In the 'artistic' scheme, the different pulses have been slightly temporally shifted with respect to each other after the crystal, in order to show the possible group velocity mismatch during propagation into the crystal, as well as for visualization purpose. The Idler has its polarization axis perpendicular to the ones of the Pump and the Signal since we represent a type-I phase-matched parametric process.

section, we will describe the development of such laser sources at the Advanced Laser Light Source, at INRS.

1.2 Development of the high-energy OPA at ALLS

1.2.1 Generation 10 mJ 5-cycles pulses around 1.8 μm

In this subsection, we will explain how we used the 80 mJ 100 Hz Ti:Sa laser system of the Advanced Laser Light Source to build a cutting-edge intense mid-IR source. To do so, we will use a cascade of Optical Parametric Amplification (OPA) [Wang et al. 1965] stages. The physical principal behind OPAs is rather simple. First, we need a (weak) signal beam (λ_s), which is the beam that will get amplified in the OPA process. Second, we need a (strong) pump beam (λ_p), that will be used to parametrically transfer energy to the signal beam. Last, we need a birefringent crystal, which acts as the second-order nonlinear material. This crystal must enable the beams to travel at a similar group velocity, to fulfill the phase-matching condition. As the acronym suggests, OPA is a parametric process, which means that the initial and the final quantum state of the nonlinear crystal is the same. This implies that there is no energy, momentum or angular momentum exchanged between the light fields and the nonlinear crystal. As a consequence, when the pump beam (*e.g.* $\lambda_p = 800$ nm, $E_p = 1.55$ eV) transfers energy to the signal beam (*e.g.* $\lambda_s \sim 1440$, nm $E_p \sim 0.86$ eV), a third beam, called the Idler ($\lambda_I \sim 1800$, nm $E_p \sim 0.69$ eV) is generated due to the energy conservation constrain of the parametric process (Fig. 1.1).

Nowadays, Optical Parametric Amplifier pumped by Ti:Sa laser systems are routinely used for generating spectrally tunable femtosecond pulses in the mid-IR spectral range, with the Signal and Idler easily covering from ~ 1.2 μm to ~ 2.5 μm [Yakovlev et al. 1994]. It is also possible to use the Signal and the Idler to drive Difference Frequency Generation (DFG), in order to reach much longer wavelength ($\sim$ up to 20 μm) [Rotermund et al. 2000]. Last, the output of the OPA can be used to generate tunable shorter wavelength. Indeed, using harmonic generation (*e.g.* SHG) and Sum Frequency Generation (SFG), one can deliver tunable pulses in the visible and ultraviolet spectral range down to ~ 200 μm [Reed et al. 1994]. OPA, combined with other nonlinear frequency conversion process, is thus a simple solution to produce femtosecond pulses, with multi-octave (more than 10) spectral tunability. This is particularly useful, for example, to tune the laser wavelength in resonance with a given quantum state, or to study the wavelength scaling of nonlinear

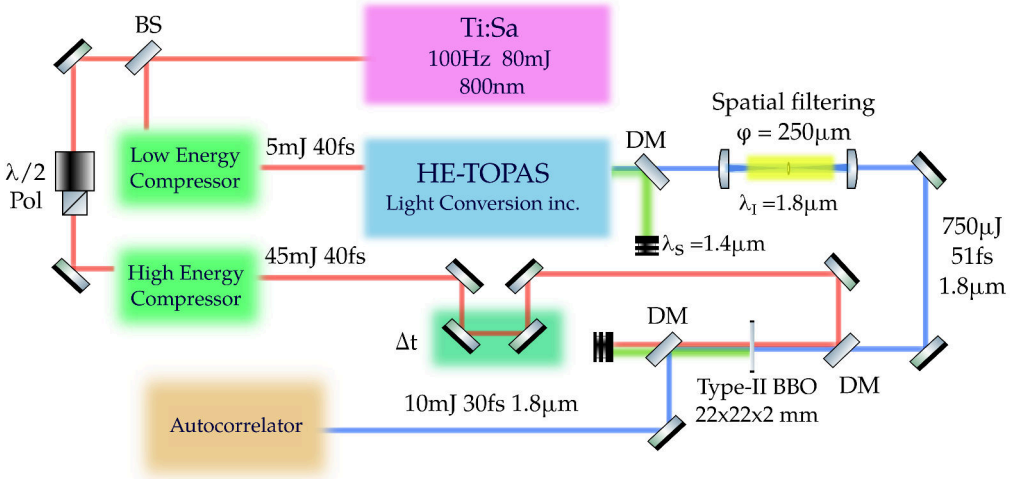

Figure 1.2: Experimental setup for the generation of high peak power tunable mid-IR pulses. BS: Beam splitter; DM: Dichroic mirror; Pol: Polarizer; φ: Pinhole diameter used for spatial filtering; Autocorrelator: Home build all reflective second harmonic autocorrelator; λ_I: central wavelength of the Idler; λ_S : central wavelength of the Signal. This figure is adapted from [Thiré et al. 2015].

phenomena like HHG [Shiner et al. 2009] or THz generation [Clerici et al. 2013].

OPA is not the only scheme to generate intense mid-IR femtosecond pulses. Optical Parametric Chirped-Pulse Amplification (OPCPA)[Dubietis et al. 1992] schemes have recently been developed, allowing the generation of tunable ultrashort pulses, with unprecedented peak intensity. OPCPA combines the advantages of OPA together with the ones of Chirped Pulse Amplification (CPA) [Strickland et al. 1985]. By driving the parametric amplification process using strongly chirped pulses, OPCPA allows the synthesis of tunable, Carrier-Envelope Phase (CEP)-stable, multi-terawatt (multi-TW) few-cycle pulses. While the first generations of OPCPA were pumped by Ti:Sa laser systems, there is currently a transition towards the Ytterbium (Yb) technology. Yb laser technology, which is now getting pretty mature, is currently revolutionizing the field of femtosecond laser development by delivering kW-class laser, to pump OPCPA, for example, [Lai et al. 2015]. Even if OPCPA has several advantages (generation of shorter and more intense pulses), their architectures remain orders of magnitude more complicated to implement than conventional OPA. Our primary goal is to be able to generate intense, few-cycle mid-IR laser pulses, but we would like to do so using a simple and robust architecture. This is why we designed a high-energy OPA instead of going for an OPCPA scheme.

Prior to the development of our high-energy OPA, the state of the art, using the same kind of architecture, was a 10 Hz OPA delivering 7 mJ pulses of 40 fs duration at a central wavelength of 1.4 μm (0.175 TW peak power) [Takahashi et al. 2008]. In the following, we will demonstrate that we can further push the peak power of OPAs by using a simple and robust optical setup.

A scheme of the experimental setup is shown in Fig. 1.2. The laser used to pump the different stages of the OPA is a standard CPA Ti:Sa laser system. This laser, installed at the Advanced Laser Light Source, at INRS, delivers up to 80 mJ, prior to the grating compressors, at a repetition rate of 100 Hz. We pick up a small fraction of the uncom-

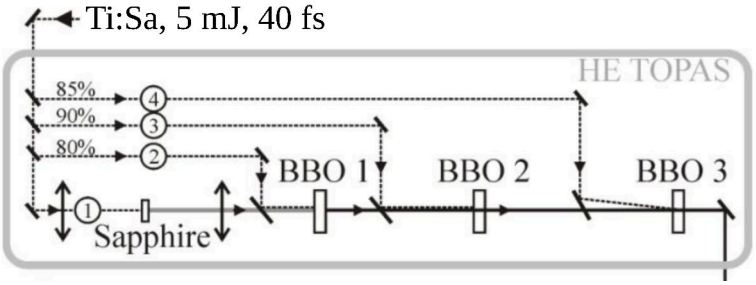

Figure 1.3: Schematic of the multistage commercial optical parametric amplifier (HE-TOPAS, Light Conversion Inc.). First, the incoming beam (800 nm, 5 mJ, 40 fs) is separated in different arms; one arm for generating the seed and three pump arms. The arm labeled '1' generate a white-light supercontinuum in a sapphire plate, which will act as the seed in the next stage. In the first BBO crystal, the pump beam labeled '2' (λ_P) amplify a specific spectral range of the seed, which in this case is the red wing of the supercontinuum, around 1.45 μm (Signal, λ_S). During this parametric amplification process, an Idler beam (λ_I) is generated. In the next two amplification stages, the pump beams labeled '3' and '4' amplify the Idler (of the first stage) beam through optical parametric amplification process. After all these nonlinear amplification stages, roughly 900 μJ of Idler, centered around 1.8 μm. After the last OPA stage of the HE-TOPAS, the Idler duration is typically $\sim$ 50 fs. This figure is adapted from [Schmidt et al. 2011].

pressed beam (7 mJ) and send it into a first grating compressor (Low Energy Compressor Fig. 1.2) to compress the pulses down to 40 fs. These pulses, containing $\sim$ 5 mJ after the compressor, are used to pump a commercial white-light seeded high-energy OPA (HE-TOPAS, Light Conversion Inc.). The optical scheme of the HE-TOPAS is shown in Fig. 1.3. Briefly, a white-light supercontinuum is generated by focusing a small fraction of the 800 nm beam into a sapphire plate. In a first BBO crystal (type-II, $\theta = 27°$), a pump beam (800 nm) parametrically amplifies the seed Signal around 1.45 μm. Note that we choose to amplify the seed Signal around 1.45 μm, but this value is tunable. An Idler beam, centered around 1.8 μm is thus generated in this first parametric amplification stage. Next, the Idler is amplified in two other stages, which also rely on parametric amplification in BBO crystals pumped with 800 nm beams. After the last amplification stage (*i.e.* at the output of the HE-TOPAS), the 1.8 μm Idler contains $\sim$ 0.9 mJ while the 1.45 μm Signal typically contains 1.1 mJ. This corresponds to a conversion efficiency of 40 %, which is pretty good considering the fact that we went through 3 stages of nonlinear parametric amplification. The Signal and the Idler can be separated using a dichroic mirror located at the exit of the HE-TOPAS. The two beams, which are temporally synchronized and mutually coherent, can thus be used together or independently to drive other nonlinear processes (*e.g.* DFG) or to perform experiments (*e.g.* Signal pump - Idler probe, or vice-versa). After going through all the optics and nonlinear crystals, the spatial profile of the Signal and the Idler are usually far from being perfect. In order to solve this issue, we have built a spatial filtering device. To do so, we focus the Idler beam using a 30 cm lens in a 50 cm long KF40 tube connected to a vacuum scroll pump. A metallic pinhole with a 250 μm diameter is placed at the focus of the lens. The spatial profile at the focus is the Fourier transform of the spatial profile of the collimated beam. By placing a pinhole at the focus, we thus filter out all the high spatial frequency components of the beam, directly in the Fourier domain (at focus). These high spatial frequencies originate from diffraction patterns, hot spot and other defects associated with the poor spatial quality of the beam. After the spatial filter, which transmits roughly 75-80 % of the total beam energy, the beam profile of the 1.8μm Idler is very good. Note that the same procedure can be applied to the Signal

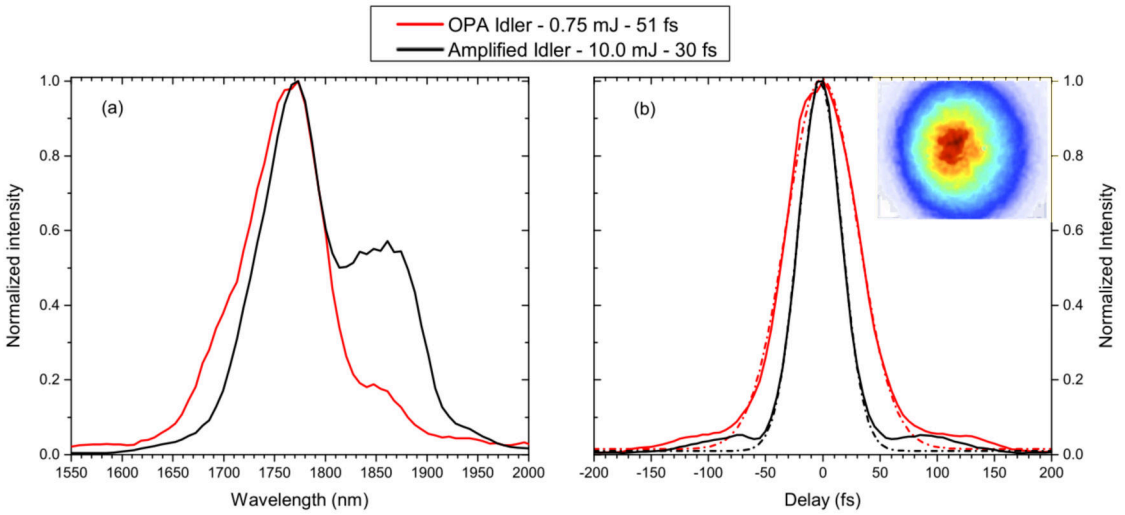

Figure 1.4: Spectral and temporal pulse characterization. (a) The spectrum of the OPA Idler, prior (red) and after (black) the last external parametric amplification stage. (b) The autocorrelation trace of the Idler, prior (red) and after (black) the last external parametric amplification stage. The red and black dotted-dashed curves are Gaussian fit of the autocorrelation traces. This figure is adapted from [Thiré et al. 2015].

beam by simply changing the beam splitter at the output of the HE-TOPAS. At the output of the spatial filter, we have characterized the root-mean-square and the peak-to-peak energy fluctuations using a photodiode connected to an oscilloscope. We obtained a RMS energy stability better than 2% while the peak-to-peak one is about 6%. It is also important to mention that at this point, the CEP of the Idler in passively stabilized, as previously measured on a similar setup at ALLS by Schmidt *et al.* [Schmidt et al. 2011].

After the spatial filtering, we have a 1.8 μm Idler beam containing $\sim$ 750 μJ per pulse, with a pulse duration of 51 fs. The spectrum (measured with an Ocean Optics NIR 256 spectrometer) and the autocorrelation trace (measured with a home-built all reflective SHG-based autocorrelator) of the Idler are shown in Fig. 1.4. The Idler spectrum at the output of the OPA has a 95 nm bandwidth, corresponding to Fourier transform limited pulses (FTL) of 50 fs. This is very close to the measured 51 fs, meaning that the spectral phase of the pulse is quite flat. A frequency-resolved characterization technique, *i.e.* FROG, would definitely be more appropriate, providing all information necessary to retrieve the spectral amplitude and phase, allowing for a complete temporal characterization of the pulse (neglecting the possible spatiotemporal coupling effects [Akturk et al. 2010]).

Many strong-field experiments can be performed by directly using the output of the HE-TOPAS. However, as we explained before, our goal is to build a cutting-edge mid-IR source with unprecedented peak power. In order to do so, we have to add an external parametric amplification stage. To pump this stage, we use the remaining (major) part of the Ti:Sa energy, which is compressed down to 40 fs using a second grating compressor (High Energy Compressor, Fig. 1.2). We can control the energy that we inject in this second grating compressor using a motorized half-wave plate in front a polarizer. The double compressor configuration enables us to tune the energy of the high energy line without affecting the beam that pumps the HE-TOPAS. After the grating compressor, up to 45 mJ of pump energy (800 nm) is available. The Idler (1.8 μm, 750 μJ, 51 fs) and the pump beam are sent into a large (22 mm x 22 mm x 2 mm) type-II ($\theta = 30°$) BBO crystal, where parametric amplification occurs.

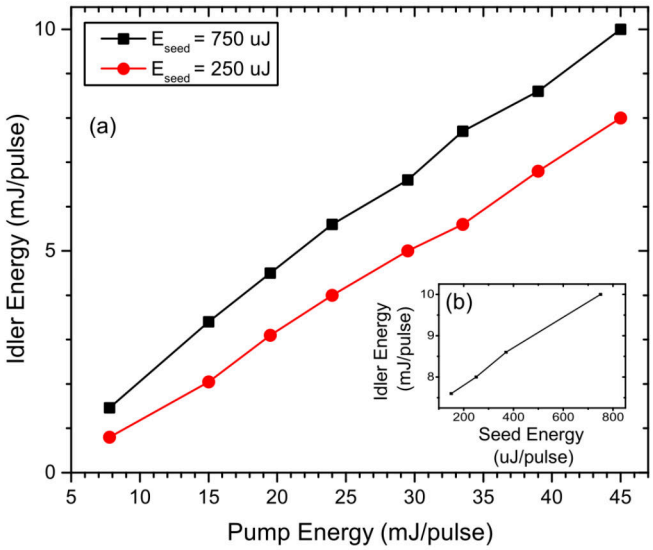

Figure 1.5: Scaling of the high-energy parametric amplification stage. (a) Amplified Idler energy per pulse as a function of Ti:Sa pump energy (seed energy was kept constant). In black, the seed energy is fixed at 750 μJ and in red at 250 μJ. (b) Amplified Idler energy per pulse as a function of seed energy (pump level was kept constant at 45 mJ). This figure is adapted from [Thiré et al. 2015].

Using a large aperture BBO crystal is of prime importance. The amplification efficiency increases with the intensity of the pump beam. However, if the pump intensity is too high, detrimental nonlinear effects (*e.g.* self-phase modulation) start to have a negative impact on the amplification process. We thus reduced the size of the pump beam down to the point where we observed spectral broadening of the pump after propagation into the BBO crystal (spectral broadening is a smoking-gun signature of self-phase modulation). It turns out that the $1/e^2$ size of the 45 mJ 800 nm pump beam corresponding to an intensity close to the self-phase modulation threshold in our BBO crystal is roughly 20 mm diameter. This pump beam diameter sets the size of the BBO required for the last amplification stage. Further upscaling of the parametric amplification process using higher pump energy would require larger nonlinear crystals. The availability of high-quality nonlinear crystals with high apertures is a technological challenge (and sometimes a limitation) for very high-energy OPA.

The spectrum and the autocorrelation trace of the amplified Idler beam are shown in Fig. 1.4. Looking at the spectrum before and after the last parametric amplification stage, we can notice that the gain is strongly inhomogeneous over the spectral bandwidth of the pulse. This inhomogeneous spectral gain was experimentally achieved (on purpose) by slightly tuning the BBO crystal angle to favor the proper phase-matching of the red wing of the spectrum. We have experimentally noticed that doing so allows us to increase the spectral bandwidth of the Idler pulses and thus to produce shorter pulses. Indeed, the spectrum of the amplified Idler can support FTL pulses of 28 fs. The autocorrelation trace of the pulse indicates a pulse duration of 30 fs, close to the FTL pulse duration. Tailoring the spectral gain by tuning the BBO crystal angle thus has a dramatic effect, enabling a 40 % reduction of the pulse duration. Moreover, in the upper right corner of Fig. 1.4 (b), one can see the spatial profile of the unfocused amplified Idler beam. The measurement of the beam profile has been performed using a Si-based CCD camera. Even after amplification, the spatial quality of the Idler beam remains remarkable.

Next, we studied the scaling of the last parametric amplification stage as a function of the seed (Idler) and the pump energy (Fig 1.5). First, let us focus on the red curve in Fig. 1.5 (a). In this case, the seed (1.8 μm) energy is kept constant (250 μJ). The 800 nm pump energy is varied from 8 mJ to 45 mJ. One can notice the growth of the amplified Idler energy with respect to the pump energy, reaching 8 mJ when pumped with 45 mJ. By increasing the seed energy to 750 μJ and by doing the same pump energy scan (black curve, Fig. 1.5 (a)), we see that the amplified Idler energy still increases with the pump energy and reaches 10 mJ when pumped with 45 mJ. Fig. 1.5 (b) shows the amplified Idler energy as a function of the seed energy, when the pump energy was kept constant (45 mJ). When using the maximum available energy, both for the 1.8 μm seed (750 μJ) and the 800 nm pump (45 mJ), we could thus generate 13 mJ of 1.44 μm Signal and 10 mJ of 1.8 μm Idler. This corresponds to a conversion efficiency of 50 % in the last parametric amplification stage. Moreover, by looking at the energy scaling curves, we can notice that we are clearly not reaching the amplification saturation limit, meaning that our OPA can still be up-scaled by pumping with more energy. However, one would also need to increase the crystal size at one point (and buy a bigger pump laser).

To briefly conclude about the design and implementation of our high-energy mid-IR OPA, let us first recall our initial goal. Our motivation was to build a cutting-edge laser source that would enable us to push as far as possible the HHG cut-off, while keeping the photon flux as high as possible. To do so, ultrashort and intense long-wavelength pulses are needed. Using a simple and robust OPA scheme, we have generated 10 mJ, 30 fs pulses centered around 1.8 μm with very good spatial proprieties, at a repetition rate of 100 Hz. This corresponds to a peak power of 0.33 TW, which is one of the most powerful OPA in this spectral region ever reported. This mid-IR source is relatively easy to operate and robust. The next step is to reduce the duration of the pulses to reach the few-cycle regime.

1.3 Compression of the pulses down to the few-cycle regime

1.3.1 Hollow-core fiber post-compression of the high-energy OPA at ALLS

The generation of high-energy few-cycles pulses is a challenging task. Ti:Sa oscillator, can be ingeniously designed to deliver nJ-class sub-4 fs (sub-2 cycles) pulses at $\sim$ 80 MHz repetition rate [Rausch et al. 2008]. The energy per pulse is however too low for most strong-field physics experiments, in particular for driving HHG. To achieve sufficient pulse energies, one needs to amplify the pulses to the micro- or millijoule level, using, for example, Chirped Pulse Amplification (CPA) [Strickland et al. 1985]. Let us take the example of the previously mentioned sub-4 fs Ti:Sa oscillator. The output spectrum of such oscillator typically spans from $\sim$ 600 nm to $\sim$ 1200 nm (octave-spanning spectrum). When amplified in a Ti:Sa crystal using the CPA technique, the spectral gain will not be homogeneous over the spectral bandwidth of the pulse. In the case of Ti:Sa, the gain function is maximum around 800 nm, with a slightly asymmetric gain profile, which decreases more smoothly on the red side of the spectrum (700-950 nm FWHM spectral gain). Such an inhomogeneous spectral gain results in a narrowing of the bandwidth of the pulses as they get amplified. This phenomenon is known as *gain narrowing* and sets the limits for the achievable bandwidth of multi-mJ class Ti:Sa lasers. The spectral bandwidth of most multi-mJ CPA Ti:Sa laser system thus allows to generate pulses which are $\sim$ 25 fs Fourier transform limited or longer. This limitation may be overcome by designing fancy OPCPAs, but such configurations are not commercially available and are relatively complicated to set up in the lab. Therefore, post-compression subsequent to multi-cycle pulse CPA amplification remains the most widely spread doorway to achieved few-cycle

high-energy pulses. The post-compression of multi-cycle pulses can be split into two key steps. First, the spectrum of the pulse needs to be sufficiently broaden. Indeed, the spectral bandwidth of the pulse sets the lower limit for the pulse duration. Second, to reach the shorter duration allows by this time-bandwidth product, the spectral phase of the pulse must be frequency independent (*i.e* no chirp). The second step of post-compression is thus to compensate the residual spectral phases that have been accumulated during the spectral broadening and the propagation through air/optics, in order to achieve pulse duration as close as possible to the Fourier limit.

Spectral broadening is usually achieved by taking advantage of a nonlinear effect called self-phase modulation (SPM). When an intense Gaussian pulse (intensity profile $I(t)$) travels in a medium, it induces a temporally varying reflection index. This is due to the optical Kerr effect,

$$n\big(I(t)\big) = n_0 + n_2 I(t) \tag{1.1}$$

where $n\big(I(t)\big)$ is the time-dependent refractive index, n_0 and n_2 are respectively the linear and the second-order nonlinear refractive index. This intensity-dependent refractive index leads to a modulation of the instantaneous phase $\phi(t)$ of the pulse,

$$\phi(t) = \omega_0(t) - \frac{2\pi}{\lambda_0} n\big(I(t)\big) L \tag{1.2}$$

where ω_0, λ_0 are respectively the central frequency and wavelength of the incoming pulse and L is the propagation length. The instantaneous frequency $\omega(t)$, which is the time derivative of the instantaneous phase $\phi(t)$, is thus also modified,

$$\omega(t) = \frac{d\phi(t)}{dt} = \omega_0 - \frac{2\pi L}{\lambda_0} \frac{dn\big(I(t)\big)}{dt} \tag{1.3}$$

The last term of equation 2.2 is thus responsible for the creation of new spectral components. On the rising (trailing) edge of the pulse, $dn\big(I(t)\big)/dt$ is positive (negative), leading to the generation of red (blue) shifted spectral component. For spectrally Gaussian pulses, self-phase modulation leads to a symmetric broadening of the laser pulse spectrum. The spectral broadening increases linearly with the propagation distance L.

The two most popular techniques to broaden the spectrum using SPM are self-guided filamentation [Hauri et al. 2005; Stibenz et al. 2006] and hollow-core fiber (HCF) [Nisoli et al. 1996]. Concerning the filamentation technique, the setup is strikingly simple to implement. The beam is loosely focused in air, the physics operates by itself. Simply speaking, while going through the focus, a balance between self-focusing induced by Kerr-effect and plasma defocusing (triggered by ionization) lead to self-guiding of the laser, over a distance much larger than the Rayleigh range. The intensity in the self-guided propagation range is typically $\sim 10^{13} - 10^{14}$ W/cm^2. The fact that the beam is self-guided at such high intensity over a significant distance leads to huge spectral broadening, through self-phase modulation. However, the beam characteristics (pointing, spectrum, spatial profile) after filamentation are usually not very stable.

Guided propagation into a hollow-core fiber (HCF) filled with rare gas is harder to implement but leads to a much more stable output laser beam, with high spatial quality. We thus choose this technology to compress the pulses from our high-energy OPA. The challenge of nonlinear propagation in a HCF is to achieve a large spectral broadening

n_2	n_e	P_{cr}	α
$\frac{n_2(\lambda_1)}{n_2(\lambda_2)} = \left[\frac{n_0^2(\lambda_1)-1}{n_0^2(\lambda_2)-1}\right]^4$	$n_e \propto \sqrt{1-\frac{\rho_e q_e}{\varepsilon_0 m_e}\left(\frac{\lambda}{2\pi c}\right)^2}$	$\propto \frac{\lambda^2}{n_2}$	$\propto \frac{\lambda^2}{A^3}$

Figure 1.6: Wavelength scaling of different important parameters for hollow-core fiber post-compression. From left to right: nonlinear refractive index (n_2), free electron refractive index (n_e), critical power for self-focusing (P_{cr}), and waveguide attenuation (α). A is the fiber aperture and ρ_e is the free electron density. This figure is adapted from [Cardin et al. 2015].

(using SPM), while avoiding detrimental nonlinear effects like ionization, nonlinear mode coupling, and self-focusing, to name few [Nurhuda et al. 2003]. Using Ti:Sa lasers, the state of the art of HCF post-compression is the generation of 5 fs, 5 mJ pulses at 1 kHz repetition rate, demonstrated in the group of Prof. Midorikawa (Riken, Japan) [Bohman et al. 2010]. To achieve such output characteristics, they focused 9.5 mJ, 27 fs pulses in a 2.2 m long, 500 μm diameter HCF filled with a pressure gradient of He (1800 mbar at the output and < 1 mbar at the input).

However, when using longer wavelength pulses, the scaling of several physical quantities needs to be taken into account, in order to properly scale the experimental parameters. Indeed, the second-order nonlinear refractive (n_2), the contribution of electrons to the refractive index (n_e), the waveguide attenuation (α) and the self-focusing critical power (P_{cr}) are all strongly affecting the nonlinear propagation into the HCF and they all depend on the incoming laser wavelength. We have summarized the wavelength scaling of these physical quantities in Fig. 1.6.

First, let us consider the nonlinear refractive index of argon, when driven by a λ_1 = 1800 nm (our OPA) or a λ_2 = 800 nm (Ti:Sa) laser. In this case, the nonlinear refractive index decreases with wavelength $\left(n_2(1800nm) = 0.59n_2(800nm)\right)$ [Wang et al. 2013]. Due to this smaller n_2, the mid-IR intensity needs to be higher to accumulate the same nonlinear phase shift. This increase of the laser intensity will subsequently lead to the increase of the ionization rate. The contribution of free electron to the refractive index (n_e) increases with the electron density (ρ_e) and the laser wavelength ($n_e^2 \propto \rho_e \lambda^2$). Thus, compensating the lower nonlinear refractive index by the laser intensity or the gas pressure with ultimately lead to the increase of the free electron density, which is detrimental for the nonlinear propagation into the waveguide.

One solution to avoid ionization, by keeping the same input peak power, is to use a large hollow-core fiber aperture (A), which will lead to a reduction of the intensity. Using a large fiber aperture also lead reduces the attenuation of the fundamental mode, which scale as $\propto \lambda^2/A^3$. However, the lowering of the intensity not only leads to the reduction of the unwanted ionization but also reduces the accumulated nonlinear phase shift. It is thus necessary to increase the propagation length in order to achieve the same spectral broadening (see equations 1.2 and 2.2). For a long time, the hollow-core fiber based on a perforated stiff fused silica rod mounted on a V-shaped groove was the only technological option for HCF spectral broadening [Bohman et al. 2008; Nisoli et al. 1996; Nisoli et al. 1997; Schmidt et al. 2010; Schmidt et al. 2011]. These fibers usually have a limited length of $\sim$ 1 m. This limitation is due to the technical challenge of drilling a perfectly straight hollow channel of few hundreds of microns diameter over a long distance. A few years ago, Nagy *et al.* [Nagy et al. 2008; Nagy et al. 2011] demonstrated the new design of an HCF which is mechanically stretched, enabling a really good straightness over a distance

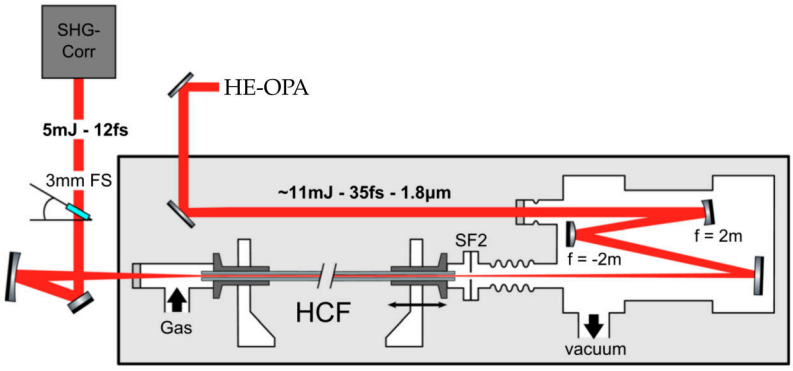

Figure 1.7: Schematic of the stretched hollow-core fiber setup at the Advanced Laser Light Source. The stretched hollow-core fiber is 3 m long and has a 1 mm inner diameter. The focusing telescope effective focal length is 3.8 m with a $1/e^2$ beam waist of 750 μm diameter. SF2: Spatial filter pinhole; SHG-Corr: all-reflective second harmonic auto-correlator. This figure is adapted from [Cardin et al. 2015].

of 3 m. The drawback of this technique is the fact that the mechanically stretch fiber is enclosed in a rigid metal tube, where the fiber ends are fixed permanently.

Inspired by the design of Nagy *et al.* [Nagy et al. 2008; Nagy et al. 2011], we have improved the concept of the stretched hollow-core fiber to allows to change easily the fiber length and inner diameter depending on the required experimental parameters.

We will now describe the implementation of the HCF setup, used to spectrally broaden the output of our high-energy OPA. First, we need to couple the beam into the waveguide. We focus the beam to a size which matches the size of the hollow waveguide. Theoretically, in order to have the best transmission of the fundamental propagation mode, the $1/e^2$ beam size should be $\sim 0.64\ A$, where A is the waveguide aperture [Marcatili et al. 1964]. In our case, we planned to use a 1 mm inner diameter capillary, meaning that we needed to focus the beam to reach a $1/e^2$ beam size of $\sim 640\ \mu m$. We installed an all-reflective folded telescope composed of a f = 2 m concave mirror places 1.05 m before a f = -2 m convex mirror (see Fig. 1.7). This folded telescope has an effective focal length of 3.8 m, with a compact footprint. The $1/e^2$ beam size was measured to be 750 μm at the entrance of the HCF. Note that we used a ratio between the $1/e^2$ beam waist over the aperture of 0.75 instead of the theoretically required value of 0.64. We empirically found that this ratio gave us a better coupling to the TEM_{00} output mode. Just before the entrance of the HCF, we placed a spatial filtering pinhole (labeled SF2 in Fig. 1.7) which has the same diameter as the fiber, to avoid any damage the fiber tip, in case of a drift of the beam pointing. The position of the pinhole in the plane perpendicular to the laser propagation axis can be finely adjusted using alignment screws located outside vacuum. The fiber is a flexible, 3 m long, 500μm inner diameter with a 300 μm thick fused silica cladding surrounded by a thin polymer layer. Some metallic sleeves are glued at both ends of the fiber, to allow the fiber to be clamped with three screws to the holders, which are fixed on the optical table. By finely tuning the three screws which clamp the fiber to the holder, one can adjust the position and the tilt of the entrance and the exit of the fiber, allowing to maximize the transmission and the spatial mode at the exit of the fiber. The output holder allows straightening the fiber by rotating a screw which results in the translation of the holder along the optical axis, as indicated by the arrow in Fig. 1.7. A two-dimensional transition stage also enables moving the position of the entrance tip of the fiber, in the plane perpendicular to the optical axis. The entrance and the exit holder

are connected to KF vacuum tube. Each tube ends with a transparent 2 mm Fused Silica window through which the beam enters and exits vacuum. We introduce the rare gas of our choice at the output of the fiber while continuously pumping the entrance KF tube. This differential pumping allows obtaining a pressure gradient, which ensures a lower pressure at the entrance of the fiber, where the laser intensity is higher. This reduces detrimental nonlinear effects (ionization and self-focusing) which are favored when both the intensity and the gas density are high. This is important because ionization reduces the transmission efficiency, the stability, and the output mode quality.

Concerning the rare gas used for post-compression, there is a trade-off between the nonlinear refractive index and the ionization potential. Going from Xenon, Krypton, Argon, Neon to Helium, the n_2 decreases while the ionization potential increases. If one wants to spectrally broaden a low-intensity beam, Xenon would be a good candidate since the nonlinear refractive index is high, ensuring a significant accumulation of nonlinear phase shift upon propagation, and the small ionization potential should not be a problem, since the intensity is low (electron density will remain low). However, if one wants to push the HCF post-compression to very high-energy pulses, Helium would be a better candidate because of its high ionization potential, avoiding to have a high ionization fraction. The small nonlinear refractive index of He would, in this case, be balanced by the high-intensity, ensuring a significant accumulation of nonlinear phase shift. For a given fiber length and laser intensity, the nature and pressure of the rare gas should be chosen to balance the detrimental ionization and the nonlinear phase shift (and thus the spectral broadening) that need to be accumulated.

In our case, to compress the 1800 nm, 11 mJ output of the high-energy OPA, we put $\sim$ 700 mbar of Ar at the exit of the fiber while continuously pumping the input (0.4 mbar residual pressure at the input). We choose Ar become it is a good compromise, with properties between Xe and He. The transmission of the fiber setup (including vacuum windows, vacuum optics, and the spatial filter SF2 in front of the fiber), under these Ar gas condition, is exactly the same as under vacuum, which leads us to conclude that the ionization level in the fiber is probably very low. The normalized spectrum with (blue) and without (red) gas are shown in Fig. 1.8 (a). After nonlinear propagation through the HCF, we achieved a spectral bandwidth spanning from 1200 nm to 2200 nm (almost an octave). The Fourier limit of this spectrum is 11.3 fs. The general shape of the spectrum is rather typical of self-phase modulation, but shows a significant asymmetry, with a stronger red wing (1900 nm to 2200 nm) compared to the blue wing (1200 nm to 1700 nm). The weaker blue wing is spectrally broader than the strong red wing. This asymmetric shape is known to be due to self-steepening during the propagation into the fiber [Anderson et al. 1983; Nagy et al. 2011]. Self-steepening is a consequence of the intensity-dependent refractive index, which induces a slower propagation of the intense part of the beam. The trailing edge of the pulse steepens, producing a strongly blue-shifted spectral component (the time derivative of the nonlinear refractive index becomes more negative on the trailing edge when self-steepening occurs, see eq. 2.2). The broader and weaker bump on the blue side of the spectrum, compared to the narrower and stronger red-shifted bump, is thus characteristic of the interplay between self-phase modulation and self-steepening during nonlinear propagation in gas-filled hollow-core fiber.

We have temporally characterized the laser pulses using our home-build all-reflective SHG autocorrelator. In this case, the 11 mJ input pulse had a duration of 35 fs (Fig. 1.8, in blue). After the nonlinear propagation into the HCF, the spectrum is significantly broader but the pulse is not shorter, since the pulse is not Fourier transform limited (*i.e.* it is chirped). In order to obtain few-cycle pulses, the positive Group Delay Dispersion (GDD)

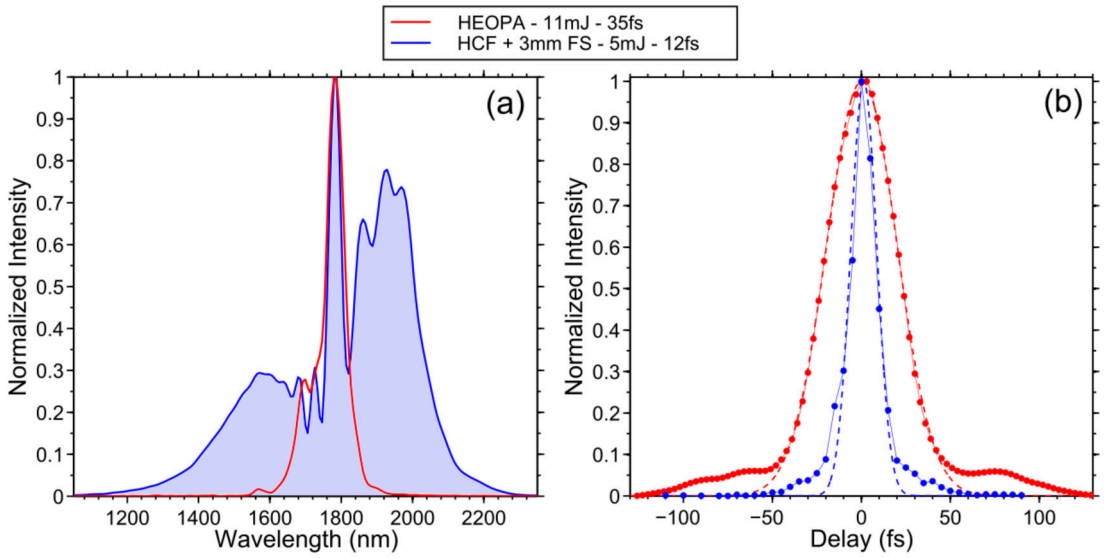

Figure 1.8: Characterization of the laser pulses at the fiber input and output. (a) The spectrum of the fiber input pulse (output of the high-energy OPA), in red, compared with the broad spectrum after spectral broadening, in shaded blue. (b) Autocorrelation signal of the input pulse in red and of the post-compressed 2-cycle pulse. Dotted lines denote Gaussian fits. This figure is adapted from [Cardin et al. 2015].

(positive chirp) accumulated by propagation through the fiber, optics, and air must be compensated. In the visible and near-IR (NIR) spectral range, all optical materials have a positive GDD, and it is necessary to use so-called '*chirped mirrors*', specially designed dielectric mirrors that induce negative GDD upon reflection. In the MidIR range, however, it is possible to find materials with negative GDD. For instance, the zero dispersion point of fused silica lies around $\sim$ 1300 nm and the GDD of this material is negative above this wavelength. Our 1800 nm pulse can thus be compressed by linear propagation into the appropriate thickness of fused silica. The pulse duration after the HCF and linear propagation through 3 mm of fused silica are shown in Fig. 1.8 (b). The measured pulse duration (12 fs) is found to be very close to its FTL duration (11.3 fs). It is important to note that the negative Third-Order Dispersion (TOD) induced by self-steepening is also partially compensated by the positive TOD of fused silica (see [Schmidt et al. 2010]). This bulk material GDD-TOD compensation scheme is strikingly cheap and simple to implement.

To conclude, we have improved the design of stretched hollow-core fiber scheme introduced by Nagy *et al.*[Nagy et al. 2008; Nagy et al. 2011] and have demonstrated the compression of 1.8 μm pulses down to 2 optical cycles (12 fs). These pulses are containing up to 5 mJ, at 100 Hz repetition rate (0.5 W). This scheme can be for sure up-scaled, for the post-compression of more energetic pulses, by using Ne or He gas, and/or by increasing the length of the fiber. Now, our cutting-edge laser source fulfills all the requirement to efficiently drive the generation of ultrashort soft-X-ray pulses via HHG. The developments presented in this section led to the creation of a spin-off company by Bruno Schmidt, few-cycle inc.

1.3.2 Hollow-core fiber post-compression of the Aurore laser system at CELIA

After developing the stretched hollow-core fiber post-compression in Montréal, I brought this technology to CELIA-Bordeaux. The goal was then to build a new setup to perform

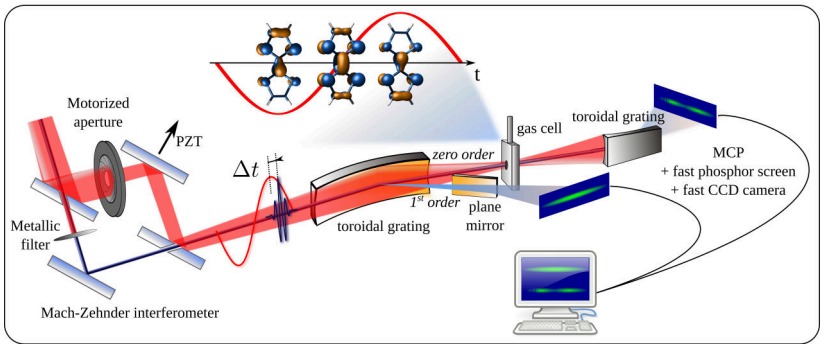

Figure 1.9: Scheme of the ATAS setup. The copropagating isolated attosecond pulse and few-cycle IR pulse are split and temporally delayed by a Mach-Zehnder interferometer using a piezoelectric translation state (PZT). A first XUV spectrometer would record the reference XUV spectrum while a second spectrometer would record the XUV spectrum transmitted through the gas cell. One reference and one transmitted spectrum would be acquired for each laser shot, allowing for very precise differential single-shot transient absorption measurement.

Attosecond Transient Absorption Spectroscopy (ATAS) in relatively large molecules (for a nice review on the theory behind ATAS experiments, see [Wu et al. 2016]). The scheme of the setup that we wanted to build is shown in Fig. 1.9. One of the key steps of this setup is the generation of isolated attosecond pulses (IAP) [Chini et al. 2014a]. IAPs can be generated by using few-cycle pulses and temporal gating techniques to drive high-order harmonics (*e.g.* ionization [Ferrari et al. 2010] or polarization gating [Sansone et al. 2006]).

The Aurore laser system of CELIA delivers up to 25 mJ per pulses centered at 800 nm at 1 kHz. The pulses are usually split, in order to feed two different experiments at the same time. Thus, at the entrance of our lab, we have up to 10 mJ of uncompressed 800 nm pulses. After the grating compressor, installed at the entrance of our experimental room, we obtain 28 fs pulses containing 7-8 mJ. In order to generate few-cycle pulses, from Aurore multi-cycle pulses, we have installed a post-compression setup.

The design of the setup for HCF post-compression is very similar to the one used at ALLS and is the commercial version provided by Few-cycle (Fig.1.10). Details are given in the caption of Fig. 1.10. We had to use a 17.5 mm diameter pinhole to clip the wings of the collimated beam prior to the focusing telescope in order to have a nicer spatial profile at the focus. The optimal pinhole diameter was determined by optimizing the fiber transmission. To avoid the drift of the beam pointing, which could damage the fiber tip, and to improve the shot-to-shot spectral and power stability at the output of the fiber, we installed an 'Aligna 4D' beam pointing stabilization system, which was purchased from '*TEM Messtechnik GmBH*'. The Aligna4D setup is an automated, high precision beam alignment that can lock the beam, both at a given 2D position (x,y) with a sub-micrometer precision, and with fixed propagation angles (θ,χ) with sub-microradians precision, using two steering mirrors and two PSDs (Position Sensitive Detector). In addition, a photodiode measures a signal proportional to the output power after the HCF. This signal is used as an input for a feedback loop which optimizes the fiber transmission by fine-tuning the beam positions and angles (x,y,θ,χ) using the steering mirrors SM1 and SM2. As soon as a rough manual alignment of the beam is enough to ensure some transmission though the fiber, the automated optimization procedure finds the optimal alignment of the laser beam with the fiber axis, the alignment which leads to optimal transmission. The parameters can be saved in the Aligna4D microcontroller and can be called from one day to the next to retrieve exactly the same alignment. The optimization procedure can be kept running

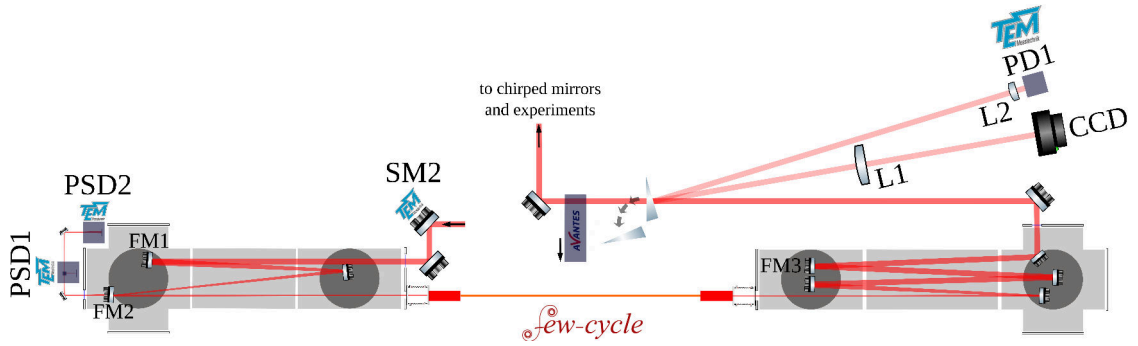

Figure 1.10: Schematic of the HCF setup and associated diagnostics. The setup is not at scale. A focusing telescope, composed of a convex mirror (FM1, f = +1250 mm), a flat mirror and a concave mirror (FM2, f = -250 mm) is installed under vacuum (ISO160 cross and tubes) in order to focus the laser beam inside the 1.5 m long and 500 μm diameter stretched HCF. The distance between FM1 and FM2 is 915 mm and the distance between FM2 and the entrance of the fiber is 850 mm. The effective focal length of the telescope is roughly 3.5 m. The reflectivity of FM2 is roughly 99 %. We picked up the leak of FM2 to image the beam pointing fluctuation using two positions sensitive detector (PSD) of the 'Aligna4D' beam pointing stabilization system. One of the detectors (PSD1) is place at the focus of the beam and a second detector is placed after few tens of centimeter after to focus (PSD2). The positions of the beam on the PSD1 and PSD2 are the input of a feedback loop which stabilizes the beam pointing by steering two motorized mirrors (SM1 (not shown) and SM2), each of them equipped with controllable motors and piezo to actively stabilize the beam pointing. At the output of the fiber, the beam is folded using flat low-dispersion silver mirrors and a convex mirror (FM3, f = +3600 mm), placed at $\sim$ 3500 mm distance from the exit of the HCF to collimate the diverging beam. After the fiber, one can either put a wedge in the beam, which allows multidimensional diagnostics of the fiber output or send directly the beam toward the chirped mirrors (and thus toward the experiments). If the wedge is in the beam, its spectrum is recorded using the transmitted beam, the spatial profile is imaged using a lens (L1) and conventional CCD camera using the front reflection of the wedge and the output intensity is recorded by focusing (L2) the back reflection of the wedge onto a photodiode (PD1). The signal of the photodiode can be injected in an optimization loop which steers the SM1 and SM2 to optimize the coupling in the HCF.

during experiments to compensate for thermal drifts and air fluctuations, for example. When the software is working properly, this setup is amazingly robust and useful. On a daily basis, the fact that one does not need to align precisely and optimize the coupling in the HCF, is a positive game changer. Indeed, the only drawback of this stabilization device is the complexity of the software.

We first investigated the spectral broadening using relatively low input energy per pulse (1.3 mJ). At such low energy, with the large aperture (500 μm diameter) of our hollow-core fiber, we need to use a gas with a high n_2 in order to accumulate sufficient nonlinear phase shift during propagation. We thus chose Argon, which has a significantly high n_2 and which is also cheap. The input of the fiber was continuously pumped by an ACP40 (Adixen dry roughing pump). The input energy was set to 1.3 mJ and the output energy was roughly constant as a function of the Argon pressure (0.73 mJ, transmission of 56 %), indicating that ionization did not play a major role in these energy/pressure conditions. Note that the overall poor transmission of the setup may have been caused by a damaged mirror under vacuum during these measurements. The spectrum at the output of the fiber was measured by an Avantes AvaSpec2048 spectrometer. Its spectral response was calibrated by using a blackbody lamp, which emits light spanning from the visible to the mid-IR range with a well-known emission spectrum. We found out that its

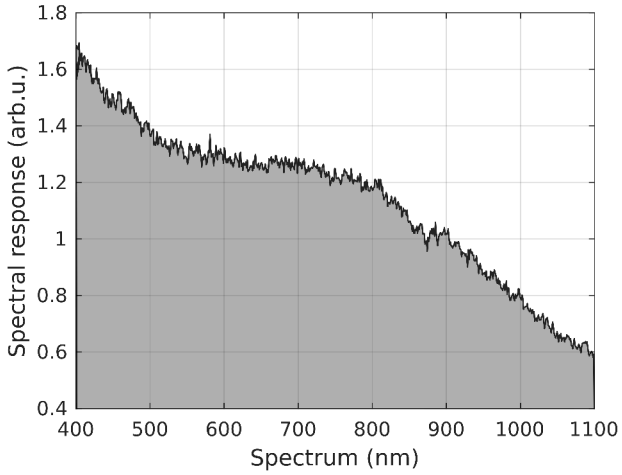

Figure 1.11: Spectral response of the Avantes spectrometer (AvaSpec2048) measured using a blackbody lamp. All the spectra shown in the Fig. 1.12 and 1.13 have been corrected by this transfer function of the spectrometer.

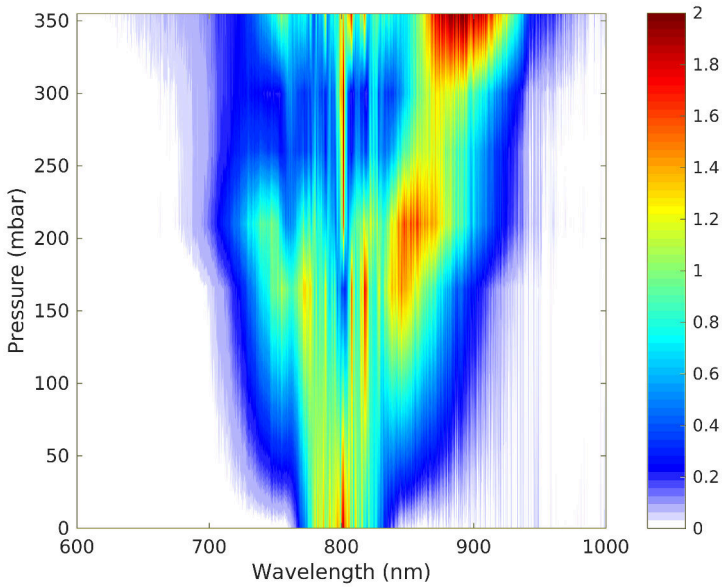

Figure 1.12: Spectral broadening in Argon. The spectrally broaden spectrum as a function of the pressure at the output of the fiber is presented. The pressure at the entrance of the fiber was less than 1 mbar, ensuring a pressure gradient inside the HCF. 1.3 mJ is injected into the HCF, and 0.73 mJ was measured after the fiber, the collimating optics, the vacuum windows, and the chirped mirrors, resulting in a total transmission of 56 % (at the highest gas pressure, *i.e.* 355 mbar).

spectral response was far from being flat (Fig. 1.11). This calibration procedure is thus very important when dealing with very broad spectrum. All spectra which are presented later on have been corrected by this spectral response.

Fig. 1.12 shows the evolution of the output spectrum as a function of the Argon pressure at the exit of the HCF. At low Argon pressure (< 150 mbar), the spectral broadening is more or less symmetric with respect to the input central wavelength (800 nm). At higher pressure, the spectrum started to be slightly asymmetric, which is the signature

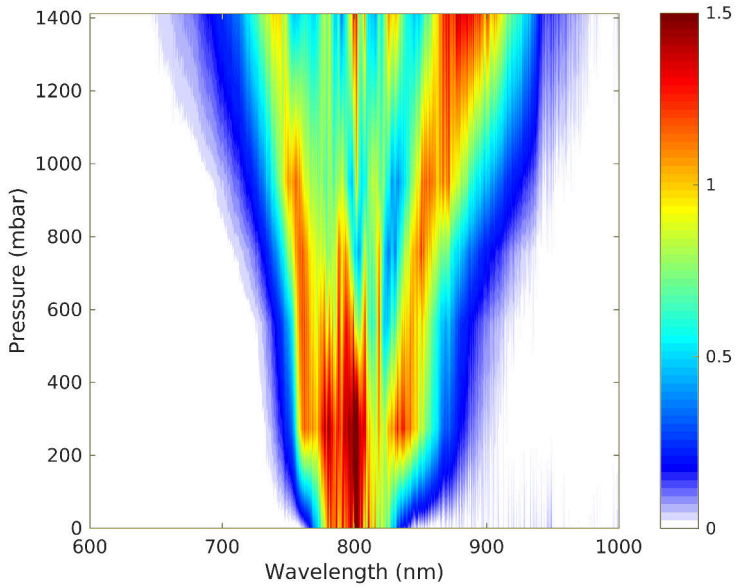

Figure 1.13: Spectral broadening in Neon. The spectrally broaden spectrum as a function of the pressure at the output of the fiber is presented. The pressure at the entrance of the fiber was less than 1 mbar, ensuring a pressure gradient inside the HCF. 3.98 mJ is injected into the HCF, and 2.15 mJ was measured after the fiber (at the highest gas pressure, *i.e.* 1412 mbar), the collimating optics, the vacuum windows, and the chirped mirrors resulting in a total transmission of 54 %.

of self-steepening competing with self-phase modulation [Anderson et al. 1983]. At 355 mbar, the spectrum can support a Fourier transform limited pulse duration of $\sim$ 6 fs. Unfortunately, when these data were acquired, we did not have a properly working Frequency-Resolved Optical Gating (FROG) [Trebino et al. 1997] apparatus to measure the pulse duration. The full temporal characterization of the pulses has thus not been performed. However, using a single-shot autocorrelator compatible with few-cycle pulses measurement, we have seen that after reflection onto 16 chirped mirrors (PC70, Ultrafast Innovations) and linear propagation into few millimeters of fused silica, we could tailor the spectral phase in order to obtain 7 fs pulses with $\sim$ 700 μJ energy. This is sufficient for most static HHG experiments. However, for pump-probe experiments, where the beam is split into multiple arms, generally require more energy. Furthermore the use of temporal confinement methods to produce single attosecond pulses, such as the double optical gating technique [Mashiko et al. 2008], dramatically decrease the laser peak intensity. It would thus be interesting to try to scale the output of the hollow-core fiber.

The HCF fiber setup was designed to handle the full energy available in our experimental room (7-8 mJ). One of the major challenges was the implementation of compact (doubly folded) telescope with long effective focal length to couple the beam into the fiber. The beam size is quite small ($\sim$ 5 mm ($1/e^2$)) on the last mirror (defocussing, FM2 Fig.1.10). We thus bought a dielectric mirror with high damage threshold coating, which was supposed to handle the fluence, even when using the full power of the laser. However, when using more than $\sim$ 4 W (4 mJ at 1 kHz), irreversible damages appeared onto the defocusing mirror, leading to a drop in transmission of the overall HCF setup. This issue could have been solved by testing other coatings or changing the geometry of the telescope. However, we never found the time to solve this issue. In the present work, we restricted ourself to a maximum input power of 4 W.

In order to spectrally broaden energetic pulses while keeping the same fiber length and hollow-core diameter, we used a gas with lower n_2 but higher ionization potential. In Fig. 1.13, we present the output spectrum as a function of the Neon pressure at the exit of the fiber. The spectral broadening behavior as a function of gas pressure is similar to the one observed in Argon at lower energy, but the gas pressure is much higher. This is due to the fact the n_2 is much smaller in Neon than in Argon. The spectrally broaden spectrum as a function of Neon pressure at the output of the fiber is presented in Fig. 1.13. The pressure at the entrance of the fiber was less than 1 mbar, ensuring a pressure gradient inside the HCF. 3.98 mJ is injected into the HCF, and 2.15 mJ was measured after the fiber, the collimating optics, the vacuum windows, and the chirped mirrors, resulting in a total transmission of 54 %. At around 1400 mbar of Neon, we obtained 2.15 mJ per pulse, with a bandwidth supporting Fourier-transform limited pulses of sub-7 fs.

1.4 Conclusions

The development of strong-field and attosecond science is driven by the evolution of ultrafast laser technologies. For example, the first experimental demonstrations of Above-Threshold Ionization [Agostini et al. 1979] and High-order Harmonic Generation [Ferray et al. 1988; McPherson et al. 1987] have been possible in the late 70s and 80s, respectively, when the available laser technologies allowed for reaching intensity above 10^{13} W/cm^2. With the fast-growing ability to generate intense, few-cycles, spectrally tunable at high-repetition-rate laser pulses, many experiments that would have been non-realistic to think of a few years ago are now accessible to researchers. More importantly, the incredible improvement of the laser capabilities is and will enable to experimentally answer scientific questions that were out of reach in the past.

The development of the light sources, both at ALLS and at CELIA, presented in this chapter, are based on well-known physical principles and concepts but relies on their clever implementations. They are surely not the fanciest light sources that are available nowadays, *i.e.* with the development of large-scale facility like ELI-ALPS, for example, the next generation drivers for strong-field and attosecond physics are now reaching crazy 'beyond cutting-edge' characteristics. However, an important aspect of the sources developed here is their reliability and robustness. In the next chapters, we will present several experiments that required acquisitions of several hours, during which the laser had to be perfectly stable. We also will see how the stability and the tunability of the laser sources enabled us to reveal subtle features in high-order harmonic generation, that led us to discover new effects in the HHG process, more than 30 years after its discovery.

2. Novel degrees of freedom in High-order Harmonic Generation

2.1 Simple Picture of High-order Harmonic Generation

When low-frequency ultrashort laser pulses are focused at an intensity of $\sim 10^{13} - 10^{15}$ W/cm^2 in an atomic or molecular gas jet, a great variety of phenomena occurs. One of the dominant processes is strong-field ionization, which is triggered by the non-linear absorption of many photons of the laser pulse. Each time the electric field of the laser goes through a maximum (in linearly polarized field, twice per optical cycle), electron wavepackets are liberated in the continuum by strong-field ionization. Afterwards, the free electrons are driven by the same strong laser field that triggered ionization. The precise timing at which the electrons are liberated into the continuum, with respect to the phase of the electric field (*i.e.* the ionization time, t_i), will govern the fate of these field driven electrons.

Some ionization times t_i will lead to electrons which will be accelerated away from the parent ion and which will never come back close to it (Fig. 2.1 (b)). These electrons are the ones leading to 'direct' Above-Threshold Ionization (ATI) [Agostini et al. 1979], and have a maximum kinetic energy of $2U_p$, as can be semi-classically predicted [Gallagher 1988]. Other electrons, born in the continuum within a specific time window, will be accelerated by the field and subsequently driven back to the vicinity of their parent ion. Three main processes are then possible. (i) They can experience a *soft* forward scattering with the parent ion (low-momentum transfer) which leads to characteristic low-energy structures (LES) in photoelectron spectra [Blaga et al. 2009; Guo et al. 2013] (Fig. 2.1 (c)). (ii) They can experience a *hard* backward scattering (high-momentum transfer), ending up with up to $10U_p$ kinetic energy [Paulus et al. 1994; Yang et al. 1993] (Fig. 2.1 (d)). (iii) They can radiatively recombine to their parent ion, leading to the coherent emission of XUV photons [Corkum 1993; Ferray et al. 1988; McPherson et al. 1987] (Fig. 2.1 (e)). In the latter phenomenon, the energy of the emitted photons is determined by the kinetic energy gained by the electron in the continuum. In this chapter, we will focus on this last phenomenon, which is known as High-order Harmonic Generation (Fig. 2.2).

Because it occurs twice per optical period, when driven using multicycle pulses,

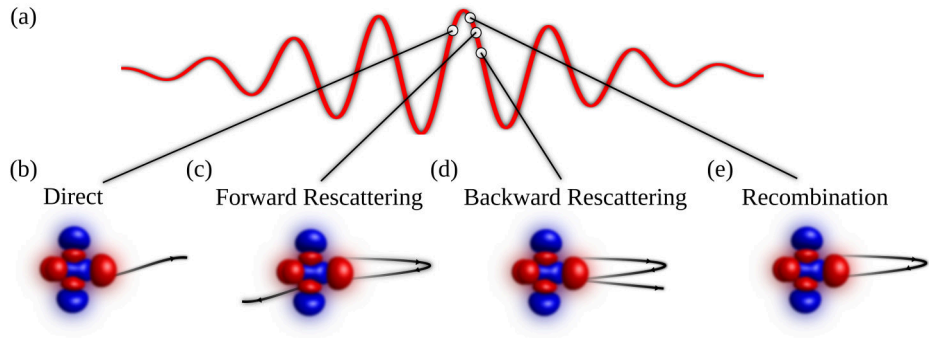

Figure 2.1: Schematic of few different processes that can occur after the removal of an electron through strong-field ionization. In (a), a scheme of a Gaussian-shaped few-cycle electric field. The white dot represents the time at which the electron is liberated in the continuum. In (b), the electrons that are born in the continuum just before the maximum of the field are directly accelerated away from the ionic core. In (c), the electrons which are born significantly after the maximum of the electric field can experience forward rescattering. In (d), the electrons which are born later after the maximum of the electric field can experience backward rescattering. In (e), the electrons which are born just after the maximum of the electric field can experience radiative recombination. Note that more complicated trajectories, for example, multiple rescattering trajectories or long-trajectories leading to radiative recombination can also occur. For sake of simplicity, we have ignored these trajectories in this figure.

HHG emerges in the time-domain as a femtosecond train of attosecond bursts. Each burst is emitted though the recollision of a strong-field driven electron. The bursts are thus temporally separated by half the optical period of the driving laser ($\sim$ 1.3 fs for a wavelength of 800 nm) [Paul et al. 2001]. The total duration of the train is typically a fraction ($\sim$ third or fifth) of the duration of the driving pulse. In the frequency domain, HHG emerges as an XUV comb made of odd high harmonics of the driving laser, with a rather constant conversion efficiency over a broad spectral range (plateau), followed by an abrupt cutoff.

An example of a spatially-resolved harmonic spectrum generated in Argon is presented in Fig. 2.3. This spectrum is adapted from Catoire *et al.* [Catoire et al. 2016]. This HHG spectrum was taken in our lab (at CELIA) during the Ph.D. thesis of Amélie Ferré, few months before the beginning of my Ph.D. One can first notice a comb of odd harmonics, spanning from H13 ($\sim$ 20 eV) to H27 ($\sim$ 42 eV). The highest detected harmonic (E_{co}) corresponds to the maximum kinetic energy that the electron can gain between ionization and recombination, which can simply be established by calculating the classical electron dynamics in a laser field. The E_{co} is given by $E_{co} = I_p + 3.2U_p$, where $U_p = 9.33 \cdot 10^{-14} \cdot I[\mathrm{W/cm^2}] \cdot (\lambda[\mu m])^2$. Here, by plugging the peak intensity of 1.5x10^{14} W/cm^2, the wavelength of 0.8 μm and the I_p of argon (15.76 eV), we find an HHG cutoff energy of $E_{co} \sim 42$ eV, in good agreement with the spectrum, produced using these laser parameters, presented in Fig. 2.3. Looking at the spectrum in Fig. 2.3 in more details, we notice two spatially distinct contributions for each harmonic. First, there is a strongly collimated on-axis component, and second, more divergent ring-like structures. These two distinct contributions originate from different families of electron trajectories that lead to HHG emission and which emerges in both the framework of the semi-classical three steps model and of a quantum reformulation of this model, which is called the Leweinstein model. Because it will be very important later on to describe more finely the HHG process, let us introduce briefly the basis of this quantum model.

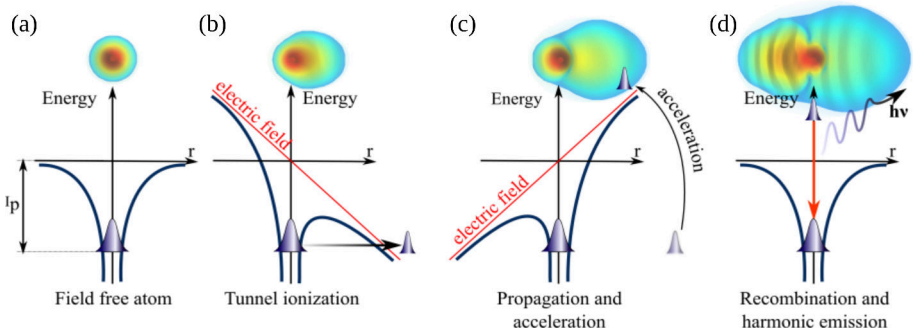

Figure 2.2: The three-step model. In (a), the Coulomb potential of a field-free atom is represented. The 2D Gaussian distribution represents the electronic density of the ground electronic state of the field free atom. In (b), the laser + Coulomb potential of the dressed atom is represented. A part of the electronic wavefunction can be released in the continuum through laser-assisted tunnel ionization. The tunneling induced outgoing electron flow is also visible in the 2D electronic density. In (c), the laser + Coulomb potential of the dressed atom is represented, one half-cyle later, where the sign of the electric field has reversed. The laser-driven electron is driven back in the vicinity of the parent ion. In (d), the radiative recombination of the freed electron onto the ground electronic state, leading to the coherent emission of XUV photon, is depicted. On the upper part of (d), one can see that in the quantum mechanical description of HHG, the emission of XUV photons is coming from the oscillating dipole resulting from the interference between the recolliding electron wavepacket and the bounded part of the electronic wavefunction.

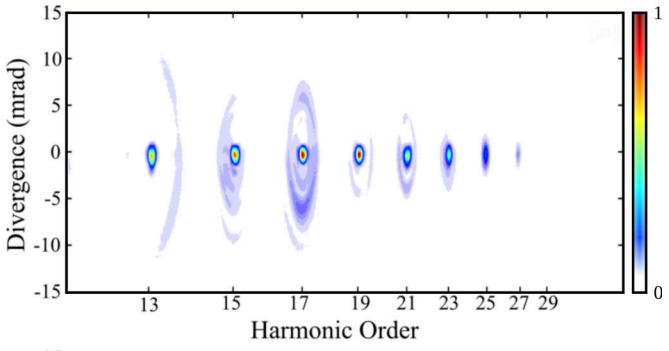

Figure 2.3: Spatio-spectrally resolved HHG spectrum. To generate such spectrum, 28 fs laser pulses from Aurore laser system (800 nm, 1 kHz) were focused to an intensity of $\sim 1.5\text{x}10^{14}$ W/cm^2 into a continuous gas jet of Argon (250 μm nozzle with $\sim$ 400 mbar backing pressure). The precise position of the gas jet with respect to the laser focus was adjusted in order to see the contribution of both short and long trajectories. The figure is adapted from [Catoire et al. 2016].

The quantum mechanical reformulation of the semi-classical model was established by Lewenstein *et al.* [Lewenstein et al. 1994], who used three main approximations to simplify the quantum treatment of the complexity underlying HHG: 1) Only the ground state of the atomic target is taken into account; the excited states are not expected to play any role, 2) the electron liberated into the continuum is treated as a free particle, it does not interact with the Coulomb potential of its parent ion (Strong Field Approximation, SFA) and 3) the depletion of the electronic ground state in neglected. This description, and in particular the SFA, is expected to be valid only if the kinetic energy of the recombining electron is high enough, *i.e.* for HHG emission well above the ionization threshold. This quantum formulation allows to calculate the high-harmonic emission process using the proper description of some effects which cannot be described in term of classical mechanics, *e.g.*

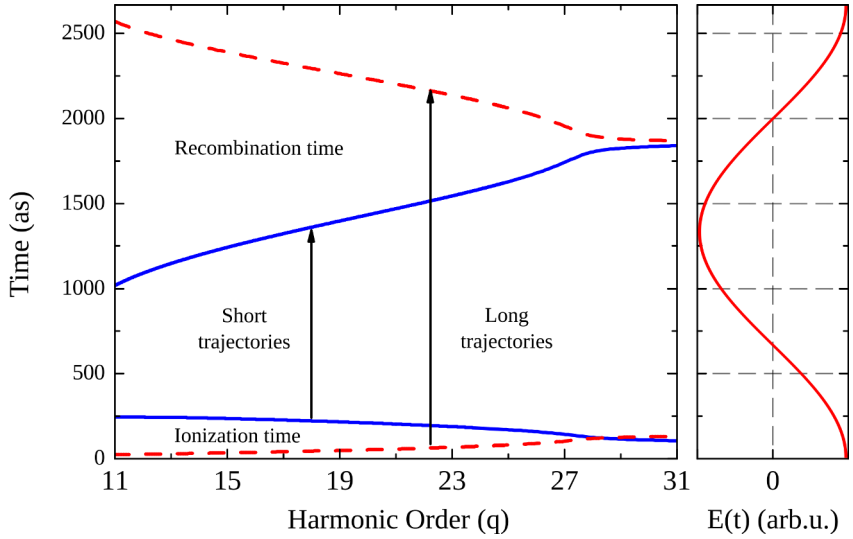

Figure 2.4: Real part of the ionization and recombination time for short (solid blue) and long (dashed red) quantum paths. These ionization and recombination times are extracted by solving the saddle point equation, using the Lewenstein model [Lewenstein et al. 1994]. These ionization and recombination times have been calculated for a laser peak intensity of 1.5 x 10^{14} W/cm^2 (at a central wavelength of 800 nm). This figure is adapted from the thesis manuscript of Yann Mairesse [Mairesse 2005].

tunnel ionization and quantum mechanical diffusion of the electronic wavepacket.

In both the semi-classical and the Lewenstein model, two electron trajectories are found to lead to the emission of each harmonic (see Fig. 2.4). There is a family of trajectories (dashed red lines in Fig. 2.4) which are born (ionization time, t_i) just after the maximum of the electric field and which radiatively recombine to the parent ion (recombination time, t_r) just before the next electric field maximum. They are called 'long-trajectories' since their excursion time ($t_r - t_i$) in the continuum is almost one optical cycle (2.66 fs for an 800 nm pulse). There are also electrons which are born later after the maximum of the laser field and which radiatively recombine to their parent ion roughly one half-cycle later. These are the so-called 'short trajectories'. The pioneering work of Shafir *et al.* [Shafir et al. 2012] allows for the experimental extraction of these ionization and recombination times, for short trajectories, which are in striking agreement with the times calculated using the Lewenstein model.

Looking at the relationship between ionization time (t_i), recombination time (t_r) and photon energy (harmonic order), in Fig. 2.4, one can see that the harmonic spectrum provides a spectro-temporal mapping of the sub-cycle dynamics occurring between ionization and recombination. Indeed, a given electron trajectory (s,l) leading to a given high-harmonic order (q) have its own characteristic travel time in the continuum ($t_r - t_r$). This time-frequency mapping has been used, for example, by Baker *et al.* [Baker 2006], to extract the nuclear dynamics between ionization and recombination, when HHG were generated in CH_4/CD_4. This mapping, inherent to HHG, provides a temporal resolution of $\sim$ 100 attosecond.

The fact that each q-th order high-harmonic results from trajectories (s,l) that have their own characteristic traveling times in the continuum, has another strong consequence on the emitted light. Indeed, in quantum mechanics, the action, which is associated to the time integral of the system's Lagrangian along the 'path' (here the electron trajectory), defines the accumulated phase (ϕ) for a time-evolving quantum system. So, in the context

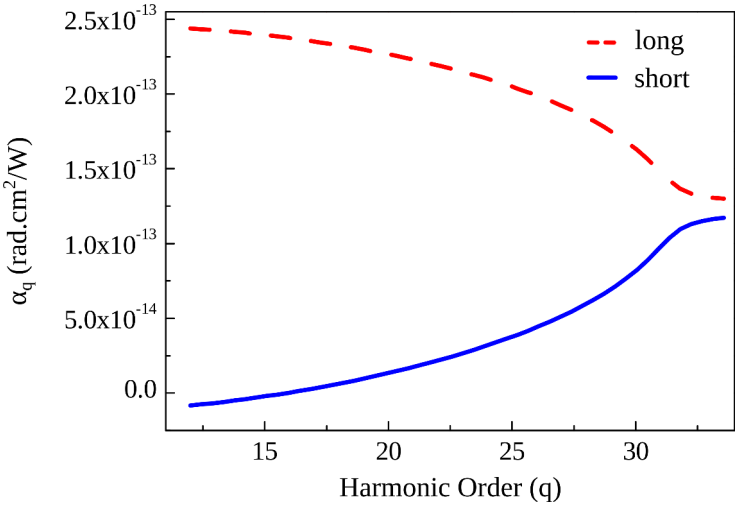

Figure 2.5: Atomic dipole phase coefficient $\alpha_q^{s,l}$ as a function of the harmonic order (q), for short (solid line) and long (dashed line) trajectories. These $\alpha_q^{s,l}$ values have been calculated for a laser peak intensity of 1.5 x 10^{14} W/cm^2, and for a central wavelength of 800 nm. This figure is adapted from the thesis manuscript of Yann Mairesse [Mairesse 2005].

of HHG, since each q-th order harmonic results from trajectories (s,l) characterized by a unique excursion time in the continuum, the phase of each harmonic, for each short and long trajectory ($\phi_q^{s,l}$), is unique. Moreover, since the ionization and recombination time depend on the laser intensity $I_0(r,t)$, which is a function of both time and space, the phase of each harmonic/trajectory is also a function of space and time $\phi_q^{s,l}(r,t)$. Using the Lewenstein model, the exact relationship between the phase $\phi_q^{s,l}(r,t)$ and the laser intensity $I_0(r,t)$ can be derived. The result is strikingly simple.

$$\phi_q^{s,l}(r,t) \approx -\alpha_q^{s,l} I_0(r,t) \tag{2.1}$$

where $I_0(r,t)$ is the laser pulse intensity. $\alpha_q^{s,l}$ is called the 'atomic dipole phase coefficient' and is a proportionality coefficient between the phase $\phi_q^{s,l}(r,t)$ and the laser intensity, and is unique for each harmonic order and short/long trajectories. The $\alpha_q^{s,l}$, which depend on the excursion time of the electron in the continuum $(t_r - t_i)$, leads to a spatio-spectral shaping of the phase of each q-th order harmonic ($\phi_q^{s,l}(r,t)$), emitted by short or long trajectories (s,l) [Gaarde et al. 2002]. The spatial, spectral and temporal properties of each harmonic, thus strongly depend on the laser intensity and its atomic dipole phase coefficient $\alpha_q^{s,l}$. Examples of $\alpha_q^{s,l}$ values, for q-th order harmonics, are shown in Fig. 2.5.

As shown is Fig. 2.5, for the plateau (low-order) harmonics, the $\alpha_q^{s,l}$ values are very different for short (solid blue line) and long (dashed red line) trajectories. This is because of the very different excursion times for these two type of trajectories in the plateau (see Fig. 2.4). For cut-off harmonics, since the short and long trajectories coalesce, their $\alpha_q^{s,l}$ are very similar.

Equation 2.1 shows that the harmonic phase depends linearly on the laser intensity. Since the laser intensity is a function of both the space and time, it means that the harmonic phase not only depends on $\alpha_q^{s,l}$ but also on space and time. Lets first pay attention to the impact of the atomic dipole phase coefficient on the near-field profile of the atomic dipole phase (related to the XUV phase). In the near-field, the XUV intensity is proportional

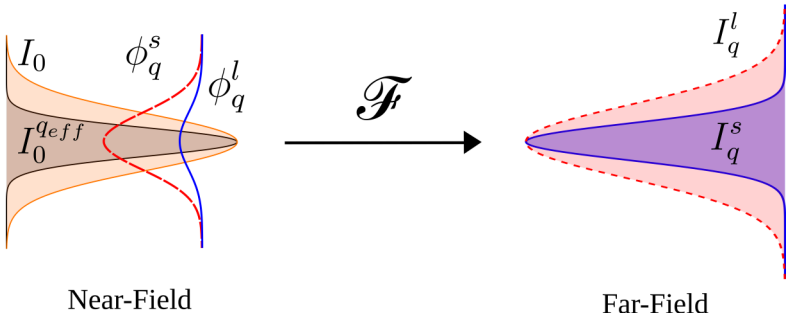

Figure 2.6: Schematic of the near- and far-field properties of the atomic dipole intensity and phase.

to the near-field driving laser intensity $I(r,t)$ to the power of the effective nonlinearity coefficient (q_{eff}) of the HHG process, so that $I_q(r,t) \sim I_0(r,t)^{q_{eff}}$. The effective nonlinearity coefficient can, for example, be measured by looking at the scaling of the intensity of a given harmonic ($I_q(r,t)$) as a function of the driving laser intensity ($I_0(r,t)$) (q_{eff} is the slope when representing $I_q(r,t)$ vs $I_0(r,t)$ as a log-log plot). The near-field profile of the atomic dipole phase ($\phi_q^{s,l}(r,t)$) is given by equation 2.1, and is shown to depend on both the atomic dipole phase coefficient ($\alpha_q^{s,l}$) and the near-field laser intensity ($I_0(r,t)$), see Fig. 2.6.

For short trajectories, the atomic dipole phase coefficient α_q^s is nearly zero for threshold harmonics and increases with the harmonic order q [Gaarde et al. 2002]. The curvature of the atomic dipole phase thus also increases with q. On the contrary, for long trajectories, the atomic dipole phase coefficient α_q^l, and thus the curvature of the atomic dipole phase, is huge for threshold harmonics and decreases with the harmonic order q, reaching the same value for cut-off harmonics. This means that the phase curvature of the harmonic emission will be very different between short and long trajectories, in the plateau spectral region.

In the experiments, we measure the spatio-spectral profile of the harmonics in the far-field. To connect the near-field to the far-field properties, one needs to use the Fraunhofer diffraction equations. Using simple wave optics, Fraunhofer demonstrated that the near-field amplitude and phase profile of a diffracting object (*e.g.* at the focus of a lens) and the far-field image of this object (*e.g.* at infinity) are simply connected by a Fourier transform. In our case, it means that the far-field spatial intensity of the harmonics is simply the modulus squared of the Fourier transform of the near-field atomic dipole (XUV amplitude and phase).

Because of this Fourier transform connection between the near- and the far-field, it is very easy to intuitively retreive the effect of the atomic dipole phase coefficient $\alpha_q^{s,l}$ on the spatial profile of the different harmonics/trajectories in the far-field. If the atomic dipole phase is spatially flat in the near-field, the far-field spatial profile will be Fourier transform limited (FTL), *i.e.* will have the smallest divergence allowed by the spatial width of the XUV in the near-field. As the atomic dipole phase gets away from being flat (as its curvature increase), the divergence will increase and thus the far-field size of the harmonics will also increase (see Fig. 2.6). For short (long) trajectories, since α_q^s (α_q^l) increase (decrease) with q, the divergence also increase (decrease) with q. The spatial properties of harmonics are thus very different for plateau harmonics and coalesce for cut-off harmonics.

After paying attention to the effect of the atomic dipole phase on the spatial properties

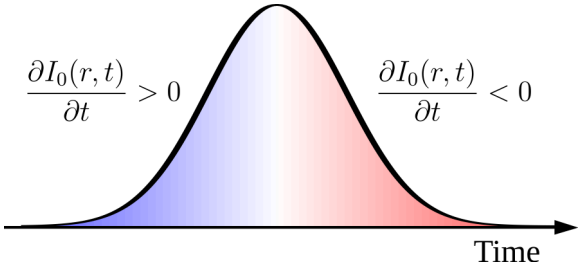

Figure 2.7: Schematic of the spectral shift of the harmonics. The harmonics generated on the rising edge of the laser pulse envelope are blue-shifted while the harmonics generated on the trailing edge are spectrally red-shifted.

of harmonics, we will now focus on its effect on the spectral properties of HHG. Since the atomic dipole phase ($\phi_q^{s,l}$) is proportional to the time-dependent intensity of the driving laser pulse $I_0(r,t)$ (see equation 2.1), the instantaneous phase of the emitted harmonics, and thus their instantaneous frequency $\Omega_q^{s,l}$, are also time-dependent.

$$\Omega_q^{s,l}(r,t) = \frac{\partial \phi_q^{s,l}(r,t)}{\partial t} = q \cdot \omega_0 + \alpha_q^{s,l} \frac{\partial I_0(r,t)}{\partial t} \tag{2.2}$$

Looking at equation 2.2, one can see that the instantaneous frequency of the q-th order harmonics ($\Omega_q^{s,l}(r,t)$) is given by $q \cdot \omega_0$, which is pretty intuitive since HHG results in a net absorption of q photons from the driving laser (ω_0), plus a second term which appear because of the instantaneous phase modulation of the emission by the interplay of the atomic dipole phase coefficient and the driving laser pulse intensity. If the atomic dipole phase coefficient vanishes, this second term also vanishes and the harmonics instantaneous frequency is time-invariant and is centered around $q \cdot \omega_0$. If the atomic dipole phase coefficient is non-zero, the harmonics generated on the rising (trailing) edge of the driving laser pulse are spectrally blue (red)-shifted (since $\partial I_0(r,t)/\partial t$ is positive (negative)). In most cases, the HHG process is equally efficient on the rising and on the trailing edge of the driving laser pulse, leading to a perfect balance between spectrally blue- and red-shifted harmonic emission. This nonadiabatic term thus leads to symmetric spectral broadening of the harmonics around $q \cdot \omega_0$. Thus, in the same fashion as spatial atomic dipole phase curvature leads to spatial broadening, the temporal atomic dipole phase curvature leads to spectral broadening. Note that this phenomenon is very similar to self-phase modulation, which has been explained in great details in the previous chapter. In the case of HHG, the atomic dipole phase coefficient $\alpha_q^{s,l}$ plays the same role as the nonlinear refractive index (n_2) in self-phase modulation. Indeed, both physical quantities are coefficients in front of the time-derivative of the driving laser intensity, which is the term giving rise to spectral broadening. Since the atomic dipole phase coefficient is larger for long trajectories, the spectral broadening is more efficient for these trajectories. Moreover, the concentric ring structures present on long trajectories is a signature of spectral interference, similar to the one observed during self-phase modulation. Also, note that as the absolute value of the time-derivative of the laser intensity increases, the spectral broadening also increases. Driving HHG using really short and intense pulses thus give rise to a large spectral broadening of the harmonics.

While the nonadiabatic spectral broadening of q-th order harmonics is usually symmetric around $q \cdot \omega_0$, there are some specific cases where this symmetry can be broken. Indeed, if the HHG process is more efficient on the leading or on the trailing edge of the

driving pulse, the spectral blue- or red-shift will be dominant, respectively. For example, if one drives HHG at an intensity above the saturation intensity, the ground state of the atomic or molecular target will be depleted prior to the laser peak intensity. Within this scenario, the harmonics are emitted on the rising edge of the laser pulse (prior to ground state depletion), leading to a nonadiabatic spectral blue-shift. This blue-shift was observed in experiments, where the intensity was set above the saturation intensity [Shin et al. 1999]. This spectral blue-shift due to the ground state depletion should not be confused with the free-electron dispersion induced spectral blue-shift of the fundamental driving laser, which also translates a blue-shift of the harmonics [Froud et al. 2006]. While intensity is an easy knob to favor the HHG emission on the rising edge of the laser pulse, experimental demonstration of harmonics emission preferentially on the trailing edge of the pulses was never demonstrated yet. Later in this chapter, we will demonstrate a new HHG mechanism which involves highly-excited states of the atomic target and which is dominant on the trailing edge of the laser pulse. We will see that this new mechanism can be directly observed in the spectral domain by looking at red-shifted spectral features in the HHG spectra. This feature will be shown to spectrally shift with increasing laser intensity. Moreover, we will show an elegant experimental measurement of the emission delay of this new spectral feature with respect to the laser pulse envelope, using the attosecond lighthouse effect [Quéré et al. 2014; Vincenti et al. 2012].

Before going into more complex cases of HHG, let us present the results of our effort to extend the high-harmonic generation cut-off over the entire Water Window spectral range, by using the simple idea developed within the framework of the semi-classical and the Leweinstein model.

2.2 Extending HHG to the Water Window spectral range

In the previous section, we have presented the basic concepts behind extreme nonperturbative frequency up-conversion from the IR to the XUV spectral range, through the process of high-order harmonic generation. In this section, we will demonstrate that this phenomenon can be used to develop coherent soft-X-ray light source, in a spectral range which is typically hard to access in conventional scale laboratory. We will go back to the main goal that drove the development of the high-energy OPA, at ALLS, Montréal, presented in the previous chapter: pushing the cut-off of the harmonic to the water-window spectral range. We will see that the relatively simple picture of HHG described in the previous section is enough refined to understand all the strategies behind the extreme cut-off extension that will be presented below.

2.2.1 Why is the Water Window spectral range interesting ?

X-ray absorption spectroscopy is one of the most used techniques to obtain information about structural and electronic properties of matter, in particular in the condensed phase. Near edge X-ray absorption fine structure (NEXAFS) spectroscopy, which is based on the multiple scattering of the excited electron onto the neighboring atoms, gives a lot of information about the environment from which the electron is excited (coordination, chemical environment). Moreover, looking at the extended X-ray absorption fine structures (EXAFS) gives information about the distance between atoms that form the lattice. It is of particular interest to use such powerful x-ray absorption spectroscopy techniques in an aqueous solution, to obtain information about molecules in the environment where most of the bio-relevant chemistry occurs. One technical challenge of x-ray spectroscopy in aqueous media is the fact that water strongly absorbs in the x-ray spectral range. It is

thus usually hard to extract the small absorption signals coming from the solute compare to the large absorption coming from the aqueous solvent. Fortunately, there is a spectral-range, between $\sim$ 285 to 530 eV, where water is more transmissive than most bio-relevant molecules (containing carbon, sulfur and oxygen atoms, for example). This spectral range, which is defined by the range between the carbon K-edge (285 eV) and the oxygen K-edge (530 eV) is thus very attractive to characterize bio-relevant molecules embedded in water. This type of experiment is usually performed in synchrotron facilities, where tunable water-window x-ray photons are accessible. However, the access to synchrotron is rather limited, and they generally deliver long pulses, preventing ultrafast time-resolved studies. It is therefore of great interest to develop bright, table-top, ultrafast soft-x-ray sources in the water window spectral range. Benchmark static NEXAFS experiments, using HHG-based source, in the gas-phase, have been recently demonstrated [Cousin et al. 2014; Johnson et al. 2016]. Moreover, first demonstrations of table-top femtosecond time-resolved NEXAFS in gas-phase molecules have been demonstrated in 2017 by Pertot *et al.* [Pertot et al. 2017], who studied the dissociation of CF_4^+ and by Attar *et al.*, who follow an ultrafast electrocyclic ring-opening reaction [Attar et al. 2017]. In the following, we will show the results of our effort to build an ultrafast soft-x-ray source that spans the entire water-window spectral range, based on HHG driven by the high-energy OPA presented in the previous chapter.

2.2.2 HHG scaling with long wavelength drivers

Extending the high-order harmonic emission to the X-ray range requires pushing the HHG cut-off energy (E_Ω^{co}), which is given at the single atom level by $E_\Omega^{co} = I_p + 3.2U_p$. To produce macroscopic (measurable) XUV signal, the emission from different atoms in the laser focus need to be in phase, in order to coherently add up. This means that the IR driver and the XUV need to propagate at the same velocity in the medium. This can be expressed as a linear relationship between the wave-vectors of the driver (k_{IR}) and of the q-th order harmonic (k_q).

$$\Delta k = qk_{IR} - k_q = \Delta k_g + \Delta k_n + \Delta k_p + \Delta k_d = 0 \tag{2.3}$$

Δk_g is the wave-vector mismatch induced by the Gaussian beam phase gradient along z, and is always negative. Δk_n and Δk_p are the wave-vector mismatches induced by the dispersion of the neutral and of the free electrons, respectively. They have opposite signs and are both proportional to the gas pressure. Δk_d is induced by the gradient of the atomic dipole phase. It is small for short trajectories (which have a small atomic dipole phase coefficient), and we will, therefore, neglect it here. In order to minimize the wave-vector mismatch (and optimize the XUV signal), we thus need to cancel the plasma dispersion and Gaussian beam phase gradient with the neutral dispersion. To be able to balance these contributions, the ionization fraction needs to be small enough to ensure that the contribution due to the neutral dispersion Δk_n dominates over the dispersion due to free electrons Δk_p. This critical ionization fraction sets a critical intensity (which depend on the I_p of the gas and the driving laser wavelength) that one can use to generate phase-matched harmonics. If the intensity is increased above the critical intensity, the ionization fraction is too high and its contribution to wave-vector mismatch cannot be compensated with neutral dispersion. Because of this critical intensity, there is a so-called phase-matching cut-off, which limits the maximum photon energy that can be generated and phase-matched. This cutoff depends on the generating medium (because of I_p) and on the driving wavelength, as can be seen in Fig.2.8.

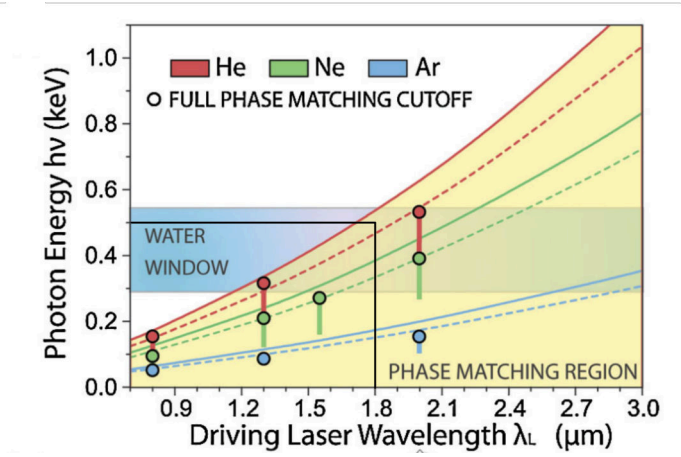

Figure 2.8: Phase-matching cut-offs for different driving wavelength and generating media. The solid (dashed) lines represent the case where HHG are driven by laser pulse of three (eight) optical cycles duration. The black line shows that using a 1.8 μm, with a duration of 5 cycle pulses, one can generate phase-matched XUV photons up to $\sim$ 500 eV. Solid circles represent the observed phase matching cutoff at 1.3μm and 1.55μm from [Popmintchev et al. 2009; Takahashi et al. 2008], and at 2 μm from [Chen et al. 2010]. This figure is adapted from [Chen et al. 2010].

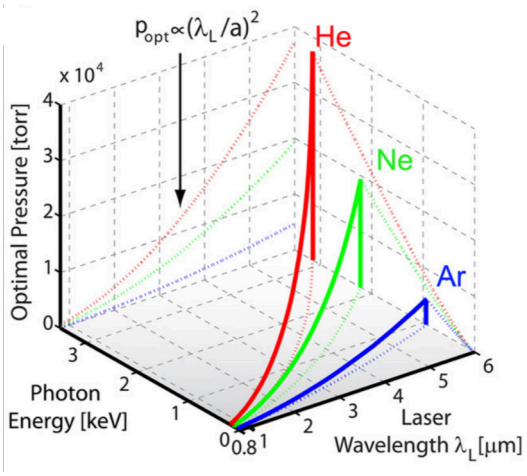

Figure 2.9: Optimal pressures needed to reach efficient phase-matching condition, for different driving laser wavelength and generating media. One can see the predicted optimal pressure scale quadratically with the wavelength. This figure is taken from [Popmintchev et al. 2009].

Figure 2.8 shows that the phase matching cut-off increases with the driving wavelength and with the ionization potential of the target (I_p), like the single-atom cut-off. The solid (dashed) lines represent the case where HHG is driven by three (eight) optical cycles. We can see that the phase-matching cut-off is higher for shorter laser pulses. This is due to the fact that the ionization fraction accumulates over the whole laser pulse duration. For a given peak intensity, the ionization fraction will be smaller for a shorter pulse. A shorter pulse thus allows using higher peak intensities before reaching the critical ionization fraction. As presented in the previous chapter, the high-energy OPA developed at ALLS allows us to generate 5-cycles pulses centered around 1.8 μm. Looking at the phase-matching curves in Fig. 2.8, we can see that focusing these pulses in Helium, we can expect the phase-matching cut-off to reach $\sim$ 500 eV.

Even if phase matching pushes us to use longer driving wavelengths, we have to keep

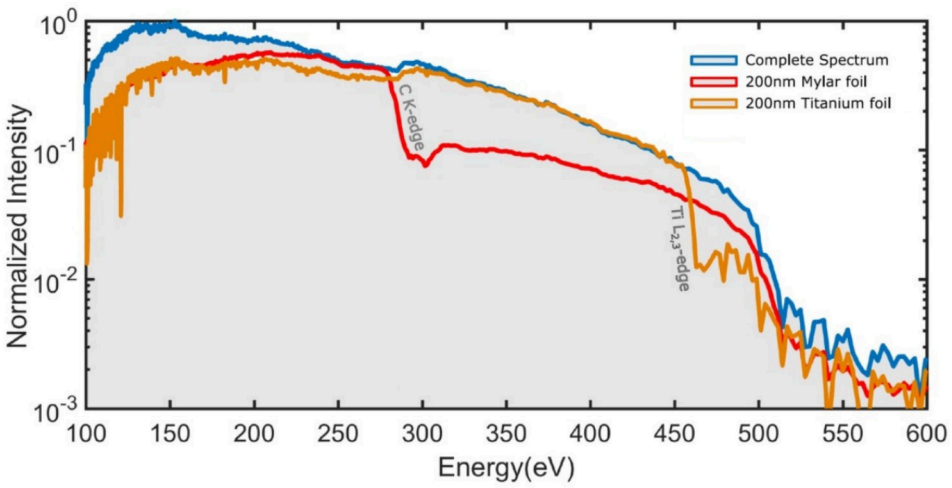

Figure 2.10: Water window HHG spectra obtained by driving Helium (50 bar backing pressure) with 7 mJ, 35 fs pulses centered around 1.8 μm, with spectra after going through a 200 nm Mylar (biaxially-oriented polyethylene terephthalate, edge at 285 and 530 eV) and a 200 nm Ti filters (edge at 453 eV). The unfiltered spectrum (blue curve) is acquired over 2000 laser shots.

in mind that increasing the laser wavelength induces a dramatic decrease of the single atom harmonic yield. Shiner *et al.* [Shiner et al. 2009] have demonstrated a $\sim \lambda^{-(6)}$ scaling of the HHG efficiency, over the 800-1850 nm range. This could be a major limitation for the development of high brightness HHG-based water-window sources. Fortunately, the decrease of the single-atom response can be partially compensated by increasing the number of emitters, *i.e.* by increasing the gas pressure. Indeed, the optimal pressure needed to fulfill the phase matching condition scales quadratically with the driving laser wavelength (see Fig. 2.9). Since the harmonic signal scales quadratically with pressure, we can expect to regain a factor $\lambda^{(4)}$, compensating the drop of the single atom response.

2.2.3 Experimental results

We produced high-order harmonics in He atoms using 7 mJ, 35 fs pulses centered around 1.8 μm at ALLS. The pulses were focused by a lens of 75 cm focal length. The gas was injected using a 100 Hz Parker pulsed valve. Figure 2.10 shows typical HHG spectrum (in log scale) that we obtained experimentally, without and with filters (Mylar and Titanium filters in this case). The backing pressure that maximized the HHG signal was found to be $\sim$ 50 bar. The Mylar (carbon k-egde at 285 eV and oxygen k-egde at 530 eV) and Titanium (at 453 eV) filters were introduced to calibrate the photon energy axis. The discrete harmonic peaks are too close to each other (separated by $\sim$ 1.4 eV) to be resolved by our spectrometer, in this spectral range. The HHG spectrum extends up to $>$ 500 eV, which is in good agreement with the predicted phase matching cut-off described above.

The photon flux was measured using a calibrated X-ray camera from Princeton instruments and found to be $> 10^5$ photons/shot in the water window spectral range (285 to 530 eV). In order to demonstrate the usefulness of this source, we performed single-shot absorption experiment using the Mylar filter as a target. The results are presented in Fig. 2.11. Note that the color scale is linear (not log). The carbon K-edge, located around 4.4 nm, is clearly visible in single shot spectra. This demonstrates the potential of this soft-X-ray source for spectroscopic applications. Unfortunately, we did not demonstrate any application in the water-window using this beam line. On the contrary, the group of Jens Biegert and the group of Jon Marangos very recently demonstrated examples of static near

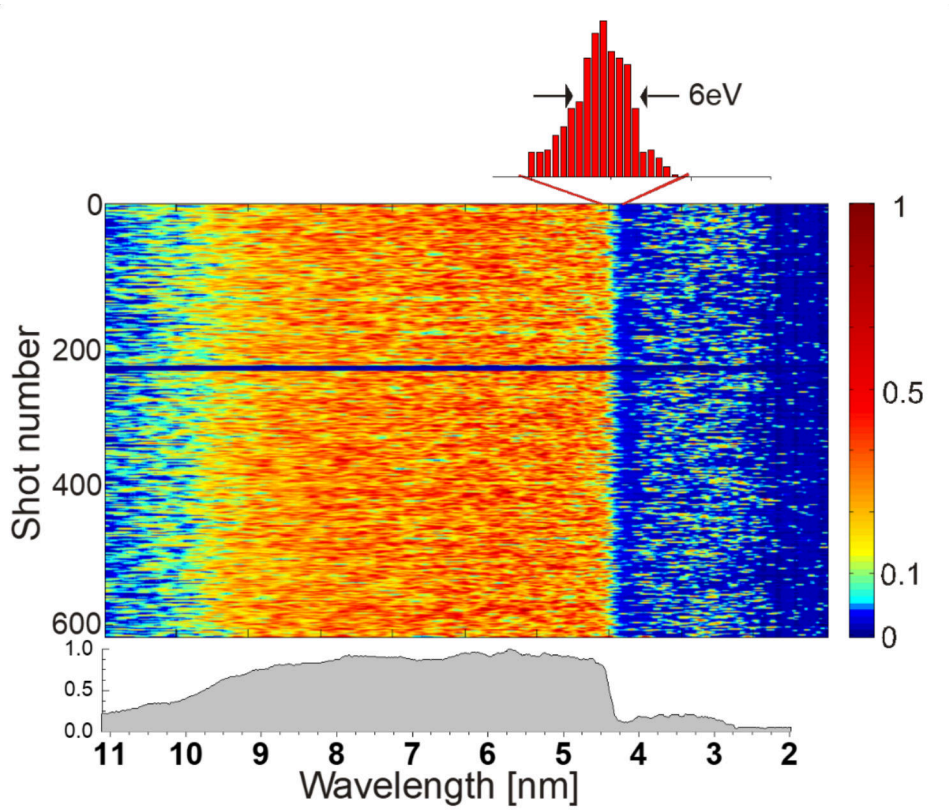

Figure 2.11: Single-shot carbon K-edge absorption spectra. The histogram bins represent the position of the measured edge as retrieved by a simple edge-detection algorithm. The grey spectrum represents the normalized sum of the 600 shots on a linear scale. The laser was blocked for shot 220 to record the noise level.

edge X-ray absorption fine structure (NEXAFS) using their HHG-based water-window sources, driven by intense few-cycle, long wavelength pulses [Cousin et al. 2014; Johnson et al. 2016]. As mentioned earlier, the dream of table-top time-resolved carbon K-edge absorption spectroscopy has also been demonstrated, both in Geneva [Pertot et al. 2017] and in Berkeley [Bhattacherjee et al. 2017].

2.2.4 Partial conclusions and perspectives

By using the simple HHG cut-off scaling law developed within the framework of the semi-classical 3-step model, one can immediately recognize that one need to push both the laser intensity and wavelength in order to increase the maximum photon energy that is generated using HHG. We have used the 100 Hz high-energy mid-IR OPA developed at ALLS to demonstrate an HHG-based soft-X-ray source spanning almost the entire water-window spectral range. We have demonstrated a soft-X-ray source extending above 500 eV photon energy, with a flux of $> 10^5$ photons/shots in the water-window spectral range. The possibility of recording single-shot measurement of carbon K-edge absorption feature has been demonstrated. This source is currently used at the Advanced Laser Light Source to study ultrafast demagnetization dynamics via time-resolved Resonant magnetic x-ray scattering. One of the major drawbacks of this source is its repetition rate. Developing high-repetition rate HHG-based soft-X-ray source is currently triggering a lot of technological development and research efforts around the world.

2.3 Beyond the Simple Picture of High-order Harmonic Generation

As we have seen in the two previous section, the pioneering semi-classical three-step model has been amazingly successful in describing the general features underlying high-order harmonic general (HHG) [Corkum 1993]. Indeed, it greatly explains the origin of the surprising 'plateau' behavior in the HHG spectrum as well as the intensity and wavelength scaling of the photon energy at which it abruptly goes to zero (cut-off). This semi-classical model also leads to excellant estimation of the ionization and recombination time underlying the generation of each harmonic. This analysis also allowed to discover that two types of electrons trajectories lead to the emission of each harmonic. Later, a refined quantum mechanical description of HHG by Lewenstein [Lewenstein et al. 1994] *et al.* led to a more precise determination of the ionization and recombination time, by taking into account quantum effects that are intrinsically intractable using classical mechanics. Its model also led to a much better understanding of spatial, spectral and temporal properties of HHG, by introducing a path integral formalism, which allows to determine the harmonic dipole phases. Many experimental works have demonstrated the validity of different aspects of the Lewenstein model, see for example [Bellini et al. 1998; Shafir et al. 2009]. So, even without taking into account the role of excited states, the electron-ion interaction during propagation in the continuum and the ground state depletion, the Lewenstein model have been shown to be truly successful in describing general aspect of HHG.

However, the approximation made within the Leweinstein model, which were used to simplify the resolution of the Time-Dependent Schrödinger Equation, also comes with some major limitations. Let us give a simple and famous example. In 1993, Wahlström *et al.* observed the appearance of a local minimum in the high harmonic emission from Argon atoms [Wahlström et al. 1993]. This minimum was immediately recognized to be associated to the Cooper minimum previously observed in XUV photoionization of argon [Cooper 1962]. In photoionization, it is well understood that this local (Cooper) minimum is due to a vanishing transition dipole moment between the p-type ground state wavefunction of Argon to the d-type continuum wavefunction of the outgoing electron for a photon energy about 48 eV. Because the calculation of photorecombination rate involves the same (but time-reversed) transition dipole matrix element than in single-photon ionization, it is thus obvious to intuitively think that local minima in the photoionization cross-section would also be present in the HHG spectrum, due the same minima in the photorecombination cross-section. Such minima have been subject to a lot of investigation in the field of XUV photoionization, because they clearly are invaluable features against which theoretical models can be tested. However, it was shown that in the framework of the Lewenstein model, where continuum wavefunctions are described as plane waves (PW), this Cooper minimum cannot be reproduced. Later on, it was shown that when using models that take into account the role of ionic potential on the shaping of the recolliding electron wavepacket, the Cooper minimum clearly shows up in the HHG spectrum. Example of such theoretical methods, which are adapted from SFA, are Quantitative Rescattering Theory (QRS) [Le et al. 2009] and Classical-Trajectory Monte Carlo Quantum Electron Scattering (CTMC-QUEST) [Higuet et al. 2011].

At this point, a new field of research, called high-order harmonic spectroscopy (HHS) emerged. This research field aims at retrieving static and dynamical structural information about the target from which the high-order harmonic emission occurs. In the past few years, as the level of accuracy and sophistication of experiments increased, the requirements for the level of accuracy of the theoretical methods used to try to tackle the physics underlying these experiments also increased, and several other important approximations

broke down. For instance, many experiments have shown that the assumption that a single bound state is involved in HHG, made within the Leweinstein model, was often violated. Several experiments demonstrated that in molecular HHG, where many valence orbitals are energetically close to each other, many of these orbitals can be strong-field ionized, opening multiple channels for HHG [Ferré et al. 2015a; McFarland et al. 2008; Rupenyan et al. 2013]. Since the overall harmonic emission is given by the coherent superposition of these all these channels, high-harmonic spectroscopy is thus a remarkably sensitive technique to probe multi-orbital effects. Another example of a multichannel effect that can have a huge impact on the XUV emission is the resonant laser-driven transition between different orbital of the molecular ion, between the ionization and the recombination step. These sub-cycle resonant transitions lead to multi-channel interference that has huge impact on the emitted harmonic amplitudes and phases, reflecting the shape and location of the hole left in the molecule by strong-field ionization. Few years ago, Mairesse *et al.* [Mairesse et al. 2010] used High-order Harmonic Spectroscopy (HHS) to study the attosecond dynamics of this light-driven hole wavepacket. These snapshots of the multi-electron dynamics during HHG is one of the most elegant examples of the sub-Angstrom spatial resolution and attosecond temporal resolution of High-order Harmonic Spectroscopy (HHS).

One other important approximation in the Lewenstein model is the one assuming the continuum wavefunctions to be flat, *i.e.* to be free from any resonance. However, it is well known from photoionization theory and experiments that ionic continua are often full of resonances, which lead to enhancements of the amplitude and jumps in the spectral phase of the photoionization dipole matrix element. If an electron wavepacket (EWP) is released in the continuum of its parent ion with a kinetic energy matching a continuum resonance, it can be trapped in a quasi-bound state for a while before leaving the vicinity of the ionic core. Since photorecombination can be seen a time-reversed photoionization event, if the recolliding EWP, in HHG, is coming back in the vicinity of its parent ion with a kinetic energy matching the continuum resonance, it can be trapped in the quasi-bound state for a while before radiatively recombining onto the electronic ground state. Taking into account such resonant effects in photorecombination has led to a refined model, known as the 4-step model of HHG, which was introduced by Strelkov in 2011 [Strelkov 2010]. The modulations of the photoionization (photorecombination) spectral amplitude and phase near the continuum resonances reflect the change in the ionization (recombination) dynamics in the time-domain when occurring near a resonance. These continuum resonances can also be used to generate highly-elliptical XUV photons, when driven by slightly elliptical driving laser pulses [Ferré et al. 2015a].

One of the last approximation made within the Leweinstein model that has been shown to breakdown is the participation of excited states of the neutral molecules during HHG. In 2014, Chini *et al.* demonstrated enhancement of narrow bandwidth VUV spectral components just below the ionization threshold of Argon [Chini et al. 2014b]. These resonantly enhanced structures (RES), measured by Chini *et al.*, are shown in Fig. 2.12.

Chini *et al.* demonstrated that these enhancements occur at the field-free Argon Rydberg states energies [Chini et al. 2014b]. They studied the CEP and ellipticity dependence of these below-threshold enhancements, and showed that the narrow spectral features behaved similarly as above-threshold harmonics. From simple Fourier transform arguments, the narrow spectral width of these spectral features suggests that they are emitted during on a long time-scale. Indeed, a recent theoretical paper by Camp *et al.*, had reported on the resonant emission mechanism from these highly-excited states during HHG [Camp et al. 2015]. They had demonstrated that the narrow-band emission at field-free Rydberg states

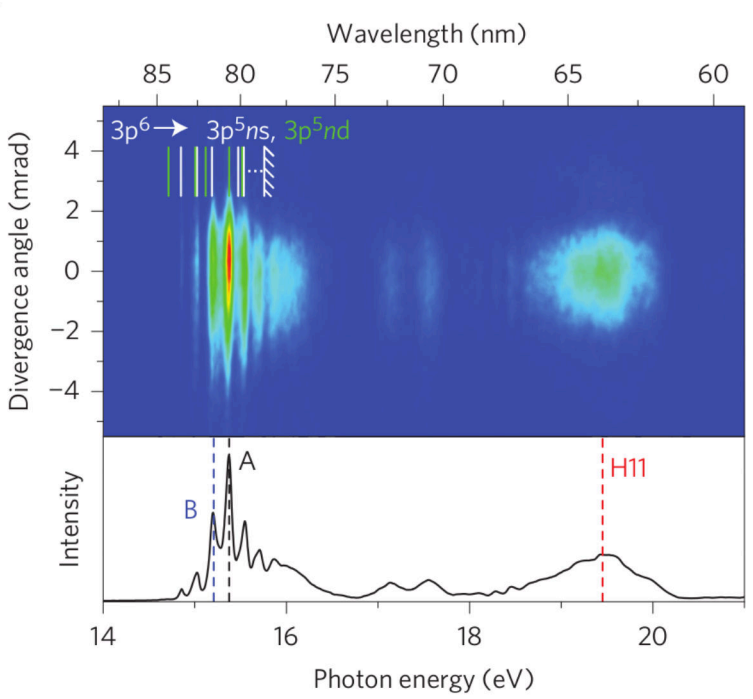

Figure 2.12: HHG spectrum recorded by driving Argon atom using few-cycle pulses, at an intensity of $\sim$ 3.3 x 10^{13} W/cm^2. The spectrum is characterized by resonant enhanced structures (for example, RES A and B) which lie within the energy range of the labelled $3p^6 \rightarrow 3p^5ns$ (white vertical lines) and $\rightarrow 3p^5nd$ (green vertical lines) Rydberg resonance of argon, concomitant with to the relatively broad, standard high harmonic (H11). This figure have been taken from [Chini et al. 2014b].

energies is emitted for times much longer than the pulse duration. On the other hand, following their CEP and ellipticity dependence of these resonant enhanced structures (RES), Chini *et al.* [Chini et al. 2014b] suggest that polarization gating technique could be used to temporally confine the below-threshold enhanced features. This would imply that these RES, at field-free Rydberg states energies, are associated with a sub-cycle process, with attosecond temporal structures.

The nature and the mechanism of the emission process near the ionization threshold and near resonances was thus still an open question. These paper were indeed published at the very beginning of my Ph.D. thesis, which stresses that all the subtleties behind HHG were not yet fully understood. In the next sub-section, we will show experimental strategies which aim at disentangling the contributions of subcycle electron recollisions and slower radiative processes, through the investigation of the spectral and temporal properties of HHG from argon, near the ionization threshold.

2.3.1 Searching for signatures of near-threshold resonant enhanced structures

In order to study the temporal properties of near-threshold resonant XUV emission, one first needs to be able to observe spectral features related to this emission. In the paper of Chini *et al.*, the below-threshold narrow bandwidth resonant enhanced structures (RES) have been observed while driving HHG in Argon using ultra-broadband NIR pulses of 5 fs duration and of moderate intensity ($\sim$ 3x10^{13} W/cm^2), see Fig. 2.12. Here, we will start by searching for spectral signature of RES in the emission spectrum of Argon, as a function of driving laser intensity for relatively long pulses (28 fs, directly after the grating

compressor) and for short pulses (7 fs, after the hollow-core fiber and chirped mirrors, as described in the previous chapter).

Before presenting the results, let us first describe briefly the experimental setup. The experiments were conducted using the AURORE laser system at CELIA, which delivers pulses centered around 800 nm, with 28 fs FWHM duration and containing up to 8 mJ at 1 kHz repetition rate. This beam can be directly used to drive HHG. The other option is to go through a post-compression setup, in order to generate few-cycle pulses. The post-compression setup installed at CELIA has been described in details in the last chapter of this thesis. Briefly, in this very precise experiment, we have focused up to 2 mJ into a 1.5 m long stretched hollow-core fiber which has a $\phi = 500\ \mu m$ inner diameter. The fiber was filled with a pressure gradient of Argon ($\sim$ 0 mbar at the entrance and $\sim$ 400 mbar at the exit of the fiber). The spectrally broadened pulses were compressed close to their Fourier transform limit by tailoring their spectral phases using 16 reflexions onto chirped mirrors (-50 fs^2 per bounce, PC70 Ultrafast Innovations) and linear propagation into a few millimeters of fused silica. The pulse energy was tuned by rotating a superachromatic half waveplate (Fichou), which was located in front of a broadband polarizer (Femtolaser).

The (multi-cycle or few-cycle) pulses were focused into a $\sim$ 250 μm thick effusive gas jet of Argon using a low-dispersive f = 37.5 cm spherical silver mirror located inside the (so-called 'generation') vacuum chamber. A differential pumping tube was installed between the generation chamber and the XUV spectrometer. The pressure was usually $\sim 10^{-2}$ mbar in the generation chamber and few 10^{-6} mbar in the XUV spectrometer. The XUV spectrometer was constituted of an entrance slit, a 1200 grooves/mm flat-field grating (Shimadzu) and a set of dual microchannel plates coupled to a fast P46 phosphor screen (Hamamatsu) that collect the first diffraction order of the grating. The fast decay time of the phosphor screen (99 % decay within $\sim 10^{-6}$ second) allowed us to make single-shot measurement of the HHG spectrum at 1 kHz. A 12-bit cooled CCD camera (PCO) is used to image the phosphor screen and to record the spatially resolved harmonic spectra.

We first studied the HHG spectrum of Argon driven by 28 fs pulses as a function of laser intensity, in order to determine if RES can be observed in these conditions. Figure 2.13(a) shows the spatially-resolved harmonic spectrum obtained using 7x10^{13} W/cm^2 pulses. The spectrum is constituted of a comb of narrow, equally spaced odd harmonics, separated by twice the laser frequency $2\hbar\omega_0$ = 3.1 eV. The field-free first ionization potential of Argon (15.76 eV) lies in between harmonic 9 and 11, and these two harmonics show rather similar spectral and spatial characteristics. The evolution of the spatially-integrated harmonic spectrum is shown in Fig. 2.13 (b) as the laser intensity increases from 2.5 to 7.0 x 10^{13} W/cm^2. There is no trace of RES or of any other resonant enhancement of the harmonic emission. This might be because the 'narrow' bandwidth of the laser pulses does not allow any multiphoton transition between the ground state and any Stark-shift excited states. It could also be that within these conditions, the RES emission is orders of magnitude weaker than the HHG emission, below the dynamical range of our XUV spectrometer.

In a second attempt to observe spectral signature of RES, we decided to use the same approach as Chini *et al.* and to drive HHG in Argon using few-cycle pulses. When the laser pulse duration decreases from 28 fs to 7 fs, the harmonic spectrum looks very different (Fig. 2.14(a)). First, the harmonics are much broader spectrally. This reflects the fact that the pulse train is composed of only few attosecond bursts. Moreover, the spectral bandwidth increases with the harmonic order. This is because the cut-off harmonics are emitted only during the few most intense sub-cycles of the laser pulse, resulting in a larger spectral

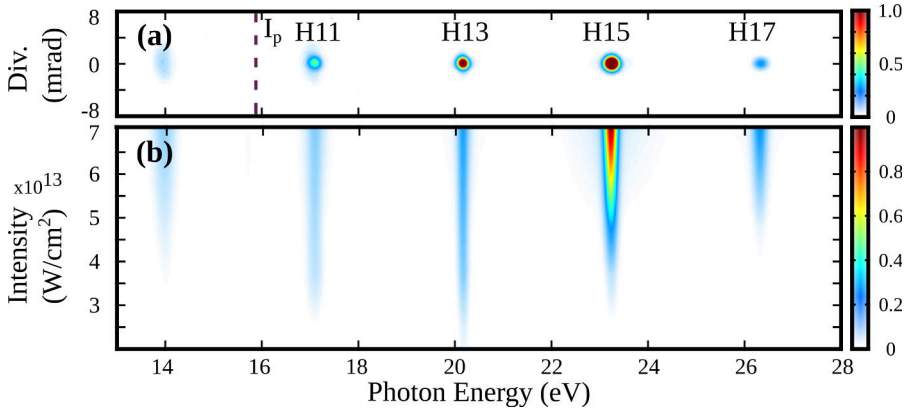

Figure 2.13: Intensity scaling of HHG in Argon using 28 fs drivers. In (a), the spatially resolved spectrum for an intensity of 7x10^{13} W/cm^2. In (b), the spatially integrated spectrum as a function of the driving laser intensity.

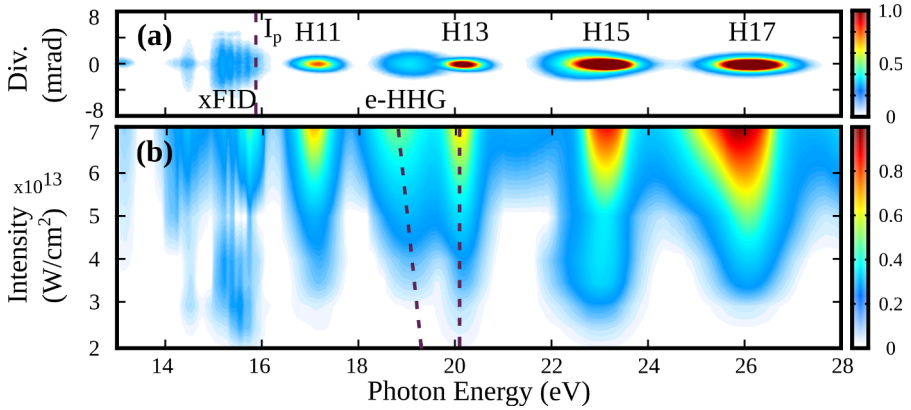

Figure 2.14: Intensity scaling of HHG in Argon using 7 fs drivers. In (a), the spatially resolved spectrum for an intensity of 7x10^{13} W/cm^2. In (b), the spatially integrated spectrum as a function of the driving laser intensity. This figure is adapted from [Beaulieu et al. 2016a].

bandwidth.

Apart from the spectral broadening of the harmonics, we also see new emission frequencies in the HHG spectrum driven by few-cycle pulses. First, there is a series a narrow spectral lines lying between 14.2 eV and 15.6 eV, *i.e.* just below the ionization threshold of Argon. This is clearly the signature of RES, as seen previously by Chini *et al.* [Chini et al. 2014b]. Second, we see a spectrally broad peak around 19 eV (between H11 and H13), which is slightly more divergent than the other harmonics. Last, we also observe a distinct shoulder on the red-wing of the H15, around 23 eV. The origin of these two new spectral features was, at this point, really puzzling to us.

2.3.2 Origin of near-threshold resonant enhanced structures

In the paper of Chini *et al.* [Chini et al. 2014b], the narrowband enhanced spectral component were overlapping with harmonics 9 (H9). In our case, these narrow spectral lines at Rydberg state field-free energies are lying in between H9 and H11. This suggests that these Rydberg lines are not resonantly enhancing the overlapping harmonics, but instead, it seems that they originate from a completely different emission mechanism, which seems to be decoupled from HHG. Digging into the literature, we found a recent paper by Camp *et al.*, that interpret these narrowband emissions as coming from XUV Free Induction Decay

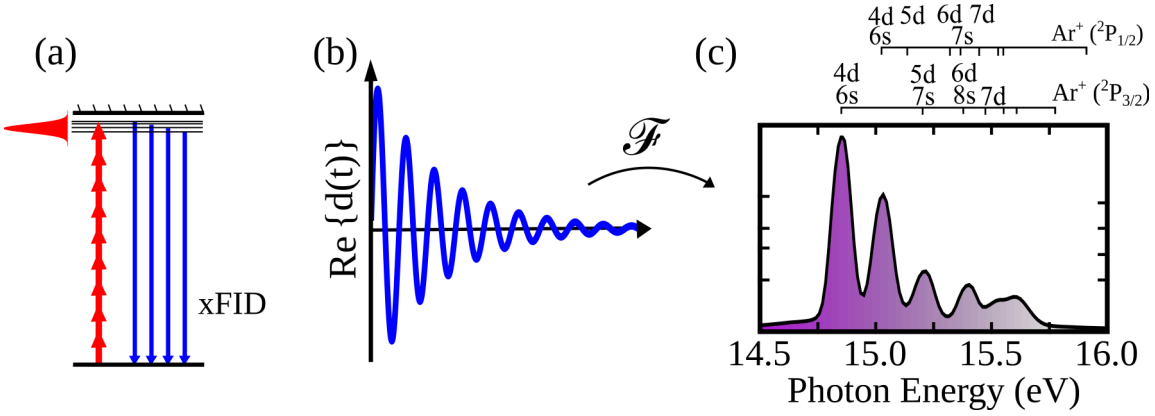

Figure 2.15: Schematic of xFID emission mechanism. (a) Multiphoton excitation creates an electronic wavepacket, made of the ground and few Rydberg states, in Argon atoms. This wavepacket can emits XUV radiation through xFID. (b) Schematic view of real part of the atomic dipole induced by the creation of an electronic wavepacket. (c) Spectrum of the emitted xFID radiation, upon the creating of an electronic wavepacket. The emission end up at the field-free Rydberg state energies.

(xFID) [Camp et al. 2015]. Moreover, we got aware that the group of Johan Mauritsson, in Lund, were working on laser-control of xFID induced by absoption of XUV pulses [Bengtsson et al. 2017]. Let us briefly describe what we mean by xFID. For a schematic representation of the xFID emission mechanism, see Fig. 2.15

When argon atoms in their ground state (E_g) are illuminated by a moderately strong laser pulse, few excited states E_n can be coherently populated by the multiphoton transition from the ground state. The creation of this electronic wavepacket leads to a time-dependent atomic dipole that oscillates at all frequencies corresponding to all level spacing within the wavepacket. A schematic of the time-dependent atomic dipole is shown in Fig. 2.15. In the absence of decoherence, these oscillations are damped by the lifetime of the excited states. The lifetime of this superposition of states (wavepacket) is typically much longer than the duration of the laser pulse. These oscillating atomic dipoles are associated with the coherent emission of light, at energies $E_n - E_g$. This dipole emission mechanism is what we call xFID. This mechanism is similar that fluorescence. However, FID is coherent while fluorescence is incoherent.

In order to gain more information about these new spectral features, we decided to monitor the XUV spectrum as a function of driving laser intensity (Fig. 2.14(b)). Let us first focus on the xFID lines. Their position is remarkably stable with increasing laser intensity. This is due to the fact that xFID occurs mostly after the laser pulse, *i.e.* is emitted by field-free atoms. As the intensity increases, new xFID lines appear at lower photon energies. The laser-induced Stark-shift increases the energy the low Rydberg states, bringing them in resonance with an 11 photon transition from the ground state. These populated states decay radiatively after the laser pulse is off, and emit at their field-free energy.

The spectrally broad feature located around 19 eV exhibits a completely different intensity dependence. This peak appears at an intensity of $\sim$ 3.5 x10^{13} W/cm^2 and undergoes a linear spectral red-shift, with a slope of $\sim 1.2 \times 10^{-11}$(meV $\cdot$ cm^2)/W. The shift indicates that this spectral component is emitted when the laser field is on (on the contrary that xFID). However, at this point, the sign of the slope (red-shifting with intensity) and more fundamentally, the origin of this component was still not understood. We thus asked our colleague Fabrice Catoire to perform TDSE simulation in order to try to

grasp the origin of this new spectral feature in HHG.

2.3.3 1D TDSE and the origin of new spectral component in HHG

Fabrice Catoire performed Time-Dependent Schrödinger Equation calculations of HHG in Argon using few-cycle laser pulses. In its most general form, the TDSE is expressed as:

$$i\hbar\frac{\partial}{\partial t}|\psi(\mathbf{r},t)\rangle = \hat{\mathcal{H}}|\psi(\mathbf{r},t)\rangle \tag{2.4}$$

where $|\psi(\mathbf{r},t)\rangle$ is the quantum mechanical wavefunction of the system, which depends on both space $\mathbf{r}$ and time t and where $\hat{\mathcal{H}}$ is the Hamiltonian describing the field-free atom and its electric dipole interaction with the laser field.

Solving exactly the 3D-TDSE for a real (multielectron) Argon atom in a strong laser field is impossible. One thus needs to make several approximations. In our case, we used the well known *Single Active Electron* (SAE) approximation, in which only one electron interacts with the laser field while all others act as frozen spectators. While this greatly simplifies the resolution of the TDSE, this prevents tackling physical effects involving multi-electrons interaction (*e.g.* autoionization or giant resonance). In addition, in order to speed up the calculation time, we reduced the 3D problem to a single dimension (1D-TDSE). This kind of reduced-dimensionality model is very useful to extract qualitative information about the ongoing physics. The wavefunction can thus be rewritten in 1D $|\psi(\mathbf{x},t)\rangle$.

To mimic the Argon atom, Fabrice used a soft-core model potential with asymptotic Coulomb tail and with the same ionization potential than Argon. The spectrum of this potential does not only support a ground state but also many excited states, enabling us to study the possible effects of excited states in HHG. Alternatively, one can use a screened Coulomb potential, which does not have any excited states, to remove any possible effect of excited states in the response of the atom to the strong laser field. The external laser field that is plugged into the TDSE is a 7 fs FWHM Fourier transform limited pulse centered around 800 nm, which is really similar to the pulses used in the experiments. Solving the TDSE gives us the time-dependent wavefunction of the system. Using $|\psi(\mathbf{x},t)\rangle$, the full HHG spectrum $S(\Omega)$ can be calculated:

$$S(\Omega) = \left|\mathcal{F}\left[\langle\psi(\mathbf{x},t)|\hat{d}|\psi(\mathbf{x},t)\rangle\right]\right|^2 \tag{2.5}$$

where $\mathcal{F}$ represents the Fourier transform and where $\hat{d}$ is the dipole operator [1]. The harmonics spectrum can thus be seen as the Fourier transform of the time-dependent dipole (or dipole velocity, or dipole acceleration) of the laser-driven atom. Moreover, the distribution of the XUV field in the near-field (at the focus of the driving laser) was calculated by solving the TDSE for different laser pulse peak intensities. This allows to obtain the spatial distribution of the XUV in the far-field by calculating the Hankel transform [2] of the near-field distribution. This procedure neglects the longitudinal phase matching effects, which is justified by the thin nature of the gas jet used in the experiments, compared to the laser beam confocal parameter.

It is important to note that these calculations should only be compared qualitatively with the experiment, since the approximation that we made render the simulation blind to

[1] The HHG spectrum can, in principle, be calculated using the dipole, the velocity and the acceleration forms.

[2] The Hankel transform is an extension of Fourier transform, for a 2D function in polar coordinate.

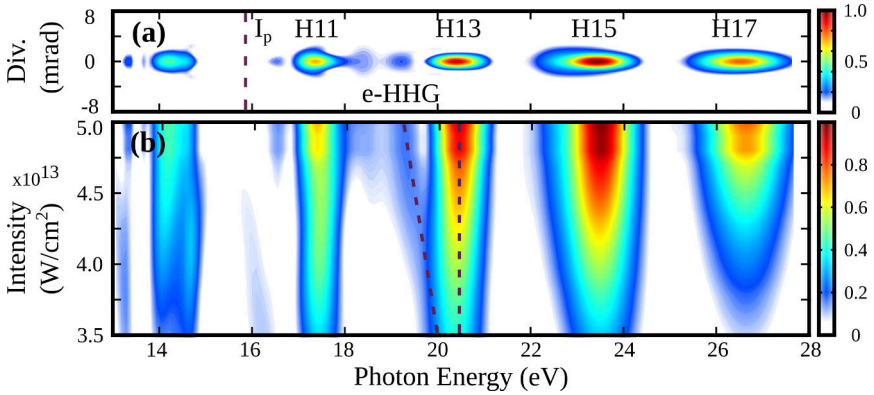

Figure 2.16: 1D TDSE simulation of HHG in Argon using 7 fs drivers. In (a), the spatially resolved spectrum for an intensity of 5 x 10^{13} W/cm^2. In (b), the spatially integrated spectrum as a function of the driving laser intensity. This figure is adapted from [Beaulieu et al. 2016a].

a lot of physics that can append 'in real life'. First, the excited states of the model potential lie at very different energies than the ones in a real Argon atom. Second, the number of excited states is also very different in the model than in the real atom. Furthermore, the fact that we solve the reduced-dimensionality 1D-TDSE significantly reduces the computational cost of the calculations and allows us to explore a greater sub-space of laser parameters, but it comes with a price to pay: some information about the symmetry of the Rydberg states are lost, for example. However, while keeping these limitations in mind, we will see how 1D-TDSE calculations helped up to grasp the origin of these new 'mysterious' spectral features in HHG.

Figure 2.16 (a) shows the far-field spatio-spectral distribution of the XUV calculated for a peak intensity of 5 x 10^{13} W/cm^2. Remarkably, the spectral component between H11 and H13 (around 19 eV) and the shoulder on the red-wing of the H15 show up in the simulated spectrum. The xFID lines are not clearly visible since we did not take into account the dipole response of the system after the end of the laser pulse. Figure 2.16 (b) shows the intensity dependence of the spatially integrated HHG spectrum. The spectral component around 19 eV experiences a spectral red-shift with increasing intensity, exactly like in the experiment. This observation seems to indicate that the 1D-TDSE is able to tackle the main physical features behind the generation of this new spectral feature. The slope of the spectral shift is found to be $\sim$ 2.5 x 10^{-11}(meV $\cdot$ cm^2)/W, which is roughly twice larger than the experimental value. The calculation was repeated by replacing the soft-core potential with a screened Coulomb potential. Unlike the soft-core potential, the screened Coulomb potential does not support any excited state. Using the screened Coulomb potential, the spectral feature around 19 eV completely disappears, indicating the fundamental role of the excited states in the generation of this component. The data are not presented here.

We are now convinced that the excited states play a central role in the generation of the new spectral component around 19 eV. From now on, we will thus call this new spectral component e-HHG (which stands for excited states-HHG). The next step of our analysis will be to try to answer the following question: do the excited states play a role in the photoionization or in the photorecombination step, for the generation of e-HHG? To do so, we recalculated the harmonic spectrum by projecting the total wavefunction onto different eigenstate (n) of the Hamiltonian. By doing so, we can isolate the contribution of each state in the photorecombination step, *i.e.* we can extract the emission resulting from recombination on each eigenstate of the system. The results are shown in Fig. 2.17.

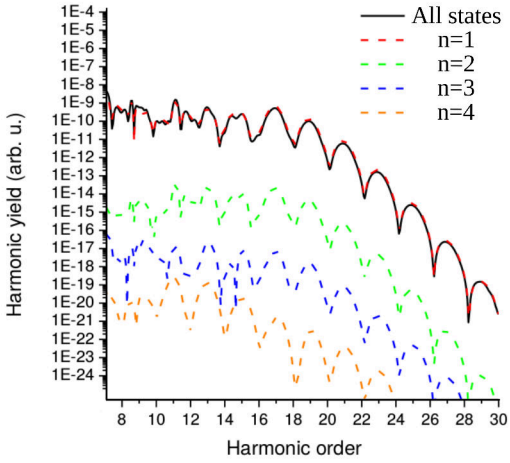

Figure 2.17: Analysis of the state on which the radiative recombination occurs. By projecting the dipole operator on different eigenstates (n) of the Hamiltonian, we can see the contribution of recombination on specific eigenstate to the total HHG yield.

The solid black curve is the HHG spectrum when recombination onto all eigenstates of the system is taken into account. The dashed red, green, blue and orange curves are respectively the HHG spectra produced by photorecombination on n=1 (ground state), n=2, n=3 and n=4 states. This analysis tells us that the recombination (almost) always occurs onto the ground electronic state of the system. Thus, the role excited state in the generation of the new spectral component around 19 eV must somehow be important during the photoionization step.

At this point, we know that the generation of e-HHG involves the excited states in the photoionization step. However, we still do not understand i) the details of the generation mechanism and ii) the reason of the spectral red-shift with laser intensity, which is observed in both the experiment and the calculation. In the next subsection, we will perform a time-frequency analysis (Gabor transform) of the time-dependent dipole calculated using 1D-TDSE is order to track the temporal dynamics of the emission of this new spectral feature (e-HHG).

2.3.4 Gabor transform of the time-dependent dipole

In order to extract the information about the time-dependent emission of harmonics, we will use a powerful tool which is called time-frequency analysis. Time-frequency analysis allows one to study a signal in time and frequency domain simultaneously. Let us consider a one-dimensional time-dependent signal. The Fourier transform of this signal would give the amplitudes and phases of all frequency components that compose the time-dependent signal. However, the spectral (frequency) content can evolve within the time duration of the signal. In order to time-resolve the frequency content of a signal, one can use short-time Fourier transform methods, which consists of Fourier transforming local sections of a signal. More sophisticated methods based on wavelet transforms also exist, but were not found to be necessary here. The equation governing the short-time Fourier transform is relatively simple:

$$G(\Omega,\tau) = \int_{-\infty}^{+\infty} d(t)W(t-\tau)e^{-i\Omega t}dt \tag{2.6}$$

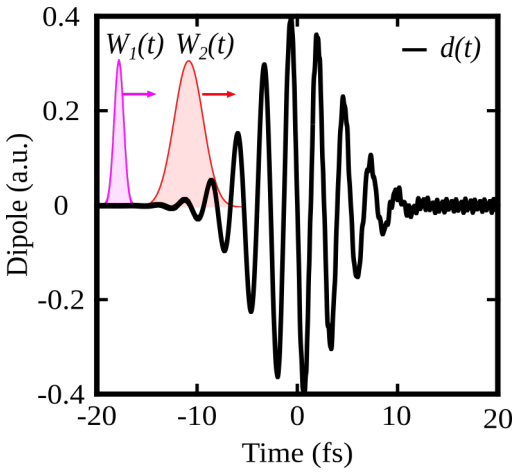

Figure 2.18: Scheme of the Gabor transform of the time-dependent dipole calculated using 1D-TDSE (in black). In pink ($W_1(t)$) and in red ($W_2(t)$), are examples of different Gaussian window functions that can be used to perform the Gabor transform.

where $G(\Omega,\tau)$ is the time-frequency representation of the signal $d(t)$, $W(t)$ is the so-called window function and τ is the temporal offset between the center of the window function and the center of the signal. This equation represents the Fourier transform of the $d(t)$ multiplied by the window function ($W(t)$), evaluated a time $t-\tau$. By sliding the window function across the signal, one can thus obtain the frequency content of the signal as a function of τ. This lead to a 2D time-frequency representation (also called spectrogram) of the signal. When the window function is a Gaussian function, the short-time Fourier transform is called Gabor transform.

Figure 2.18 is schematic representation of the Gabor transform of the time-dependent dipole $d(t)$ calculated using 1D-TDSE (solid black line). $W_1(t)$ and $W_2(t)$ represents two Gaussian window function of different widths. By Fourier transforming the $d(t)W_1(t-\tau)$ as a function of τ, we can reconstruct the time-frequency map of the HHG emission. Moreover, because time and frequency are conjugated variables, the width of the window function defines the temporal and the spectral resolution of the spectrogram. If the width of the window function is narrow, we obtain a good time resolution but a poor spectral resolution. On the contrary, by using a broad window function, the temporal resolution is poor while the spectral resolution is high. This can also be seen as a consequence of the convolution theorem. One thus needs to adapt the width of the window function to the needed temporal and spectral resolution. Unfortunately, one cannot have the cake and eat it too.

To extract the dynamics underlying the harmonic emission, we will now present the Gabor analysis of the time-dependent dipole obtained by solving the 1D-TDSE. Figure 2.19 (a) shows the spectrogram of HHG using a 0.75 optical cycle ($\sim$ 2 fs) FWHM Gaussian window function. This window function is temporally sufficiently broad to resolve the emission of each discrete harmonic peaks. However, it does not provide enough temporal resolution to resolve the sub-cycle dynamics of the HHG emission. Figure 2.19 (b) shows the laser electric field used in the TDSE. The emission of H5 to H19 increases monotonically on the leading edge of the laser pulse, from the beginning to roughly 1 fs. The femtosecond chirp of the harmonics can be seen (redshift with time) for the highest harmonics. The most interesting physics emerge after the maximum of the laser pulse. First, long-lasting lines of xFID emission appear between 7 and 14 eV. They correspond to the dipole emission from the coherent superposition between ground and excited states

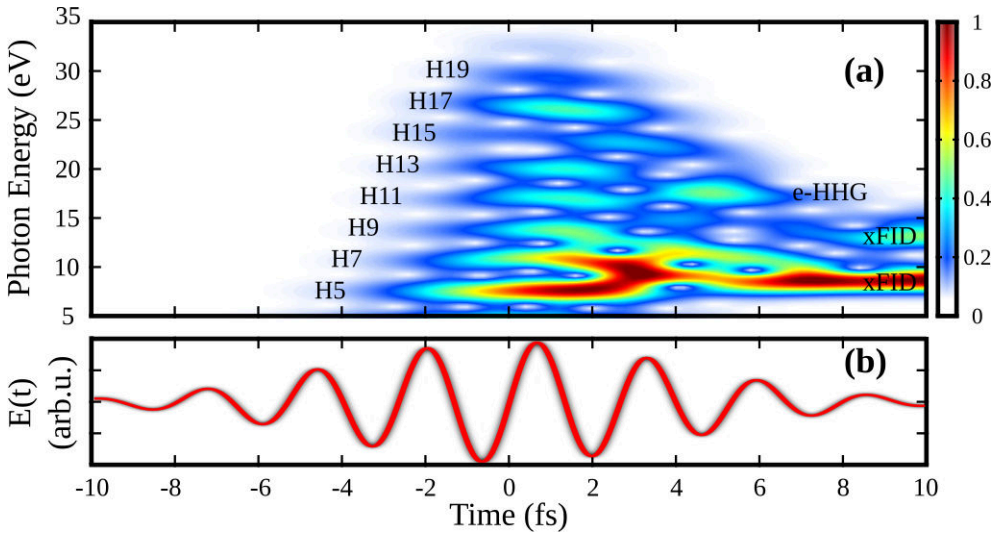

Figure 2.19: Gabor analysis of the TDSE dipole, at $I_0 = 5.0 \times 10^{13}$ W/cm^2 (a) Gabor analysis using a 0.75 optical cycle FWHM Gaussian window function (b) Laser electric field used in the calculations. This figure is adapted from [Beaulieu et al. 2016a].

that still lasts after the laser pulse. In addition, one can see a spectrally and temporally localized emission between H11 and H13 roughly 4 fs after the maximum of the field. This localized emission in the time-frequency space is exactly at the energy where we expected the new spectral component to show up. The Gabor analysis tells us that this spectral component is emitted in a well-defined region in the falling edge of the pulse. This is exactly the kind of information that was missing to explain the origin of the red-shift of this spectral component with increasing laser intensity.

As explained above (see Fig. 2.7 and equation 2.2), the HH emitted on the rising edge of the pulse are spectrally blue-shifted while the HH emitted on the trailing edge are red-shifted. This can be explained by the fact that the instantaneous frequency of the q-th order harmonic (short (s) and long (l) trajectories) is described by : $\Omega_q^{s,l}(t) = q \cdot \omega_0 + \alpha_q^{s,l} \partial I_0(t)/\partial t$. Because the e-HHG component is emitted on the trailing edge, $\partial I_0(t)/\partial t$ is negative, and the emission should experience a red-shift with respect to HH emitted symmetrically on both edges of the pulse. Moreover, as the intensity is increased, $\partial I_0(t)/\partial t$ becomes more negative, and the red-shift should be larger. The origin of the spectral red-shift of the e-HHG is thus now well understood in terms of delay in the emission, thanks to the TDSE calculation.

In order to reveal the sub-cycle dynamics of the HHG process, we will now perform the Gabor analysis of the time-dependent dipole using a much narrower window function (0.2 optical cycle, $\sim$ 530 as). Before presenting the results, let us discuss what is expected, within the Lewenstein model [Lewenstein et al. 1994]. Indeed, by solving the Leweinstein saddle point equations, we can retrieve the emission times (which are the recombination times), for each trajectory (short and long) leading to each harmonic and that, for each laser sub-cycle [Lewenstein et al. 1994]. The results of this analysis are presented in Fig. 2.20 (a). The calculations were performed by running the Lewenstein/SFA code written by Baptiste Fabre. It reveals branches associated with the emission of attosecond pulses from short and long trajectories, with respectively a positive and negative slope. These slopes are associated to the chirp of the attosecond emission (attochirp [Mairesse 2005; Varju et al. 2005]). We can also notice that in the cut-off, only one trajectory is observed. These branches thus provide a lot of powerful insights into the spectro-temporal dynamics

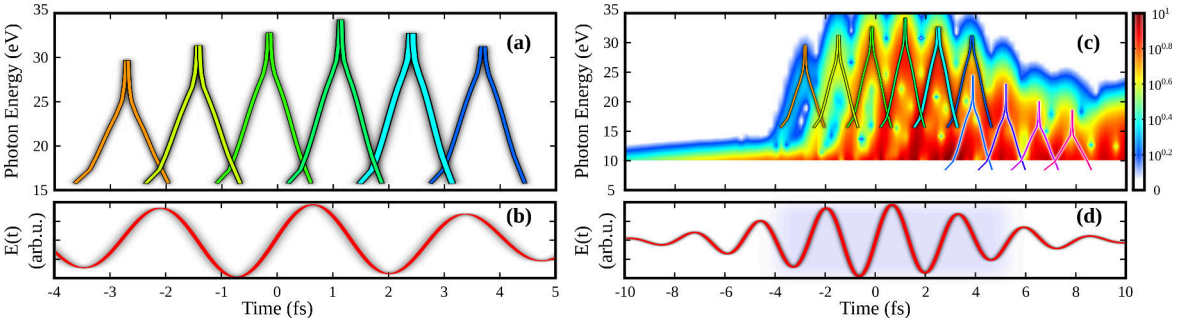

Figure 2.20: Attosecond dynamics underlying high-order harmonic generation. In (a) recombination (emission) time for short- and long- quantum trajectories calculated using the Lewenstein model. In (c) Gabor analysis of the TDSE dipole, at $I_0 = 5.0 \times 10^{13}$ W/cm^2, using a 0.2 optical cycle FWHM Gaussian window function. The superimposed colored branches represent the emission times from short- and long- quantum trajectories calculated with the Lewenstein model. The upper branches (from -10 fs to 4 fs) correspond to both ionization and recombination from/to the ground state. The lower branches (4 fs to 10 fs) involve ionization from the excited state and recombination to the ground state. In (b) and (d),is the laser electric field used for the TDSE calculation. This figure is adapted from [Beaulieu et al. 2016a].

of HHG emission.

In Fig. 2.20 (b), we have superimposed these branches, calculated using the Lewenstein model, to the high temporal resolution Gabor analysis of the dipole. We notice that up to $\sim$ 4 fs, the high temporal resolution Gabor analysis of the dipole and SFA branches results are in remarkable agreement. However, after $\sim$ 4 fs, lower energy components show up and dominate the emission. These late-time low energy components cannot be explained using the conventional emission time of the Lewenstein model anymore.

Because we know that the e-HHG, emitted on the trailing edge of the pulse, involves the participation of excited states in the ionization step, we formulated the hypothesis that this process could be initiated by multiphoton excitation of electrons, followed by ionization, acceleration, and recombination. From the Gabor analysis of the TDSE (see Fig. 2.19 (a)), we see from the xFID emission after the laser pulse that an excited state lying around 8.9 eV is strongly populated. We thus calculated the SFA quantum trajectories for the scenario where the ionization takes place from the excited state at 8.9 eV followed by the recombination on the ground state. This process produces an additional comb of high-order harmonics red-shifted in energy by 8.9 eV, in agreement with the Gabor analysis of the dipole obtained using TDSE calculations 2.20. Since, in this situation, the ionization potential is reduced to 6.9 eV (I_p of the ground state: 15.76 eV, minus the energy of the excited state: 8.9 eV), the cutoff of this second harmonic spectrum is predicted to appear around 20 eV. Thus, the component emitted around 19 eV at $\sim$ 4 fs can be assigned to the cutoff of the e-HHG process.

We now have a pretty good interpretation of this new e-HHG mechanism. In the trailing edge of the pulse, when the ground state is in multiphoton resonance with the Stark-shifted excited states, it can help to initiate quantum trajectories which are described by ionization from the excited state and recombination onto the ground state. This emission is temporally delayed with respect to the maximum of the laser field (and with respect to non-resonant HHG), which explains its spectral redshift with increasing laser intensity. Together with the theory group from Louisiana State University (Seth Camp, Kenneth Schafer and Mette Gaarde), we recently published a follow-up paper where we studied in great details the delayed (and spectrally-shifted) resonant-enhanced near-

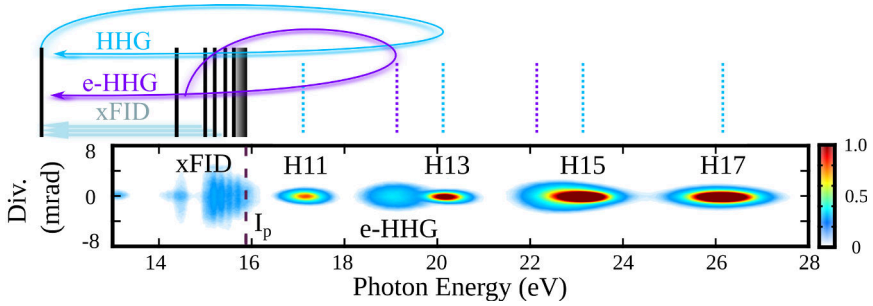

Figure 2.21: Scheme of the different process governing the near-threshold emission of strong-field-driven Argon atoms. Below the threshold, xFID emission occurs as a consequence of the creation of a coherent superposition of electronic states. Above the ionization threshold, standard harmonic (H11 to H17) are observed. Moreover, between standard non-resonant HHG, we also observe e-HHG emission, characterized by ionization from excited states and recombination onto the ground state.

threshold HH emission [Camp et al. 2018]. Figure 2.21 summarizes the different processes governing the near-threshold emission of strong-field-driven Argon atoms. We will now use the experimentally measured spatial profile of e-HHG and neighboring non-resonant HH to extract the atomic dipole phase coefficient of this new type of resonantly initiated quantum trajectories.

2.3.5 Experimental determination of the atomic dipole phase coefficient of e-HHG

As explained at the beginning of this chapter, the far-field spatial profile of the XUV (I_q^{far}) encodes information about its near-field spatial intensity (I_q^{near}) and phase ($\phi_q^{s,l}$) distributions. The harmonic phase front is determined by the atomic phase : ($\phi_q^{s,l} = \alpha_q^{s,l} I_0^{near}$, where I_0^{near} is the near-field laser intensity profile and $\alpha_q^{s,l}$ is the atomic dipole phase coefficient, which is directly determined by the excursion time (time between ionization and recombination) of the quantum trajectories giving rise to harmonic q. Thus, measuring the far-field divergence of a given harmonic can provides information on the sub-cycle electronic dynamics leading to its emission.

Let us first compare the far-field spatial profile of the non-resonant H13 (Fig. 2.22(a)), of e-HHG (Fig. 2.22(b)) and of xFID (Fig. 2.22(c)) as a function of the driving laser intensity. The emission of above-threshold non-resonant H13 is very collimated, with a ≈ 1 mrad divergence while the fundamental laser divergence is above 10 mrad. This emission hardly shows any spatial broadening as the laser intensity increases. This means that the harmonic phase front in the generating medium is quite independent of the laser intensity, i.e. $\alpha_{13}^{s} \approx 0$, and that the far-field spatial profile of H13 I_{13}^{far} is Fourier transform limited. This profile and its Gaussian fits are shown in Fig. 2.23 (a)(I_{13}^{far}).

The spatial profile in the far-field is given by the Fraunhofer diffraction of the radiating dipole in the near-field (and vice-versa),

$$I_{13}^{near} = \left| \mathcal{F}\left(\sqrt{I_{13}^{far}} \right) \right|^2 \tag{2.7}$$

Because we know that the far-field spatial profile is Fourier transform limited (flat atomic dipole phase in the near-field), we can retrieve the intensity profile of H13 in the near-field using equation 2.7. Since HHG is a highly non-linear phenomenon, we

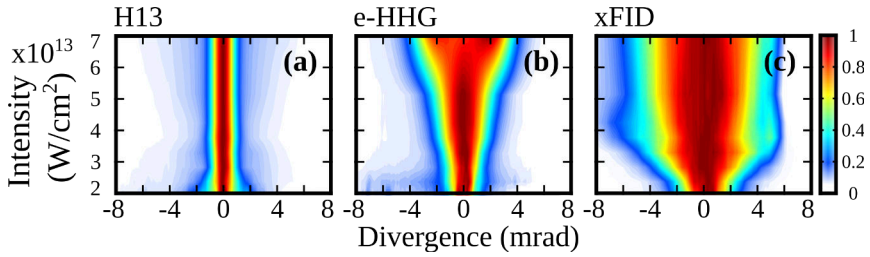

Figure 2.22: Divergence as a function of intensity for different spectral features. In (a) for non-resonant H13 ($\sim$ 20 eV), in (b) for e-HHG ($\sim$ 19 eV) and in (c) for xFID ($\sim$ 15 eV) . Note that the saturation of the xFID divergence at high intensity, in (c), is due to clipping onto a limited aperture in the experimental setup. This figure is adapted from [Beaulieu et al. 2016a].

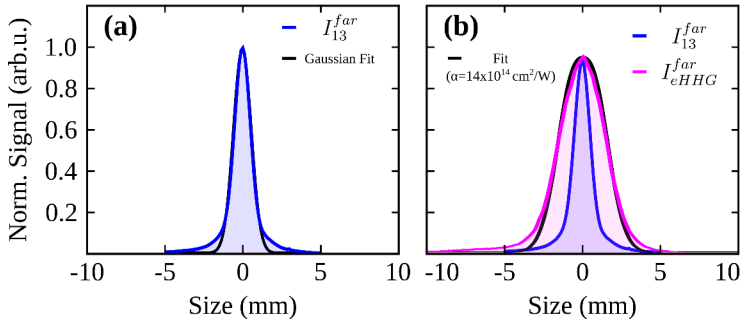

Figure 2.23: Experimental determination of the atomic dipole phase coefficient α of e-HHG. In (a) the spatial profile of the H13 in the far-field (blue), and in black, its Gaussian fit. In (b), the pink line represents the far-field spatial profile of the e-HHG emission. The blue line represents the spatial profile of H13 in the far-field. The black line represents the fitted spatial profile of e-HHG in the far-field using α as a free parameter. The peak intensity of the laser field was 7 x 10^{13} W/cm^2.

also know that the near-field intensity profile of the XUV (I_{13}^{near}) is given by the laser intensity profile I_0^{near} to the power of the effective nonlinearity q_{eff} of the non-linear process: $I_{13}^{near} = (I_0^{near})^{q_{eff}}$. Measuring the H13 harmonic signal as a function of the driving laser intensity enables us to determine the effective non-linearity, which is, in this case, $q_{eff} = 3.9$. Using this experimentally measured quantity, we can thus find the intensity profile of the fundamental laser beam in the near-field I_0^{near}. This quantity is important since it is involved in determining the curvature of the harmonic phase in the near-field through the relationship $\phi_q^{l,s} = -\alpha_q^{l,s} \cdot I_0^{near}$.

Next we determine the effective nonlinearity of the e-HHG emission by measuring the total e-HHG signal as a function of laser intensity, and deduce the near field harmonic profile I_{eHHG}^{near}. We fit the far field profile I_{eHHG}^{far} using the following equation, with α_{eHHG} as a fitting parameter:

$$I_{eHHG}^{far} = \left| \mathcal{F}^{-1}\left(\sqrt{I_{eHHG}^{near}} \cdot e^{i\alpha_{eHHG} I_0^{near}} \right) \right|^2 \tag{2.8}$$

This procedure allows us to experimentally extract the value of α_{eHHG}.

The results of this fitting procedure are shown in Fig. 2.23 (b), where the far-field intensity profile for H13 (in blue) and e-HHG (in pink) are compared. The non-zero atomic dipole phase curvature of e-HHG leads to a much larger divergence compared to the Fourier transform limited H13. By using equation 2.8 to fit the far-field intensity profile of e-HHG, we found $\alpha_{eHHG} = (14 \pm 1) \cdot 10^{-14}$cm^2/W. The error bar was obtained by

repeating the fitting procedure for different laser intensities. This value of the atomic dipole phase coefficient typically corresponds to long trajectories of the end of the plateau, close to the cut-off (see Fig. 2.5). This agrees well with the e-HHG mechanism described above, where the quantum trajectories are initiated from the excited states and radiatively recombine into the ground state. The new information provided by this analysis is the fact that the quantum trajectories leading to e-HHG are near cut-off long trajectories, *i.e.* trajectories with long excursion time in the continuum.

We have performed the same analysis for the xFID emission and found a $\alpha_{xFID} = (33 \pm 5) \cdot 10^{-14}\text{cm}^2/\text{W}$. However, one needs to keep in mind that the xFID emission mechanism in fundamentally different that the one of HHG. Thus, the relation between the α_{xFID} and the excursion time is meaningless in the case of xFID. This large values of α_{xFID} tell us that the phase of the xFID is very sensitive to the laser intensity. We will see why this is the case in the next section of this chapter.

Our understanding of this new mechanism called e-HHG is getting pretty refined. Indeed, we know that this emission involves long quantum trajectories initiated by multi-photon resonance from the ground to excited states. We also observed that this spectral feature undergoes a spectral red-shift when intensity is increased. This behavior can be explained using the Gabor analysis of the time-dependent dipole calculated using TDSE which reveals that the e-HHG emission is temporally delayed, *i.e.* is emitted on the falling edge of the laser. At this point, we would like to be able to experimentally demonstrate this temporal emission delay of e-HHG with respect to the non-resonant HHG. However, this delay is theoretically predicted to be less than 2 optical cycles (sub-5 fs). A conventional pump-probe scheme thus does not seem to be well suited to experimentally access this relatively small delay. We decided to use an ingenious scheme to access the emission time of harmonics on the optical cycle time-scale: the attosecond lighthouse.

2.3.6 Experimental time-frequency mapping of HHG using the attosecond lighthouse

One of the great challenges of attosecond science is to be able to gate the HHG emission in order to produce Isolated Attosecond Pulse (IAP) instead of Attosecond Pulse Train (APT). As mentioned in the previous chapter, researchers have developed different gating schemes (ionization gating [Ferrari et al. 2010], amplitude gating [Goulielmakis et al. 2008], polarization gating [Sansone et al. 2006] and double optical gating [Mashiko et al. 2008]) in order to temporally confine the HHG emission to a single half-cycle, resulting in the generation of IAP. In 2012, Vincenti and Quéré [Vincenti et al. 2012] came with a very elegant idea, that they called the *attosecond lighthouse*, to isolate a single attosecond burst from an attosecond pulse train, by using *Spatio-Temporal Couplings* (STC) in ultrashort light beams.

It is often assumed that electric field of laser pulse $E(\mathbf{r},t)$ can be decomposed in a product a of a spatio-dependent electric field $E_{\mathbf{r}}(\mathbf{r})$ and a time-dependent electric field $E_t(t)$: $E(\mathbf{r},t) = E_t(t) \cdot E_{\mathbf{r}}(\mathbf{r})$. This separation implies that the spatial properties of the electric field are time-independent and that the temporal properties are homogeneous in space. Such beam is said to be free of any *Spatio-Temporal Coupling* (STC). However, when working with ultrashort laser pulses, which are characterized by their extremely broad spectral bandwidth and their high intensity, it is usually hard to avoid STC. For instance, intense laser beams experience self-phase modulation when they propagate into any medium. This nonlinear effect induces a change of the spectral properties of the pulses, which depends on the local laser intensity and is thus intrinsically inhomogeneous, inducing STC. The situation is more critical when laser pulses travel through angularly dispersive media (*e.g.* a prism), because each spectral component propagates at a different

angle and group velocity in such medium. Working with ultrashort laser pulses thus requires careful alignment of such optical components (*e.g.* grating and prism compressor) to avoid the introduction of any STC in the beam.

When focusing an intense broadband Gaussian laser beam free of any STC, to generate HHG for example, all the spectral components are focused at the same position. This means that the spectral and temporal properties are homogeneous across the laser focus. This also implies that the wavefront at the focus is flat. Since the attosecond bursts are emitted perpendicular to the instantaneous wavefront of the laser, and because the wavefront of an STC-free beam is time-independent, all the attosecond bursts that form the attosecond pulse train propagate together, in the same direction than the driving laser pulse.

The attosecond lighthouse effect relies on the introduction of a controlled STC in a laser beam, to send consecutive attosecond bursts from the train in different directions [Vincenti et al. 2012]. The schematic of the experimental implementation is shown in Fig. 2.24, taken from [Kim et al. 2013]. The technique makes ingenious use of angularly dispersive optical element (wedges) to introduce an ultrafast wavefront rotation (WFR) at the focus of the beam. By placing a pair of well-misaligned wedges in the collimated beam, angular dispersion is introduced in the beam, which translates in a spatial chirp at the focus: the blue and red edges of the laser spectrum are focused into different places, vertically shifted (Fig. 2.24(b)). This spatial chirp induces an ultrafast WFR, meaning that the wavefronts for differents half-cycle are not parallel (Fig. 2.24(c)). Because XUV bursts are emitted perpendicular to the laser wavefront, each attosecond burst propagates in a different direction, as one can see in Lewenstein/SFA calculations presented in Fig. 2.24 (d). The spatially resolved spectrum of the XUV light produced by driving HHG using a beam with ultrafast WFR is shown in Fig. 2.24 (e) (also Leweinstein/SFA calculations). In combination with spatial filtering in the far-field, the attosecond lighthouse effect can thus be used to produce a source of multiple IAP. Recently, Hammond *et al.* [Hammond et al. 2016] performed a temporal characterization (streaking measurement) of the three most intense beamlets generated by the attosecond lighthouse, and confirmed that they were isolated attosecond pulses.

Another advantage of the attosecond lighthouse is that it is relatively easy to implement in the laboratory: all you need is to put wedges in the beam. A short duration of the laser pulse ensures a better angular separation of the beamlets in the far-field; it is thus better to drive the attosecond lighthouse effect using few-cycle pulses. The propagation direction of the beamlets also depends on the CEP of the laser pulse. Thus, one need to have a CEP stable laser in order to send the beamlets is the same direction from shot-to-shot. On the others hand, in the first paper introducing the attosecond lighthouse effect, Vincenti and Quéré formulated the idea of using the single-shot far-field profile of the XUV emitted from the attosecond lighthouse to perform an *in situ* tagging of the CEP of the laser [Vincenti et al. 2012]. However, this idea was never demonstrated experimentally.

Here, we decided to use the attosecond lighthouse effect to a completely different end, *i.e.* to perform a spatio-temporal mapping of the XUV emission and to obtain temporal information on the generation mechanism. This is the experimental analog of Gabor transforming the time-dependent dipole calculated TDSE. We will see that the attosecond lighthouse can, in fact, be an invaluable tool to study the electronic dynamics governing HHG on the time-scale of the optical cycle.

In order to introduce an ultrafast wavefront rotation in our experiment, we introduced a pair of wedges in the few-cycle laser beam and drove HHG in argon. We looked at the spatially-resolved spectrum of the driving laser at its focus to make sure that we

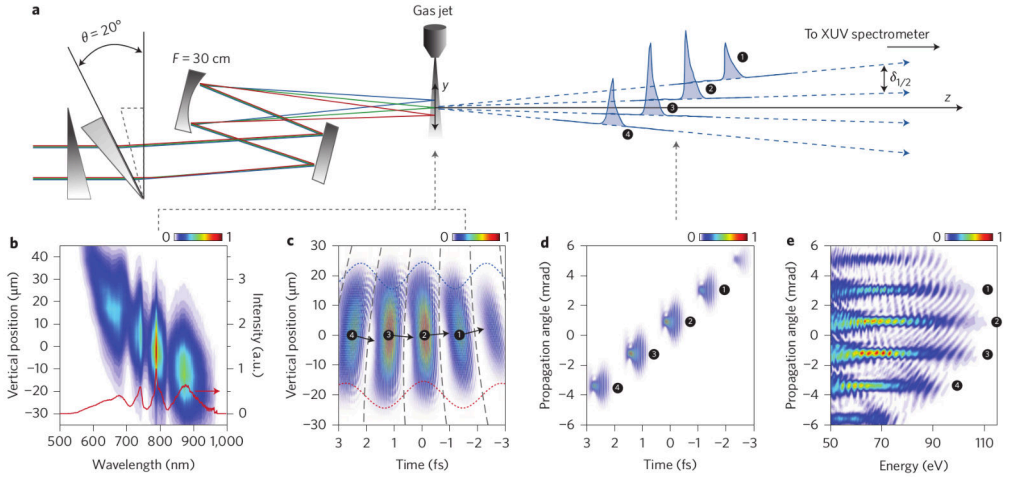

Figure 2.24: Schematic of the attosecond lighthouse effect. This figure has been taken from [Kim et al. 2013]. In (a) is a schematic of the experimental set-up. By putting a pair of misaligned wedges in the collimated beam, angular dispersion of the different spectral components is imposed. The angular dispersion leads to spatial chirp at the focus of the beam. In (b), the spatially chirped spectrum measured using an imaging spectrometer is presented. The red curve represents the spatially integrated spectrum of the driving laser. In (c) is the calculated temporal profile of the harmonics at the exit of the gas jet. One can see that the ultrafast wavefront rotation of the IR in imprinted onto the XUV radiation. The 4 principle attosecond bursts of the attosecond pulse train are label 1-4. In (d) is the calculated temporal profile as a function of the propagation angle in the far-field. One can see that each attosecond bursts are well separated in time and space. In (e), the calculated spatially resolved XUV spectrum is presented. We notice the good spatial separation of the different attosecond burst in the far-field. The calculation shown in (c)-(e) are SFA simulation. For more information, see the supplementary materials of [Kim et al. 2013].

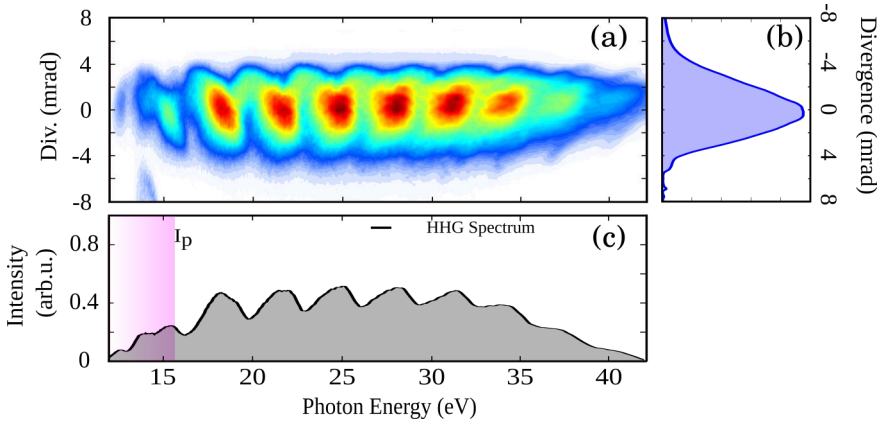

Figure 2.25: Attosecond lighthouse technique using CEP unstable laser. (a) Spatially-resolved harmonic spectrum driven by a spatially chirped laser pulse. (b) Spectrally integrated harmonic spatial profile. (c) Spatially integrated harmonic spectrum.

introduced a large spatial chirp using the wedges. To do so, we kept one of the two wedges fixed, while rotating the other one vertically. We choose the wedge angle that lead to the largest spatial chirp, using the spatially-resolved spectrum of the driving laser at its focus. Next, we finely reoptimized the wedge angle in order to see well contrasted spatial fringes in the single-shot far-field HHG spectrum. Moreover, we also noticed that slightly changing the gas pressure in the hollow-core fiber, resulting in tailoring the spectral broadening, and thus of the temporal properties of the laser pulse, was a pretty

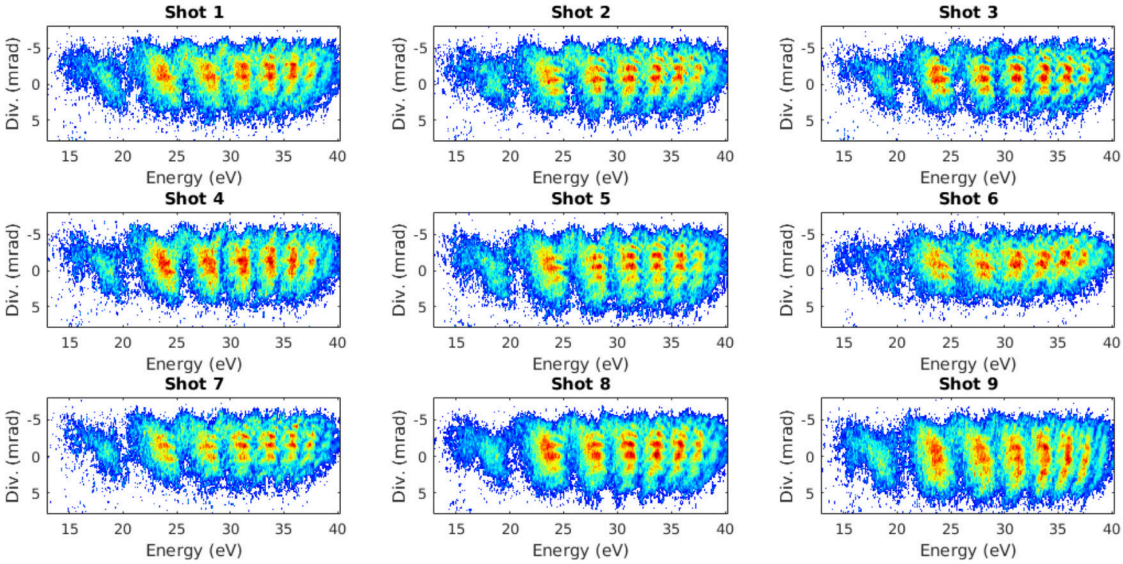

Figure 2.26: Single shot measurement of the spatially-resolved HHG spectrum, when driven using spatially chirped pulses.

efficient experimental parameter to tune to optimize the contrast of the spatial fringes in the single-shot far-field HHG spectrum.

A spatially-resolved HHG spectrum integrated over 100 laser shots is shown in Fig. 2.25 (a). We note that the harmonics are more divergent when driven with spatially chirped pulses (see 2.25 (a)) than with STC-free pulses (see 2.14 (a)). This is the signature of the angular spreading of the XUV using the attosecond lighthouse. However, the usual discrete horizontal fringes which result from the angular separation of the different attosecond beamlets are not visible in this measurement. The spatial profile of the XUV is rather Gaussian (see Fig. 2.25(c)). This can be explained by the fact that our laser system is not CEP stable. The different CEPs lead to the generation of beamlets that propagate in different directions. The random CEP fluctuation of the laser thus completely wash out the discrete spatial fringes which are expected to emerge when driving HHG using the attosecond lighthouse.

Rather than stabilizing the CEP of our laser source, which is far from being trivial, we decided to record spatially-resolved HHG spectra in a single-shot manner and to use the relationship between the CEP and the propagation direction of the beamlets to *a posteriori* sort the data acquired with different CEP. The single shot acquisition (< 1 ms exposure time because of the 1kHz laser repetition rate) is possible due to the fast decay time of our P46 phosphor screen. An example of 9 HHG spectra recorded for 9 laser shots is shown in Fig. 2.26.

On these single-shot spatially-resolved HHG spectra, we notice the emergence of horizontal spatial fringes, which are characteristics of angularly spread attosecond bursts of light. The signal-to-noise ratio of HHG spectra recorded in a single shot is not exceptional but is more than enough to extract the phase of the spatial fringes using Fourier analysis, in a shot-to-shot manner. As explained previously, the phase of the spatial fringes is directly related to the *in situ* CEP of the driving laser.

Figure 2.27 shows the spatial profile of the HHG for two different laser shots (shot 2 and shot 7). The CEP fluctuation results in a change of the phase of the spatial fringes. When integrating the signal for all CEPs, this results in a smearing of the fringes (see

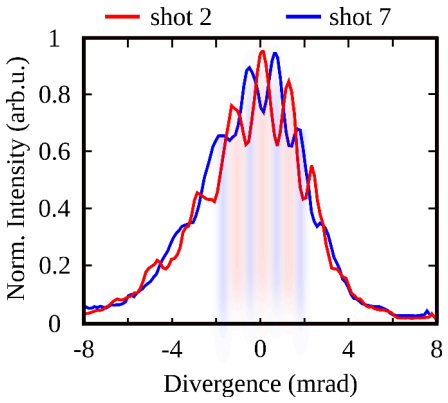

Figure 2.27: Spatial profile of the HHG for laser shot 2 and laser shot 7. We can see that the phase of the spatial fringes can be use for *in situ* tagging of the CEP.

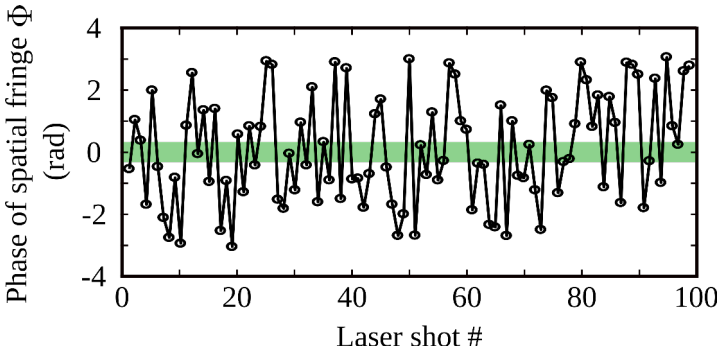

Figure 2.28: Phase of the spatial fringes extracted using Fourier analysis, for each laser shot. The green area represents the window used for CEP sorting the data, used to produce the Fig. 2.29.

Fig. 2.25(a)). Figure 2.28 presents the single-shot extraction of the phase of the spatial fringes, using Fourier analysis. This is equivalent to tag the relative *in situ* CEP in a shot-to-shot manner. One can see that over 100 laser shots, the CEP fluctuations seem to be pretty random. We can thus *a posteriori* sort the different spectra according to the phase of their spatial fringes (Φ) and sum them together to increase the signal-to-noise ratio. In the following, we will take all the spectrum where we found -300 mrad$< \Phi <$300 mrad (green area in Fig. 2.28) and sum them together. Note that this is the first demonstration of single-shot CEP tagging of a CEP unstabilized laser, using the attosecond lighthouse technique.

The spatially-resolved HHG spectrum of Argon generated from the attosecond lighthouse, after CEP sorting, is presented in Fig. 2.29 (a). This spectrum provides a spatiotemporal mapping of the XUV emission. The signal which is detected at the bottom of the detector is emitted on the rising edge of the pulse while the signal measured on the upper part of the detector is emitted on the trailing edge of the pulse. Well separated horizontal fringes are visible. Since we know that each of these fringes is separated by 1.3 fs (half-cycle), they can be used to calibrate the spatiotemporal mapping provided by the attosecond lighthouse effect. The level of sub-cycle temporal confinement of the harmonic emission can be evaluated by measuring the contrast of the spatial fringe pattern, using Fourier analysis. If the XUV is emitted continuously during the laser pulse duration, it will not exhibit any fringe. If the emission is temporally confined on the attosecond time-scale, the fringe contrast will be large (assuming a good enough angular separation). The results are shown in Fig. 2.29(b). Above threshold, the harmonics exhibit significant spatial fringe

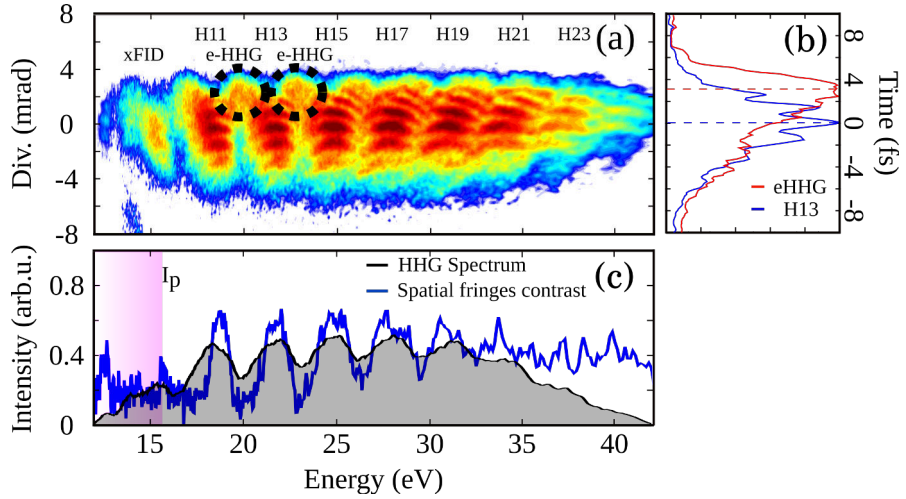

Figure 2.29: Time-frequency mapping of HHG using the attosecond lighthouse technique. (a) Spatially-resolved harmonic spectrum driven by a spatially chirped laser pulse. (b) Spectrally integrated harmonic spatial profile for e-HHG (in red) and for H13 (in blue). The interfringe was used to transform the spatial axis into a time axis. (1 interfringe = 1.3 fs) (c) Spatially integrated harmonic spectrum (black) and contrast of the spatial fringes (blue). This figure is adapted from [Beaulieu et al. 2016a].

contrast, which is a signature of the sub-cycle (attosecond) confinement of their emission. On the other hand, this contrast falls down drastically below the ionization threshold, at the spectral position of where we expect xFID emission to occur. As the photon energy further decreases, the contrast increases again around the non-resonant H9. The spatial fringe visible for below- and above-threshold HHG is a signature of their attosecond pulse train temporal profile. The fact that spatial fringes are not observed for the xFID indicates that the emission is not confined on the attosecond time-scale. This confirms our initial hypothesis about the lack of sub-cycle structure in the xFID emission.

A closer look at the near-threshold part of the angularly-streaked spectrum reveals that there are indeed two spatially separated components: a main comb, centered around the laser propagation axis, which shows well contrasted spatial fringes, characteristic of the emission of well-confined attosecond pulses (see the cut of H13 in Fig. 2.29(b)); and a secondary, spectrally shifted comb, showing no spatial fringes and centered up on the detector (see the black dashed circles in Fig. 2.29(a)). The spatial shift of this second component, associated to e-HHG, is the signature of the delayed emission time, which can be quantified by calibrating the space-time mapping onto the detector using the fringe spacing (1.3 fs). The secondary component, associated to e-HHG, is found to be maximum around 4 fs (see the cut of e-HHG in Fig. 2.29(b)), which is in good agreement with the emission delay predicted by the Gabor analysis of the TDSE, which was also ~ 4 fs. The attosecond lighthouse thus enables us to experimentally resolve the emission delay of e-HHG. This measurement extends the scope of the attosecond lighthouse technique, from a way to generate isolated attosecond pulses to a metrology tool that enables the measurement of ultrafast electronic dynamics during HHG.

2.3.7 The Hyper-Raman lines interpretation

The participation of excited states in the high-order harmonic generation process was recognized in the early day's simulation of HHG. Indeed, after identifying experimental signatures of the role of excited states in HHG, we dug into 'old' literature and found

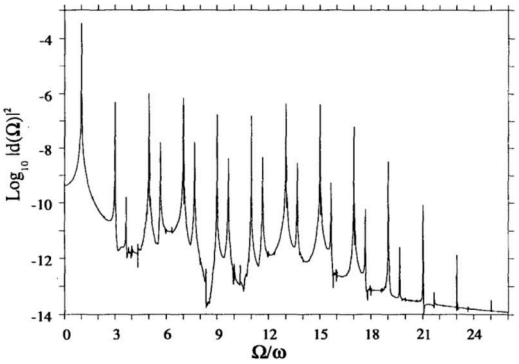

Figure 2.30: Scattered light spectrum from a 1D-model system driven with a long multi-cycle 570 nm pulse. In this case, the system was shown to be in a coherent superposition of states after the 'turn-on' ramp of the electric field. The figure was taken from [Millack et al. 1993].

many papers that were addressing the problem of HHG from a system in a coherent superposition between its ground and excited state(s) [Balcou et al. 1996; Bandarage et al. 1992; Di Piazza et al. 2001; Millack et al. 1993]. These paper demonstrated that when HHG is generated from a system in a coherent superposition of states, new spectral lines, concomitant with standard HHG, were visible in the calculated scattered spectrum of strong-field driven atom. These spectral lines, located somewhere between the usual high-order harmonics, were called Hyper-Raman lines (HRL). They have been observed is classical [Bandarage et al. 1992] and many quantum [Balcou et al. 1996; Di Piazza et al. 2001; Millack et al. 1993] calculations of the scattered light spectrum of strong-field driven atoms. They have also been observed in many other theoretical calculations which are not cited here. One example of a calculated spectrum showing HRL concomitant with HHG is shown in Fig. 2.30. This spectrum was simulated using a 1D-model system driven with a long multi-cycle 570 nm pulse. We can see that besides the usual odd order harmonics, the spectrum presents weak additional peak in between each harmonic. These peaks are the Hyper-Raman Lines.

In the paper of Millack *et al.*, Hyper-Raman Lines were shown to appear in the strong-field driven atom emission spectrum when the system is in a coherent superposition of states (let say states of energies E_1 and E_2) [Millack et al. 1993]. When driven by a single color field of frequency ω_0, the frequencies of HRL of q'-th order $\Omega_q'^{HRL}$ are given by:

$$\Omega_q^{HRL} = \frac{(E_2 - E_1)}{\hbar} \pm 2q'\omega_0 \tag{2.9}$$

The HRLs are thus interpreted as originating from a high-order Raman process, where many photons are absorbed from a state of energy E_2, followed by the emission of a high-energy photon to relax to the state of energy E_1. For the emission to be coherent, the states of energy E_1 and E_2 must be in a coherent superposition prior to the high-order Raman process. A scheme of the simultaneous generation of HHG, xFID, and HRL from a system in a coherent superposition of electronic states is shown is Fig. 2.31.

Because HRL where often observed in simulation, but were never observed experimentally, a lot of tentative arguments for the absence of HRL in experimental spectra have been formulated in some 90s [Millack et al. 1993; Pons et al. 1996] and early 00s [Di Piazza et al. 2001] papers. The main arguments are the following:

i) The creation of a coherent superposition of states, necessary for the generation of HRL, by a strong low-frequency far off-resonance pulse, is strongly sensitive to the laser

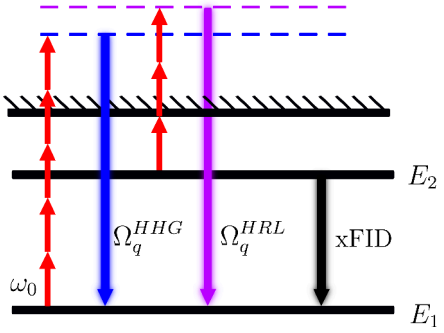

Figure 2.31: Schematic of the simultaneous generation of HHG and Hyper-Raman Lines (HRL) in strong-field driven system. The driving laser photon are represented as red arrows, the HHG emission is represented as a blue arrow and the HRL emission is represented as a purple arrow. The black arrow represents the fact that the state of energy E_1 and E_2 are in coherent superposition, leading to xFID emission at $\Omega_{xFID} = (E_2 - E_1)/\hbar$.

pulse parameters. To observe HRL, one thus needs to be in a regime where the coherent superposition of states triggered by multiphoton resonant transition is efficient. For HHG, no such condition is necessary since the process is (usually) purely non-resonant.

ii) The instantaneous frequencies of the HRL strongly vary within the laser pulse (both in time and space) since the states leading to HRL experience AC-Stark-shift, which depends on the instantaneous and local strength of the field. The HRLs are thus strong when calculating the single-atom response, with a temporally flat-top pulse and without including focal averaging effects. However, when the Gaussian temporal shape of the pulse and/or the focal averaging are included in the calculations, the HRLs are washed out and appear as a weak continuous background between the harmonic peaks, prohibiting their clear experimental identification. The use of high laser intensity goes hand in hand with efficient generation of HHG and with the smearing of the HRL.

The phenomenon that we have described as e-HHG earlier seems to be somehow related to HRL. Indeed, it involves the ionization from excited states and photorecombination onto the ground state, leading to new spectral lines in the scattered spectrum of light-driven atoms. However, since the multiphoton creation of the coherent superposition of states is a dynamical process involving the dynamically Stark-shifting excited states, it leads to the temporally inhomogeneous emission of e-HHG. It can thus be seen as a special case of inhomogeneous generation of Hyper-Raman Lines. In order to try to render the situation simpler, by partially decoupling the creation of a superposition of electronic states and the generation of HHG and HRL, we decided to perform a two-color experiment.

Our idea is to use a first pulse to create a coherent superposition of electronic states, and a second pulse to drive HHG and HRL from this wavepacket. The results of this experiment are presented in Fig. 2.32. First, to prepare the coherent superposition of states, we choose to use the second harmonic of our Ti:Sa laser, which is centered around 400 nm. Using this driving laser wavelength, the excited Rydberg states are accessible through a resonant 5 photons transition from the ground state. This allows us to prepare the coherent superposition of states using a 400 nm intensity which is much below the intensity needed to efficiently generate high-order harmonics. The first step of our experimental approach was to optimize the $\sim$ 400 nm pulse parameter (central wavelength, intensity, chirp) to maximize the xFID emission at Rydberg states field-free energies. Fig. 2.32(a) shows that using the 400 nm pulse alone, the spectrum is dominated by H5 and xFID (and very weak H7). Because we have an experimental observable which allows us to directly monitor the

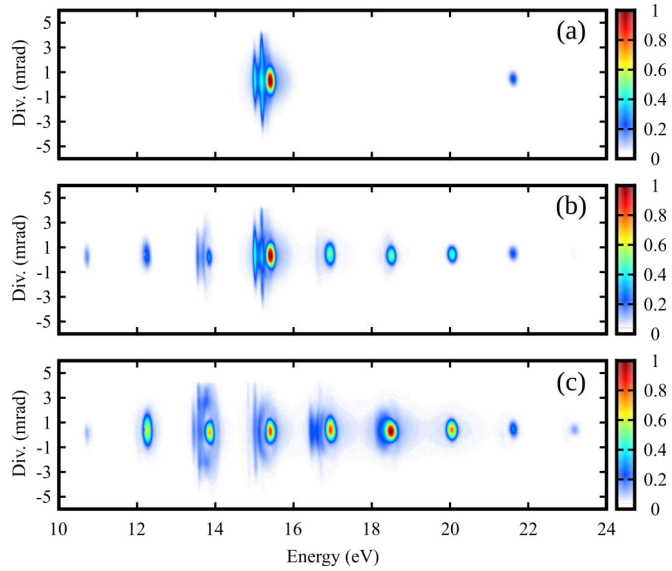

Figure 2.32: Simultaneous observation of Hyper-Raman Lines (HRL) and High-order Harmonic Generation in Argon, using two-color laser pulses. In (a), a spatio-spectrally resolved spectrum of light emitted by Argon driven by 400 nm pulses. In (b), same as in (a) but the Argon atoms are driven by a two-color (400 nm + 800 nm) field, where the power of the 800 nm is 98 mW. In (c), same as (b) but the power of the infrared was increased to 250 mW.

efficiency with which we are preparing the coherent superposition between ground and Rydberg states (xFID), it is straightforward to find the perfect experimental conditions that prepare the system in the required superposition of states.

Next, we added a spatially and temporally synchronized relatively weak 800 nm pulse. The combination of the 400 nm and the 800 nm allows the generation of even and odd harmonics as well as clear HRL, which are located $\pm q\hbar\omega_{800}$ from the xFID emission ($\Omega_{xFID} = (E_2 - E_1)/\hbar$). The fact that we observe clear HRL indicates the IR induced Stark-shift in not sufficient to wash-out their signature in the spectrum.

In a situation where we decoupled the preparation of the superposition of states and the generation of HHG, we clearly observed well defined HRL concomitant with standard non-resonant HHG. This is the first unambiguous experimental demonstration of these Hyper-Raman Lines during HHG. As the phenomenon that we have called e-HHG, HRL involves the ionization from excited states and recombination onto the ground state. We think that these two phenomena are somehow intimately related. We are currently collaborating with Vasily Strelkov and Baptiste Fabre, to try to unify our understanding of these resonant phenomena occurring during HHG.

2.3.8 Perspectives and partial conclusions

This story began when a paper by Chini *et al.* [Chini et al. 2014b] triggered our interest about the temporal properties of near-threshold resonant high-order harmonics. We were particularly interested in the resonant HHG process because the CELIA team had recently demonstrated that it could be used as a way to produce quasi-circularly polarized XUV beams [Ferré et al. 2015a]. Our attention focused on the appearance of narrow spectral lines in the XUV spectrum, which turned out to be xFID lines. By trying to find the good experimental condition to observe them, we accidentally observed a new and strange broad spectral component between H11 and H13. By carefully measuring the spectral and spatial properties of this new spectral component as a function of driving laser intensity

and helped by TDSE calculation, we succeed in explaining its origin. We found that the multiphoton transition from the ground to excited states not only leads to xFID, but can also initiate quantum trajectories which are described by the ionization from excited states and recombination onto the ground state. We called this mechanism e-HHG (excited-states HHG). We theoretically found that the emission of e-HHG is delayed by few-femtosecond with respect to the maximum of the laser field (and with respect to the non-resonant HHG). This time delay in the e-HHG emission explains its significant non-adiabatic spectral red-shift with increasing laser intensity, which was measured experimentally. We used the attosecond lighthouse effect to spatio-temporally map the XUV emission, revealing an emission delay of the e-HHG which is in good agreement with the one theoretically predicted.

The discovery of e-HHG has turned our attention away from the xFID for few months. However, we will present in the next section a complete study of the physics behind xFID emission. Indeed, by using pump-probe scheme, we will see that xFID can be used as an analog technique to XUV transient absorption spectroscopy [Beck et al. 2014; Cao et al. 2016b; Warrick et al. 2016].

2.4 Laser-induced XUV Free Induction Decay

2.4.1 Analogy with Attosecond Transient Absorption Spectroscopy (ATAS)

When a quantum system in its ground state (E_g) is illuminated by a coherent broadband pulse of light, a coherent superposition of states (wavepacket) made of states (of energy E_n) which are energetically accessible ($\hbar\omega_0 = E_n - E_g$, where ω_0 is within the bandwidth of the pulse) and which are transition dipole allowed ($\langle\psi_g|\hat{d}|\psi_n\rangle \neq 0$) is launched. The wavepacket relaxes by coherently emitting photons at energies $E_n - E_g$, a process which is called Free Induction Decay (FID). These photons, coherently emitted by the wavepacket, (destructively) interfere with the incoming broadband spectrum of the exciting pulse. Thus, by subtracting the transmitted spectrum with the incoming spectrum, we get the absorption spectrum of the quantum system. The dynamics of the wavepacket created by the absorption of light from the incoming pulse is partially encoded in the spectral width and the spectral lineshape of the absorption lines.

A schematic of a static absorption spectroscopy experiment using an isolated attosecond pulse (IAP) is shown in Fig. 2.33 (a) and (d). The incoming pulse has a broadband spectrum centered around 30 eV (Fig. 2.33 (a)) and we assume that it has a flat spectral phase, such that its temporal profile is Fourier limited (Fig. 2.33 (b)). When this IAP interacts with a quantum system which can be excited by absorption of one photon around 23 eV, an absorption line appears in the spectrum of the transmitted light (Fig. 2.33 (c)). In the temporal domain (Fig. 2.33 (d)) a long-lasting component appears: the FID. The spectral hole created around 23 eV is the result of the spectral interference between the incoming electric field and the long-lasting dipole emission of the wavepacket (FID). Its spectral width gives information about the coherence time of the excited states and its spectral lineshape encodes information about the phase of the dipole emission of the wavepacket. This is the basis of static absorption spectroscopy.

Since absorption spectroscopy provides invaluable information about the eigenstates of a quantum system, this technique is very interesting for dynamical studies. One can pre-excite a quantum system with a pump pulse and measure its absorption spectrum with a broadband probe pulse as a function of pump-probe delay. This technique is called Transient Absorption Spectroscopy (TAS), and has become one of the most powerful workhorses of ultrafast science. Indeed, TAS in the extreme ultraviolet (XUV) range is a

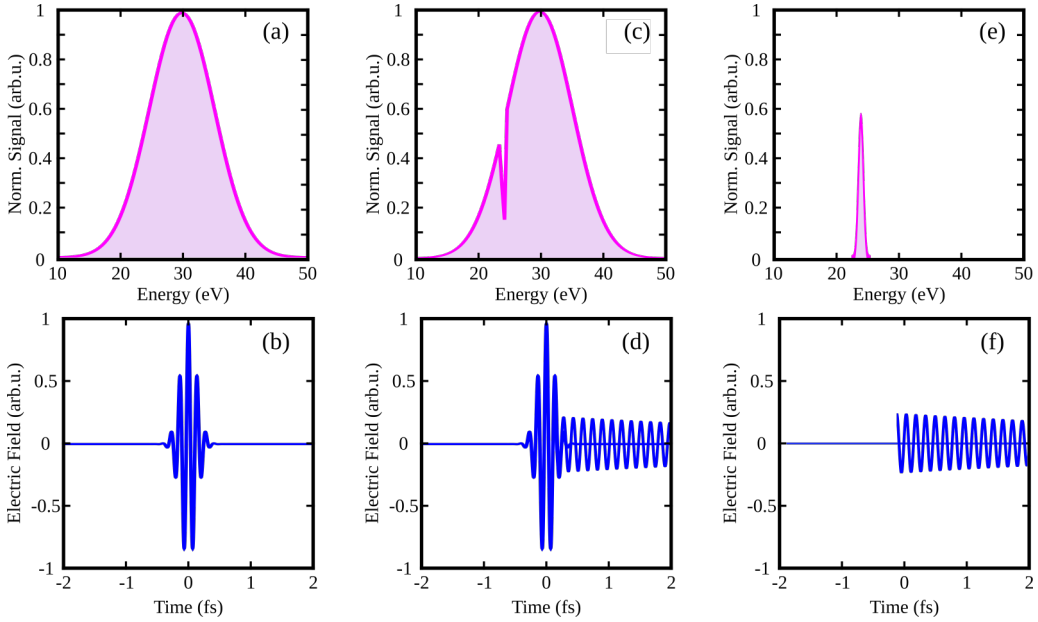

Figure 2.33: Schematic of absorption and xFID 'emission' spectroscopy. In (a) a broadband Gaussian spectrum centered around 30 eV and in (b) the associated electric field (assuming a flat spectral phase). In (c) is a schematic of the spectrum after interaction with a quantum system characterized by a dipole-allowed excited state 23 eV above the ground state. In (d) is the electric field associated with the spectrum in (c). In (e) is the emission spectrum of a wavepacket made of two states separated by 23 eV and in (f) is the associated electric field. All these subplots are schematic; they are not extracted from simulation.

powerful technique for ultrafast dynamical studies, from the gas phase [Goulielmakis et al. 2010; Holler et al. 2011; Wang et al. 2010] to the solid-state [Lucchini et al. 2016; Schultze et al. 2014]. The recent developments of attosecond pulse generation, combined with the ability to synchronize them with few-cycle IR pulse, with tens of attosecond precision, have led to the birth of ATAS – Attosecond Transient Absorption Spectroscopy.

In the most intuitive scheme for ATAS, the IR pulse excites the system and the delay-dependent absorption of photons from ultrabroadband attosecond XUV pulse probes its time-evolution. This scheme was the first one to be experimentally demonstrated by the Garching group. In 2010, Goulielmakis *et al.* succeed to follow the ultrafast coherent hole dynamics initiated by strong-field ionization of krypton [Goulielmakis et al. 2010]. Later, it was realized that performing ATAS experiments in the configuration where the IR and XUV pulse temporally overlap can give access to a lot of information about the IR-dressed atomic or molecular states. This second ATAS scheme has allowed the observation of light-induced states [Chen et al. 2012; Reduzzi et al. 2015] and sub-cycle AC-Stark-shifts [Chini et al. 2012], for example. The information obtained using this ATAS configuration can be of great interest for the field of High Harmonic Spectroscopy (HHS), where, the systems under study are always embedded in a strong laser field, whose effect on the system can be difficult to disentangle. The last ATAS scheme, which is the less intuitive but which turned out to be the most widely used, uses the XUV pulse as a pump and the IR as a probe. The XUV creates a broadband superposition of quantum states through single-photon absorption. The time-delayed IR pulse is used to follow and/or to control the wavepacket dynamics, modifying the spectrum of the transmitted XUV light. In order to have a cool acronym for our extension of this technique, later on, we will call this third ATAS scheme [Beck et al. 2014; Cao et al. 2016b]: Transient Reshaping of the Absorption

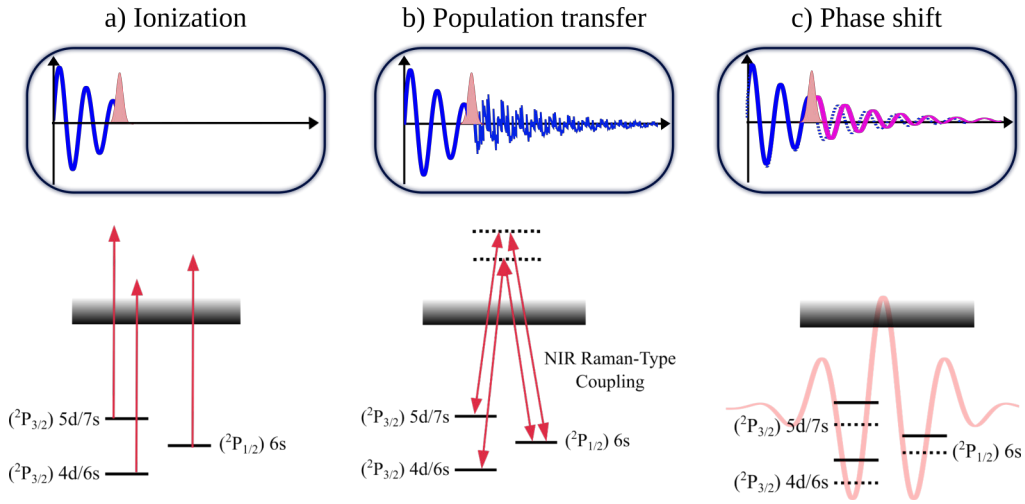

Figure 2.34: Schematic of the three principal effects of the time-delayed IR probe pulse in TRAX experiments. The upper panels illustrate the effects from a time-domain perspectives while the bottom panels illustrate the effects from energy-domain perspectives. In (a), we represent the effect of IR-induced ionization, *i.e.* it can irreversibly promote excited electrons to the continuum. In (b), we represent the effect of IR-induced population transfers, through 2-photons Λ- (1 photon up, 1 photon down), which spectrally reshapes the wavepacket, and thus, its dipole emission. In (c), we represent the effect of AC-Stark-shift of the quantum states of the system, leading to a phase shift of the emission.

spectrum of the XUV light (TRAX).

In the following, we will focus on the TRAX scheme. In TRAX experiments, the time-delayed IR probe pulse can have three main effects on the dipole emission of the wavepacket initiated by the broadband XUV excitation. These three effects are explained below, and schematized in Fig. 2.34

i) It can irreversibly promote excited electrons to the continuum (ionization). This effect will quench the xFID emission. In the transmitted spectrum, the effect of ionization is visible by a weakening and a spectral broadening of the absorption features [Wang et al. 2010].

ii) It can couple different excited states of the wavepacket, leading to population transfers, through 2-photons Λ- (1 photon up, 1 photon down), V- (1 photon down, 1 photon up) or ladder-coupling (2 photons up or down). For population transfer to be possible, the energy difference between the two excited states must be contained within the laser bandwidth. With a larger bandwidth, population transfer between more energetically separated states is possible. IR-induced population transfers show up as a beating of the absorption at the frequency corresponding to the energy difference between the two field-coupled states, as demonstrated in atoms [Beck et al. 2014; Cao et al. 2016b] and molecules [Warrick et al. 2016].

iii) The IR can lead to an AC-Stark-shift of the quantum states of the system. This energy shift of the states produces a phase modulation of the emitted radiation. Let us take for example an excited state (e) lying at energy $E_e = \hbar\omega_e$. The instantaneous phase ($\phi(t)$) linearly depends on the instantaneous energy of the state $\omega_e(t)$. The phase of the quantum mechanical wavefunction determines the phase of the emitted XUV radiation. Thus, the Stark-shift of the states leads to a phase-shift of the XUV emitted by the wavepacket. The

phase shift of the xFID is given by:

$$\Delta\phi_{xFID} = \int_{-\infty}^{+\infty} \delta E(t) dt \tag{2.10}$$

where $\Delta\phi_{xFID}$ is the laser-induced phase shift of the xFID and $\delta E(t)$ is the instantaneous Stark effect induced energy shift of the excited states. This phase shift is called the *Laser Imposed Phase*. The phase of the xFID that interferes with the incoming light determines the spectral lineshape of the absorption feature. Thus, this laser-imposed phase can enable full control over the absorption lineshapes, from Lorentz to Fano profiles, and vice-versa. This laser-imposed phase controlled over spectral lineshape of absorption feature is, in my opinion, one of the most elegant uses of ATAS demonstrated up to date [Ott et al. 2013]. The laser imposed phase can also be used to perform spatial control of the emitted radiation: by slightly misaligning the IR beam that perturbed the xFID emission, one can impose a Stark-shift gradient in the medium, creating a tilt of the xFID wavefront, which allows to angularly deflect the xFID radiation [Bengtsson et al. 2016].

The combination of the different physical effects and observables mentioned above (see Fig. 2.34), makes TRAX a very rich tool for ultrafast spectroscopy and strong-field physics. However, TRAX suffers from several limitations, which make its experimental implementation and interpretation pretty hard. First, the phase sensitivity of the xFID, which is important for many TRAX applications, is based on the interferometric nature of the detection, which records the coherent superposition of the incoming XUV and radiated xFID light. This interference is encoded is the spectral lineshape of the different absorption features. The extraction of the phase of the xFID is thus indirect and requires a theoretical modeling of the laser-atom interaction. It would be of great interest to have a way to extract the xFID phase directly from the experimental measurement, *i.e.* without any theoretical input. Second, the XUV absorption cross sections are usually small. The contribution of the incoming XUV is generally much stronger than the contribution of the xFID emitted by the wavepacket. This leads to poor signal-to-noise ratio, which means that the experimental setup must be really stable and that acquisition time are long. Since the absorption scales with the number of atoms/molecules that interact with the pulses, one appealing solution is to increase the pressure-length product of the absorbing medium. However, this solution comes with some important drawbacks: recent works have demonstrated that increasing the pressure-length product of the absorbing medium caused significant modifications of the absorption lineshapes due to resonant effects in the XUV pulse propagation, which complicates the interpretation [Liao et al. 2015].

2.4.2 Using xFID as a background free alternative to absorption spectroscopy

In the last section, we have shown that driving Argon atoms with few-cycle IR pulses lead to the emission narrow spectral xFID lines just below the ionization threshold [Beaulieu et al. 2016a]. These lines result from the creation of an electronic wavepacket made of the ground and Rydberg states. In this case, the wavepacket was created by absorption of multiple IR photons, instead of by single XUV photon transition like in TRAX experiments. The spectrum of the exciting light (IR spectral region) does not overlap anymore with the spectrum of the emitted radiation (XUV spectral region). This provides a background-free measurement of xFID (see Fig. 2.33). Here, we propose to use this idea of laser-induced background-free xFID to overcome some limitations of TRAX. In the experimental scheme that we propose, we will first use an optical pulse (400 nm) to create a coherent superposition of quantum states through a multiphoton transition, and a time-delayed IR

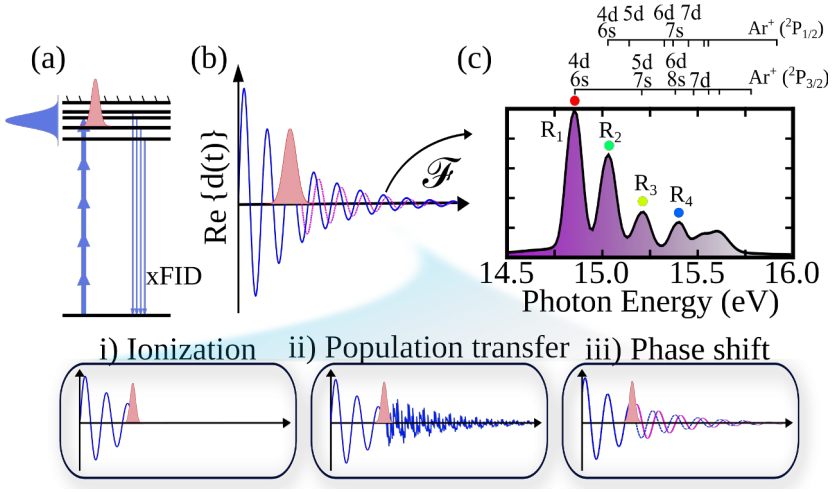

Figure 2.35: Principle of a T-REX experiment: (a) Multiphoton excitation creates an electronic wavepacket in Argon atoms, which emits XUV radiation through xFID. A time-delayed 800 nm laser pulse perturbs the xFID emission. (b) Schematic view of real part of the unperturbed and IR-perturbed atomic dipole with the different effects induced by the IR pulse, i.e. ionization, population transfer and Stark-shift induced phase shift. (c) Experimental xFID spectrum, obtained in Argon using 400 nm driving pulses. This figure is adapted from [Beaulieu et al. 2017a].

pulse (800 nm) to manipulate the wavepacket and thus its xFID emission. We call this new technique Transient Reshaping of the Emission spectrum of the XUV light (T-REX, which is the cool acronym that we were talking about earlier). A schematic of T-REX is shown in Fig. 2.35.

In order to demonstrate the feasibility of T-REX, we decided to use Argon as a first candidate, since it has been previously studied using TRAX [Cao et al. 2016b] and since we had already observed static xFID emission when driving Argon with few-cycle IR pulses. These ultrashort IR pulses might not be the most well-suited ones to excite the states between 14.8 and 15.6 eV in Argon. Indeed, they lie in between the 9 and 11 photons absorption region, assuming that the pulses are centered around 1.55 eV (800 nm). To significantly populate these levels using 800 nm pulses, and thus to see a strong xFID signal, one needs to tune the intensity of the driving laser such that the Stark-shifted Rydberg states are resonant with an odd number of IR photons. By using a 400 nm (photon energy of 3.1 eV) driving pulses, the Rydberg states manifold between 14.8 and 15.6 eV would be resonantly populated by 5 photon transitions from the ground states, without the need of any Stark shift. Using 400 nm instead of 800 nm should thus lead to a much stronger xFID signal.

The experimental setup required for T-REX is fairly simple. The Aurore laser beam was sent into a Mach-Zehnder interferometer. The high-energy arm (90%) was frequency-doubled by a 200 μm thick type-I BBO crystal (θ=29.2°, ϕ=90°). In the low-energy 800 nm arm (10%), the laser power was varied by rotating a superachromatic half-wave plate in front of a broadband polarizer. The dispersion in each arm of the Mach Zehnder was adjusted using silica plates to achieve optimal durations of both the 400 nm and 800 nm pulses. The two arms were recombined using a dichroic mirror and focused by a f = 1.5 m lens into a 250 μm thick effusive gas jet of Argon. The pump intensity I_{400nm} was on the order of few 10^{12} W/cm^2. The XUV emission was analyzed by the flat-field XUV spectrometer described in the previous section.

Fig. 2.36 shows a typical spatially-resolved spectrum obtained by driving Argon using

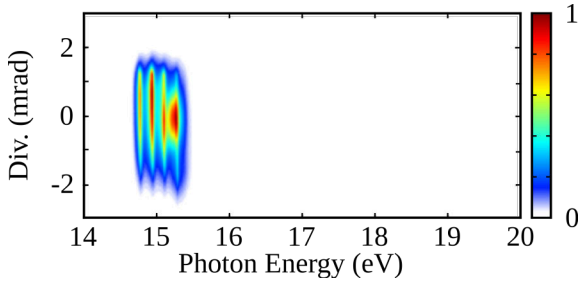

Figure 2.36: Spatially resolved spectrum of Argon driven by 400 nm pulses. The spectrum is only constituted of xFID emission around 15 eV. The laser intensity was kept below low enough to ensure that only xFID is visible in the spectrum (no HHG).

moderately intense multi-cycle ($\sim$ 40 fs) 400 nm pulse, at an intensity of 10^{12} W/cm^2. The spectrum shows narrow spectral xFID lines around 15 eV, demonstrating that the 400 nm pulses efficiently create a Rydberg wavepacket. The intensity of the 400 nm is set such that no high-order harmonics are generated. When it increases, the spectrum gets dominated by HHG rather than xFID.

As a first experiment, we investigated the role of the driving laser parameters on the unperturbed xFID emission spectrum of Argon. Because of the $\Delta\ell = \pm 1$ selection rule for the single XUV photon emission, only the ns- and nd- Rydberg series (where n is the principal quantum number) radiatively decay to the 3p ground state of Argon and can be observed in the xFID spectrum. These Rydberg manifolds converge to two different spin-orbit coupled ionic cores, $Ar^+(^2P_{3/2})$ and $Ar^+(^2P_{1/2})$, with ionization potential of $I_p(^2P_{3/2}) = 15.76$eV and $I_p(^2P_{1/2}) = 15.94$eV. The observed Rydberg states are spectroscopically identified according to the VUV absorption measurement and assignment of Yoshino [Yoshino 1970]. In Fig. 2.37(a), the driving wavelength was changed by steps of 1 nm by slightly tilting the BBO crystal, while keeping the intensity roughly constant. At 'long' wavelength ($\sim$ 405 to 403 nm), only three low-lying Rydberg states are energetically accessible and contribute to the xFID emission. When the laser wavelength decreases (photon energy increases), higher-lying Rydberg states start to be energetically accessible through resonant 5 photon absorption and appear on the xFID spectrum. The driving laser wavelength is thus an easily tunable parameter to control the different spectral components of the wavepacket leading to xFID emission.

Because of the nonlinear nature of the excitation process, the laser intensity is also a tunable parameter that might modify the spectral content of the wavepacket. The results obtained at a fixed wavelength ($\lambda_c = 403$ nm) show that the laser intensity mostly affects the overall transition efficiency from the ground to the Rydberg states, without significantly affecting the xFID spectrum shape (Fig. 2.37(b)).

2.4.3 Time-resolved xFID spectroscopy

Because of their non-stationary nature, wavepackets evolve in time. We, therefore, used a time-delayed NIR pulse to investigate the possibility to obtain dynamical information on the evolving Rydberg wavepacket by manipulating the xFID emission. In order to determine the coherence time of the xFID emission, we first measured the time-dependent ionization damping of the xFID signal, using an IR probe pulse at $\sim 10^{13}$ W/cm^2. The xFID signal increases with delay, since the later the IR pulse arrives, the more XUV emission has occurred prior to ionization (see Fig. 2.34). Figure 2.38(b) shows the spatio-spectrally integrated signals for the different spectral components within the wavepacket. The data were fitted with an error function multiplied by an exponential function. The time

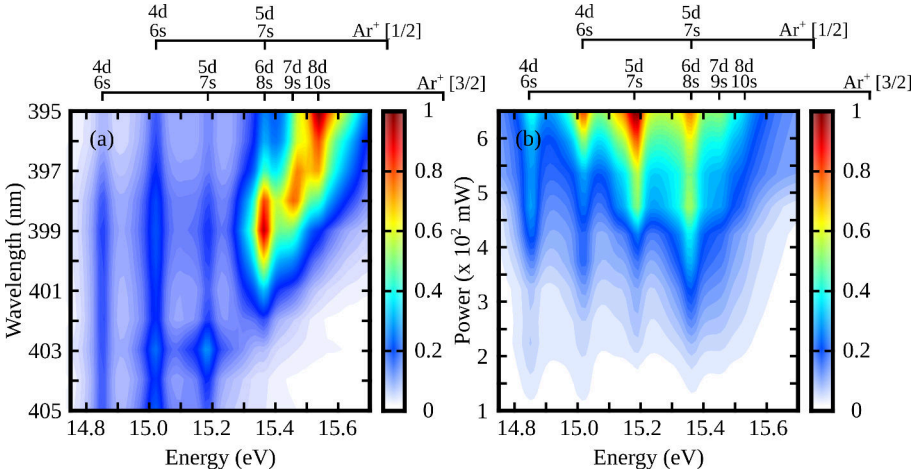

Figure 2.37: Controlling the xFID spectrum using the properties of the driving laser. In (a), the xFID spectrum as a function of the wavelength of the driving laser, which is tuned by slightly changing the angle of the doubling BBO crystal. The intensity is kept roughly constant for each wavelength. In (b), the scaling of the xFID signal as a function of the driving laser power.

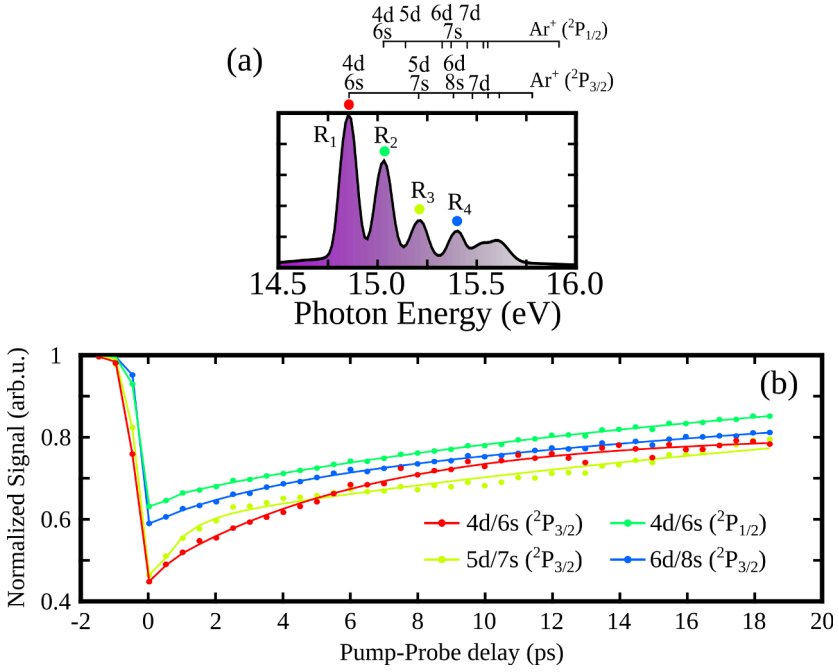

Figure 2.38: Time-resolved ionization damping of xFID. In (a) a static xFID spectrum obtained using the 400 nm pulse only. In (b) picosecond time-resolved xFID for R_1 (4d/6s ($^2P_{3/2}$)) in red, R_2 (5d/7s ($^2P_{3/2}$)) in light green, R_3 (4d/6s ($^2P_{1/2}$)) in dark green and for R_4 (6d/8s ($^2P_{3/2}$)) in blue. The intensity of the IR probe pulse was $\sim 10^{13}$W/cm^2. The Argon backing pressure was 8 mbar. The dots are the measurement points and the lines are the fits. This figure is adapted from [Beaulieu et al. 2017a].

constant of the exponential function, associated with the characteristic xFID emission time, were then retrieved for each Rydberg states. The fits provide rising times of 6.3 ps for R_1, 30.8 ps for R_2, 21.6 ps for R_3 and 33.6 ps for R_4. These are much shorter than the typical nanosecond lifetime of the Rydberg states, indicating the importance of homogeneous broadening and decoherence in the measurement. The same measurement was repeated using different Argon backing pressures. We observed a strong shortening of the xFID

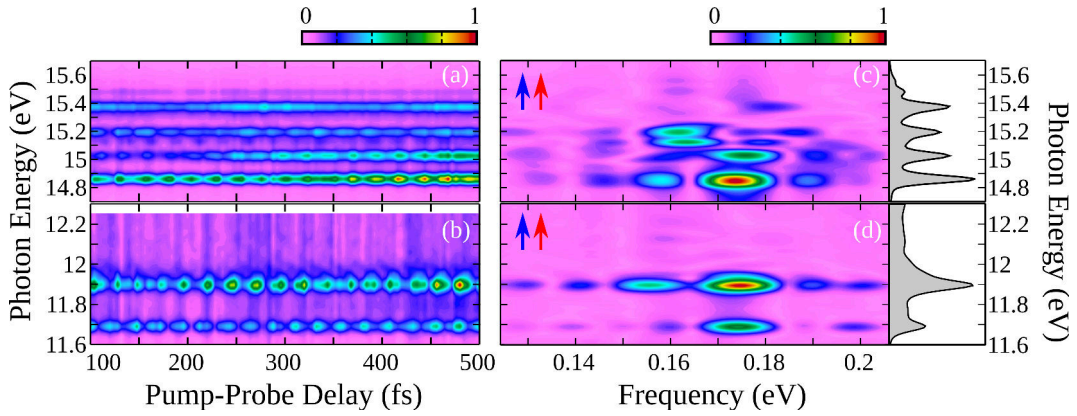

Figure 2.39: Laser-induced population transfer in T-REX. Evolution of the Rydberg (a) and valence (b) emission spectrum as a function of pump-probe delay, in parallel pump-probe polarization configuration. (c-d) show the 2D spectra obtained by Fourier transforming each spectral slice along the pump-probe axis. The Argon backing pressure was 5 mbar and the probe intensity $I_{800nm} \sim 2$ x 10^{12}W/cm^2. The cross-correlation time between the pump and the probe pulse is roughly 70 fs. This figure is adapted from [Beaulieu et al. 2017a].

coherence time with increasing pressure: the coherence time was found to decrease by a factor 5 when the backing pressure increased from 10 to 1000 mbar. We will come to this issue later in this section.

Next, we decided to perform pump-probe scans with much smaller time steps (4 fs). The goal of this measurement was to try to observe oscillation of the xFID spectral components as a function of the pump-probe delay. These oscillations would reveal the IR-induced population transfer between different states within the wavepacket. The results are shown in Fig. 2.39 (a). Most of the xFID spectral components show well-contrasted oscillations when the delay between the pump and probe is scanned. We analyzed these modulations by performing Fourier transform along each spectral slice (Fig. 2.39(c)). The resulting energy-energy 2D spectrum gives information about the laser-induced population transfer of individual Rydberg states with their neighboring bound states. The two lower Rydberg states, R_1 and R_2, show a main Fourier peak at 0.174 eV, which corresponds to the frequency difference (0.1737 eV) between the 6s ($^2P_{3/2}$) and 6s ($^2P_{1/2}$) spin-orbit states (according to the assignment of [Yoshino 1970]). This Fourier peak tells us that population transfer occurs between R_1 and R_2 states. This is allowed through a two-photon Λ-/V-type coupling. The emission from R_3 (15.19 eV) oscillates with a 0.164 eV frequency, corresponding to the difference between 6s ($^2P_{1/2}$) and 7s ($^2P_{3/2}$) (0.16341 eV). The highest peaks hardly show modulations, but a slow beating with a $\sim$ 200 fs period is visible in the R_4 (15.35 eV) signal. This beating must be caused by two oscillations that are too fast to be resolved in our experiments, but which are separated by $\sim$ 0.02 eV energy.

Looking at Fig. 2.39(b), we see other spectral components between 11.6 and 12 eV which are modulated with the pump-probe delay. This emission was not observed when using 400 nm pulse only. This spectral region is associated with the 4s valence states of Argon (11.7229 eV and 11.8228 eV). It is energetically accessible through resonant 4 photons transition from the ground state. However, for parity argument, the even parity 4s valence states cannot be populated by absorption of an even number of photons from the odd parity 3p ground state of Argon. The population of the 4s states at positive pump-probe delays originates from laser-induced ladder type population transfer between Rydberg states. The fact that the 4s xFID amplitude oscillates with the pump-probe delay

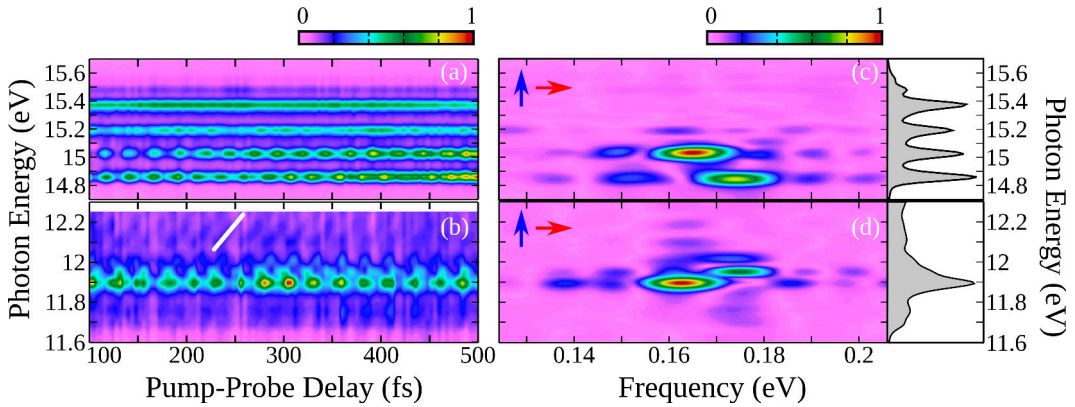

Figure 2.40: Evolution of the Rydberg (a) and valence (b) emission spectrum as a function of pump-probe delay, in perpendicular pump-probe polarization configuration. The other experimental parameters are the same as in the parallel polarization configuration. (c-d) show the 2D spectra obtained by Fourier transforming each spectral slice along the pump-probe axis. The white line in (d) serves as a guide to the eyes to emphasize the linear dephasing of the beating with photon energy. This figure is adapted from [Beaulieu et al. 2017a].

indicates that the population transfer occurs from several Rydberg states. The oscillation frequencies that are visible in Fig. 2.39 are imposed by the energy differences between the Rydberg states from which the population transfer originates, and are thus the same as in the Λ-/V-type coupling modulating the Rydberg xFID lines.

Next, we repeated the experiments after rotating the probe pulse polarization by 90°, *i.e.* using an orthogonal pump and probe polarizations. The transition between the ground and the Rydberg states involves five 400 nm photons, and thus imposes a given orientation of the atomic dipole along the pump polarization axis. By changing the polarization of the probe pulse from parallel to perpendicular to the orientation of the atomic dipole, we aimed at determining the sensitivity of 2D xFID spectroscopy to the anisotropy of the dipole excitation. The results are presented in Fig. 2.40. The perpendicular polarization case indeed reveals different modes in the oscillating xFID signal (see Fig. 2.40(c)). In this polarization configuration, the dominant mode modulating the R_2 emission was the weakest one in the parallel case (see Fig. 2.39(c)). This is a clear evidence that the population transfers between some Rydberg states are polarization-dependent. This observation is a signature of the angular dependence of the two-photon transition dipole matrix element. Performing this kind of scan by continuously tuning the polarization angle between the pump and probe would allow us to build a complete angular map of the laser-induced population transfer strength between each Rydberg states, which could be of great interest to benchmark quantum theory involving the description of highly excited (Rydberg) states.

We now turn our attention to the spectral region where we see emission from the 4s states. In the parallel case, two spectral components ($\sim$ 11.7 and 11.9 eV) were visible in the xFID spectrum (for positive pump-probe delay only). In the perpendicular configuration, the lower spectral component almost vanishes (see Fig. 2.40(b) and (d)). Again, this is a signature of the angular-dependence of the ladder-type two-photon transition dipole matrix elements that govern the population transfer from the Rydberg states to the lower 4s valence states. More intriguingly, we also observe the appearance of a weak and broad spectral component that extends from several hundreds of meV above the energy of the highest 4s state to significantly below the first 4p state (12.9 eV). The fact that this emission occurs in an energy range where there is no field-free eigenstate indicates that it probably

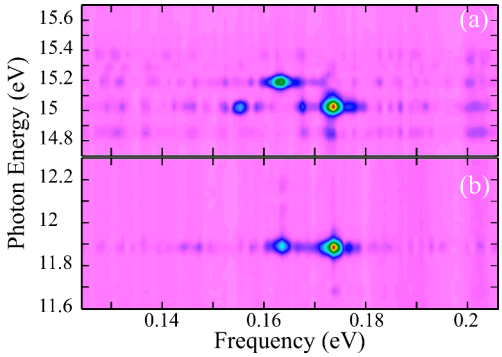

Figure 2.41: High-resolution 2D xFID spectrum for (a) Rydberg states and (b) 4s valence states. We used a parallel relative polarization configuration and the Argon backing pressure was 10 mbar. This figure is adapted from [Beaulieu et al. 2017a].

comes from the Stark-shifted 4s state when the probe laser field is on. Indeed, even though the xFID emission occurs mostly when the probe IR pulse is off and is thus insensitive to this Stark-shift, a small fraction of the emission does occur during the probe pulse, *i.e.* from Stark-shifted states. This can create a high-energy tail on the xFID lines. We observe that the oscillation phase of this broad spectral component linearly depends on its energy (it is represented as a tilted thick white line in Fig. 2.40). This could be a signature of a linear dependence of the transition dipole matrix element that governs the transition from Stark-shift Rydberg state to the ground state to the instantaneous field strength.

The energy resolution ($\delta\xi$) of Fourier transform spectroscopy is set by the number of oscillation periods of the beating that we scan. In the previously shown data, we restricted the scan from 100 to 500 fs, i.e. over a range of $\Delta\tau$ = 0.4 ps. This ensures a short acquisition time for each scan. The energy resolution associated with these scan is thus $\delta\xi \propto 1/\Delta\tau \approx 10$ meV. We performed additional measurements with a larger scanning range, from 100 to 2400 fs, also by steps of 4 fs. The resulting 2D spectrum is shown on 2.41. One can see that the spectral resolution is improved by $\sim$ one order of magnitude, reaching $\delta\xi$=1.72 meV. This resolution could be easily improved by increasing the pump-probe delay scanning range, to reach the sub-meV range. In the high-resolution 2D spectrum, we now see many components which were not resolved by the XUV spectrometer nor by the 2D spectrum with tens of meV spectral resolution. This high resolution measurement reveals additional modulations at 0.168 eV for R_1 and R_2 (population transfer between $4d(^2P_{3/2})$ and $6s(^2P_{1/2})$), and an additional 0.155 eV modulation for the R_2 peak corresponding to the coupling between $4d(^2P_{3/2})$ and $6s(^2P_{3/2})$ (0.1552 eV). By performing high-resolution T-REX spectroscopy, we beat by more than one order of magnitude the resolution of our spectrometer ($\sim$ 60 meV around 15 eV). T-REX is thus shown to allow for high-resolution XUV spectroscopy, without using XUV pulses.

2.4.4 Direct measurement of the xFID phase using two-source interferometry

In conventional absorption spectra, the frequency, the characteristic emission time and the phase of each spectral component of the xFID are mapped onto the position, the linewidth and the spectral lineshape of the associated absorption feature, respectively. For example, let us consider the xFID emitted by a coherent superposition of two states of energies E_1 and E_2, where the dynamics is characterized by dipole emission at the frequency $\epsilon = (E_2 - E_1)/\hbar$ with a mono-exponential decay function with a characteristic time of $\Delta\tau$ (as in Fig. 2.43 (a)-(b)). A scheme of the process in shown in Fig. 2.42(a).

The associated spectral line shape would be a Lorentzian peak centered around ($\epsilon =$

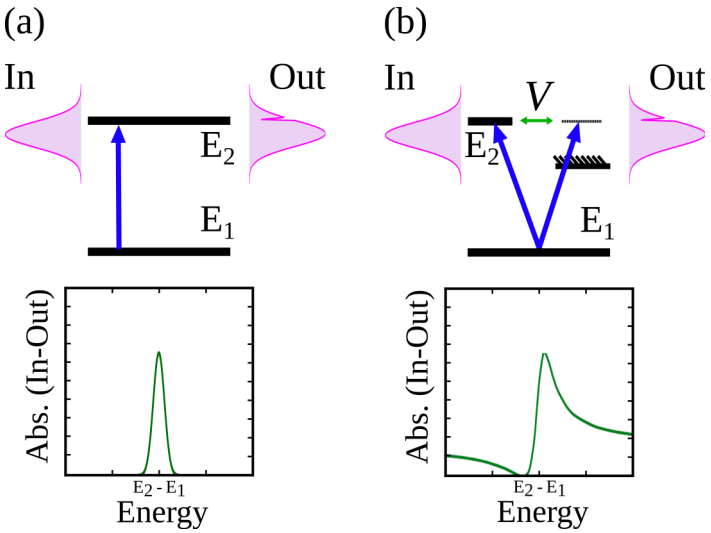

Figure 2.42: Schematic of different scenario giving rise to Lorentz (a) and Fano (b) spectral lineshape. In (a), the coherent superposition of two bound states characterized by mono-exponential decaying of the dipole emission gives rise to Lorentzian lineshape. In (b), the excited (bound) state is coupled via Configuration Interaction (V) with the equienergetic continuum state (*e.g.* autoionization), which lead to the production of an asymmetric (Fano) spectral lineshape. The upper panels represent the incoming (In) and transmitted (Out) spectra. The bottom panels represent the absorption spectra (Abs.), where Abs. = In - Out.

$(E_2 - E_1)/\hbar$), of linewidth $\Delta\epsilon \propto 1/(\Delta\tau)$). If a continuum state is equienergetic to the excited state (at E_2), the dynamics might get more complicated. The light at frequency $\epsilon = (E_2 - E_1)/\hbar$ can either lead to direct continuum absorption (ionization) or can create a coherent superposition between the ground (E_1) and the excited (bound) state (E_2) that emits xFID. The excited (bound) state is coupled via Configuration Interaction (CI) with the equienergetic continuum state. The spectral interference between the direct continuum absorption (delta-like in the time domain) and the exponentially decaying component produces an asymmetric (Fano) spectral lineshape. The asymmetry of the Fano spectral lineshape is determined by the phase shift (ϕ_{Fano}) of the long-lived exponentially decaying component compared to the Lorentzian case. The spectral lineshape thus gives information about the electron dynamics near resonances.

We have previously seen that a time-delayed (IR) laser pulse can induce a phase shift of the xFID, which is governed by the time-integral of the Stark-shift over the laser pulse duration (see equation 2.10 and Fig. 2.43 (f)). By controlling the laser pulse parameters (duration, intensity, wavelength), one can thus tailor the time-integral of the Stark-shift over the laser pulse duration, leading to a control over the *Laser-Imposed Phase*, ultimately leading to a full control over the absorption lineshape. As one can see in Fig. 2.43, the laser-induced phase-shift (Fig. 2.43 (e)-(f)) can be used to control the lineshape and mimic a case where Fano profile would have been obtained after a complex multielectron dynamics, near an autoionization, for example (Fig. 2.43 (c)-(d)) This general and universal scheme for controlling the spectral lineshape, from Lorentz to Fano, and vice-versa, has been demonstrated by Ott *et al.* [Ott et al. 2013].

The interference between the incoming light and the xFID emitted by the excited medium *indirectly* encodes the xFID phase in the spectral lineshape resulting from this interference, in a heterodyne-like detection scheme. In T-REX, there is no spectral overlap between the exciting light (400 nm) and the xFID ($\sim$ 82 nm (15 eV)). T-REX measures

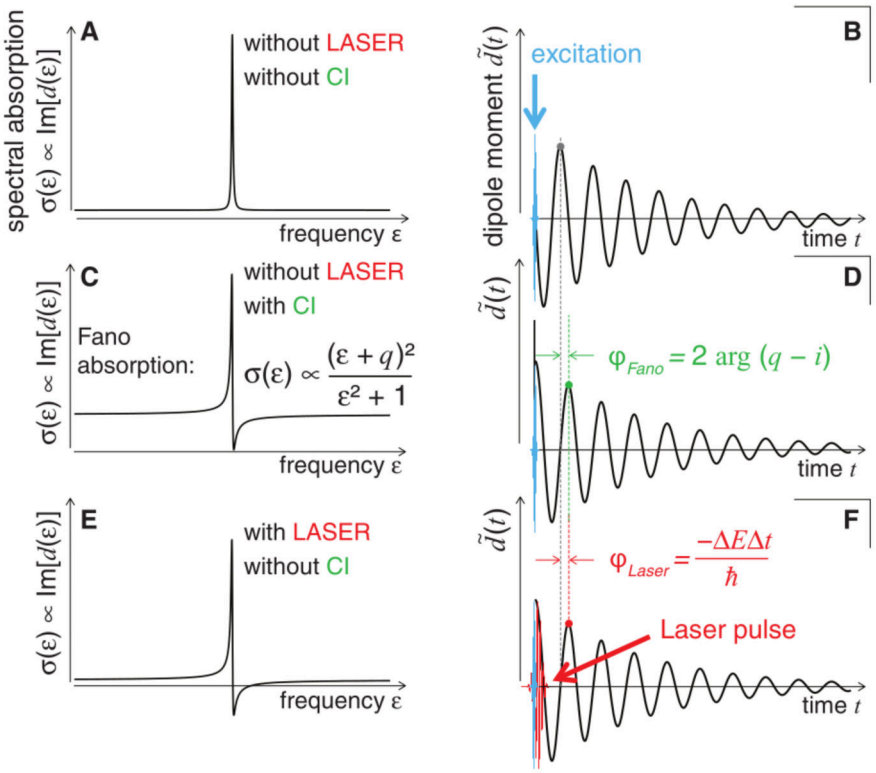

Figure 2.43: Schematic of the origin of different spectral lineshapes and their laser control. In (a), the Lorentzian absorption lineshape. In (b), the temporal dipole response function associated with a Lorentzian absorption lineshape. It is characterized by a simple mono-exponential decay. In (c), an example of an asymmetric Fano spectral absorption lineshape. In (d), the temporal dipole response function associated with the Fano spectral lineshape. The asymmetric Fano lineshape emerges because of a phase shift (ϕ_{Fano}) dipole compared to the Lorentzian case. This phase shift (ϕ_{Fano}) is governed by configuration interaction (CI), which is associated to the multielectron interaction in the case of Fano resonance. In (e) and (f), a laser pulse dynamically Stark-shift the excited state, which leads to a phase shift of the xFID emission (see equation 2.10). This so-called *Laser-Imposed Phase* will transform the originally Lorentzian shaped absorption feature in a Fano-like absorption lineshape. This figure is adapted from [Ott et al. 2013].

background-free xFID emission, which significantly improve the signal-to-noise ratio. However, using this background-free technique, we seem to have lost the interferometric (heterodyne) nature of the detection, and thus the xFID phase information. Would it still be possible to recover the xFID phase information, using T-REX ?

In the following, we will show that using the 'Two-Source Interferometry' (TSI) technique, one can *directly* measure the laser-imposed xFID phase. The TSI technique consists of creating two spatially separated source of xFID radiation in the near-field. These two sources interfere in the far-field, like two high-order harmonic sources [Bellini et al. 1998], and their relative phase is mapped onto the phase of the interference fringe. In the lab, we did so by inserting a dry-etched fused-silica plate which acted as a 0-π phase mask in the 400 nm laser beam and split its focus into two spots [Camper et al. 2015]. This 0-π phase mask was provided by S. Guilet and brought to Bordeaux by L. Barreau, who participated to the two-source interferometry experiments. The resulting focal spot of the UV beam is shown in Fig. 2.44 (a). We overlapped the probe IR beam to one of these sources, in order to induce a dephasing of the xFID through Stark-shift, while the other source was unperturbed and was used as a reference. By measuring the phase of the

spatial interference fringe, one can thus *directly* extract the Laser-Imposed Phase (LIP) in the perturbed source. The fringe pattern was recorded as a function of the IR intensity, at a delay of 400 fs, in order to avoid pump-probe overlap effects. We performed the scan for both parallel and perpendicular relative polarizations between pump and probe pulses.

The interference fringes show a linear shift with increasing laser intensity, as can be seen in Fig.2.44(a), reflecting a linear behavior of the laser-imposed phase. In addition, the total signal decreases as the intensity increases, because of the damping by ionization. The amplitude of the signal as a function of laser intensity is shown in Fig. 2.44 (b). The ionization damping of the xFID is clearly more efficient when the polarization of the ionizing pulse is parallel to the exciting one. This means that it is easier to ionize the Rydberg states with a laser pulse that is parallel to the quantization axis of the atomic dipole. A similar behavior is well known for tunneling ionization from valence orbitals [Pavicic et al. 2007; Shafir et al. 2009; Young et al. 2006]. At first sight, it may seem quite surprising to observe a similar alignment effect at the low intensity used in our measurement. However, our experiment lies in an exotic regime where the I_p of the excited atoms is less than 1 eV, such that even at the intensity in the 10^{12} W/cm^2 range, the Keldysh parameter is close to 1. This proximity to the tunneling regime explains the strong dependence of the ionization yield on the polarization direction, as previously shown in strong-field ionization of the valence orbitals of atom and molecules in their ground state. This result shows that relatively weak laser fields can be used to transpose strong-field physics studies to highly excited states.

We now turn our attention to the laser-induced phase shift of the xFID (Fig. 2.44 (c)). This phase shift is determined by the time-integral of the AC-Stark-shift of the Rydberg states during the laser pulse. Usually, the energy of the electronic ground state is assumed to be rather insensitive to the laser intensity, while the Stark-shift ($\Delta E^{(S)}$) of states lying close to the ionization threshold is assumed to be equal to the ponderomotive energy $U_p \propto I_0 \lambda^2$. For lower-lying Rydberg states, like the ones involved in our T-REX experiment, the Stark-shift is expected to be smaller than U_p because as the electrons get more deeply bound, their polarizability decreases. Our measurement can, in fact, be used to measure this Stark shift. Knowing the laser pulse duration, and IR peak power, we can calculate the laser-induced phase shift that corresponds to a Stark shift of U_p. We can then compare the slope of the xFID phase as a function of intensity to this value, and extract the amplitude of their Stark-shift, compared to U_p. For the Rydberg states measured in our experiment we find slopes of $0.77 \cdot \phi_{U_p}$ for R_4, $0.72 \cdot \phi_{U_p}$ for R_3 and $0.66 \cdot \phi_{U_p}$ for R_2. Our experimental results show that when Rydberg states are closer in energy to the ionization threshold, the value of ζ gets closer to 1, which is pretty intuitive given the explanation above.

Phase-resolved T-REX thus provides a direct evaluation of the AC-Stark-shifts, a quantity which is fundamentally important, but not easy to accurately determine experimentally [López-Martens et al. 2000]. The measured values are between 66 and 77 % of the ponderomotive shift, meaning that the Coulomb interaction between the low-lying Rydberg electrons and the ionic core is not negligible with respect to the effect of the electric field of the laser on the Rydberg electron dynamics. Moreover, our experiment shows that while the ionization yield is strongly affected by the relative polarization between pump and probe, the AC-Stark-shift is remarkably independent of this parameter. The precision of this method to determine the Stark-shift is limited by the precision with which we are able to determine the laser pulse duration and intensity. In this case, we retrieved the pulse duration (30 fs), using a single-shot SHG autocorrelator. The intensity was determined by using the highest energy per pulse available in the 800 nm arm to generate HHG in Argon, and to retrieve the peak intensity using the HHG cut-off scaling

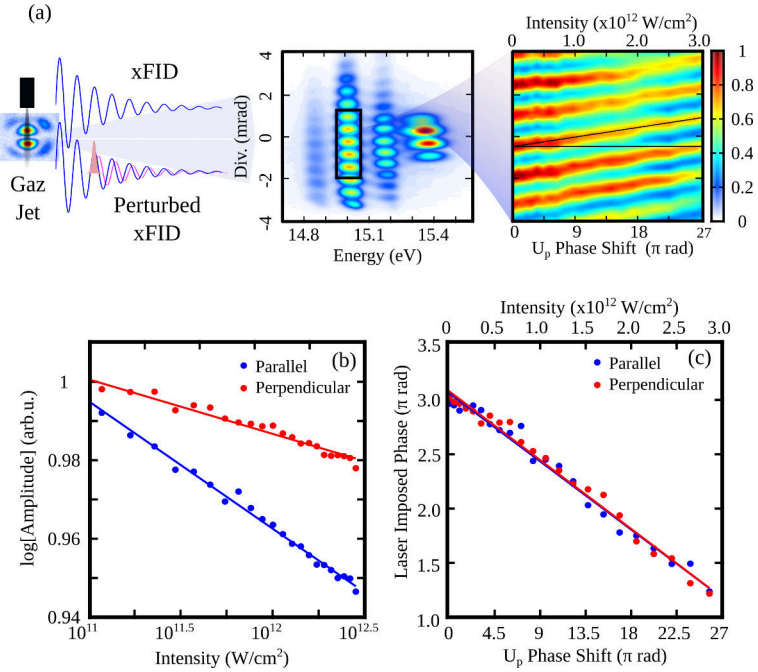

Figure 2.44: Direct measurement of the xFID phase and its laser control. (a) Schematic representation of the two-source interferometry experiment. Two sources of xFID are created by introducing a 0-π phase mask in the collimated beam. The xFID emission in one of the sources is perturbed by an IR pulse with tunable intensity and polarization state, while the other one is used as a reference. The middle panel shows the spatially-resolved xFID spectrum when using the 0-π phase mask. The right panel shows the spatial profile of the R_2 xFID emission as a function of the IR pulse intensity at a pump-probe delay of 400 fs. (b) Amplitude, and (c) phase of the xFID emission of R_2 as a function of IR intensity, with parallel (blue) and perpendicular (red) pump-probe polarizations. The dots are the experimental points and the solid lines are linear fits. The Argon backing pressure was 10 mbar. This figure is adapted from [Beaulieu et al. 2017a].

law. The low-intensity values, used for the TSI experiments, extrapolated by using the measured maximum peak intensity (known from the HHG cut-off) multiplied by the transmission of the attenuator made of a half-wave plate and a polarizer.

2.4.5 Pressure dependence of the xFID emission dynamics

We now turn our attention to the pressure scaling of the xFID signal. We have first carried out a static investigation of the pressure dependence of the xFID signal, of a below-threshold harmonic (H5) and of an above threshold harmonic (H7). The results are presented in Fig. 2.45. In the low-pressure range (0-120 mbar Argon backing pressure, Fig. 2.45(a)), the harmonics exhibit a quadratic growth as a function of the backing pressure. On the contrary, the evolution of the XFID signal is remarkably linear. As the backing pressure of Argon is further increased (see Fig. 2.45(b)), the signal from above-threshold H7 increases up to 475 mbar, after which it suddenly starts to decrease. This behavior is the signature of strong reabsorption. For the below-threshold harmonic (H5) and xFID signals (R_2 and R_3), the signals continue to grow, up to the end of the pressure scaling scan (1600 mbar).

Because both HHG and xFID are coherent processes, one would expect a quadratic growth of both signals with the atomic density (or the backing pressure), at least, until reabsorption effects start playing a role. In order to stay away from the case where reabsorption is playing a role, we will focus on the low-pressure range (Fig. 2.45(a)). From

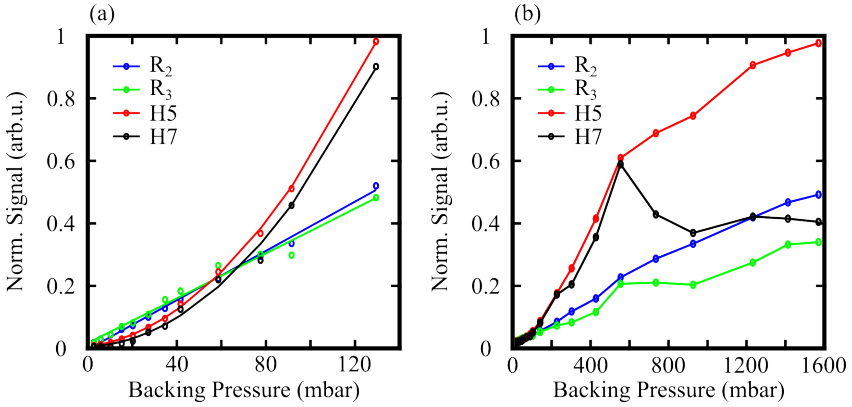

Figure 2.45: Pressure scaling of harmonic and xFID signals. R_2 and R_3 are the xFID signals for the $5d/7s(^2P_{3/2})$ and $4d/6s(^2P_{1/2})$ Rydberg states. H5 and H7 are the below-threshold harmonics 5 and above-threshold harmonic 7, respectively. In (a), for the low-pressure range (The dots are experimental data and the lines represent linear fitting for R_2, R_3 and quadratic fitting for H5 and H7.) and in (b), up to 1600 mbar Argon backing pressure. This figure is adapted from [Beaulieu et al. 2017a].

0-120 mbar, H5 and H7 show the expected quadratic scaling behavior with atomic density. In the same condition, the xFID exhibits a linear scaling with atomic density. In order to explain this, we have to take into account the effect of collisions in the experiment. Because the xFID emission takes place on a very long timescale (tens of picoseconds), atomic collisions between the spatially extended electronic excited states can play a role in the scaling of the signals with pressure, even causing spectral reorganization of the xFID lines, as shown in Fig. 2.47. A simple model derived in [Beaulieu et al. 2017a] shows that the xFID signal scales linearly with pressure if the collision rate is faster than the emission rate. This approximation is justified by the fact that the typical timescale of the Rydberg states lifetime is on the order of nanoseconds, but our experimental measurements indicate picosecond coherence times. This suggests that the collision rate dominates over the emission rates. Thus, even if the Argon density is rather low in the jet (at least one order of magnitude lower than the backing pressure), the delocalized nature of the Rydberg electrons causes significant collisional effects.

In order to further investigate the influence of pressure, we compared the time-dependent ionization damping of signals (like in Fig. 2.38), which is the equivalent of measuring the coherence time of each spectral components, for different backing pressures (Fig. 2.46). We found out that the characteristic coherence time decreases with increasing backing pressure, which can be explained by the higher collision rate.

Last, we measured the effect of pressure in the fine femtosecond T-REX scans that reveal the beating (as in Fig. 2.39 and 2.40). The results are presented in Fig. 2.48 (a)-(c). As the pressure increases ((a) 8 mbar, (b) 100 mbar and (c) 500 mbar), the oscillations of $\sim$ 25 fs period, which reflect the electronic wavepacket reshaping by the IR-induced population transfer, disappear, and a new spectral component down-shifting in energy as the pump-probe delay increases. This dramatic influence of pressure on the femtosecond T-REX scans was at first really puzzling to us. In order to understand it, we need to take into account the different contributions to the final xFID signal measured onto the detector. First, there is the xFID signal emitted before the arrival of the IR pulse. This signal contains the unperturbed dipole emission. There is also the xFID signal emitted when the IR laser pulse is on. It contains xFID signal from field-dressed (Stark-shifted) Rydberg states. Last, there is the xFID signal emitted after the probe pulse. It contains the

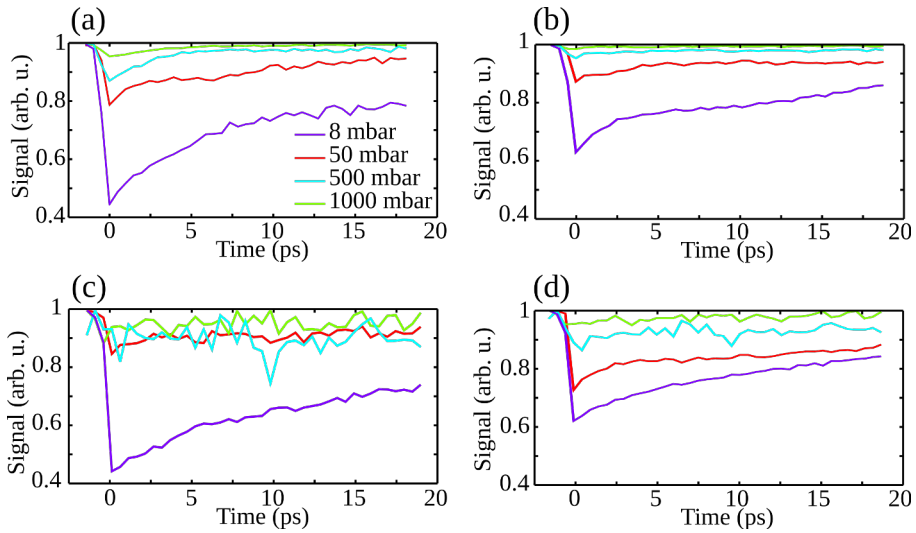

Figure 2.46: Time-resolved ionization damping of the xFID for different Argon backing pressure. In (a) for R_1 (4d/6s ($^2P_{3/2}$)), in (b) for R_2 (5d/7s ($^2P_{3/2}$)), in (c) for R_3 (4d/6s ($^2P_{1/2}$)) and in (d) for R_4 (6d/8s ($^2P_{3/2}$)). The signals are normalized to unity (negative pump-probe delay) for each pressure and each Rydberg state. This figure is adapted from [Beaulieu et al. 2017a].

signal of the laser-induced population transfer between the different Rydberg states. At very low pressure (for example Fig. 2.48(a)), the coherence time of the xFID is very long. The signal is thus dominated by the component emitted after the probe pulse, and shows strong signatures of the laser-induced population transfer between the different Rydberg states (beatings). These are the ideal experimental conditions to perform 2D T-REX. At very high pressure (for example Fig. 2.48(c)), the coherence time of the xFID emission is strongly reduced by collisional effects. In this regime, a large fraction of the total signal is emitted before and during the probe laser pulse, which leads to the disappearance of the beating of the xFID signal. It also leads to the appearance of a time-dependent energy shift of the spectral lines, which is signature of the Stark-shifts occurring during the probe pulse. High pressures, leading to collisional broadening, are thus clearly prohibitive to perform 2D T-REX. However, they provide a bright and relatively short, narrow band source of VUV light. For intermediate pressures (for example 2.47(b)), the spectrogram contains both the features of the beating and the Stark-shift, indicating a balance between the xFID signal emitted during and after the laser pulse.

Pressure effects have also been previously investigated in TRAX experiments, where XUV and IR pulses are used. The disappearance of the beating with the increasing pressure has been observed by Cao *et al.* [Cao et al. 2016a]. It has been interpreted as resulting from the reshaping of the propagating XUV exciting pulse by the strongly dispersive absorbing medium. Here, because we used multiphoton excitation by VIS pulses, the reshaping of the pump pulse cannot play a role. We thus provide a new interpretation of the origin of beating disappearance at high pressure, based on collisional effect arguments. T-REX is thus a good technique to decouple pulse propagation and pressure (collision) effects, which are usually coupled in TRAX experiments.

2.4.6 Partial conclusions and perspectives

We have demonstrated that using multiphoton transitions to create an electronic wavepacket made of the ground and few Rydberg states provides an interesting background-free alternative to XUV transient absorption spectroscopy, in the case where the XUV comes before

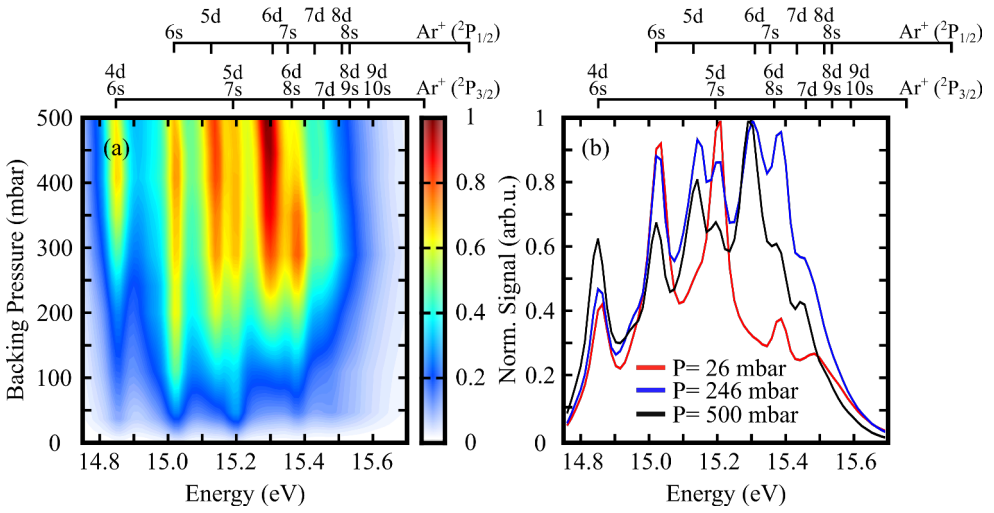

Figure 2.47: Spectral reshaping of xFID at high pressure. (a)-(b) xFID spectrum as a function of the Argon backing pressure.

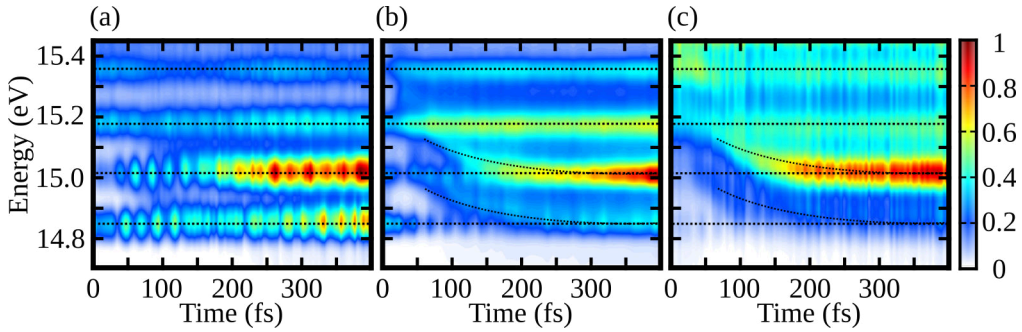

Figure 2.48: Pressure effect in the femtosecond T-REX scans. The xFID spectrum as a function of pump-probe delay for different backing pressure: (a) 8 mbar, (b) 100 mbar and (c) 500 mbar, with parallel pump-probe polarizations. The dashed black lines serves as a guide to the eyes.

the IR pulse (which is the most widely used ATAS configuration). In our T-REX scheme, the fact that the pump pulse does not spectrally overlap with the xFID emission from the wavepacket leads to a tremendous improvement of the signal-to-noise ratio. In a similar fashion as in ATAS, T-REX can measure the coherence time of the xFID emission as well as the laser-induced population transfer dynamics. We have shown that T-REX provides an easily way to perform high-resolution XUV Fourier transform spectroscopy, without the use of any XUV pump or probe pulses. This enables an intrinsic decoupling between resonant XUV pulse propagation and collisional effect, which usually occur at the same time in ATAS experiments when the density of the medium is increased. Last but not least, we have shown that 'Two-source interferometry' (TSI) allows to *directly* measure the xFID phase with respect to a reference xFID source. By controlling the xFID emission in one source using a second laser pulse, we have shown that TSI allows measuring the 'Laser-Imposed Phase', a phase which is at the heart of many ATAS experiments. This ultimately leads to the determination of the Stark-shift of each Rydberg states emitting xFID, a physical quantity which is fundamentally important and usually hard to access experimentally.

T-REX also comes with some limitations. First, the states that can be excited are limited by the narrow bandwidth of the pump pulse (compared to XUV pulses used in ATAS).

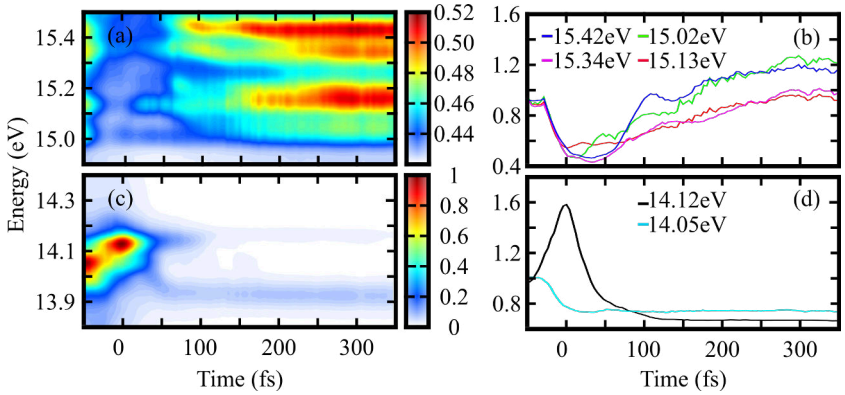

Figure 2.49: Demonstration of time-resolved xFID in N_2. The delay was vary by step of 4 fs. Under the same experimental conditions, oscillations in the time-resolved xFID spectra were observable in Ar.

The use of a tunable UV-VIS or IR source as a pump would allow tuning the pump wavelength in multiphoton resonance with states of interest, considerably extending the scope of this scheme. However, the maximum bandwidth of wavepacket will always be smaller for T-REX than with ultrabroadband XUV continuum pump. Moreover, the temporal resolution is also much better when using a combination between few-cycle IR and isolated attosecond pulses.

One of the possible perspectives of T-REX is to study the xFID dynamics in molecules. In the molecular case, one could investigate static and time-resolved xFID emission as a function of the angle between the pump (or probe) pulse and the molecular axis (using impulsive molecular alignment). This would give access to the angular-dependence of the multiphoton transition dipole matrix element involved in the creating of the wavepacket (by the pump) and involved in the population transfer between different states of the wavepacket. Moreover, the non-adiabatic coupling between electronic and nuclear degrees of freedom might lead to significantly different wavepacket dynamics, which might be encoded in the time-resolved xFID spectrum. As a first test, we performed a time-resolved xFID scan in N_2, which have roughly the same I_p as Argon. The fact that Argon and N_2 have the same I_p ensures that there will be some Rydberg states accessible through 5x400 nm photons transition from the ground state in both systems when using the same experimental parameters. A first attempt of time-resolved xFID in N_2 is shown in Fig. 2.49. We can see that the dynamics of several spectral components strongly departs from the simple case of monoexponential decay, indicating more complicated and rich wavepacket dynamics than in Argon. Moreover, we were not able to see any oscillation of the xFID spectrum as a function of the pump-probe delay. This might be a molecular orientation averaging smearing effect, meaning that the different molecular orientation could lead to different oscillation frequencies and phases (coupling with different states at different delays), leading to a smearing of the oscillations when the signal is averaged over all molecular orientations. Molecular T-REX is thus an interesting and easily implementable all-optical technique that could be investigated in the future, in impulsively aligned molecular ensemble.

2.5 High-order Harmonic Generation driven by Laguerre-Gaussian beam

2.5.1 Generality about angular momentum conservation in HHG

In the previous sections, we have shown how the coherently populated excited states of the system can be used to generate new spectral components though the highly non-linear interaction of light with excited atoms. In this section, we will show how we can tailor the spatial properties of light to transfer angular momentum to the XUV light emitted though HHG.

Light is known to carry two different type of angular momentum, namely spin- and orbital- angular momentum (SAM and OAM, respectively). The SAM is associated with the circular polarization of light: at a single photon level, SAM can takes values of $\pm\hbar$, associated with left- or right-handed circular polarization. A linearly polarized beam of light is considered as made of a linear combination of left- and right- circularly polarized photons. The OAM is associated with the light field wavefront. A beam with a flat wavefront does not carry any OAM. On the contrary, a light beam with twisted wavefront carries OAM.

High-order harmonics are typically driven by linearly polarized Gaussian beams, whose transverse (electric and magnetic) field amplitude profiles can be described by a Gaussian function and by a flat wavefront profile (plane wave, no OAM). This Gaussian spatial profile and the linear polarization properties of the IR pulse are usually transferred to the XUV beam that is generated through the extreme nonlinear frequency upconversion process of HHG. Such simple case, where the SAM and the OAM of the IR and thus of the XUV beam are null, is not fundamentally interesting to study the role of angular momentum in HHG.

The transfer of SAM from the IR to the XUV in HHG has recently been subject to intense research effort. Studying the SAM transfer in highly nonlinear processes is not only fundamentally interesting but is also of great interest for application requiring the use of circularly polarized XUV light. Despite its broad range of potential applications, the transfer of OAM in highly nonlinear phenomena have, however, attracted much less attention. Indeed, in the visible spectral range, beams carrying OAM have been used, for example, to produced OAM entangled photon pair for quantum cryptography [Mair et al. 2001], to overcome the Abbe diffraction usually limiting STED microscopy [Hell et al. 1994], to detect spinning objects [Lavery et al. 2013] and even to optically trap particles [Kuga et al. 1997]. It would be of great interest to extend these innovative ideas to the XUV spectral range, where OAM can be used to control different aspects of light-matter interaction. One of the most obvious interests of OAM in XUV spectral range, is the possible transfer of OAM from the light beam to the electronic degrees of freedom, for example in photoionization [Picón et al. 2010]. In the following, we will quickly describe the scheme which is generally used to impose a given curvature to the driving laser wavefront and briefly review the different experiments that have tackled the questions of OAM transfer during HHG.

To convert a typical Gaussian beam, which does not carry OAM, into a beam carrying OAM, the most simple solution is to propagate the beam into a transparent material with well defined transverse spatial inhomogeneity, named spiral phase plate (SPP). A schematic of such SPP is depict in Fig. 2.50. When $d = \ell\lambda$, the SPP converts the incoming plane wave into a beam carrying non-zero and well defined OAM (ℓ). This yields to a

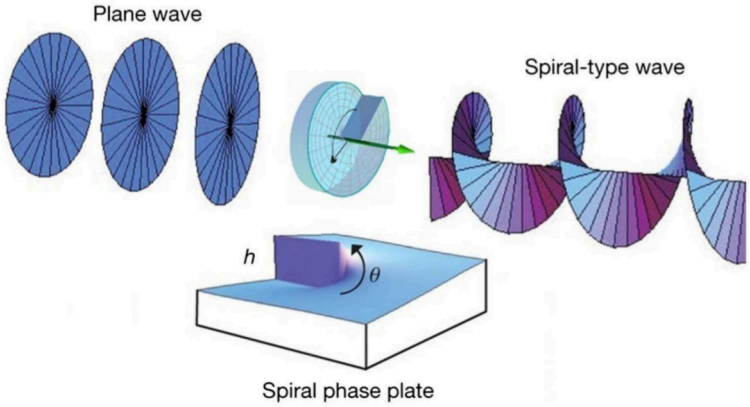

Figure 2.50: Schematic of the generation of light carrying OAM with a Spiral Phase Plate (SPP). The plate, which is characterized by a well defined transverse spatial inhomogeneity, is converting a plane wave into a twisted wave. This figure is adapted from [Massari et al. 2015].

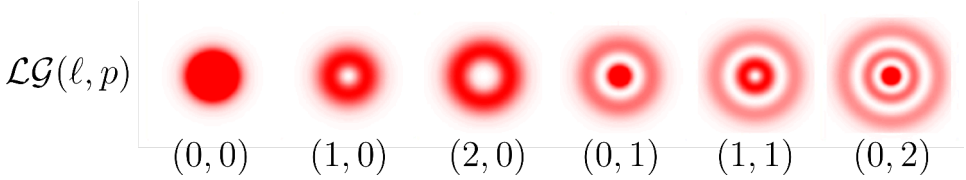

Figure 2.51: Schematic of the intensity profile for few Laguerre-Gaussian modes $\mathcal{LG}(\ell,p)$.

so-called 'Laguerre-Gaussian mode' ($\mathcal{LG}$) which is described by the following expression:

$$E_{\ell,p}(r,\theta,z) = \frac{e^{i\ell\theta}}{w(z)}\left(\frac{r}{w(z)}\right)^{|\ell|} L_p^{|\ell|}\left(\frac{2r^2}{w^2(z)}\right)\cdot e^{\left(\frac{r}{w(z))}-ik\frac{r^2}{2R(z)}-ikz+i(2p+|\ell|+1)\chi(z)\right)} \tag{2.11}$$

where $w(z)$, $R(z)$ and $\chi(z)$ are the beam waist, wavefront curvature, and Gouy phase, respectively. $L_p^{|\ell|}$ are the generalized Laguerre polynomials. The $\mathcal{LG}$ modes are indexes by two mode numbers, denoted the azimuthal (ℓ) and the radial (p) indexes, $\mathcal{LG}(\ell,p)$. The name of the indexes stem from the fact the phase of these modes goes as $\ell\theta$ along the azimuthal coordinate θ (see Fig. 2.50) and their radial distribution can be described by $p+1$ concentric rings, for $\ell > 0$. A few examples of the intensity profile of some $\mathcal{LG}(\ell,p)$ modes are shown in Fig. 2.51.

Based on momentum conservation argument, the XUV light generated by HHG should obey the multiplicative law for OAM transfer, as previously observed for low-order, perturbative nonlinear phenomena (second harmonic generation, for example, [Dholakia et al. 1996]). The mode of the q-th order harmonics generated by driving the nonlinear interaction using a beam with a $\mathcal{L},\mathcal{G}(\ell,0)$ mode should be a $\mathcal{L},\mathcal{G}(q\ell,0)$ mode. Unexpectedly, the first measurement of the OAM a harmonic generated though HHG showed a violation of this multiplicative momentum conservation rule [Zurch et al. 2012]. Zurch *et al.* measured the OAM of a single harmonic and showed that $\ell_1 = \ell_q$, where ℓ_1 and ℓ_q are respectively the azimuthal indexes of the driving laser and the q-th order harmonic. They claimed that the departure from the multiplicative momentum conservation rule was due to a parametric instability in the medium, which prevented the macroscopic propagation of the XUV high-order $\mathcal{L},\mathcal{G}(\ell > 1,0)$ mode to the detector. These results were somehow controversial. Later, an elegant interferometric measurement of the OAM of three harmonics was performed by Gariepy *et al.* [Gariepy et al. 2014]. In this experiment, it was shown

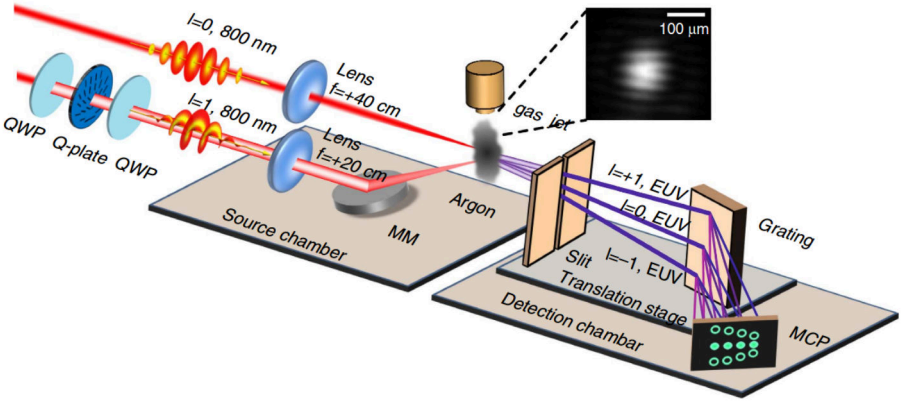

Figure 2.52: Schematic of the experimental setup of Kong *et al.* [Kong et al. 2017]. A strong IR Gaussian beam is focus into an Argon gas jet. A non-collinear perturbative $\mathcal{LG}$ IR beam is overlapped to the strong IR Gaussian beam. The interference between the two pulses create a fork-like structure in the gas jet (see the inset). Since the atomic dipole phase depends on intensity, this fork structure is imprinted onto the phase of the emitting atomic dipole. The emitted harmonics, carrying OAM, are analyzed using an XUV imaging spectrometer. QWP stands for quarter wave plate, MCP stands for microchannel plate and MM stands for a motorized mirror. This figure is adapted from [Kong et al. 2017].

that the HHG process follows the expected multiplicative momentum conservation rule. It is thus possible to generate XUV beam with high ℓ values.

More advanced control of the OAM of high-order harmonics was recently achieved in two experiments published simultaneously by Kong *et al.* [Kong et al. 2017] and Gauthier *et al.* [Gauthier et al. 2017]. These works demonstrated the ability to control the OAM of each harmonic by using a non-collinear HHG scheme, which had been introduced a few years ago by Bertrand *et al.* [Bertrand et al. 2011]. They added to the strong IR Gaussian generating beam a weak non-collinear IR [Kong et al. 2017] or 400 nm [Gauthier et al. 2017] $\mathcal{LG}$ beam, and showed the perturbative control over the OAM of the generated harmonics.

Last, the influence of OAM on the temporal profile of the high-order harmonic generation was investigated by Géneaux *et al.* [Géneaux 2016]. They used the RABBITT technique to show that the coherent superposition of a few harmonics q with $\ell = q$ lead to a helically shaped attosecond pulse train, an effect which was theoretically predicted by Hernandez-Garcia *et al.* [Hernández-Garcıa et al. 2013].

2.5.2 Radial index of Laguerre-Gaussian modes in high-order harmonic generation

As one can notice, from the few examples given above, most of the attention has been paid to the effect of the azimuthal index (ℓ) during HHG, while the effect of the radial index (p) of the $\mathcal{LG}$ modes is usually ignored. The situation was, for a long time, similar in the visible spectral range, where p was called the “forgotten quantum number". Nonetheless, people have later realized the importance and the great potential of p, for example, to prepare quantum states of high dimensionality [Salakhutdinov et al. 2012]. $\mathcal{LG}$ with high p values were also shown to exhibit self-healing properties [Mendoza-Hernández et al. 2015]. It is thus of fundamental interest to investigate the role of the radial index in HHG driven by $\mathcal{LG}$ mode. This might pave the way to the addition of a new degree of freedom in our ability to shape XUV beams, and also, it might pull p out from its dormant state of forgetfulness, in the field of extreme nonlinear optics.

In the following, we will present a joint theoretical and experimental effort to understand the role of the radial index of Laguerre-Gaussian modes in HHG. It will be shown that the generation of harmonics with non-vanishing p indexes is intimately related to the contribution of quantum trajectories with large atomic dipole phase coefficients (*long quantum paths*). The experimental results were taken during a visit to LIDYL-Saclay, where I worked with Romain Géneaux and Thierry Ruchon. I brought the different optical components necessary to build the atypical XUV spectrum needed for these experiments. I assembled the spectrometer, performed the experiments and took the experimental data with Romain Géneaux and Thierry Ruchon. The theoretical calculations that will be shown below were performed by Thierry Auguste.

2.5.3 Theoretical description of HHG driven by $\mathcal{LG}$-beam

The first step of our investigation was to look at the theoretical calculations of the spatially-resolved HHG spectrum generated with a $\mathcal{LG}$ beam. The single-atom response was calculated within the Lewenstein model [Lewenstein et al. 1994] framework, where both "short" and "long" quantum path are generally well described. However, at a single-atom level, the Laguerre-Gaussian beam is seen as a plane-wave. The single-atom response is thus not affected by the presence of OAM in the driving beam. On a macroscopic scale, the different emitters are illuminated by parts of the driving beam which are characterized by different instantaneous phases. This will influence the macroscopic response of the light-driven medium, whose calculation is thus essential. To do so, an IR Gaussian beam of 50 fs duration was propagated through a spiral phase plate, which generated the $\mathcal{LG}(1,0)$ mode, characterized by a specific transverse phase profile. The propagation of this beam in a 500 μm wide Lorentzian Argon gas jet, where the XUV photons are emitted, was also included in the model. Details about this 3D SFA model are given in a paper by Géneaux *et al.* [Géneaux 2016]. The relative position between the focus and the gas jet (z_0) is known to modify the relative contribution of short and long quantum paths. Thus, the calculations were performed for three different z_0 values ($z_0 > 0$, $z_0 = 0$ and $z_0 < 0$).

The computed intensity profiles of harmonic 21 are presented in Fig. 2.53. When $z_0 < 0$, the contribution of the short quantum paths dominates the XUV emission. In this case, the computed intensity profile of H21 shows a single ring pattern (Fig. 2.53 (a)), which is the signature of $\ell \neq 0$. According to the multiplicative law for OAM transfer, we expect the H21 of a driving laser with a $\mathcal{LG}(1,0)$ mode to be described by a $\mathcal{LG}(21,0)$ mode. This ring pattern describing the spatial profile of H21 is thus not surprising. The fact that the intensity profile shows only one ring is the signature of a $p = 0$ mode. For $z_0 > 0$, where the contribution of long quantum paths is expected to be strong, we observe the presence of multiple concentric rings, which are the signature of $p > 0$. In the intermediate case of $z_0 = 0$, the contributions from both short and long quantum paths lead to a rich and complicated far-field profile of H21. In order to interpret this profile, one can separate the contribution of each quantum path to the total signal, by taking only one solution of the saddle-point equation (within the Leweinstein/SFA framework). The results of separated contribution from short and long quantum path are shown in Fig. 2.53 (d)-(e). This analysis leads us to conclude that short quantum paths are associated to the generation of single-ring intensity pattern ($\mathcal{LG}(q,0)$) while the long quantum paths lead to the emission of a multiple-ring pattern ($\mathcal{LG}(q, p \neq 0)$). We can also conclude that the complex intensity profile computed for $z_0 = 0$ is associated with the interplay between short and long trajectories.

The numerical results presented above show that signatures of the azimuthal and radial indexes of the harmonics generated with a $\mathcal{LG}(1,0)$ driving mode can be observed

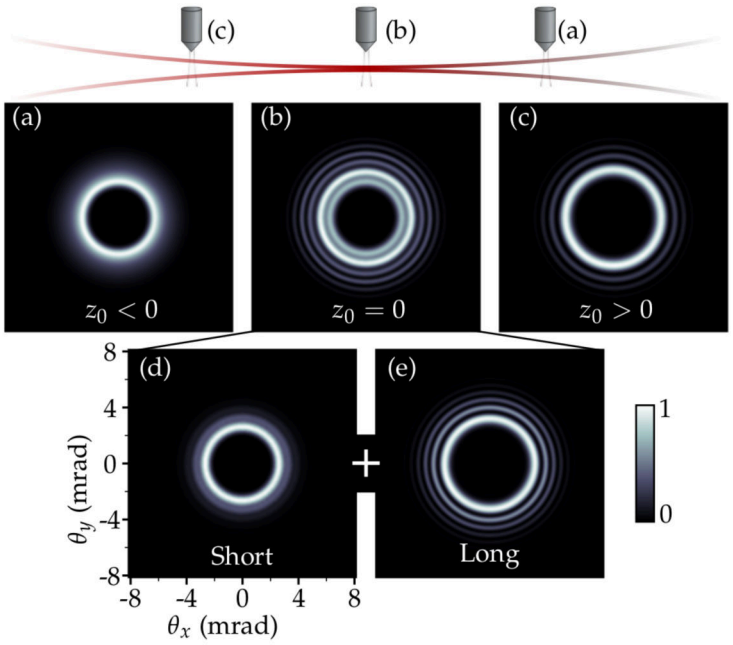

Figure 2.53: Theoretical investigation of the role of the long and short quantum path in HHG driven with a $\mathcal{LG}(1,0)$ beam. The far-field intensity of the H21 is computed for (a) $z_0 < 0$, (b) $z_0 = 0$ and (c) $z_0 > 0$. In (d) and (e), we show the intensity profile in the far-field, for $z_0 = 0$, when only the short or the long quantum path is selected, respectively. This allows isolating the contribution of each quantum path to the total intensity profile measured in the far-field. This figure is adapted from [Géneaux et al. 2017].

in their 2D spatial profile. Most HHG experiments do not resolve this 2D profile, but measure a spatially resolved spectrum, such as the ones shown previously in this chapter. In order to access the 2D profile of each harmonic, it is necessary to use a monochromator. We have used a scheme designed by Hartmut Ruf during his Ph.D. thesis at CELIA [Ruf 2012], see Fig. **LGHHG_Setup**

2.5.4 Experimental results of HHG driven by $\mathcal{LG}$-beam

The experimental setup is shown in Fig.2.54. We used the LUCA laser system at LIDYL, which delivers up to 30 mJ, 50 fs pulses centered around 800 nm, at 20 Hz repetition rate. The very high quality of the spatial profile is ensured by a stage of spatial filtering just before the compressor. This provides almost perfect Gaussian mode [Mahieu et al. 2015], which is important for its subsequent conversion into a Laguerre-Gaussian mode. The beam is sent through a 16-level spiral phase plate (SPP) (SILIOS technologies), to convert the Gaussian mode into a 77.5% pure $\mathcal{LG}(1,0)$ mode [Sueda et al. 2004]. The impurities of the mode are due to fact that the radial variation of the thickness of the spiral phase plate (SPP) is discrete rather than continuous. The beam is subsequently focused with a 1 m lens (L) into a gas jet of Argon delivered by a piezoelectric driven pulse valve (Attotech). Examples of the IR spatial profile at the focus are shown in Fig.2.55, for different values of ℓ.

The diverging XUV radiation produced via the highly nonlinear light-matter interaction is sent onto a toroidal mirror (TM) and a silica plate (SP), which respectively refocus and filter out most of the copropagating IR beam. The XUV beam is then reflected at $\sim 10^\circ$ incidence angle by a B_4C spherical mirror (Fraunhofer Institute). This B_4C has a reflectivity

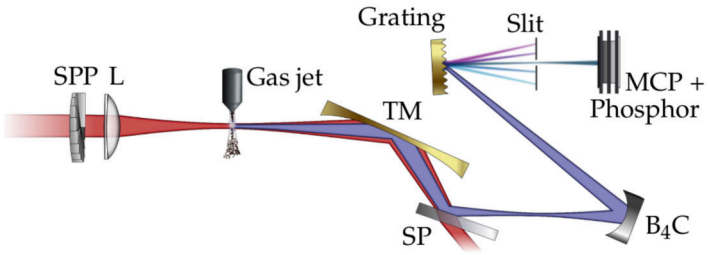

Figure 2.54: Schematic of the experimental setup. SPP: Spiral phase plate, L: Lens, TM: Toroidal mirror and SP: Silica plate. This figure is adapted from [Géneaux et al. 2017].

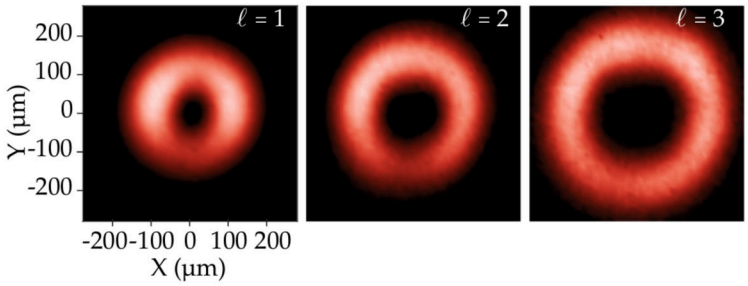

Figure 2.55: Spatial intensity profile of the IR laser beam, focused using a 1 m focal lens. In (a), the beam have propagated through a $\Delta\ell = 1$ SPP, in (b) through a $\Delta\ell = 2$ SPP and in (c) in both $\Delta\ell = 1$ and $\Delta\ell = 2$ SPP. The SPP were always placed before the lens. This figure is adapted from [Géneaux et al. 2017].

higher than 10% in the 1.55 - 40 eV spectral range. This ensures a high-reflectivity in the XUV spectral range of interest. Near the focus of the B_4C mirror, the XUV beam hits a flat diffraction grating (600 grooves/mm, Spectrogon) at an angle of incidence of $\sim 6°$. The grating is mounted on a motorized rotational stage, allowing a spectral selection of different harmonics using a slit, placed in front of the detector. The detector is made of MCP coupled to a phosphor screen, which is imaged by a 12-bit CCD camera (Basler). The 'Ruf' XUV monochromator has the advantage of being very cheap, easy to implement and allows one to measure the 2D spatial profile of each harmonic, with a really small amount of spatio-spectral couplings.

The experiment aimed at observing similar structures as in the numerical simulations. We generated high-order harmonics using a $\mathcal{LG}(1,0)$ beam, and analyzed their far-field 2D spatial profile. Since the numerical simulation demonstrated that the p content of the XUV strongly depended on the nature of the quantum paths leading to HHG emission, we performed the experiment for different z_0 values, which enabled us to change the relative weight of the short and long quantum paths. The far-field 2D spatial profile of H11 to H15, for different z_0 position, are presented in Fig. 2.56.

First, the fact that the signal shows up as cylindrically symmetric rings is a confirmation that the 'Ruf' XUV monochromator introduces a negligible amount of spatio-spectral couplings. When $z_0 < 0$, we expect no contribution from long quantum trajectories. For $z_0 = -0.2$ cm, the spatial profiles of H13-H15 can be described by single ring patterns, which is a signature of $p = 0$. For $z_0 > 0$, one can see that more divergent concentric rings appear in the spatial profiles of the harmonics. For these $z_0 > 0$, long quantum paths are expected to significantly contribute to the HHG signal. Moreover, as mentioned above, the appearance of these more divergent concentric rings in the spatial profile of the harmonics is related to the generation of $p > 0$ Laguerre-Gaussian modes. These observations thus

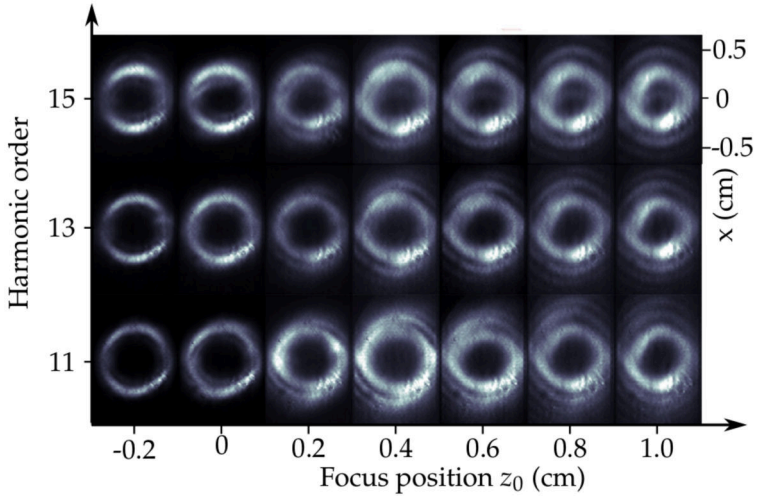

Figure 2.56: Experimental measurement of the 2D transverse spatial profile of H11 to H15 using a $\mathcal{LG}(1,0)$ driver. The measurements were performed using the 'Ruf' XUV spectrometer. The 2D transverse spatial profiles of H11 to H15 are presented for different value of $z_0 = 0$. To control the value of z_0, the generating lens is translated over 1.2 cm. The intensity of each harmonic, for each position of the lens, is normalized to 1. The $z_0 = 0$ position is known from previous HHG experiments using Gaussian drivers on this beamline. This figure is adapted from [Géneaux et al. 2017].

suggest that the generation of $p > 0$ Laguerre-Gaussian is due to the long quantum paths during HHG. Why would short and long quantum paths respond differently to OAM?

2.5.5 Origin of the production of harmonics with $\mathcal{LG}(\ell, p \neq 0)$ modes

In order to understand the origin of the high harmonic OAM, we need to understand the physics behind the p mode index. It was recently demonstrated that p is actually a quantum number related to an operator acting on the light field [Karimi et al. 2014; Plick et al. 2015]. In a similar manner as linear momentum is associated to translational displacement, or as angular momentum is associated to a rotation, the p quantum number is associated with the dilation of a light beam along the radial coordinate. The next step of our analysis is thus to focus on the radial properties of HHG.

The far-field spatial profile of the high-order harmonics is given by the Fourier transform of the near-field harmonic field. The field amplitude profile of the near-field q-th order harmonic emission E_q is determined by the driving laser field amplitude E_0 and by the effective nonlinearity of the HHG process q_{eff}: $E_q = E_0^{q_{eff}}$. The nonlinearity of HHG can thus modify the p content of the beam. The phase of the harmonic emission also plays a crucial role in the spatial shaping of the far field profile. The near-field phase is set by the atomic dipole phase $\phi_q^{s,l}$, which depends linearly on the infrared intensity $I_0(r,\theta)$: $\phi_q^{s,l}(r,\theta) = -\alpha_q^{s,l} I_0(r,\theta)$, where $\alpha_q^{s,l}$ is the atomic dipole phase coefficient. When HHG is driven by $\mathcal{LG}$ mode, the $\phi_q^{s,l}(r,\theta)$ will present ring-shaped modulation (if $\alpha_q^{s,l} > 0$), that will lead to a modification of the XUV profile in the far-field, and thus to its p content.

To study the effect of the nonlinearity of HHG and of the atomic dipole phase in the generation of XUV with $p > 0$, we will go back to numerical simulations. In order to be able to launch calculations over a large parameters space, one needs to reduce the computation time of each calculation. This can be achieved by reducing the gas jet to an infinitely thin sheet of atoms, neglecting the longitudinal effects during HHG. This

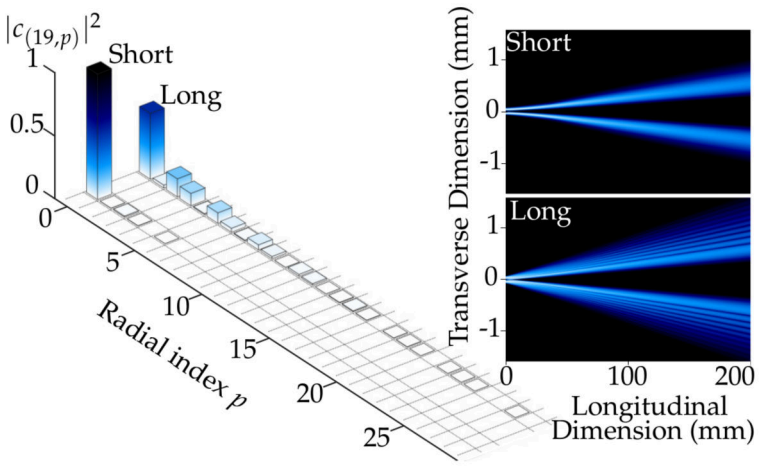

Figure 2.57: Decomposition of the far-field spatial profile (20 cm propagation distance) of short and long quantum paths contribution to the H19 onto Laguerre-Gaussian basis. Figure adapted from [Géneaux et al. 2017].

approximation was shown to be valid for thin gas jet [Beaulieu et al. 2016a; Catoire et al. 2016; Rego et al. 2016]. For long interaction medium, as in the experiment of Zurch *et al.* [Zurch et al. 2012], the longitudinal phase-matching effects start to be too important to use this kind of model.

For these simulations, a hybrid approach was used: the ionization rate was calculated with ADK [Ammosov et al. 1986] and the harmonic emission was determined using the framework of Strong Field Approximation [Lewenstein et al. 1994]. The simulations were run using a near field $\mathcal{LG}(1,0)$ beam, with a peak intensity of $1.2 \times 10^{14}\mathrm{W/cm^2}$. The far-field spatial profile of the harmonics was decomposed onto the Laguerre-Gaussian basis. The coefficients of this decomposition, denoted as $c_{\ell,p}$, give the contribution of the Laguerre-Gaussian mode $\mathcal{LG}(\ell,p)$ to the 2D transverse spatial profile. By selecting only one solution of the saddle point equations (Leweinstein/SFA), one can isolate the contribution from the short and long quantum to HHG emission. The decomposition of the far-field spatial profile onto the Laguerre-Gaussian basis was done for the short and long quantum path individually. As one can see in Fig. 2.57, the short trajectory lead to an almost pure $\mathcal{LG}(19,0)$ mode. This means that in this case, the highly nonlinear frequency upconversion follows the multiplicative law for OAM conservation, but does not lead to any spatial dilation associated with $p > 0$ mode. This observation leads us to conclude that the nonlinearity of the HHG process is probably not at the origin of the production of high p values $\mathcal{LG}$ mode.

On the contrary, the long quantum path contribution shows a completely different behavior. Its spatial profile decomposition onto Laguerre-Gaussian basis shows that the mode, containing a series of concentric circles, can be decomposed into modes with p values ranging from 0 to $\simeq 30$. The major difference between the short and long quantum paths lies in their atomic dipole phase coefficients. Indeed, as one can see in Fig. 2.5, the atomic dipole phase coefficient is much larger for long quantum paths, in the early plateau region. For the case presented here, $\alpha_{19}^{l} \sim 20 \times 10^{-14}\mathrm{cm^2/W}$, while $\alpha_{19}^{s} \sim 1 \times 10^{-14}\mathrm{cm^2/W}$. We can thus conclude that the trajectories with large atomic dipole phase coefficients can lead to the generation of XUV characterized by multi-ringed pattern spatial profile. Controlling the relative weight between short and long quantum paths, by changing the relative position between the focus and the gas jet, is thus an easy knob to control the p

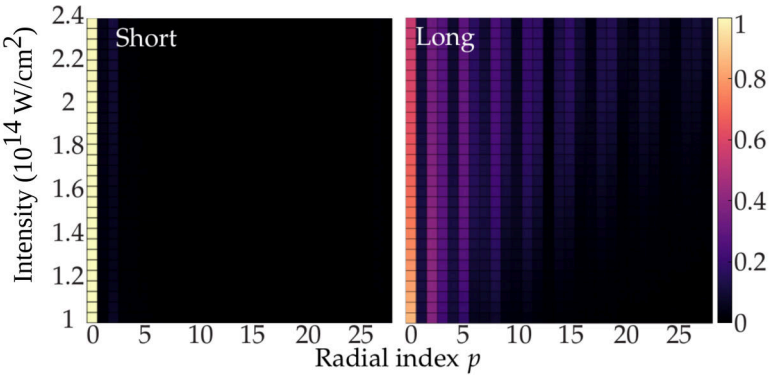

Figure 2.58: Laguerre-Gaussian mode decomposition as a function of driving laser intensity, for both short and long quantum paths of H19. This figure is adapted from [Géneaux et al. 2017].

content of the XUV emission.

The modulation of the atomic dipole phase does not only rely on the atomic dipole phase coefficient. It is also governed by the laser intensity $I_0(r,\theta)$: $\phi_q^{s,l}(r,\theta) = -\alpha_q^{s,l} I_0(r,\theta)$. The laser intensity is thus also an easy knob to tune to control the atomic dipole phase modulation in the near-field, and thus, to control the p content of the XUV emission. In order to numerically demonstrate this possibility, the previous calculation was repeated for different IR intensities, ranging from 1 to 2.4×10^{14}W/cm^2. The far-field profile of H19 was decomposed on a Laguerre-Gaussian basis (Fig. 2.58). As expected, the short trajectory contribution is always strongly dominated by the $\mathcal{LG}(\ell = 19, p)$ mode. At high laser intensity, we can see a small contribution from $p > 0$ modes. This means that even if the atomic dipole phase coefficient is small, driving short trajectories with high-intensity can yield to a sufficient atomic dipole phase modulation, necessary to generate $p > 0$ modes. However, the contribution $p > 0$ always remains weak. For long trajectories, the $p > 0$ is shown to continuously increase with the driving laser intensity. This is the signature of strong atomic dipole phase modulation in the near-field.

2.5.6 Partial conclusions and perspectives

Driving high-order harmonics using beam carrying orbital angular momentum is currently the subject of intense research efforts, because of the fundamental interest to understand the transfer of angular momentum in extreme nonlinear optics, but also because of the perspectives of applications for controlling the properties of ultrafast XUV pulses. It was recently demonstrated that q-th order harmonic generated with Laguerre-Gaussian ($\mathcal{LG}$) beam of ℓ_1 azimuthal quantum number is characterized by $q\ell_1$ [Gariepy et al. 2014; Géneaux 2016]. Non-collinear HHG using perturbative ($\mathcal{LG}$) mode leads to the generation of angularly separated beams with controllable and well defined azimuthal quantum number [Gauthier et al. 2017; Kong et al. 2017]. However, the radial index of the emitted extreme ultra-violet vortices had never been subject to any study.

The production of a beam with non-vanishing radial indexes is associated to a spatial profile made of concentric rings. We have experimentally shown that large atomic dipole phase modulation in the near-field can lead to the generation of such beam. The XUV emission through long quantum trajectories thus leads to such large atomic dipole phase modulations, given the large values of their atomic dipole phase coefficients. The physics behind the generation of XUV beam with non-vanishing radial index, when driven by $\mathcal{LG}$ IR beam, is thus related to the physics behind the generation of multi-ring pattern, associated with long trajectories, in conventional HHG driven by a Gaussian beam ([Carlström

et al. 2016; Catoire et al. 2016]). It is also closely related to the physics underlying self-phase modulation (SPM), where strong modulation of the spectral phase through non-linear propagation lead to spectral broadening and spectral interference. These phenomena are associated with the strong modulation of the atomic dipole phase, or of the spectral phase, for the case of SPM.

The doughnut intensity profile produced at the focus of a $\mathcal{LG}$ mode leads to a different modulation of the atomic dipole phase than at the focus of a Gaussian profile. In the context of HHG driven by $\mathcal{LG}$, the control over both ℓ and p of the emitted harmonics is now possible. These are new degrees of freedom that add to the atto-toolbox in the quest of generating complex and refined attosecond XUV pulses.

2.6 Conclusions

In this chapter, we have studied the generation and the control of the properties of light in the VUV, XUV and soft-x-ray spectral range, generated through the extremely non-linear response of atoms to strong (low-frequency) laser fields. One of the key phenomena which have been studied is High-order Harmonic Generation (HHG). From a spectral domain point of view, HHG usually leads to the emission of frequency combs made of odd harmonics of the driving laser. The mechanism behind the generation of HH is based on the radiative recombination of field-driven attosecond electron wavepacket onto the parent ion from which they originated. In the time-domain, HHG usually produces attosecond pulse trains, which make it very attractive as a light source for pump-probe experiments requiring high photon energy and high temporal resolution. Indeed, in one of the first section of this chapter, we have shown that one can use intense long-wavelength pulse to drive HHG up to the water-window spectral range (285-530 eV). This table-top ultrafast soft-x-ray source can be of fundamental interest for future applications, as mentioned earlier in the chapter.

On the other hand, the amplitude, the phase and the polarization state of the emitted photons encode very rich information about the structure and dynamics of the atoms or molecules from which they have been emitted. In the most simple (and frequent) case, the electrons are assumed to be removed from- and to recombined to the electronic ground state (outermost valence orbital) of the system. In more complex and interesting cases, electrons from many orbitals can participate in the HHG process. In such case, it is possible to retrieve the underlying sub-cycle multi-electron dynamics, including the dynamics of electrons upon ionization, by looking at properties of the emitted XUV photons. This is a good example of possible applications of High Harmonic Spectroscopy [Smirnova et al. 2009]. Nevertheless, the highly-excited states are usually assumed to play no role in HHG. In this chapter, we have demonstrated how we have accidentally observed many different phenomena that can be as efficient as HHG, when excited states start to be populated, in the presence of strong driving laser field. In different regimes, we have demonstrated that the creation of a coherent superposition of electronic states, in the presence of a (moderately) strong laser field, can lead to:

1) the direct emission of XUV photon through XUV Free Induction Decay (xFID). We have, moreover, used this xFID emission as a background-free and phase-resolved alternative to XUV transient absorption spectroscopy [Beaulieu et al. 2017b], which is one of the workhorses of our community.

2) the ionization from the excited states and recombination to the ground state. The emission coming from this process has been shown to be temporally delayed by few-femtosecond compared to non-resonant HHG. We have experimentally measured this delay by making elegant use of the attosecond lighthouse effect [Beaulieu et al. 2016a].

3) the emission of Hyper-Raman Lines between each HH. This is the weak-field (multiphoton) analog as the effect described just above. Concomitant generation of Hyper-Raman Lines and HHG have been predicted long time ago [Bandarage et al. 1992; Millack et al. 1993; Pons et al. 1996], but here, we presented the first experimental evidence for it.

These observations lead us to conclude that in some special cases, the simple description of HHG breakdown and the participation of the excited states to the process can lead to the emission of new spectral features, which contain information about the interplay between the bound wavepacket dynamics and the rich electronic dynamics going on during HHG. From this point of view, I think that even if, 25 years after the seminal paper of Corkum *et al.* [Corkum 1993], our understanding of HHG is pretty refined, there are also still unexplored subtle features and degrees of freedom underlying HHG that need to be examined. For example, in this chapter we also studied, for the first time, the possibility to generate Laguerre-Gaussian XUV beam with high radial indexes, using HHG. HHG, which gave birth to the field of Attosecond science, remains full of surprises and possibilities, whose discovery is associated to the improvement of experimental techniques.

3. Nuclear and electronic dynamics in simple molecules

3.1 Introduction

It is common knowledge that at a temperature of 0 K, molecules would be in their ground state, from the point of view of all their degrees of freedom. In the presence of thermal or light excitation, translational, rotational, vibrational and electronic excited states can be populated. The energy spacing between the different eigenstates of each degree of freedom increases in the same order as they have been introduced in the previous sentence. This implies that the typical timescale of electronic dynamics is much faster than the one of vibrational dynamics, which is itself much faster than the timescale of rotational dynamics, and so on. The separation of the timescales for the different degrees of freedom (*e.g.* vibrational and electronic) is at the heart the famous Born-Oppenheimer approximation (BOA). This approximation, named after the physicists Max Born and Julius Robert Oppenheimer, is based on the assumption that the motion of the nuclei and of the electrons, in a molecule, can be fully decoupled due to the different timescale on which they are undergoing dynamics, which is a consequence of their very different masses. This implies that the total molecular wavefunction can be decomposed as the product of an electronic and a nuclear wavefunction. This approximation is ubiquitous in quantum chemistry calculations of the molecular wavefunction and potential energy surfaces (PES).

In a typical quantum chemistry calculation of the PES, one would clamp the position of the nuclei, and calculate the electronic energy of the molecule, for this given nuclear geometry (using the time-independent Schrödinger equation, for example). This calculation would be repeated for different positions of the nuclei. The energy of the electronic states, calculated as a function of the nuclei position, forms the adiabatic (Born-Oppenheimer) potential energy surface (PES). In other words, within the BOA, the electronic energy depends only parametrically on the nuclear coordinates. When the energy spacing between the different PES becomes small, the timescale of the electronic dynamics becomes on the same order than the one of nuclear dynamics, leading to strong non-adiabatic coupling between the electronic and nuclear degrees of freedom. This represents a scenario where

the BOA breaks down. In that case, the parametric dependence of the electronic energy on the nuclei coordinates become a functional one. Indeed, in region where electronic states are close to each others, small nuclear perturbations can result in significant changes in the electronic character. The set of nuclear geometries where the PES are degenerate (intersect) and where the non-adiabatic couplings between these states are non-vanishing is called conical intersection. As we will see later on, conical intersections are of major importance in many photochemical processes like photoisomerization, photosynthesis, the primary event of animal vision and the photostability of DNA.

The Born-Oppenheimer approximation leads to the formulation of other important principles in photochemistry, such as the Franck-Condon principle. This principle is a rule that dictates the intensity of the vibronic transitions when a molecule simultaneously changes its electronic and vibrational states upon absorption of light. The Franck-Condon approximation assumes that upon the absorption of light, the transition is vertical, *i.e.* the nuclei do not move while the molecule is transiting from the initial to the final electronic state. Thus, assuming that the transition is vertical, one can calculate the so-called Franck-Condon factors, which give the intensity of each vibronic transition. The Franck-Condon factors strongly depend on the shape of the initial and final PES. They are determined by the overlap integral between the initial and final vibrational wavefunctions. If the initial and final PES are parallel, the vibrational distribution remains unchanged upon electronic excitation ($\Delta v = 0$). This is, for instance, the case for the ionization of high-lying Rydberg states, whose PES curves are roughly parallel to ones of the ion. A secondary consequence of the Franck-Condon principle is that the transition dipole matrix elements of a given transition (excitation or ionization) should be fully independent of the vibrational states of the system. In the case of molecular ionization, this implies that the molecular continuum features should be fully independent of the vibrational state of the cation. This means that the branching ratio and the MF-PAD (Molecular Frame Photoelectron Angular Distribution), for example, should be the same for all vibrational modes or quanta. Deviations from this approximation are known to occur for instance in the vicinity of shape resonances in the molecular continuum [West et al. 1980] or across Cooper minima [Powis et al. 2017].

Another interesting example of the breakdown of the BOA is Vibrational Circular Dichroism (VCD). VCD is the differential absorption cross-section of chiral molecules illuminated with left- or right-circularly polarized infrared light. As in conventional (electronic) CD, VCD results from the interference between electric and magnetic dipole transitions in the absorption cross-section. In the theoretical treatment of VCD, one needs to include the electronic charge flow induced by vibrational motion in order to calculate non-vanishing values of VCD [Nafie 1997]. This electronic current induced by vibrational motion does not exist within the BOA. The distinction between two chiral molecules using vibrational IR spectroscopy is thus intrinsically an example of the breakdown of the Born-Oppenheimer approximation. This example is particularly interesting for us since it involves both the breakdown of BOA and chiral molecules, which will be extensively studied in the next chapters.

An important example of concomitant nuclear and electronic dynamics, which does not necessarily requires the breakdown of the Born-Oppenheimer approximation, is the attosecond charge localization during dissociative ionization [Sansone et al. 2010]. An intuitive (and simplified) picture of this process can be formulated: at an internuclear distance smaller than a given critical distance, the electron can 'jump' back and forth from one fragment to the other. At an internuclear distance greater than the critical distance, the electron cannot 'jump' back to the other fragment, and remains asymptotically localized on

one of the dissociating moiety. The fragment on which the electronic density is localized when the molecule reaches the critical internuclear distance is governed by the relative phase between electronic eigenstate within the wavepacket. The attosecond electronic dynamics can thus dictate the faith of charge-directed reactivity of dissociating small polyatomic molecules, which occurs on a much slower timescale.

What kind of experimental techniques and related observables are required to study coupled vibrational and electronic dynamics? The most well-established technique to probe both electronic configurations and vibrational dynamics in the gas phase is time-resolved photoelectron spectroscopy (TR-PES). In the Koopmans' approximation [Koopmans 1934], the ionization from different valence states (*e.g.* α or β) leads to the production of cation in different electronic states (*e.g.* α^+ or β^+). Because of the ionization potential difference between $\alpha \rightarrow \alpha^+$ and $\beta \rightarrow \beta^+$, monitoring the energy-resolved photoelectron spectra provides a direct way of looking at the electronic transition from α to β, or vice-versa [Blanchet et al. 1999]. Indeed, following the electronic transition from α to β, the kinetic energy of the photoelectrons is expected to shift. One can also concomitantly follow the coupled nuclei dynamics via the vibrational structure within each photoelectron peak. Moreover, because the symmetries of the outgoing electron partial waves are related to the symmetry of the electronic state undergoing ionization, a transition between two-electronic states, during a non-adiabatic process, would also lead to a significant modification of the photoelectron angular distribution [Bisgaard et al. 2009]. Following the photoelectron angular distribution as a function of the pump-probe delay is thus another observable which encodes the signature of non-adiabatic relaxation processes. The sensitivity of such measurement is greatly improved by pre-aligning the molecular sample and/or measuring the PAD in the molecular frame.

Recently, time-resolved high-order harmonic spectroscopy emerged as a complementary technique to probe coupled electronic and nuclear dynamics in photochemical reactions. In a TR-HHS experiment, the observable is the XUV high-order harmonic radiation produced by the interaction of the probed molecule with a strong laser pulse. The XUV radiation is generated by radiative recollision of electrons driven by the strong laser field. This recollision process is the reverse process of photoionization, and is thus intrinsically sensitive to the electronic configuration and geometry of the molecule. Furthermore, the high-order harmonic generation process is a coherent mechanism, in which phase plays an important role. HHS is thus very sensitive to wavepacket motions on PES because of the changes of vertical ionization potential which induces a phase modulation of the harmonic emission. A pioneering experiment of TR-HHS in photoexcited NO_2 molecules (400 nm pumped), which is known to undergo non-adiabatic dynamics at a conical intersection, showed the high sensitivity of the technique to the wavepacket dynamics [Wörner et al. 2011]. However, the origin of the harmonic signal modulation by the wavepacket dynamics in still debated. Indeed, Ruf *et al.* claimed that the origin of the HHG signal modulation is due the molecular vibration on the first excited diabatic state [Ruf 2012], while Kraus *et al.* claimed it was purely due to electronic population dynamics [Kraus et al. 2012]. TR-HHS is thus an interesting emerging technique to probe non-adiabatic dynamics in photoexcited molecules, but understanding the origin of signal modulation in such complex experiments is still a challenging task. Important work has been recently performed in the Ottawa group to carefully examine the advantages and drawbacks of TR-HHS and TR-PES [Forbes et al. 2017; Wilkinson et al. 2014], showing that the combination of these two techniques was probably the best general strategy to look at such dynamics.

While TR-HHS and TR-PES show high sensitivity to non-adiabatic dynamics, the interpretation of the measured spectra can be complicated. In this chapter, we will see that

time-resolved Coulomb explosion imaging (TR-CEI) allows, through the measurement of the 3D momentum vector of photofragments, to obtain direct information on the ultrafast nuclear motion of molecules [Ibrahim et al. 2014; Légaré et al. 2005]. While this technique is (almost fully) blind to the electronic structure of the molecules, we will see how it can be used in conjunction with theoretical calculations to elucidate non-adiabatic dynamics in simple polyatomic molecules.

The breakdown of the BOA leads to a rich myriad of effects, which can govern the dynamics of excited molecules. In this chapter, we will present two very different examples where the nuclear and electronic dynamics leads to interesting features in the behavior of diatomic and polyatomic molecules. In the first example, we will study the ultrafast photoisomerization of acetylene cation into vinylidene cation. This prototypical isomerization reaction occurs thanks to the passage through a conical intersection, which provide a 'funnel' between the excited cationic state of acetylene and the ground cationic state of vinylidene. For this experiment, we have used the ionic fragment detected in coincidence as the observable. This allows us to follow the nuclear rearrangement in the molecular frame, during the ultrafast nonadiabatic dynamics leading to the isomerization of the acetylene cation. In the second example, we will see how we have used the OPA from ALLS to coherently control of the electron localization in dissociating H_2^+, using long-wavelength phase-locked two-color pulses.

3.2 Hydrogen migration in Acetylene cation

3.2.1 Acetylene: a benchmark molecule to study photoisomerization

Photoisomerization is one of the most fundamental chemical reactions. It is a chemical process, triggered by electronic excitation via light absorption, by which one molecule is transformed into another one which has exactly the same molecular formula (the same atoms), but where the atoms have a different arrangement. Photoisomerization reactions imply a change in the electronic structure coupled to ultrafast nuclear motions, which makes them spectroscopically very interesting. One photoisomerization reaction is particularly famous because of its importance in the life of every animal (including humans): the photoisomerization of the retinal molecule which is the first key step in animal vision. When the 11-*cis*-retinal chromophore, located in our eyes, absorbs a visible photon, it photoisomerizes from the 11-*cis* state to the all-*trans* state [Abe et al. 2005; Hasson et al. 1996; Kobayashi et al. 2001; Prokhorenko et al. 2006]. These dynamics occurs in few hundreds of fs, when retinal molecules are embedded bacteriorhodopsin, a small protein in which retinal is encapsulated in our body. Beyond this fundamental example, there are many technological devices that rely on photoisomerization, like rewritable CDs and DVDs as well as molecular switches [Mammana et al. 2011] and motors [Vachon et al. 2014]. In all the examples states above, the molecular system undergoing photoisomerization is too large to perform accurate and quantitative *ab initio* calculations, to try to understand the underlying physical mechanism that drives these complex and coupled nuclear and electronic dynamics. It would thus be nice to have a simple polyatomic benchmark molecule that undergoes photo-induced isomerization and which would be simple enough to be well described using state-of-the-art models of vibronic dynamics. We will see below that the acetylene (C_2H_2) molecule fulfills these conditions and is therefore 'the' benchmark molecule for studying photoisomerization.

For decades, the photoinduced isomerization of acetylene into vinylidene has been used as a prototype to understand the subtleties of such complex nonadiabatic dynamics. Despite its rich electronic structure ($1\sigma_g^2 1\sigma_u^2 2\sigma_g^2 2\sigma_u^2 3\sigma_g^2 1\pi_u^4$), the acetylene molecule is

simple enough to allow time-resolved quantitative quantum chemistry calculations to be performed, making this system perfect for benchmark studies of nonadiabatically driven photoisomerization. In C_2H_2, proton migration can occur in various charge states. The first experimental evidence of the formation of neutral vinylidene isomer was found in the photodetachment spectrum of the vinylidene anion in the late 80's [Ervin et al. 1989]. Since this observation, the mechanism of neutral acetylene-vinylidene isomerization has been subject to a lot of studies and controversies in the molecular spectroscopy community [Jacobson et al. 2000]. For the case of dicationic acetylene, there are numerous electronic states that can lead to 'barrierless' (or direct) vinylidene formation. One simple way to initiate the proton transfer dynamics in the doubly charged acetylene is by the population of the $^1\Sigma_g^+$ state, which is the first electronically excited state of $C_2H_2^{2+}$. The population of this state is achieved through the removal of two electrons from the least bounded orbital ($^1\Pi_u^{-2}$) [Osipov et al. 2008]. Because strong-field ionization by infrared fields is dominated by the removal of electrons from the highest occupied molecular orbital (HOMO), launching proton transfer dynamics in the dicationic charge state has been possible after double ionization ($1\Pi_u^{-2}$) with standard commercially available amplified Ti:Sa laser systems (800nm). For instance, the pioneering work of Hishikawa *et al.* [Hishikawa et al. 2007] and Masuda *et al.* [Matsuda et al. 2011] observed the recurrently migrating deuterium atom in the d_2-acetylene dication with a strong field 800 nm - 800 nm pump-probe setup and found an isomerization time of 90 fs with a recurrence time of 280 fs. Other papers confirmed that after strong field 800 nm ionization, the dissociation of $C_2H_2^{2+}$ into $C^+ + CH_2^+$ arises from proton transfer occurring in the dicationic charge state (and not the cationic charge state) [Alnaser et al. 2006; Wells et al. 2013]. The proton migration - isomerization - dynamics in the acetylene cation was much less studied than in the neutral and in the doubly charged acetylene. We will see in the next section that launching the proton transfer dynamics in the singly charged acetylene is indeed technologically harder, but that it leads to very rich dynamics involving the passage through a conical intersection, which is a hallmark of nonadiabatic dynamics.

3.2.2 Launching proton transfer dynamics in excited cationic state

In the one-electron picture of ionization (Koopmans approximation [Koopmans 1934]), when an electron is removed from the least bounded molecular orbital of the acetylene, the ground ionic state is populated ($X^2\Pi_u$). An isomerization barrier of ~ 2 eV separates the state of the linear $D_\infty h$ acetylene cation from the ground state of the Y-shaped C_{2v} vinylidene cation [Boyé-Péronne et al. 2006] (for a scheme of few-electronic state as a function of the molecular geometry, see Fig. 3.1). This large potential barrier prevents the formation of vinylidene cation after the population of the ground ionic state of acetylene ($X^2\Pi_u$). Thus, since 800 nm strong field ionization of acetylene is largely dominated by the population of $X^2\Pi_u$ (ionization from the HOMO), one cannot efficiently launch hydrogen migration dynamic in the cation upon ionization with standard Ti:Sa laser system. However, if an electron is ionized from the HOMO-1 orbital (lying 5.3 eV below the HOMO), the first excited state of the ion ($A^2\Sigma_g^+$) is populated. Following HOMO-1 ionization, the vibrational wavepacket launched on this ionic state is known to undergo an ultrafast (τ = 40-60 fs) non-adiabatic relaxation through a conical intersection with the $\tilde{X}^2A_1$ electronic ground state of the vinylidene cation. Understanding this ultrafast non-Born-Oppenheimer relaxation in the excited acetylene cation has recently been subject to extensive theoretical studies [Madjet et al. 2013; Madjet et al. 2011]. The first experimental observation of hydrogen migration in cationic acetylene was demonstrated using XUV pump - XUV probe (38eV) photons from the Free Electron Laser in Hamburg (FLASH)

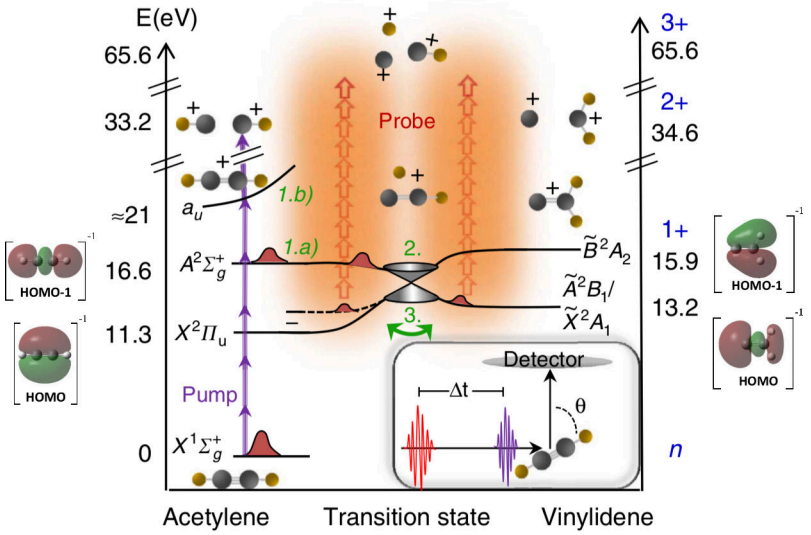

Figure 3.1: Schematic of the experiments. (1.a) The third harmonic of the Ti:Sa (266 nm) pump-pulse populates the first excited state $A^2\Sigma_g^+$ of $[HC=CH]^+$ through a four-photon ionization process. Hydrogen migration pathway: within 40 fs, the wavepacket enters a region of strong non-adiabatic coupling with the ground $X^2\Pi_u$ state of $[HC=CH]^+$. The passage through this region involves relaxation to the X-state via a conical intersection. Following this transition, the molecule, now in a highly vibrationally excited state, may undergo isomerization to the vinylidene cation $[C=CH_2]^+$. A to and fro isomerization between acetylene and vinylidene takes places, indicated by the green double arrow. Dissociation pathway: (1.b) while the 32-fs pump-pulse is present, a fifth photon can be absorbed on the A-state thus exciting population to higher lying states. To probe the nuclear structure, either further 266 nm photons are absorbed to reach the dication of acetylene and vinylidene (single-pulse experiment) or a second time-delayed 800 nm pulse leads to Coulomb explosion of the charged molecule (pump-probe experiment). With the latter, we reach the doubly charged as well as the triply charged ionic states and thus correlate either two fragments ($CH^+ + CH^+$ or $C^+ + CH_2^+$) or three fragments ($CH^+ + C^+ + H^+$) with each other. In the inset, a sketch of the experimental setup with orientations of molecules, laser pulses and time of flight (TOF) are shown, with θ being the angle between the molecular axis and laser polarization. Molecules being oriented parallel to the laser field correspond to $\theta = 0°$. This figure is adapted from [Ibrahim et al. 2018].

using a reaction microscope (REMI/COLTRIMS) detection system [Jiang et al. 2010; Jiang et al. 2013]. This work showed that single-photon ionization by XUV radiation was an efficient way to populate the $A^2\Sigma_g^+$ cationic excited state and to subsequently observe the hydrogen migration. However, this experiment suffered from some intrinsic FEL characteristics, namely the low repetition rate (bad statistic) and high temporal jitter (low temporal resolution).

In our experiment, we explored an intermediate ionization regime, which lies between single XUV photon (using FEL) and tunnel ionization (using Ti:Sa), namely few-photon ionization (using Ti:Sa 3rd harmonic, 266 nm, 4.66 eV). We aimed at determining if this intermediate regime enabled launching population in the first cation excited state and measuring the nonadiabatic proton transfer dynamics. In the next subsection, we present our detection scheme and the physical observable that we have measured in this experiment.

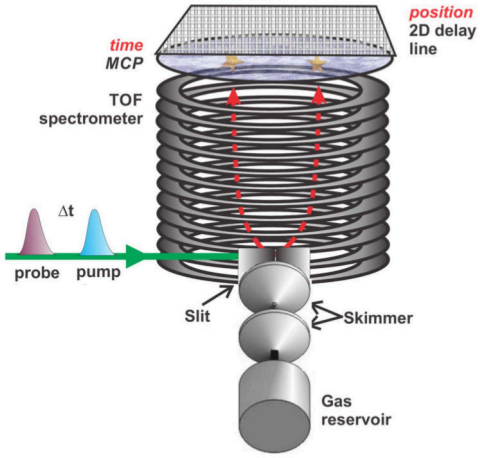

Figure 3.2: Schematic of the experimental apparatus used for Coulomb Explosion Imaging (CEI). We used a position and time-sensitive detector for ion detection in coincidence. It is composed of a time-of-flight mass spectrometer, where the MCP are used to measure the TOF, a 2D delay line detector for position sensitive detection and a doubly skimmed molecular gas jet. The delayed pump and probe laser pulses are also shown in the schematic of the experimental setup. This figure is adapted from [Ibrahim et al. 2018].

3.2.3 Probing molecular geometries using laser-induced Coulomb Explosion Imaging (CEI)

Throughout this thesis manuscript, we have up to now discussed two different observables to extract information about the ultrafast light-matter interaction and atomic/molecular dynamics: the emitted VUV-XUV light and the ejected photoelectrons. In both cases, the rearrangement of the molecular structure would modulate the observed signal, *i.e.* both observable are sensitive to the geometry of the molecule. However, in both cases, retrieving clear information about the ongoing nuclear dynamics is not trivial, since the nuclear rearrangement is not directly mapped on the measured observables. The changes in the molecular structure modify the photoionization/photorecombination transition dipole matrix elements, thus modifying the electron/light spectrum in a photoelectron or high-harmonic spectroscopy experiment. However, linking the modulation of these observables to a given nuclear motion in a molecule is really not trivial and generally requires advanced experiments and intensive theoretical investigations. Here, we present a technique, named Coulomb Explosion Imaging (CEI), which enables measuring the 3D momentum vector of fragments produced upon dissociation. We will show that measuring the 3D momentum vector of all the ions produced upon molecular fragmentation gives us direct insights into the geometry of the molecule, prior to fragmentation.

Our experimental apparatus used for laser-induced CEI is shown in Fig. 3.2. The experiments were performed at ALLS, Montréal. A laser pulse (or a sequence of pulses) was sent inside an ultra-high vacuum chamber, where it was focused with parabolic mirror (f = 100 mm) on a cold and collimated gas jet. The gas jet was produced using an expansion from a gas-reservoir, followed by double-skimmer stages and a passage through a motorized piezoelectric slit, which allows selecting only the coldest molecules. It produced a highly collimated beam with an effective transverse translational temperature of ~ 1 μK. As we will show later, this cold molecular gas jet enables achieving high-resolution time-of-flight mass spectrometry, since these cold temperatures are associated with the negligible spread of initial velocities along the time-of-flight mass spectrometer

axis. The strong laser pulse(s) ripped off multiple electrons from the cold molecule, producing multiply charged molecule that undergoes dissociation or Coulomb Explosion [1]. The ionic fragments resulting from Coulomb Explosion produced in the laser focus volume were accelerated towards the detector by the spectrometer internal electric field. The ion TOF spectrometer uses a static field throughout the whole flight region. This field is produced by a stack of 17 nonmagnetic stainless steel ring electrodes with different positive potential on each electrode. The resulting static electric field accelerates the ionic fragment towards a time- and position-sensitive detector (RoentDek Handels GmbH). The ions are converted into electron by MCPs and detected by a delay line anode detector, which is able to measure the 2D position (x^i, y^i) of the electrons produced by the MCPs (and thus of the ion hits). In addition, we detect the electronic signal produced by the MCPs to measure the time-of-flight of the ion (t^i). Moreover, we know that in the center-of-mass frame of a fragmenting molecule, the conservation of momentum law requires that the electronic and ionic fragment momenta sum to zero. Because the electrons are much lighter than the ions, we can make the approximation that the net momentum of the ionic fragments is also zero. By using the x^i, y^i and t^i information for each fragment, for each laser shot, as well as the momentum conservation restriction describe above, we can reconstruct the full 3D momentum vector of each fragment (p_x^i, p_y^i and p_z^i), coming from the same Coulomb Explosion (or dissociative ionization) event. By doing that, we have a direct information about the molecular geometry, at the time of the fragmentation. In order to work properly, only one Coulomb explosion event can occur within each laser shot. If more than one event occurs, fragments coming from two different molecules would be detected in a narrow time window, which would render the coincidence analysis based on the momentum conservation restriction impossible. Thus, we need to keep the gas jet density and the laser intensities low enough that less than one molecule is exploded within each laser shot. Working in such low count rate regime significantly increases the data acquisition time. As we will see in the general conclusion of the thesis, a very high-repetition-rate laser system is thus perfectly well suited for coincidence experiment working in the so-called 'counting' regime, to be able to concomitantly produce high-quality scientific data and have hobbies and passions, apart from research in AMO physics. For analysis of data, we used a newly designed coincidence detection algorithm, written by our collaborators from UWaterloo (Benji Wales and Joe Sanderson) that significantly enhanced the true coincidence events yield by relaxing the TOF window definitions. For more details about the algorithm, see [Wales et al. 2012].

By using CEI in a time-resolved fashion, one can thus think about initiating a dynamics involving nuclear rearrangement using a short pump pulse, and Coulomb exploding the molecule using a time-delayed short probe pulse, to take a snapshot of the molecular geometry at a given pump-probe delay. By doing so, for different pump-probe delays, one can record the evolution of the nuclei within a molecule undergoing a dynamics induced by the pump pulse. Let us stress here that, using CEI, we have a lot of information about the geometry, but very few information about the electronic states of the probed molecules. Indeed, because we do not detect the photoelectrons, we lose the 'direct' information about the electronic configuration of the system. However, as we will see later, looking at the angular distribution of the fragments can give us insight into the electronic states of the probed molecules.

[1] When the Coulombic repulsion in multi-charged ion becomes too strong, the bonds that hold the molecule together breaks apart and the ionic fragments fly in different direction.

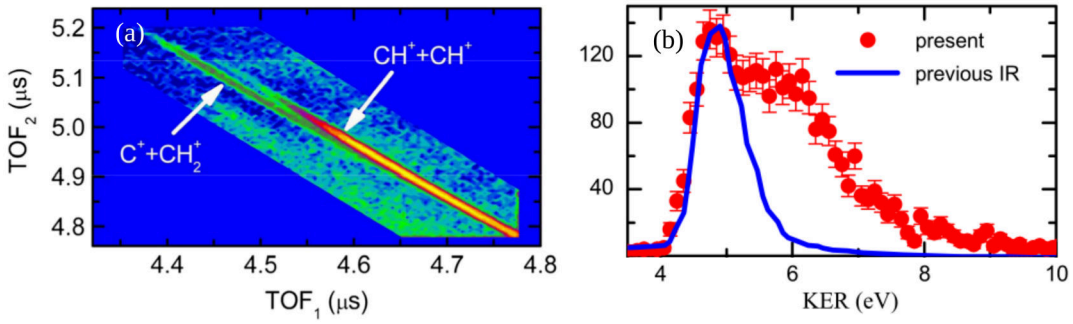

Figure 3.3: Identifying the proton migration in the cationic acetylene at FEL. In (a), TOF of the firstly detected fragment vs TOF of the second fragment. The data are integrated over time delays $|\Delta\tau|$ = 360 fs. In (b), Kinetic energy release (KER) spectra for coincident fragments from the two body vinylidene break-up channel $C^+ + CH_2^+$. The red circles represents the data obtained at FEL using 38 eV pump - 38 eV probe, integrated over all pump-probe delays and the solid blue line represents the data using a strong IR pulse, extracted from [Alnaser et al. 2006]. This figure is adapted from [Jiang et al. 2010].

3.2.4 Confirmation of hydrogen migration in single pulse experiments

We have explained above that proton migration dynamics was observed in the acetylene cation at the FEL, using 38 eV pump photon, while it was never observed using strong field 800 nm pump photons. Let us first determine what are the observables that allow determining that proton migration dynamics in the cationic acetylene is present or not in the experimental data. To do so, we will look at the FEL experimental data published by Jiang *et al.* [Jiang et al. 2010].

Figure 3.3 (a) shows the time of flight of the second detected ion as a function of the time of flight of the firstly detected ion. In such a plot, each diagonal is associated with a correlated break-up channel, because of total energy sharing between the two ions. In Fig. 3.3 (a), the lower right diagonal is associated with the correlated symmetric break-up channel $CH^+ + CH^+$. We will not focus on this channel for now. The upper left diagonal is associated to the correlated asymmetric break-up channel $C^+ + CH_2^+$. The presence of the CH_2^+ fragment within this channel is a smoking gun evidence that the proton has migrated on the other end of the molecule, prior to fragmentation. However, no information about the charge state on which this proton transfer dynamics occurred can be directly extracted just by looking at this diagonal. In Fig. 3.3 (b), the kinetic energy released (KER) of the $C^+ + CH_2^+$ channel, which is the sum of the kinetic energy of C^+ and CH_2^+ fragments which have been detected in coincidence, is presented. The KER spectrum of the vinylidene break-up channel measured at FEL (38 eV photons) is compared to the one measured by Alnaser *et al.* [Alnaser et al. 2006], where strong IR pulses were used. The KER spectrum obtained using strong IR pulses shows a single energy component centered around 4.8 eV. The KER peak has been assigned to isomerization on the doubly charged acetylene. The KER spectrum obtained using 38 eV photons shows a double peak structure: a peak centered around 4.8 eV and a high energy tail starting above 5 eV and extending up to $\sim$ 8 eV. By scanning the pump-probe delay (38 eV pump - 38 eV probe), they have shown that the high-energy peak increased with time while the low-energy peak was time-independent [Jiang et al. 2010]. They thus claimed that the high-energy peak was associated with proton transfer dynamics in the singly charge acetylene, while the low energy peak was associated with the isomerization on the doubly charged acetylene, in good agreement with previous finding [Alnaser et al. 2006]. Based on these observations, we will use the high-energy part of KER spectrum (above $\sim$ 5 eV), as a signature of the

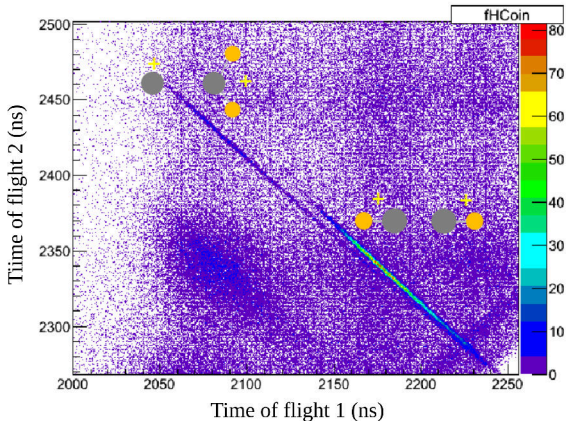

Figure 3.4: Time of flight of the second detected ion as a function of the time of flight of the firstly detected ion. The diagonal lines represents correlated ionic fragments. The upper (lower) diagonal is associated with the vinylidene $C^+ + CH_2^+$ (acetylene $CH^+ + CH^+$) break-up channel.

proton transfer on the acetylene cation charge state. We will try to see if going from 800 nm to 266 nm pulses allows us to initiate the dynamics that we are interested in, namely the nonadiabatic proton transfer on the acetylene cationic charge state, using simple table-top setup instead of using 38 eV photon from a FEL, which would allow better statistics and better temporal resolution.

The experiments were carried out using a multi-kHz amplified Ti:Sa laser system (2.5 kHz, 800 nm, 4 mJ, 30 fs). The intense 266 nm pulses were obtained by sum frequency generation of the fundamental beam (ω = 800 nm) with its second harmonic (2ω = 400 nm) into a 80 μm (and 250 μm for long pulse) thick type-I phase-matching β-Barium borate (BBO) crystal. Our setup included a very simple and efficient approach to control the 266 nm pulses duration. By changing the number of round trips on chirped mirrors (which add negative chirp) (Ultrafast Innovation) and/or by linear propagation through a controlled amount of fused silica (which add positive chirp), we were able to control the pulse duration from Fourier transform limited (32 fs) to above 200 fs, chirped pulses. 266 nm pulses can either be used alone, in single pulse experiments or can act as a pump to launch the dynamics in a pump-probe scheme. The pulse characterization was performed with a home-built all reflective transient-grating frequency-resolved optical gating (TG-FROG) setup. For the pump-probe experiments an 800 nm, 40 fs pulse was synchronized to the 266 nm to Coulomb-explode the molecules undergoing dynamics. An example of the time of flight of the second detected ion as a function of the time of flight of the firstly detected ion is shown in Fig. 3.4. One can see that we are clearly able to resolve the vinylidene two-body break-up channel ($C^+ + CH_2^+$, upper left diagonal).

We now study the KER spectrum of the vinylidene two-body break-up channel ($C^+ + CH_2^+$) as a function of the laser wavelength and look for the appearance of a high-energy peak, which is the signature of a proton migration that occurred in the singly charged acetylene. In Fig. 3.5, one can see that the dissociative double ionization of acetylene into $C^+ + CH_2^+$ fragments with 800 nm laser pulses only leads to the well-known 4.5 eV KER-peak, which confirms that IR strong field ionization only leads to proton migration in the doubly charged acetylene. The blue curve (rounded-dot symbol) represents the $C^+ + CH_2^+$ fragments generated by dissociative double ionization using second harmonic of the Ti:Sa laser (λ = 400 nm). Despite the very weak increase of signal in the high energy shoulder, which is not truly convincing, there is no significant difference

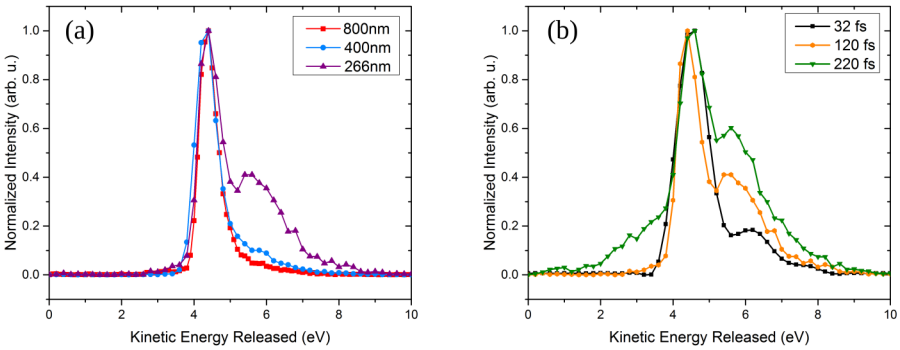

Figure 3.5: Wavelength and pulse dependence of the KER spectrum of the $C^+ + CH_2^+$ fragments detected in coincidence. In (a) the black curve represents KER spectra from ionization with 800 nm, 60 fs, 80 μJ pulses, in red, with 400 nm 130 fs 11.2 μJ and in blue, with 266 nm, 120 fs, 8.0 μJ pulses. In (b), the pulse duration dependence. In black, KER spectra from ionization with 266nm, 32fs, 4.8 μJ pulses. In orange, with 266 nm, 120 fs, 8.0 μJ pulses and in olive with 266 nm, 220 fs, 11.2 μJ pulses.

between the KER spectrum with λ = 400 nm and λ = 800 nm. However, when double ionization is produced by the third harmonic, λ = 266nm, (purple curve with filled-triangle dot) the KER spectrum of the $C^+ + CH_2^+$ fragments clearly show a second peak centered around 5.8 eV, which is the characteristic signature of the proton migration on the cationic charge state [Jiang et al. 2010]. This observation shows that using tabletop UV (266 nm) few-photon ionization enables the population of the electronically excited state $A^2\Sigma_g^+$ leading to the formation of vinylidene cation.

How can we explain that the 266 nm pulses are able to ionize the HOMO-1 while the 800 nm pulses cannot? In 2009, Telnov *et al.* [Telnov et al. 2009] used an all-electron TDDFT approach to study the angular-resolved multi-orbital contribution in strong field ionization of diatomic molecules (N_2, O_2 and F_2) with 800 nm pulses (photon energy of 1.55 eV). They found out that the HOMO-1 contribution was negligible in O_2 and F_2 but significant in N_2, and concluded that this was due to the energy gap between the HOMO and HOMO-1. This gap is much larger than the photon energy in O_2 and F_2 (4.6 eV and 3.2 eV, respectively), but it is only 1.4 eV in N_2. According to these observations, it is not surprising to see, in our results, that multiphoton ionization with photon energies of 1.6 eV (800 nm) and 3.2 V (400 nm) is not sufficient to reach the $A^2\Sigma_g^+$ state which lies 5.3 eV above the electronic ground state of acetylene cation. However, going to a photon energy (266 nm = 4.6 eV) close to the HOMO/HOMO-1 gap is an efficient way to increase the contribution from first inner-lying orbital, which is seen in our case by the high-KER-peak in the $C^+ + CH_2^+$ KER spectrum.

As a second experiment, we investigated the effect of 266 nm pulse duration on the KER spectrum of the $C^+ + CH_2^+$ fragments. We varied pulse duration from 32 fs to 220 fs (Fig. 3.5 (b)). The peak intensity was kept relatively constant. The high-KER-peak is already present with short 32 fs pulses but it increases drastically with the laser pulse duration. This observation can be interpreted as an accumulation effect. Indeed, for the high energy $C^+ + CH_2^+$ fragments to be detected, they have to undergo a full three-step sequence during the laser pulse envelope: i) population of the $A^2\Sigma_g^+$ states through strong field ionization from HOMO-1 orbital, ii) ultrafast nonadiabatic proton transfer dynamics and iii) dissociative second ionization into $C^+ + CH_2^+$ fragments, which are detected by our ion imaging spectrometer. As the pulse duration is increased, the probability that a

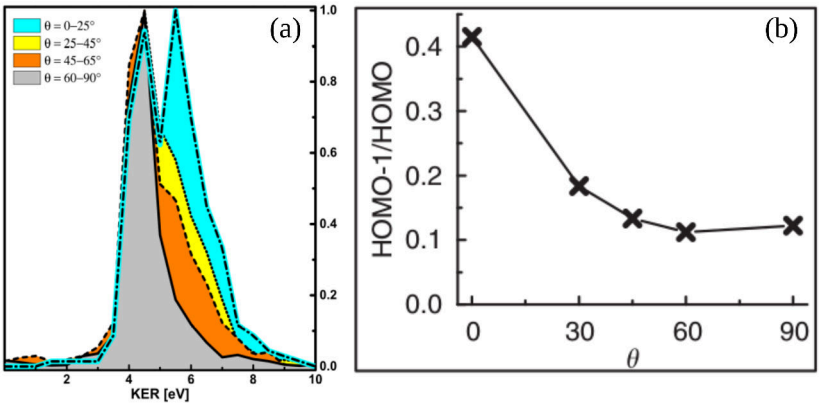

Figure 3.6: Angular dependence of the KER spectrum. We used 266 nm pulses, of 110 fs FWHM duration, at an intensity of $\sim$ 1 x 10^{14}W/cm^2. In (a), we represent the KER spectrum as a function of the angle θ between the laser electric field and the molecular principal axis. Cyan corresponds to angles θ between 0–25 °, yellow corresponds to 25-45 °, orange to 45-60 ° and grey to 60–90 °. All curves are normalized to the peak maximum. In (b), TDDFT calculations showing the ratio of ionization rate of HOMO-1 to HOMO versus angle θ. The pulse parameters used in the simulation were: 266 nm, 24 fs, 3 x 10^{14}W/cm^2. The calculations were performed by Emmanuel Penka Fowe and André Dieter Bandrauk, from Sherbrooke University. This figure is adapted from [Ibrahim et al. 2014].

molecule is able to undergo these three steps also increases. At very long pulse duration (220 fs), a second interesting feature appears in the KER spectrum: the KER distribution broadens in the low energy region, down to roughly 1.5 eV. We will see later that this feature is due to dissociation along the C=C bond.

3.2.5 Time-resolved nonadiabatic hydrogen migration dynamics in acetylene cation

In the previous subsection, we have demonstrated that few-photon (266 nm) ionization of acetylene can efficiently populate the $A^2\Sigma_g^+$ first excited state of the cation, a state which is known to undergo ultrafast nonadiabatic isomerization. We are now interested in time-resolving the proton transfer dynamics. To do so, we used a 32 fs 266 nm pulse to photoionize the molecule to the $A^2\Sigma_g^+$ (pump pulse) and a time-delayed 800 nm 40 fs pulse to remove one or two other electrons to the molecule, which leads to dissociation ($C^+ + CH_2^+$, $CH^+ + CH^+$ or $C^+ + CH^+ + H^+$). The fragments were detected in coincidence using the CEI apparatus described above.

We first focus on the KER spectrum of the two body break-up channels ($C^+ + CH_2^+$ and $CH^+ + CH^+$, see Fig. 3.7). First, we analyze the isomerization process. As in the single-pulse experiments, proton migration dynamics shows up in pump-probe experiments in the high-energy region obtained by correlating two fragments. These dynamics corresponds to the region V3 of the vinylidene channel ($C^+ + CH_2^+$) in Fig. 3.7(a). We observe an increase of the yield in this high-energy shoulder at early pump-probe delay (60 - 100 fs) followed by a decrease. We will leave the details about the proton migration dynamics and vinylidene formation until we have direct evidence from three-fragment correlations in the next section.

The mid-energy region (V2) in Fig.3.7(a) has been previously assigned to proton migration occurring in acetylene dication [Alnaser et al. 2006; Jiang et al. 2010]. This peak is thus time-independent and pretty boring (for us). In addition, we observe a new peak emerging in the low-energy region (V1). This peak is first visible around 80 fs, and occurs as well in the low-energy region (A1) of the acetylene channel ($CH^+ + CH^+$; Fig.3.7(b))

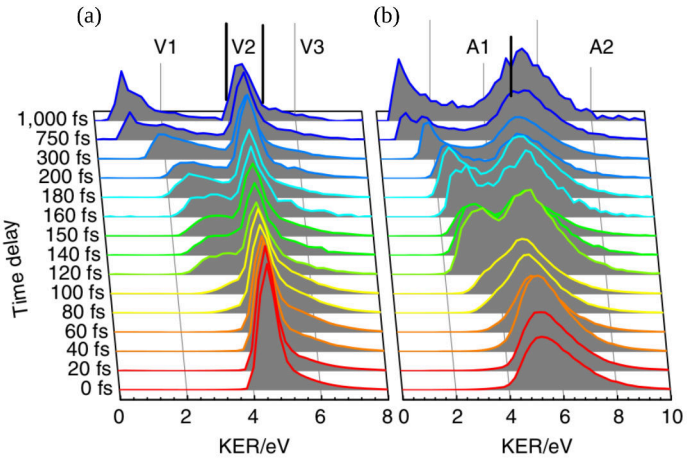

Figure 3.7: Two body breakup channel KER spetra. Vinylidene break-up channel $C^+ + CH_2^+$ is shown in (a) and acetylene break-up channel $CH^+ + CH^+$ in (b) as a function of pump-probe delay. For the analysis, we will separate the vinylidene spectrum in three different regions: V1: below 4 eV; V2: between 4 and 5 eV; and V3: above 5 eV. We will also divide the acetylene channel into two regions: the low-energy region A1: below 5 eV, and A2: above 5 eV. Spectra are normalized by the number of correlated counts, to account for varying acquisition times at different time steps, as well as for minor fluctuations in pulse power or gas pressure. This figure is adapted from [Ibrahim et al. 2014].

and has, to our knowledge, never been observed before. Since it occurs for both vinylidene and acetylene, we attribute it to a stretching of the C=C bond. In both channels, it shifts to smaller energies (indicating an increase in the C=C internuclear distance) with increasing time delay. The peak strength continuously increases with increasing time delay, which is consistent with a lowering of the ionization potential as the C=C bond length increases. Assuming purely Coulombic potential (which is far from being the case), the peak at 1 eV would correspond to an elongation of the C=C bond to more than 4 times its equilibrium distance, implying that the molecule has largely dissociated. While none of the low-lying electronic states of $[HC = CH]^+$ are dissociative along the C=C stretch coordinate, if a fifth photon is absorbed during the pump pulse, enough energy is transferred to the molecule so that it can reach states which are dissociative along C=C coordinate. Since the dissociation dynamics occur in both the acetylene and vinylidene channels, they are likely to be triggered by the same event, namely absorption of a photon to higher lying excited states of the cation. From there, dissociative states of the vinylidene cation are reached.

The KER spectrum of the two body break-up channels ($C^+ + CH_2^+$ and $CH^+ + CH^+$) gave us a few important insights about the ongoing proton migration and dissociation occurring in the acetylene cation. However, these two body break-up channels do not provide direct and clear information about the molecular geometry, *i.e.* they do not allow us to tell where the flying proton is within the molecule, as a function of time. In order to track the motion of the migrating hydrogen atoms, we will use the same data set, but we will look into the three body break-up channel ($C^+ + CH^+ + H^+$).

In the three-body breakup channel, we have access to the direction in which the proton is emitted, allowing us to follow the proton migration process in detail. At its simplest, if the proton trajectory is close to the direction of the CH^+ fragment, it means that the molecule was close to the vinylidene geometry while undergoing Coulomb explosion. On the other hand, if the proton is close to the C^+ fragment direction, the molecule is closer to acetylene geometry. Such simple analysis allows following the proton migration

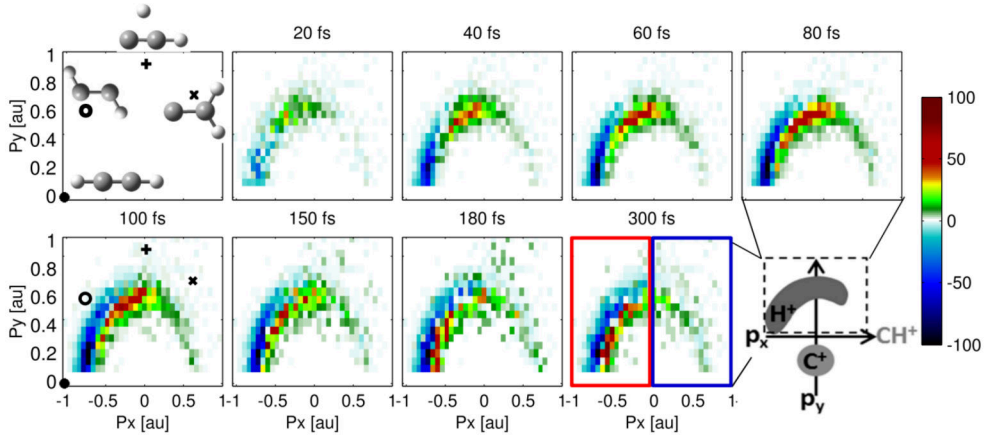

Figure 3.8: Newton plots filtered in energy for total KER larger than 13eV. In the upper left panel, symbols show classically calculated results (assuming purely Coulombic potentials) for different geometry (linear configuration, trans-configuration, transition state, and vinylidene). As indicated in the lower right panel, all molecular fragments are rotated such that the momentum vector of CH^+ points towards the positive x-axis, the relative momentum of C^+ is confined to the negative y-axis (not shown here). This transformation allows to look at the data in the molecular (recoil) frame. We plot only the momentum vector of H^+ after subtracting the distribution at $\Delta t = 0$. The plots show the evolution of H^+ momenta with increasing time delay from 0 to 300fs. This figure is adapted from [Ibrahim et al. 2014].

dynamics in momentum space. Key frames of this nonadiabatic isomerization dynamics are represented by the Newton plots in Fig. 3.8. [2] In Fig. 3.8, proton fragment momenta are presented in the molecular frame. As indicated on the lower right panel, all molecules are rotated such that the momentum vector of CH^+ points towards the positive x-axis and that the relative momentum of C^+ is confined to the negative y-axis (not shown in the other panels). We plot only the data of the momentum vector of H^+ after subtracting the distribution at $\Delta t = 0$. Because time zero distribution has been subtracted for each positive delay distributions, white colors correspond to zero, blue colors to negative signal (that is, where the signal originates) and other colors to positive contributions (that is, where the signal is going). In the higher left panel of Fig. 3.8, we show the classically calculated values of the proton momentum for different geometry (shown as symbols) assuming Coulomb potentials. It represents the expected position of the signal, for different molecular geometries. If the signal is in the bottom left, the molecule is in an acetylene-like geometry. If the signal is in the top part (in P_y) and in the middle (in P_x), the molecule is in transition-state-type geometry. If the signal moves to the middle-right region of the momentum space, it is in a vinylidene-like geometry. The plots show the evolution of H^+ momenta with increasing time delay from 0 to 300fs. Let us first look at the first panel (20 fs pump-probe delay). We see a blue contribution around the lower-left corner of the momentum space and a green contribution around the upper-middle region. This indicates a negative signal for acetylene-like geometry and a positive signal for the trans-bent and transition state-like geometries. It means that molecules are going from acetylene-like geometry to trans-bent and transition state-like geometries. As the delay increases, the signal becomes more negative around the acetylene-like geometry region,

[2] Since proton migration in the acetylene cation initiated on the $A^2\Sigma_g^+$ state results in a bound vinylidene cation (that is, non-dissociative), its Coulomb explosion yields a high KER. Therefore, the dynamics of interest (proton migration) were isolated by filtering the total three-body KER data, selecting only correlated events above 13 eV and thereby excluding the signal coming from the C=C bond dissociation.

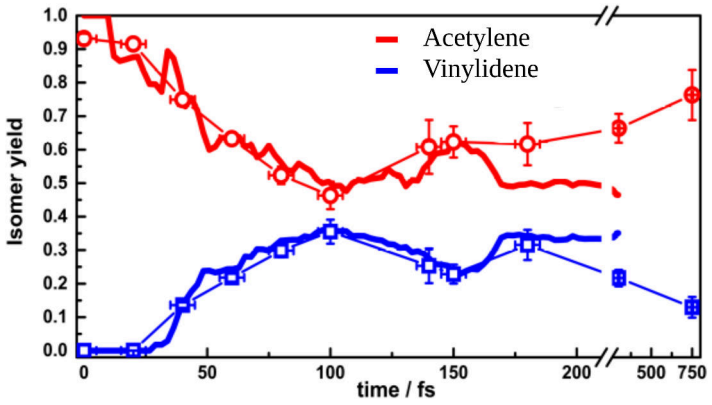

Figure 3.9: Comparison between the theoretical (thick lines) and the experimental (thin lines and dots) time-dependent yield of acetylene (red) and vinylidene (blue). The experimental values are obtained by summing over the left (acetylene) and right (vinylidene) part of the Newton plot presented in Fig. 3.8 (see the red and blue boxes). Experimental data are corrected by offset and scaling factor to fit the theoretical points. The theoretical data are obtained by looking at the molecules which are in the acetylene or vinylidene geometry.

and more positive around the transition state-type geometry region, and even extends in the region where we expect the vinylidene-like geometry to end-up in the momentum space. Since the triply charged states populated in the experiment substantially deviate from a Coulomb potential, the observed momentum in the experiment is lower than the classically calculated one (upper left panel, Fig. 3.8). Despite this deviation, the agreement between this simple calculation and the experimental data is very good.

In order to follow in a more quantitative way the dynamics of acetylene-vinylidene nonadiabatic isomerization, we integrated the $P_x > 0$ and $P_x < 0$ signals, which can be defined as the cationic vinylidene-like and acetylene-like population (see the red and blue square, in the lower right panel of Fig. 3.8). The results of this integration are presented in Fig. 3.9, where they are compared with theory. Briefly, the excited nonadiabatic molecular dynamics on the $A^2\Sigma_g^+$ state was simulated using the full-multiple spawning approach [Ben-Nun et al. 2002], a semi-classical method. More details about the theoretical method are presented in [Ibrahim et al. 2014]. The calculations were performed by Michael S. Schuurman from NRC Ottawa. The recurrent isomerization behavior of Fig. 3.9 is perfectly reproduced by the ab initio trajectory simulations of the vibronic dynamics as shown by solid lines in Fig. 3.9. We see the first maximum in the vinylidene-like population around 100 fs, followed by a local minimum, which is followed again by a local maximum around 180 fs, indicating a recurrently migrating proton. While a single recurrence had also been observed in $[DC=CD]^{2+}$ [Hishikawa et al. 2007; Matsuda et al. 2011], we now see further recurrence associated with the evolution of the nuclear wavepacket. We deduce from these results the following proton migration process: Both $X^2\Pi_u$ and $A^2\Sigma_g^+$ are populated in a three- and four-photon process, respectively; (Fig. 3.1). According to our calculations, the $A^2\Sigma_g^+$ state population is depleted by roughly half in the first 40–50 fs via a trans-bent conical intersection to hot vibrational states of the ground electronic state of $[HC=CH]^+$. The initial X-state population does not contribute to isomerization since its energy is too low to overcome the isomerization barrier. The solid lines in Fig. 3.9 represent the total ground- and excited-state populations of acetylene (red) and vinylidene (blue) cation. As one can notice in Fig.3.9, the agreement is excellent up to 150 fs. From a single exponential fit, we estimate the initial isomerization time to be $\tau = 41$ fs (theory) and $\tau = 43 \pm 10$ fs (experiment), which is in agreement with previous results [Jiang et al. 2010]. We can thus

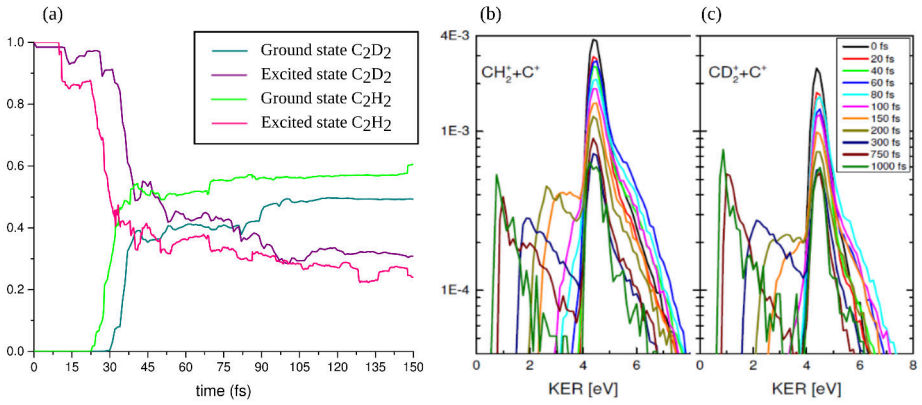

Figure 3.10: Theoretical (a) and experimental (b)-(c) investigation of the isotopic effects in the nonadiabatic hydrogen migration dynamics in acetylene and d_2-acetylene cations. In (a) is the population in the ground and excited states of the acetylene and d_2-acetylene cations as a function of time after which the wavepacket have been launched on the excited cationic state. In (b) and (c) is the total KER for the 'vinylidene' ('d_2-vinylidene') two body break-up channel ($C^+ + CH_2^+$) and ($C^+ + CD_2^+$), respectively, as a function of the pump-probe delay.

add ourselves to the long list of people who have recorded the 'first' molecular movie!

3.2.6 Isotopic effect in the nonadiabatic hydrogen migration dynamics in acetylene cation

In the previous subsection, we have seen that we were able to follow the ultrafast isomerization dynamics of acetylene cation, which occur by the passage through a conical intersection. This constitutes a typical scenario where the Born-Oppenheimer approximation breakdown. Conical intersections provide an efficient mechanism for radiationless electronic relaxation: they can act like "funnels" for the nuclear wave function. In our case, we have shown that proton transfer was an important nonadiabatic doorway for the relaxation of electronically excited acetylene cation.

Because proton migration represents one of the most fundamental processes in chemistry and biology, it is important to use benchmark molecules like C_2H_2 to study the subtle details of such unimolecular reaction. One simple strategy often used to gain information about the ongoing vibronic dynamics, is to perform the same experiment using two different isotopologues. Isotopologues are molecules which different solely in their isotopic composition. For example, in our case, it would be interesting to compare the isomerization dynamics in acetylene (C_2H_2) and in deuterated acetylene (C_2D_2). For isotopologue molecules, the electronic potentials are identical, but vibrational levels are shifted depending on the mass of the nuclei. Thus, the conical intersection itself, as well as the wavepacket dynamics in its vicinity, will be affected by the isotopic switching of one atom in the molecule. Moreover, because the nuclei are heavier for C_2D_2 than for C_2H_2, the nuclear wavepacket involving the motion of H/D will be slower in the deuterated isotopologue. Here, we present very preliminary experimental and theoretical results where we have compared the dynamics in the two different isotopologues mentioned above. We have performed the exact same experiments (266 nm pump - 800 nm probe), in acetylene and is isotopologue d_2-acetylene. Michael S. Schuurman has also performed calculations of the excited nonadiabatic molecular dynamics on the $A^2\Sigma_g^+$ state, using the full-multiple spawning approach, in both acetylene and is isotopologue d_2-acetylene. The results of his calculation are presented in Fig. 3.10 (a).

In the results presented in Fig. 3.10 (a), the simulations started with a wavepacket on the excited $A^2\Sigma_g^+$ electronic state, and the lines show the population in the excited state and in the ground state (after nonadiabatic relaxation through the conical intersection), for both isotopologue. From these populations dynamics, we can draw two conclusions, which are pretty intuitive. The first conclusion is that the lighter the nuclei are, the faster the nuclear wavepacket reaches the conical intersection, which allows to nonadiabatically relax through the ground state. Indeed, we can see in Fig. 3.10 (a) that the ground state population starts to grow earlier in acetylene that in its deuterated isotopologue. The second conclusion is that the lighter the nuclei are (faster nuclear wavepacket), the more efficient the nonadiabatic passage through the conical intersection is. We can see that more population is transferred to the ground state via the conical intersection in the case of acetylene, where the nuclear wavepacket is expected to move faster. This observation is in good agreement with the Landau-Zehner formula, which describes the nonadiabatic transition probability in the vicinity of conical intersection [Liekhus-Schmaltz et al. 2016]. This formula indeed tells us that faster wavepackets have a higher probability to make nonadiabatic transitions around a conical intersection. Replacing a light atom with a heavy one will thus slow the nuclear wavepacket and leads to a decrease of the nonadiabatic transitions rate around a conical intersection. This is exactly what is observed in the calculations. Let us now look at the experimental results. We will look into the KER spectrum of the vinylidene two body break-up channel $C^+ + CH_2^+$, since, as explained previously, the presence of a high-KER-peak is a smoking gun signature of the formation of vinylidene by nonadiabatic relaxation through a conical intersection. The dynamics high-KER-peak will thus serve as the signature of the passage through the CI. By looking at the high-KER-peak ($C^+ + CH_2^+$, Fig 3.10 (b) and $C^+ + CD_2^+$, Fig 3.10 (c)), we can see that the two conclusions extracted from the simulations (and from the Landau-Zehner formula [Liekhus-Schmaltz et al. 2016]) are confirmed experimentally. The high-KER-peak rise faster and higher for $C^+ + CH_2^+$ than for $C^+ + CD_2^+$, indicating that the conical intersection is reached faster and that the nonadiabatic transitions probability around a conical intersection is more efficient for lighter nuclei.

These results are still under analysis, in order to extract more quantitative conclusions about the isotopic effect on the nonadiabatic dynamics around a conical intersection. From this very preliminary analysis of the data, we can see that substituting some atoms in a molecule enables controlling the speed of the associated nuclear wavepacket, which has a tremendous effect on the nonadiabatic vibronic dynamics.

3.2.7 Partial conclusions

In summary, we have shown that dynamics initiated in the first excited cationic states could be launched without using XUV free-electron lasers, by using a few-photon ionization scheme, where the photon energy is close to the HOMO/HOMO-1 energy gap. Given the limited availability, repetition rate, pulse stability and timing jitter of FELs, our approach offers tremendous benefits in terms of statistics and temporal resolution. Combining multiphoton absorption of UV light pump with Coulomb Explosion Imaging probe opens the door to time-resolved imaging of chemical reactions involving nonadiabatic dynamics through conical intersections. These nonadiabatic dynamics are at the heart of modern femtochemistry. Combined with theoretical simulations, we believe that our results present the most complete picture of proton migration in $[HC=CH]^+$ to date. These experiments were performed by using the ionic fragments detected in coincidence, which enables the reconstruction of the 3D momentum vector of each ionic fragments produced upon dissociation. This is possible for relatively small molecules. Even if this detection

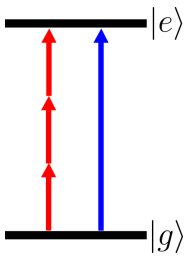

Figure 3.11: Brumer-Shapiro scheme for non-linear coherent control of the amplitude of a bound-bound transition using the interference between a single and a three-photon transitions.

scheme is blind to the electronic structure, it was shown to be very useful to extract structural information in molecules undergoing dynamics. It is a technique which is very powerful to follow dynamics involving large modification of the nuclear geometry of molecules. Exotic dynamics in small polyatomic molecules, like 'roaming' in formaldehyde [Houston et al. 2017; Mauguière et al. 2015; Townsend et al. 2004], are currently under study with the CEI setup at ALLS.

3.3 Subfemtosecond control of electron localization during dissociation

3.3.1 Coherent control using the Brumer-Shapiro scheme

Developing tools and schemes to control the outcome of chemical and physical transformations with light has been a long-standing goal for a large community of scientists. In 1986, Paul Brumer and Moshe Shapiro proposed a scheme, termed *Coherent Control*, that laid the foundation of controlling the quantum dynamics of matter with photons [Brumer et al. 1986]. The Brumer-Shapiro scheme is based on a multiple-pathway interference of light-induced transitions, leading to the control of simple chemical and physical processes like light absorption, ionization, and dissociation, for example. A schematic of a typical Brumer-Shapiro experiment is shown in Fig. 3.11.

The Brumer-Shapiro coherent control scheme relies on the interference between transitions of different multiplicities. Starting from the ground state of a system ($|g\rangle$), the excited state ($|e\rangle$) can be reached by two (or more) different pathways, through the absorption of n or m photons. The selection rules governing the transition from $|g\rangle$ to $|e\rangle$ dictate the acceptable n and m combinations. For example, for atomic bound-bound transitions, the initial and final states have a well-defined parity, which defines if an even or odd number of photons are necessary for this transition to be allowed. Because the absorption of each photon is associated with a change of parity of the quantum state, n and m must be odd (even) if the initial and final states have the opposite (same) parity. One of the most simple and intuitive implementations of the Brumer-Shapiro coherent control scheme is the so-called 'ω - 3ω' scheme. As depicted in Fig. 3.11, a three-photon transition using light at fundamental frequency ω as well as a single photon transition using light at third-harmonic frequency 3ω are concomitantly involved in the transition from the ground to the excited states.

$$\sigma_{ge}^{tot} = \left|\sigma_{ge}^{(3)} + \sigma_{ge}^{(1)}\right|^2 = \left|A_\omega e^{3i\phi_\omega} + A_{3\omega} e^{i\phi_{3\omega}}\right|^2 \tag{3.1}$$

As shown in equation 3.1, the total photoabsoption cross-section from the ground to the excited state σ_{ge}^{tot} can be calculated by evaluating the modulus square of the sum of

the cross-section for the single ($\sigma_{ge}^{(1)}$) and the three-photon transition ($\sigma_{ge}^{(3)}$). Expanding the square modulus in equation 3.1 leads to equation 3.2.

$$\sigma_{ge}^{tot} = \left|\sigma_{ge}^{(1)}\right|^2 + \left|\sigma_{ge}^{(3)}\right|^2 + A_{3\omega}A_{\omega}\cos(3\phi_{\omega} - \phi_{3\omega} + \delta_{13}) \tag{3.2}$$

This equation is the sum of the square modulus of the cross-section for the single photon transition ($\sigma_{ge}^{(1)}$), the square modulus of the cross-section for the three-photon transition ($\sigma_{ge}^{(3)}$), and of an interference (cross) term which is at the heart of the coherent control mechanism. This interference is dictated by δ_{13}, which is the phase difference between the single and the three-photon transition dipole matrix elements (phase lag or atomic/molecular phase, depending to who you are talking to), and ϕ_{ω} and $\phi_{3\omega}$ which are the phases of the two fields used for the coherent control. By tweaking the relative phase between the two laser pulses ($\phi_{\omega} - \phi_{3\omega}$), one can control whether the interference between the two transitions is destructive or constructive, leading to a control over the total photoabsorption cross-section, for example. Moreover, for the control to be efficient, the amplitude of the single photon transition $A_{3\omega}$ and the three-photon transition A_{ω} should be similar. Because a three-photon transition is (typically) much less probable that the single photon transition using the third harmonic 3ω, the fundamental ω field strength needs to be much higher than the one of the third harmonic. This constraint on the relative field amplitude is pretty good news for experimentalists since the generation of harmonics (third harmonic in this case) of the fundamental laser frequency is generally not very efficient. Very early demonstrations of this coherent control scheme were reported in the 1990s, to control the total ionization rate of an atom [Chen et al. 1990], the photodissociation rate of a molecule [Kleiman et al. 1995], as well as the directionality of the laser-induced current in a semiconductor [Dupont et al. 1995].

Many variants of the Brumer-Shapiro scheme can be implemented, to control different observables. For instance, one could think of using the interference between two-photon transition induced by the fundamental and single-photon transition by its second harmonic (ω - 2ω). However, changing from ω - 3ω to ω - 2ω scheme comes with a change in the selection rules. Starting from the same initial state, a single-photon (at 2ω) and a two-photon (at ω) transitions would lead to final states with different parities. This scheme can therefore not be used to control the transition rate from two bound states, since they have well-defined parity. However, the ω - 2ω scheme can be used to control the angular distribution of electrons emitted upon bound-continuum transitions. Consider an atom in its s- ground state. A single-photon transition, where $2\hbar\omega > I_p$, would produce a free-electron described by a p-type partial wave, because of the $\Delta\ell = \pm 1$ selection rule for a single photon transition. A two-photon transition, using photons of ω frequency, would produce a free-electron described by a linear combination of s- and d-type partial waves, because of the selection rule described above. By simultaneously photoionizing the atom using (two) ω and (one) 2ω photons would produce photoelectron at a well-defined energy, described by a linear combination of s-, p- and d- type partial waves. The relative weight of the partial waves is governed by the differential transition dipole matrix elements, while their relative phases depend on both the differential phase of the transition dipole matrix elements and the relative phase between the ω and 2ω fields. By changing the delay between the two fields, one can thus control the relative phase between the different partial waves constituting the photoelectron wavepacket, at a given energy, leading to a control over its angular distribution. Few years after the seminal paper of Brumer and Shapiro, such a scheme was used to control the angular distribution

of photoelectrons [Yin et al. 1992; Yin et al. 1995] and photofragments [Kim et al. 1997]. We will see later that the interference between different two-photon transitions (XUV+IR), which is conceptually very similar to the Brumer-Shapiro scheme, is at the heart of one of the most used attosecond metrology tool, which is called *Reconstruction of Attosecond Beating By Interference of Two-photon Transitions* (RABBITT) [Paul et al. 2001].

In the next subsection, we will present how such ideas, introduced by Brumer and Shapiro, can be used to control the electron localization during the photodissociation of the 'world simplest molecule', or the 'world simplest atom with one extra proton', which is the favorite molecule of the attosecond science community, namely H_2^+ (and its isotopologue D_2^+).

3.3.2 How to control the electron localization in dissociating H_2^+ and D_2^+ ?

Controlling chemistry with lasers comes with the hope that one can dictate the faith of a chemical process in a different way that it would naturally occur thermally. One could argue that the most simple chemical reaction is the dissociation of the H_2^+ molecule into H + H^+. Indeed, H_2^+ is composed of two nuclei and one electron. The ground state of H_2^+ is a *gerade*[3] $|\sigma_g\rangle$ state, which is bound. The first excited state of H_2^+ is an *ungerade* $|\sigma_u\rangle$ state, which is dissociative (see Fig. 3.12). At low-temperature, an ensemble of H_2^+ molecules are in their ground state, and nothing interesting happens. If we heat an ensemble of H_2^+ molecules, the excited states $|\sigma_u\rangle$ can be thermally populated and a fraction of the molecules will undergo dissociation into $H + H^+$. In fact, if we could distinguish between the two hydrogen atoms, the excited molecular ion could dissociate into $H + H^+$ or $H^+ + H$. Statistically, the two chemical reactions have the exact same probability to occur. In the following, we will see how it is possible to apply Brumer-Shapiro schemes to control the yield and the directionality of this prototypical chemical reaction. We choose this very simple photoinduced chemical transformation since the dynamics of H_2^+ can be described with high accuracy using *ab initio* theoretical methods and since its dynamics in strong laser field have been subject of many theoretical and experimental studies (for a recent review, see [Ibrahim et al. 2018]).

Let us first consider the control of the yield of the photodissociation rate ($H_2^+ \rightarrow H + H^+$) using the ω-3ω Brumer-Shapiro scheme. The demonstration of the coherent control of the photodissociation rate has been shown by Xu *et al.* [Xu et al. 2016]. They used a ω-3ω (1800 nm - 600 nm) two-color phase-locked field to photoionize H_2 and to control the dissociation yield ($H + H^+$ yield). They measured the ion yield and directionality using a COLTRIMS detector. At the peak of the two-color pulses, the H_2 molecules are singly ionized to the ground $|\sigma_g\rangle$ ionic state. Because the neutral H_2 molecule has a smaller equilibrium geometry than the ionic ground state H_2^+, a nuclear wavepacket motion is induced in the molecular ion upon ionization of the neutral molecule. When H_2^+ reaches the internuclear distance where the energy difference between ground $|\sigma_g\rangle$ state and first dissociative $|\sigma_g\rangle$ excited state equals the energy of a 3ω photon, the molecular ion can be excited to the dissociative $|\sigma_g\rangle$ state via a single 600 nm photon or a three 1800 nm photons dipole allowed transitions. As explained earlier, by scanning the delay between the ω and 3ω field, one can control whether the interference between the single- and the three-photon transition is constructive or destructive, leading to a control over the dissociation yield. Using this scheme, Xu *et al.* demonstrated a control of the dissociation yield of $H_2^+ \rightarrow H + H^+$ with a contrast of more than 50 % [Xu et al. 2016], over of broad range of H^+ fragment kinetic energy, which is impressive.

Now that we have explained how Xu *et al.* used the ω-3ω Brumer-Shapiro scheme to

[3] *gerade* and *ungerade* means even and odd, respectively, in German.

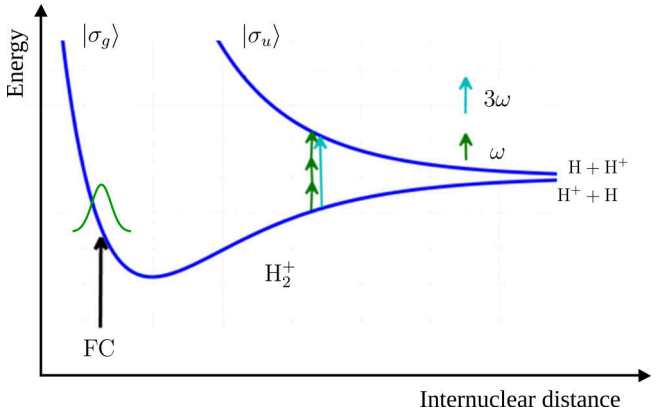

Figure 3.12: Potential energy curves of the $|\sigma_g\rangle$ and $|\sigma_u\rangle$ states of H_2^+. The *gerade* $|\sigma_g\rangle$ state is bounded while the *ungerade* $|\sigma_u\rangle$ is dissociative. Possible dissociation pathways are shown (three ω photon absorption and one 3ω absorption). The potential energy surface have been taken from [Xu et al. 2016].

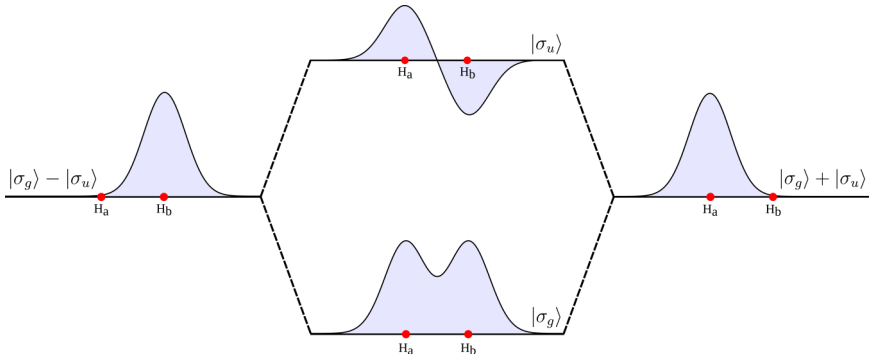

Figure 3.13: Schematic of the electron localization using a linear combination of molecular orbitals. This scheme can be seen as an 'inverse' LCAO case, where LCAO stands for Linear Combination of Atomic Orbitals and is a well-known theory for the construction of molecular orbital using a linear combination of orbital of the atoms forming the molecule. Indeed, by creating a coherent superposition of *gerade* $|\sigma_g\rangle$ and *ungerade* $|\sigma_u\rangle$ molecular orbital, the electron can be localized on one of the two nuclei, depending on the relative phase between the molecular orbitals.

control the yield of the dissociation of the H_2^+ molecular ion into $H + H^+$ fragments, we will see how one can use the ω-2ω scheme to control the directionality of the dissociation process, *i.e.* on which of the two nuclei the electron will be localized asymptotically. Let us first describe the very general conditions to control the directionality of the dissociation of H_2^+. The most general requirement for coherent control is that one needs to have two different pathway that trigger an event in order to be able to control it. Two other conditions are necessary to achieve the directional control of electron localization: (i) the two pathways must result in states of opposite parity (*gerade* $|\sigma_g\rangle$ and *ungerade* $|\sigma_u\rangle$, see Fig. 3.13) and (ii) the kinetic energy of the fragments produced by the two pathways must overlap in order to allow interference to occur. Moreover, to have a strong contrast in the coherent control, the relative probabilities of the two interfering pathways need to be similar to each other. In Fig. 3.14, a scheme of the different pathway that can lead to dissociative ionization is presented.

Before discussing our experimental strategies and results, we need to mention that we were not the first team to tackle the question of electron localization during photodissociation of diatomics. Several groups have implemented few-cycle CEP-stable schemes [Kling

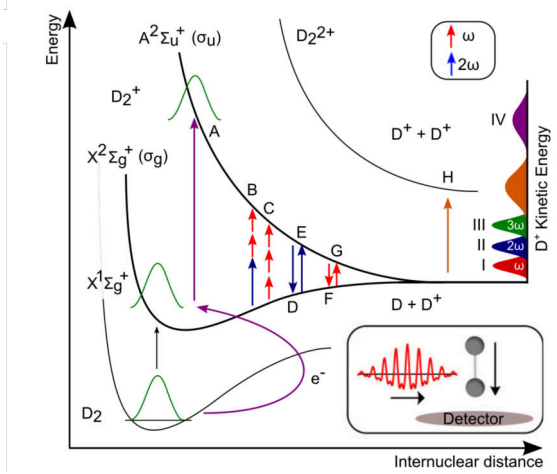

Figure 3.14: Schematic of the experiment. The figure represents the different pathway leading to the formation of D^+ ions: bond softening (red KE region), above-threshold dissociation (blue KE region), three-photon dissociation (green KE region), charge-resonance-enhanced ionization (orange KE region) and recollision excitation (purple KE region). Capital letters correspond to different pathways and roman numerals indicate different control channels, as discussed in the text. The inset shows the geometry of the experimental setup. This figure is adapted from [Wanie et al. 2016].

et al. 2006; Kremer et al. 2009; Xu et al. 2013; Znakovskaya et al. 2012; Znakovskaya et al. 2009], XUV attosecond pulses synchronized with near-infrared (NIR) schemes [Kelkensberg et al. 2011; Sansone et al. 2010; Singh et al. 2010] as well as two-color phase-locked ω-2ω schemes [Gong et al. 2014; Ray et al. 2009; Song et al. 2017], to control the dissociation of diatomic molecules. The control of the directionality of the dissociation process using few-cycle CEP-stable scheme has mostly been performed using $\sim$ 800 nm central wavelength. The only experiment which used few-cycle mid-IR pulses [Znakovskaya et al. 2012] demonstrated unprecedented charge-directed reactivity. This better control over the charge directionality was attributed to the better match between the (longer) optical cycle and the time it takes for the nuclear wavepacket to reach the internuclear separation where the radiative transitions can occur [Znakovskaya et al. 2012]. Moreover, it was shown that using multicycle two-color fields (400 nm - 800 nm) also lead to much higher control of the charge-directed reactivity, compared to few-cycle 800 nm pulses. One could thus think that combining the multi-cycle aspect of two-color fields with the long wavelength (mid-IR) pulses would lead to a much better degree of control than previously achieved. With the availability of the mid-IR sources from the OPAs at ALLS, as presented in the first chapter of this thesis, we had the idea to try to improve the level of control of the directionality of the electron localization by using multicycle phase-locked mid-IR (1800 nm - 900 nm) pulses.

Fig. 3.14 illustrates the dynamics and pathways of interest concerning our experiment leading to the dissociation of D_2^+ [4]: the two-color laser pulse first removes an electron from the ground state of the neutral molecule via strong-field ionization. A vibrational wavepacket is then launched on the ground electronic state $|\sigma_g\rangle$ of the cation. During the evolution of the nuclear wavepacket, many different mechanisms involving different quantum pathways are likely to occur upon absorption of further photons, and lead

[4] When we describe processes in D_2^+, it could also apply to H_2^+. In our experiments, we will see later than we have compared the degree of control in both isotopologues and observed a better contrast for D_2^+. This is why, in the following, we will describe the different phenomena for D_2^+.

to fragmentation on different electronic states and to fragments with different kinetic energies:

1) The molecule may dissociate in the bond softening (BS) region, *i.e.* at internuclear distance where a single-photon is resonant with the $|\sigma_g\rangle \rightarrow |\sigma_u\rangle$ transition [Bucksbaum et al. 1990]. This internuclear distance is different for the ω and 2ω photon. For the 1800 nm, this process is indicated as G, in Fig. 3.14, and results in dissociation via the $|\sigma_u\rangle$ cationic state (red region on the D^+ kinetic energy (KE) axis in Fig. 3.14). Furthermore, the second color (900 nm) of a two-color field can also lead to BS (indicated as E, in Fig. 3.14) and populate the $|\sigma_u\rangle$ state (blue region).

2) Dissociation can also occur via above-threshold dissociation (ATD) [Giusti-Suzor et al. 1990]. For example, the absorption of three photons (indicated as C, in Fig. 3.14) followed by stimulated emission of one photon (indicated as F, in Fig. 3.14) may lead to the dissociation of the molecule via the $|\sigma_g\rangle$ cationic state (blue region in Fig. 3.14).

3) A wavepacket avoiding the previously mentioned light-induced process may reach an internuclear distance where the ionization probability is significantly increased, leading to the ionization of the second electron. This behavior is known as charge-resonance-enhanced ionization (CREI) [Zuo et al. 1995]. Because the process generates two ions ($D^+ + D^+$, *i.e.* no electron left), the concept of electron localization in meaningless for this channel. Nevertheless, we will see later on that we detect these ions in our experiments (indicated as F and leading to KE region shown in orange in Fig. 3.14).

4) Apart from radiative coupling with the laser field, recollision-induced excitation (RCE) can lead to molecular dissociation. Under the influence of the laser field, the ionized electron may recollide with the molecular ion and cause an excitation of the molecule to the $|\sigma_u\rangle$ dissociative state (indicated as A, in Fig. 3.14). Because this excitation event occurs within a single laser cycle, the excitation occurs at a small internuclear distance (the molecule does not have time to significantly stretch between ionization and recollision), leading to an ion with high KE (the purple region in Fig. 3.14).

In our experiments, using multicycle 1800 nm + 900 nm pulses, we will see control of molecular dissociation via the interference of multiple of these dissociation pathways (see Fig. 3.14). As an example, because BS (pathway E) and ATD (pathways C+F) fulfill the two essential criteria for two transition to be amenable for coherent control, namely the energy overlap of the ions and the dissociation on electronic states with different parity ($|\sigma_g\rangle$ and $|\sigma_u\rangle$), the resulting interference allows us to coherently control the charge-directionality of the dissociation process, as will be presented in the discussion section.

3.3.3 Experimental Methods and Results

The mid-IR source that was used for the coherent control experiments was slightly different from the one presented in the second chapter of this thesis manuscript. Since we did not need a lot of energy per pulse, we chose to use the 2.5 kHz laser from INRS instead of the 100 Hz laser, in order to increase the signal-to-noise ratio (statistics) in the experiments. From a 30 fs, 800 nm pulse, we generated the (ω) 1800 nm beam using a commercially available (Light Conversion) white light seeded optical parametric amplifier (OPA). The generation and the synchronization of the (2ω) field were performed using an in-line simple setup. A 200 μm thick BBO crystal was used to generate the 900 nm second harmonic field. To compensate the group delay between the two pulses, a second 500 μm thick BBO crystal combined with a calcium fluoride window was used. Next, because the 2ω is generated orthogonal to the ω field, a zero-order half-waveplate was employed to rotate the 1800 nm polarization parallel to the one of its second harmonic. We finally propagated the two-colors through 2 mm fused silica window. Because of the different

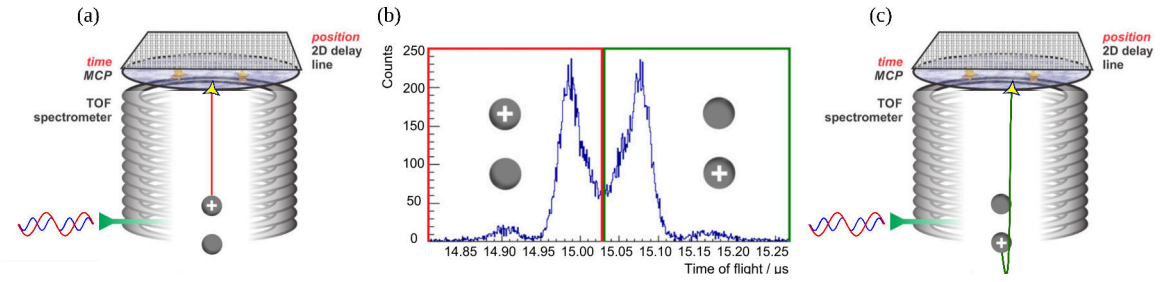

Figure 3.15: Disentangling the localization of the electron in the experiment. In (b), D^+ time of flight spectrum is presented. The calibration allows to define the time of arrival for fragments with a zero initial momentum p_z in the direction of the detector (here, the $p_z = 0$ correspond to a TOF of ~ 15.03 μs). Fragments that arrive before (red rectangle and panel (a)) and after (green rectangle and panel (c)) correspond to electron localization (ion emission) in opposite direction (on different nuclei).

index of refraction of FS at ω and at 2ω, rotating the FS plate around its vertical axis enables a fine control over the relative phase (delay) between the ω and the 2ω field. The pulse duration of the 1800 nm field was evaluated to be 50 fs using second harmonic generation autocorrelation. The resulting two-color laser pulses were focused into a Coulomb explosion imaging (CEI) apparatus with a spherical mirror of 100 mm effective focal length. The CEI apparatus is the same as described in the previous section. The laser intensity at 1800 nm in the interaction region was determined from the distribution of the recoil momentum transferred to H_2^+ and D_2^+ ions, when ionized by circularly polarized laser pulses [Alnaser et al. 2004].

The experimental procedure is relatively simple. For different relative phases between the ω and 2ω, we measured the momentum vector (and thus the kinetic energy) of the detected D^+ ions, emitted upon the dissociation of D_2^+ into $D^+ + D$ or upon the dissociation of D_2^{2+} into $D^+ + D^+$. How can we distinguish between the electron localization on one of two nuclei in our experiment? The answer to this question resides in the symmetry breaking of the interaction using the geometry of our detection scheme. The ionization of neutral D_2 molecules to the cationic ground state is much more efficient if the laser electric field is aligned along the molecular principal axis. Thus, as the first step of our experimental coherent control scheme is the preparation of D_2^+ through strong-field ionization, the molecular ions will be naturally preferentially aligned along the laser electric field. By using a linearly polarized two-color field with its electric field pointing in the direction of the time-of-flight of the CEI machine, the ions that are generated with an initial momentum towards (down) or away (up) from the detector can be distinguished by their flight time (see Fig. 3.15). The TOF peaks will be spit in two, corresponding to ions emitted upward or downward with respect to the detector plane. For each relative phase between the two colors of the laser field, observing a preferential emission direction (upward or downward) of the fragments, reflected in the asymmetry of the TOF (see Fig. 3.15), is thus a direct measurement of the electron localization. To quantify the control over the electron localization, we define the asymmetry parameter $A(\phi, E)$,

$$A(\phi, E) = \frac{N_{up}(\phi, E) - N_{down}(\phi, E)}{N_{up}(\phi, E) + N_{down}(\phi, E)} \tag{3.3}$$

where $N_{up}(\phi, E)$ and $N_{down}(\phi, E)$ correspond to the number of fragments emitted in the corresponding direction, in the laboratory frame, with a kinetic energy E and for a specific relative phase ϕ between ω and 2ω. The experiments were performed for intensities

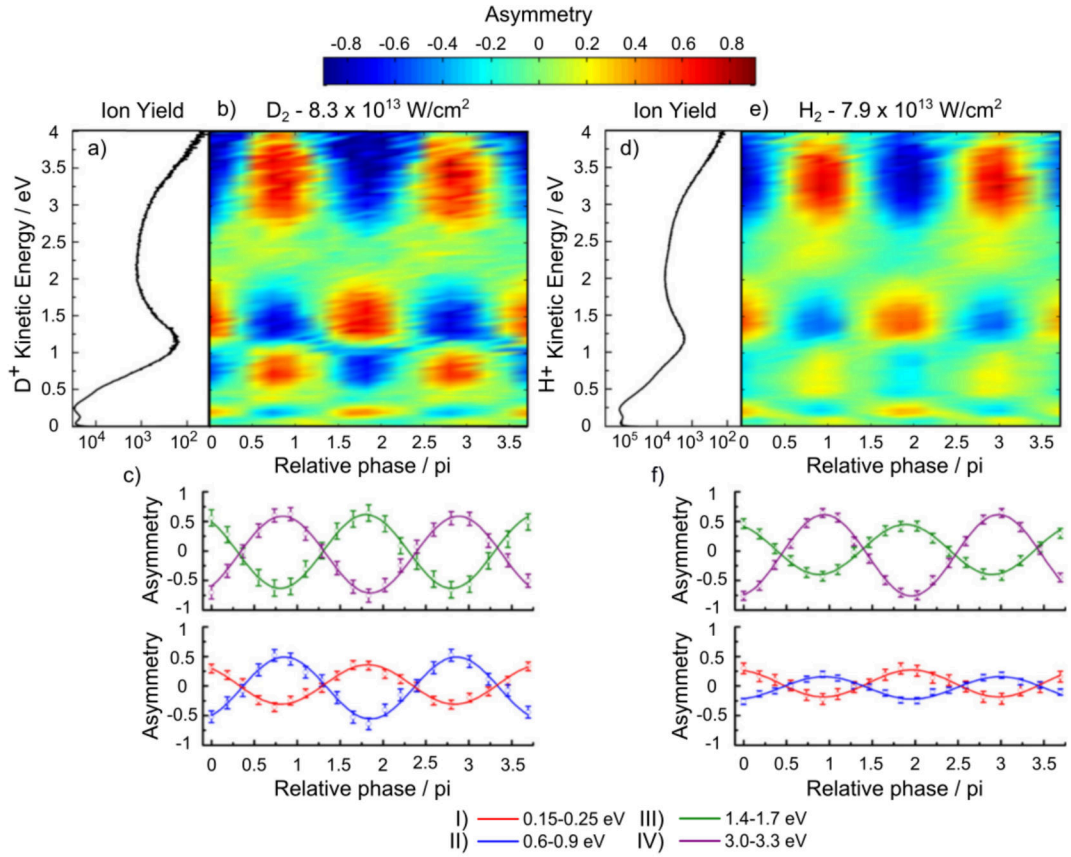

Figure 3.16: (a) Kinetic energy distribution for the detected D^+ fragments at an intensity of 8.3 x 10^{13}W/cm^2, in logarithmic scale ; (b) Experimental electron localization asymmetries; (c) Averaged asymmetries for the specified KER cuts; (d)–(f) same for H^+ at an intensity of 7.9 x 10^{13}W/cm^2.

ranging from 5.5 x 10^{13}W/cm^2 to 8.5 x 10^{13}W/cm^2 for both D_2^+ and H_2^+ molecules. At the lowest intensity, no significant control of electron localization could be observed. The main features are present for all the other ones. Figure 3.16 shows the results for intensities showing the strongest asymmetries for each isotope. Figure 3.16(a) depicts the kinetic energy distribution of the detected D^+ fragments at 8.3 x 10^{13}W/cm^2. Clear oscillations are observed, with different phases depending on the kinetic energy. In Fig. 3.16 (b), which depicts the asymmetry parameter $A(\phi, E)$ for D^+ ions with a kinetic energy up to 4 eV, four channels in which efficient directional control is achieved can be distinguished. The corresponding energy cuts are illustrated in Fig. 3.16(c): (I) from 0.15 to 0.25 eV with a maximal asymmetry of $\sim$ 30 %; (II) from 0.6 to 0.9 eV with maximal asymmetry of $\sim$ 50 %; (III) from 1.4 to 1.7 eV and (IV) from 3.0 to 3.3 eV, both with a maximal asymmetry of $\sim$ 60 %. We assign the kinetic energy region in which we do not observe any control (vanishing asymmetry parameter), around 2.5 eV, to Charge-Resonance Enhanced Ionization (CREI) where all the electrons are removed from the molecules: if there are no electrons left, we cannot control their localization. Figure 3.16 (d)–(f) shows the corresponding results for H_2^+, demonstrating control of the same photodissociation channels. Smaller asymmetries are observed, except for the highest energy region where the asymmetry reaches $\sim$ 65 %.

We will now perform a more detailed analysis of the control of the electron localization for different kinetic energy range. First, we will look at the control of the asymmetry parameter for the high-energy ($\sim$ 3-4 eV) channel, which has been interpreted as coming from the recollision-induced excitation (RCE). In RCE, the electron that has been removed

from the neutral molecule is driven back by the laser field in the vicinity of the parent ion, where it can rescatter and excite the molecular ion to the $|\sigma_u\rangle$ state. Following the population of the dissociative $|\sigma_u\rangle$ state, the internuclear distance starts to increase. As the molecular ion is stretching, the energy difference between the electronic states of the cation decreases and enables population transfers between the $|\sigma_u\rangle$ and the $|\sigma_g\rangle$ state via radiative coupling with the laser field. This leads to high-energy nuclear wavepacket dissociating along both the $|\sigma_u\rangle$ and the $|\sigma_g\rangle$, which produces ionic fragments overlapping in energy. This is exactly what is needed for the coherent control to be possible. The electron localization following the RCE mechanism was previously described by Kling *et al.* [Kling et al. 2006], who used few-cycle CEP stable pulses centered around 800 nm to control the directionality of the dissociation, observing a maximum asymmetry of $\sim$ 25 % [Kling et al. 2006; Znakovskaya et al. 2012]. By using phase-locked NIR two-color (800 nm and 400 nm) pulses, Ray *et al.* demonstrated $\sim$ 50 % asymmetry for the RCE channel [Ray et al. 2009]. This shows that controlling the relative phase of two-color pulses can enable more efficient control over the electron localization than using the CEP of an ultrashort pulse. Here, we report an asymmetry up to $\sim$ 65 % using phase-locked mid-IR two-color (1800 nm and 900 nm) pulses, demonstrating the great potential of such scheme to control electron localization in dissociating molecules, which is an elegant example of laser-controlled (really simple) chemistry.

We will now focus on the low-KER region (0-2 eV), where several channels exhibit asymmetry parameters with different amplitudes and opposite phases. As we have seen in the schematic Fig. 3.14, many different processes, like ω (labeled F,G in Fig. 3.14) and 2ω (labeled E,D in Fig. 3.14) bond softening (BS), 3xω (labeled C in Fig. 3.14) and 2xω+1x2ω (labeled B in Fig. 3.14) can lead to ions production involving dissociation on electronic states of different parity, and overlapping in energy.

The first 'low-energy channel', labeled as I in Fig. 3.14, located between 0.15-0.25 eV, can be reached by two-pathways where there is a net absorption of one ω photon. Since we observe a control of the electron localization for this channel, we know that these two pathways are characterized by dissociation on electronic states with different parities. The first pathway can be described by absorption of a single 2ω photon, indicated as E in Fig. 3.14 ($|\sigma_g\rangle \rightarrow |\sigma_u\rangle$), followed by the emission of a single ω photon, indicated as F in Fig. 3.14 ($|\sigma_u\rangle \rightarrow |\sigma_g\rangle$). The second pathway can be described by the absorption of a single ω photon, indicated as G in Fig. 3.14 ($|\sigma_g\rangle \rightarrow |\sigma_u\rangle$). The interference of these two pathways leads to a maximum degree of control of the electron localization of $\sim$ 30 % in D_2^+ and $\sim$ 20 % in H_2^+. For this channel and for a given relative phase between the two laser pulses, the electron is preferentially localized on the other nuclei that in the case of the RCE channel. The relative timing between the nuclear wavepacket propagation and the time-dependent electric field of the laser pulse defines the final electron localization yield. Therefore, depending on the dissociation pathways involved in each channel, different phase dependences are observed. Moreover, because the nuclear dynamics is faster in H_2^+ than D_2^+, their timing with respect to the electric field is expected to be different, leading to a different degree of control of the electron localization.

The second 'low-energy channel', labeled as II in the Fig. 3.14, located between 0.6-0.9 eV, can be reached by two pathways where there is a net absorption of two ω photons. Again, the clear control observed in the experiment proves that these two pathways involve dissociating states with different parities. The first pathway can be described by absorption of a three ω photon, indicated as C in Fig. 3.14 ($|\sigma_g\rangle \rightarrow |\sigma_u\rangle$), followed by the emission of a single ω photon, indicated as F in Fig. 3.14 ($|\sigma_u\rangle \rightarrow |\sigma_g\rangle$). The second pathway can be described by the absorption of a single 2ω photon, indicated as E in Fig.

3.14 ($|\sigma_g\rangle \rightarrow |\sigma_u\rangle$). The interference of these two pathways leads to a maximum degree of control of the electron localization of $\sim$ 60 % in D_2^+ and $\sim$ 30 % in H_2^+. For this channel and for a given relative phase between the two laser pulses, the electron is preferentially localized on the same nuclei that in the case of the RCE channel.

The third 'mid-energy channel', labeled as III in the Fig. 3.14, located between 1.4-1.7 eV, can be reached by two-pathway where there is a net absorption of three ω photons. The first pathway can be described by absorption of a one 2ω and three ω photon, indicated as B in Fig. 3.14 ($|\sigma_g\rangle \rightarrow |\sigma_u\rangle$), followed by the emission of a single ω photon, indicated as F in Fig. 3.14 ($|\sigma_u\rangle \rightarrow |\sigma_g\rangle$). The second pathway can be described by the absorption of a three ω photons, indicated as C in Fig. 3.14 ($|\sigma_g\rangle \rightarrow |\sigma_u\rangle$). The interference of these two pathways leads to a maximum degree of control of the electron localization of $\sim$ 60 % for both D_2^+ and H_2^+. For this channel and for a given relative phase between the two laser pulses, the electron is preferentially localized on the other nuclei that in the case of the RCE channel.

In order to be well reproduced by the theory (not shown here, see [Wanie et al. 2016]), the initial vibrational distribution in H_2^+ (upon ionization of H_2), needs to be calculated beyond the Franck-Condon approximation. Indeed, using the simple vibronic transition amplitude calculated within the Franck-Condon framework, the theoretical level of control and relative phase between the channels is in strong disagreement with the experimental data. By using initial vibrational distributions that are non-Franck-Condon, the theory can reproduce the level of control and relative phase between the channels achieved in the experiment.

3.3.4 Comparison with previous experimental works

Comparing our results to previous single pulse control experiments, we observe the following: in the first experimental demonstration of electron localization in D_2^+ by Kling *et al.* [Kling et al. 2006], only the recollision channel (RCE) could be controlled efficiently. This is because 5 fs, 800 nm CEP stabilized pulses at an intensity of 1 x 10^{14}W/cm^2 are not well suited to induce the population transfers between the $|\sigma_g\rangle$ and $|\sigma_g\rangle$ states, which lead to the control of the electron localization during of NIR induced dissociation. Indeed, because of the very short laser pulse duration, the internuclear distances where these transfers occur are reached at times where the intensity of the pulse is very low. To observe any electron localization asymmetry with 800 nm pulses, one needs to use longer pulses and/or study a faster dynamic, such as H_2^+ dissociation, where the critical internuclear region would be reached more rapidly, since the nuclear wavepacket motion is faster in H_2^+ than in D_2^+. These solutions were employed by Kremer *et al.* and Xu *et al.* [Kremer et al. 2009; Xu et al. 2013], who observed asymmetries involving BS for the H_2^+ dissociation using 6 fs NIR pulse. To control the slower D_2^+ dissociation dynamics, the pulse duration has to be increased. The first option is to use longer wavelengths, where the few-cycle CEP stabilized pulses are longer than in the NIR spectral range (for the same number of optical cycles). This approach combines both the few-cycle duration, necessary for the CEP to be a relevant parameter (or in other words, necessary for the up-down symmetry of the field to be significantly broken) and the total duration of the pulse long enough to let the molecules stretch to the critical internuclear distance, upon the ejection of the first electron. Znakovskaya *et al.* have demonstrated this CEP-stable few-cycle mid-IR (2100 nm) approach to efficiently control dissociation involving BS in D_2^+ [Znakovskaya et al. 2012]. However, in all the previously mentioned CEP-stable pulses based experiments, the maximal asymmetry which was achieved was $\sim$ 40 % [Xu et al. 2013]. As an alternative to mid-IR CEP stable pulses, the pulse duration can also be increased by using a phase-locked

two-color laser field. Our results confirm that this experimentally much simpler technique is capable to induce really efficient localization of the electronic density in dissociating molecules. The obtained asymmetries, for most of the dissociation channels, is much higher than what has been previously reported (up to 60 % for dissociation in the BS region in D_2^+ and 65% for RCE in H_2^+). This increase of asymmetry using a two-color field in the NIR (800/400 nm) was also observed by Ray *et al.* [Ray et al. 2009], but extending this strategy to the mid-IR spectral range opens up the control of an additional dissociation channel, 'the net 3-photons channel', involving the absorption of a 2ω photon and three ω photon followed by the emission of a single ω photon (channel III, Fig 3.14).

3.3.5 Partial conclusions and perspectives

In conclusion, we used a MIR two-color (1800 nm and 900 nm) laser field to control the electron localization in H_2^+ and D_2^+ dissociative ionization, which led for the first time to the simultaneous control of four dissociation channels. The control of electron localization during MIR induced dissociation was interpreted by interferences between processes involving the net absorption of n and n+1 photon(s), such as BS (n = 1), ATD (n = 2) and three-photon dissociation (n = 3). Our experiment confirms that the use of a two-color laser field is more efficient to localize the electronic density in photodissociating molecules. From this technique, which is easier to implement experimentally, the level of control is stronger than what was obtained by using CEP stable pulses as a control tool. To the best of our knowledge, we measured the strongest asymmetry reported to date both for MIR (60 %) and RCE (65 %) induced dissociations. By comparing the level of control and the phase dependence of each photodissociation channel measured in the experiment and found using TDSE calculations (see [Wanie et al. 2016]), we have learned that going beyond the Franck-Condon approximation is essential for the theory to match the experiment results. Coherent control in simple diatomic molecules is thus really important to benchmark theoretical models involving the breakdown of the commonly used picture of decoupled nuclear and electronic degrees of freedom.

This coherent control scheme using CEP-stable or phase-locked two-color pulses is very general [Roudnev et al. 2007] and has recently applied to control the directionality of dissociation in more complex system like CO [Song et al. 2017], CO_2 [Endo et al. 2017; Endo et al. 2016] and C_2H_2 [Alnaser et al. 2014; Kübel et al. 2016], for example. However, in the case of directionality control of dissociation channels, because of the higher dimensionality of the nuclear wavepacket, controlling a given dissociation channel in such polyatomic molecules becomes increasingly hard (small degree of control) with increasing size of the molecules.

3.4 Conclusions

In the first example presented in this chapter, we have measured ultrafast non-adiabatic dynamics leading to the photoisomerization of acetylene cation, triggered by ionization from HOMO-1 orbital. We have followed structural modification within the cationic acetylene molecule undergoing dynamics, by looking at the 3D momentum vector of each cationic fragment produced upon laser-induced Coulomb explosion. The photoisomerization of the acetylene cation into vinylidene cation was enabled through the passage through a conical intersection. Our method, which provides invaluable information about the geometry of the molecule prior to Coulomb explosion, is however blind to its electronic structure. Performing this experiments by detecting the photoelectrons and photoions in coincidence would definitely be a very interesting benchmark experiment,

which could correlate the time-dependent geometry of the molecule with the evolution of the photoelectron angular distribution, for example.

In the second example, we have not only measured the electron localization during photodissociation of H_2^+ and D_2^+, but have also controlled it. With the two-color multiple pathway Brumer-Shapiro coherent control scheme, using phase-locked 1800 nm - 900 nm pulses, we have demonstrated a high level of control of multiple dissociation pathways. We have seen that even in simple systems like H_2^+ and D_2^+, the energy-resolved control of electronic localization leads to complex patterns which can not be easily tackled by theory. Indeed, in order to get good agreement with the experimental data, the theory needs to include a non-Franck-Condon initial vibrational distribution on the H_2^+ and D_2^+, demonstrating again the breakdown of the approximation that the electron and nuclei are fully decoupled.

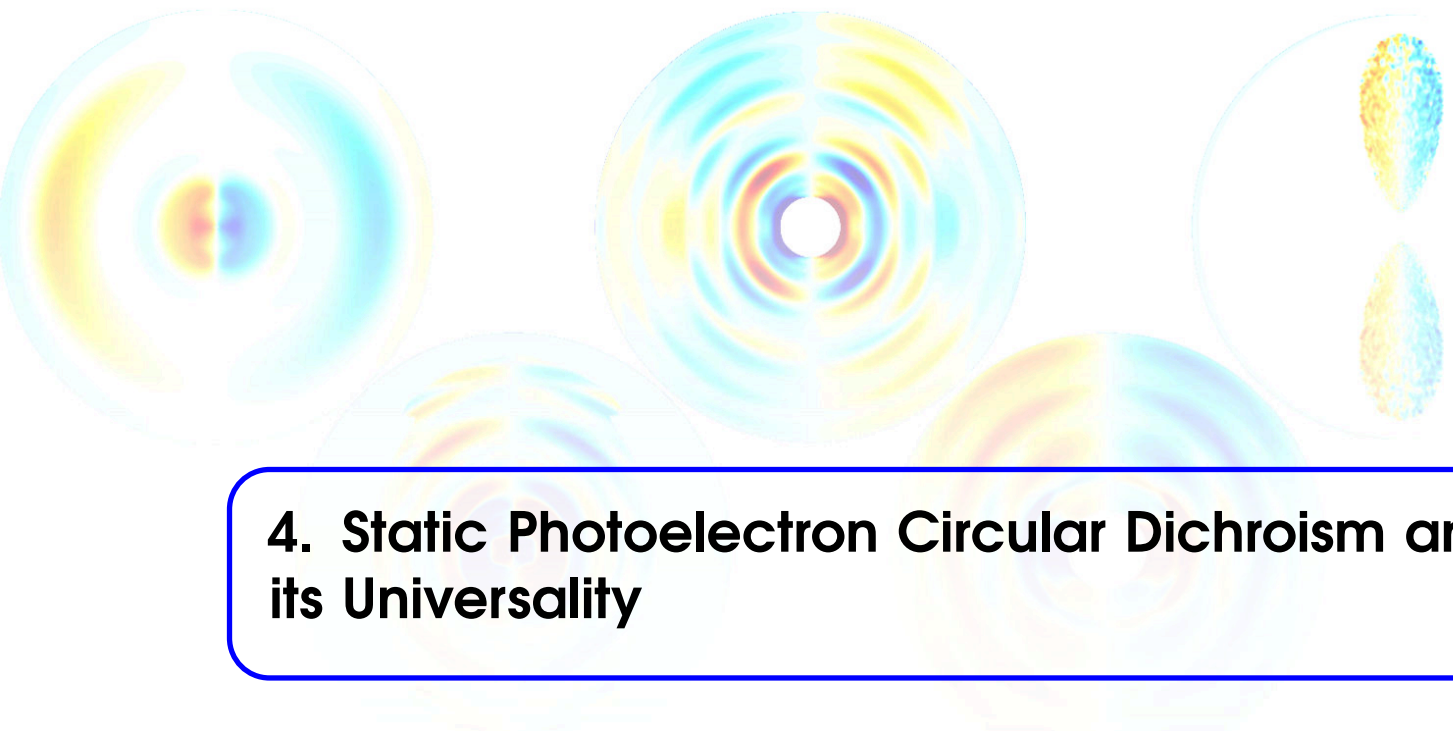

4. Static Photoelectron Circular Dichroism and its Universality

4.1 Introduction

Chirality is a geometrical property of an object to be non-superposable to its mirror image. It is a ubiquitous concept in many branches of science, from chiral symmetry breaking in subatomic particles [Nambu et al. 1961], to the preferential chiral coiling of snail shells [Asami et al. 1998], to the formation of spiral-shaped chiral galaxies [Kondepudi et al. 2001]. At the molecular level, chirality plays a capital role, because the two mirror images (enantiomers) of a chiral molecule behave very differently when embedded in a chiral environment. A striking and famous example is the biological effect of a chiral molecule called thalidomide [Eriksson et al. 1995]. The (-)-thalidomide can be used as a drug to fight against nausea and morning sickness of pregnant women. However, its other enantiomer, the (+)-thalidomide, can cause malformation of the limbs and blindness of children when ingested during pregnancy. This drug was prescribed as a racemic mixture (equal amount of both enantiomers) to pregnant women in the 1950's and caused the malformation of about 10,000 children.

The reason why biology is so sensitive to chiral is at the heart of a deeply fundamental question, which is the origin of the homochirality of life [Bonner 1995]. The quasi-totality of amino-acids, the building blocks of proteins, which are found in nature have the same handedness. The same observation is also true for natural sugars. The exact origin of this mirror-symmetry breaking of life is still an unresolved question. A lot of work is thus conducted during planetary missions to try to find a chiral imbalance in probiotic molecules, in the quest to unravel the possible origin of the homochirality of life [MacDermott et al. 1996]. The development of experimental techniques that can measure precisely the enantiomeric excess in a chiral mixture in therefore very important.

The used of circularly polarized light (CPL) to probe molecular chirality is one of the most commonly used technique. Since the circularly polarized light is chiral, its interaction with a chiral object of a given handedness can depend on its helicity. A conventional circular dichroism (CD) experiment consists of measuring the difference in the photoabsorption cross section of a molecule with a given handedness using right-CPL

or left-CPL. The chiral asymmetry factor g, is obtained by taking the normalized difference of the absorption signal obtain using left- (I_l) or right-CPL (I_r); $g = 2(I_l - I_r)/(I_l + I_r)$. The difference in the absorption cross section of left-CPL and right-CPL is usually three to five orders of magnitude smaller than the cross-section itself, leading g-factor values on the order 0.01%. Consequently, these really small relative signals are very challenging to measure. Usually, CD experiments need to be performed in the condensed phase (liquid or solid), where a large density of particles is naturally achieved, increasing the signal to noise ratio. One of the major problems of performing the experiment in the condensed phase is the interaction of the molecules of interest with their environment. The molecules can indeed interact with the solvent or other neighboring compounds, leading to a CD signal which departs from the pure isolated molecular CD response.

The weakness of the CD signals arises from the fact that they originate from the interference between the electric (E_1) and the (very weak) magnetic dipole (M_1) interaction terms. Note that if the magnetic dipolar interaction is replaced by an electric quadrupolar (or higher-order) interaction, CD can also arise. The incommensurate balance between the magnitude of the two components ($E_1 >> M_1$) leading to the interference term ($E_1 \cdot M_1$) explains its small values. One exception to this rule arises when a transition is forbidden by electric-dipole interaction but allowed by magnetic dipole interaction. In this particular case, the E_1 and M_1 terms can have the same order of magnitude, which strongly enhances the $E_1 \cdot M_1$ driven CD signal [Balavoine et al. 1974].

In this context, a universal and sensitive probe of molecular chirality in a dilute, interaction-free, environment would thus be of a great interest. In the next section, we will see that Photoelectron Circular Dichroism fulfills these requirements and is a very powerful tool to probe chirality in the gas phase.

4.1.1 Photoelectron Circular Dichroism

When an ensemble of randomly oriented enantiopure chiral molecules is photoionized by circularly polarized light, a strong forward-backward asymmetry appears in the angular distribution of the ejected electrons. For a given enantiomer and a given light helicity, more electrons are ejected in the forward direction than backwards, with respect to the light propagation axis ($\vec{k}$). This effect, called Photoelectron Circular Dichroism (PECD), reverses with molecular handedness or photon helicity [Böwering et al. 2001; Ritchie 1976].

A simple 'threaded rod and nut' mechanical analogy, borrowed from a review paper of Ivan Powis [Powis 2008], can help to understand the phenomenon of PECD. One can imagine a threaded rod (representing a chiral molecular potential) and a threaded nut (representing the electron). An external observer takes his/her hand (representing the CPL) to screw the nut by turning it clockwise around the threaded rod. The nut will then travel away from the observer and be ejected in the 'forward' direction. If the threaded rod is rotated by 180° and the same operation is performed, the nut will still be ejected in the 'forward' direction. On the contrary, if the observer uses her/his left hand and rotates the nut anticlockwise (with the other helicity of light, in our analogy) the nut will travel and be ejected in the opposite ('backward') direction. Also, considering a given spinning direction (*e.g.* clockwise), if the right-handed thread is replaced by a left-handed thread (switching the molecular enantiomer), the nut will also change is propagation direction. This simple mechanical analogy is well suited to enlighten that because both the threaded rod and the action of spinning the nut are chiral, both the handedness of the rod and the spinning sense of the nut govern the translation direction of the nut perpendicular to its rotation plane. This is also the case in PECD, where the chiral molecular potential

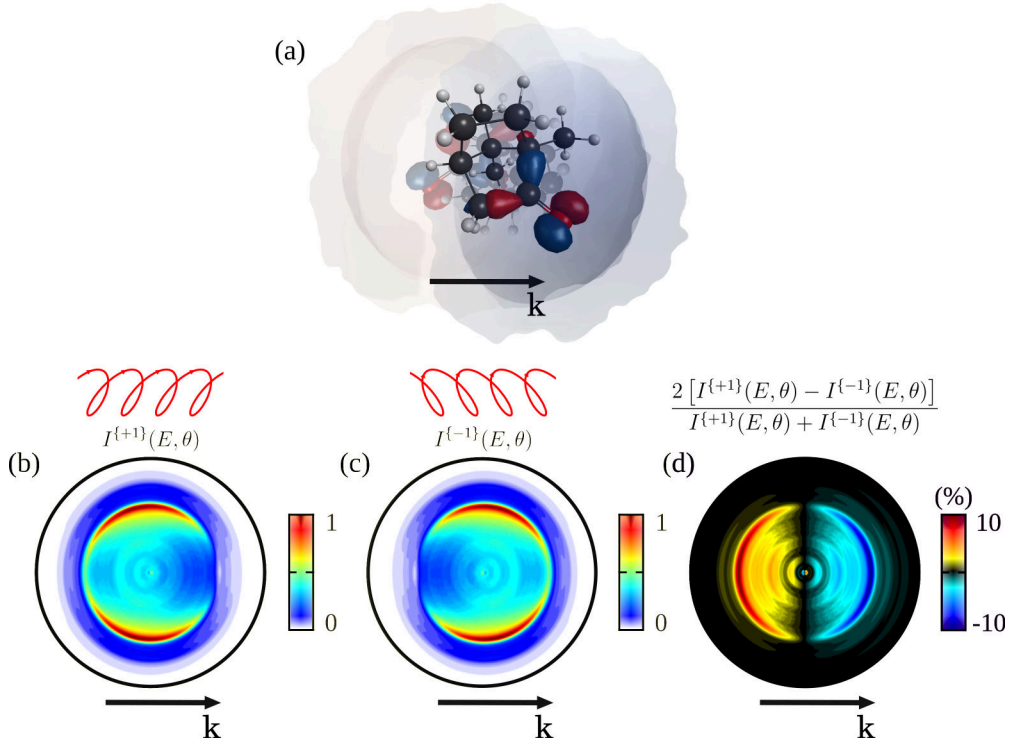

Figure 4.1: Principle of a PECD experiment. (a) Scheme of an ensemble of randomly oriented (+)-camphor molecules. The HOMO orbital is located on the C=0 bond. The light blue/red wiggly spheres represent the outgoing electron following photoionization. Example of photoelectron angular distribution (PAD) upon photoionization with left-CPL (b) and right-CPL (c). One can notice that more electrons are emitted in the backward (b) or forward (c) direction with respect to the light propagation axis (**k**). The normalized difference between PADs obtained using left- and right-CPL (d). The asymmetry, which is antisymmetric with respect to **k**, is typically in the order of 1-20 %. Note that from an experimental point of view, artifacts in the experiment often leads to not perfectly antisymmetric PECD images. During the data analysis, we only keep the antisymmetric part of the images. This procedure removes the experimental artifacts.

converts the rotation of the electrons in the laser polarization plane in a net translational displacement in the direction perpendicular to it. The translational direction (forward or backward) is reversed if the handedness of the light or the molecule is inverted.

In order to be more quantitative than this simple mechanical analogy, let us describe mathematically the photoelectron angular distribution (PAD). It is usually assumed that the PAD $I^{\{p\}}(E,\theta)$ can be expressed as:

$$I^{\{p\}}(E,\theta) = \sum_{j=1}^{2N} b_j^{\{p\}}(E) P_j(cos(\theta)) \tag{4.1}$$

where p represents the polarization state of light ($p = 0$ for linear photons and $p \pm 1$ for circular photons), N is the number of absorbed photons, $P_j(cos(\theta))$ is the j-th order Legendre polynomials, $b_j^{\{p\}}(E)$ is the associated j-th order Legendre coefficient and θ is the photoelectron ejection angle with respect to the light propagation direction, for circular photons and with respect to the electric field vector, for linear photons. The summation up to $2N$ results from the Yang's theorem [Yang 1950], which is a result of angular momentum conservation.

In the specific case of single photon ionization of an atom or an ensemble of randomly oriented achiral molecules, the expression 4.1 simplifies to:

$$I^{\{p\}}(E,\theta) = b_0^{\{p\}}(E)P_0(cos(\theta)) + b_2^{\{p\}}(E)P_2(cos(\theta)) \tag{4.2}$$

Indeed, from symmetry consideration, only the even Legendre coefficients, which are symmetric along the light propagation direction, contribute to the PAD. Note that $b_2^{\{0\}} = \beta$ and $b_2^{\{\pm1\}} = -\frac{1}{2}\beta$, where β is the so-called anisotropy parameter. It provides information about the angular anisotropy of the PAD. This formulation was used for decades to study the atomic and molecular PAD resulting from single photon ionization.

In the 1970's, a seminal paper from Ritchie [Ritchie 1976] pointed out that under some very precise symmetry condition, the odd Legendre polynomials $P_1(cos(\theta))$ could also contribute to the PAD, leading to the following equation:

$$I^{\{p\}}(E,\theta) = b_0^{\{p\}}(E)P_0(cos(\theta)) + b_1^{\{p\}}(E)P_1(cos(\theta)) + b_2^{\{p\}}(E)P_2(cos(\theta)) \tag{4.3}$$

Ritchie demonstrated that the $b_1^{\{p\}}$ term could survive over molecular orientation averaging when the photoionized molecules where chiral, and when the ionizing photon was circularly polarized. Because $P_1(cos(\theta))$ is antisymmetric along the azimuthal angle, *i.e.* along the forward-backward direction with respect to $\vec{k}$, it leads to a forward/backward asymmetry in the PAD. This means that the electrons signal in the forward hemisphere is greater than in the backward hemisphere (or vice-versa), with respect to $\vec{k}$. The magnitude of the electron signal difference between the forward/backward hemispheres is $2b_1^{\{p\}}$. Changing the light (or the molecular) handedness reverses the F/B asymmetry, while it would leave the anisotropy parameter unchanged. In other words,

$$b_1^{\{+1\}} = -b_1^{\{-1\}}, b_2^{\{+1\}} = b_2^{\{-1\}} \tag{4.4}$$

One really important feature of PECD is that it appears within the electric dipole approximation framework. This means that the emergence of the forward/backward asymmetry in the PAD does not require any magnetic dipolar or electric quadrupolar effects. The fact that PECD is purely electric dipolar is the reason why its amplitude is several orders of magnitude larger than most conventional chiroptical techniques.

As it is well known from photoionization theory, the angular structure of the outgoing electron wavepacket is governed by the interference between the final state partial-waves with different angular momentum (ℓ). From a quantum mechanical point of view, PECD thus finds its origin in the forward/backward asymmetries of the photoelectron scattering phases, which render the resulting electron interferogram forward/backward asymmetric. More precisely, $b_1^{\{p\}}$ is proportional to the sine of the phase differences between adjacent partial waves, $b_1^{\{p\}} \propto sin(\eta_\ell - \eta_{\ell'})$, where $\ell' = \ell \pm 1$. Because the sine function varies rapidly and changes its sign around zero, it provides a very sensitive and sign-dependent mapping of small variations of its argument. The fact that $b_1^{\{p\}} \propto sin(\eta_\ell - \eta_{\ell'})$ renders PECD ultra-sensitive to tiny variations in the scattering dynamics of the outgoing electron in the chiral molecular potential.

Unlike $b_1^{\{p\}}$, $b_0^{\{p\}}$ does not contain any information about the scattering phases since it is proportional to the integrated photoionization cross section. The $b_2^{\{p\}}$ coefficient, which

is related to the anisotropy parameter $\beta^{\{p\}}$, is proportional to the cosine of the phase differences between partial waves, $b_2^{\{p\}} \propto cos(\eta_{\ell-1} - \eta_{\ell+1})$. Since the cosine function is almost flat near zero, it is much less sensitive than $b_1^{\{p\}}$ to small difference of scattering phases. An exhaustive derivation, and associated discussions, of all these relationship can be found in a very complete review by I. Powis [Powis 2008].

Last, let us mention that PECD should not be confused with the asymmetries in photoelectron angular distributions which exist in the photoionization of aligned, non-chiral molecules by CPL. These asymmetries, called CDAD (Circular Dichroism in the electron Angular Distributions), arise in the plane perpendicular to the light propagation axis, because of the symmetry breaking associated to the detection of electrons associated to a given molecular orientation [Dubs et al. 1986; Sen et al. 2017].

In conclusion, PECD leads to F/B asymmetries in the PAD that are orders of magnitude larger that conventional chiroptical signals. Furthermore, the asymmetry is extremely sensitive to the scattering of the outgoing electron in the chiral potential. PECD is thus a genuine and powerful chiral observable which can provide rich information about molecular chirality, in gas-phase media.

4.1.2 Experimental detection of Photoelectron Circular Dichroism

There are several kinds of apparatus that allow the experimental detection of PECD. The minimal requirement is to be able to discriminate between electrons that are emitted in the forward and in the backward hemisphere with respect to the light propagation axis.

In the most simple scheme, one would collect the angularly- and energetically-integrated photoelectrons emitted in the forward and in the backward hemisphere, without performing any coincidence with the parent ion or fragment from which the electron has been ionized. This very simple, compact and cheap solution would be perfectly suited for purely analytical purposes, *e.g.* determining the handedness and the enantiomeric purity of a molecular sample. This kind of apparatus was recently developed by Miles *et al.* [Miles et al. 2017]. Coupling this simple and clever instrument with a high-repetition-rate laser, they were able to monitor the enantiomeric excesses of chiral mixtures at a few percents level of accuracy in an *almost* real-time fashion. A schematic view of the apparatus is shown in figure 4.2.

While this detection scheme was shown to be a very powerful analytical tool for detecting enantiomeric excesses, it is clearly not well suited for more fundamental studies of PECD. Integrating over electron ejection angles and energies is a pity since PECD exhibits rich features which depend on these two parameters. Indeed, as we will see both the angular and energy dependence of PECD provide a lot of information about the photoionization dynamics of chiral molecules.

In order to energetically and angularly resolve the photoelectron emission process, one could use a Velocity Map Imaging Spectrometer (VMIS). This is the apparatus that was used in most of the PECD experiment presented in this thesis. A schematic representation of a VMIS is shown in figure 4.3. The heart of the VMIS is its interaction zone, where the focused ionizing radiation intersects a molecular jet at a right angle to create the charged particles (electrons and ions). In this region also lies the electrostatic focusing optics. The electrostatic lens is made of three electrodes: the repeller, the extractor, and the ground electrode. High voltages are applied on the repeller and on the extractor. The polarity of the high voltage applied on the repeller and on the extractor allows detecting either ions or electrons. In our case, we will focus mostly on the electron detection. The extractor and the ground electrodes are both circular ring-shaped in order to allow to send the electrons towards the detector. After being produced at the intersection between the laser

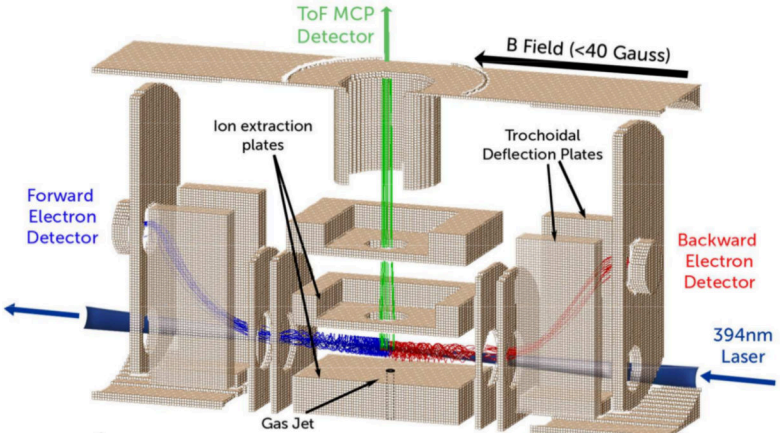

Figure 4.2: Schematic of an experimental apparatus to detect the angularly- and energetically-integrated PECD. The applied static electric and magnetic field allows one to steer the electrons that are emitted in each hemisphere towards their respective electron multiplicator detector regardless their ejection angle or energy. The figure is adapted from [Miles et al. 2017], where all the details can be found.

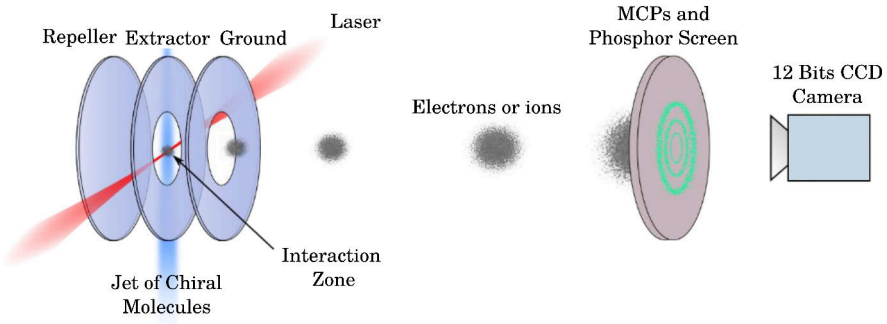

Figure 4.3: Schematic representation of a VMIS. This figure is adapted from the thesis manuscript of Charles Handschin [Handschin 2013].

focus and the molecular jet, the charged particles are extracted from the interaction region by the electrostatic lens. The role of the ground electrode is to ensure a field-free flight zone after the extraction of the electrons from the interaction zone. Finally, the electrons hit a detector located at the end of the time-of-flight (TOF) tube. The detector is made of a stack of microchannel plates (MCPs) and a phosphor screen which is imaged by a 12-bits cooled charge-coupled device (CCD) camera. When an electron hits the MCPs, it creates about a million secondary electrons by avalanche effect in the channels of the MCP. These electrons are accelerated towards the phosphor screen and are converted into visible photons through the phenomenon of luminescence. This visible light can thus be imaged using a standard high dynamical range CCD camera.

Because the PAD is a function of the three coordinates of space (3D) and because our detector in only two-dimensional (2D), the distribution that we experimentally measure is the 2D projection along the TOF axis of the 3D PAD. It is, however, possible to reconstruct the 3D PAD from the 2D VMIS images if the symmetry of the photoionization geometry is sufficient. Indeed, when using a linear polarization parallel to the detector or when using a circular polarization, the electron ejection is cylindrically symmetric with respect to the detection plane and some exact and unique mathematical reconstruction techniques of the 3D PAD are thus possible. Several algorithms have been developed to retrieve the

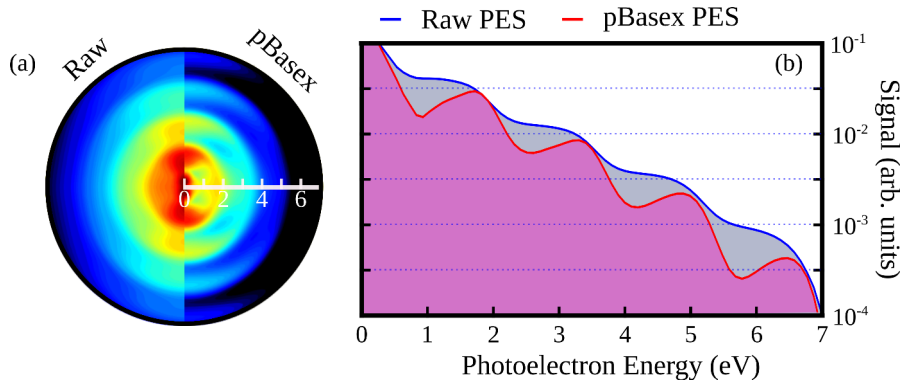

Figure 4.4: In (a), the left panel represent a raw 2D VMIS projection and the right panel represent its inversed 2D projection using pBasex algorithm. In (b), angularly-intergrated PAD of raw (in blue) and the pBasex inverted images (in red). The photoelectrons were produced using strong left- (L) or right- (R) circularly polarized 800 nm pulses focused in a effusive gas jet of (+)-liomonene. The PAD is defined as (L+R)/2.

3D PAD using its 2D projection in that case. One method is based on the Fourier-Hankel algorithm and was developed by Smith *et al.* [Smith et al. 1988] in the 1980's. Another widely used technique based on the inverse Abel transform was developed by Heck *et al.* [Heck et al. 1995] in the 1990's. Later, a pseudo-Gaussian basis-set expansion (BASEX, which stand for *BAsis Set EXpension*) technique was introduced by Dribinski and Reisler [Dribinski et al. 2002]. Garcia *et al.* improved the BASEX algorithm by implementing it in polar coordinate (pBasex) [Garcia et al. 2004] and showed its high computational speed as well as its high accuracy in retrieving the 3D PAD. At CELIA, Baptiste Fabre wrote a pBasex algorithm that has been used to invert almost every 2D VMIS projection images presented in this thesis. An example of pBasex inversion is given in figure 4.4.

In the case where the cylindrical symmetry is broken, by use of elliptically polarized photons, for example, the retrieval of the 3D PAD using the aforementioned algorithm is not exact anymore. One solution to this issue is the use of the tomographic reconstruction technique. To do so, one needs to record 2D VMIS projections of the 3D PAD while rotating the main polarization axis with respect to the detection plane. While rotating the polarization axis, one also rotates the 3D PAD and thus take 2D VMIS projection of the PAD from different angles. Well known algorithms, like inverse Radon transform, for example, can be used to reconstruct the 3D PAD using the set of 2D projections. Tomographic reconstruction is used in a broad range of applications, spanning from medical x-ray imaging [Shepp et al. 1978] to quantum information processing [D'Ariano et al. 2001]. In photoelectron spectroscopy, the tomographic reconstruction technique has been used by several group [Maurer et al. 2012; Smeenk et al. 2009; Wollenhaupt et al. 2009]. This technique is very powerful but is time-consuming since it requires recording several 2D projections in order to reconstruct a single 3D PAD.

In standard experiments, electrons can be ejected from different species which are present in the gas jet. For example, if there is a mixture of monomer and clusters of different size, the total photoelectron signal will be the incoherent sum of the photoelectron coming from all the different species. Thus, detecting the photoelectrons in coincidence with the photoions allows one disentangle all these photoionization events and access photoionization measurement from many species in a single experiment.

A i^2PEPICO spectrometer (which stand for double imaging - PhotoElectron PhotoIon COincidence), is a very powerful apparatus that enables the measurement of the 2D

photoelectron images (like in a VMIS) in correlation with the mass, the kinetic energy and the recoil direction of a given ionic species [Bodi et al. 2012; Garcia et al. 2013a]. In a PECD experiment, for example, this gives the advantage of being able to separate the different PES associated with different ionic species. One can thus measure simultaneously and independently the PECD of the electrons coming from the parent ion and the different fragments. However, as in a standard VMIS, the i^{2}PEPICO does not resolve the velocity component of electrons perpendicular to the detector plane. This means that the cylindrical symmetry with respect to the detection plane also needs to be preserved in order to be able to reconstruct the 3D PAD, using standard inversion algorithms. If one was able to resolve this third velocity component of the electrons, it would be in principle possible to reconstruct the PECD directly in the molecular frame, *i.e.* for all different molecular orientation with respect to the quantization axis of the light.

The grail of charged particle imaging techniques is, without a shadow of a doubt, the Cold Target Recoil Ion Momentum Spectroscopy (COLTRIMS) spectrometer. As in i^{2}PEPICO, the COLTRIMS measures the velocity components of ionic species, in coincidence with the photoelectrons. However, by adding a static magnetic field that guides the electrons towards a time- and position-sensitive detector, the full reconstruction of the 3D momentum vectors of the photoelectrons is also possible. This is also something that is possible, in principle, using i^{2}PEPICO. However, the magnetic field that guides the electrons toward the COLTRIMS electron detector allows for a better energy resolution. The 3D PAD is thus fully accessible, in coincidence with the with 3D momentum vector of each ionic species, even in the case where the cylindrical symmetry is not preserved. Since the 3D PAD can be fully retrieved using experimental observable, no image inversion (*e.g.* Abel inversion or pBasex) is needed. As will be explained in the next section, the COLTRIMS technique has allowed the measurement of PECD in the molecular frame of methyloxirane, showing a large enhancement compared to orientation average measurement of PECD in the laboratory frame [Tia et al. 2017].

4.1.3 Early days of PECD at synchrotron facilities

It is quite surprising that after the theoretical prediction of PECD by the seminal paper of Ritchie [Ritchie 1976] in 1976, and the development of a quantum theory of photoelectron angular distribution from a chiral molecule by Chereokov in 1982 [Cherepkov 1982], one had to wait until the 2000s to see the field of PECD emerging. First, Powis performed the first theoretical evaluation of the amplitude of PECD in a real molecule [Powis 2000]. Soon after, benefiting from the growth in the expertise of producing circularly polarized VUV radiation at synchrotron facilities, the first experimental PECD was reported in 2001 by Böwering *et al.* [Böwering et al. 2001]. They reported the measurement of PECD up to 3 % from an ensemble of randomly oriented enantiopure bromocamphor molecules, using 16.2 eV photons. To measure the PECD, they used two electron spectrometers placed at opposite direction from the light propagation axis. The PECD was measured at fixed angles with respect to the light beam. They also reported that the PECD was varying with the binding energy of the ionized orbital.

Since this first proof of principle experiment, a lot of theoretical and synchrotron-based experimental efforts have been dedicated to understand the subtlety behind the phenomenon of PECD. The very large number of published synchrotron-based PECD papers forced us to make a selection for this discussion. More references can be found in two review papers: [Nahon et al. 2015; Powis 2008]. In 2003, Garcia *et al.* reported the first measurement of the fully angular-resolved PECD, for the near-threshold photoionization of the prototypical camphor molecules [Garcia et al. 2003]. To do so, they used a correlated

photoelectron–photoion velocity spectrometer, the ancestor of the i^{2}PEPICO spectrometer described above. The year after, Hergenhahn *et al.* measured PECD resulting from the inner shell ionization of the carbonyl C 1s orbital of camphor molecules [Hergenhahn et al. 2004]. These results are remarkable since the ionized orbital has a non-chiral spherically symmetric structure. This enlightens the important role of the chirality of the final (continuum) states in the emergence of the PECD. Their results were backed by electron multiple scattering calculations done by Ivan Powis.

In 2006, Nahon *et al.* [Nahon et al. 2006] performed a systematic study of PECD in camphor molecules, by scanning the ionization photon energy from 8.85 to 26 eV. Theses experiments using energetically tunable source enabled to reveal in greater details the effect of initial orbitals on PECD. They observed that the magnitude and even the sign of PECD depend on the ionization channel (*i.e.* on the ionized molecular orbital). They also reported that within a single ionization channel, PECD strongly depends on the final photoelectron kinetic energy. They measured a large enhancement of the asymmetry in the vicinity of a shape resonance roughly 10 eV above the ionization threshold, which also demonstrated the high sensitivity of PECD to the shape of the molecular potential from which the electron scatters off.

The next important question was the role of conformational isomerism on PECD. Conformational isomerism is a form of isomerism in which the isomers can be interconverted solely by a rotation of a moiety along a single bond. No chemical bond needs to be broken to interconvert between two conformational isomers (or conformers). Because the free energy difference between two conformers is usually small (tens of meV), many different conformers can be present in a gas jet, depending on its temperature. The conformer distribution is determined by Maxwell-Boltzmann statistics. In 2008, Garcia *et al.* demonstrated both theoretically and experimentally that different conformers of glycidol lead to different PECD [Garcia et al. 2008]. They were able to demonstrate the capability of PECD to identify the most abundant conformer present in the gas jet. Later, Turchini *et al.* performed a similar joint theoretical and experimental work to further extend the study of the effect of conformational isomerism on PECD. They were able to reveal conformer population effects in the valence-state PECD of Alaninol [Turchini et al. 2009]. More recently, Tia *et al.* used the conformer sensitivity of PECD to reveal a difference in the conformers of alanine, produced in the gas phase using two different vaporization methods, by aerosol thermodesorption or by a resistively heated sample oven [Tia et al. 2014].

Another kind of isomerism is encountered when molecules have the same chemical formula but have different bonding patterns: structural isomerism. To switch from a structural isomer to another one, one would need to break a chemical bond and to connect the broken moiety somewhere else on the molecular frame. For example, camphor and fenchone are two structural isomers ($C_{10}H_{13}O$). They are both rigid bicyclic ketones with very similar molecular structures. They have been often studied comparatively because their Highest Occupied Molecular Orbitals (HOMO) are very similar and because they have comparable absorption spectra. In 2008, Powis *et al.* studied the PES and PECD of both fenchone and camphor in the same experimental conditions [Powis et al. 2008]. They showed that despite their very similar PES, the PECDs from camphor and fenchone were strikingly different. That observation established the sensitivity of PECD to structural isomerism.

The sensitivity of PECD to the chemical substitution was also demonstrated both theoretically and experimentally. Stener *et al.* performed B-splines Density Functional Theory (DFT) calculation of PECD for chiral derivatives of oxirane and identified trends on the effect of the electronic character of the substituent on the calculated PECD [Stener

et al. 2004]. Later, Garcia *et al.* performed experiments on methyloxirane and trifluoromethyloxirane and confirmed the dramatic effect of chemical substitution on the measured PECD of the outermost orbitals [Garcia et al. 2014]. Last, PECD from Van der Waals complexes was investigated. In cold molecular beams, the internal temperature of molecules is very low and several molecules can bond together to form clusters. By performing mass-selected photoelectron spectroscopy in a cold jet of epichloridyn, Daly *et al.* were able to unambiguously differentiate the monomer and dimer PECD [Daly et al. 2011]. Other works also reported the effect of clustering on PECD [Nahon et al. 2010; Powis et al. 2014].

All these examples demonstrate that PECD is a very sensitive probe of molecular structure. PECD should thus be a good probe of molecular dynamics, such as vibrations. Within the Born-Oppenheimer approximation (BOA) framework, the vibrational and electronic degrees of freedom are fully decoupled. A consequence of the BOA is the assumption that when a molecule absorbs a photon, the transition should be vertical (the nuclei are frozen during the electronic transition). Within the BOA, the properties of the continuum should be completely independent of the associated cationic vibrational energy (Franck-Condon principle, or the Franck-Condon approximation). This principle implies that the PECD associated with different vibrational states of the cation should be strictly identical. In 2014, Garcia *et al.* demonstrated a spectacular violation of this statement, measuring a sign inversion of PECD upon vibrational excitation of the cationic methyloxirane [Garcia et al. 2013b]. This clear breakdown of the Franck-Condon approximation established the sensitivity of PECD to coupled electronic and nuclear dynamics in the photoionization of chiral molecules [Garcia et al. 2013b].

4.2 VUV-PECD in Fenchone and Camphor at SOLEIL Synchrotron

4.2.1 Context

In February 2015, with a delegation from CELIA (Valérie Blanchet, Baptiste Fabre, Bernard Pons, Vincent Wanie and myself) and from the LIDYL-Saclay (Romain Géneaux), we went to the DESIRS beamline at SOLEIL French National Synchrotron Facility to perform PECD experiments. We were working with Laurent Nahon and Gustavo Garcia, who are responsible for the beamline and are experts in PECD.

DESIRS stands for Dichroïsme Et Spectroscopie par Interaction avec le Rayonnement Synchrotron (dichroism and spectroscopy through interaction with synchrotron radiation). This beamline can deliver light from 5 to 40 eV photon energy, with a flux of 10^{10} to 10^{14} photons/second, depending on photon energy and bandwidth. One of the key features of the beamline is the fully tunable polarization state of the photons. The synchrotron emission results from the wiggle of electrons in an undulator, which is an array of magnets. By controlling the undulator geometry, it is possible to shape the electron trajectories to obtain any polarization ellipse of the radiation [Nahon et al. 2004].

The polarization state of a light beam can be fully described through the 4 Stokes parameters (S_0, S_1 S_2 and S_3), where S_0 is the total intensity and where S_1, S_2 and S_3 characterize the polarization rate and the axis of polarization of the light. The *in situ* measurement of the full polarization ellipse is achieved using a home-build VUV polarimeter [Nahon et al. 2012]. The absolute circular polarization rate (S_3) can reach up to 0.99 ± 0.01 over whole spectral range [Nahon et al. 2012]. One of the permanent endstations of the beamline is a i^2-PEPICO spectrometer [Garcia et al. 2013a]. As described in the previous section, this is a well-suited apparatus to perform mass-tagged PECD experiments.

The primary goal of our synchrotron run was to compare the PECD measurement using the *almost*-perfectly circularly polarized photons of the synchrotron, to the PECD measurement done at CELIA using the HHG-based elliptically polarized VUV sources [Ferré et al. 2015b], in order to use the PECD to retrieve the full polarization state of the HHG-based VUV source. Indeed, Ferré *et al.* have performed PECD experiment using HHG based highly elliptically polarized VUV [Ferré et al. 2015b], which was achieved by driving resonant-HHG in SF_6 with slightly elliptically polarized UV pulses. The tilt of the polarization ellipse with respect to the photoelectron detection plane was unknown. Moreover, because they used a rotating VUV analyzer, Ferré *et al.* could only determinate the upper bound ellipticity (ε_{ub}) of the harmonics, $\varepsilon_{ub} = [1 - (S_1^2 + S_2^2)]^{\frac{1}{2}}$. This limitation comes from the fact that recording a Malus law using a rotating polarizer cannot discriminate between circularly polarized and unpolarized light. Owing the fact that in single photon ionization, the measured PECD linearly depends on the absolute circular polarization rate (S_3), PECD = $2b_1 \cdot S_3^{VUV}$, one can determine the pure molecular response (b_1) by measuring the PECD using a well characterized VUV source (S_3^{VUV}). After this benchmarking procedure, one could perform PECD experiment using the same molecular sample in order to retrieve the S_3 of a 'not-fully characterized' VUV source.

We recorded mass-tagged PECD in fenchone ($C_{10}H_{16}0$) at five different photon energies (9.3 eV, 12.4 eV, 15.5 eV, 18.6 eV and 21.7 eV). These photon energies correspond to the harmonic 3 to 7 of a 400 nm driving laser beam. The HHG-based VUV source developed by Ferré *et al.* contains only the odd harmonics, but measuring the PECD corresponding to even harmonics is interesting as well in the perspective of comparing the result of single-photon absorption and multiphoton ionization by 400 nm pulses. A preliminary attempt to use these data to characterize the HHG-based VUV source polarization state is presented in the thesis of Romain Géneaux [Géneaux 2016]. It was however concluded that some damages on the VMIS detector and the presence of background noise on the HHG-based VUV PECD data render the unambiguous determination of the absolute circular polarization rate impossible. During the entire duration of my thesis, we had the plan of redoing carefully this HHG-based VUV PECD experiment. We did conduct measurements on harmonic 3 using a VUV quarter waveplate but did not reach the point of redoing the whole experiment with several harmonics. The synchrotron data were however used, in combination with similar data obtained in camphor in a previous synchrotron run, to show the great analytical potential of VUV-PECD and to further demonstrated its sensitivity to structural isomerism.

In the following subsections, we will show that high-quality synchrotron-based PECD data can be used to quantify the enantiomeric purity of a chiral sample. The enantiomeric excess determined using PECD data will be compared to an independent analysis done using a well-established chromatographic technique. Moreover, by comparing the PECD from various low-lying orbitals for both fenchone ($C_{10}H_{16}0$) and camphor ($C_{10}H_{16}0$), we will extend the previous knowledge on the sensitivity of PECD to structural isomerism.

4.2.2 Experimental Methods

Each studied molecule was introduced into the i^{2}PEPICO apparatus by heating an oven at 40°C. The resulting vapor pressure was carried by a 0.5 bars helium flow through a 70 μm nozzle, where it expanded in the vacuum. The molecular jet went through two ϕ = 1 mm skimmers placed from either side of a differentially pumped chamber, to finally cross the ionizing radiation at a right angle. The electrons and ions created following VUV photoionization were detected using the DELICIOUS III i^{2}PEPICO spectrometer [Garcia et al. 2013a; Tang et al. 2015], which measured the mass-tagged PECD, resolved in energy

and in angle. The mass-tagged VMI images can be inverted using pBasex algorithm.

The enantiomeric excess (*ee*) of each sample, defined as $ee = ([R] - [S])/([R] + [S])$, was calibrated using multi-dimensional gas-phase chromatography coupled to time-of-flight mass spectrometry (GC x GC-TOFMS) [Meinert et al. 2012]. This is a well-known technique in the analytical chemistry community. The *ee* are found to be +96.7 $\pm$ 0.9 % for R-(+)-camphor and -98.7 $\pm$ 0.1 % for S-(-)-camphor while for fenchone, the *ee* are +82.1 $\pm$ 0.5 % for R-(-)-fenchone and -99.90 $\pm$ 0.03 % for S-(+)-fenchone [1]. The ee_R/ee_S ratio is thus found to be 0.979 for camphor and 0.821 for fenchone.

The measurements were conducted by acquiring the photoelectron and photoion spectra in coincidence during a total time of 300 minutes, at a given photon energy, alternating left (LCP) and right (RCP) circular polarizations every 15 minutes to average out drifts.

4.2.3 Analytical Power of VUV-PECD

First, the PECD using 12.3 eV photon energy was recorded for both camphor enantiomers. The raw and inverted difference VMIS images (LCP-RCP), without performing any mass-tagging are shown in figure 4.5 (a). One can see that the magnitude and the sign of PECD change with the photoelectron kinetic energy (*eKE*). In order to quantify the PECD, one can calculate the difference between the number of electrons ejected in the forward and backward hemispheres. As introduced earlier in the chapter, this quantity is given by $2b_1$, where b_1 is the first odd Legendre coefficient.

The PES (LCP+RCP) and the extracted PECD ($2b_1$) are shown in figure 4.5 (c). The x-axis is in now in Ionization Energy (*IE*) units, which is defined as $IE = \hbar\omega_{VUV} - eKE$. It is known that the measured photoelectron asymmetries will scale linearly with the enantiomeric purity of the sample. For example, in a racemic mixture (equal amount of both enantiomers), the $ee = 0$ and the PECD vanish. The data presented here were thus all corrected taking into account the *ee* measured with GC x GC-TOFMS, leading to an almost perfect mirroring of the PECD.

One can see that the PES is characterized by a peak centered around 8.7 eV, corresponding to the ionization of the HOMO orbital, and a region of quasi-continuous signal starting around 9.7 eV. The ionization of the HOMO orbital leads to a stable ground state camphor cation, while when the ionization energy exceeds 9.7 eV, lower-lying orbitals start to be ionized, leading to dissociative excited cationic states. The PECD exhibits rich oscillating features between 10 and 12 eV, which show an almost perfect mirroring when switching the enantiomer. The mirroring is studied in greater details by plotting the mean value (or baseline, *BL*), which is define as $BL = \frac{1}{2}[PECD_R - PECD_S]$. In a 'perfect' experiment, the *BL* would be zero, since the PECD for both enantiomers is supposed to be purely antisymmetric. A non-vanishing *BL* could be the result of the statistical error (different signal to noise ratio) or systematic errors (residual instrumental asymmetries, for example). In our experiment, the *BL* is always below the 3 % level (see figure 4.5 (d)).

The i^2-PEPICO spectrometer also allows us to mass-tag the photoelectron images. In figure 4.6, one can see the raw and inverted difference (LCP-RCP) photoelectron images, the corresponding PES as well as the extracted PECD ($2b_1$) associated to the coincidence with the parent ion mass. We clearly see a very good isolation of the photoelectron signal

[1] One can see that there is two different chiral labeling here. The R/S (*rectus/sinister*, which stands for right and left-handed in Latin) labeling is coming from the Cahn-Ingold-Prelog priority rules, which determined the absolute configuration of a chiral center [Cahn et al. 1966]. The (+) and (-) labeling only dictate if an enantiomer rotates a polarized light beam in the clockwise or anticlockwise direction. It does not provide any information about the absolute configuration of a chiral center.

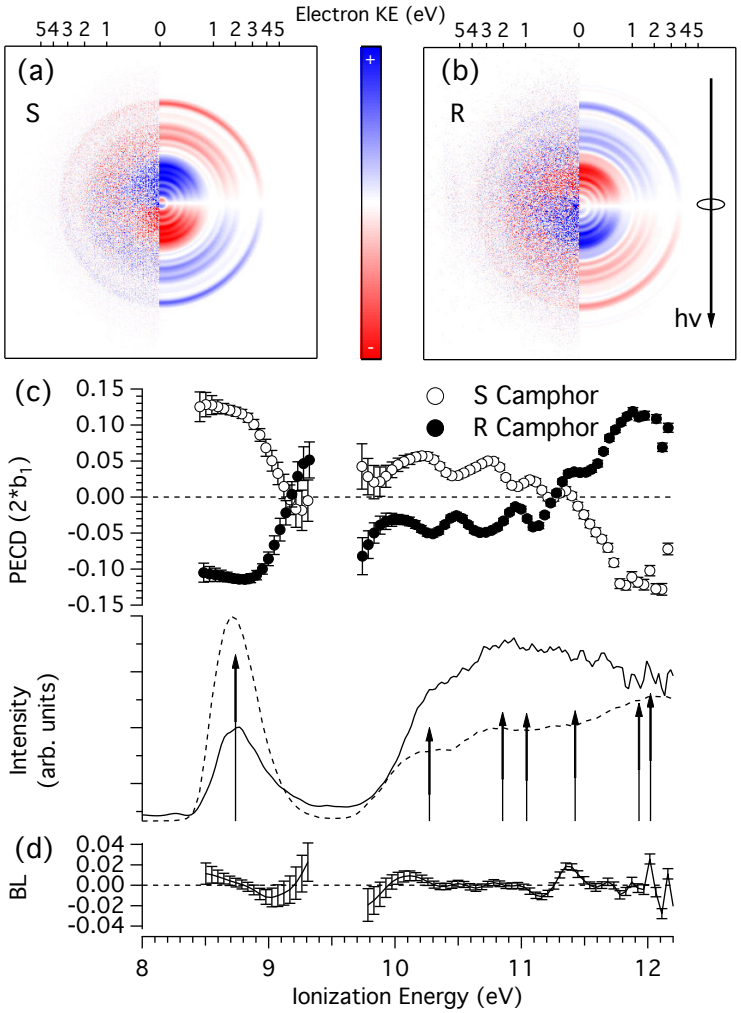

Figure 4.5: VMI difference images (LCP–RCP) recorded at 12.3 eV photon energy for 1S,4S-camphor (a) and 1R,4R-camphor (b) enantiomers. The left-half images show raw 2D-projections, and the right half the corresponding inverted image (c) PECD (open and filled circles) and PES (solid line) extracted from inversion of the total and difference images. The data have been normalized by S_3 and the *ee* measured by GC x GC-TOFMS. (d) PECD baseline (BL) obtained as the mean value of the S and R PECD curves. A PES obtained at 95 eV photon energy is also represented (dashed line) along with the calculated values (arrows), both taken from [Rennie et al. 2002]. This figure is adapted from [Nahon et al. 2016].

coming from the HOMO orbital. The error bars are smaller in figure 4.6 than in figure 4.5, enlightening the relevance of mass-tagging the photoelectron images.

The high accuracy of the PECD measurement enables extracting the enantiomeric excess of the two samples. To obtain this value, we analyzed the mass-tagged PECD raw data, without using any correction by the GC x GC-TOFMS *ee* measurement. The retrieved ee_R/ee_S for both camphor and fenchone are compared to the GC x GC-TOFMS results in Table 4.1. There is a striking agreement between *ee* ratio obtained by the two methods. These remarkable results demonstrate that synchrotron-based VUV-PECD is an accurate enantiomeric excess analytical tool in the gas phase, with a precision in the percent range.

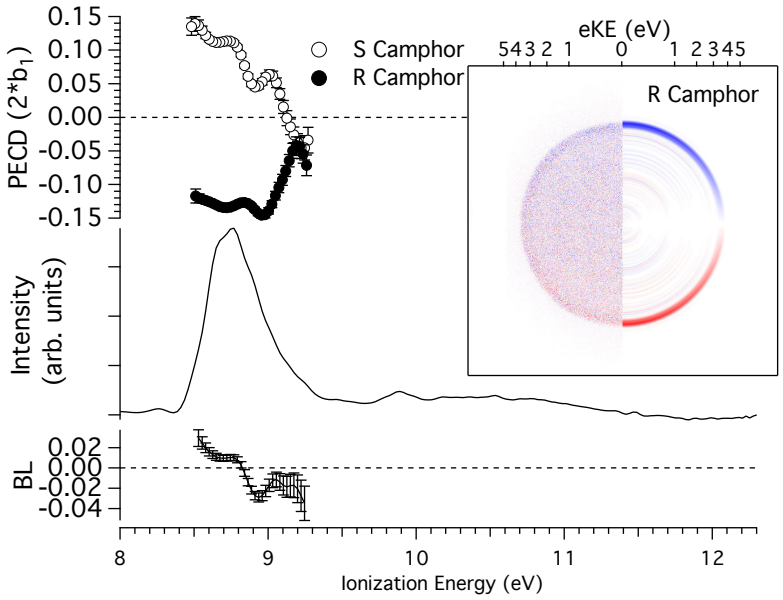

Figure 4.6: PECD (open and filled circles) and PES (solid line) extracted in coincidence with parent ions (m/z 152, 153 and 154 to take into account the ^{13}C contributions) recorded for 1R,4R- and 1S,4S-camphor at 12.3 eV photon energy. The data have been normalized by S_3 and the *ee* measured by GC x GC-TOFMS. The bottom panel represents the PECD baseline (BL) extracted as the mean value of the R and S PECD curves. The inset shows the raw (left) and inverted (right) difference image for 1R,4R-camphor corresponding only to photoelectrons correlated to parent ions. This figure is adapted from [Nahon et al. 2016].

	GC × GC-TOFMS			PECD
Sample	Enantiomeric excess (%)	Chemical purity[b] (%)	$\lvert ee_R/ee_S \rvert$	$\lvert ee_R/ee_S \rvert$
R-(+)-Camphor	$+96.7 \pm 0.9^a$	>99.9	$0.979(9)^a$	$0.97(2)^c$
S-(−)-Camphor	-98.7 ± 0.1^a	>99.9		
R-(−)-Fenchone	$+82.1 \pm 0.5^a$	>99.9	$0.821(5)^a$	$0.82(1)^c$
S-(+)-Fenchone	-99.90 ± 0.03^a	>99.9		

[a] 3σ error bars. [b] Not considering non-volatile or solvent species. [c] 1σ error bars.

Table 4.1: GC x GC-TOFMS analysis of the supplied fenchone samples, along with the relative *ee* measured by PECD. This figure is adapted from [Nahon et al. 2016].

4.2.4 Sensitivity to structural isomerism

The sensitivity of PECD to structural isomerism was already discussed by Powis *et al.*, who compared the PECD of camphor and fenchone using a variety of photon energies between 13 eV and 23 eV [Powis et al. 2008]. Camphor and fenchone both have rigid structures with a single conformer, and differ solely by the shift of two methyl groups from a top position to a side one. The methyl groups are not attached to a chiral center in either of the two molecules. The HOMO orbital of both species is a localized 2p lone pair of the carbonyl oxygen. The isomeric changes are thus remote from the chiral centers and the HOMO orbitals. However, the PECDs of camphor and fenchone were shown to be strongly different, which emphasizes the role of the final continuum states in PECD.

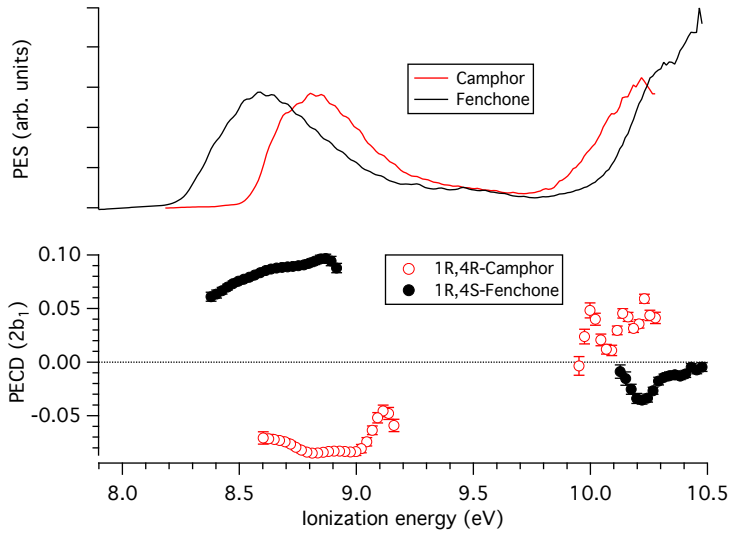

Figure 4.7: PES and PECD for R-camphor (red) and R-fenchone (black) recorded at photon energies of 10.3 eV and 10.5 eV, respectively. The data have been normalized to S_3 and the absolute *ee* as provided by GC x GC-TOFMS. This figure is adapted from [Nahon et al. 2016].

The photon energy range used in this previous experiment did not enable the measurement of PECD in the near-threshold ionization regime originating from the ionization of the HOMO, a region known to be the most sensitive to the molecular potential [Nahon et al. 2015], and thus potentially to structural isomerism effects. We have extended these measurements to shed light on the influence of structural isomerism on the PECD of threshold (slow) photoelectrons.

Figure 4.7 shows the PES and PECD obtained in R-camphor and R-fenchone using 10.3 eV and 10.5 eV photon energy respectively, without performing any mass-tagging. The 200 meV photon energy difference should not have a dramatic effect since it only slightly modifies the kinetic energy of the photoelectrons; the data can thus be directly compared. The R-(+)-camphor and R-(-)-fenchone have the same absolute configuration, *i.e.* the same spatial arrangement of the atoms around the chiral centers.

Their two PES are really similar. They present a broad peak maximizing around 8.5-9.0 eV, corresponding to the ionization of the HOMO, and the beginning of the quasi-continuous peak, starting around 10 eV, corresponding to the dissociative ionization from inner orbitals. The small offset between the two HOMO peaks originates from the difference between the first ionization potential (I_p) of fenchone and camphor. The I_p of fenchone is 180 meV lower than the one of camphor. Quite remarkably, the PECD of fenchone and camphor have an opposite sign. The two molecules behave almost like opposite enantiomers, even if their HOMOs orbitals are nearly identical and their absolute configuration is the same. This striking observation enlightens the role of long-range molecular potential effects: the different position of the two remote methyl groups is enough to affect the electron scattering and inverse the sign of the chiroptical signal. This is confirmed by state-of-the-art theoretical calculation ($CMS - X\alpha$), detailed in [Nahon et al. 2016].

4.2.5 Partial Conclusions

In conclusion, this work has shown the ability of the synchrotron-based PECD experiment to provide high accuracy measurement of the chiroptical signal from an ensemble of

randomly oriented chiral molecules. Using a well-characterized polarization state of light, and using a mass-tagging of the photoelectron images, it was possible to measure precisely the enantiomeric excess ratio between samples of different enantiomers. The *ee* ratio measured with PECD was compared with values obtained using the well-known GC x GC-TOFMS technique. The agreement between the two technique is excellent. Moreover, we have demonstrated that the threshold PECDs of fenchone and camphor molecules with the same absolute configuration have opposite signs, revealing the deep sensitivity of PECD to structural isomerism.

As we will see in the next section, a new generation of PECD experiments using table-top UV-VIS femtosecond pulses has also emerged in the last few years. These experiments imply that many photons need to be absorbed before reaching the continuum, with the possibility of populating intermediate resonance. The resulting PECD will thus be more challenging to interpret compared to the case of single photon VUV-PECD. The accurate PECD measurement presented here will thus also serve as a benchmark to interpret these complicated multiphoton PECD signals.

4.3 Universality of PECD

4.3.1 Early days of multiphoton PECD

In the last section, we went through the genesis of the PECD research field, from its first theoretical prediction [Ritchie 1976], to its first experimental observation [Böwering et al. 2001] and going through a broad range of different VUV-XUV PECD investigations. In these single photon ionization experiments, the only experimental knobs that were available were either to change the molecule or to tune the photon energy. The main path that this research field took was, from my point of view, the 'chemist' way: you change a sub-part of a molecule and you look what happens to your signal; you take two similar molecules, you compare their responses to something, and try to understand why their signals are different. This procedure enabled establishing the sensitivity of this new chiroptical observable to important molecular properties like conformational/structural isomerism and chemical substitution, for example. The fact that the photon energy was also an available knob lead to the demonstration of the capital role of the orbital from which the electrons are departing, as well as the final continuum state on which it ends up. The synchrotron-based single photon PECD experiments thus laid solid foundations of this new and exciting research field. However, the small amount of 'free knobs' and the difficult access to synchrotron beamtime are obstacles that need to be overcome in order to broaden the scientific community using PECD.

In 2012, a pioneering experiment by Lux *et al.* broke these barriers by demonstrating that PECD could be measured using a table-top visible femtosecond laser (400 nm) [Lux et al. 2012]. Using a resonance-enhanced multiphoton ionization (REMPI) [2+1] scheme and a VMIS to detect the photoelectrons, they measured PECD up to 10% in both prototypical camphor and fenchone molecules. In that kind of REMPI experiments, a two-photon transition resonantly brings the molecules to intermediate excited states, where they can absorb one more photon to reach the continuum. They reported that the angular distribution of the PECD was very different for camphor and fenchone. The angular dependence of the PECD constitutes a new observable compared to synchrotron measurements. Indeed, as described in equation 4.1, the number of contributing odd Legendre polynomials to the angular distribution of the PECD (and PES) depends on the number of photons that have been absorbed. This is a consequence of angular momentum conservation. In single photon PECD experiments, only the first odd Legendre coeffi-

cient (b_1) is non-zero, leading to the same angular distribution for every molecule, at all photoelectron kinetic energy. In this case, the information is only encoded in the energy dependence of b_1. By contrast, when multiple photons are absorbed, like in the experiment of Lux *et al.*, many odd Legendre polynomials can contribute to PECD (b_1, b_3,..., b_{2N+1}), leading the angular structuration of the PECD, which depends on the amplitude and sign of each contributing Legendre coefficient, at each energy. This proof-of-principle experiment thus not only showed that the PECD effect also existed in REMPI, but also that it provided rich information about the photoionization dynamics of chiral molecules, encoded in the energy dependence of many odd Legendre coefficients.

Table-top femtosecond lasers enable the use of new experimental knobs to study multiphoton PECD, by bringing all the ingredients of ultrashort laser science: pulse duration, bandwidth, chirp, intensity, and wavelength, for example. These new experimental knobs will be important to try to answer a bunch of new questions raised by this first multiphoton PECD experiment. Is multiphoton PECD sensitive to the same molecular parameters as VUV-PECD? What is the role of the intermediate resonance? Can PECD also exist in a purely non-resonant case? How does PECD depend on the ionization regime, *i.e.* on the laser intensity and wavelength? Is different information encoded in the different Legendre coefficients? So, after Lux *et al.*'s pioneering experiment in 2012 [Lux et al. 2012], a few experimental groups started the quest of answering these challenging questions.

In 2013, Lehmann *et al.* performed an exhaustive REMPI-PECD investigation in camphor by detecting photoelectron images in coincidence with the photoions [Lehmann et al. 2013]. They demonstrated that the use of two different driving laser wavelength, 380 nm, and 400 nm, lead to different PECDs. They interpret their result by arguing that when changing the wavelength, different intermediate (Rydberg) states are populated after the resonant two-photon absorption, which leads to different photoelectron asymmetries. They also briefly discussed the possible effect of the partial molecular axis alignment induced in the excited states, after the resonant two-photon transition. Later, the same group performed a similar experiment by using [2+1] ionization scheme in limonene [Rafiee Fanood et al. 2015] and a [3+1] ionization scheme in methyloxirane [Rafiee Fanood et al. 2014], both using 420 nm photons, demonstrating the generality of the REMPI-PECD technique. They also demonstrated that this mass-tagged table-top REMPI-PECD technique has a very powerful analytical potential [Fanood et al. 2015]: they achieved identification of chiral molecules enantiomeric excesses in multi-component mixtures, which is a really challenging task in the gas phase, and reached a remarkable level of accuracy (10 % level).

In 2014, Lux *et al.* studied the variation of the PAD and the PECD as a function of the driving laser intensity [Lux et al. 2015]. Over the narrow intensity range that was scanned, they observed a power scaling law of the ions that lead to the conclusion that the [2+1] REMPI pathway was strongly favored compared to the non-resonant 3 photons absorption from the ground state. This means that the ionization mostly occurs from the intermediate Rydberg state. They confirmed this finding by looking at the kinetic energy of the photoelectron as a function of intensity. They found that the photoelectron peak was not shifting ponderomotively with the increase of laser intensity, suggesting a Freeman resonance-type phenomenon [Freeman et al. 1987] (*i.e.* that the ionization occurs from the Stark-shifted Rydberg states). They also found that the PECD was slightly decreasing as the laser intensity was increasing. They also mentioned in this paper, and reported in the following article [Lux et al. 2016], that significant chiral asymmetry was also observed on the first Above-Threshold Ionization (ATI) peak.

Again, we did not perform an exhaustive review of all the works that have been

done in the field of REMPI-PECD. Some important papers in the field that have not been mentioned yet but will be discussed later in the section.

At the beginning of my thesis, the exact role of the intermediate resonance and of the laser intensity in multiphoton PECD was not fully understood. To try to resolve this important question, we performed two different studies: i) First, to determine the influence of the laser intensity/ionization regime on PECD, we performed a variety of PECD experiments in a broad range of ionization regime: single photon, multiphoton, above-threshold and tunnel ionization. We showed that PECD is a universal effect in the photoionization of chiral molecules using circularly polarized light, that appears whatever the ionization regime. ii) Second, to gain more insight into the role of intermediate resonances, we used two-color laser fields, where the polarization state of each color can be controlled independently, to completely decouple the excitation and the ionization step.

Before our study on the universality of PECD with respect to the ionization regime, PECD was experimentally found to exist in synchrotron-based single photon ionization [Böwering et al. 2001], in [2+1] [Lux et al. 2012] and [3+1] [Rafiee Fanood et al. 2014] REMPI scheme, as well as on the first order ATI peak ([2+2]) [Lux et al. 2016]. Moreover, a pioneering theoretical paper by Dreissigacker *et al.* had demonstrated that PECD could also exist in multiphoton ionization, even in the absence of any intermediate resonance [Dreissigacker et al. 2014]. To do so, they theoretically investigated the PECD in camphor and fenchone molecules within the framework of the Coulomb-corrected Strong Field Approximation (ccSFA) (the SFA is described in the HHG section of this manuscript). One of the main pillars of the SFA is the assumption that the electron is insensitive to the potential of its parent ion once it has been released into the continuum, meaning that the continuum states are pure plane waves. Within the SFA framework, the continuum states do not have any signature of the chirality of molecular potential. This is the reason why Dreissigacker *et al.* found that the pure SFA treatment of ionization always leads to vanishing PECD. When correcting the continuum states by taking into account the influence of the Coulomb potential (ccSFA), they showed that a nonzero PECD appeared. Because ccSFA does not take into account any resonant phenomena, this finding indeed means that PECD can exist in purely non-resonant multiphoton ionization scheme.

One of the questions raised by the work of Dreissigacker *et al.*, is whether or not this forward-backward asymmetry in the PAD would exist in the tunneling ionization regime? In this regime, the ponderomotive energy ($U_p \propto I \cdot \lambda^2$) is large compared to the binding energy of the electron, and the outgoing electron dynamics is almost solely governed by the laser field (and not by the ionic potential). The tunneling ionization regime is usually assumed to be perfectly well suited for the applying the Strong Field Approximation. Studying the photoionization of chiral molecules using CPL in the tunneling regime is thus a good probe of the validity of SFA: if we observe a PECD, this will mean that the ionic potential still plays a significant role on the outgoing electron dynamics, indicating a departure from pure SFA. On the contrary, if the PECD vanishes, this will mean that the outgoing electron is solely driven by the laser and does not feel the chirality of the molecular potential, which corresponds to a 'pure' SFA case.

Within this context, we decided to perform a series of measurement to investigate the ionization of chiral molecules with circularly polarized light in *all* ionization regime. We investigated PECD in the single-photon HHG-based VUV regime, in the REMPI regime, in low- and high-order ATI regime as well as in the deep tunneling ionization regime. A schematic of the different ionization pathways that were studied is presented in Fig. 4.8. We found that PECD is a universal effect when chiral molecules are photoionized with

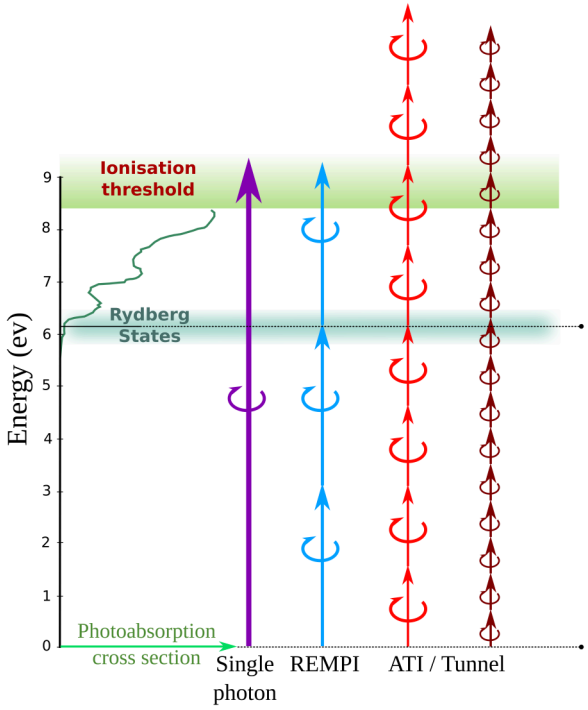

Figure 4.8: Photoionization schemes that will be used in the PECD measurements discussed in this section, by photons at 133, 400, 800 and 1850 nm, from left to right. The photoabsorption cross section of fenchone is adapted from Pulm *et al.* [Pulm et al. 1997]. This figure is adapted from [Beaulieu et al. 2016c].

circularly polarized light.

4.3.2 PECD using HHG-based VUV source

As we have seen in the previous section, single-photon VUV-PECD using synchrotron radiation is a powerful tool to study molecular chirality in dilute media. However, the access to these huge facilities is limited. It is thus of great interest to develop table-top circularly polarized VUV/XUV source. We have shown in the previous chapter that driving the process of High-order Harmonic Generation (HHG) in atoms or molecules using VIS/IR laser could lead to a table-top, bright and coherent VUV/XUV source. Unfortunately, the HHG mechanism has an intrinsic preference for linearly polarized light. This is a consequence of the mechanism underlying the generation of the high harmonics. When the driving laser is elliptically polarized, the minor component of the electric field drives the electron wavepacket away from its parent ion, strongly suppressing the radiative recombination process. For example, driving HHG with 20 % ellipticity decreases the HHG efficiency by one order of magnitude with respect to the case of linear polarization [Budil et al. 1993]. Moreover, the ellipticity of the HHG emitted using elliptically polarized driving laser remains lower than the driving laser [Antoine et al. 1997]. At first sight, achieving highly-elliptical VUV sources by driving HHG with an elliptically polarized laser does not seem to be the way to go.

Since the HHG mechanism is much more efficient using linear polarization, a way to achieve circular XUV photons can be to *a posteriori* convert the linear polarization to a circular one. In the visible or infrared spectral, this is easily achieved by using a quarter-wave plate. In the XUV spectral range, there is no such a device. Fortunately, one

can use multiple reflexions on metallic surfaces to produce circular XUV photons, using an incoming linear polarization [Vodungbo et al. 2011; Willems et al. 2015]. One important drawback of this technique is the low-reflectivity of the surfaces in the XUV spectral range, leading the strong decrease of the photon flux.

In the past few years, a few different HHG-based schemes to directly generate high-brightness circular XUV photon have emerged. The first scheme relies on the temporal shaping of the driving field by using a combination of counter-rotating fundamental ω and second harmonic fields 2ω. This combination of two counter-rotating electric fields results in a trefoil knot shaped electric field. Driving HHG which such a field leads to circularly polarized harmonics with alternatively left or right polarizations [Fleischer et al. 2014]. Because in molecular photoionization, each harmonic with sufficient energy can open many different ionization channels, which lead to highly congested and overlapping photoelectron spectra, the use of a comb of harmonics with alternating polarization states is not well suited for PECD experiments. However, it was shown to be a really efficient solution for the investigation of X-ray Magnetic Circular Dichroism (XMCD) in the condensed phase [Kfir et al. 2015]. Recent theoretical results have shown that it may be possible to kill one harmonic out of two in the generation process by proper selection of the generating medium [Medisauskas et al. 2015].

Another scheme that has been developed is the non-collinear generation of angularly isolated circularly polarized high harmonics [Hickstein et al. 2015]. This scheme uses a combination of two counter-rotating pulses of the same frequency that are non-collinearly focused in a gas jet. Because of momentum conservation, the different harmonics of the fundamental laser emerge at different angles, and left- and right- circularly polarized harmonics are sent at opposite angles. One can thus select a given harmonic with a given helicity by using a spatial filter (*e.g.* a slit) in the intermediate/far field. This technique can in principle be used for PECD experiments if one is able to manipulate the XUV beam propagating in different directions in order to send them to the molecular target. We had in mind to try it, but we did not have time to perform the experiment.

The third solution, which is the one we use in our experiment, is based on the shaping of the recollision process in the HHG mechanism using resonant high-harmonic generation. In single-photon ionization, resonances in the continuum can have a tremendous influence on the outgoing electron dynamics. In the vicinity of autoionizing or shape resonances, the photoionization cross-section is greatly enhanced. Moreover, these resonances strongly modify the anisotropy parameter β of the outgoing electrons, leading to a modification in the photoelectron angular distribution [Piancastelli 1999]. Recent experiments performed in the time-domain using attosecond interferometry enlightened the fact that the spectral phase of the EWP was also strongly distorted across the resonance [Gruson et al. 2016; Kotur et al. 2016]. Because the photorecombination step in HHG is the time-reverse analog of XUV photoionization, resonances in the continuum will also influence the last of the three steps in the HHG mechanism. If the returning electron kinetic energy matches the energy where is located a shape resonance, for example, the electron gets trapped into the potential well associated with the shape resonance before being able to radiatively recombine to the electronic state from where it originated. The population trapping into the resonance during HHG adds a fourth step to the so-called 3 step model, as established by Vasily Strelkov [Strelkov 2010]. The effect of the shape resonance is not only to enhance the harmonic yield. Calculations performed by Bernard Pons and Baptiste Fabre, from CELIA, show that the resonance creates a strong orthogonal component to the harmonic electric field when HHG is driven by a slightly elliptical electric field [Ferré et al. 2015b]. This results in a quasi-circular XUV emission. This phenomenon is illustrated in figure 4.9.

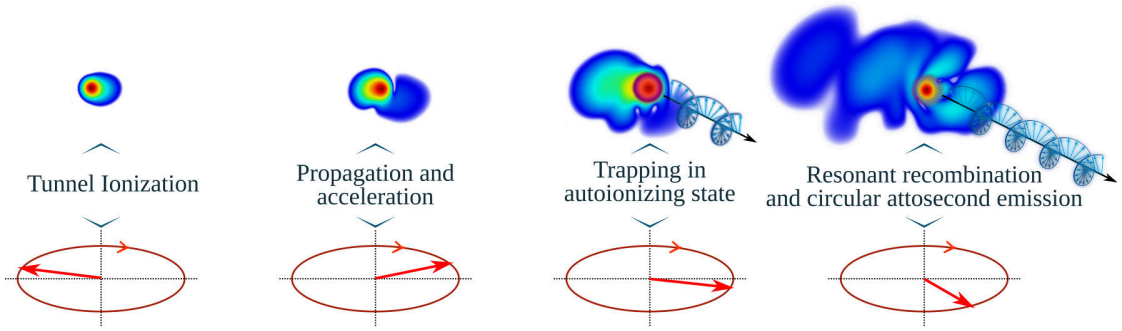

Figure 4.9: Mechanism of elliptical resonant high-harmonic generation. The top color plot represents the electronic density from a 2D quantum calculation, evolving in an elliptical laser field whose instantaneous direction is depicted at the bottom.

This property of resonant HHG has been observed experimentally for the case of shape resonance in SF_6 molecules (around 22-23 eV) and for the case of below-threshold Rydberg resonances in argon atoms (around 15 eV) [Ferré et al. 2015b]. We have used this bright and highly elliptical VUV source to perform table-top single photon PECD in fenchone molecule.

The PECD measurements were performed using the 1 kHz Aurore laser system at CELIA, which delivers 25 fs, 7 mJ pulses centered around 800 nm. The laser pulses were frequency doubled in a 200 μm thick type-I BBO crystal and focused by a 50 cm lens in a 3 mm long cell filled with SF_6 molecules. Using 400 nm rather than 800 nm pulses for HHG increase the energy spacing between odd harmonics from 3.1 to 6.2 eV, easing the assignment of the photoelectron spectra. The laser ellipticity was controlled using a motorized zero-order half waveplate in front of a fixed zero order quarter wave- plate, in order to keep the orientation of the polarization ellipse fixed in space. The harmonics were directly sent into the interaction region of the VMIS, without any focusing optics to avoid modifying the XUV polarization state. A motorized aperture was tuned to limit the size of the XUV beam to achieve a good resolution of the photoelectron images. A sample of enantiopure (+)-fenchone molecules at room temperature was connected to the heated metallic nozzle (390 K) with a 300 μm diameter located 7 cm away from the interaction zone. The pressure in the interaction region was $2 \cdot 10^{-6}$ mbar ($5 \cdot 10^{-8}$ mbar background pressure). In order to remove the influence of slow drifts in the experiments, the polarization state was switched every 10 seconds. Typically few 10^5 laser shots were accumulated to obtain each of the LCP and RCP images.

By using the recorded VMI images obtained with LCP (S_{+1}) and RCP (S_{-1}), we can add them to retrieve the PAD ($PAD(E,\theta) = \frac{1}{2}[S_{+1} + S_{-1}]$) or we can take the normalized difference to obtain the PECD ($PECD(E,\theta) = 2(S_{+1} + S_{-1})/(S_{+1} - S_{-1})$). As described before, the Legendre coefficients are extracted by least-squares fitting of the experimental distributions (pBasex). The experimental results are presented in figure 4.10.

The PAD and its associated PECD are shown in figure 4.10(a) and (b), respectively. Because of the single-photon ionization nature of this experiment, only the first odd Legendre polynomials contribute to the PECD. The $b_0(E)$ (shaded gray area) and $b_1(E)$ are shown in figure 4.10(c). The $b_0(E)$ presents a huge peak around 0.5 eV, a broad distribution between 1 and 5.5 eV and a tiny bump around 6.75 eV. To assign these spectral features, Bernard Pons and Baptiste Fabre performed Time-Dependent Density Functional (TDDFT) calculations of the electronic structure of fenchone using the GAMESS-US package [Schmidt et al. 1993]. The equilibrium geometry of the ground state fenchone

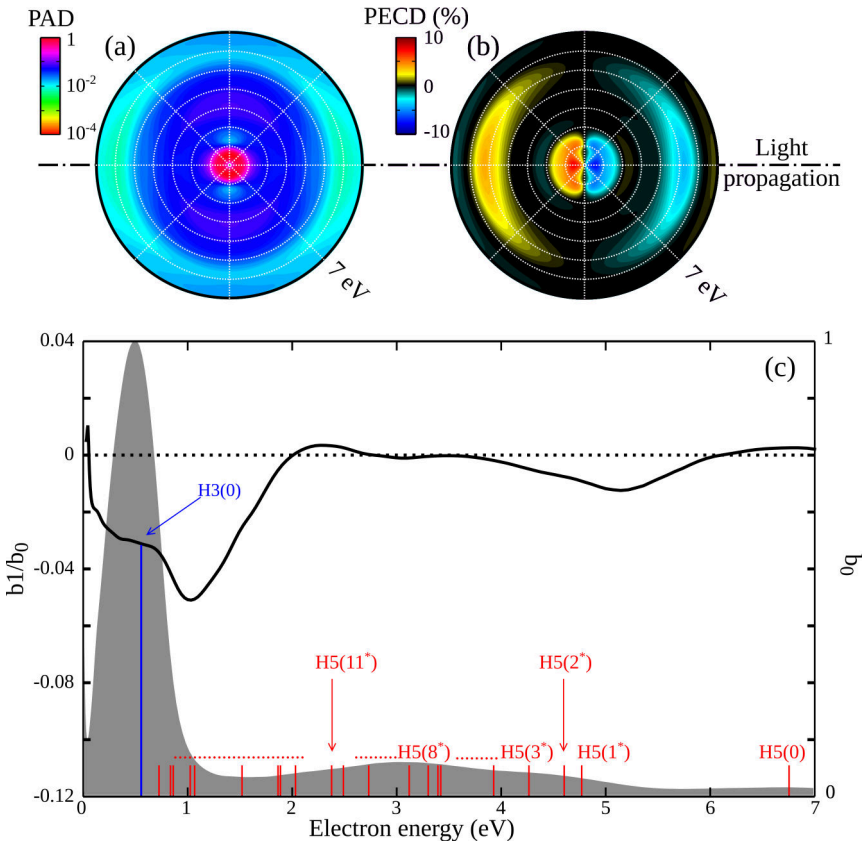

Figure 4.10: Single-photon ionization of (+)-fenchone by elliptical harmonics 3 to 7 of a 400 nm. PAD (a) and PECD (b); the light propagation axis is horizontal and the radius extends from 0 to 7 eV. (c): b_0 (grey area) and normalized b_1/b_0 (black line) Legendre coefficients as a function of electron kinetic energy; positions of PES peaks expected from TDDFT calculations are shown in blue and red and are labeled by $Hq(i^*)$, which is a shortcut of the $Hq(0 \rightarrow i^*)$ notation employed in the text. This figure is adapted from [Beaulieu et al. 2016c].

molecule was optimized using a $6-311++G^{**}$ basis set and the CAMB3LYP hybrid exchange-correlation functional. The same geometry was used for the electronic structure calculation of the cationic fenchone, yielding a first vertical ionization potential from the ground state neutral (0) to the ground state cationic (0) fenchone $I_p^{0\rightarrow 0}$ = 8.74 eV, which is in very good agreement with the experimental values (8.72 eV). The TDDFT calculation also provides the vertical ionization from the neutral ground state (0) and excited cationic states (i^*). The vertical ionization potential for each ionization channel $(0 \rightarrow i^*)$ is labeled $I_p^{0\rightarrow i^*}$. These ionization potentials can be used to identify the different photoelectron peaks associated to ionization channel $(0 \rightarrow i^*)$ opened by the absorption of the qth order harmonic $Hq(0 \rightarrow i^*)$. The photoelectron associated with the $Hq(0 \rightarrow i^*)$ ionization channel will end up at a final energy given by $E_k = q\hbar\omega - I_p^{0\rightarrow i^*}$, following simple energy conservation rule.

The 3rd harmonic photon energy is 9.3 eV. This harmonic can only open the $H3(0 \rightarrow 0)$ ionization channel, giving rise to the strong peak at 0.5 eV in the $b_0(E)$. The photon energy of harmonic 5 is 15.5 eV. In a large molecule like fenchone, the energy separation between molecular orbitals is small. The 5th harmonic can thus open a large number of ionization channels. As shown in figure 4.10 (c), the tiny bump around 6.75 eV is associated to the $H5(0 \rightarrow 0)$ ionization channel. The large bump between 1 and 5.5 eV can be attributed to ionization that leaves the cation in excited states, after the absorption of a 15.5 eV

photon $H5(0 \rightarrow i^*)$. One can see that a lot of excited states are energetically accessible, explaining why this peak is so broad. Also, we know from the mass-tagged experiment at the synchrotron that ionization from inner orbital lead to fragmentation of the cationic fenchone. By performing coincidence with the parent ion, this large peak would thus probably disappear.

Now we will focus on the PECD. The first thing that we notice is that even if there is a myriad of states that contribute to the PES, the PECD is remarkably simple. Indeed, we can see that while the PECD is really strong ($2b_1/b_0 \sim 10\%$) for the $H3(0 \rightarrow 0)$ ionization channel, the PECD associated to large peak from 1 to 5.5 eV coming from the many $H5(0 \rightarrow i^*)$ channels is almost zero. One can also see a significant PECD ($2b_1/b_0 \sim 3\%$) for the $H5(0 \rightarrow 1^*)$ channel. The fact that the PECD vanishes in the spectral region where a lot of ionization channels overlap can be explained as the following: each contributing channel has is own circular dichroism, which can have different amplitude and sign. We can tentatively assume that the alternating positive and negative PECD average to $\sim$ zero when taking into account a large number of contributing channels.

Another remarkable feature is that $b1/b0$ does not maximize at the locations of PES peaks but on their falling edges. This could be due to the inherent dependence of $b1$ on the electron energy, or because of overlapping contributions of adjacent $H5(0 \rightarrow 1^*)$ channels.

Using the bright table-top elliptically polarized VUV source developed by Ferré *et al.* [Ferré et al. 2015b], we were able to record PECD in fenchone. This kind of experiment does not provide any new information about the physics underlying this chiroptical effect. It is exactly like performing a synchrotron-based PECD experiment with multiple wavelengths simultaneously. However, this proof-of-principle experiment paves the way towards a new generation of PECD studies in which the ultrashort characteristic of the light source could be used to track ultrafast dynamics. We will come back to this in the next chapter.

4.3.3 Role of resonant enhancement in REMPI-PECD

We will now focus on the role of the resonant enhancement in [2+1] REMPI-PECD. To investigate this, we monitored the PES and the PECD of (+)-limonene as a function of the laser wavelength (409 nm, 401 nm, and 396 nm). When the photon energy is slightly modified, the 2 photons absorption step of the REMPI scheme will photoselected different resonant intermediate states. The oscillator strength and the electronic character of the intermediate state can thus be easily tuned.

The experimental procedure to acquire the PECD data is similar as in HHG-based VUV-PECD. The experiments were conducted using the Aurore laser system. The laser pulses are frequency doubled in a 200 μm thick type-I BBO crystal, whose orientation was adjusted to tune the central wavelength of the pulses between 396 nm and 409 nm. The detection scheme (VMIS), the source of gas-phase chiral molecules and the data acquisition and inversion procedures were exactly the same as described in the HHG-based VUV-PECD section. However, because three photons are involved in the photoionization process, high-order odd Legendre coefficients can contribute to the PECD. This will lead to the more complex angular dependence of the PECD.

In the case where many photons are involved, we need to introduce a new quantity which is called the multiphoton PECD (MP-PECD). As in the case of the single photon defined as PECD = $2b_1$, MP-PECD corresponds to difference between electron emission in the forward and backward hemispheres, normalized by the average number of electrons per hemisphere, and is defined as [Lehmann et al. 2013; Lux et al. 2015]. MP-PECD can

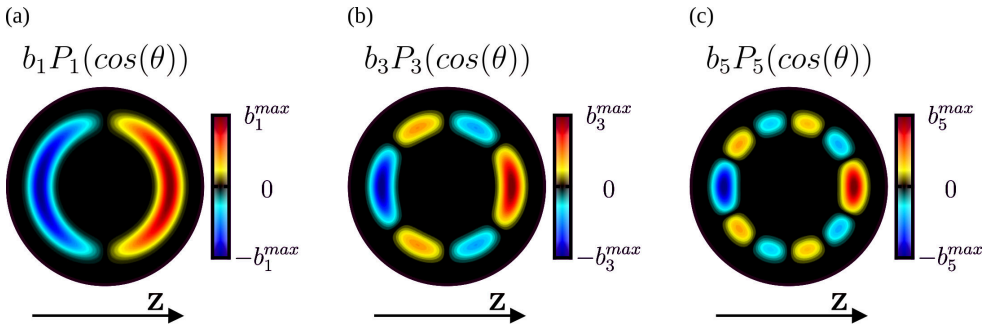

Figure 4.11: Scheme of the individual contribution of different odd Legendre polynomials to the asymmetric part of a hypothetical photoelectron image. In (a), the first order, (b) third order and (c) fifth order Legendre polynomials. **z** is the laser propagation direction.

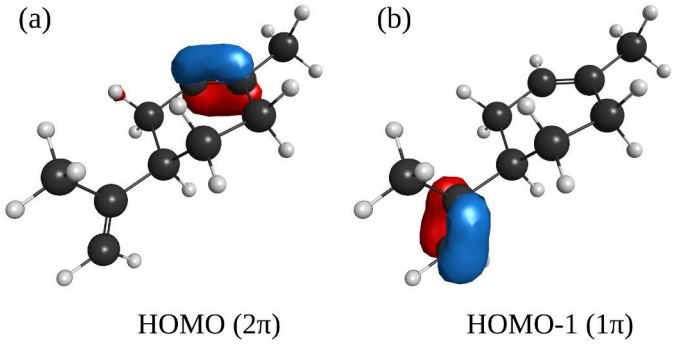

Figure 4.12: Equilibrium geometry of the most stable conformer of (+)-limonene in gas phase at room temperature as well as the representation of the (a) HOMO (2π) and (b) HOMO-1 (1π) orbitals. The ground state geometry was optimized using density functional theory (DFT) with CAMB3LYP functional and a 6-311++G(d,p) basis.

also be express as a linear combination of Legendre coefficients,

$$\mathrm{MP-PECD}(E) = \frac{1}{b_0(E)}\left[2b_1(E) - \frac{1}{2}b_3(E) + \frac{1}{4}b_5(E) - \frac{5}{32}b_7(E) + ...\right] \tag{4.5}$$

A schematic example of the contribution of the first three odd order Legendre polynomials is presented in Fig. 4.11.

Figures 4.13 (a)–(c) show the measured PADs, and Fig. 4.13(d)–(f) their associated PECD. Using the same notation as above and by using the ionization potentials $I_p^{0\to i^*}$ from the ground state of limonene (0) to the ground (0) and excited (i^*) states of the associated cation given in [Smialek et al. 2012], we calculated the expected positions of the $3\hbar\omega(0 \to 1^*)$ and $3\hbar\omega(0 \to 0)$ ionization pathways, depicted as continuous circles. Within the Koopmans approximation, they correspond to the removal of one electron from the highest occupied molecular orbital (HOMO, outer circle) and the HOMO-1 (inner circle) respectively. The $I_p^{0\to 0}$ is 8.52 eV and the $I_p^{0\to 1^*}$ is 8.9 eV. The equilibrium geometry, as well as the representation of the HOMO and HOMO-1 orbitals of limonene, are shown in figure 4.12. Looking at the PAD and the PECD, we can notice that the angular distributions are more complex than when using VUV ionizing radiation. At some given energies, the PECD is maximum around 45°, which is a signature of the contribution of high-order odd

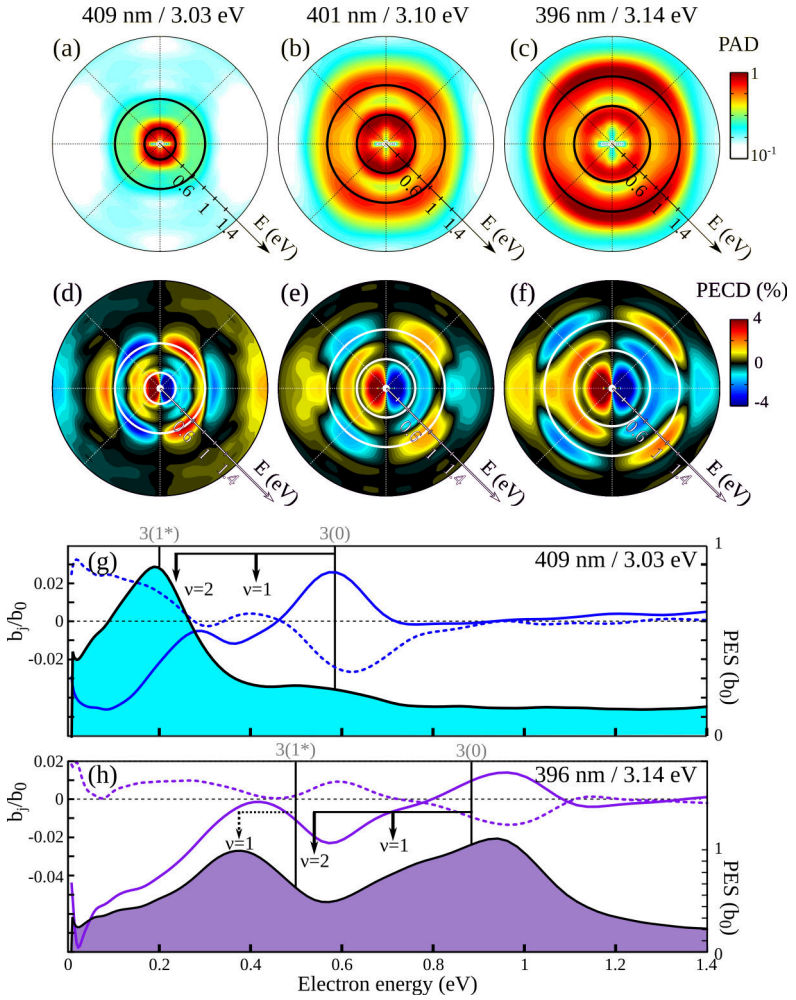

Figure 4.13: Multiphoton ionization of (+)-limonene molecules. PAD (a)–(c) and PECD images (d)–(f) for $\lambda = 409$ (a), (d), 401 (b), (e) and 396 nm (c), (f). The light propagation axis is horizontal and the radius extends from 0 to 1.4 eV. (g), (h): PESs (shaded area) and normalized b_1/b_0 (solid line) and b_3/b_0 (dashed line) as functions of E, for $\lambda = 409$ nm (g) and 396 nm (h). The theoretical positions of the PES peaks are marked by $k(i^*)$, as a shortcut of the notation $k\hbar\omega(0 \rightarrow i^*)$ employed in the text; the arrows refer to vibrational quanta of energy. This figure is adapted from [Beaulieu et al. 2016b].

Legendre coefficients (when only b_1 contributes to PECD (single photon ionization), it maximizes around 0°).

As the laser wavelength varies, the most striking feature in the PAD is a strong change in the intensity of the higher energy peak: the signal increases by around one order of magnitude when the wavelength changes from 409 to 396 nm. In addition, the angular distribution of the photoelectrons ejected from the higher energy peak is modified, showing a sign change of the b_2 Legendre coefficient (related to the anisotropy parameter, β) from positive to negative. This indicates a clear modification of the ionization pathway. Indeed, changing λ from 409 to 396 nm brings different Rydberg states of limonene in 2 photons resonance: from 3s to the lowest 3p state according to the assignment made in [Smialek et al. 2012]. Comparison of figures 4.13(d) and 4.13(f) unambiguously shows that similar PECDs are obtained at both wavelengths for the higher energy peak, with the same sign, and in the 4% range. This observation suggests that the different intermediate resonances selected in our wavelength scan do not lead to very different PECD.

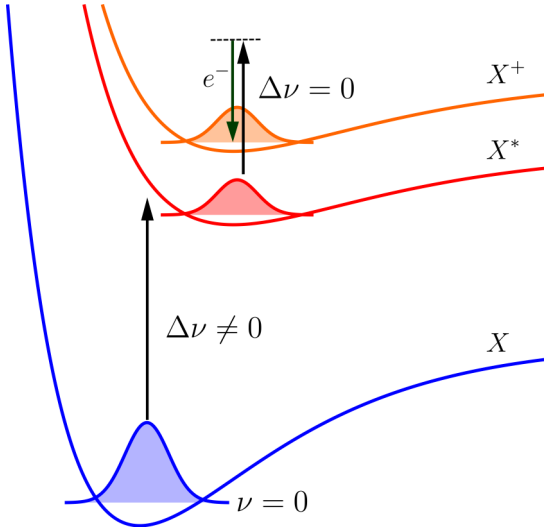

Figure 4.14: Schematic of the propensity rule for the photoionization of Rydberg states. The ground state of the neutral (X) does not have the same equilibrium geometry as the Rydberg states (X^*). This typically leads to $\Delta\nu \neq 0$ upon vibronic transition. The populated vibrational states of the excited states depend on the Franck-Condon factor. Upon photoionization, because the Rydberg state (X^*) and the molecular ion (X^+) typically have parallel potential energy surfaces, the vibrational state remain invariant ($\Delta\nu = 0$).

By using Legendre polynomials least-square fitting of the 2D projection of the PAD (and associated PECD), we can perform a more accurate spectroscopic assignment of the experimental data. The extracted odd Legendre coefficients are shown in figure 4.13(g) and (h). Note that odd Legendre coefficients up to the 7th order can contribute to the PECD. However, the contributions of the 5th and 7th order polynomials are very small, so only b_1/b_0 and b_3/b_0 are present, for sake of clarity. The spectroscopic assignment is based on the vibronic states accessible with the resonant 2 photons transition and with the electron kinetic energy associated with the third photon absorption, taking into account the $\delta\nu = 0$ propensity rule that holds for the ionization of (intermediate) Rydberg states. A scheme explaining the origin of this propensity rule is presented in Fig. 4.14.

In Fig. 4.13(g), using 409 nm central wavelength, the high-energy peak can be assigned to a resonant transition from the HOMO to the vibrational ground state of the 3s Rydberg states ($2\pi \rightarrow 3s(\nu = 0)$), followed by the ionization leaving the cation in its vibrational and electronic ground state $3\hbar\omega(0 \rightarrow 0)$ ($\nu = 0$). We can notice a maximum of b_1/b_0 and b_3/b_0 (with opposite sign) around the maximum of this PES peak. Roughly 0.17 eV below, we can notice that both b_1/b_0 and b_3/b_0 switch signs and maximize again. This 0.17 eV shifted PECD peak corresponds to one quantum of vibrational energy, for the C=C bond located within the six-membered ring, in the ground electronic state of the ion [Smialek et al. 2012]. The low energy peak can come either from the ionization of the HOMO-1 orbital (1π), leaving the cation in its first excited state ($3\hbar\omega(0 \rightarrow 1^*)$ ($\nu = 0$)) or from the ionization of the HOMO orbital leaving the cation with two quantum of C=C vibrational energy ($3\hbar\omega(0 \rightarrow 0)$ ($\nu = 2$)). The b_1/b_0 and b_3/b_0 show large values around this PES peak.

Decreasing the wavelength to 396 nm give also rise to a lot of rich vibrational features. Indeed, the PES shows a shoulder around the expected electron energy for an ion left in $\nu = 1$ excited state, and the associated PECD sign is again opposite to that corresponding to $\nu = 0$. The magnitude of the PECD increases to reach a maximum around E = 0.57 eV,

which roughly corresponds to the electron kinetic energy release for a limonene cation in the $v = 2$ state. In addition electron kinetic energy effects between the $3\hbar\omega(0 \rightarrow 0)$ and $3\hbar\omega(0 \rightarrow 1^*)$ thresholds might also play a role. Sign reversals in PECD from vibrationally excited ions have recently been observed in one XUV-photon absorption and interpreted as a signature of non-Frank-Condon transitions [Garcia et al. 2013b]. Our present findings generalize this observation in the REMPI regime and show that PECD enables resolving vibrational features invisible in the PADs.

Our study shows that whereas the laser wavelength has a dramatic influence on the photoelectron spectrum and angular distribution, which we attribute to a change in the resonant intermediate state, the PECD is rather insensitive to excitation wavelength. This suggests that while PECD is remarkably sensitive to the initial and final states, resonant multiphoton PECD is not necessarily sensitive to the electronic character of the resonant state.

A recent study of REMPI-PECD in fenchone molecules by Kastner *et al.* demonstrated that selecting different intermediate resonances during the REMPI pathway could lead to PECD with opposite signs [Kastner et al. 2017]. We can thus conclude that the exact role of intermediate resonance in REMPI-PECD strongly depends on the molecular system.

4.3.4 PECD in the Above-Threshold Ionization regime

In a recent paper, Lux *et al.* reported the existence of a strong PECD signal in the first ATI peak of fenchone, camphor, and norcamphor [Lux et al. 2016]. This proof-of-principle experiment showed that low-order ATI electrons also carry a signature of the molecular chirality. However, one important question that remained unanswered was: How does this chiroptical signal evolve as a function of the ATI order? In VUV-PECD, it was already pointed out that the PECD amplitude is stronger for near-threshold photoelectrons. This is a consequence of the fact the high energy electrons are less sensitive to the molecular potential and thus do not carry its chiral character. Here, we will extend the work of Lux *et al.* and monitor the PECD in fenchone as a function of the ATI order, for different laser intensity. The wavelength will be fixed at 402 nm. We will use the fenchone VUV-PECD data taken during the synchrotron run described in the previous section to compare with the ATI-PECD data.

The PECD images obtained at 402 nm for $I \sim 5 \times 10^{12}$ and $4 \times 10^{13}\mathrm{W/cm^2}$ are presented in Fig. 4.15 (a) and (b), respectively. The associated PES and the so-called multiphoton PECD (MP-PECD) are shown in Fig. 4.15 (c). For the lower intensity, the PES presented in Fig. 4.15 (c) shows two distinct ATI combs, each with a comb spacing of $\hbar\omega = 3.09$eV. These two combs, beginning at E = 0.53 eV and 1.57 eV, respectively, originate from different ionization channels. As for the case of limonene, presented above, our theoretician colleagues from CELIA performed TDDFT calculation of the electronic spectra of neutral and cationic fenchone in order to identify the different ionization channels which contribute to the experimental PES. The thin lines labeled $k(i)$ indicate the positions of PES peaks expected from the calculations. The ATI comb starting around 1.57 eV is associated to the $k\hbar\omega(0 \rightarrow 0)$, with $3 \leqslant k \geqslant 6$, ionization channel while the ATI comb starting around 0.53 eV comes from the $k'\hbar\omega(0 \rightarrow 1^*, 2^*)$, with $3 \leqslant k' \geqslant 7$.

The signal from the former ATI comb is about one order of magnitude stronger than the one from the latter. The TDDFT calculations validate the Koopmans approximation for states $i^* \leqslant 11$. This means that cationic states up to $i^* = 11$ can be associated with electron removal from the HOMO-i^* orbitals. The two series can thus be safely interpreted as ionization from the HOMO and HOMO-1,2, respectively, where the energy difference between the HOMO-1 and HOMO-2 is too small to be resolved experimentally. For highly

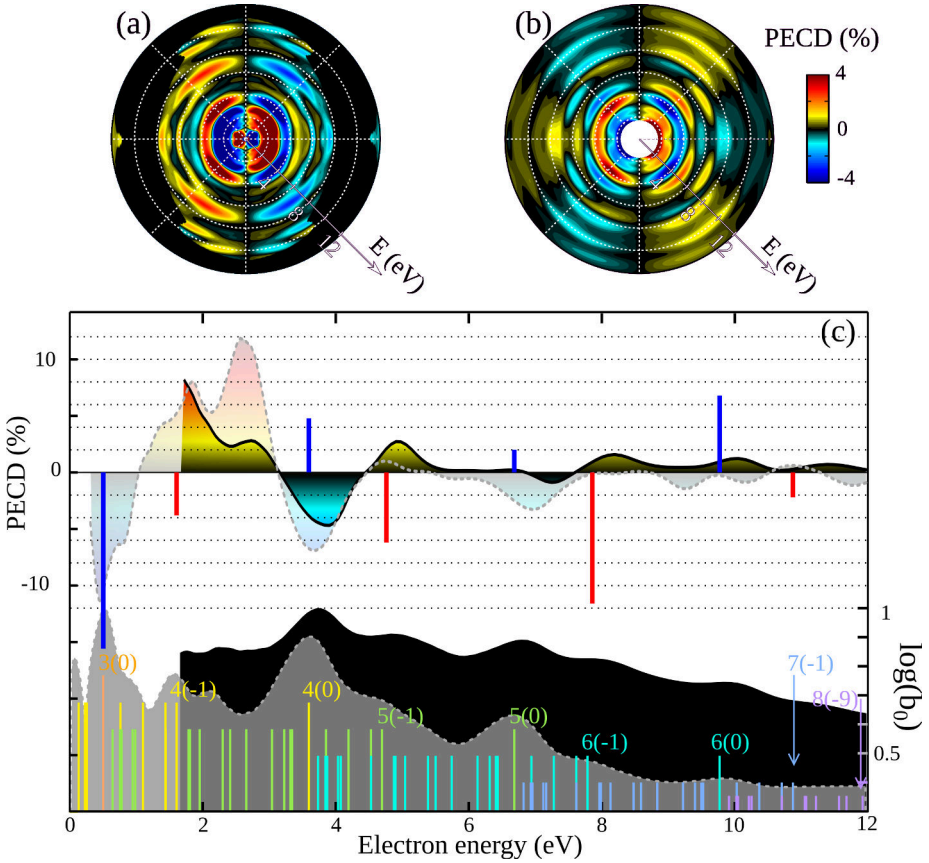

Figure 4.15: PECD of (+)-fenchone by 402 nm pulses in the ATI regime. PECDs for $I \sim 5 \times 10^{12}$ (a) and 4×10^{13}W/cm^2 (b). The light propagation axis is horizontal and the radius extends from 0 to 12 eV. (c): corresponding PES and MP-PECD for $I \sim 5 \times 10^{12}$W/cm^2 (lightest shaded area) and $I \sim 4 \times 10^{13}$W/cm^2 (darkest shaded area); the dark (blue) and light (red) thick vertical lines are the one-photon PECD values from the HOMO and HOMO-1,2, respectively, measured in [Nahon et al. 2016]; the thin lines labeled k(i) indicate the positions of PES peaks expected from our calculations. This figure is adapted from [Beaulieu et al. 2016b].

excited cationic state $i^* > 11$, the Koopmans approximation breaks down and the states start to be described as two-hole-one-particle configurations which are accessible from the ground state of the neutral through excitation + ionization processes.

The angle-resolved PECD presented in Fig. 4.15 (a) shows that the forward/backward asymmetry in the photoionization maximizes around $\theta = 0°$ for the low-order ATI peaks. As the number of absorbed photons increases (*i.e.* higher ATI orders), the PECD maximizes at higher values of θ, which is a signature of the contribution of higher order Legendre coefficients. This behavior was already observed on the first ATI peak, in the experiment of Lux *et al.*. Our experimental data confirm that this behavior is even more dramatic as the ATI order increases.

We can now turn our analysis to the absolute magnitude of the PECD as a function of the ATI order. The MP-PECD from the HOMO channel decays from $\sim -12\%$ just above the ionization threshold (k = 3) to $\sim -1\%$ for 6-photon ionization (k = 6) (figure 4.15(c)). This reflects the fact that as the electron gets more energy through sequential absorption of photons, it is less sensitive to the molecular chiral potential. This result qualitatively agrees with the case of single-photon VUV-PECD, where PECD is also found to vanish for electrons of high kinetic energies. We can also use the fenchone VUV-PECD data that we

have to obtain at the synchrotron facility [Nahon et al. 2016] to quantitatively compare ATI-PECD and VUV-PECD.

The values of the HOMO and HOMO-1,2 PECDs obtained by a single-photon XUV ionization experiments [Nahon et al. 2016] are presented as blue and red thick vertical line, respectively, in Fig. 4.15 (c). While the results are remarkably similar for the 3-photon (3 $\hbar\omega$ = 9.3 eV) and single-photon ($\hbar\omega$ = 9.3 eV) ionization of the HOMO, the single-photon PECD switches sign above this energy, whereas it remains negative in the multiphoton regime. Well above the threshold, the single-photon PECD is much stronger than the multiphoton one. This could be the signature of a better isolation of the HOMO contribution by coincidence electron-ion detection in the single-photon experiment, while background from other channels may decrease the ATI-PECD. Also, in the case of single-photon ionization, the transition is only sensitive to the initial (molecular orbital) and the final (continuum state) while in ATI, there are multiple continuum-continuum transitions that can affect the resulting PECD. The fact that multiple continuum states are involved in the production of high-order ATI electrons might also explain their weaker PECD compared to VUV-PECD.

The evolution of PECD with ATI order being established, we can now study the influence of laser intensity on ATI-PECD. We increased the laser intensity from $I \sim 5 \times 10^{12}$ to 4×10^{13}W/cm^2. Figure 4.15 (b) shows that the overall amplitude of the PECD is lower for higher laser intensity. This can be explained by the fact that as the laser field is increased, its influence on the outgoing electron dynamics become greater than the one from the molecular chiral potential, which leads to weaker chiroptical signals. The PECD is even found to switch its sign for photoelectrons above 5 eV.

One other interesting feature can be observed by looking at the PES (figure 4.15 (c)). At lower intensity, the contribution of the HOMO-1,2 ATI comb was one order magnitude smaller than the one from the HOMO orbital. At 4×10^{13}W/cm^2, both ATI combs are almost of the same magnitude, revealing the more efficient ionization yield of inner-orbitals at a higher intensity. Another intriguing observation is the spectral blueshift of the two ATI comb with increasing laser intensity. In the case of purely non-resonant photoionization, one might expect a redshift of the ATI comb with increasing laser intensity, due to the ponderomotive shift of the ionization threshold. To tentatively explain the observation of the blueshift of the PES with laser intensity, one needs to take into account the role of two-hole-one-particle states. Indeed, the ATI comb that was attributed to HOMO-1,2 now maximizes around the neighbor $k\hbar\omega(0 \rightarrow i^*)$ transitions, with $i = 12 - 14$ and $k = 6 - 8$. Interestingly, TDDFT associates $i \geqslant 11$ excited states of the cation to two-hole-one-particle configurations which are accessible from the ground state of the neutral through excitation + ionization processes. Similar processes, with even higher i in the range 16–20, may also come into play in the close neighborhood of the main HOMO peaks. In both cases, the juxtaposition of one-electron direct ionization and higher-order (excitation + ionization) processes could lead to the observed shift of the PES peaks. It would also lead to modifications of the PECD picture, inducing sign changes in the high-energy range where the magnitude of the high-order ATI peaks associated to one-electron direct ionization is low. Thus, tuning the laser intensity enables probing different responses of the molecule: the pure one-electron PECD response at low intensity, and higher order processes, beyond the Koopmans theorem, at a higher intensity.

4.3.5 A transition from ATI to tunneling ionization

Does PECD still exist in the tunneling regime? This was one of the major questions raised at the beginning of the section. The survival of PECD in this extreme ionization

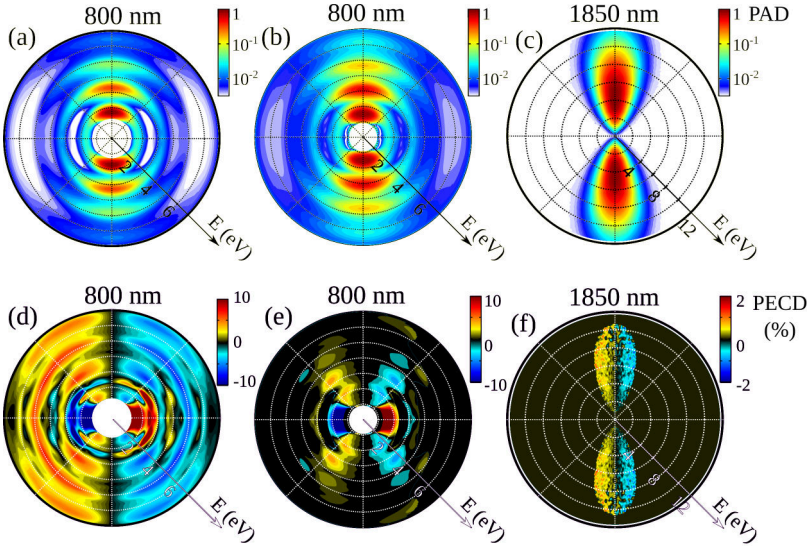

Figure 4.16: Photoionization of (+)-fenchone from ATI to the tunneling regime. PAD and PECD for $\lambda = 800$nm pulses with $I \sim 9 \times 10^{12}$W/cm^2 (a), (d) and $I \sim 1.2 \times 10^{13}$W/cm^2 (b), (e). (c)–(f) Raw projection of the PAD and PECD for $\lambda = 1850$nm pulses with $I \sim 4 \times 10^{13}$W/cm^2. The light propagation axis is horizontal and the radius extends from 0 to 7 eV in (a), (b), (d) ,(e) and 0 to 12 eV in (c), (f). This figure is adapted from [Beaulieu et al. 2016b].

regime would be an elegant experimental demonstration of the failure of the Strong Field Approximation, which completely neglects the role of the atomic/molecular potential on the outgoing electron dynamics. Also, because tunnel ionization is at the heart of attosecond and strong-field physics, the demonstration of the existence of PECD in this regime could bridge the gap between the PECD and attosecond communities and lead to important advances in ultrafast metrology of chiral photoionization. This will be the subject of the last section of the thesis.

When an atom or a molecule is embedded in an oscillating electric field, the ionization regime is characterized by the Keldysh parameter γ, which depends on the ratio between the ponderomotive energy and the ionization potential of the atom $\gamma = [I_p/2U_p]^{\frac{1}{2}}$. A $\gamma \gg 1$ is characteristic of the multiphoton regime while $\gamma \ll 1$ is characteristic of a pure tunneling regime. The ponderomotive energy (U_p) is proportional to the laser intensity (I) and grows quadratically with its wavelength ($U_p \propto I\lambda^2$). To explore the deep tunneling regime, one can thus increase the laser intensity and/or increase the laser wavelength.

In order to move towards the tunneling regime, we decided to photoionize the fenchone molecules using the fundamental wavelength of our Ti: Sa laser (800 nm) rather than its second harmonic (400 nm). The PAD and PECD using λ = 800 nm, at two different laser intensities are shown in Fig. 4.16 (a), (b) and (d), (e). The PADs are constituted of a comb of photoelectron peaks separated by $\hbar\omega = 1.55$eV, which is characteristic of the ATI regime. The comb originating from the HOMO-1,2 ionization channel, which was present when using 402 nm pulse, does not show up anymore in the PAD. This observation goes hand in hand with a recent study of molecular strong field ionization which showed that ionization to excited cationic states was significantly suppressed if the gap between the ground and excited states was higher than the photon energy [Zhao et al. 2014]. In other words, ionization from orbitals deeper than $\hbar\omega$ from the HOMO is unfavored. Since in fenchone, the HOMO and HOMO-1 orbitals are separated by $\sim$ 2eV, the isolation of the HOMO ionization signal is possible when ionization is driven by 800 nm ($\hbar\omega = 1.55$eV),

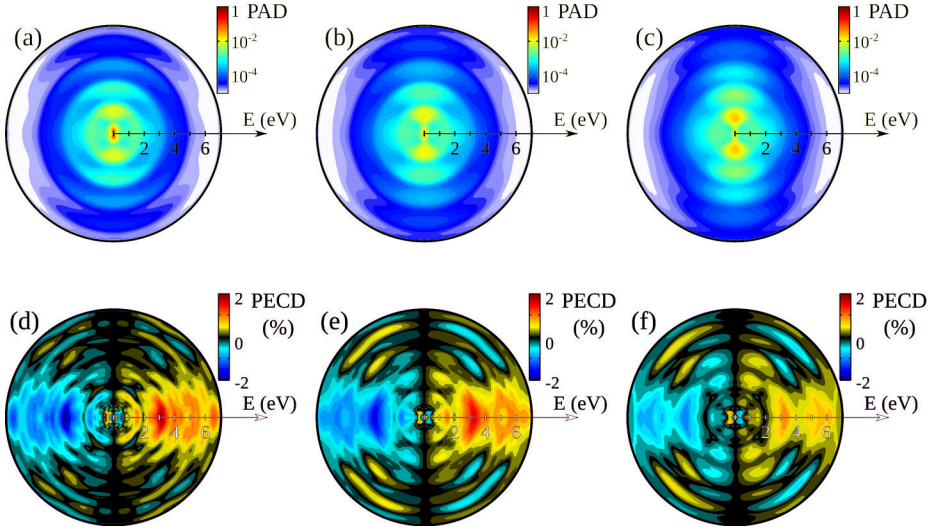

Figure 4.17: Laser intensity dependence of the PAD (a), (b) and (c) and the PECD (d), (e) and (f) of (+)-limonene using 800 nm pulses. The PAD are in logarithmic scale. The PECD is defined as 2(L-R)/(L+R). The energy scale goes from 0 to 7 eV. The laser energy per pulse was 10.5 μJ (a)/(d), 14.3 μJ (b)/(e) and 18.4 μJ (c)/(f). This figure is adapted from [Beaulieu et al. 2016b].

but less favorable when using 400 nm pulses ($\hbar\omega = 3.1$eV).

In order to enlighten the above-explained behavior, we have performed similar measurements in (+)-limonene molecules, where the HOMO/HOMO-1 gap is ~ 0.38 eV, i.e. smaller than the photon energy (1.55 eV). At the lowest laser intensity (Fig. 4.17(a)), the PECD is maximum along the laser propagation axis and has the same sign for all ATI peaks. As the laser intensity increases, the ATI peaks undergo a spectral broadening as well as an angular shrinking along laser polarization axis. This behavior is well known when approaching the tunnel ionization regime. At the same time, we see the appearance of repeatedly regular PECD features. Two combs separated by ~ 0.4 eV, with opposite sign and which maximize at a different angle with respect to the propagation axis are visible in the PECD in Fig. 4.17(c). These two combs most probably originate from the population of the ground- and the first-excited cationic state of limonene during strong-field ionization, which, in the Koopmans approximation, represents the ionization from the HOMO and the HOMO-1 orbitals, respectively. These results show that using 800 nm light is sufficient to isolate the contribution of the HOMO from lower-lying orbitals in fenchone (HOMO/HOMO-1 gap ~ 2eV), but is not sufficient in limonene (HOMO/HOMO-1 gap ~ 0.38eV).

Going back to the case of fenchone, (Fig. 4.16) the PES peaks show a global downshift in energy with respect to the positions inferred from field-free TDDFT calculations, which increases with laser intensity. This is the signature of the laser-induced ponderomotive shift, which is a typical feature of non-resonant ATI processes. As the intensity increases, the PECD diminishes, becomes blurred in energy, and the PAD shrinks angularly towards the laser polarization plane, i.e. the direction perpendicular to the light propagation axis (Fig. 4.16 (e)). These two features are signatures of being in the vicinity of the tunneling regime. Indeed, the Keldysh parameter associated to Fig 4.16 (b,e) is $\gamma = 1.9$, which is rather close to the limiting value of 1 which signs the entrance in the tunneling regime.

The last observations, using intense 800 nm pulses, give us indications that the PECD still exist at the entrance of the tunneling regime. However, with these irradiation conditions, we were still at the frustrating border between the multiphoton and tunneling

regime, where you cannot really claim to be well located on one side or the other of this frontier. To go deeply in the tunneling regime and make a strong conclusion, we decided to use 1850 nm, $I \sim 4 \times 10^{13}\mathrm{W/cm^2}$ pulses, corresponding to $\gamma \approx 0.6$. To do so, we needed frequency down-converted our Ti: Sa laser (800 nm) to the mid-infrared by using a High-Energy Optical Parametric Amplifier (HEOPA by *Light Conversion, Inc.*), similar to the one described in the first chapter of the thesis. Figure 4.16(c) and (f) presents the experimental 2D projections of the PAD and PECD. The shape of the PAD, strongly peaked about 90°, is typical of tunnel-ionized electron distributions. It extends up to energies corresponding to the absorption of more than 30 photons from the HOMO. Because of this really high number of absorbed photons, the Legendre polynomials decomposition would require a basis set with more than 60 polynomial orders, which would require very long calculation time. This is the reason why we present raw PAD and PECD and not the inverted one, as in previous figures. Also, because of the exponential decay of tunneling ionization rate with increasing I_p, only the HOMO orbital can be ionized.

The main difficulty in this experiment was related to the quality of the quarter wave plate used to produce LCP and RCP pulses. The 1850 nm pulses have a rather large bandwidth ($\sim$ 90 nm FWHM). We used achromatic waveplates to go from linearly to circularly polarized pulses, but it turned out that the subtraction of LCP and RCP images would never give an antisymmetric signal. This is because the two 'circularly polarized' pulses were, in fact, elliptical, with slightly different ellipticities, leading to slightly different intensities. To circumvent this issue, we performed measurements in the two opposite enantiomers of fenchone, and finally combined the sets of 4 measurements obtained with the two enantiomers and helicities to obtain the PECD. As a result, we were able to detect a clear PECD, in the order of $1-2\%$, from the threshold to electron kinetic energy up to 12 eV. We can notice that the PECD does not seem to get smaller as the electron kinetic energy increases, which is somehow remarkable. This demonstrates that the PECD still persists in this extreme ionization regime, even high above the threshold. This is a clear indication that the effect of the molecular potential on the outgoing electron dynamics is still significant, even in the tunneling regime.

4.3.6 Classical mechanics perspectives on PECD

The fact that PECD survives such high-intensity laser field is somehow remarkable, given the usual approximations that are made in such ionization regime. Numerical simulations could be of great help to understand how the molecular potential succeeds in imprinting its chirality on the outgoing electron wavepacket, in the presence of such high laser field. One possible way to do it is to solve the Time-Dependent Schrödinger Equation (TDSE) for toy-model chiral molecules in a strong CPL laser field. Indeed, fully solving the TDSE for a molecule as large as fenchone, embedded in a strong laser field is computationally far from reach. Also, the other drawback of TDSE calculations is that even if they provide accurate results, it is not trivial to extract intuitive information about the physics going on during the simulation. An alternative technique that can provide an intuitive picture of the electron dynamics in the combined laser+molecular field is Classical Trajectory Monte Carlo (CTMC) [Abrines et al. 1966] [Botheron et al. 2009]. These calculations were performed by our theoretician colleagues at CELIA, Bernard Pons, and Baptiste Fabre. CTMC methods make uses of repeated random sampling to simulate a system with of a lot of coupled degrees of freedom. They applied CTMC to the photoionization from the HOMO orbital of the fenchone molecule, in the single active electron and the fixed-nuclei approximation. The latter approximation consists of using a point-charges description of the ionic potential. To do so, they placed the nuclei and effective charges

on a 3D grid to mimic the quantum mechanical potential calculated using Hartree-Fock calculation [Schaftenaar et al. 2000]. The nuclei are not allowed to move during the simulation, meaning that we are in the Born-Oppenheimer approximation framework. After having determined the point-charge effective potential and after choosing a relevant initial phase-space distribution of the electrons, the temporal evolution of the system was calculated using the Liouville equation. This classical analog of TDSE takes into account (i) the interactions of the active electron with the inactive cloud of electrons, (ii) the electron-nuclei interactions and (iii) the interactions with the laser electric field (within the dipole approximation framework).

The CTMC simulation consisted of calculating the motion of $\mathcal{N} = 10^6$ independent trajectories for a single molecular orientation. The final (E,θ)- distribution of freed electrons is simply defined by counting among the $\mathcal{N} = 10^6$ independent electron trajectories those with positive energy at the end of the interaction (positive energy means above the ionization threshold). The calculation was then repeated for an ensemble of molecular orientations defined in terms of Euler angles with regular spacing $\Delta\alpha = \Delta\beta = \Delta\gamma = \pi/8\,\mathrm{rad}$, to simulate the random alignment of molecules in a gas sample. To mimic the photoionization of fenchone HOMO orbital in the tunneling regime, an 800 nm pulse of half-cycle duration, with a peak intensity of $I_0 = 10^{14}\mathrm{W/cm^2}$ was used. This condition corresponds to a Keldysh parameter of $\gamma \approx 0.85$, which is reasonably close to the experimental Keldysh parameter which is $\gamma \approx 0.6$. In the purely classical CTMC description, there is no such thing as tunnel ionization. However, some electron trajectories are able to jump over the potential barrier and be released in the continuum, mimicking the tunnel ionization step. Several studies of strong-field phenomena using CTMC have shown that this description was indeed quite accurate to describe even subtle features of the strong-field interaction [Higuet et al. 2011; Soifer et al. 2010].

A typical trajectory is shown in figure 4.18(a). One can see that the electron scatters many times onto the molecular potential before leaving its parent ion. This is the main source of PECD within the CTMC framework. The PAD and its associated PECD are shown in figure 4.18(b), on the bottom and the upper panel respectively. The classical simulations are in very good qualitative agreement with the experimental results of Figures 3(c) and (f). In the commonly accepted picture of tunneling, the electron is freed at a distance $r, \sim \mathrm{I_P}/\mathrm{F_0}$ from the center of the target, where $\mathrm{F_0}$ is the maximum strength of the pulse electric field. Using Hartree–Fock results for $\mathrm{I_P}$, this yields $r \sim 7$ a.u. The ionic potential still presents small chiral anisotropy beyond such distances, which can thus induce small PECD. However, as stated earlier, the main source of PECD is expected to be due to the multiple scattering of the outgoing electron onto the chiral molecular potential when driven by CPL field.

Purely classical calculation is able to reveal the origin of PECD in the deep tunneling regime. Since single-photon ionization can also be studied using classical simulations, one can try to bridge the gap between our understanding of the emergence of PECD in single-photon and in strong-field ionization. To do so, we will now focus on single-photon ionization of fenchone, using the sudden approximation. Within this framework, the absorption of a photon, at a random time within the laser cycle, instantaneously modifies the electron momentum without affecting its position. The electron is given an energy of $\hbar\omega - \mathrm{I_p}$ and its subsequent dynamics is simulated over three laser cycle, during which the electric field is linearly ramped down to zero. In the simulation, a photon energy of 9.3 eV was used, which is $\sim 0.5eV$ above the ionization threshold. The resulting PAD and PECD are presented in figure 4.18 (c). Both the angular and the energy distributions of the photoelectrons are, as expected, completely different from the case of tunnel ionization. A

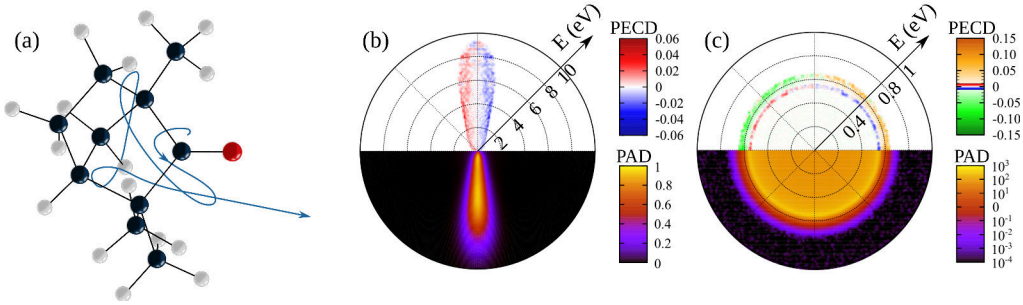

Figure 4.18: Typical ionizing CTMC electron trajectory in fenchone embedded in a circularly polarized laser pulse with $\lambda = 800,\text{nm}$ and $I = 10^{14}\text{W/cm}^2$ (a). PAD (bottom half) and PECD (top half) from CTMC calculations in the tunneling (b) and single-photon (c) ionization regimes. The light propagation axis is horizontal and the radius extends up to 10 eV in (b), and up to 1 eV in (c). This figure is adapted from [Beaulieu et al. 2016b].

narrow ring of energy is obtained from the PAD. At the maximum of the PAD, the PECD is quite weak ($\sim \pm 1\%$). However, on the blue wing of the PAD, the PECD changes sign and reaches $\sim \pm 15\%$. This observation means that the classical description of the single-photon ionization within the sudden-approximation framework is able to tackle the kinetic-energy dependence of the PECD, *i.e.* the different scattering dynamics onto the chiral potential for electrons with different kinetic energies. This kinetic energy dependence is well known from experimental results as well as from advanced quantum mechanical calculations [Powis 2008; Stener et al. 2004].

4.3.7 Partial conclusions and perspectives

We have studied PECD in a broad range of ionization regimes, ranging from single-photon to tunnel ionization. We have shown that PECD is a universal effect in the photoionization of chiral molecules using circularly polarized radiation. The chiral character of the molecular potential is able to imprint its signature onto the PAD, whatever the ionization regime, which is quite remarkable. In this work, we have bridged the gap between the generality of one-photon XUV PECD and the versatility of femtosecond laser sources by demonstrating that PECD could be observed in non-resonant multiphoton/tunnel ionization. The fact that PECD still exists in the strong-field regime is indeed not so intuitive because this regime is often successfully described using the strong-field approximation, in which the influence of the chiral molecular potential is neglected. Our CTMC calculations have revealed that even in a strong laser field, the chiral potential was able to significantly affect the ionizing electrons, imprinting a forward/backward asymmetry. We have shown that this effect was qualitatively similar to the one at the origin of one-photon PECD. Thus, strong-field PECD should be a general effect, as XUV PECD is. Its magnitude will, of course, depend on the molecules, and it may be very weak in some specific cases.

The fact that PECD exists in the case of purely non-resonant photoionization is a fairly good news for the future application of table-top multiphoton-PECD scheme for analytical purposes. Indeed, it can be envisioned that using of a high-repetition rate ('turn-key/alignment-free') Yb-based laser coupled to a well-suited photoelectron detection technique will enable the chiral discrimination in the gas-phase almost in real-time, which could potentially be a highly attractive technique for people doing stereospecific synthetic chemistry, for example. The fact that PECD is universal and exists even in the purely non-resonant ionization scheme will allow using a single wavelength to performed chiroptical analysis on a broad scope of molecules, without having to tune the laser wavelength to hit

an electronic resonances, which are located at different energies for different molecules, like it is the case in REMPI-PECD.

From a more fundamental point of view, the variety of ionization regimes in which PECD can be measured offers interesting perspectives to obtain complementary pictures of the chiral response. Tuning the wavelength and intensity of the driving laser in the multi-photon and ATI ranges enables probing different electronic ionizing states, from one-electron (Koopmans) to two-hole-one-particle configurations. Vibrationally resolved PECD is also accessible in the multiphoton regime. All of this opens the route to more sophisticated multi-color ionization experiments, were laser pulse parameters can be fully controlled independently, to enable multi-dimensional coherent control of PECD.

The fact that PECD exists in the strong-field ionization regime also paves the way towards its link with attosecond science. The fact that strong-field ionization occurs in a really short (attosecond) time window is one of the pillars of attosecond science. It is the fundamental reason of the attosecond confinement of electron wavepackets during strong field ionization, and one of the reasons of the attosecond duration of XUV pulses produced during high-order harmonic generation. Extending well-established attosecond metrology techniques to the photoionization of chiral molecules with circularly polarized strong fields can potentially enable tracking the F/B asymmetric electron dynamics on their natural timescale. This type of studies will be presented in the last chapter of this thesis.

One of the questions that remain open after this extensive study is the role of intermediate resonances in REMPI-PECD. Because we were using a single laser pulse configuration, the transition from the electronic ground state to intermediate excited states and the ionization from the intermediate to the continuum states were naturally intertwined. Indeed, it was not possible to tune a laser parameter that would have affected only one of the two steps and thus help us to decoupled their individual role in the build-up of PECD. In the following section, we will use multi-color pulses with fully controllable polarization states to decouple the excitation and ionization step in REMPI-PECD.

4.4 Role of Bound-Bound and Bound-Continuum Transitions in REMPI-PECD

4.4.1 Introduction

Resonance Enhanced Multiphoton Ionization (REMPI) can be described as a sequential two-steps mechanism, where a n photon(s) transition resonantly promotes an electron to an excited state (bound-bound transition) and a m photon(s) transition drives a bound-continuum transition from the excited state. This REMPI scheme is labeled $[n+m]$. In REMPI of chiral molecules using CPL pulses, the role of bound-bound and bound-continuum transitions on the emergence of F/B asymmetry in the PAD is currently the subject of many experimental and theoretical investigations. It is of capital importance since laser-based PECD, where resonant enhancements are often involved, promises to become a powerful and easily implementable chiroptical analytical tool. Experimentally, it is not trivial to decouple the role of the two-steps because when changing an experimental parameter, one will often influence both steps simultaneously, preventing to make a conclusion about the physics behind each step of the REMPI process.

As we will see later, one of the goals of this thesis was to bring a new dimension to PECD, namely the time-resolution. In order to perform time-resolved PECD, we have built two-color (199 nm + 396 nm and 396 nm + 800nm) Mach-Zehnder interferometers allowing to fully control the polarization state of each color independently. We had the idea of using these setups to try to learn something about the role of intermediate

states in REMPI-PECD. The idea was the following: because a chiral object responds in a stereospecific way only when it interacts with another chiral object, we can decouple the bound-bound and bound-continuum steps of REMPI by rendering one of the two steps non-chiral. For example, if the bound-bound transition is driven by CP (LP) photon(s) and the bound-continuum transition with LP (CP) photon(s), only the first (second) step should be chirosensitive. In addition, we can also drive the different transitions with a different combination of helicity (LCP/RCP) and study the effect of the relative chirality of the light fields on the measured PECD. We thus measured PECD using two-color fields (in [1+1'] (199 nm + 396 nm) and [2+2'] (396 nm + 800 nm) configurations), for various polarization states in an ensemble of limonene molecules.

During the analysis of these results, a theoretical paper on REMPI-PECD by Goetz *et al.* [Goetz et al. 2017] came out and helped us a lot to extract conclusions from our experimental data. In this paper, Goetz *et al.* introduced an approach to model the prototypical [2+1] REMPI-PECD scheme, which has been the most widely studied, in particular in the pioneering experiment in fenchone and camphor molecules [Lehmann et al. 2013; Lux et al. 2012]. They used *ab initio* model to calculate the ground- to intermediate-states two-photon transition dipole matrix elements (bound-bound transition). Following this first step, they used perturbation theory to calculate the single photon ionization from the intermediate states (bound-continuum transition). Like in our proposed experimental scheme, the great advantage of their theoretical framework is the ability to fully decouple the excitation and the ionization. In particular, they can analyze the influence of the laser polarization state for each individual step of the [2+1] ionization process and determine the requirement for yielding non-zero PECD.

The theoretical paper of Goetz *et al.* draws several conclusions which are deeply connected to our experimental investigation: (i) First, their calculations showed that the main role of the bound-bound transition is to break the isotropy of the molecular ensemble, due to the angular dependence of the bound-bound transition dipole matrix elements. Indeed, molecules with a given orientation with respect to the polarization plane will be photo-selected by the transition, yielding an anisotropic distribution of molecular orientation in the excited intermediate state. (ii) They showed that this symmetry breaking by the bound-bound transition leads to the appearance of more complex angular distribution of the PECD, reflected by the contribution of high-order Legendre coefficients. Indeed, if the bound-bound transition is isotropic, then the single photon ionization step occurs from an isotropic ensemble, as in XUV-PECD, and only the first odd Legendre polynomials contribute to the PECD. One could thus indirectly reveal the anisotropy of the bound-bound transition from the high-order odd Legendre coefficients (b_{2N-1}, where $N > 1$). (iii) They demonstrated that driving the bound-bound transition with circularly polarized photons was not necessary to produce PECD. Only the ionizing photon(s) need to be circularly polarized to observe PECD, which is pretty intuitive given the conclusion (i).

4.4.2 Experimental details

This experiment was performed using the 1kHz Ti: Sapphire Aurore laser system from CELIA. For the 396 nm + 800 nm experiments, the pulses were sent in a (50%/50%) Mach-Zehnder interferometer, where one of the two arms was frequency-doubled in a 200 μm thick type I BBO crystal. In each arm, we placed a broadband zero order quarter wave plate to control the polarization states of the 800 nm and the 396 nm pulses independently. After the quarter wave plates, all the reflective optical components were at $\sim 0^o$ incidence angle to preserve circular polarizations. The pulses were recombined by a dichroic mirror and were focused by using a 1000 mm focal lens into a velocity map imaging spectrometer.

The (+)-limonene molecules were introduced as a continuous flow through a 200 μm nozzle heated at 60^{o}C and located 7 cm away from the laser focus. The pressure in the interaction chamber was typically 1x10^{-6} mbar, with a background pressure of 7x10^{-8} mbar.

For the 199 nm + 396 nm experiments, the setup was slightly different. One part of the laser beam was used to generate the 199 nm pulses by sum frequency generation between the fundamental 800 nm and its third harmonic (267 nm) in a 100 μm thick BBO crystal. The second arm was frequency doubled from 800 nm to 396 nm in a 100 μm BBO crystal. The pulses were focused with a 250 mm and a 600 mm lens into a pulsed (1 kHz) molecular beam produced by an Even-Lavie valve [Even et al. 2000] with a 250 μm conical nozzle, at a temperature of 60^{o}C and backed with a carrier gas of helium to avoid cluster formation.

In all experiments, the photoelectrons were imaged by an electrostatic lens onto a set of two micro-channel plates (MCP) coupled to a phosphor screen (P43), and recorded by a cooled 12 bit CCD camera. The PECD was measured by recording the photoelectron spectra with left (LCP, $p = +1$) and right (RCP, $p = -1$) circularly polarized laser pulses. In order to remove the influence of slow drifts in the experiments, the polarization state was switched every 10 seconds. Typically, $\sim$3x10^5 laser shots were accumulated to obtain the LCP or RCP images. Measurements using different polarization states were conducted at constant pulses energies. In two-color measurements, the pulse energies were kept low enough to observe ionization only when the two pulses were present. The data analysis and the Legendre coefficients extraction procedure was the same as described earlier in this chapter.

4.4.3 Results and discussions

The first step of our study was to record PECD in a [2+1] REMPI-scheme, using single 396 nm pulses. All the photons involved in the transition have the same helicity. This situation will later be used for comparison with the two-color [1+1'] and [2+2'] cases, where a different combination of linearly and circularly polarized photons can be used. Fig. 4.19 shows the comparison between raw and inverted PES and PECD of (+)-limonene using a [2+1] photoionization scheme at 396 nm. The figure is presented in order to emphasise the high quality of the experimental data, even before pBasex inversion.Figure 4.20 (b) shows the PES (bottom panel) with two well-defined broad peaks centered about 0.3 eV and 0.9 eV. As described earlier in this chapter, the spectroscopic identification of ionization channels is based on energy conservation, on two-photon accessible resonant intermediate states and on the $\Delta\nu = 0$ propensity rule for photoionization of Rydberg states. The first adiabatic ionization threshold of limonene being at 8.52 eV [Smialek et al. 2012] the peak around 0.9 eV can be assigned to ionization of the HOMO leaving the ion in the electronic and vibrational ground state ($2\pi^{-1}(\nu = 0)$) (3 x 3.13 eV - 8.52 eV = 0.87 eV). This assignment is in good agreement with the one of Rafiee Fannod *et al.* [Rafiee Fanood et al. 2016], when they were using 392 nm (3.16 eV) pulses. The spectroscopic assignment of the low-energy (0.3 eV) peak is, however, more challenging. Indeed, based on simple energy conservation consideration, this peak could come from two different pathways: the production of a vibrationally excited ground state cation ($2\pi^{-1}(\nu = 3)$) or by the production of a cation in its first vibrational and electronic excited states ($1\pi^{-1}(\nu = 1)$). Recently, a clever comparison between VUV PES (9.5 eV) and REMPI-PES (3 x 392 nm) of limonene allowed assigning this low-energy peak to the formation of an electronically excited cationic state ($1\pi^{-1}$) [Rafiee Fanood et al. 2016]. We will thus assume that this spectroscopic assignment is valid and assign our 0.3 eV peak to the formation of an

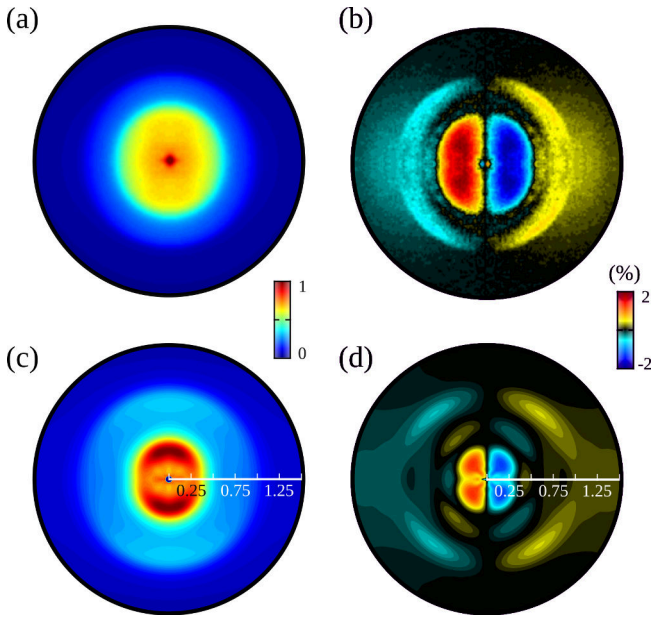

Figure 4.19: Comparison between raw and inverted PES and PECD of (+)-limonene using a [2+1] photoionisation scheme at 396 nm. (a) and (b) are the raw VMI images of the PES and PECD, respectively. In (c) and (d) are the pBasex inverted PES and PECD, respectively. The laser propagation axis is horizontal.

electronically excited cationic state ($1\pi^{-1}$), which, in the Koopmans approximation, results from the ionization of HOMO-1 orbital. It is important to note that the vibrational quanta referred above is associated to a vibrational excitation of the ring C=C stretching mode ($\sim$ 1500 cm^{-1} = 185 meV). This mode was identified as the dominant mode in previous PECD studies on limonene [Rafiee Fanood et al. 2016] [Lehmann et al. 2013] [Smialek et al. 2012]. A vibrational progression scheme, using this 185 meV vibration quantum, for the ionization of the two lower-lying orbitals, is plotted above the b_i decomposition of the PAD and PECD to ease their spectroscopic assignment (see for example Fig. 4.20).

Now that we have assigned the main PES peaks, we will focus on the PECD of (+)-limonene in the one-color [2+1] photoionization scheme 4.20. Note that all the measured PECD (in their Legendre polynomials decomposition) will be presented in a synthetic Table 4.2. In the upper hemisphere of Fig. 4.20(a), the 2D map representing the difference image (L-R) have been normalized by the absolute maximum of the PES ((L-R)/max(L+R)). This normalization, compared to the usual normalized PECD=2(L-R/L+R), is useful to avoid spuriously large PECD values where the PES (L+R) is small. However, as one can see in Fig. 4.20(b), we have normalized the extracted odd Legendre coefficients by the energy-resolved PES ($b_i(E)/b_0(E)$), in order to give quantitative physical quantities. Since the number of ionizing photons is $N = 3$, Legendre polynomials up to the 5^{th} order (b_5) can contribute to the PECD. However its experimental value ($b_5/b_0 < 0.1$ %) being negligible compared to the ones of b_1/b_0 and b_3/b_0, we do not plot it for sake of clarity. The limonene PECD shows three peaks at $\sim$ 0.90, 0.60 and 0.25 eV, maximizing around $\theta = 45^o$. While the PECD peaks around 0.9 eV and 0.25 eV clearly correlate with the PES channels identified above ($2\pi^{-1}(\nu = 0)$) and $1\pi^{-1}(\nu = 1)$, respectively), the PECD peak around 0.6 eV is not associated with a clear feature in the PES. However, as assigned in a previous study [Beaulieu et al. 2016b], this PECD peak is associated with the production of a cation in the $2\pi^{-1}(\nu = 2)$ state. This is a good example of one of the great powers of

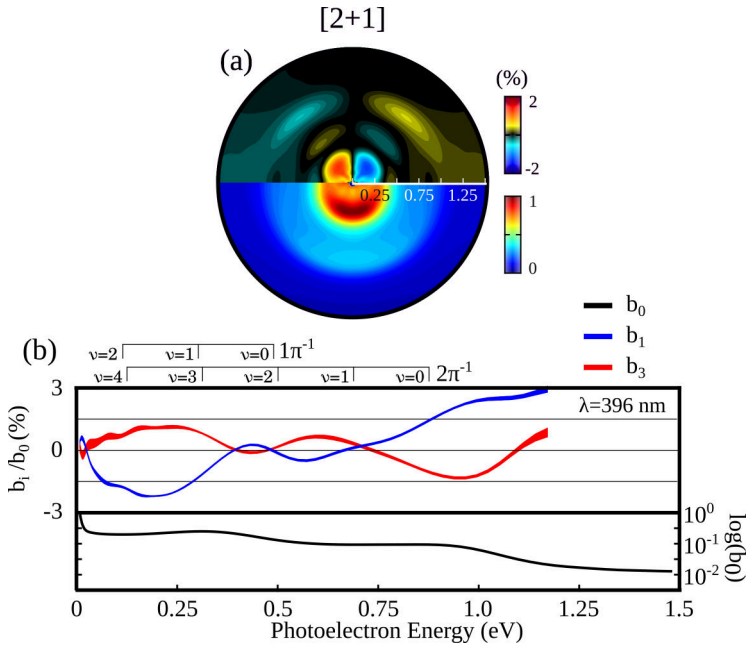

Figure 4.20: PECD of (+)-limonene using a [2+1] photoionisation scheme at 396 nm. In (a), the lower hemisphere is a cut of the 3D-PAD, in linear scale. The upper hemisphere represents the a cut of the 3D-PECD (pBasex) that has been further normalized by the absolute maximum of the PES signal. The radius represents the energy of the photoelectrons, in eV. The laser propagation axis is horizontal. In (b), the upper panel shows the normalized $b_i(E)/b_0(E)$ (i=1,3) odd Legendre coefficients. The thickness of the lines ($b_i(E)/b_0(E)$) represent the 90 % confidence interval determined using Student's statistics, based on 25 individual measurements of $b_i(E)/b_0(E)$ (each individual measurement is an average over 10000 laser shots, for each helicity). The PES $b_0(E)$ is shown in logarithmic scale in the lower panel. Above (b) is a spectroscopic identification of the vibrational progression for the population of cationic ground- ($2\pi^{-1}$) and excited-state ($1\pi^{-1}$). As in [Rafiee Fanood et al. 2016] [Lehmann et al. 2013] [Smialek et al. 2012], we assume a vibrational excitation of the ring C=C stretching mode ($\sim$ 1500 cm^{-1} = 185 meV)

PECD: some features that are hidden in PES due to spectral overlap of an adjacent peak can sometimes be revealed in PECD spectrum due to its differential nature. At 0.9 eV, both the b_1 and b_3 have opposite signs compared with the two other PECD peaks. These results thus indicate sign changes of the REMPI-PECD upon vibrational excitation of the ion, and between adjacent molecular orbitals, two properties that are often observed in single-photon VUV PECD measurements [Daly et al. 2011; Garcia et al. 2014; Nahon et al. 2006; Powis et al. 2008]. Note that the thickness of the $b_i(E)/b_0(E)$ lines, in Fig. 4.20(b), represents the 90 % confidence interval determined by performing the pBasex analysis for 25 individual PES and PECDs, and by a statistical analysis on the resulting Legendre coefficients. The statistics being similar in all our measurements, we only include the error bars on this figure.

We have presented in great detail the case of single pulse [2+1] PECD of limonene. From this simple ionization scheme, we have seen that we can learn a lot about the PECD from different ionization channels. However, as explained earlier, because of the single pulse nature of this scheme, the excitation and the ionization step of the REMPI pathway are intertwined. In an attempt to decouple these two steps, we used multicolor fields with fully tunable polarization states. First, we kept the photoexcitation step identical (2 photons at 396 nm) but we replaced the photoionization step by a two-photon transition (2 photons at 800 nm), which results in a [2+2'] instead of a [2+1] ionization scheme. To

ease the comparison with the single pulse [2+1] scheme, we start by using co-rotating CPL photons for both 396 nm and 800 nm. The two 396 nm photon leads to the population of the same states around 6.26 eV. However, the absorption of the first 800 nm photon from the low-lying 3s Rydberg states leads to an energy range where many high-lying Rydberg states can be populated ($\sim$ 7.8 eV). This scheme can thus be considered as a [2+1'+1'] scenario (Fig. 4.21(a)). Since the 800 and 396 nm pulses are synchronized, this scheme is in competition with others, such as for instance [1+2'+1]. We expect the [2+1'+1'] pathway to be dominant because of its doubly resonant character. The PAD and PECD obtained, in this case, are very differents from those from the [2+1] case (Fig. 4.21(a)). The PES shows a shoulder at $\sim$ 0.17 eV and a peak around 0.65 eV. The PECD peaks around 0.25 eV with negative b_1 and b_3 values, both weaker than in the [2+1] scheme. It shows a complicated angular and energy dependence. We interpret this as the result of the high number of Rydberg states that can be populated around 7.8 eV by the 2+1' transition [Smialek et al. 2012]. PECD is known to be highly sensitive to molecular orbitals and vibrational excitation. Here, many different electronic and vibrational excited states contribute to the signal, with possibly different signs, energy and angular dependences of PECD. As a result, the total PECD, which is the incoherent sum of the PECD from different excited states, is weak and strongly modulated. This REMPI pathway involving the population of many high-lying Rydberg states does not seem to be well suited to make neither qualitative nor quantitative comparison with the single pulse [2+1] case. We will thus move to another REMPI scheme.

In order to investigate the influence of the photoexcitation pathway in REMPI-PECD, we replaced the two-photon excitation (2 x 396 nm) by a single (199 nm) photon excitation, while driving the bound-continuum transition with a single (396 nm) photon. Again, to ease the comparison with the single pulse [2+1] case, we start by using co-rotating two-color fields. The PES and PECD obtained in this co-rotating [1+1'] scheme are shown in Fig. 4.21(b),(c). On the contrary to the [2+2'] ([2+1'+1']) case, here the PES and the PECD shows simple features which can be compared with the single pulse [2+1] case. For the low energy peak, the PECD has the same sign and angular structures as in the [2+1] scheme while its magnitude is a bit weaker. The PECD peak around 0.6 eV present in the one-color [2+1] scheme, which was assigned to originate from the $2\pi^{-1}(\nu = 2)$ channel, is absent in the [1+1'] scheme.

For the high energy peak ($2\pi^{-1}(\nu = 0)$), the sign of the PECD reverses compared to the [2+1] case, while its angular dependency stays similar. These results reveal a significant influence of the excitation scheme on the PECD. They may seem surprising at first sight because we do not expect selection rules to lead to the excitation of different Rydberg states in such a large polyatomic molecule. However, another effect is at play: the orientation-dependence of the photoexcitation process. This dependence breaks the isotropy of the sample, leading to a partial alignment of the electronically excited molecular ensemble in the polarization plane.

Recent measurements of single-photon ionization of chiral molecules in the molecular frame showed that PECD could have opposite sign for molecules aligned parallel or perpendicular to the light propagation direction, which considerably reduces the value of PECD after averaging over all molecular orientations [Tia et al. 2017]. Indeed this is greatly illustrated by Fig. 4.22, which is the PECD measured upon dissociative ionization from the oxygen 1s orbital of methyloxiran as a function of both the electron ejection angle and the molecular orientation angle. This effect is consistent with our observations. The two-photon excitation of the [2+1] leads to a sharper alignment distribution than the single-photon process of the [1+1']. The overall value of the PECD is thus expected to

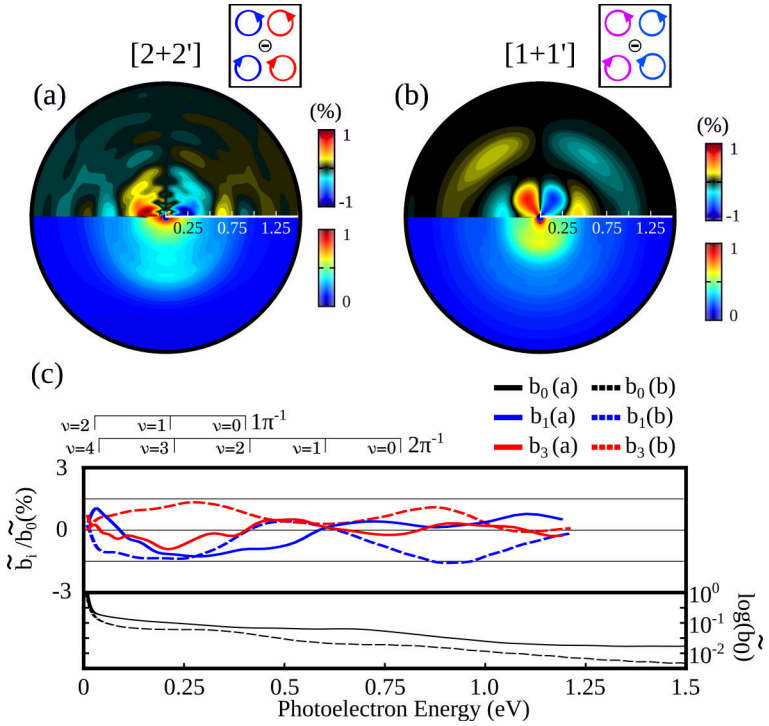

Figure 4.21: PECD of (+)-limonene using corotating two-color laser fields. In (a), we used a [2+2′] (396 nm + 800 nm) scheme while in (b), we used a [1+1′] (199 nm + 396 nm) ionization scheme. As in figure 4.20, the lower hemisphere is the photoelectron angular distribution (PAD) in linear scale, while the upper one is the PECD normalized by the absolute maximum of the PES (L-R/max(L+R)). In (c), the upper panel show the normalized polynomials decomposition of the PECD. The thick (dashed) blue line represent the $b_1(E)$ for the [2+2′] ([1+1′]) scheme, while the thick (dashed) red line represent the $b_3(E)$ for the [2+2′] ([1+1′]) scheme. For the lower panel, the thick (dashed) line represent the PES for the [2+2′] ([1+1′]) ionization scheme.

be larger in the two-photon excitation case. Furthermore, since PECD can change sign depending on the orientation, different alignment distributions can lead to different signs of PECD, as observed in the high-energy peak, around 0.9 eV.

Controlling the number of photons involved in the photoexcitation and photoionization steps is not the only degree of freedom in our experiment. Since we have a full control over the polarization states of both color independently, we can further decouple the role of bound-bound and bound-continuum transitions. We will now record the photoelectrons coming from the photoionization of (+)-limonene by using [1+1′] REMPI scheme, with a different combination of relative polarizations, including linear polarization cases. The simultaneous use of linearly and circularly polarized radiation breaks the cylindrical symmetry which is necessary to retrieve the photoelectron angular distribution from its projection on the velocity map imaging spectrometer by Legendre polynomials decomposition. In order to extract the PAD and PECD, we would need to directly resolve the 3D photoelectron distribution using another type of detector [Dörner et al. 2000] or to perform a tomographic reconstruction by rotating the polarization direction of the linearly polarized pulses [Wollenhaupt et al. 2009]. Nevertheless, we still decompose the projected images into Legendre polynomials to extract a PAD and PECD. In the case where the cylindrical symmetry is broken by the use of linearly polarized photon(s), we will thus use the followed notation: $\tilde{b_i}$, $\widetilde{PES}$ and $\widetilde{PECD}$.

As a reminder, the idea behind using linearly polarized photon in one of the two-steps

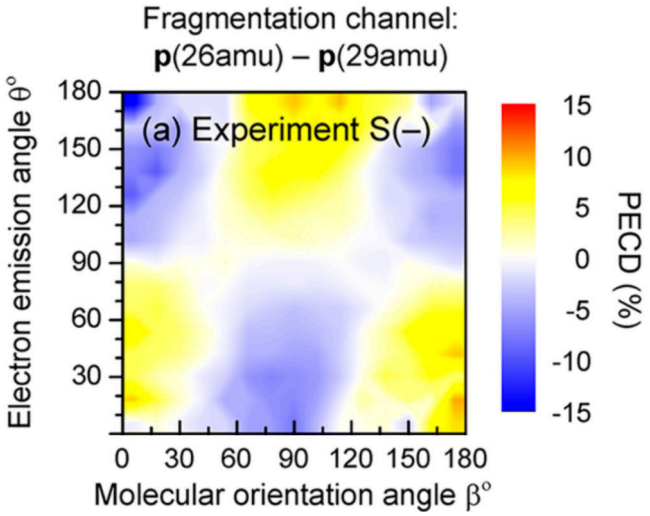

Figure 4.22: Photoelectron circular dichroism measured in S-(-)-methyloxiran enantiomer as a function of the photoelectron emission angle θ and the molecular orientation angle β. The molecules have been ionized from the oxygen 1s orbital, which triggers the dissociation of methyloxirane into 26 amu and 29 amu fragments. The coincidence detection of both fragments and photoelectrons allow one to determine the PECD in the (uniaxially determined) molecular frame. This figure has been adapted from [Tia et al. 2017].

of REMPI is to render it completely non-chiral. When doing that, only one of the two steps (photoexcitation or photoionization) will be sensitive to the chirality of the molecular potential. Figure 4.23(a) shows the results obtained by driving the bound-bound transition with a linearly polarized ($p = 0$) 199 nm photon and photoionizing with a circularly polarized ($p = \pm 1$) 396 nm photon. In this case, only the photoionization step is sensitive to the molecular chirality. The overall $\widetilde{PECD}$ is stronger than in the fully circular [2+1] and [1+1'] cases (see table 4.2). The $\widetilde{PECD}$ from the higher energy peak, associated to ionization from the HOMO, has the same sign as in the [1+1'] case and is about twice larger when driven by linear photons compared to circular. These results illustrate once again the importance of the photoexcitation anisotropy and provide interesting information on the angular dependence of $\widetilde{PECD}$. For the HOMO, ionization of molecules selected by one or two-photon circular excitation produces $\widetilde{PECD}$ with opposite signs. Because the bound-bound transition preferentially promotes the molecules that have their transition dipole parallel to the laser electric field into Rydberg states, the use of linear exciting photons photoselects a *axis*, while the use of circularly polarized photon photoselects a *plane* of molecular orientations. A schematic representation of the effect of the pump polarization state on the partial selection of molecular orientations by the photoexcitation process is shown in Fig. 4.24.

The PAD and the PECD being the incoherent sum over all molecular orientations of the Rydberg states, it is not surprising to see a difference when driving the bound-bound transition with linear or circular photons. Looking at the table 4.2, it is also clear that the use of linear photon leads to a greater enhancement on the b_3 than on the b_1, since b_3 is the observable with the larger sensitivity on the photoexcitation anisotropy. Also, the fact that the $\widetilde{PECD}$ is non-zero agrees with the finding of Goetz *et al.* [Goetz et al. 2017]: using their combined *ab initio*/perturbation theory to treat the excitation/ionization steps, respectively, they conclude that driving the bound-bound transition with linear and the

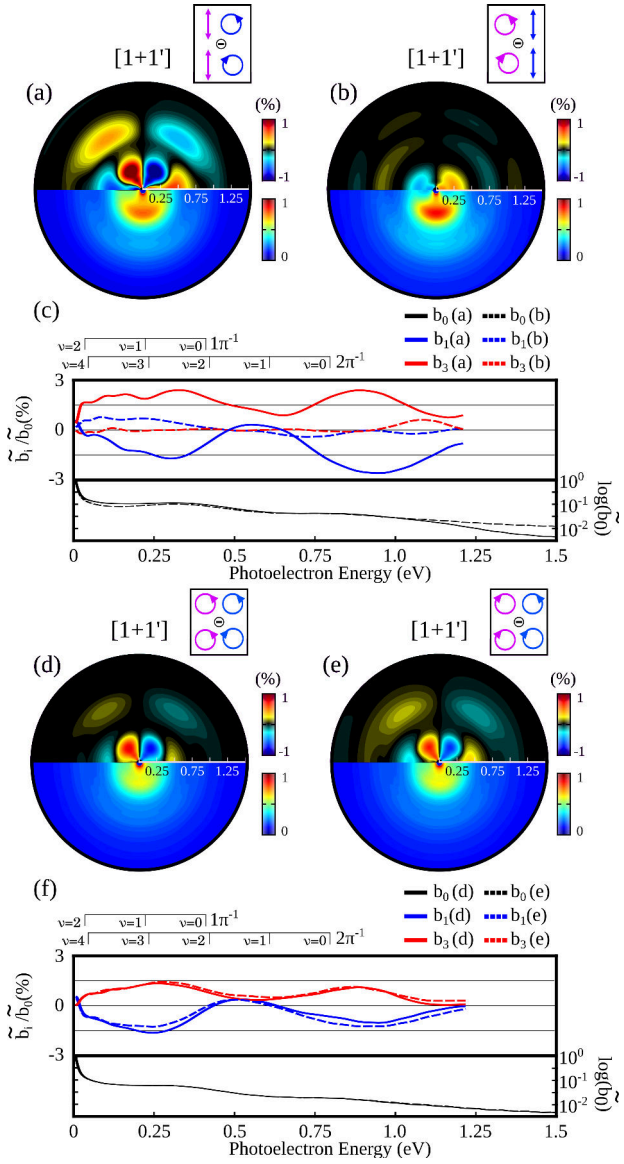

Figure 4.23: PECD of (+)-limonene in [1+1'] (199 nm + 396 nm) ionization scheme using various polarization combinations. As in previous figures (4.20 and 4.21), the upper hemisphere is the PECD normalized by the absolute maximum of the PES (L-R/max(L+R)) while the lower hemisphere is the photoelectron angular distribution (PAD). In (a), the 199 nm was linearly polarized while the 396 nm was circularly polarized. In (b), the 199 nm pulse was circularly polarized while the 396 nm was linearly polarized. In (c), the upper panel represents the normalized odd Legendre polynomials decomposition of the PECD for (a) (thick lines) and (b) (dashed lines) case. The lower panel represents the PES for (a) (thick black line) and (b) (dashed black line) case. For (d) and (e), we have done the same analysis but using different polarization scheme. As in (a) and (b), the polarization of both 199 nm and 396 nm are indicated in the square black box. The purple arrow represents the polarization state of the 199 nm pulse while the blue arrow represents the polarization state of the 396 nm pulse.

bound-continuum transition with circular photon(s) is sufficient to yield non-vanishing PECD. This finding is important in the perspective of doing time-resolved PECD. It means that in such pump-probe PECD experiment, one could initiate the dynamics with linear photons and follow the dynamics by recording PECD with alternating LCP and RCP probe. We will present the implementation of this scheme in the next chapter.

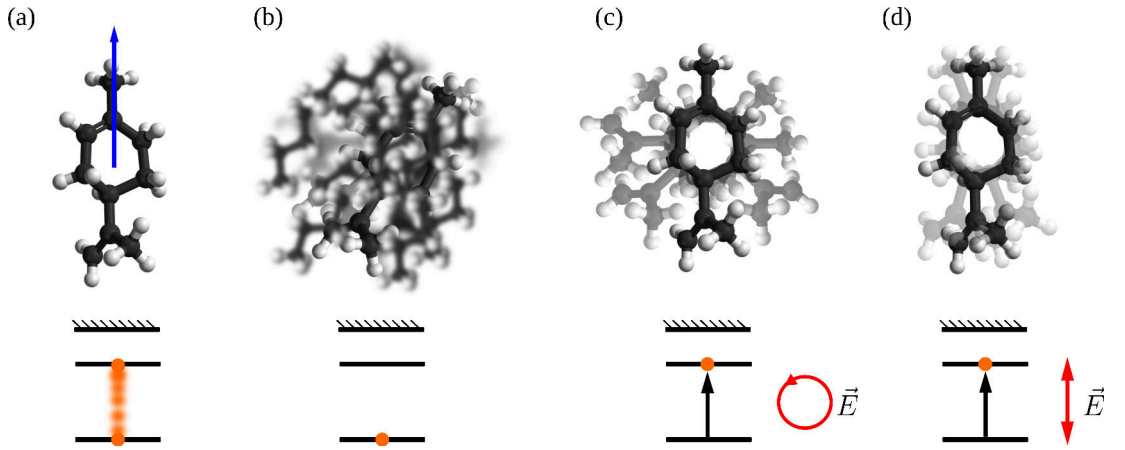

Figure 4.24: Effect of the polarization state on the photoexcitation induced molecular orientations selection. In (a), a limonene molecule with a fictive transition dipole moment (upper panel) for a transition from the ground state to a given Rydberg state (represented in the lower panel). In (b), a sample of randomly oriented limonene molecules in their ground electronic state. In (c), a sub-ensemble of limonene molecules that has been excited to a Rydberg state by a circularly polarized light (CPL). One can notice that CPL photoselect molecules which have their transition dipole moment in the plane of the light polarization. In (d), a sub-ensemble of limonene molecules that have been excited to a Rydberg state by a linearly polarized light. One can notice that linearly polarized light photoselect molecules which have their transition dipole moment with the axis of the light polarization.

Next, we can invert the polarization states of the exciting and ionizing fields to render the photoionization step completely insensitive to the molecular chirality. The only step which is chirosensitive is the photoexcitation from the ground state to the intermediate states, which is driven with CPL photon. For such bound-bound transition in chiral molecules, it is well known that the photoabsorption cross section depends on the helicity of the light, via the well-known absorption Circular Dichroism (CD). This CD is usually very weak; on the order of $10^{-4} - 10^{-5}$ with respect to the total photoabsorption cross section. We thus do not expect to measure PECD while driving the bound-bound transition with CPL and the photoionization with a linear photon. The theoretical paper of Goetz *et al.* also predicts a vanishing PECD for this polarization state configuration.

Figure 4.23(b) presents the experimental results for the latest described polarization states configuration. Remarkably, we see a clear non-vanishing forward-backward asymmetry, consisting solely of first-order Legendre polynomials (pure $\tilde{b_1}$). This measurement of non-vanishing asymmetry disagrees with the model based on perturbation theory developed by Goetz *et al.* [Goetz et al. 2017]. We will see later in this thesis that this relatively strong PECD results from a new chiroptical effect called PhotoeXcitation Circular Dichroism (PXCD), which occurs when a bound wavepacket is prepared by the CPL pump.

Last, we study the effect of the helicity of the photon that drives the bound-bound transition relative to the ionization step in PECD. We can do this by comparing the PECD obtained from molecules photoexcited by a left and right photons (Fig. 4.23(d,e,f)). We drive the bound-bound transition with a given circular polarization of the 199 nm pulse ($p = +1$ in (d) and $p = -1$ in (e)) and ionize alternatively with $p = +1$ and $p = -1$ circularly polarized 396 nm pulse in order to measure the difference between the PAD driven with co-rotating and counter-rotating two-color fields. Both cases lead to very similar PADs and PECDs. This observation strengthens the conclusion that the role of

Ionisation Scheme		[2+1]	[1+1′]	[1+1′]	[1+1′]	[1+1′]	[1+1′]	[1]
Polarization State		(1,1)-(-1,-1)	(1,1)-(-1,-1)	(0,1)-(0,-1)	(1,0)-(-1,0)	(1,1)-(1,-1)	(-1,1)-(-1,-1)	
Figure		Fig. 4.20 (a)	Fig. 4.21 (b)	Fig. 4.23 (a)	Fig. 4.23 (b)	Fig. 4.23 (c)	Fig. 4.23 (d)	Ref. [Rafiee Fanood et al. 2017]
$2\pi^{-1}$	b_1/b_0 (0.90 eV)	1.7 %	-1.6 %	-2.5 %	0 %	-1.0 %	-1.2 %	-1.0 %
$2\pi^{-1}$	b_3/b_0 (0.90 eV)	-1.2 %	1.0 %	2.5 %	0 %	1.0 %	1.0 %	-
$2\pi^{-1}$	*MPPECD* (0.90 eV)	4.0 %	-3.7 %	-6.3%	0 %	-2.5 %	-2.9 %	-2.0 %
$1\pi^{-1}$	b_1/b_0 (0.30 eV)	-1.3 %	-1.1 %	-1.8 %	0.5 %	-1.5 %	-1.1 %	-2.0 %
$1\pi^{-1}$	b_3/b_0 (0.30 eV)	0.9 %	1.4 %	2.5 %	0 %	1.3 %	1.4 %	-
$1\pi^{-1}$	*MPPECD* (0.30 eV)	-3.1 %	-2.9 %	-4.9 %	1.0 %	-3.7 %	-2.9 %	-4.0 %

Table 4.2: Odd Legendre polynomial coefficients decomposition of the forward-backward asymmetry for the different photoionisation and polarisation schemes in R-(+) Limonene. For the polarisation state description, we used the (p_{bb},p_{bc}) notation, where p_{bb} is the polarisation of the photon(s) that drive the bound-bound transition, where p_{bc} is the polarisation of the photon(s) that drive the bound-continuum transition and where $p_i = 1$ for LCP, $p_i = -1$ for RCP and $p_i = 0$ for linearly polarised photon(s). Note that for the all [1+1′] ionization schemes, the quantities b_0, b_1, b_3 and *MPPECD* are approximated quantities ($\tilde{b_0}$, $\tilde{b_1}$, $\tilde{b_3}$ and $\widetilde{MPPECD}$) since the cylindrical symmetry of the interaction is broken.

the bound-bound transition is to photoselect some given molecular orientations (an axis for $p = 0$, or a plane for $p = \pm 1$). Since the left- and the right-CPL photon is expected to select the same molecular orientations, it is not surprising to measure similar PECD. The small discrepancy between figure 4.23(d) and (e) might be due to the PXCD induced by the circular excitation step.

A synthetic view of the different cases studied is given in Table 4.2, which provides the values of the odd Legendre coefficients associated with the dominant ionization channels. These coefficients are normalized by the PES to enable direct quantitative comparison.

4.4.4 Conclusions and perspectives

We have studied the role of resonances in Resonant Enhanced Multiphoton PECD of (+)-limonene. Using two-color fields with fully tunable polarization states, we were able to disentangle the role of bound-bound and bound-continuum transitions. The main role of the bound-bound transition is clearly to break the molecular ensemble isotropy through the angular dependence of the transition dipole matrix elements. We have also demonstrated experimentally that the bound-bound transitions do not need to be driven with circular photon in order to observe PECD, as recently theoretically predicted [Goetz et al. 2017]. Indeed, in our case, the PECD is found to be enhanced when the bound-bound transition is driven with linearly polarized photon. Moreover, we have shown that the helicity of the pulse that drives the bound-bound transitions hardly modifies the measured PECD.

We have focused here on the case where the two pulses overlap temporally. However, the population of excited states following the bound-bound transition will inherently lead to ultrafast vibronic dynamics, which might influence the chiroptical response of the molecules. Moreover, after the excitation of the excited states, the molecules are allowed to rotate, and the isotropic distribution of the molecular orientation will asymptotically be recovered. As we have seen during this chapter, static PECD is sensitive to electronic and vibrational characters of the initial state, as well as the molecular ensemble orientation distribution. Even if this observable seems perfectly well-suited for the time-dependent study of chiroptical dynamics, time-resolved PECD experiment had never performed before the beginning of this thesis. Our idea was thus to use pump-PECD probe schemes to follow the ultrafast vibronic and sample anisotropy dynamics following photoexcitation, to establish the sensitivity of PECD as a time-dependent observable. This will be discussed in the next chapter.

5. Ultrafast dynamics in chiral molecules

In the previous chapter, we have extensively studied the photoelectron circular dichroism (PECD) which emerges when an ensemble of randomly oriented chiral molecules is photoionized by circularly polarized light. We have seen that PECD leads to really strong chiroptical signals, orders of magnitude stronger than most standard CD signal, which enables probing molecular chirality in gas-phase sample. We have seen that PECD is very sensitive to the initial, intermediate and final states involved in the photoionization processes. For example, we have presented a systematic investigation of REMPI-PECD in limonene molecules, in which the electrons transit to excited bound states before being released in the continuum. We have shown that the bound-bound transition in the REMPI breaks the isotropy of the molecular ensemble by orientation-dependent photoexcitation. Since both the excited Rydberg states and the photoinduced anisotropy in the sample are non-stationary, this REMPI-PECD study triggers two specific questions; i) Is PECD sensitive to the dynamics launched in the low-lying Rydberg states? ii) Can the rotation of the molecules in the ensemble dynamically wash-out the effect of photoinduced anisotropy? More generally, at this point, we started to think about the possibility to use PECD as a probe of ultrafast rotational, vibrational and electronic dynamics in chiral molecules.

In the first example that is presented here, we will show the first experimental realization of time-resolved PECD experiments, where a linearly polarized pump pulse launches dynamics in Rydberg states of chiral molecules and where a linearly polarized probe pulse photoionizes the molecules. The time-resolved forward-backward asymmetry of the photoelectron angular distribution will be shown to be sensitive to the both nuclear and electronic dynamics. In the second example, we will show that using the same experimental setup, but by using a counterintuitive polarization configuration, led to the accidental discovery of two new chiroptical effect named PhotoeXcitation Circular Dichroism (PXCD) and PhotoeXcitation induced Electron Circular Dichroism (PXECD). We will see that PXCD is characterized by an enantiospecific forward-backward oscillations of the bound electronic density, which emerges when a wavepacket is created in chiral molecules

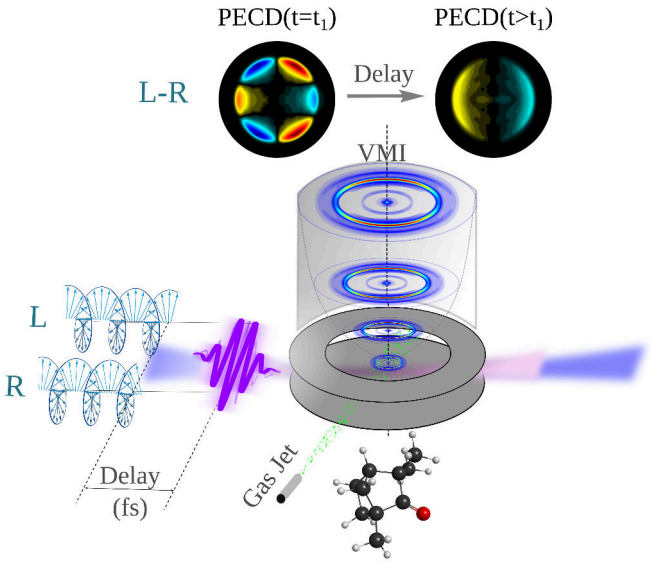

Figure 5.1: Schematic of a time-resolved PECD experiment. A linearly polarized pump pulse is focused into a gas jet of a randomly oriented ensemble of enantiopure chiral molecules. The pump pulse excites some molecules within the ensemble. A circularly polarized probe pulse photoionize the excited molecules. The unexcited molecules within the ensemble cannot be ionized by the probe pulse. In our experiment, the 2D projection of the 3D PAD, for each (left- and right-) helicity of the probe pulse is measured. The evolution of the PECD can be followed as a function of time, by looking at the difference between the VMI images obtained using left- and right-circularly polarized probe pulse.

using chiral light. This electronic charge oscillation can be created upon the creation of a vibrational wavepacket, which is a striking manifestation of the breakdown of the BOA. Photoionizing different bound states within the wavepacket to the same final state, using linear (non-chiral) photon, leads to the emergence of a forward-backward asymmetry in the angular distribution of the photoelectrons. This phenomenon is called PXECD, and is also a new type of chiral observable.

5.1 Time-resolved Photoelectron Circular Dichroism

5.1.1 Why, and how to do TR-PECD ?

In this section, our goal is to establish the sensitivity of PECD to ongoing dynamics in photoexcited chiral molecules. We want to determine if time-resolved photoelectron circular dichroism (TR-PECD) can be the chiral analog to the well known and powerful technique of time-resolved photoelectron spectroscopy (TR-PES). This is particularly important since, before the work presented here, no sub-picosecond chiral dynamics had ever been measured in the gas phase. Indeed, differential signals obtained in most Circular Dichroism techniques rely on the interference between electric and magnetic dipole transitions and are too small to be used in dilute media. High enantiosensitivity can be achieved by microwave spectroscopy [Medcraft et al. 2014; Patterson et al. 2013b] but this spectral range is prohibitive for ultrafast measurements on the sub-picosecond timescale, because the period of the microwave radiation is tens of nanoseconds.

The experimental scheme of a prototypical TR-PECD experiment is presented in Fig. 5.1. In its most general form, a pump pulse is focused in a gas jet of chiral molecules to create a non-stationary wavepacket that evolves in time. In our case, the linearly polarized

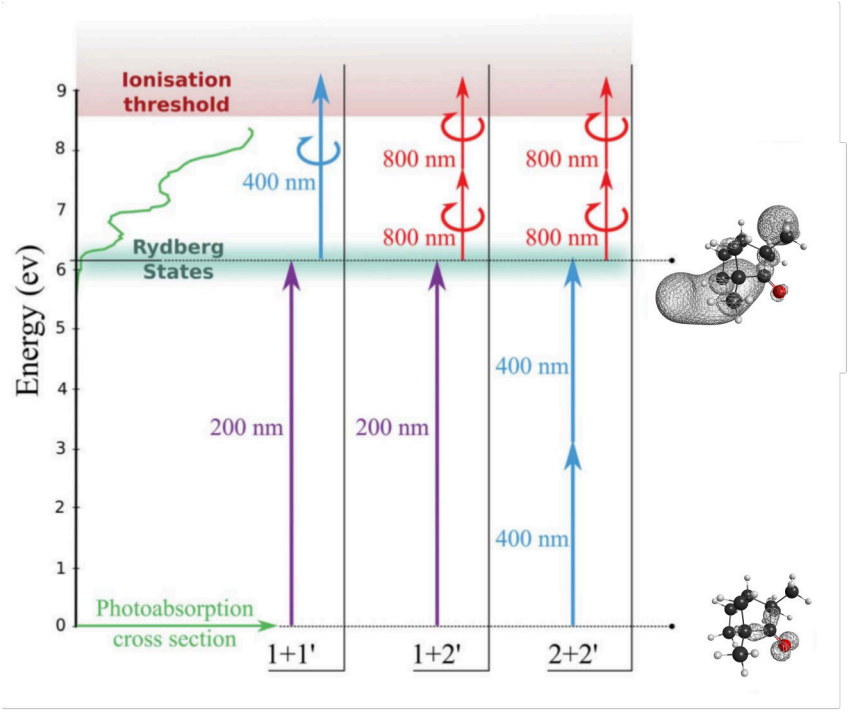

Figure 5.2: Schematic of the different pump and probe configuration ([1+1′], [1+2′] and [2+2′]) that will be used in our time-resolved photoelectron circular dichroism measurements, in fenchone molecules. Schematic of electronic density for the highest-occupied and 3s Rydberg state molecular orbitals are shown. This figure is adapted from [Beaulieu et al. 2016c].

pump pulse will photoexcite randomly orientation enantiopure fenchone molecules to their low-lying Rydberg bands, lying $\sim$ 6.2 eV above the electronic ground state S_0. A time-delayed (left- or right-) circularly polarized probe pulse will photoionize the excited molecules. The photoelectron angular distribution will be measured for different pump-probe delays and for both (right- (R) and left- (L)) helicities of the probe pulse. The evolution of the forward-backward asymmetry of the ejected electrons as a function of delay encodes the chiral relaxation dynamics of the photoexcited system. Using the time-resolved PES and PECD, our basic knowledge of photochemistry, and appropriate theoretical modelling, we will then need to try to understand the dynamics induced by the pump, through the goggles of our observables [1].

As we did for the static REMPI-PECD study of limonene (see previous chapter), we will use different pump-probe scheme ([1+1′] (201 nm + 404 nm), [1+2′] (201 nm + 800 nm) and [2+2′] (400 nm + 800 nm)) to study the dynamic of the photoexcited 3s Rydberg state of fenchone. A schematic representation of these different excitation/ionization configuration is shown in Fig. 5.2. The use of a different number of pump photons possibly leads to different quantum states, but also produces a different distribution of molecular orientation photoselected by the transition.

It is trivial to understand that the photoexcited Rydberg states will somehow decay to lower-lying electronic states and ultimately go back to the electronic ground state. Less trivial is to try to guess how TR-PECD would be sensitive to such dynamics. First, as

[1] By that I mean that observables rarely provides all the information that we need to retrieve the information that we are looking for. One needs to choose the physical observables which are sensitive to the physical process of interest. The goal here is to make the first attempt at establishing to what kind of dynamics PECD is sensitive.

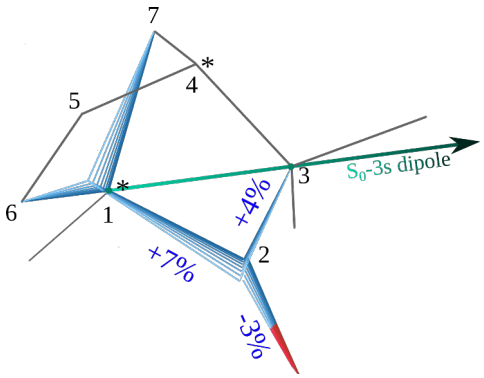

Figure 5.3: Electronic photoexcitation induced modification of the molecular geometry of the fenchone molecule. After the excitation from the ground electronic state to the 3s Rydberg state, the molecule undergoes a nuclear rearrangement, which is despites as the blue and red lines (from the TDDFT calculations). This figure is adapted from [Beaulieu et al. 2016c].

any femtochemistry experiment, we are limited by the 'ionizing energy window' of our probe photons. If the system relaxes to a state where $I_p > \hbar\omega_{probe}$, the probe will not be able to photoionize the system anymore. The evolution of the total signal is thus expected to reflect the population decay of the Rydberg states. Second, the $S_0 \rightarrow 3s$ transition induced by the pump launches a vibrational dynamics in the excited electronic states, since the equilibrium geometry of S_0 and $3s$ is not the same. The change of equilibrium geometry upon $S_0 \rightarrow 3s$ excitation is shown in Fig. 5.3 [2]. It will be interesting to measure the sensitivity of PECD to such vibrational dynamics.

5.1.2 (1+1') TR-PECD in fenchone

The first experiment that we proposed is the most intuitive and simple TR-PECD experiment that one can think of, a [1+1'] pump-probe experiment in the 'benchmark' fenchone molecule (a molecule so used in PECD measurements that it could be considered as the H_2^+ of the PECD community). The measurements were performed on the 'Aurore4' (Aurore 4 is an experimental room which use Aurore laser system to pump different nonlinear frequency conversion setup for femtochemistry. There is also a VMI built by V. Blanchet) setup at CELIA. In this scheme, a linearly polarized 201 nm (6.27 eV, 30 meV FWHM bandwidth, $\sim 2\ \mu$J) photoexcite the fenchone molecules to their first (3s) Rydberg states. The 201 nm pulses were generated by sum-frequency between the third harmonic (267 nm) and the fundamental (800 nm) of the 1 kHz Ti:Sa laser in a BBO crystal. They were focused to an intensity of $\sim$ 5x10^{11} W/cm^2 in a gas jet of enantiopure fenchone molecules injected using an Even-Lavie 1 kHz pulsed valve. The molecules were introduced placing fenchone-soaked fiberglass into a heatable cartridge in the body of the Even Lavive Valve. Heating the valve to 60° degrees results in a vapor pressure of fenchone of only few tens of mbars, which is insufficient to operate the Valve. A high backing pressure carrier gas (Helium, $\sim$ 12 bars) was used. The advantage of this setup is that it produces a cold supersonic beam and consumes much less compound than a continuous jet. On the other hand, clusters can be formed during the supersonic expansion. We observed some signatures of clusters under some specific experimental conditions, but all the features

[2] The equilibrium geometry of S_0 and $3s$ states have been calculated using a complete active space self-consistent field (CASSCF) approach which optimizes the energy and geometry by allowing excitation of 4 valence electrons into 7 molecular orbitals, referred to as CASSCF(4,7). More details about the calculation can be found in the Supporting Information of [Comby et al. 2016].

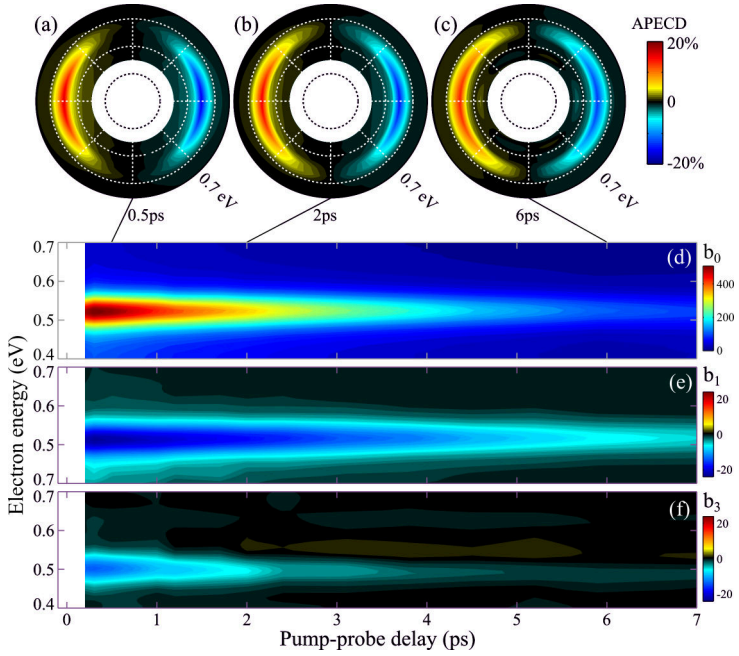

Figure 5.4: Time-resolved [1+1′] PECD measurements in enantiopure fenchone molecules. In this experiment, we used a 201 nm linearly polarized pump and a 404 nm circularly polarized probe pulse. The upper plots show the PECD snapshots for three different pump probe delays: 0.5 ps in (a), 2 ps in (b) and 6 ps in (c). The light propagation direction is along the horizontal axis. The radius of the polar plots, which reprensents the photoelectron kinetic energy, extends from 0 to 0.7 eV. The lower contour plots depict the evolution of the Legendre coefficients b_0 (d), b_1 (e) and b_3 (f) as a function of photoelectron kinetic energy and pump probe delay. This figure is adapted from [Beaulieu et al. 2016c].

presented here were found to be robust against fine-tuning of the jet, indicating that they come from monomers. A time-delayed 404 nm (3.07 eV, 35 meV FWHM bandwidth) probe pulse, generated by SHG in a BBO crystal, was propagated into a quarter waveplate to convert its polarization state to circular and focused into the gas jet at in intensity of $\sim 10^{11}$ W/cm^2, using an independent lens (not the same lens that was used to focus the 201 nm). The intensity of both the pump and the probe were set such that almost no electron/ion was produced using the pump or the probe only. The duration of the laser pulses were not Fourier transform limited because of the dispersion in the focusing optics and in the entrance window of the VMI. As a consequence, the temporal resolution of this experiment was limited by the relatively long cross-correlation time of $\sim$ 170 fs. The photoelectrons were collected using a VMI, whose working principle and geometry have been detailed in the previous chapter. To avoid the influence of slow drifts in the experiment, for each pump-probe delay, the probe laser helicity was switched every 45 000 laser shots to record a series of left and right images. The pump-probe delay was then scanned consecutively ten times to further smooth out slow drifts in the experiment. Background images corresponding to the probe pulse alone were recorded for each helicity and subtracted from each image.

A summary of the experimental data is presented in Fig. 5.4. Figure 5.4 (d) shows the evolution of the PES as a function of the pump-probe delay. The PES is defined as the half-sum of the images ((L+R)/2) obtained using left (R) and right (L) circularly polarized probe pulse. The PES is centered around 0.52 eV, which correspond to a [1+1′] transition where all the excess energy goes to the photoelectron (6.27 eV (E_{pump}) + 3.07 eV (E_{probe})

- 8.72 eV (I_p) = 0.52 eV (E_{kin})). The PES does not spectrally shift as a function of the pump-probe delay. The signal evolution is characterized by a single exponential decay with a decay time of 3.3 ps. This means that the 3s Rydberg states decay to a state which is not in the 'ionization energy window' of the probe pulse, in a characteristic time of 3.3 ps. This gives us the lifetime of the 3s Rydberg states. We now turn our attention to the forward-backward antisymmetric part of the signal, *i.e.* the PECD. Here, the PECD is defined as the difference between images obtained using a left- and right- circularly polarized probe, normalized by the maximum of the PES (2(L-R)/max((L+R))). Fig. 5.4 (a), (b) and (c) show snapshots of the PECD for 0.5 ps, 2 ps and 6 ps pump-probe delay, respectively. The first general observation is that a significant PECD is observed, which is remarkable given the fact that the electron is ionized from highly excited Rydberg states. The ionization from this state constituted of an electron 'orbiting' quite far away from the ionic core by the circularly polarized probe pulse is sufficient to imprint a strong chiral forward-backward asymmetry to the ejected electrons. In fact, this result can be seen as the time-dependent analog to the static experiments in limonene, presented in the previous chapter (see Fig. 4.23(a)). While carefully looking into the time evolution of the PECD, we can notice that the magnitude of this asymmetric signal slightly decreases and becomes angularly more dispersed as the pump-probe delay is increased.

In order to tackle the subtle feature of this dynamical evolution of the PECD, we now focus on the time- and energy-resolved Legendre polynomials decomposition of the signals. This will provide details of the angularly-resolved time evolution of the chiroptical signal. Since we have used pBasex inversion in a situation where the cylindrical symmetry of the light-molecule interaction is broken by the simultaneous use of linearly and circularly polarized photons, we will use the previously introduced $\tilde{b_i}$ notation (we will use $MPPECD^*$, instead of $\widetilde{MPPECD}$, for aesthetic consideration). The time- and energy-resolved first and third Legendre coefficients ($\tilde{b_1}$ and $\tilde{b_3}$) are shown in Fig. 5.4 (e) and (f), respectively. Both $\tilde{b_1}$ and $\tilde{b_3}$ are centered at the same energy as the PES ($\sim$ 0.52 eV). At short delay, their superposition leads to a rather sharp PECD distribution along the laser propagation axis. Interestingly, we notice that $\tilde{b_3}$ decays much faster than $\tilde{b_1}$. In fact, exponential fitting of the odd Legendre coefficients gives characteristics decay time of 3.9 ps for $\tilde{b_1}$ and 1.4 ps for $\tilde{b_3}$. When $\tilde{b_3}$ has vanished, the situation is very similar as in the single photon case, *i.e.* only $\tilde{b_1}$ contributes to the PECD.

What is the origin of the fast decay of $\tilde{b_3}$? To answer this question, one needs to remember the conclusions of the previous chapter as well as those of the theoretical paper of Goetz *et al.* [Goetz et al. 2017]. In REMPI-PECD, the contribution from higher-order Legendre polynomials mainly comes from the sample isotropy breaking induced by the bound-bound transition to the intermediate Rydberg states (because the excitation probability is maximized for given molecular orientations). So just after the excitation, the ensemble of molecules in excited Rydberg states is strongly anisotropic, leading to a large contribution of $\tilde{b_3}$. Because of thermal agitation ($k_bT \neq 0$, where k_b is the Boltzmann constant and T the temperature of the molecular ensemble), the molecules are freely rotating in space. After the pump pulse, the photoexcitation induced anisotropy will quickly decay as the molecule freely rotates under the action of thermal agitation [Blokhin et al. 2003]. The characteristic decay time of the $\tilde{b_3}$ would thus be determined by the moment of inertia of the molecules and rotational temperature of the gas jet.

Another interesting feature is the general decay of the $\widetilde{PECD}$ as a function of time. The multiphoton $\widetilde{PECD}$ can be quantified by integrating the Legendre coefficients around the peak of the PES and calculating the $MPPECD^*$ as defined in the previous chapter (see equation 4.5), where the sum is here restricted to its first two terms since the transition is a

two-photon process (*i.e.* $MPPECD^* = (1/\tilde{b_0})[2\tilde{b_1} - (1/2)\tilde{b_3}]$). The detailed investigation of the $MPPECD^*$ at short delays, presented in [Comby et al. 2016], shows a fast decrease with a minimum around 0.4 ps, followed by an increase to reach the limit value of 14%. If PECD was simply sensitive to the population decay of the Rydberg states, then the $MPPECD^*$, which is a normalized quantity, should remain constant with the pump-probe delay. The fact that the TR-PECD is evolving with time is probably a signature of a vibronic dynamics which is not revealed by the TR-PES. We can thus argue that this first [1+1′] TR-PECD experiment has laid the foundation of the sensitivity of this observable to both rotational dynamics of the anisotropic excited molecular ensemble, and subtle vibronic dynamics which is not resolved by conventional TR-PES.

5.1.3 (1+2') TR-PECD in fenchone

Now that we know how to perform TR-PECD experiments and that we have (partially) established its sensitivity to ongoing molecular dynamics, we will perform experiments using different pump-probe wavelengths, in the same fashion as we did for static limonene experiments (see previous chapter or [Beaulieu et al. 2018b]). First, we will keep the same pump wavelength (201 nm) and change the probe wavelength to 800 nm. This will lead to a [1+2′] scheme, where two photons are needed to reach the ionization continuum from the 3s Rydberg states. The fact that two-photon are needed in the probe step makes the story more complicated, since the electrons transit from the 3s Rydberg states ($\sim$ 6.2 eV) to the highly excited states ($\sim$ 7.7 eV) before reaching the continuum. This two-photon 'probe' configuration has been shown to lead to a complex angular structure of the PECD, in static experiments in limonene [Beaulieu et al. 2018b]. On the other hand, this probe configuration also comes with a better temporal resolution ($\sim$ 100 fs cross-correlation for [1+2′] compared to $\sim$ 170 fs for [1+1′]), since the 800 nm pulse duration is only $\sim$ 30 fs. Let us now look at the results of this [1+2′] TR-PECD experiment in fenchone.

Fig. 5.5 presents the evolution of the PES (d), of the odd Legendre coefficients $\tilde{b_1}$ (e), $\tilde{b_3}$ (f) and $\tilde{b_5}$ (g) as well as three snapshots of PECD at 0.3 ps (a), 0.9 ps (b) and 7 ps (c) pump-probe delay. The PES is centered at the same energy as in the [1+1′] case ($\sim$ 0.52 eV). However, its spectral bandwidth is significantly larger than in the previous case, reflecting the broader bandwidth of the 800 nm probe pulse with respect to the bandwidth of the 404 nm probe pulse. By performing an exponential fit of the PES signal, we retrieve a decay constant of $\sim$ 3.2 ps, which agrees well with the 3s Rydberg states lifetime found in the [1+1′] ($\sim$ 3.3 ps). This is not surprising since the dynamics induced by the pump pulse is exactly the same in both configurations. Now, we will focus on the TR-PECD signals. First, we notice that the PECD is much weaker and presents more complex angular features that in the [1+1′] case. In the static PECD limonene experiment presented in the previous chapter [Beaulieu et al. 2018b], we encountered the same situation where the 2-photon transition from Rydberg states to the continuum led to a weak and angularly complex PECD. We have interpreted this observation as the result of a large number of Rydberg states that can be populated around 7.7 eV prior to reach the continuum. Indeed, PECD is known to be highly sensitive to molecular orbitals and vibrational excitation. Here, many different electronic and vibrational excited states contribute to the signal, with possibly different signs, energy dependences and angular distributions of their PECD. As a result, the total PECD, which is the incoherent sum of the PECD from different excited states, is weak and strongly modulated.

We will now look at the dynamics of the different Legendre coefficients. The high-order odd coefficients, $\tilde{b_3}$ and $\tilde{b_5}$, reveal the existence of two energetic components with very different dynamics. Below 0.6 eV, $\tilde{b_3}$ is negative and decays with a characteristic time of 1.1

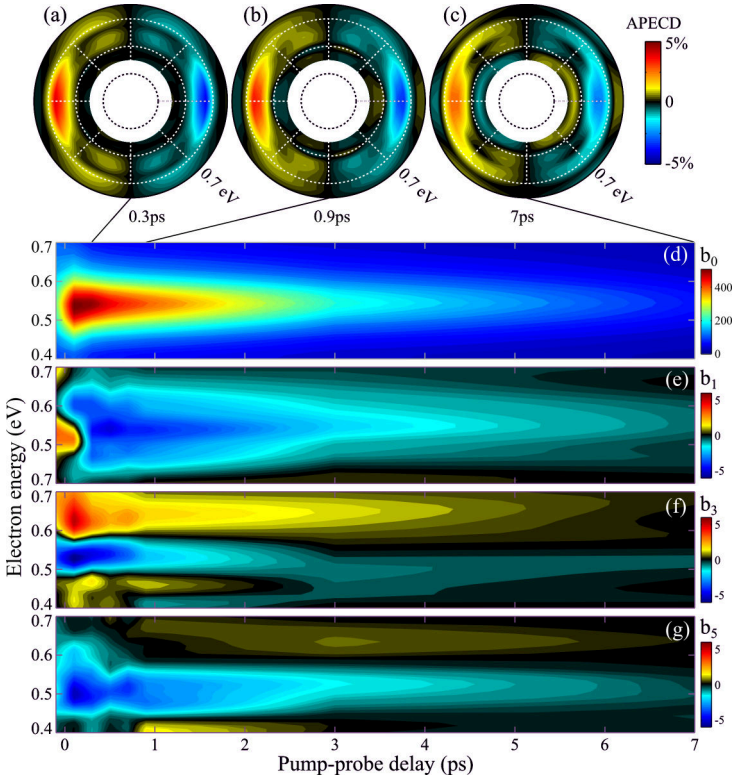

Figure 5.5: Time-resolved [1+2′] PECD measurements in enantiopure fenchone molecules. In this experiment, we used a 201 nm linearly polarized pump and a 800 nm circularly polarized probe pulse. The upper plots show the PECD snapshots for three different pump probe delays: 0.3 ps in (a), 0.9 ps in (b) and 7 ps in (c). The light propagation direction is along the horizontal axis. The radius of the polar plots, which reprensents the photoelectron kinetic energy, extends from 0 to 0.7 eV. The lower contour plots depict the evolution of the Legendre coefficients b_0 (d), b_1 (e), b_3 (f) and b_5 (g) as a function of photoelectron kinetic energy and pump probe delay. This figure is adapted from [Beaulieu et al. 2016c].

ps. This is very similar to what was observed in the [1+1′] scheme (Fig. 5.4). In this energy range (*i.e.* below 0.6 eV), a strong $\tilde{b_5}$ component also exists. The interplay between b_3 and b_5 can be seen directly in the PECD snapshots (Fig. 5.5 (a)-(c)), which show lobes peaking around $\theta \sim \pm 60°$ and 120°. Above 0.6 eV, these lobes disappear. This corresponds to the energy range where $\tilde{b_3}$ change sign (becomes positive) and shows a slower characteristic decay time of 3.3 ps, and where $\tilde{b_5}$ is zero.

The PECD measurements show a transition at 0.6 eV between two energy components separated by $\sim$ 100 meV, which are invisible in the PES. We will now try to understand the origin of these components. For that, we will use the [1+1′] case as a reference. There are two main differences between the [1+1′] and the [1+2′] scheme. First, as explained in great details above, while the ionization process is a single photon transition from the 3s Rydberg states to the continuum in the [1+1′] case, the ionization is characterized by a 2-photon REMPI process for the [1+2′] scheme. The transition to a spectral region where the density of Rydberg state is high (around 7.7 eV) might be a possible explanation why the resulting PECD has different energetic structures which show different dynamics. The first hypothesis is that the two energetic components that we observe are associated with different intermediate states. The second difference between the [1+2′] case compared to the [1+1′] measurement is the larger spectral bandwidth of the probe pulses, which inherently produce broader photoelectron peaks. Since PECD results from the scattering of

the electrons in the combined electric field and molecular potentials, it is very sensitive to the electron kinetic energy, especially for low-kinetic energy photoelectrons. For instance, the $\tilde{b_1}$ parameter measured in single-photon ionization from the HOMO of camphor and fenchone was shown to vary abruptly between 0 and 1 eV [Nahon et al. 2016]. The [1+2′] scheme, which produces broader photoelectron peaks, allows sampling a larger range of photoelectron kinetic energy, which can be helpful to reveal kinetic energy effects on the PECD. The second hypothesis is thus that the transition observed at 0.6 eV is a near-threshold kinetic energy effect. The development of a theoretical model for the accurate and quantitative description of multiphoton PECD would be of great help to discriminate between the first and second hypothesis.

In addition to these relatively slow picosecond dynamics, the first Legendre coefficient $\tilde{b_1}$ shows a sign change in the first few hundreds of femtoseconds. Since this coefficient dominates the $MPPECD^*$, this means that the overall forward-backward asymmetry reverses in this range. This spectacular behavior could be a signature of fast internal vibrational relaxation (IVR) dynamics launched in the excited states (see Fig. 5.7). It would be interesting to perform the same kind of experiment with a higher temporal resolution, in order to try to tackle more subtle and faster dynamics. To do so, we will moved to a [2+2′] (400 nm + 800 nm) scheme.

5.1.4 (2+2') TR-PECD in fenchone

The goal of this last experiment is to have a better temporal resolution than in the [1+1′] and [1+2′] cases, using a [2+2′] (400 nm + 800 nm) scheme. In this configuration, the absorption of two linearly polarized 400 nm photons brings the molecules in the 3s Rydberg states, as in the other configurations. The probe pulse photoionizes the excited molecules through a two-photon transition to the continuum. The cross-correlation of pump and probe pulse was measured to be less than 50 fs, which is a significant improvement compared to the [1+1′] ($\sim$ 170 fs) and in the [1+2′] ($\sim$ 100 fs) configurations. These experiments were performed using the Aurore1 setup at CELIA (Aurore1 is qn experimental room using Aurore laser system equipped of tools for attosecond and femtosecond spectroscopy), and the fenchone source was here the continuous nozzle described in the static PECD measurements, instead of the 1 kHz Even-Lavie pulsed gas jet.

In this [2+2′] scheme, the PECD is found to be much weaker than in both previous configurations, reaching a maximum value of $\sim$ 2 %. The PECD also shows a nice modulated angular structure. Looking to the snapshots of the angle-resolved PECD in Fig. 5.6(a)-(c), we can notice that they undergo very fast evolution. In order to reduce the dimensionality of the data interpretation [3], we will now monitor the Legendre coefficients averaged over the width of the PES peak, as a function of pump-probe delay. The PES (b_0) decays smoothly while the odd Legendre coefficients and the $MPPECD^*$ seem to show oscillations as a function of the pump-probe delay. For example, the $MPPECD^*$ maximizes at 80 fs, with equally strong but with opposite sign contribution of $\tilde{b_1}$ and $\tilde{b_3}$. At 320 fs, the $MPPECD^*$ maximizes again, with now a dominant contribution of $\tilde{b_3}$. At 600 fs, $\tilde{b_1}$ is almost zero, which makes the PECD almost exclusively composed of the $\tilde{b_3}$ term.

We can thus claim that there is a drastic change of the $\tilde{b_1}/\tilde{b_3}$ ratio between the [1+2′] and [2+2′] schemes. The major difference between the two scheme is the fact that the

[3] Because, to be honest, as we saw in the last [1+2′] case, were multiple photons are involved in the probe step, looking at the time- and energy-resolved Legendre coefficients lead to rich but complex data interpretation. It is thus hard to extract simple conclusions from this way of plotting data in such complex scheme.

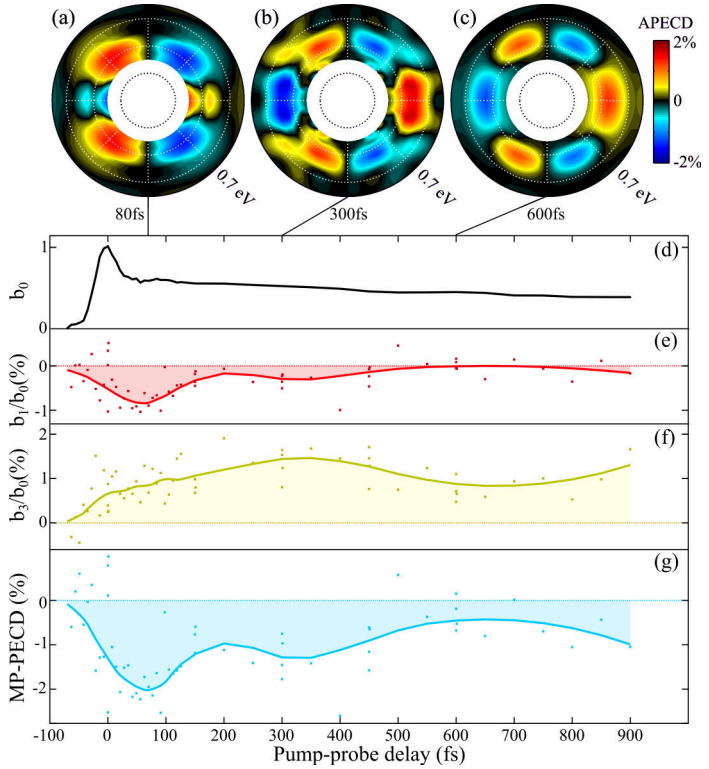

Figure 5.6: Time-resolved [2+2′] PECD measurements in enantiopure fenchone molecules. In this experiment, we used a 400 nm linearly polarized pump and a 800 nm circularly polarized probe pulse. The upper plots show the PECD snapshots for averaged around three different pump probe delays: 80 ± 20 fs in (a), 300 ± 50 fs in (b) and 600 ± 50 fs in (c). The light propagation direction is along the horizontal axis. The radius of the polar plots, which reprensents the photoelectron kinetic energy, extends from 0 to 0.7 eV. The lower contour plots depict the evolution of b_0 (d) the normalized Legendre coefficients b_1/b_0 (e), b_3/b_0 (f) and the MPPECD (g) as a function pump probe delay. This figure is adapted from [Beaulieu et al. 2016c].

ground- to Rydberg states transition is driven either with one or two-photon(s) transition. To tentatively try to rationalize the reason for that, we again go back to the conclusions of the static limonene experiments presented in the last chapter [Beaulieu et al. 2018b], and the conclusions of the theoretical study of Goetz *et al.* [Goetz et al. 2017]. The two-photon bound-bound transition is expected to be more selective than a single photon transition to the molecular orientations selected by the transition. According to Goetz *et al.* [Goetz et al. 2017] and our previous results [Beaulieu et al. 2018b], this type of selective excitation is expected to enhance the contribution of high-order odd Legendre coefficients ($\tilde{b_3}$, $\tilde{b_5}$, ...). The fact that $\tilde{b_3}$ is much stronger in [2+2′] thus makes sense, according to these conclusions.

The most striking feature observed in Fig. 5.6 is the oscillations in $\tilde{b_1}$ and thus in the $MPPECD^*$. Our intuition was that these oscillations were the signature of a quasi-periodic change in the molecular geometry in the excited Rydberg state. Martial Boggio-Pasqua from LCPQ, Toulouse, performed TD-DFT calculations to determine the dominant motion of the wavepacket launched by the pump pulse on the 3s Rydberg state potential energy surfaces. He found that the main gradient of this surface corresponds to the $C_1 - C_2$ stretching (see Fig. 5.3 and Fig. 5.7). We expect that this main vibrational motion will be accompanied by energy transfers to other vibrational modes, as well as by internal conversion onto lower valence states.

The detailed understanding of the PECD signal would require a complete calcula-

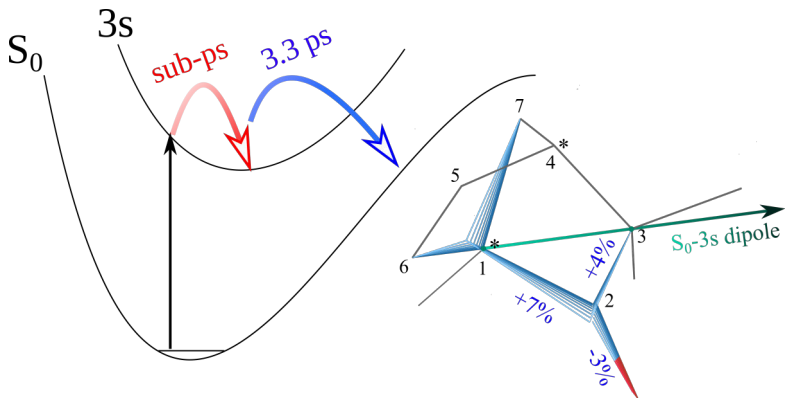

Figure 5.7: Schematic of the relaxation processes of photoexcited fenchone molecule, revealed in the our TR-PECD experiments. The red curved arrow represents the sub-picosecond IVR process and the curved blue arrow represents the few-picosecond electronic relaxation process. The bond length changes between the equilibrium geometry within the ground and 3s Rydberg state are indicated in %. The green arrow represents the transition dipole moment for the transition from the electronic ground to 3s Rydberg state.

tion of the wavepacket dynamics, which is far beyond the scope of this work. Indeed simulating accurately the wavepacket dynamics of such a large polyatomic molecule and quantitatively calculating the associated PECD spectra is at the edge of the current capabilities. Let us stress that the dynamics revealed by the TR-PECD measurements are invisible in the conventional TR-PES signal, confirming the relevance of photoelectron circular dichroism as a probe of ultrafast dynamics of chiral molecules.

Even if we do not understand all the features of our complex TR-PECD data, we have undoubtedly demonstrated the sensitivity of PECD to rotational and vibronic dynamics. In static multi-pulse multi-polarization PECD experiments in limonene, presented in the previous chapter [Beaulieu et al. 2018b], we have seen that changing the number of photons in the pump and/or in the probe could lead to a qualitative understanding of the role of bound-bound and bound-continuum transition in REMPI-PECD. Here, we have shown that using the same strategies, but in a time-resolved fashion, also leads us to gain a lot of information about the sensitivity of the different observables ($MPPECD^*$, $\tilde{b_1}$, $\tilde{b_5}$, ...) to the ongoing dynamics in TR-PECD experiments. Now we will also use another important strategy that we have presented in the previous chapter: to look at structural isomerism effects.

5.1.5 Structural isomerism effects in TR-PECD: fenchone vs camphor

Camphor and fenchone both have rigid structures with a single conformer, and differ solely by the exchange of two methyl groups from a top position to a side one. The methyl groups are not attached to a chiral center in either of the two molecules. The HOMO orbital of both species is a localized 2p lone pair of the carbonyl oxygen (see Fig. 5.8(a) and (c)). The isomeric changes are thus remote from the chiral centers and the HOMO orbitals. However, we have shown in the previous chapter that single-photon PECDs of camphor and fenchone were strongly different. Because the initial state of both molecules is similar, and the single-photon transition directly promotes a 'HOMO electron' to the continuum, this observation emphasizes the role of the final continuum states in PECD. Here, we will present preliminary TR-PECD data in both camphor and fenchone, which will enlighten the role of intermediate state and its relaxation dynamics on the TR-PECD signals. Indeed, looking at Fig. 5.8, we can notice that the transition

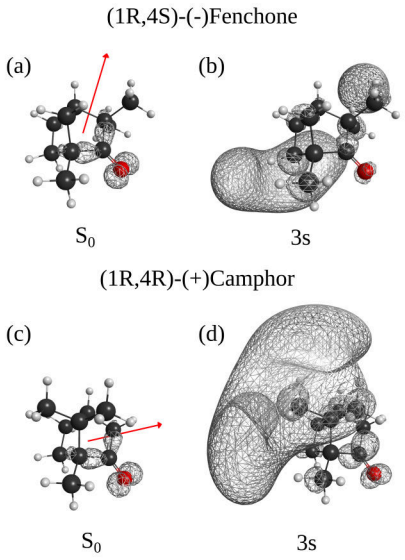

Figure 5.8: Representation of the electronic density in the ground and 3s Rydberg states of fenchone (a-b) and of camphor (c-d). The red arrows represent the transition dipole moments when a HOMO hole is created to excite the 3s Rydberg states. These calculations were performed using the GAMESS-US software [Schmidt et al. 1993]. First, the ground state geometry was optimized using density functional theory (DFT) with CAMB3LYP functional and 6-311++G(d,p) basis. Then, the energies and transition dipoles of the first 20 excited states of camphor and fenchone were computed using Time-Dependent density functional theory (TDDFT) with the same functional and basis functions.

dipole moment describing the transition from HOMO to 3s Rydberg states, as well as the electronic density of the 3s Rydberg states are strongly different for fenchone and camphor.

Lets us now compare the raw experimental data of TR-PES and TR-PECD in camphor and fenchone. As shown in the previous examples of TR-PECD, the most intuitive and 'clean' way of performing such experiment is to use a [1+1'] excitation/ionization scheme, since using a multiphoton pump or multiphoton probe somehow makes the signals and their interpretation more complicated. The experiment was carried out using a 201 nm (6.26 eV, 250 meV FWHM bandwidth, 3 μJ/pulse) pulse to photoexcite the molecules to their 3s Rydberg states, and a time-delayed 400 nm (3.1 eV, 100 meV FWHM bandwidth, 8 μJ/pulse) to photoionize the molecule. The cross-correlation, measured using the time-dependent ion yield signal, was determined to be $\sim$ 200 fs. These TR-PECD data are still under analysis and interpretation. We will thus solely give a brief outlook of what has been measured and use it as a perspective for future TR-PECD investigations.

Lets first pay attention to the PES dynamics. In both fenchone and camphor, the dynamics of PES can be described by a monoexponential decay, with a slower decay time in fenchone ($\tau = 3.3$ ps) than in camphor ($\tau = 2.2$ ps). These different characteristic decay times of the PES tell us that the dynamics launched in the 3s Rydberg states is somehow different in camphor and fenchone. Very generally, this could be an effect of the different geometry of the molecules (position of the methyl) combined with the different electronic density of the 3s Rydberg states that lead to very different vibronic wavepacket dynamics [4]. Moreover, because the energies of 3s Rydberg states are not exactly identical for both

[4]This is a very generic explanation, but we cannot be much more quantitative than that (for now), concerning the monoexponential decay time of the PES in such large polyatomic chiral molecules.

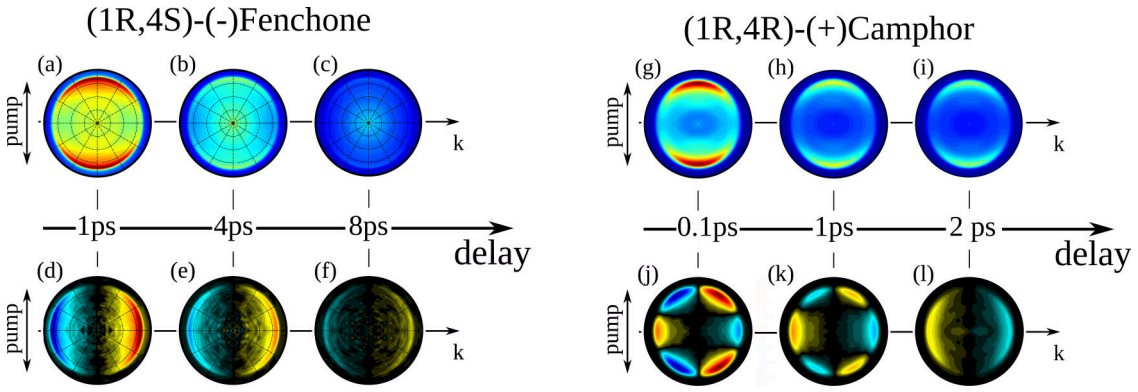

Figure 5.9: Snapshots of the PES (L+R) and the PECD (L-R) at different delays, taken from the time-resolved [1+1′] experiments in fenchone and camphor molecules.

isomer, the vibrational energy which is deposited in the excited states is not the same in fenchone and camphor. This might also affect the wavepacket dynamics in the Rydberg states.

We now turn our attention to the structural isomerism effect in TR-PECD data. The early delay PECD images of fenchone and camphor reveal a huge difference in the angular dependence of the forward-backward asymmetry (Fig. 5.9 (d,j)). In fenchone, the PECD angular structure is characteristic of a case with a strong contribution of $\tilde{b_1}$ and weak $\tilde{b_3}$, where $\tilde{b_1}$ and $\tilde{b_3}$ have the same sign [5]. In camphor, the PECD angular structure is characteristic of strong contribution of both $\tilde{b_1}$ and $\tilde{b_3}$, where $\tilde{b_1}$ and $\tilde{b_3}$ have opposite signs. This larger contribution of $\tilde{b_3}$ in camphor is a signature of a stronger anisotropy of pump excitation [Goetz et al. 2017]. This large $\tilde{b_3}$ is found to decay very quickly (characteristic time τ = 0.75 ps). Indeed, the PECD snapshot measured at 2 ps delay shows an almost pure $\tilde{b_1}$ contribution (Fig. 5.9(l)). The evolution of the $\tilde{b_1}/\tilde{b_3}$ ratio is less drastic in fenchone. Concerning the evolution of MPPECD with time, in camphor, we have measured a fast increase from $\sim$ 7 % to $\sim$ 9 % within the first hundred of fs, followed by a fast monoexponential decay to a value of $\sim$ 1.5 % in a characteristic decay time 0.73 ps. At longer time delays, the MPPECD is time-invariant ($\sim$ 1.5 %). This means that the rotational and vibronic dynamics that modifies the PECD is much faster than the 3s Rydberg states lifetime ($\tau = 2.2$ ps). In fenchone, the MPPECD shows a fast decrease from $\sim$ 11 % to $\sim$ 9 % in the first hundreds of fs, followed by a slow increase up to $\sim$ 14 % in a characteristic time of 3.2 ps. At long time-delay (again up to 10 ps, where the signal-to-noise ratio start to be very small), the $MPPECD^*$ is more or less constant ($\sim$ 14 %).

The physics underlying the origin of these structural isomerism effects in TR-PECD experiments is still not (quantitatively) deeply understood. Experiments in other similar molecules are currently being performed at CELIA to increase the number of available data, in an attempt to draw general conclusions. Moreover, from a theoretical point of view, theoreticians from Bordeaux (Baptiste Fabre, Bernard Pons, and Alex Clergerie) are developing models that provide good descriptions of the molecular continuum states, which might help us in our quest to understand the exact nature of the signal evolution in TR-PECD.

[5] The figure of the evolution of the Legendre coefficients and MPPECD is not presented here since a publication is under preparation.

5.1.6 Partial conclusions and perspectives

In this section, we have presented the first time-resolved photoelectron circular dichroism (TR-PECD) experiments ever performed [Beaulieu et al. 2016c; Comby et al. 2016]. First, using the most intuitive and simple scheme ([1+1']), we have followed the relaxation of fenchone molecules photoexcited in their 3s Rydberg states. We have shown that PECD could reveal ultrafast dynamics that are invisible in time-resolved photoelectron spectra (TR-PES). The different Legendre coefficients encode different information about the dynamics going on in the molecular ensemble. These first results mark the birth of ultrafast time-resolved measurements of chirality in the gas phase. In a similar fashion as in our static PECD study of limonene, we have changed the wavelength of the pump and/or of the probe, to determine the influence of the number of absorbed photons in each of these steps, on TR-PECD. This comparison shows spectacular differences in the angular distribution of the PECD, which are an additional illustration of its sensitivity. The use of shorter laser pulses in the multiphoton pump multiphoton probe experiments reveals that ultrafast vibronic dynamics takes place within a few hundreds of femtoseconds. On the other hand, increasing the number of photons also increases the complexity of the data. On the long term this could, of course, be a good thing, because richer data carries richer information on the dynamics, but for now, given the difficulties in interpretation and the level of the theoretical modeling, this complexity could be problematic.

Fully understanding the outcome of the measurements will require an extensive theoretical work. However, the parametric study that we have performed should enable determining what key parameters are at play. An essential aspect of future experiments will be to increase the temporal resolution, in order to track the fastest vibronic dynamics with high contrast. The development of ultrashort (sub-10 fs) UV pulses with significant spectral tunability would be ideal for femtosecond TR-PECD. Such sources are currently under development, for instance in the group of Francesca Calegari (Milan/Hambourg). One other aspect that needs to be improved in our experiments is the detection scheme. As explained several times throughout the thesis manuscript, the simultaneous use of linear and circular photons breaks the cylindrical symmetry of the interaction, preventing the rigorous retrieval of the 3D PAD from 2D VMI projections (using pBasex or Abel inversion technique, for example). We always inverted the images, by making the assumption that this departure from the cylindrically symmetric case would not have a dramatic effect on the general conclusions that were drawn from these inverted images. However, for fine spectroscopic applications or for experiments requiring precise calibration of the photoelectron energy axis, it would be more secure to use a detection scheme where no assumption about the interaction geometry is made, *i.e.* where the 3D PAD can be fully reconstructed. As we will see later, tomographic reconstruction of the 3D PAD using VMI projections offers one solution to this issue [Maurer et al. 2012; Smeenk et al. 2009; Wollenhaupt et al. 2009]. Another solution is to directly measure the 3D PAD using delay-line anodes. A COLTRIMS (Cold Target Recoil Ion Momentum Spectroscopy) [Dörner et al. 2000] spectrometer is currently being built at CELIA to this end. This apparatus will work in electron-ion coincidence mode, enabling the measurement of mass-tagged 3D PAD. This mass tagging will also be an important asset to disentangle the possible contributions from different channels in the TR-PECD measurements.

Our results confirm that PECD is a sensitive enough observable to measure ultrafast dynamics of chiral molecules in the gas phase. In that sense, the development of TR-PECD could open a new era for ultrafast chiral metrology, enabling to tackle fundamental questions related to dynamical aspects of chirality (chiral recognition, mechanism of the transfer of chirality from nuclear to electronic degrees of freedom ...). Indeed, the extreme

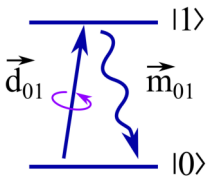

Figure 5.10: Ladder diagram representation of Circular Dichroism (CD). CD requires an electric dipole transition up and a magnetic dipole transition down and vice-versa. The figure is adapted from [Beaulieu et al. 2018a].

.

sensitivity of PECD to molecular orientation [Tia et al. 2017], initial electronic states [Powis et al. 2008], molecular geometry [Comby et al. 2016], molecular conformation [Garcia et al. 2008; Tia et al. 2014], vibrational excitation [Garcia et al. 2013a; Rafiee Fanood et al. 2017], clustering [Powis et al. 2013] and structural isomerism [Nahon et al. 2016; Powis et al. 2008] demonstrates the great potential of this observable to study ultrafast dynamics in excited chiral molecules. On the other hand, this sensitivity to many parameters also means that understanding the complex data from TR-PECD experiments will not be straightforward. We are nevertheless optimistic that the joint development of experimental and theoretical TR-PECD investigations will make this technique a standard ultrafast chirality measurement method.

5.2 Photoexcitation Circular Dichroism

5.2.1 First experimental signature of PXCD

In the previous section, we have presented an intuitive scheme to perform time-resolved PECD experiments, *i.e.* pumping the system using linearly polarized photon(s) and photoionizing it using circularly polarized light. Using this scheme, the forward-backward symmetry of the light-matter interaction is solely broken during the photoionization step, as in conventional PECD experiments. Using the experimental setup described above, it is very easy for us to change the relative polarization states between the 201 nm and the 405 nm pulses. We were curious to try a very counterintuitive scheme, where we would photoexcite the chiral molecules using right- or left- circularly polarized pulse and photoionize them using linearly polarized pulse. In this scheme, the forward-backward symmetry of the interaction would be solely broken during the pump (excitation) step. The electrons would be ripped off from the excited states using non-chiral light.

Photoexcitation of chiral molecules by circularly polarized radiation can be the subject of a standard absorption Circular Dichroism. For example, the probability to excite a chiral molecule from its ground state $|0\rangle$ to an excited state $|1\rangle$, using light at ω_{01} frequency (where $\Delta E_{01} = \hbar\omega_{01}$), will be different if the light is right- or left-circularly polarized ($\Delta\rho_{01}$). This CD originates from the interference between electric ($\vec{\mu}_{01}$) and magnetic dipole transition ($\vec{m}_{01}$). This is illustrated in Fig. 5.10. Because magnetic dipole transition amplitudes are typically several orders of magnitude smaller than electric dipole transition amplitudes, the CD signal is typically extremely weak (hundredth-thousandth of %). The CD effect, which is an angularly-integrated quantity, should slightly modulate the total photoelectron signal in a [1+1'] circular pump - linear probe experiment, but such low modulations ($10^{-5} - 10^{-6}$ relative) are difficult to detect in the gas phase because of the low target density (associated to a limited signal-to-noise ratio). However, in our experiments, we measure angularly-resolved photoelectron spectra. We will thus be able to determine

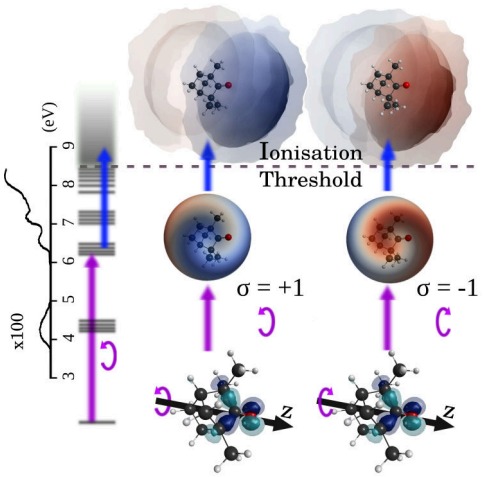

Figure 5.11: Artist view of the experiment. Absorption of circularly polarized femtosecond pulse at 201 nm with helicity $\sigma = \pm 1$ promotes an electron from the highest occupied molecular orbital to Rydberg bands. A linearly polarized femtosecond probe pulse at 405 nm photoionizes the molecule, and the angular distribution of the photoelectrons is recorded for both helicity of the pump pulse $\sigma = \pm 1$. The absorption spectrum of fenchone is adapted from [Pulm et al. 1997]. The figure is adapted from [Beaulieu et al. 2018a].

.

if we can extract dichroism information which would be hidden in angularly-integrated measurements.

The experimental setup is the same as the one used '[1+1'] TR-PECD. A circularly polarized femtosecond pump pulse at 201 nm (6.27 eV photon energy, 80 meV at $1/e^2$ electric field bandwidth) photoexcited enantiopure fenchone molecules to Rydberg bands through single-photon absorption. A time-delayed, linearly polarized probe pulse at 405 nm (3.1 eV photon energy, 85 meV at $1/e^2$ of the electric field bandwidth) induced one-photon ionization of the excited molecules. The cross-correlation of the pump and the probe pulses was 170 fs. The photoelectrons were accelerated and projected by an electrostatic lens onto a set of dual microchannel plates and imaged by a phosphor screen and a CCD camera. The (L) and (R) photoelectron images were recorded alternatively using left and right circularly polarized pump pulses respectively. The difference (L-R) and sum (L+R) of these two images were fitted by a linear combination of Legendre polynomials using a least-square fitting algorithm (p-Basex [Garcia et al. 2004]). The difference is given by (L-R) image while the (L+R) image reflects the angle-resolved photoelectron spectrum (PES). Fig. 5.11 present an artistic view of the experimental scheme.

Figure 5.12 show snapshots of the photoelectron forward-backward asymmetry (2(L-R)/(L+R)) for (+)- and (-)-fenchone, at a pump-probe delay of 700 fs, to avoid any pump-probe overlap effects. There is a large asymmetry in the photoelectron angular distribution, which reaches up to 3 % (several order of magnitude stronger than conventional CD) and which appears along the light propagation axis. This observation is absolutely astonishing, given the linearly polarized nature of the probe pulse. In fact, before we carried out the experiment, several of our colleagues had told us that in this polarization configuration, we should observe no asymmetry. This asymmetry reverses when we switch between the two fenchone enantiomers (Fig. 5.12). This is a signature that the (unknown) effect that produces this asymmetry is a genuine chiral effect, *i.e.* it changes sign upon symmetry operation of space inversion (switching the light or the molecular

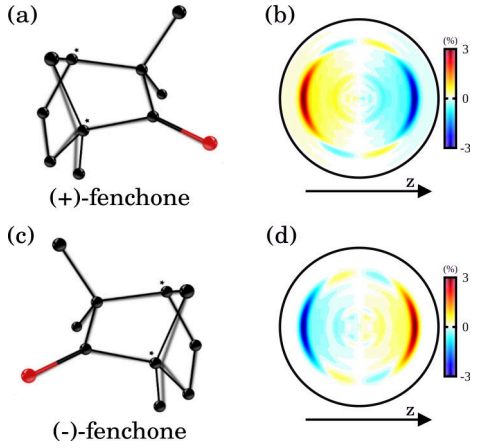

Figure 5.12: Snapshot of the photoelectron forward-backward asymmetry (2(L-R)/(L+R)) for (+)- and (-)-fenchone, at a pump-probe delay of 700 fs. In (b) and (d), the images have been pBasex inverted. The figure is adapted from [Beaulieu et al. 2018a].

handedness). These properties are very similar to the ones of PECD, but the underlying physics is fundamentally different since the electrons are removed from the Rydberg states by a linearly polarized photon. In analogy to PECD, we will now call this new chiroptical effect PhotoeXcitation induced Electron Circular Dichroism (PXECD). What is the physical mechanism underlying PXECD? This is the question that we will try to answer in the next few pages.

5.2.2 Understanding PXCD and PXECD: analytical theory perspective

The observation of forward-backward asymmetry in the PAD using linearly polarized ionizing radiation remained a puzzle to us for several months. As often when you have data that you do not understand, you ask your theoretician friends to help you. In order to unravel the mystery behind these observations, the problem was attacked from two different theoretical perspectives: i) our colleagues Bernard Pons and Baptiste Fabre performed hardcore quantum mechanical calculations mimicking similar conditions to the ones used in the experiments and ii) the group of Olga Smirnova, from MBI, developed a general analytical theory of the interaction of the light-chiral molecules. We will see how the synergy between analytical theory, numerical simulations and experimental results led us to understand the new chiroptical phenomenon inherent to the excitation of chiral molecules using ultrafast chiral pulses followed by photoionization using non-chiral pulses.

First, we will present the main results of the analytical theory developed by the MBI group. A complete derivation of this theory can be found in one of our recent paper [Beaulieu et al. 2018a], and in a series of two follow-up theory papers by the group of Olga Smirnova [Harvey et al. 2018; Ordonez et al. 2018]. Before dealing with the photoionization step, which involves electron removal from excited states using linear photon, we need to understand the dynamics launched in the bound states by the circularly polarized pump field. The first step is to look for any novel circular dichroism effects in the photoexcitation step (PhotoeXcitation Circular Dichroism, PXCD).

The molecule is described as a three-level system ($|0\rangle$, $|1\rangle$ and $|2\rangle$) and the laser-molecule interaction is described using first-order perturbation theory, within the dipole approximation. In the experiment, the pump field is circularly polarized and the measured photoelectron asymmetry is along the light propagation direction (z). The pump-induced

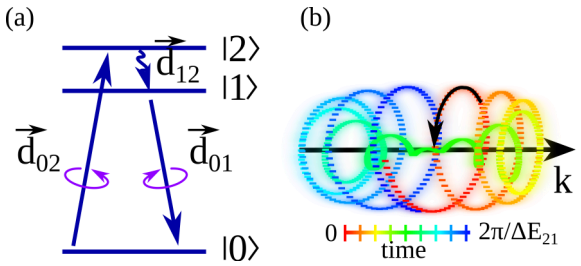

Figure 5.13: Ladder diagram representation of Photoexcitation Circular Dichroism (PXCD). PXCD requires a coherent excitation of two states by ultrashort circularly polarized pulse. (b) The map of the induced dipole as a function of time. One can notice that this induced dipole maps out a helix as a function of time. The figure is adapted from [Beaulieu et al. 2018a].

dipole is thus calculated along the z direction (d_z^{PXCD}), and averaged over all possible molecular orientations. The orientation-averaged induced dipole is shown to have a non-vanishing component along the light propagation direction z.

$$d_z^{PXCD} \propto \sigma[\vec{d}_{01} \times \vec{d}_{02}]\vec{d}_{12} \sin(\Delta E_{21} t), \tag{5.1}$$

where $\sigma = \pm 1$ is the light helicity, $\vec{d}_{01}$, $\vec{d}_{02}$ and $\vec{d}_{12}$ are the dipole transition vectors connecting the ground $|0\rangle$ and the two excited electronic states $|1\rangle, |2\rangle$ (Fig. 5.13 (a)), ΔE_{21} is the energy spacing between the two excited states. For more than two excited states, equation 5.1 will contain the sum over all pairs of excited states n, m, leading to oscillations of the dipole at all relevant frequencies ΔE_{nm}.

Despite its compact form, equation 5.1 provides very rich insights about the physics going on in the excited bound states. It shows that the coherent excitation of electronic states leads to a charge displacement along the light propagation direction. Hence, a dipole d_z^{PXCD} is created, with a chiral current (Fig. 5.13(b)) oscillating out of phase for the two enantiomers of a chiral molecule. The triple products (in this case $[\vec{d}_{01} \times \vec{d}_{02}]\vec{d}_{12}$) are characteristic measures of chirality. As any pseudoscalars [6], they must change sign upon reflection. Since such reflection transforms a random ensemble of left-handed molecules into a random ensemble of right-handed molecules, the triple-products will also have opposite signs for left-handed and right-handed molecular ensembles. For ensembles of non-chiral molecules, the dipole is equal to zero. In that case, reflecting the polarization plane will not change the molecular ensemble and hence the z-component of the current must remain the same, *i.e.* null. Remarkably, the derivation of equation 5.1 did not require any magnetic dipolar or electric multipolar effects. This means that the PXCD effect *could be* orders of magnitude stronger than standard photoabsorption CD, since its a pure electric dipolar effect.

Moreover, inspecting in greater details equation 5.1, we notice that PXCD arises only if the excitation dipoles $\vec{d}_{01}$, $\vec{d}_{02}$ are non-collinear: it is proportional to $\sigma \sin(\phi)$, where ϕ is the angle between the two transition dipoles. Since $\sigma = \pm 1$, $\sigma \sin(\phi) = \sin(\sigma\phi) = \sin(\sigma\omega\tau)$, where ω is the light frequency and $\tau = \phi/\omega$ is the time required by the light field to rotate by the angle ϕ. This gives an intuitive picture of PXCD, in analogy to conventional photoabsorption CD. Photoabsorption CD relies on the helical pitch of the laser field in space, which is given by the wavelength of the absorbed light, $\lambda > 2500$Å (1Å $= 10^{-8}$ cm). This pitch is barely noticeable on the molecular scale of ~ 1Å, leading to very weak signals. While photoabsorption CD exploits the helical pitch of the laser field in *space*, PXCD takes

[6] The hallmark of a chiral system is that it can support time-even pseudoscalar observables [Barron 2004]

advantage of the subcycle rotation of the light field in *time* and is inherently ultrafast. This makes PXCD a very sensitive effect, and also provides it with an intrinsic ultrafast temporal resolution. Last, let us note that PXCD vanishes if the coherence between excited states $|1\rangle$ and $|2\rangle$ is lost. PXCD is thus an effect which is sensitive to coherence, and not only to population.

Up to now, we have (*implicitly*) assumed that the states $|1\rangle$ and $|2\rangle$ were excited electronic states. What if these states are vibrational states? Can a vibrational wavepacket induce PXCD? The analytical theory from MBI shows that vibrational states within the same electronic state can also fulfill the PXCD condition, as long as their transition dipoles are not collinear. As shown in the Supplementary Information of [Beaulieu et al. 2018a], this non-collinearity condition requires the breakdown of the Franck-Condon approximation. This means that the electronic wavefunction must strongly vary with the position of the nuclei. Such dependence leads to the appearance of electronic currents stimulated by the nuclear motion, which is triggered by the pump pulse: vibrational PXCD is intertwined with the underlying chiral motion of electrons. The PXCD current can thus be induced with circularly polarized light either by direct coherent excitation of electronic states or by vibrational excitations involving a strong coupling between electronic and vibrational degrees of freedom. Note that this strong dependence of the electronic wavefunctions on the nuclear positions naturally arises in the vicinity of conical intersections between electronic potential surfaces. Thus, we expect that PXCD could be used to excite and reveal coherent chiral dynamics at conical intersections. Moreover, note that the case of vibrational-induced PXCD is fundamentally similar to the case of vibrational circular dichroism (VCD), where the nuclear motion driven directional electronic current lead to a (small) circular dichroism in the IR photoabsorption cross-section, which is an angularly-integrated physical observable. In our case, we have shown that looking at a vectorial observable (dipole, or the electronic current) leads to the unveiling of an enantiospecific vibrational-induced electronic current, which expresses as a dynamical (and large) forward-backward asymmetry in the bound electronic density (PXCD).

So at this point, we have presented, based on a very general analytical theory, a new chiroptical effect named PXCD, which induces a forward-backward asymmetry in the *bound* electronic density. This is fundamentally intresting, but this cannot *a priori* be directly linked to the surprising forward-backward asymmetry in the photoelectron angular distribution, measured experimentally by using linear ionizing photon. Indeed, it is of common belief that a chiral object can only be distinguished by the interaction with another chiral object (*e.g.* circular photon).

We now present the general analytical theory of photoionization from excited chiral molecules exhibiting a non-vanishing PXCD, using linearly polarized photon. We will try to see if the photoionization of molecules characterized by forward-backward asymmetry in their *bound* electronic density results in a forward-backward asymmetric photoelectron angular distribution.

The physical quantity of interest in now the outgoing photoelectron current averaged over molecular orientations. A long and meticulous derivation of this quantity (by our collaborators from MBI), is presented in the SI of [Beaulieu et al. 2018a], and in a follow-up theory paper [Harvey et al. 2018]. Here, we will present the final results of this derivation, since it is more than enough to grasp the details of the underlying physics. The photoelectron current averaged over molecular orientations $J_z(k)$ is found to be:

$$J_z(k) = \sigma[\vec{d}_{01} \times \vec{d}_{02}]\vec{D}^{r}_{12}(k)\sin(\Delta E_{21}\tau) + \sigma[\vec{d}_{01} \times \vec{d}_{02}]\vec{D}^{i(k)}_{12}\cos(\Delta E_{21}\tau) \tag{5.2}$$

with $J_x(k) = J_y(k) = 0$ and where τ is the pump-probe delay, k is the photoelectron mo-

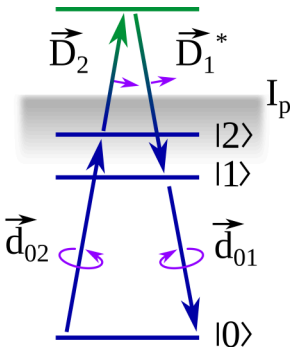

Figure 5.14: Ladder diagram representation of PhotoeXcitation induced Electron Circular Dichroism (PXECD). In PXECD (equation 5.2) the two excited states are connected by transitions via the continuum, stimulated by a linearly polarized probe pulse. The figure is adapted from [Beaulieu et al. 2018a].

mentum, $\vec{D}_{12}(k) = \vec{D}^r_{12}(k) + i\vec{D}^i_{12}(k)$ is the bound-continuum transition (photoionization) vector which connects the excited bound states via the common continuum and plays the role of $\vec{d}_{12}$ in equation (5.1). A schematic of the photoionization process from a coherent superposition of states is shown in Fig. 5.14.

Looking at equation 5.2, we can clearly notice some similarity to equation 5.1. The outgoing photoelectron current along the laser propagation direction $J_z(k)$ (Eq. 5.2) contains two triple products (pseudoscalars). Just like the triple product $[\vec{d}_{01} \times \vec{d}_{02}]\vec{d}_{12}$ which was encountered in the expression of PXCD (Eq. 5.1), both $[\vec{d}_{01} \times \vec{d}_{02}]\vec{D}^r_{12}$ and $[\vec{d}_{01} \times \vec{d}_{02}]\vec{D}^i_{12}$ will change sign upon parity inversion. Thus, the photoelectron current $J_z(k)$ in equation 5.2, which is forward-backward asymmetric, is a pseudo-scalar observable; it reverses its direction if the handedness σ of the pump pulse or of the enantiomer is swapped, showing that $J_z(k)$ is a genuine chiral effect. Let us recall that the ionizing photon is linearly polarized. This means that the forward-backward asymmetry imprinted in the excited bound states through the PXCD effect can be transferred to the ionization continuum using non-chiral pulses, which is remarkable. Moreover, as one can see in equation 5.2, the chiral nature of the response arises only if the participating bound states are coherently excited. Once the coherence is lost, the chiral signal will also disappear. The coherence underlying PXCD allows a chiral object to 'interact with itself', through a common continuum state, thus mimicking interaction with "another chiral object" and removing any need for other chiral interactions during the probe step (see Fig.5.14).

Importantly, the state of the continuum does not need to be chiral, as it only provides a link between the two chiral bound states $|1\rangle$ and $|2\rangle$ (Fig. 5.14). Let us give more details about what we mean by a chiral continuum. In an achiral molecule, the continuum is obviously achiral. In chiral molecules, tens of eV above the ionization threshold, the continuum is not chiral, *i.e.* a photoelectron ejected with very high kinetic energy does not feel the chirality of the molecular potential (plane-wave approximation). On the other hand, the continuum is said to be chiral near the ionization threshold because slow outgoing photoelectrons strongly feel the chiral molecular potential, which impacts their scattering dynamics and their final PAD. This chirality of the continuum is what leads to the PECD effect in the photoionization of chiral molecules by circularly polarized light, even when the ionized molecular orbital does not show a chiral character [Harding et al. 2005].

In order to make sure that the PXECD is not coming from a effect of the continuum chirality, the MBI team rederived the equation of $J_z(k)$ (PXECD), by assuming a plane-

wave continuum $J_z^{PW}(k)$. This procedure eliminates any possibility of chiral contributions from the continuum state (*i.e.* photoelectron scattering from the chiral potential of the ionic core). The photoelectron current along the laser propagation direction, for plane-wave continuum $J_z^{PW}(k)$, is shown to be:

$$J_z^{PW}(k) = -\sigma[\vec{d}_{01} \times \vec{d}_{02}]\vec{D}_{12}^{i,PW}(k)\cos(\Delta E_{21}\tau). \tag{5.3}$$

This equation looks roughly similar to the equation 5.2. The most important point here is that Eq. 5.3 shows that the PXECD current remains chiral for every k, even when the chiral character of the continuum is removed (by using a plane wave continuum instead). Thus, PXECD can be used as a probe which is exclusively sensitive to bound chiral dynamics. The analytical theory provides a direct link between PXCD and the forward-backward asymmetry measured upon photoionization using linearly polarized light (PXECD).

To quickly wrap up about what we have leaned from the analytical theory underlying PXCD and PXECD: the coherent excitation of an ensemble of randomly oriented chiral molecules, using a circularly polarized light, from the ground $|0\rangle$ to two excited states $|1\rangle$ and $|2\rangle$, characterized by non-collinear transition dipoles $\vec{d}_{01}$, $\vec{d}_{02}$, leads to an oscillating dipole (at frequency $\Delta E_{12}/\hbar$) in the direction of the light propagation axis. The dipole reverses when changing the handedness of the molecules or of the photons, meaning that PXCD is a genuine chiral effect. The excited electrons develop a helical motion when driven by the planar rotation of the electric field of circularly polarized light. This motion can be compared to macroscopic world examples where chiral dynamics created by helical structures convert rotations in a plane into translational motion orthogonal to it. For instance, one can think about Archimedes screw, where rotations of the screw induce a linear displacement of liquid orthogonal to the plane of rotation. Plane propellers and household fans are also good examples of devices that take advantage of the directional translational displacement induced by the rotation of a chiral object.

Next, it has been shown that photoionization with linearly polarized pulses is a good way of probing the oscillating dipole along the light propagation axis d_z^{PXCD}, leading to a forward-backward asymmetric PAD. The combination of PXCD and PXECD can thus explain the experimental observation of forward-backward asymmetry in the PAD, when the excitation of a bound wavepacket is performed using circular photon and photoionization from this wavepacket is performed using non-chiral linearly polarized photon.

5.2.3 Understanding PXCD and PXECD: quantum calculations perspective

In order to gain more quantitative insight about PXCD and PXECD, Bernard Pons and Baptiste Fabre have performed numerical quantum mechanical calculations, using a pump-probe scheme similar as in the experiment, based on first-order perturbation. Given the single-photon nature of the photoexcitation, high-order (multiphoton) processes can be depreciated. They simulated the excitation around the s- and p-manifold of Rydberg states in fenchone by a circularly polarized pump pulse. The molecular states were determined by using the Hartree-Fock level of theory using the 6-311++G** [Krishnan et al. 1980] (GAMESS package [Schmidt et al. 1993]). A lot of details about the calculation of the molecular states are given in the SI of [Beaulieu et al. 2018a]. They calculated the molecular orientation-averaged excitation probability of the Rydberg states by the pump pulse. As expected, the most populated states are the 3s and 3p Rydberg ones (Fig. 5.15 (a)). Moreover, the bound state populations, after excitation by the pump, are the same

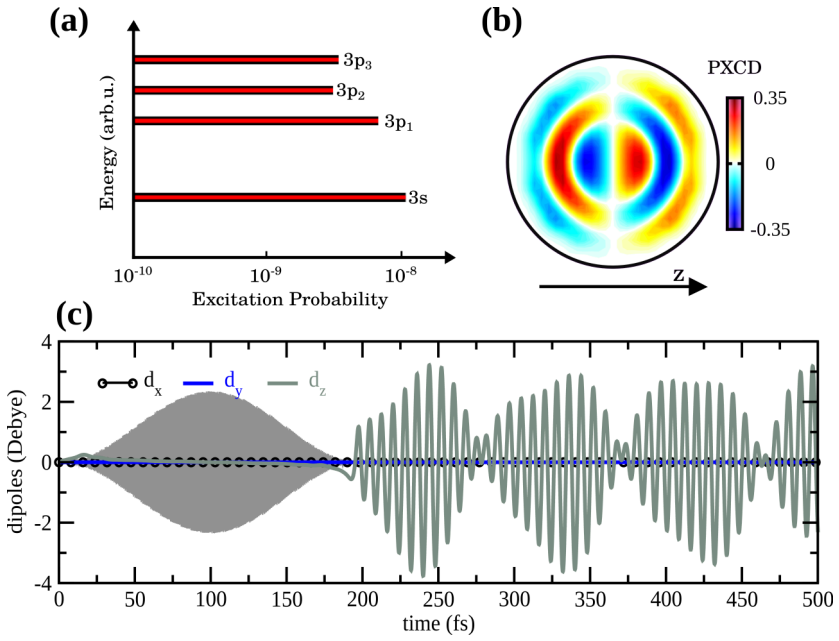

Figure 5.15: (a) Orientation-averaged bound state populations at the end of the pump pulse. The pump pulse used in the simulation are centered around 200 nm, their FWHM duration is 72 fs and the intensity is 10^{12}W/cm^2. (b) Momentum space electron density underlying PXCD. The asymmetry is formed along the light propagation direction z. (c) Temporal evolution of the x-, y- and z-components of the macroscopic dipole associated with the (3s,3p) Rydberg wave-packet created by the pump pulse (the shaded area). Only the z-component, along with the direction of propagation of the pump and probe pulses, survives orientational averaging. The figure is adapted from [Beaulieu et al. 2018a].

for both light helicity $\sigma \pm 1$. This is due to the fact that there is no absorption CD in the electric dipole approximation.

The strength of the PXCD can be quantified by the magnitude of the chiral component within the excited electron density. It was obtained by subtracting the momentum space electronic density $\mathcal{D}$ obtained with right (R) and left (L) circularly polarized light: $PXCD = 2(\mathcal{D}(L) - \mathcal{D}(R))/(\mathcal{D}(L) + \mathcal{D}(R))$. The calculated PXCD reaches very high values ($\sim$ 35 %, Fig. 5.15 (b)). In order to determine the temporal evolution of the process, the PXCD and the associated dipole moment d_z^{PXCD} were calculated as a function of time after photoexcitation. The dipole moment along the light propagation axis d_z^{PXCD} reaches values up to $\pm$ 3 Debye (Fig. 5.15 (c)) and oscillates at frequencies determined by the energy differences between the states forming the electronic wavepacket. To give a coarse feeling about the strength of the transient dipole moment induces by the PXCD effect (more than 3 Debye), the permanent dipole moment of water molecules, which is considered to be a strongly polar molecule, is only $\sim$ 1.8 Debye.

Now that the quantum mechanical calculation in fenchone has demonstrated the production of a strong PXCD effect, it would be interesting to investigate the photoionization from the asymmetric bound excited states with linear photon, in order to quantitatively study the PXECD effect. Figure 5.16 shows the PXECD computed at the end of the probe pulse (400 nm, τ = 36 fs). This theoretical result shows that PXECD is reaching up to $\sim$ 6 % amplitude. Because of the approximations made in the construction of the molecular states, we should not try to compare the experimental and simulated PXECD absolute values and angular distributions. However, the quantum calculations remarkably lead to the same conclusion that the analytical theory: the photoionization of the wavepacket ex-

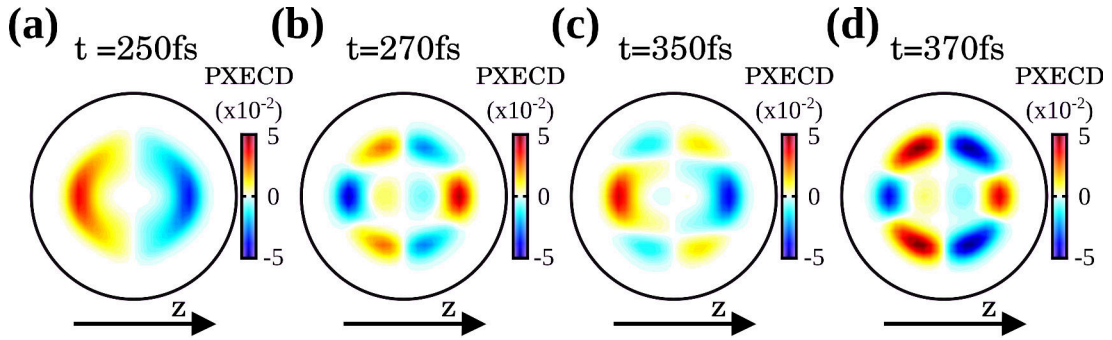

Figure 5.16: Momentum space PXECD signals at various pump-probe delays τ calculated with a probe duration of 36 fs (FWHM in intensity). The momentum scale goes from 0 to 0.6 atomic units. The figure is adapted from [Beaulieu et al. 2018a].

hibiting PXCD using non-chiral light leads to forward-backward asymmetry in the ejected photoelectron angular distribution. Moreover, one can see in Fig. 5.16 that the beating of the dipole within the bound wavepacket (Fig. 5.15 (c)) is revealed in the time-resolved PXECD signals. This means that the chiral dynamics of the bound wavepacket can be revealed by monitoring the PXECD as a function of pump-probe delay, where the probe step is the ionization with linearly polarized (non-chiral) pulses. However, the probe pulse duration is very important to resolve the d_z^{PXCD} beating using PXECD. Indeed, as shown in Fig. 5.15, the d_z^{PXCD} oscillates at all $\Delta E_{nm}/\hbar$ frequencies, where ΔE_{nm} is the energy difference between all (n,m) states within the wavepacket. Thus, the oscillation components which oscillate at a much faster frequency than the probe pulse duration will be washed out. In the simulation, where a 36 fs (FWHM) probe pulse is used, the fast (period of $\sim$ 10 fs) oscillations are blurred by the probe pulse duration while the slow (period of $\sim$ 100 fs) oscillations of the d_z^{PXCD} are revealed by the PXECD.

The experimental observation of forward-backward asymmetry in the PAD using this counterintuitive pump-probe configuration now seems to be well understood, thanks to the synergy between analytical theory (developed at MBI) and numerical simulations (performed at CELIA). We will now go back to experimental data, where we have scanned the delay between the 201 nm pump and 405 nm probe pulse, to try to follow the dynamics of the bound chiral wavepacket using PXECD as the observable.

5.2.4 Dynamics of the bound chiral wavepacket probed using TR-PXECD

Let us now present the experimental results of the TR-PXECD experiments performed in fenchone using the setup described above. As described many times throughout this thesis manuscript, the sum (L+R) and difference (L-R) images have been decomposed onto a Legendre coefficient basis sets using pBasex, even if the cylindrical symmetry is broken by the fact that we use linear and circular photons. A detailed discussion about the images inversion in a case where the cylindrical symmetry is broken is presented in the SI of the reference [Beaulieu et al. 2018a]. To emphasise the difference between PECD and PXECD, we now call the first and third Legendre polynomial coefficients α and α' instead of $\tilde{b_1}$ and $\tilde{b_3}$. The dynamics of the PES, α and α', in our TR-PXECD experiment in fenchone, are presented in figure 5.17.

The photoelectron spectrum contains a single broad component in energy, corresponding to ionization from the HOMO orbital (vertical ionization potential $\sim$ 8.72 eV). It does not spectrally shift with the pump-probe delay (Fig. 5.17 (b)) and decays monoexponentially in a characteristic time of 3.3 ps, reflecting a simple relaxation of the Rydberg

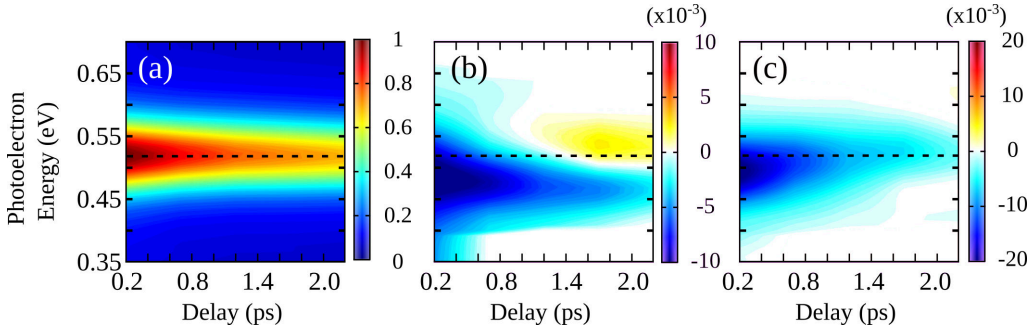

Figure 5.17: Time-resolved PXECD in fenchone. (a) Evolution of the PES and PXECD α (b) and α' (c) coefficients as a function of the pump-probe delay and the photoelectron kinetic energy, in (1R)-(+)-camphor. The black dotted lines represent the kinetic energy of the photoelectron corresponding to the maximum of PES. The decay time of the main PES component is 3.28 ± 0.05. The figure is adapted from [Beaulieu et al. 2018a].

population onto lower states which cannot be photoionized by one probe photon alone. This decay time of the Rydberg states is in good agreement with what has been found in TR-PECD experiments. The temporal evolution of the PXECD image shows much richer spectroscopic features, which can be analyzed by decomposing it in odd Legendre polynomials (Fig. 5.17(a)). We note that a sum of first- and third-order Legendre polynomials, with coefficients α and α', is enough to fit the PXECD images. Both coefficients maximize around ~ 50 meV below the maximum of the PES.

The α and α' signals can be decomposed into two components: below and above the maximum of the PES. The low-energy component of α undergoes a rather slow decay. On the contrary, its high-energy component decays very quickly and even changes sign around 1 ps. For α' the behavior is opposite, *i.e.* the high-energy component shows much slower dynamics than the low-energy part. We can also notice that we do not resolve any periodic oscillation in the PXECD. This is not surprising since the cross-correlation is ~ 170 fs. The long duration of the pulses prevents the resolution of any fast oscillation of the PXECD. Contrariwise, we see a slower dynamics that modify the PXECD on the (sub-) picosecond time scale. The electronic excitation of the molecules is expected to be accompanied by a significant vibrational excitation, since the equilibrium geometries of Rydberg states are quite different from that of the ground state. The molecules will tend to relax towards the equilibrium geometry of the Rydberg states and oscillate around it.

In order to determine the sensitivity of PXECD to the geometry of the molecule, we have performed numerical simulation of PXECD in two different geometries: the ground and the 3s Rydberg states equilibrium geometry. The results (Fig. 5.18) show that even small bond length changes ($\leq 7\%$) lead to significant modification of the PXECD signal. We also see that the vibrational motion does not only change the amplitude of the PXECD but also its angular constitution. This demonstrates the remarkable sensitivity of PXECD to molecular vibrations, which follow the electronic excitation. Molecular structural changes upon photoexcitation might be at the origin of early time-delay dynamics of the PXECD. The long time-scale dynamics might be due to the loss of coherence. Indeed, around 4 ps (not shown), the PXECD completely vanishes while the Rydberg population is still 30% of its initial value. This result unambiguously reflects the loss of wavepacket coherence.

Earlier in the section, we have explained that the PXCD current could be induced with circularly polarized light either by direct coherent excitation of electronic states or by vibrational excitations with a strong coupling between electronic and vibrational degrees of freedom. What is the origin of the PXCD current in our fenchone experiments?

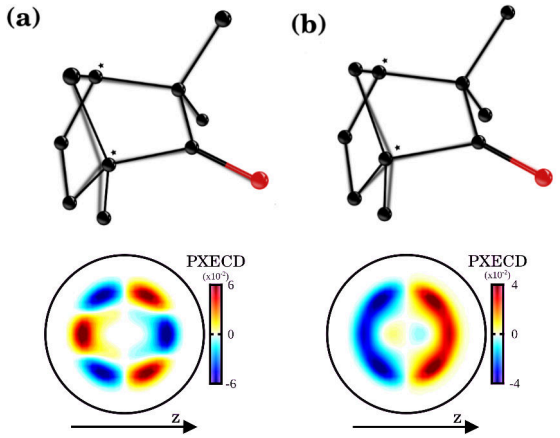

Figure 5.18: Sensitivity of PXECD in (1S)-(+)-fenchone to the evolution of the chiral molecular structure. (a) The equilibrium geometries of the ground (dark) and 3s (shadowed) electronic states, and the PXECD signal computed at $t = 370$ fs using the ground state geometry for both the pump excitation and the probe ionization. (b) The representation of the geometries are exchanged and the PXECD is now calculated for the 3s equilibrium geometry. The PXECD images are averaged over random molecular orientations and calculated with a 36 fs duration of the probe pulse. The figure is adapted from [Beaulieu et al. 2018a].

According to numerical simulation, the simultaneous population of 3s and 3p Rydberg states of fenchone, using 201 nm pulses, is possible. However, the 3s population strongly dominates over the 3p population. Since our temporal resolution is too poor to resolve the current beating, it is hard to determine if the PXECD current is induced by the excitation of a pure electronic wavepacket or by a vibronic wavepacket.

Next, we will present the experimental data of TR-PXECD experiments performed in camphor molecules. One major difference between the two structural isomers is that the *s*- and *p*- Rydberg bands of camphor are upshifted by additional several tens of meV compared to fenchone. This upshift of the bands prevents direct excitation of the *p*- states by the pump pulse. So, for the case of camphor, if we measure a non-vanishing PXECD, we will know for sure that it originates from the chiral PXCD current induced by a vibronic wavepacket. The experimental results, for two different pump wavelength (200 nm and 202 nm) are presented in Fig. 5.19.

The experiment performed in camphor still reveals a strong PXECD signal for both pump wavelengths, indicating that a chiral vibronic wavepacket, and thus a chiral PXCD current, has been created in camphor. With these results, we also demonstrate the PXCD and PXECD are highly sensitive to specific molecular structure. Indeed, the PXECD images, and their dynamics, from the two isomers (camphor and fenchone) are drastically different. The α' coefficients in camphor and fenchone are of opposite sign. This has also been seen in multiphoton [Lux et al. 2015] and one-photon PECD [Nahon et al. 2015] experiments. In our experiment, this could be a consequence of PXECD sensitivity to isomerism, but it might also be a signature of the different nature of the excited chiral electronic currents in fenchone and camphor. Changing the excitation wavelength from 202 nm to 200 nm does not affect the monoexponential decay of the PES. In contrast, a strong change is observed in the PXECD: the α' magnitude is almost twice as large and it is shifted in energy towards the red wing of the photoelectron spectrum. The drastic change observed in the PXECD signal in camphor when increasing the pump photon energy by only 60 meV illustrates the extreme sensitivity of this measurement to the excited vibrational dynamics.

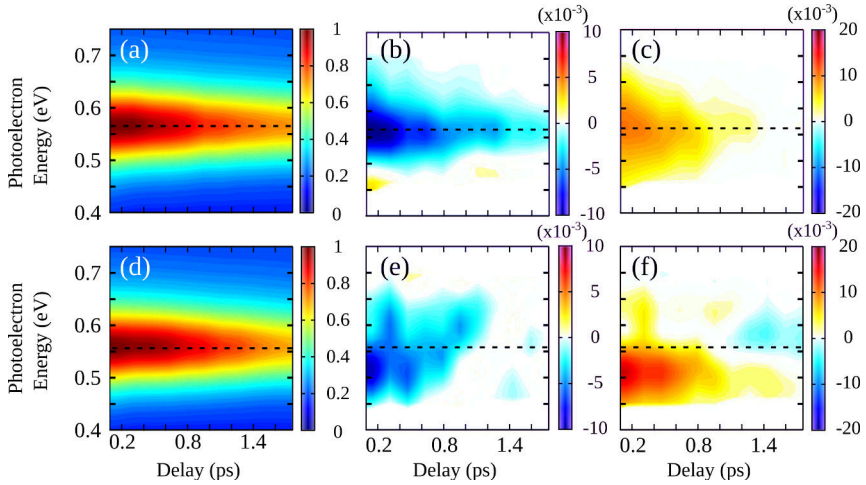

Figure 5.19: Time-resolved PXECD in camphor. For the data presented in the upper (lower) panels, we used 202 nm (200 nm) pump pulses. (a),(d) Evolution of the PES and PXECD α (b),(e) and α' (c),(f) coefficients as a function of the pump-probe delay and the photoelectron kinetic energy, in (1S)-(+)-fenchone. The black dotted lines represent the kinetic energy of the photoelectron corresponding to the maximum of PES. The figure is adapted from [Beaulieu et al. 2018a].

5.2.5 Comparison with microwave three-wave mixing in chiral molecules

After our quest to understand the PXCD and PXECD effects, helped by analytical theory and numerical simulation, we have found in the literature a similar effect which is used for chiral analysis using broadband rotational spectroscopy [Patterson et al. 2013a; Patterson et al. 2013b; Shubert et al. 2016]. The concept of chiral identification using microwave spectroscopy is illustrated in Fig. 5.20. As PXCD, the technique relies on the unique spectroscopic properties of enantiomers of a chiral molecule to have a opposite scalar triple product of three transition dipole moments $\vec{\mu}_a \cdot [\vec{\mu}_b x \mu_c]$ associated with three electric dipole allow transitions ($\vec{\mu}_a = \langle a|\vec{\mu}|b\rangle$, $\vec{\mu}_b = \langle b|\vec{\mu}|c\rangle$ and $\vec{\mu}_c = \langle c|\vec{\mu}|a\rangle$), as shown in Fig. 5.20 (a)-(b).

In this technique, the chirosensitive signal also relies on non-parallel transition dipole moments to coherently populate two excited states ($|b\rangle$ and $|c\rangle$). In this case, the excitation is performed using two linearly polarized pulses, which are mutually perpendicularly polarized, instead of a single broadband circularly polarized pulses (PXCD). As a result of this combined excitation, the wavepacket will emit Free Induction Decay (FID) radiation, in a direction orthogonal to the two exciting pulses (see Fig. 5.20 (c)). Because of the opposite sign of the scalar triple product for the enantiomers, the FID will be π-phase shifted (out-of-phase) for the two mirror images of a chiral molecule (see Fig.5.20). The phase of the microwave FID signal perpendicular to the excitation pulses thus encodes the chirality of the excited sample [Patterson et al. 2013a; Patterson et al. 2013b]. This technique can also be used to determine the enantiomeric excess in a gas phase sample [Patterson et al. 2013a; Shubert et al. 2016]. This microwave technique is similar to PXCD in the sense that it needs a three-level system to induces an oscillating dipole in a direction perpendicular to the polarization plane/axis of the exciting pulse(s), and produces dipoles that oscillate out-of-phase for the two enantiomers of a given chiral molecule. Another similar aspect of these two phenomena is their potential application for chiral separation in the gas phase. Indeed, the existence of the enantio-sensitive dipole, which occurs for both PXCD and rotational excitation, opens the way to the separation of enantiomers in isotropic racemic mixtures in the gas phase. In our case (PXCD), we envision the

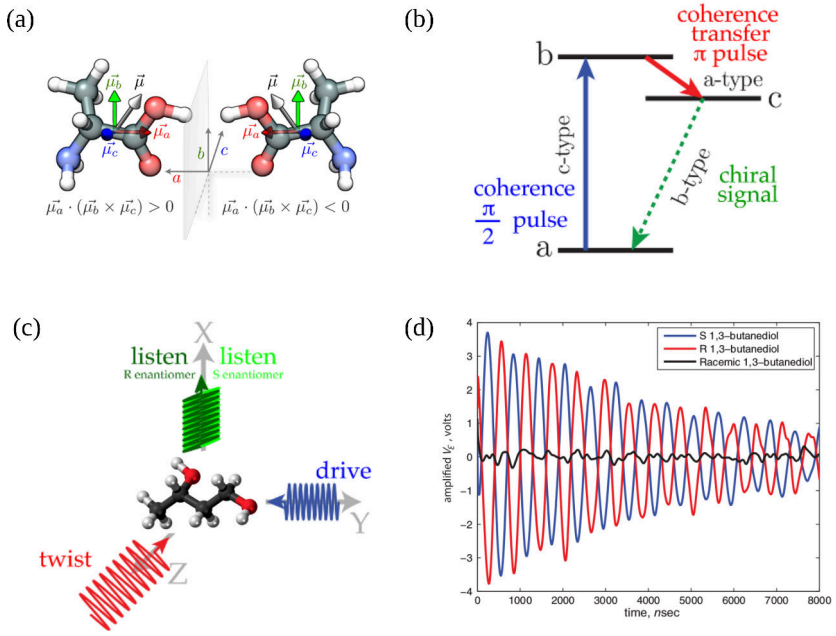

Figure 5.20: Schematic of chiral analysis using microwave three-wave mixing. In (a), we show that two enantiomers have opposite scalar triple products of the transition dipole moment components. The scalar triple product changes sign upon mirror reflection. Note that the molecules used in the experiments presented in (d) (1,3-butanediol) are not the same that the one presented in this scheme (alanine). In (b) is the energy level diagram of the microwave three-wave mixing experiments. In (c), the geometry of the experiment is presented. The driving field comes along the Y-axis and is polarized along the X-axis. The twist field comes along the Z-axis and is polarized along the Y-axis. The molecular emission triggered by this two-pulse excitation is along the X-axis and is polarized along the Z-axis. These three first panels (a-c) were adapted from [Shubert et al. 2016]. In (d) is the enantiomer dependent signals for S-, R- and a racemic mixture of 1,3-butanediol. This panel is adapted from [Patterson et al. 2013a].

application of carrier-envelope phase-controlled visible or IR fields, resonant with the electronic transition.

Even if this chiral microwave three-wave mixing is fundamentally similar to PXCD, there are also significant differences between the two phenomena. The fact that one technique manipulates the rotational degrees of freedom and the other one (PXCD) the vibrational and/or electronic degrees of freedom leads to a difference in their potential applications. One advantage of microwave three-wave mixing is that it is easy to synthesize and measure microwave radiation, both in amplitude and phase, which render probing of the chirosensitive FID relatively easy. On the contrary, these dynamics leading to the chiral discrimination is occurring in the electronic ground state of the molecules. One advantage of PXCD is the fact that its sensitive to ultrafast vibronic dynamics in chiral molecules. It thus intrinsically provides a novel probe for our understanding of dynamical chirality. In the future, it would thus be great to directly detect the (THz) FID emitted by the (PXCD) wavepacket perpendicular to the exciting pulse propagation axis, in a similar fashion as in microwave three-wave mixing.

5.2.6 Partial conclusions and perspectives

In conclusion, by using a counterintuitive polarization scheme, *i.e.* circular pump and linear probe that photoionizes chiral molecules and by detecting the angular distribution of the photoelectrons, we have discovered two new chiroptical effects, namely PXCD

and PXECD. First, PXCD can be seen as a new type of CD effect, which emerges when a wavepacket is created in chiral molecules using chiral light. PXCD should not be mixed up with CD. First, CD is an angularly-integrated (scalar) observable while PXCD is a vectorial observable. CD is sensitive to the helical structure of light in space. However, the size of the helical pitch of light is given by its wavelength and is orders of magnitude larger than the size of the molecule. The molecule can hardly feel it. It leads to an extremely weak chiral response in CD. In PXCD, we use a helix which is orders of magnitude more compact, namely the one formed by the helical motion of bound electrons excited states of a chiral molecule. Such helix not only has the right size to explore molecular chirality, but it is also inherently ultrafast, leading to strong, ultrafast chiral response. Indeed, PXCD leads to a dipole in the propagation direction of the light that was used to excite the molecules, which oscillates at all the frequencies corresponding to the energy difference of each state within the wavepacket. The sign of PXCD changes when switching the handedness of the light or of the molecular ensemble, which is the signature that PXCD is a genuine chiral observable.

This PXCD chiral dipole has been shown to be revealed by a forward-backward asymmetry in the photoelectron angular distribution upon photoionization with *linear* photon. This effect, called PXECD has been predicted by analytical theory and has been observed in both quantum mechanical simulation and experimental data. At first sight, PXECD seems to go against the common belief that a chiral object can only be distinguished by the interaction with another chiral object. The coherent nature of the superposition of states leading to PXCD allows to project them onto the same continuum states. This can be seen as making a chiral object 'interact with itself', thus mimicking interaction with "another chiral object" and removing any need for other chiral interactions during the probe step. The discovery of these new chiroptical phenomena is by itself fundamentally interesting. Moreover, our study paves the way towards selective detection of excited chiral dynamics in neutral systems without contamination by additional types of chiral interactions induced by chiral probes, in contrast to all other existing techniques.

For future experiments, we can think of different ways of probing the PXCD dipole d_z^{PXCD}. Indeed, because there is an asymmetric charge oscillation in the z axis, one could think of probing these dynamics using time-resolved x-ray diffraction, to directly follow temporal evolution of the electronic density along z. Moreover, because there is a coherent dipole oscillation along the light propagation axis (z), coherent radiation at $\Delta E_{nm}/\hbar$ frequencies will also be emitted in directions perpendicular to z (Free Induction Decay, see chapter 2). The detection of the amplitude and phase of the electromagnetic field emitted by this wavepacket would thus provide invaluable information about the ongoing chirosensitive dynamics in the photoexcited molecular ensemble.

5.3 Conclusion

In this chapter, several novel concepts have been introduced. First, we have extended the powerful technique of time-resolved photoelectron spectroscopy (TR-PES) to the study of chiral molecules undergoing dynamics in the gas-phase. TR-PES is a well-known technique which has been successful in the elucidation of the dynamical behavior of photoexcited molecules because of its sensitivity to the modification of both nuclear geometry and electronic character of the target. By looking at the time-dependence of the asymmetry of the photoelectron spectrum along the light propagation axis, in photoexcited chiral molecules, we have introduced the concept of time-resolved photoelectron circular dichroism (TR-PECD). In these experiments, a linearly polarized pump pulse launches a dynamics, and a circularly polarized probe pulse photoionized the chiral molecules. We

have shown, for the first time, the opportunities to study the picosecond and femtosecond dynamics in photoexcited gas-phase chiral molecular sample, in an enantiospecific fashion.

By using the exact same setup, our curiosity led us to perform a similar experiment but using a counterintuitive polarization configuration. We have used a chiral pump pulse to create a wavepacket in chiral molecules, and a non-chiral probe pulse to photoionize these excited molecules. If our observable had been the angularly-integrated photoelectron spectrum (scalar observable), our measurement would have been an *indirect* measurement of standard absorption circular dichroism, which would have led to really small (unmeasurable) signals. By measuring the angularly-resolved photoelectron spectrum (vectorial observable), we have seen a strong asymmetry along the light propagation in the number of ejected photoelectron, which is remarkable given the non-chiral nature of the ionizing photon. The synergy between analytical theory, quantum mechanical calculations and experimental observations has enabled to understand this asymmetry in term of two new genuine chiral phenomena: PhotoeXcitation Circular Dichroism (PXCD) and PhotoeXcitation-induced Electron Circular Dichroism (PXECD). PXCD is described in term of the emergence of an enantiospecific bounded oscillating dipole along the light propagation axis when multiple excited states are coherently populated using circular photons. The phase of the dipole oscillations reverses when switching the molecule or the pump pulse handedness, which is the hallmark of chiral observables. Photoionizing different bound states within the wavepacket to the same final state, using linear (non-chiral) photons, leads to the emergence of a forward-backward asymmetry in the angular distribution of the photoelectrons. This phenomenon is called PXECD, and is also a new type of chiral observable.

As we have seen in the previous chapter, i^2PEPICO and COLTRIMS detection schemes allow electron-ion coincidence measurements, representing the grail of photoionization-type molecular experiments. The group at CELIA is currently building a COLTRIMS apparatus (from RoentDek GmbH) as an end-station of a 166 KHz-2 MHz tunable UV-VIS-IR pump - HHG-based circular VUV-XUV probe beamline. By increasing the dimensionality of the measurement, given the tunability in both wavelength and polarization state of both UV-VIS-IR pump and VUV-XUV probe, by detecting electrons and ions in coincidence, and given the data quality expected with a multi-hundred-kHz laser system, this setup will allow to tackle important questions related to the chiral recognition in gas-phase and to the birth and death of chirality in molecular assemblies.

6. Attosecond-resolved photoionization of chiral molecules

6.1 Delays in photoionization

Since the discovery of the photoelectric effect by Albert Einstein in 1905, the ejection of electrons from matter upon light absorption was considered to be instantaneous from an experimental point of view. Nowadays, with the rapid development of attosecond metrology techniques, it is possible to measure the electron dynamics on their natural (attosecond) timescale. In this context, recent attosecond-resolved photoionization experiments have been performed, revealing that electrons take a finite time to leave their parent ion. This emerging field of research has known a spectacular development. The first measurements were conducted on solid targets in Garching [Cavalieri et al. 2007], revealing a ~ 100 as delay between electrons ejected from the 4f state and conduction band of tungsten. However the interpretation of this delay was extremely challenging because of the complexity of the system – tens of theoretical papers explained the measured delay with different models and sometimes contradicting interpretations. It was thus necessary to somehow step back and consider simpler cases. The Lund group investigated the delays between electrons ejected from 3s and 3p states of atomic argon [Klünder et al. 2011]. By carefully taking into account the influence of the laser field used in the measurement procedure, they were able to establish a general framework for the determination of photoionization delays [Dahlström et al. 2012]. The Bordeaux and Saclay teams characterized the photoionization of nitrogen molecules, revealing that electrons associated with different electronic or vibrational states of the ion were delayed, in particular close to a resonance [Haessler et al. 2009]. The influence of resonances was studied in greater details by the Lund and Saclay groups in rare gases [Gruson et al. 2016; Kotur et al. 2016], leading to the reconstruction of the temporal shape of an autoionizing wavepacket [Gruson et al. 2016]. Last, more subtle effects such as the influence of the electron ejection direction in non-resonant [Heuser et al. 2016] and resonant photoionization [Cirelli et al. 2018] were recently investigated.

Within this context, and following the investigations of photoionization of chiral molecules that we performed in this thesis, it seemed natural to address the question

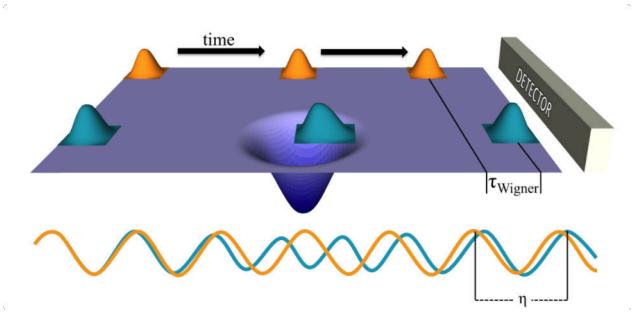

Figure 6.1: Schematic representation of Wigner time delay. In orange, a free electron wavepacket traveling with a given momentum toward a virtual detector, located asymptotically. In blue, an electron wavepacket traveling with the same momentum as the orange wavepacket, toward the virtual detector. During its propagation, the blue electron wavepacket scatters off an attractive potential, where it is transiently accelerated, leading to its arrival on the virtual detector before the free electron wavepacket (orange). This arrival time difference is defined as the Wigner time delay τ_W. Below, representation of the effect of the scattering off the potential, in term of scattering phase of the photoelectron wavepacket. The wavepacket scattering off the potential acquires an asymptotic phase shift η compared to a reference free electron (orange).

of the dynamics of the chiral photoionization process. Indeed, the forward/backward asymmetry which emerges when randomly oriented chiral molecules are photoionized by circularly polarized radiation (PhotoElectron Circular Dichroism, PECD) results from the scattering of the electrons in the chiral potential. Does this mean that electrons ejected forward and backward are delayed with respect to each other? We answer this question in this chapter.

6.1.1 Theoretical description of photoionization delays

When an atom or a molecule absorbs a photon of energy greater than its ionization potential, the transition from a bound molecular state $|\Psi_0\rangle$ to a continuum state $|\Psi_{\mathbf{k}}^{(-)}\rangle$ leads to the release of an outgoing electron wavepacket. In the electric dipole approximation, the ionization cross sections and the dynamics of this photoionization process depend on the transition dipole matrix element, $\mathcal{D}_{\mathbf{k}}^M$,

$$\mathcal{D}_{\mathbf{k}}^M = |\mathcal{D}_{\mathbf{k}}^M| e^{i\gamma_{\mathbf{k}}^M} = \langle \Psi_{\mathbf{k}}^{(-)} | \mathbf{r} \cdot \hat{E} | \Psi_0 \rangle \tag{6.1}$$

where $\hat{E}$ is the unitary electric field vector associated to the incident radiation, $\gamma_{\mathbf{k}}^M$ is the phase of the transition dipole matrix element, $|\Psi_{\mathbf{k}}^{(-)}\rangle$ is the stationary scattering state describing an electron of momentum k ejected in the direction $\hat{\mathbf{k}}$ in the molecular frame and $\mathbf{r} \cdot \hat{E}$ is the light-matter dipolar interaction term. The M exponant stresses that the transition dipole matrix element ($d_{\mathbf{k}}^M$) is expressed in the molecular frame. One can derive a physical quantity, called the Wigner time delay (τ_W^M) [Wigner 1955], which is characteristic of the outgoing electron scattering dynamics,

$$\tau_W^M = \hbar \frac{\partial}{\partial \epsilon} arg \left[\mathcal{D}_{\mathbf{k}}^M \right] \tag{6.2}$$

where ϵ is energy. The Wigner delay τ_W^M can be seen as the group delay acquired by a photoelectron wavepacket scattering off a given potential, compared to a free traveling

wavepacket. This is illustrated in a simple scheme, in Fig. 6.1. To express the molecular-frame Wigner delay in a more explicit fashion, the scattering state $|\Psi_{\mathbf{k}}^{(-)}\rangle$ can be expressed as a coherent sum over partial-waves,

$$|\Psi_{\mathbf{k}}^{(-)}\rangle = \sum_{\ell m} c_{\ell m} \psi_{\ell m}(k,\theta,\phi) \tag{6.3}$$

where a (ℓ,m) pair defines a given partial-wave scattering channel. The transition dipole matrix element can thus be rewritten, using the partial-waves decomposed scattering state,

$$\mathcal{D}_{\mathbf{k}}^{M} = \sum_{\ell m} c_{\ell m}^{*} d_{\ell m}^{M}(k,\theta,\phi) \tag{6.4}$$

where,

$$d_{\ell m}^{M}(k,\theta,\phi) = \langle \psi_{\ell m} | \mathbf{r} \cdot \hat{E} | \Psi_0 \rangle \tag{6.5}$$

and where the values of the coefficients $c_{\ell m}$ depend on the nature of the bound molecular state $|\Psi_0\rangle$. We can thus rewrite the molecular-frame Wigner delay, for a given (ℓ, m) scattering channel,

$$\tau_{W,\ell m}^{M}(k,\theta,\phi) = \hbar \frac{\partial}{\partial \epsilon} arg\left[d_{\ell m}^{M}(k,\theta,\phi)\right] = \hbar \frac{\partial}{\partial \epsilon}\left[\frac{-\ell\pi}{2} + \eta_{\ell m}\right] \tag{6.6}$$

where $\eta_{\ell m} = \sigma_\ell + \delta_{\ell m}$ is the total scattering phase, which the sum of the contribution of the Coulombic (long-range) (σ_ℓ) and the non-Coulombic (short-range) $\delta_{\ell m}$ part of the potential. Wigner delays τ_W and scattering phases $\eta_{\ell m}$ contain the same information about the effect of the atomic or molecular potential on the outgoing photoelectron wavepacket. The scattering phase $\eta_{\ell m}$ is often described as the phase accumulated by a photoelectron leaving an atomic or molecular potential, for a given scattering channel (ℓ,m).

When an atom is being photoionized, the outgoing photoelectron wavepacket scatters from a simple potential, resulting in a simple spatial pattern which can be often described with only one or few scattering (partial-wave) channel(s). However, in typical molecular photoionization, because of the strong anisotropy of the molecular potential, many (ℓ,m) scattering channels are coherently accessed. The angular distribution of the outgoing photoelectron wavepacket being imposed by the angular interferences between the partial-waves at a given energy, it is thus relevant to express the molecular Wigner time delay (group delay) $\tau_W^M(k,\theta,\phi)$ in terms of a coherent sum over all constituent channels, as introduced by Hockett *et al.* [Hockett et al. 2016],

$$\tau_W^M(k,\theta,\phi) = \hbar \frac{\partial}{\partial \epsilon} arg\left[\sum_{\ell m} c_{\ell m}^{*} d_{\ell m}(k,\theta,\phi)\right] \tag{6.7}$$

More details about the theoretical formulation of molecular Wigner delays can be found in the literature (*e.g.* [Baykusheva et al. 2017; Hockett et al. 2016]), often written using different formalisms.

To what extent the complete measurement of the Wigner time delay can be compared to others type of photoionization experiments? In principle, the Wigner delay $\tau_W^M(k,\theta,\phi)$ contains all information about the energy and angular dependence of scattering phases of individual partial-waves. In standard photoionization experiments, the scattering phases of individual partial waves, at a given energy, can be determined by fully measuring the photoelectron angular distributions. However, by only measuring the photoelectron angular distributions, it is not possible to extract the phase structure with respect to energy, *i.e.* we can only determine the scattering phase shifts for a set of partial-waves, where one of the waves serves as a reference. Because the Wigner delay $\tau_W^M(k,\theta,\phi)$ is sensitive to the energy derivative of the scattering phase shift, its complete determination can thus be seen as an elegant solution to perform a 'complete' photoionization experiment.

6.1.2 Measurement of photoionization delays

How can we measure Wigner time delays? As mentioned earlier, τ_W is the group delay of the outgoing photoelectron wavepacket (energy derivative of the spectral phase). It is well known from basic wave optics that the measurement of spectral phases requires the use of interferometric techniques. In the following, we will describe how the RABBITT (Reconstruction of Attosecond Beating by Interference of Two-photon Transitions) technique, which is one of the workhorses of attosecond science, can be used to extract the energy derivative of the outgoing photoelectron spectral phase (Wigner time delays).

In a standard RABBITT experiment, the IR driving laser beam is split into two arms. In the first arm, the IR is focused on a gas jet (*e.g.* of rare gas atoms) to generate high-order harmonics. In the time-domain, the high harmonics emerge as a femtosecond train of attosecond pulses. In the spectral domain, they emerge as a phase-locked XUV comb of odd harmonics of the driving laser. This XUV frequency comb is used to photoionize the target of interest (here, the atom or molecule from which we want to characterize the Wigner time delay). Each tooth of the comb, of energy ($E_{n\omega}$), produces a photoelectron peak at kinetic energy $E_k = E_{n\omega} - I_p$, where I_p is the ionization potential of the target. A weak (perturbative) IR pulse (ω) is superimposed spatially and temporally to the attosecond pulse train. From each photoelectron peak, created by absorption of a given harmonic, one IR photon can be absorbed or emitted, leading to the creation of photoelectron sidebands between the harmonic photoelectron peaks. The sideband of order $n+1$, at energy $E_{(n+1)\omega} - I_p$, is created via two interfering pathways: 1) the absorption of a photon from harmonic n and the absorption of one additional IR photon and 2) the absorption of a photon from $n+2$-th harmonic and the emission of one IR photon. Because of the interference between the two pathways, the amplitude of each sideband oscillates as a function of the relative delay between the XUV and IR pulses. This is very similar to the multiple pathways 'Brumer-Shapiro' interferometric scheme described in chapter 3.

In a RABBITT experiment, measuring the oscillation phase is equivalent to measuring the time delay τ_S that maximizes the signal of each sideband. This does not directly give access to the Wigner delay. Indeed, the τ_S delay is the sum of different contributions which reflect the different steps of the sideband creation [Dahlström et al. 2012]:

$$\tau_S = \tau_{xuv} + \tau_\theta \tag{6.8}$$

where τ_θ is called the atomic or molecular delay and τ_{xuv} is directly related to the spectral phase of the XUV comb. The ionization is triggered by absorption of an XUV photon at a well defined time τ_{xuv}. Next, the electron wavepacket released in the continuum scatters in the atomic or molecular potential and interacts with the weak IR field, which induces

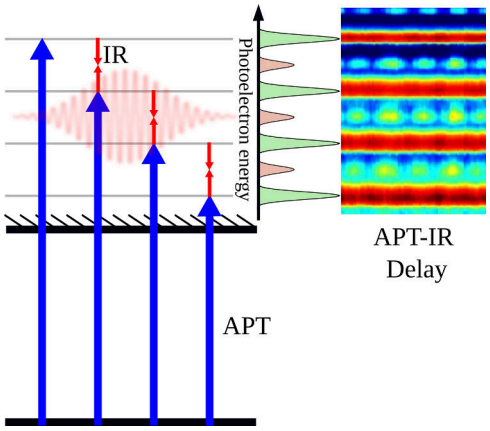

Figure 6.2: Schematic representation of a RABBITT measurement. An atom or a molecule is photoionized by a combination of an attosecond pulse train and a femtosecond IR pulse (ω). When the attosecond delay between the two pulses is scanned, it gives rise to the oscillation of the sidebands at 2ω frequency. The phase of the sideband oscillation encode the photoionization dynamics, from which the Wigner time delay can be extracted, in some specific cases.

continuum-continuum transitions from the main photoelectron peaks to the sidebands. This scattering and laser-induced dynamics introduce an additional delay τ_θ, called the atomic or molecular delay. It has been shown that well above the ionization threshold and away from resonances, the delay induced by the IR-driven transition connecting the two continuum states was insensitive to the short-range behavior of the atomic potential [Dahlström et al. 2012]. In that case, one can directly separate the τ_θ into a sum of the Wigner delay and the continuum-continuum delay, $\tau_\theta = \tau_W + \tau_{cc}$. Thus,

$$\tau_S = \tau_{xuv} + \tau_W + \tau_{cc} \tag{6.9}$$

We will see later that corrections to this approximation due to the ionic core are expected to become important near the ionization threshold and close to resonances. In the following, we will explain how we can experimentally extract τ_W from the measured τ_S.

Since tracking the precise time at which the attosecond pulse hits the target is experimentally impossible, Wigner time delay measurements are always relative. In fact, this is also the case in theoretical investigations in the temporal domain, as illustrated in the example given in Fig. 6.1, where the reference is a 'free' traveling electron wavepacket which does not scatter off any (atomic or molecular) potential. In the laboratory, we do not have access to such 'free' wavepacket reference (it would be great). To circumvent this problem, it is convenient for instance to compare the delay between photoelectrons emitted from different subshells of an atom. This idea was first demonstrated using RABBITT in a pioneering experiment by Klunder *et al.* [Klünder et al. 2011], where they measured the differential delay $\Delta\tau_S$ between electrons emitted from 3s and 3p subshell. The simultaneous measurement of two electron wavepackets liberated from two different subshells, using the same attosecond pulse train, enables removing the influence of the delay induced by the spectral phase of the XUV ($\Delta\tau_{xuv} = 0$), *i.e.* $\tau_S = \tau_\theta$. In order to extract the Wigner delays, it is still necessary to determine the contribution of the IR-driven transition connecting the two continuum states (τ_{cc}). Luckily, since the continuum-continuum transitions occur rather far from the atomic core, this term is insensitive to the short-range structure of the atomic potential but only to its long-range Coulombic tail. This tail has al-

ways the same form and it is therefore somehow universal and relatively easy to compute. To isolate the contribution of $\Delta\tau_W$ from the measured delay $\Delta\tau_S$, Klunder *et al.* computed the universal τ_{cc} and, assuming that $\Delta\tau_\theta = \Delta\tau_W + \Delta\tau_{cc}$, subtracted the contribution of the $\Delta\tau_{cc}$ [Klünder et al. 2011]. By comparing their results with theory, they showed that the experimentally retrieved $\Delta\tau_W$, between electrons ejected from the 3s and 3p subshells of Argon, was strikingly well reproduced by the theory, for photoelectron kinetic energies above 8 eV ($\sim 0.5 I_p$). For electron ejected near the ionization threshold, the experimentally measured $\Delta\tau_W$ is several standard deviations away from the theoretical value. This has been interpreted as a breakdown of the $\tau_\theta = \tau_W + \tau_{cc}$ approximation. Indeed, near the ionization threshold and close to resonances, the ionic core may play an important role in the continuum-continuum transition and its simple additive separation from the Wigner delay is not valid anymore. In such a situation, the direct extraction of $\Delta\tau_W$ is not straightforward.

Several important conclusions can be drawn from the work presented in [Klünder et al. 2011]. First, far from the ionization threshold and resonances, the continuum-continuum induced delay τ_{cc} is similar for any atoms or molecules and for any scattering channels (ℓ, m), *i.e.* it is universal. It is strongly negative for slow electrons ($\sim$ -100 as for 5 eV photoelectrons) and it monotonically decreases for faster electrons. The Wigner delay τ_W, which depends on the target, is larger for slow electrons. This is quite intuitive in the sense that slow electrons spend more time scattering in the ionic potential. As soon as the electron energy reaches a few 10s eV, the Wigner delay converges to $\sim$ zero. Last, the comparison between electrons emitted from different subshells reveals that photoelectrons escaping to a scattering channel with higher angular momentum (ℓ) are characterized by larger Wigner delays, because of the effect of the centrifugal barrier.

6.1.3 State of the art

The measurement of photoionization delays has become a hot topic in the past few years. This is illustrated for instance by the work of Schultze *et al.* [Schultze et al. 2010], who measured the delay between ionization from the 2s and 2p subshells of Neon. It is important to note that they used an isolated attosecond pulse to ionize the atoms rather than an attosecond pulse train. An isolated attosecond pulse possesses a continuous broadband spectrum, such that the RABBITT technique, which relies on the observation of interference between photoelectron peaks, cannot be used. However, an infrared laser field can still be employed to detect the photoionization delays by 'attosecond streaking' [Itatani et al. 2002], which is conceptually similar to RABBITT. Schultze *et al.* measured a delay of 21 $\pm$ 5 attosecond between electrons leaving from the 2s and 2p subshells. This measurement has triggered a lot of theoretical efforts. Even though Neon is a relatively easy system to model, not a single theoretical model succeeded in retrieving this value (see [Moore et al. 2011], for example). It was one of the greatest debate in our community. The question was: Is there an issue with the experimental measurement or are we really not able to model accurately photoionization delays in simple rare gas atoms? This problem was solved by the Lund group in 2017 [Isinger et al. 2017]. They relied on the advantage of using attosecond pulse trains rather than single attosecond pulses: APT provide both high spectral and temporal resolutions, just like frequency combs in the optical domain [Marian et al. 2004]. This property had been used for instance to measure attosecond photoionization with vibrational resolution in nitrogen molecules [Haessler et al. 2009]. In the case of neon, Isinger *et al.* showed that the photoionization produced two spectral components separated by only $\sim$ 500 meV, with different Wigner delays. These two components were indistinguishable in the original experiment of Schultze *et al.* because

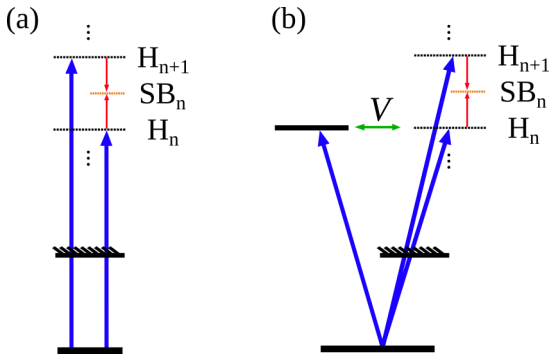

Figure 6.3: RABBITT scheme in the case of (a) non-resonant photoionization and (b) photoionization where one harmonic release an electron wavepacket near an autoionizing resonance. 'V' stands for configuration interaction coupling between the bound state and the continuum state.

of the pulse bandwidth [Schultze et al. 2010]. Using an APT enabled them to spectrally disentangle direct ionization from shake-up ionization, in which a second electron is left in an excited state, and to obtain excellent agreement with theoretical calculations [Isinger et al. 2017].

All the experiments presented above are dealing with angle-integrated photoionization delays. However, the direction of the electron emission also influences the photoionization dynamics. This effect has been investigated both theoretically and experimentally, revealing highly anisotropic photoionization delays between electrons ejected at different angles [Baykusheva et al. 2017; Heuser et al. 2016; Hockett et al. 2016] and from different sides of an asymmetric molecule [Cattaneo et al. 2016; Chacon et al. 2014].

Up to now, we have put aside the situation where photoionization occurs near the ionization threshold, or near a resonance. To focus on one of these examples, we will consider the case where an electron is released in the vicinity of an autoionization (Fano) resonance. The photoionization process involves more complicated dynamics when autoionization occurs. Photoabsorption promotes the system into a metastable bound state, which is coupled to equienergetic continuum states through configuration interaction (see Fig. 6.3). This coupling leads to autoionization of the metastable state. The interference of direct and indirect photoionization channels produces characteristic (Fano) spectral profiles [Fano 1961], associated with complex temporal dynamics (see Fig. 2.42). A very recent study of Cirelli *et al.* demonstrated that the release of photoelectrons near autoionizing resonances strongly affected the angular dependence of the photoionization time delays [Cirelli et al. 2018]. Moreover, pioneering experiments (RABBITT using tunable laser [Kotur et al. 2016] or spectrally-resolved RABBITT / Rainbow-RABBITT [Gruson et al. 2016]) in rare gases recently showed the possibility of measuring the amplitude and spectral phase across a resonance [Gruson et al. 2016; Kotur et al. 2016]. If a given high-harmonic photoionizes the target close to an autoionizing resonance (see Fig. 6.3 (b)), the spectral amplitude and phase of the corresponding photoelectron peak are strongly modulated. The adjacent harmonics ((n$\pm$1)-th orders) photoionize the target in a flat region of the continuum (*i.e.* away from resonances). The spectral amplitude and phase of the associated photoelectron peak are thus unstructured. The absorption/emission of an additional IR photon from both peaks leads to the formation of a sideband. The sideband results from the interference of the resonant photoelectron peak with the non-resonant adjacent peak. The spectral phase of the sideband thus directly provides the spectral phase of the resonant photoelectron peak, since it is heterodyned by a peak with a flat phase. By performing a Fourier transform using this spectral amplitude and phase, the temporal

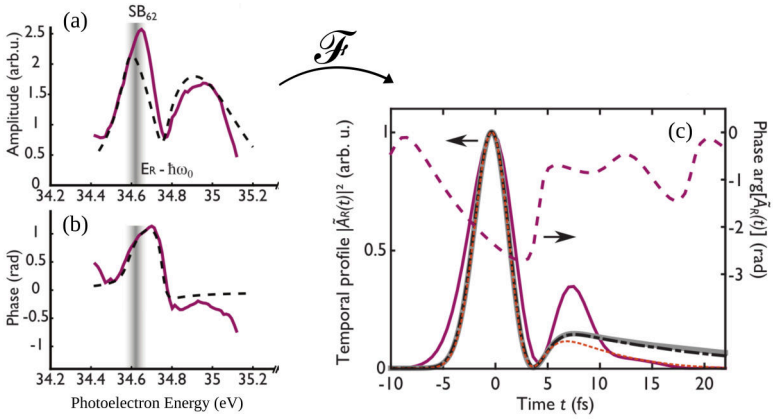

Figure 6.4: Principle of rainbow-RABBITT, introduced by Gruson *et al.* [Gruson et al. 2016]. The spectrally-resolved RABBITT allows measuring the spectral amplitude (a) and phase (b) of the sideband, created by the interference of a resonant and a non-resonant photoelectron wavepacket. By performing a Fourier transform using this spectral amplitude and phase, the temporal profile of the resonant two-photon photoelectron wavepacket can be fully reconstructed (c). This figure is adapted from [Gruson et al. 2016].

profile of the resonant two-photon photoelectron wavepacket can be fully reconstructed (see Fig. 6.4).

To briefly wrap up, for non-resonant photoionization (and away from the ionization threshold), the RABBITT technique can be used to extract the Wigner time delays, which characterize the scattering dynamics of the outgoing photoelectron wavepacket. For resonant photoionization, the approximation needed to be able to extract the Wigner time delays from a RABBITT trace are not valid anymore. However, by performing a spectrally-resolved RABBITT analysis, the temporal profile of the two-photon resonant photoelectron wavepacket can be fully characterized.

6.2 Chiral photoionization delays: An ATI RABBITT-like measurement

Our interest here is to measure the delays between electrons ejected forward and backward chiral molecules ionized with circularly polarized radiation. The most intuitive scheme would be to perform RABBITT measurement with a circularly polarized attosecond pulse train (APT). As we have seen in our synchrotron PECD experiments, the photoionization of large chiral molecules by monochromatic XUV radiation produces congested photoelectron spectra because of the contribution of multiple ionization channels. Using high-order harmonic from a 400 nm pulse enabled us to produce a frequency comb with 6.2 eV spacing between harmonics and to measure and assign a PECD from harmonic 3 and 5 (see Fig. 4.10). We thus tried to add some 400 nm light to induce sidebands and perform a RABBITT measurement. The main difficulty that arose was the competition between the H3+1 and the 2+2 REMPI photoionization processes. The ionization potential of the molecules we used is very low ($\sim$ 8.7 eV) compared to rare gases generally used in RABBITT. As soon as we increased the laser intensity to observe a sideband, we ended up with ATI peaks, promoted by resonant two-photon excitation to Rydberg states. We thus decided to replace the photoionization by an attosecond pulse train by the creation of attosecond electron wavepacket using Above-Threshold Ionization (ATI). In such a scheme, the ionization is mediated by the relatively strong laser pulses, producing ATI peaks, and a weak perturbative laser pulse at half the frequency of the strong laser field is

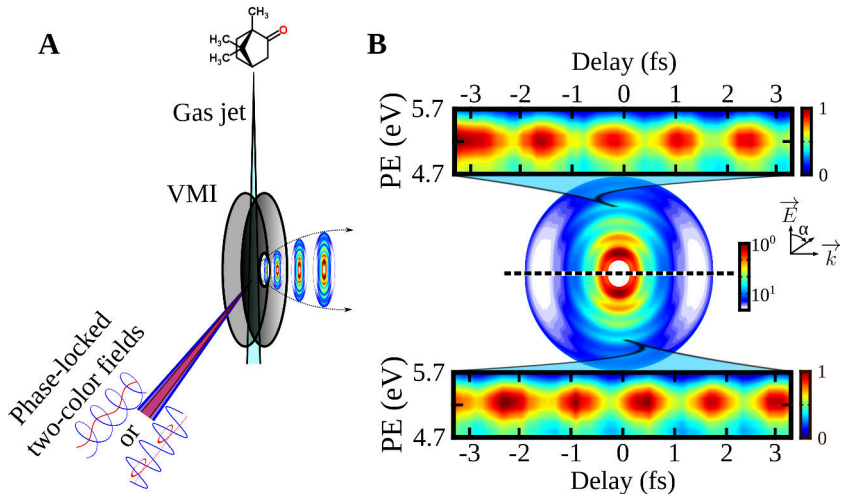

Figure 6.5: (a) Schematic experimental setup. Two phase-locked femtosecond laser pulses with linear or circular polarization are focused into a jet of enantiopure camphor molecules in the interaction zone of a velocity map imaging (VMI) spectrometer. The photoelectrons are accelerated by a set of electrodes onto microchannel plates imaged by a phosphor screen and a CCD camera, which records the 2D projection of the 3D angular distribution of the photoelectron spectrum with an energy resolution around 0.2 eV at 2 eV. (b) Typical measured photoelectron angular distribution and evolution of the second sideband as a function of delay between the two fields. The oscillations in the upper and lower half of the distribution are out of phase, reflecting the up-down asymmetry of the total ionizing electric field.

superimposed to produce sidebands, as in RABBITT (see Fig. 6.7 (a)). This scheme has the advantage to enable very easy manipulation of the polarization state of the ionizing fields, which is not the case with attosecond pulse trains.

The superposition of 800 nm and 400 nm pulses produces an electric field which is stronger in the upper or lower direction, depending on the relative delay between the two fields. As a consequence, the electrons ejected up and down are modulated in opposite phase [Skruszewicz et al. 2015; Zipp et al. 2014] (Fig. 6.5(b)). This can also be explained in the framework of the Brumer-Shapiro coherent control scheme for controlling the angular distribution of photoelectrons. Indeed, because the sideband is created via the interference between n-th order ATI peak plus one IR photon and (n+1)-th order ATI peak minus one IR photon, the number of photons absorbed in the two arms of the interferometer is different (leading to different parity of the final states), only the angular distribution of the sideband is modulated (not the total angularly integrated sideband amplitude, as in RABBITT).

In order to make the analogy with standard RABBITT and rainbow-RABBITT, let us briefly describe the general features and properties of ATI. When an intense femtosecond laser pulse ionizes an atom or a molecule, multiple photons can be absorbed above the ionization threshold. In the spectral domain, ATI produces a comb of photoelectron peaks separated by the laser photon energy [Agostini et al. 1979]. Each peak is characterized by a spectral width $\delta\omega$, and the overall ATI spectrum extends over a width $\Delta\omega$. In the time domain, the ATI process leads to the emission of attosecond electron bursts of duration δt, which form a train. The overall duration of the train Δt is set by the laser pulse duration, typically a few tens of femtoseconds. The ATI emission can last longer if an autoionizing state is populated: the lifetime of the autoionizing state increases the electron wavepacket duration.

Characterizing the temporal dynamics of the ionization process requires measuring the process on two timescales δt and Δt. The femtosecond structure of the wavepacket is encoded in the spectral intensity and phase within the bandwidth of each ATI peak: Δt is related to $\delta\omega$. On the other hand, the attosecond sub-structures are encoded in the relative amplitude and phase between the different ATI peaks: δt is associated to $\Delta\omega$. In order to have a complete picture of the temporal dynamics of the ionization process, it is thus necessary to measure the spectral phase of the ATI peaks, both within their bandwidth ($\delta\omega$) – using Rainbow-RABBITT – and from one peak to the next ($\Delta\omega$) – using RABBITT. Recently, Zipp *et al.* have measured the photoionization delays in non-resonant ATI using this type of ATI-RABBITT scheme [Zipp et al. 2014], revealing the effect of strong laser intensities on the photoionization dynamics.

In order to perform this kind of ATI-RABBITT experiment and resolve the ionization dynamics of chiral molecules, we used an experimental that is similar to the Mach-Zehnder ω - 2ω setup described earlier in this thesis manuscript (Fig. 6.6). The incoming beam is delivered by the Aurore laser system at CELIA, which provides 800 nm 25 fs pulses at 1 kHz, with up to 7 mJ energy. In one of the two arms, we frequency double the pulses by using a type-I 200 μm thick BBO crystal. The remaining 800 nm is filtered out by reflection on two dichroic mirrors. In the 800 nm arm, a delay stage is installed to temporally overlap the two beams. The control of the attosecond delay is achieved by a pair of wedges rather than by translating mirrors. This enables us to convert a rather large translation motion of one wedge into small delays (1 micron for 67 attoseconds, while a 1 micron translation of the mirrors would induce a 6.7 femtoseconds delay), releasing some constraints on the translation stage accuracy and repeatability. Motorized quarter-wave plates are placed in both arms of the interferometer, allowing to fully control the polarization of each color independently. After the quarter-wave plates, all reflections are at $\sim 0^\circ$ to avoid inducing polarization state artifacts. The 400 and 800 nm beams are recombined using a dichroic mirror and are focused into the interaction region of the Velocity Map Imaging Spectrometer. To compensate chromatic aberration induced by the lens, we have installed a lens telescope in the 800 nm arm, which allows us to focus both 400 nm and 800 nm at the exact same position in the spectrometer. In all presented experiments, the 400 nm/800 nm delay was scanned over a range of ~ 6700 as by steps of 133 as.

The enantiopure chiral samples (Sigma Aldrich, 98% purity for (1R)-(+)-camphor and 95% purity for (1S)-(-)-camphor) were heated in an oven at 60°C, carried to the VMI by a 80°C heated line, and conducted under vacuum by a 100°C heated tube to a 250 μm nozzle located 7 cm away from the interaction zone. No carrier gas was used. The pressure in the interaction chamber was typically 2×10^{-7} mbar. The velocity distribution of the photoionized electron was projected onto a set of dual microchannel plates and imaged by a phosphor screen and a CCD camera.

Camphor molecules have their first ionization potential at 8.76 eV and Rydberg states starting around 6.2 eV. They are thus ionized by $2+n$ resonance-enhanced multiphoton transitions when using a 400 nm ultraviolet (UV) field, with n being the order of the ATI peak. In the presence of a weak IR 800 nm field (ω) the sidebands appear between the ATI comb. We measured the sideband oscillation phase independently on the angularly-integrated upper and lower half of the photoelectron image and averaged the phase obtained from the upper half with the π-shifted phase obtained from the lower half. In the case where we wanted to extract chiroptical signals, we also performed the analysis independently for the forward and backward quadrants.

Figure 6.7(b) shows the photoelectron spectrum as well as the sideband oscillation phase $\varphi_{2\omega}$ as a function of the photoelectron kinetic energy E. The first sideband (SB1),

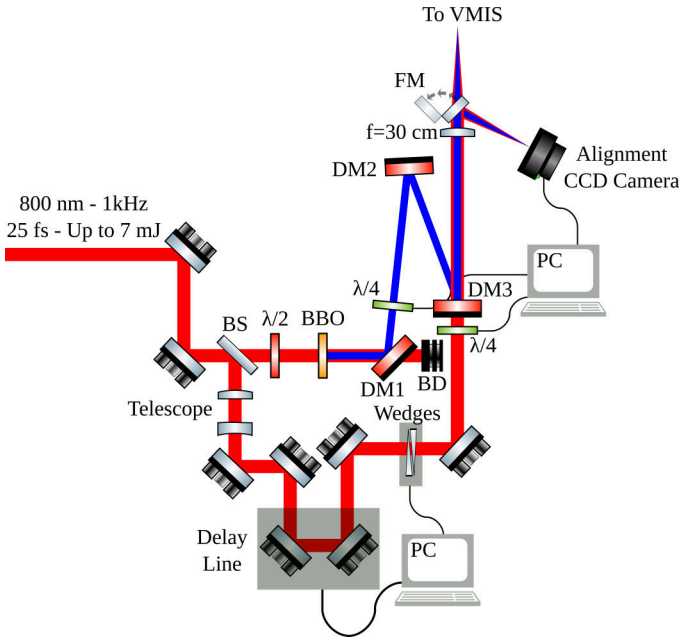

Figure 6.6: Scheme of the optical setup. BS is a 80/20 beamsplitter; $\lambda/2$ and $\lambda/4$ are half- and quarter-wave plates, respectively; BBO is a type-I 200 μm thick β-Barium borate crystal; DM are dichroic mirrors; FM is a flip mirror and BD is a beam dump. The setup is not at scale.

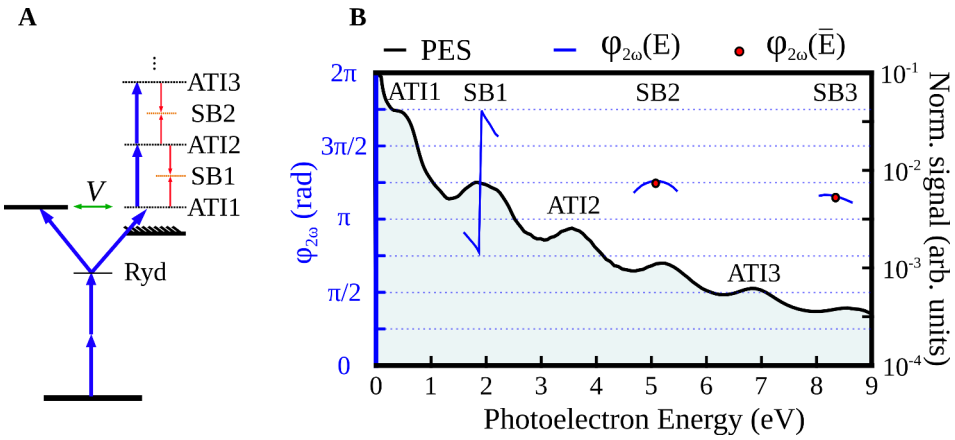

Figure 6.7: (a) Ionization scheme. The 400 nm pulse (40 fs duration, intensity $\sim 5 \times 10^{12}$ W/cm^2) induces multiphoton above-threshold ionization of the molecules. The first ionizing transition lies in the vicinity of an autoionizing resonance. The 800 nm pulse (30 fs, intensity $\sim 5 \times 10^{11}$ W/cm^2) produces additional transitions, leading to the creation of sidebands between the ATI peaks. (b) Angle-integrated photoelectron spectrum constituted of ATI peaks and n-th order sidebands (SBn). The full blue lines are the angularly-integrated spectrally-resolved 2ω-oscillation phases for each sideband and the red dots are the spectrally-averaged 2ω-oscillation phases for non-resonant SB2 and SB3.

which encodes the phase difference between ATI peaks 1-2, presents an abrupt π-phase jump around 1.9 eV. This is the signature of a resonance associated with one or the other of the two contributing ATI peaks. The second and third sidebands, which are built respectively upon ATI peaks 2-3 and 3-4, have a smooth phase variation across their bandwidth (*i.e.* without any trace of resonance).

From this experimental observation, it seems that the resonance occurs in the formation

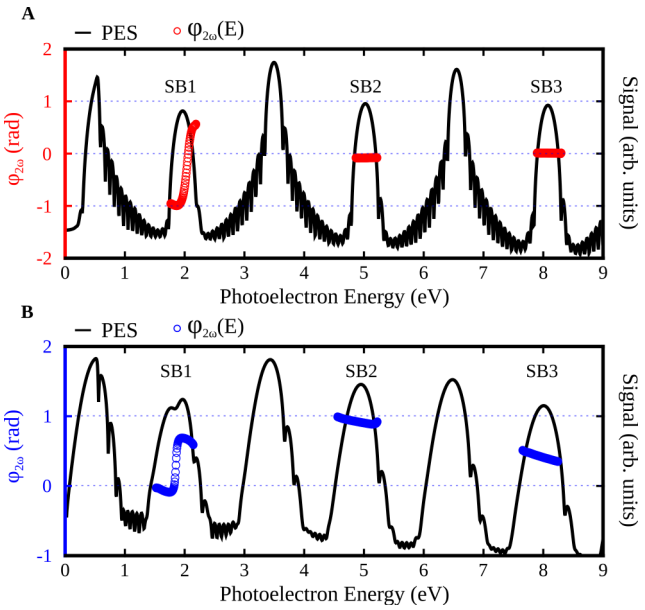

Figure 6.8: 1D-TDSE simulations of resonant photoelectron interferometry in the RABBITT (a) and ATI (b) regimes. The photoelectron spectra are shown in black. The spectrally-resolved 2ω-oscillation phase of the sidebands in the RABBITT regime (a) is shown in red, and in the ATI regime (b) is shown in blue.

of the first ATI peak (ATI1), and does not propagate to the higher ATI peaks. This conclusion may seem surprising since all ATI peaks above the first one share a common pathway through the resonance. We thus decided to ask our theoretician friends from LCPMR, Richard Taïeb and Jérémie Caillat, to perform TDSE calculations to unambiguously answer this question: Does the effect of the resonance propagate through the high-order ATI peaks, or is it localized on the resonant first ATI peak only? If the presence of the resonance on the first ATI peak is shown to influence the higher-order ATI peaks, the photoelectron interferometry technique (Rainbow-RABBITT) cannot be transposed to the ATI regime. To do so, they solved the time-dependent Schrödinger Equation for a 1D model atom, represented by a short-range Gaussian potential where they added symmetric barriers in order to mimic a shape resonance into the continuum, as in [Gaillac et al. 2016]. The parameters of the potential were adjusted to approximately match the ionization potential of the molecule as well as the energy of the resonance encountered in the experiment. The propagation was performed on a spatial grid using the Crank-Nicolson algorithm in the velocity gauge. The photoelectron spectrum was extracted from the final wavefunction thanks to the window operator.

They used two kinds of electric field, both composed of harmonics of the fundamental IR field, whose wavelength was set at 806.4 nm ($\hbar\omega = 1.5375$ eV). In the first case, dubbed 'ATI', they ionized the system with only the second harmonic (2ω) at an intensity of $I_{2\omega} = 7 \times 10^{12}$ W/cm^{-2} and a pulse duration of FWHM ~ 20 fs in intensity. In the second case, called 'RABBITT', the ionizing field was an attosecond pulse train of the same duration, made from harmonics 6, 8, 10, 12 and 14 of the IR frequency ω in order to reach the same energies as in the 'ATI' case. For the sake of simplicity, they considered that all harmonics were synchronized and of the same intensity $I_H = 3 \times 10^8$ W/cm^{-2}.

In order to observe sidebands, they added a weak IR field ($I_\omega = 8 \times 10^{10}$ W/cm^{-2}), with the same duration, and they varied its phase $\delta \equiv \omega\tau$. Following the procedure

introduced in [Gruson et al. 2016], the photoelectron spectra $S(\delta)$ as a function of delay δ were analyzed for each energy, using the following fit:

$$S(\delta) = \overline{S}\,[1 - B_2 cos(2\delta + \varphi_2) - B_4 cos(4\delta + \varphi_4)]\,, \tag{6.10}$$

where B_2 and B_4 are proportionality coefficients and φ_2 and φ_4 are the phases of the 2ω- and 4ω-oscillations.

Note that in the 'ATI' case, they analyzed the spectra in only one direction, *i.e.* $x > 0$. This is compulsory as the parity of the sideband final state is different, whether the path leading to the sideband comes from the ATI peak below or above. Therefore, there would be no sideband oscillation if the spectra were taken over all x space. This is not the case in the 'RABBITT' case, because the sideband parity is always 'even', as invariably reached by a two-photon transition. This can be explained in the framework of the Brumer-Shapiro coherent control of angular distribution (if different final states parity) and angularly-integrated quantity (if same final states parity).

As shown in figure 6.8, both RABBITT and ATI techniques show a large spectral phase jump across the bandwidth of the SB1, while the phase is mostly flat for SB2 and SB3. These results confirm that the effect of the resonance does not propagate above the resonant ATI peak. This validates that our experimental interferometric ATI scheme is well suited for the measurement of the spectral amplitude and phase of photoelectron wavepackets. Beyond this similarity, we observe some differences in the evolution of the spectral phases: the phase jumps are slightly different, and a linear phase appears on each higher ATI sidebands. These are the signature of differences between the single photon and multiphoton ionization dynamics. A systematic analysis of the role of the 'strong' ionizing laser field on the phase of the sidebands oscillation is planned to further investigate these effects.

After having demonstrated that the effect of the resonance does not propagate on higher order ATI peaks, we can now proceed to investigate the chiral (enantiospecific) photoionization dynamics in the two different regimes identified above: direct (attosecond) ionization (SB2 and SB3), and indirect (femtosecond) ionization in the vicinity of an autoionizing resonance (SB1).

6.3 Asymmetric attosecond delays in non-resonant photoionization

6.3.1 Decoupling the Wigner and continuum-continuum delays

We start by analyzing the direct (non-resonant) photoionization dynamics (SB2 and SB3). It can be obtained by extracting the oscillation phases of the signals averaged over the bandwidth of each sideband, $\varphi_{2\omega}(\overline{E})$. Neglecting the variations over the spectral width is equivalent to assuming that the photoionization process is strictly periodic from one laser cycle to the next. The spectral homogeneity of the sideband phases shown in Fig. 6.7(b) indicates that this assumption is reasonable for SB2 and SB3, but not for the resonant SB1, which will be discussed later.

To resolve the enantioselectivity of Wigner delays, we turned to chiroptical measurements comparing the sideband oscillation phases for electrons emitted in the forward vs backward directions, and extracting the difference $\Delta\tau^{f/b} = \tau^f - \tau^b$. This procedure naturally eliminates τ_{light}, which is strictly common to the forward and backward electrons. Further decoupling is achieved by using different combinations of linearly and circularly polarized light. Indeed, the forward/backward (f/b) symmetry can only be broken by the chiral nature of the interaction, that is, if a circularly polarized light pulse

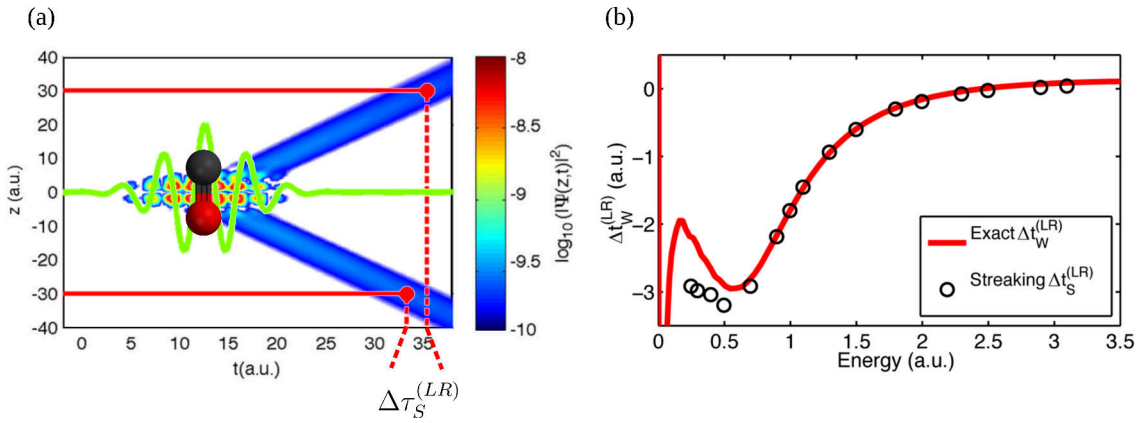

Figure 6.9: Simulation of the asymmetry of Wigner's time delay in a small molecule. In (a), electron densities as a function of the position and time for the ionization of aligned C=O molecule by an XUV attosecond pulse. The solid red lines are the equidistant positions on either side $z_d = \pm 30$ a.u. of the molecule while the red dashed lines are the corresponding arrival times onto the virtual detector, which allows measuring the differential photoionization time delay. In (b), the attosecond streaking measurement of the stereo Wigner-time delay. The plot shows the comparison between the exact single photon stereo Wigner time-delay (red) and the streaking measurement of the two-photon stereo Wigner time-delay (black dot). This figure is adapted from [Chacon et al. 2014].

is used. We can thus selectively break the f/b symmetry only in the ionization step by using a circularly polarized UV field and a linear IR field. In that case $\Delta\tau_{cc}^{f/b} = 0$ and $\Delta\tau^{f/b} = \Delta\tau_W^{f/b}$. Alternatively, we can render the Wigner delay f/b symmetric by using linearly polarized UV for ionization and circularly polarized IR probing photons to obtain $\Delta\tau_W^{f/b} = 0$ and $\Delta\tau^{f/b} = \Delta\tau_{cc}^{f/b}$.

The decoupling between Wigner and continuum-continuum delays is only possible away from resonances, and high enough above the ionization threshold. In argon, it has been shown that the simple additive relationship between the Wigner delay τ_W and the continuum-continuum delay τ_{cc} was valid above ~ 0.5 I_p [Klünder et al. 2011]. In our case, since the ionization potential is 8.78 eV, we can thus expect that the decoupling of these two delays should be applicable for SB2 and SB3 (electron energy above ~ 4.4 eV). However, some theoretical derivation has shown that in molecular photoionization, because multiple partial waves are needed to describe the intermediate continuum state (after the single photon transition), the simple separation between τ_W and τ_{cc} does not hold anymore [Baykusheva et al. 2017]. In this case, the universal τ_{cc} can be still removed from the measurement, but the remaining τ_W departs from the pure single photon ionization time delay [Baykusheva et al. 2017]. On the other hand, Chacon *et al.* recently performed numerical experiments demonstrating that in a stereo-Wigner time delay measurement, where looking at the two-photon delays between equienergetic electron ejected from different sides of a C=O molecule, the differential two-photon delays reproduces very well the differential single photon ionization time delay. The main results of Chacon *et al.* are presented in Fig. 6.9. We thus need to keep in mind that the $\Delta\tau_W^{f/b}$ measurement that we will report later on might slightly depart from the pure single photon ionization delay, even if the calculation of Chacon *et al.* leads us to be confident that this deviation should not be dramatic.

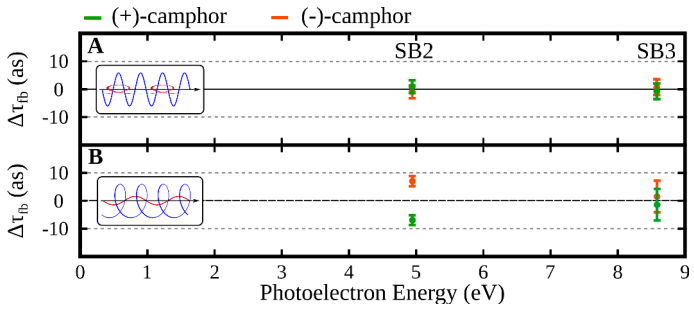

Figure 6.10: Forward/backward differential delays in non-resonant photoionization of camphor. (a) When the UV is linearly polarized and the IR is left-circularly polarized, the differential delay $\Delta\tau_{cc}^{f/b}$ is zero for SB2 and SB3. (b) When the UV field is circularly polarized and the IR is linearly polarized, the differential delay $\Delta\tau_{W}^{f/b}$ is non zero for SB2, and zero for SB3. Error bars are defined as the 95% confidence interval.

6.3.2 Overall forward and backward delays

For the first part of the analysis, the photoelectron images were separated into four quadrants, and the signal was angularly-averaged in each quadrant. A Fourier analysis of the 2ω-oscillations was conducted to determine the delay that maximized each sideband, in each quadrant. We calculated the difference between the delays measured in the forward and backward directions $\Delta\tau^{f/b}$. This procedure was repeated for left and right helicities, and for five consecutive measurements in each enantiomer. The delays measured from opposite helicities or opposite enantiomers have opposite signs, revealing that the differential f/b photoionization delay is a genuine chiral observable. In order to extract the most accurate value of the differential delay, we averaged the results obtained from the (+) and (-) enantiomers: $\Delta\tau^{f/b} = (\Delta\tau_{(+)}^{f/b} - \Delta\tau_{(-)}^{f/b})/2$.

First, we used a linearly polarized UV ionizing field and a circularly polarized IR dressing field. The Wigner component τ_W of the sideband delay was thus f/b symmetric ($\Delta\tau^{f/b} = \Delta\tau_{cc}^{f/b}$). The results are shown in Fig. 6.10(a) and reveal that the differential f/b continuum-continuum induced delay is zero (within the ~ 2 as accuracy of the present measurement), for both SB2 and SB3. This means that the laser-induced continuum-continuum transitions produce essentially the same delay on electrons emitted in the forward and backward directions, without any significant sensitivity to the chiral character of the ionic potential.

Second, we broke the f/b symmetry during the ionization step by switching the polarization state of the ionizing UV field to circular while using a linearly polarized IR field. The photoionization process is here expected to be f/b asymmetric, while the continuum-continuum coupling is f/b symmetric: $\Delta\tau^{f/b} = \Delta\tau_{W}^{f/b}$. The measurements (Fig. 6.10(b)) show a differential delay of $\Delta\tau_{W}^{f/b} = 7 \pm 2$ attoseconds for the second sideband (SB2). Our experiment is thus able to reveal a small f/b asymmetry of the Wigner delay in the photoionization of chiral molecules by circularly polarized light. The $\Delta\tau^{f/b}$ vanishes for SB3 because of the decrease of both the f/b asymmetric character of the photoionization and the absolute Wigner time delay with increasing photoelectron kinetic energy.

6.3.3 Angle-resolved analysis

In order to gain more insight about the chirality of the photoionization delays, we resolved the angular dependence of the photoionization dynamics [Aseyev et al. 2003; Cirelli et al.

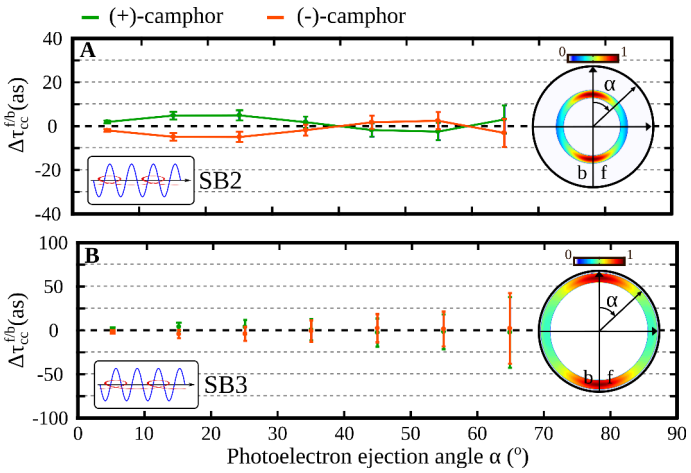

Figure 6.11: Angularly-resolved differential delays for SB2 (a) and SB3 (b), when the UV field is linearly polarized and the IR is circularly polarized.

2018; Heuser et al. 2016; Hockett 2017]. We integrated the photoelectron signal in slices of 10° around different ejection angles α from the polarization plane of the light and measured the associated differential delays. The results for SB2 and SB3, when the UV field is linearly polarized and the IR one is circularly polarized ($\Delta\tau^{f/b} = \Delta\tau_{cc}^{f/b}$) are shown in Fig. 6.11.

For electrons emitted beyond 70°, the signal level was too low to extract reliable values. A very weak, but non-zero $\Delta\tau_{cc}^{f/b}$ is measured on SB2 when electrons are ejected close to the polarization plane of the IR laser, reaching 5 $\pm$2 as at $\alpha = 25°$. This delay tends to vanish for larger ejection angles and the error bars become greater due to the lower level of signals. Measurements on SB3 show a delay of zero, whatever the ejection angle. In the commonly accepted intuitive picture of multicolor photoionization, the linear UV field induces bound-free transitions starting from the molecular core region, and the IR field subsequently drives continuum-continuum transitions while the electron is escaping from the core region. The continuum-continuum transitions are thus assumed to be rather insensitive to the details of the molecular potential (short-range potential), as confirmed by the calculations from Chacon *et al.* [Chacon et al. 2014]. The zero (or very small) overall differential delay we measured between forward and backward electrons on SB2 and SB3 is consistent with this general picture. Nevertheless, the small but non-zero delay revealed in the angle-resolved data (SB2) demonstrates that the continuum-continuum transitions can be slightly influenced by the core (chiral) region of the potential.

Before presenting the evolution of the differential photoionization delays as a function of the ejection angles, for the case where UV field is circularly polarized and the IR one is linearly polarized, let us look at the (non-differentiated) forward and backward photoionization delays, for SB2. These results are presented in Fig. 6.12. This kind of angular analysis was previously performed by Heuser *et al.* [Heuser et al. 2016] and Cirelli *et al.* [Cirelli et al. 2018], for the photoionization of Helium and Argon, respectively, using XUV+IR scheme (RABBITT). They concluded that the angular dependence of the photoionization time delays was due to the interplay between final quantum states (continuum states) with different symmetries. It thus arises naturally, whenever multiple scattering channels (partial-waves) are accessed in the continuum, which is the case in almost every photoionization scenario. Surprisingly, even if our ionization scheme and

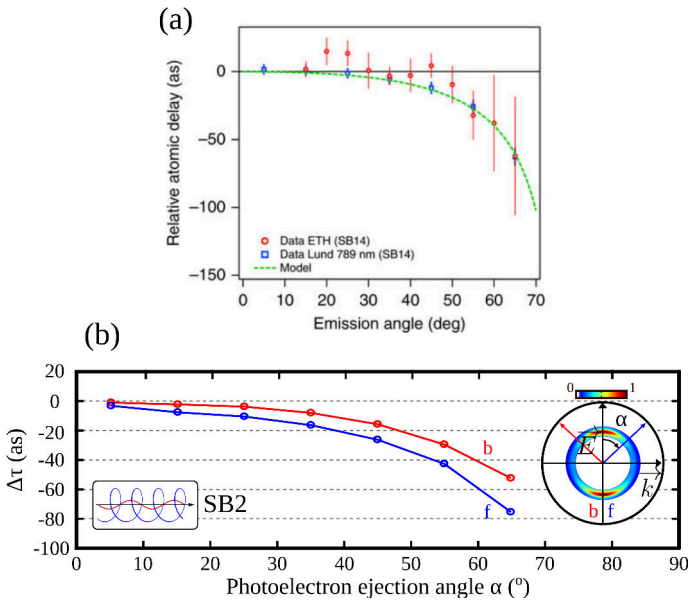

Figure 6.12: Angular dependence of photoemission delays. In (a), data taken in Argon in Lund and Zurich. The figure is taken from [Cirelli et al. 2018]. In (b), forward and backward angularly-resolved photoionization delays for SB2, in camphor, when the UV field is circularly polarized and the IR is linearly polarized.

target are very different, the angular-dependence of the photoionization delay looks very similar as in the case presented by Heuser *et al.* [Heuser et al. 2016] and Cirelli *et al.* [Cirelli et al. 2018]: the delay slowly increases as electrons get ejected away from the laser polarization plane (see Fig. 6.12). The delay increases faster as they are ejected further away from the polarization plane.

The results presented in Fig. 6.12 (b) show that the forward and backward delays are slightly different. We can thus now study the differential forward-backward Wigner delays as a function of photoelectron ejection angle, for SB2 and SB3 (Fig. 6.13). For SB2, close to $\alpha = 0°$, $\Delta\tau_W^{f/b}$ is null. This is not surprising since the PECD also vanishes in the laser polarization plane. For electrons emitted in the 60-70° slice, $\Delta\tau_W^{f/b}$ reaches 24 as. This angle-resolved analysis shows that while the average difference between forward and backward electron ionization delay is only 7 as on SB2, it strongly varies with ejection angle and can reach higher values for electrons emitted away from the laser polarization plane. Repeating this analysis for SB3 shows that the differential Wigner time delay remains zero within the error bars, for all photoelectron ejection angles. Again, this is not surprising since both the Wigner delay and PECD decrease as a function of photoelectron kinetic energy. By accessing the angular dependence of the photoionization time delays, our measurements give access to angular-dependent phase properties of the photoionization matrix elements. The determination of the underlying scattering phase shifts has been a long-standing quest of photoionization experiments, and our results show that their energy-derivative, *i.e.* the Wigner delays, are accessible with high accuracy using a relatively simple setup, in large chiral molecules.

6.3.4 Error bars and measurement accuracy

Given the accuracy of our data, one might ask the question: what determined the error bars of the measurements? The temporal resolution of our experiment is determined by

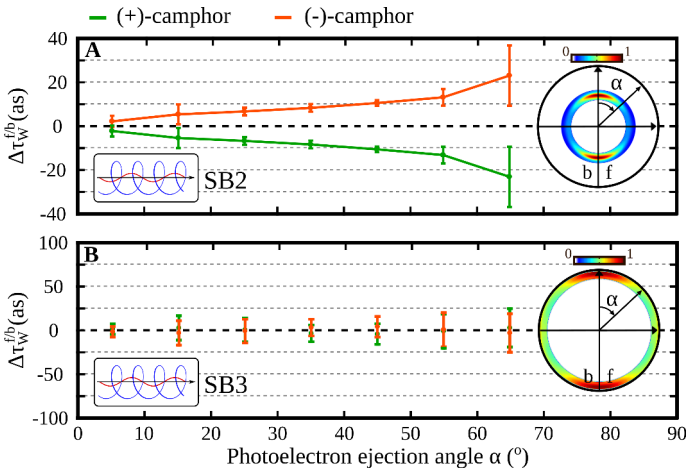

Figure 6.13: Angularly-resolved differential delays for SB2 (a) and SB3 (b), when the UV field is circularly polarized and the IR is linearly polarized.

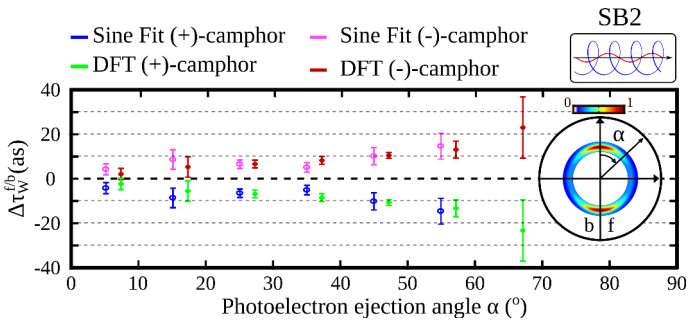

Figure 6.14: Comparaison between Discrete Fourier Transform (DFT) and 4-parameter Sine Fit methods to extract the angle-resolved $\Delta\tau^{f/b}$ for sideband 2. An offset of 2 degree was added to the point extracted with the DFT method in order to clearly see the difference between the DFT and Sine Fit methods.

the accuracy with which we are able to measure the phase of the oscillating function (sine-type function, which governs the sideband oscillations). It depends on the way we sample the sine function as well as on the algorithm used to extract the phase. From the sampling point of view, the experimental acquisition time sets a limit and imposes the total number of samples that can be acquired in a reasonable time. In our experimental conditions, we recorded 5 oscillations with 10 points per oscillations. Recording 5 oscillations fulfill the standard set by IEEE to properly sample a sine function [Sedlacek et al. 2005]. We sequentially repeated the measurement for 5 consecutive delay scans in each enantiomer. The overall acquisition time was roughly 10 hours, for the two enantiomers and the two helicities.

For the phase extraction, we have compared two methods: Discrete Fourier Transform and 4-parameter sine fitting. The method can significantly influence the accuracy of the results, as demonstrated for instance in [Sedlacek et al. 2005]. The 4-parameter fitting followed the procedure recommended by IEEE (IEEE-STD-1057). Fig. 6.14 shows the $\Delta\tau^{f/b}$ extracted from both methods as a function of electron ejection angle. The error bars are calculated by Student statistical analysis of the consecutive measurements. The results from the two methods are consistent within the error bars. The DFT provides smaller error

bars. This is why the data presented above are extracted using the DFT methods.

6.4 Calculation of differential Wigner delays in one-photon ionization

The differential Wigner delay is a signature of the asymmetric scattering process which is at the heart of the photoelectron circular dichroism phenomenon. Wigner delays are determined by the energy derivative of the scattering phase. In this section, we present a theoretical analysis of the photoionization of camphor molecules performed by Bernard Pons, Alex Clergerie and Baptiste Fabre from CELIA. This investigation aims at tracking the existence and the behavior of the asymmetric Wigner delays in a randomly oriented ensemble of molecules. Atomic units will be used throughout this section unless otherwise stated.

Within the framework of the dipolar approximation, ionization probabilities and cross sections are defined by the matrix element which reads in the molecular frame:

$$d^M_{\mathbf{k}'} = < \Psi^{(-)}_{\mathbf{k}'} | \mathbf{r} \cdot \hat{E} | \Psi_0 > \tag{6.11}$$

where $\hat{E}$ is the unitary electric field vector associated with the incident radiation, Ψ_0 is the initial molecular state, and $\Psi^{(-)}_{\mathbf{k}'}$ is the stationary ingoing scattering state describing an electron ejected in the direction $\hat{\mathbf{k}}'$ in the molecular frame. $\mathbf{r} \cdot \hat{E}$ is the dipolar interaction term, expressed in the length gauge, where $\mathbf{r}$ stands for the vectorial coordinate of the active electron. In this respect, we work in a single active electron picture where inner electrons remain frozen throughout the interaction and are accordingly described by the same molecular orbitals in both Ψ_0 and $\Psi^{(-)}_{\mathbf{k}'}$.

The optimization of molecular geometry and Ψ_0 result from Density Functional Theory calculations using the GAMESS-US package [Schmidt et al. 1993] with the 6-311++G** underlying Gaussian basis [Krishnan et al. 1980] and CAM-B3LYP exchange-correlation functional [Yanai et al. 2004]. The electric field, circularly polarized, is naturally defined in the laboratory frame so that the dipolar interaction term must be transposed into the molecular frame as

$$\begin{aligned} \mathbf{r}.\mathbf{E} = x \pm iy &= \sqrt{\frac{2\pi}{3}} r (a Y_1^{-1}(\Omega) + b Y_1^1(\Omega)) \\ &= \sqrt{\frac{2\pi}{3}} r \sum_\nu (a \mathcal{D}^{(1)}_{\nu-1} + b \mathcal{D}^{(1)}_{\nu+1}) Y_\nu^1(\Omega') \end{aligned} \tag{6.12}$$

where we have assumed $||\mathbf{E}|| = 1$ and Y_l^m are usual spherical harmonics defined either in the laboratory frame (with argument Ω) or in the molecular frame (with argument Ω'). The coefficients (a, b) are (0,-2) in the $x + iy$ case and (2,0) in the $x - iy$ one. $\mathcal{D}^{(l)}_{mn'} \equiv \mathcal{D}^{(l)}_{mn'}(\alpha, \beta, \gamma)$ are Wigner matrix elements [Amati 1960] related to the rotation, in terms of the Euler angles (α, β, γ), that brings the laboratory frame in coincidence with the molecular one.

The multi-center scattering state $\Psi^{(-)}_{\mathbf{k}'}$ is expanded in terms of partial waves [Dill et al. 1974]

$$\Psi^{(-)}_{\mathbf{k}'}(\mathbf{r}) = \sum_{l,m} i^l e^{-i\sigma_l} \Psi^{(-)}_{k'lm}(\mathbf{r}) Y_l^{m*}(\hat{\mathbf{k}}') \tag{6.13}$$

where σ_l is the Coulomb phase shift for electron wavevector k' and angular momentum l. The complex $\Psi^{(-)}_{k'lm}(\mathbf{r})$ states, which fulfill appropriate boundary conditions, are related to real states $\Psi_{k'lm}(\mathbf{r})$ through the transformation

$$\Psi^{(-)}_{k'lm}(\mathbf{r}) = \sum_{l'm'} (\mathbf{I} + i\mathbf{K})_{lm,l'm'} \Psi_{k'l'm'}(\mathbf{r}) \tag{6.14}$$

where $\mathbf{I}$ is the unitary matrix and $\mathbf{K}$ is the so-called $\mathbf{K}$-matrix (see below). The $\Psi_{k'lm}$ are real solutions of the Schrödinger equation $H\Psi_{k'lm} = \epsilon\Psi_{k'lm}$, with $\epsilon = k'^2/2$.

To solve the Schrödinger equation, our theoretician colleagues employ an approximate form of the potential felt by the electron ejected from neutral camphor, in terms of so-called ElectroStatic Potential ESP-charges [Besler et al. 1990], which basically consist of non-integer charges Z_i^{eff} located on the nuclei of the molecule, so that

$$V(\mathbf{r}) = -\sum_i \frac{Z_i}{|\mathbf{r} - \mathbf{R}_i|} + \int \frac{\rho(\mathbf{r}')}{|\mathbf{r} - \mathbf{r}'|} \sim -\sum_i \frac{Z_i^{eff}}{|\mathbf{r} - \mathbf{R}_i|} \tag{6.15}$$

on Van der Walls surfaces surrounding the molecule. Z_i and $\mathbf{R}_i$ are the real charges and locations of the nuclei while $\rho(\mathbf{r})$ is the core electron density which does not include the density associated to the active electron. Therefore $\lim_{r\to\infty} V(\mathbf{r}) = -1/r$. Subsequently to a single-center decomposition of $V(\mathbf{r})$ onto spherical harmonics [Abu-samha et al. 2010; Decleva et al. 1994], the coupled-channel Schrödinger problem is solved using the renormalized Numerov method of Johnson [Johnson 1978]. The $\mathbf{K}$-matrix elements are defined in the asymptotic r-region according to

$$\Psi_{k'lm}(\mathbf{r}) \sim \frac{1}{\sqrt{\pi k' r}} \sum_{l''m''} (\sin(\theta_{l''})\delta_{l'm',l''m''} + \cos(\theta_{l''})K_{l'm',l''m''}) Y^{m''}_{l''}(\hat{\mathbf{r}}) \tag{6.16}$$

where $\theta_{l''} = k'r - l''\pi/2 - (1/k')\ln(2k'r) + \arg\Gamma[l'' + 1 - i/k']$.

Once the $\Psi_{k'l'm'}$ states and $\mathbf{K}$-matrix elements are known, the dipolar amplitudes $a_{klm\nu}$ can be computed

$$a_{klm\nu} = < \Psi^{(-)}_{klm} | r Y^{\nu}_1 | \Psi_0 > \tag{6.17}$$

using eq. (6.14). According to eqs. (6.11)-(6.13), the dipole in the molecular frame is thus simply

$$d^M_{\mathbf{k}'} = \sqrt{\frac{2\pi}{3}} \sum_{lm\nu} (-i)^l e^{i\sigma_l} a_{k'lm\nu} (a\mathcal{D}^{(1)}_{\nu-1} + b\mathcal{D}^{(1)}_{\nu+1}) Y^m_l(\hat{\mathbf{k}}'). \tag{6.18}$$

Performing the inverse rotation on Y^m_l to pass from the molecular frame to the laboratory one provides the dipole in this latter

$$d^{(lab)}_{\mathbf{k}} = \sqrt{\frac{2\pi}{3}} \sum_{lm\nu\mu} (-i)^l e^{i\sigma_l} a_{klm\nu} (a\mathcal{D}^{(1)}_{\nu-1} + b\mathcal{D}^{(1)}_{\nu+1}) \mathcal{D}^{(l)*}_{m\mu} Y^{\mu}_l(\hat{\mathbf{k}}) \tag{6.19}$$

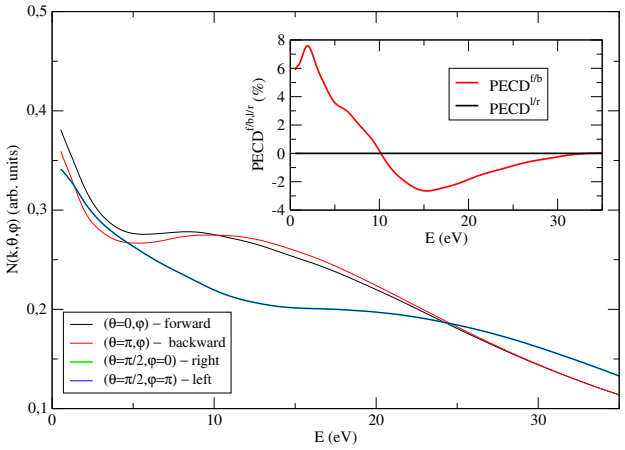

Figure 6.15: Differential electron production $\mathcal{N}$, defined in eq.(6.21), along the forward, backward, left and right directions of electron ejection, for (1S)-(-)-camphor irradiated by a left circularly polarized radiation. In the inset are displayed the PECDs in the forward/backward and left/right directions.

which can be evaluated for any direction of electron ejection $\hat{\mathbf{k}} = (\theta, \varphi)$ in the laboratory. Introducing the simple notation $d^{(lab)}_{\mathbf{k}} = |d^{(lab)}_{(k,\theta,\varphi)}|e^{i\varphi(k,\theta,\varphi)}$, the Wigner delay can be computed in the case of an oriented molecule as in [Baykusheva et al. 2017; Chacon et al. 2014; Goldberger et al. 1962; Wigner 1955]

$$\tau_W(k,\theta,\varphi) = \frac{\partial}{\partial\epsilon}\varphi(k,\theta,\varphi) \equiv \frac{1}{k}\frac{\partial}{\partial k}\varphi(k,\theta,\varphi). \tag{6.20}$$

However, this delay is defined for a given orientation $\hat{R}$ while the experiment deals with samples of randomly oriented molecules. An orientation-averaged delay $\bar{\tau}_W(k,\theta,\varphi)$ thus has to be defined, within which the contribution of a particular orientation $\hat{R}$ is weighted by its contribution to the total electron production

$$\mathcal{N}(k,\theta,\varphi) = \int d\hat{R}|d^{(lab)}_{\mathbf{k}}(\hat{R})|^2, \tag{6.21}$$

according to [Baykusheva et al. 2017]

$$\bar{\tau}_W(k,\theta,\varphi) = \int d\hat{R}\tau_W(\hat{R};\mathbf{k})\frac{|d^{(lab)}_{\mathbf{k}}(\hat{R})|^2}{\mathcal{N}(\mathbf{k})}. \tag{6.22}$$

In practice, the integrations on $\hat{R}$, with $d\hat{R} = \frac{1}{8\pi^2}d\alpha\sin(\beta)d\beta d\gamma$, are performed by (Simpson) numerical quadratures with angular spacing $\Delta\alpha = \Delta\beta = \Delta\gamma$ small enough to ensure convergence of the computed $\bar{\tau}_W$ values.

The one-photon counterpart to the measured differential Wigner delay is then evaluated by subtracting the $\bar{\tau}_W$ values in the forward and backward directions:

$$\Delta\bar{\tau}^{f/b}_W(k) = \bar{\tau}_W(k,0,\varphi) - \bar{\tau}_W(k,\pi,\varphi), \tag{6.23}$$

the axis z of quantization being collinear with the direction of propagation of the incident direction. The delay difference is also inspected between the left and right directions:

$$\Delta\bar{\tau}_W^{l/r}(k) = \bar{\tau}_W(k,\pi/2,\pi) - \bar{\tau}_W(k,\pi/2,0). \tag{6.24}$$

Note that similar quantities can be evaluated for a fixed orientation, $\Delta\tau_W^{f/b}(\hat{R};k) = \tau_W(\hat{R};k,0,\varphi) - \tau_W(\hat{R};k,\pi,\varphi)$ and $\tau_W^{l/r}(\hat{R};k) = \tau_W(\hat{R};k,\pi/2,\pi) - \tau_W(\hat{R};k,\pi/2,0)$.

Finally, the calculations also enable to estimate the PhotoElectron Circular Dichroism (PECD) in the forward/backward and left/right directions as

$$PECD^{f/b}(k) = 2\frac{\mathcal{N}(k,0,\varphi) - \mathcal{N}(k,\pi,\varphi)}{\mathcal{N}(k,0,\varphi) + \mathcal{N}(k,\pi,\varphi)} \tag{6.25}$$

$$PECD^{l/r}(k) = 2\frac{\mathcal{N}(k,\pi/2,\pi) - \mathcal{N}(k,\pi/2,0)}{\mathcal{N}(k,\pi/2,\pi) + \mathcal{N}(k,\pi/2,0)}. \tag{6.26}$$

$$\tag{6.27}$$

All the following results have been obtained using $\Delta\alpha = \Delta\beta = \Delta\gamma = \pi/32$ which guaranteed convergence of all computed observables.

We first present in Fig. 6.15 the differential electron production $\mathcal{N}$, defined in eq. (6.21), along the forward, backward, left and right directions of electron ejection, for (1S)-(-)-camphor irradiated by a left circularly polarized radiation. While $\mathcal{N}$'s are strictly identical in the left and right directions, they significantly differ in the forward and backward directions for electron energies E less than 30 eV. This is a feature commonly observed in photoionization of chiral systems [Nahon et al. 2016; Ritchie 1976], which gives rise to a sizable $PECD^{f/b}$ while $PECD^{l/r} = 0$ for all E (see inset of Fig. 6.15). Interestingly the $PECD^{f/b}$ changes sign about $E = 10$ eV. Since the calculations assume that the nuclei are frozen and consider only the single outermost molecular orbital, such a sign change illustrates kinetic energy effects, *i.e.* the energy dependence of multiple electron scattering off the chiral potential [Beaulieu et al. 2016a; Nahon et al. 2016; Ritchie 1976]. The $PECD^{f/b}$ exhibits a maximum value of $\sim 8\%$ about $E = 2$ eV, and a shoulder shows up in the $E = 6 - 10$ eV region.

The differential Wigner delays, $\Delta\bar{\tau}_W^{f/b}$ and $\Delta\bar{\tau}_W^{l/r}$, defined in eqs. (6.23) and (6.24) respectively, are displayed as a function of E in Fig. 6.16. As for the PECD, we find that $\Delta\bar{\tau}_W^{l/r} = 0$ whatever is E. By contrast, $\Delta\bar{\tau}_W^{f/b} \neq 0$ and presents sizable values in the attosecond range. The forward/backward differential delay is maximum at low E, as intuitively expected since low energy electrons spend more time in the chiral potential. However, it consists in this energy region of a small fraction only of the typical Wigner delay, which is illustrated in the inset of Fig. 6.16. In practice, $\bar{\tau}_W^f \sim \bar{\tau}_W^b \sim \bar{\tau}_W^l \sim \bar{\tau}_W^r$ and the ratio $|\Delta\bar{\tau}_W^{f/b}/\bar{\tau}_W^{f,b}|$ maximizes in the intermediate energy region centered about ~ 10 eV. Kinetic energy effects also show up in $\Delta\bar{\tau}_W^{f/b}$ through a sign change about $E = 4$ eV. But more interestingly, the differential Wigner delay presents rich spectroscopic features in terms of local maxima/minima for $E > 1$ eV. These features are totally absent in the electron production signals of Fig. 6.15 and almost invisible in the usual PECD (inset of Fig. 6.15). In fact, differentiating the PECD with respect to E partially allows retrieving the structures strongly marked in $\Delta\bar{\tau}_W^{f/b}$, but with very small amplitudes. This procedure would thus be difficult on experimental data. By contrast, our present experimental

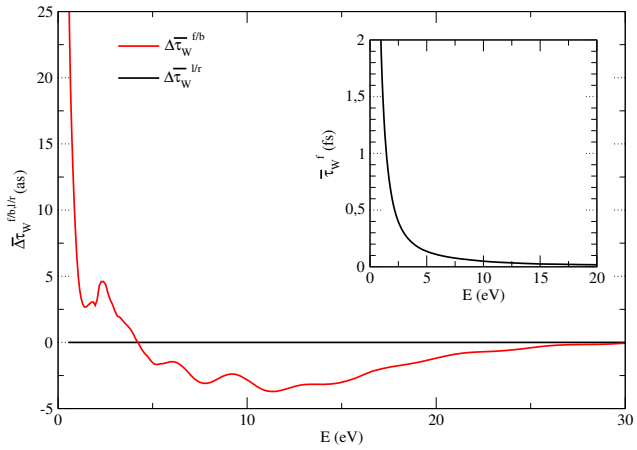

Figure 6.16: Differential Wigner delays, $\Delta\bar{\tau}_W^{f/b}$ and $\Delta\bar{\tau}_W^{l/r}$, defined in eqs. (6.23) and (6.24) respectively, for (1S)-(-)-camphor irradiated by a left circularly polarized radiation. The Wigner delay $\bar{\tau}_W^{f}$ in the forward direction is illustrated in the inset.

investigation shows that measuring differential delays is now feasible, and will surely be addressed by highly sensitive setups in the next future. In this respect, it seems that the differential delay $\Delta\bar{\tau}_W^{f/b}$ is a very valuable chiral observable which encodes subtle features of the underlying chiral potential, beyond usual (PECD) signatures.

We now investigate the origin of the features observed in the differential Wigner delays. $\Delta\bar{\tau}_W^{f/b}$ involves delays averaged on the molecular orientations. We thus looked at the delays for all underlying orientations, $\Delta\tau_W^{f/b}(\hat{R};E)$, and observed that some of them have very important values. For instance, focusing on the local maximum of $\Delta\bar{\tau}_W^{f/b}$ centered about $E = 2.5$ eV in Fig. 6.15, we found that the orientation defined by $(\alpha = 22.5°, \beta = 45°, \gamma = 0°)$ yields $\Delta\tau_W^{f/b}(\hat{R};E) \sim 2$ fs at this energy (see Fig. 6.17(a)). This important delay difference stems from a phase jump of $\sim \pi$ in the forward direction, in a narrow E-range where the phase in the backward direction behaves smoothly and thus leads to a vanishing Wigner delay (see Fig. 6.17(b)). Simultaneously the dipole modulus has ~ 0 amplitude in the forward direction (see Fig. 6.17(e)). In other words, the important delay in the forward direction is nothing else than the signature of a Cooper minimum [Cloux et al. 2015; Cooper 1962] induced by the potential shape in the $(\theta = 0, \varphi)$-electron direction for $(\alpha = 22.5°, \beta = 45°, \gamma = 0°)$ molecular orientation. This large delay difference, in the fs range, survives orientation averaging, and leads to the maximum of $\Delta\bar{\tau}_W^{f/b}$ in the as range at $E \sim 2.5$ eV (see Fig. 6.17).

In the calculations, which are based on the single-active electron approximation and employ a simplified form of the molecular potential in terms of ESP-charges, all local variations of $\Delta\bar{\tau}_W^{f/b}$ are due to such differential Cooper minima. This is illustrated in Figs. 6.17(d-f) for the oscillation appearing in Fig. 6.16 about $E = 8.5$ eV. In this case, the important negative delay computed in the forward direction for $(\alpha = 180°, \beta = 157.5°, \gamma = 0°)$ contributes positively to the averaged $\Delta\bar{\tau}_W^{f/b}$ because $\sin(\beta) < 0$. It is important to note that in the experiment, the multiphoton excitation/ionization preferentially selects

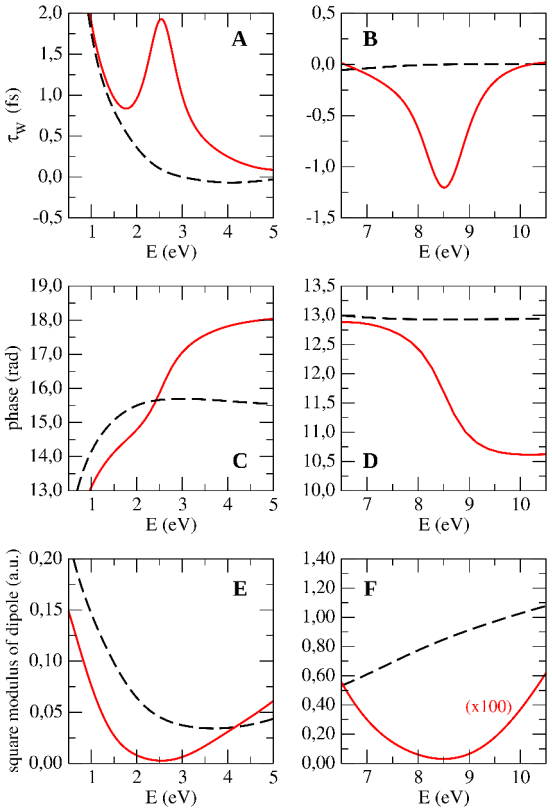

Figure 6.17: (a) Wigner delays, τ_W, in the forward and backward directions for ($\alpha = 22.5°, \beta = 45°, \gamma = 0°$); the (red) continuous line refers to the forward direction and the (black) dashed one to the backward direction. Associated variations of the phase (c) and square modulus (e) of the dipoles. (b),(d) and (f) graphs are similar to (a), (c) and (e) but for ($\alpha = 180°, \beta = 157.5°, \gamma = 0°$).

some molecular orientations within the sample of randomly oriented molecules. The calculations suggest that this photoselection can have a huge impact on the measured quantities. In the future, it would thus be of great interest to study the differential Wigner time delays within the molecular-frame of chiral molecules, using coincidence electron-ion imaging [Tia et al. 2017].

It has to be noted that not only differential Cooper minima but also differential resonances are amenable to important local variations of $\Delta\tau_W^{f/b}(\hat{R};E)$ because of underlying $\sim\pi$ phase jumps. However, the calculations presented here are based on the single-active electron approximation, which inhibits the occurrence of autoionizing resonances. Shape resonances do not show up either, at least using the simplified description of the ionic potential in terms of ESP-charges. Nevertheless, it is clear that fine differential features of chiral molecular potentials can, in general, be probed by measurements and computations of $\Delta\bar{\tau}_W^{f/b}$.

To summarize this theoretical subsection, the calculations confirm the existence of asymmetric Wigner delays, even in a randomly oriented ensemble of molecules. The theoretical forward/backward differential Wigner delay $\Delta\tau_W^{f/b}$ is of the order of 5 as for 2 eV electrons, which agrees qualitatively with the present experimental observation. Interestingly, the evolution of $\Delta\tau_W^{f/b}$ with respect to the photoelectron energy, shown in the SM, shows rich spectroscopic features that are not visible in the photoelectron spectrum and cannot be easily distinguished in the PECD signal. Thus $\Delta\tau_W^{f/b}$ is a remarkable chiral observable, which enables tracking of subtle features of the molecular potential such as, for example, the differential Cooper minima, surviving the molecular orientation averaging. This observation opens prospects for highly sensitive experiments, for instance through molecular-frame measurements [Tia et al. 2017], as well as accurate testing of advanced quantum theories of molecular photoionization.

6.5 Asymmetric resonant photoionization of chiral molecules

6.5.1 Signatures of resonant photoionization

Continuum resonances play an essential role in the photoionization of most polyatomic molecules. They can arise from the shape of the molecular potential, in a single-electron picture (shape resonances) [Piancastelli 1999], or from multi-electron dynamics involving electron correlations and couplings between different channels [Fano 1961]. In both cases, spectrally localized transition dipole moment enhancement, as well as scattering phase jump(s), are expected, reflecting the modification of the ionization dynamics. For instance, in chiral molecules, the PECD was recently shown to be enhanced in the vicinity of a Fano resonance [Catone et al. 2012]. Here we used the spectrally-resolved photoelectron interferometry technique, introduced by Gruson *et al.* [Gruson et al. 2016] (see Fig. 6.4), to directly track the asymmetric ionization dynamics of chiral molecules in the vicinity of an autoionization resonance.

As shown in Fig. 6.7(b), the SB1 presents a sharp π-phase jump around 1.9 eV, which reflects the presence of a resonance on the first ATI peak. Resonances in the continuum are generally detected through an increase of the photoionization cross section. Additional information can be obtained by resolving the ejection direction of the photoelectrons, *i.e.* measuring photoelectron angular distributions (PAD) and decomposing it on a Legendre polynomials basis. In single photon ionization, the 2nd order Legendre coefficients completely describe the angular anisotropy of the PAD and are called the anisotropy parameters (β). The anisotropy parameter provides rich information about the photoion-

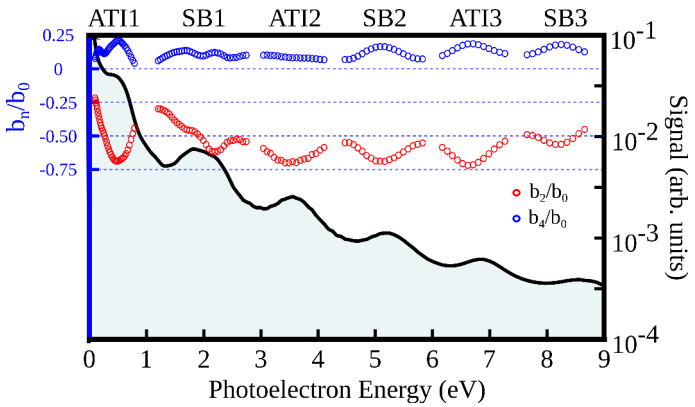

Figure 6.18: Legendre polynomials decomposition of the photoelectron angular distribution (PAD) across the ATI peaks and sidebands. The red/blue dots represent b_2/b_0 and b_4/b_0 normalized Legendre polynomials, respectively, averaged over the relative delay between the two-color fields. The blue, left-sided y-axis is associated with b_2/b_0 and b_4/b_0. The full black line represent the b_0 averaged over the relative delay between the two-color fields. The black, right-sided y-axis is associated with b_0. These data are taken when the UV was linearly polarized and the IR was circularly polarized.

ization dynamics. When multiple photons are used to ionize a target, the PAD exhibit more complex angular features and higher-order Legendre polynomials are needed to tackle the angular information encoded in the PAD. In this case, multiple high-order Legendre coefficients (b_2, b_4, ..., b_{2n}) provides information about the ionization dynamics. These high-order Legendre coefficients are known to be strongly modulated in the vicinity of a continuum resonance (shape resonance or autoionizing resonance, for example) [Kabachnik et al. 1976]. We thus decomposed the PAD to extract the Legendre coefficients and to see if the anisotropy parameters around the ATI peaks and sidebands exhibit any signature of the autoionizing resonance. The energy resolved b_2/b_0 and b_4/b_0 parameters are shown in Fig. 6.18. Higher-order Legendre coefficients (b_6, b_8, ...,b_{2n}) can also contribute to the PAD, for high-order ATI/sideband peaks. However, they are really small compared to b_2/b_0 and b_4/b_0, so for the sake of clarity, we choose to not plot them.

For the two higher-order ATI peaks and sidebands (ATI2, ATI3 and SB2, SB3), b_2/b_0 and b_4/b_0 exhibit an almost flat or monotonic single bump behavior across their spectral bandwidth. On the contrary, for the first ATI peak (ATI1), where we expect the autoionizing resonance to show up, the anisotropy parameters are highly structured: b_2/b_0 strongly varies across the bandwidth of the ATI1 peak, and b_4/b_0 shows a clear double-bump feature, which is certainly caused by the presence of the autoionizing resonance. These features are transferred to the SB1, which also presents a double-bump feature on its b_4/b_0 and a strongly modulated b_2/b_0. Both b_2/b_0 and b_4/b_0 exhibit singular behavior at 1.9 eV, the exact energy where a phase jump of π was observed in the electron interferometry results (see Fig. 6.7). The observation of the signature of the resonance only on the first sideband go hand in hand with the electron interferometry results. This further confirms that the autoionization resonance does not influence the high-order sidebands.

6.5.2 Phase-resolved photoionization of camphor

We will now go back to the photoelectron interferometry measurement. We investigate the forward/backward dependence of the spectrally-resolved sideband oscillation phase of the first ATI peak, where we have seen a $\sim \pi$-phase jump around 1.9 eV in the angularly

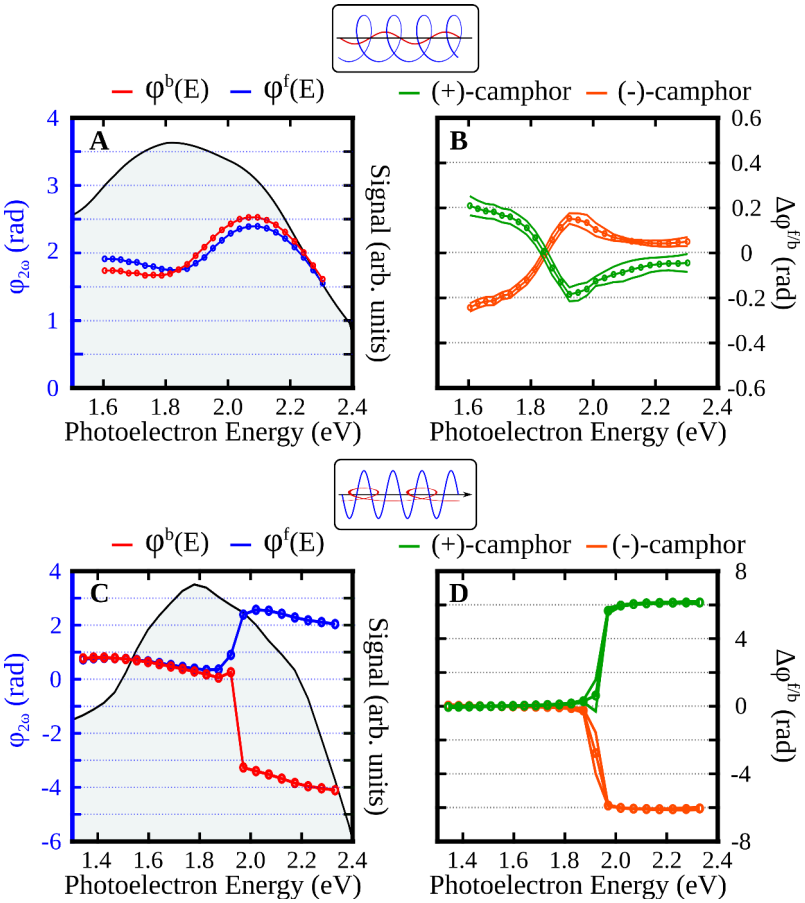

Figure 6.19: Phase-resolved resonant photoionization in camphor. (a),(c) Spectral amplitudes (black) and forward and backward spectral phases ($\varphi^f(E)$, blue and $\varphi^b(E)$, red) of SB1 in (1R)-(+)-camphor, using left-circularly polarized UV - linearly polarized IR (a) and linearly polarized UV - left-circularly polarized IR (c). (b),(d) forward backward asymmetry of the spectral phase ($\Delta\varphi^{f/b}$) in camphor, using left-circularly polarized UV - linearly polarized IR in (b) and linearly polarized UV - left-circularly polarized IR (d). In (b) and (d), the dots represent the mean values of the forward backward asymmetry of the spectral phase while the solid lines show the error bars, which are defined as the 95% confidence interval.

integrated case (see Fig. 6.7). The forward (blue) φ^F and backward (red) φ^B phases are shown in Fig. 6.19, using circularly polarized UV (a) or IR (c) light.

When the UV light is circularly polarized, the spectral phase exhibits a weak ~ 0.75 rad bump centered around 2.1 eV. A significant difference is observed between the forward and backward spectral phases. The differential phases ($\Delta\varphi^{f/b} = \varphi^F - \varphi^B$) (Fig. 6.19(b)) show a good mirroring when switching the enantiomers.

The case where the f/b symmetry is broken by the weak IR pulse (linear UV and circular IR) is more intriguing. The spectral phases show a steep $\sim \pi$ jump around 1.9 eV, in opposite directions for forward and backward electrons. After the jump, the phases become nearly identical, as they are separated by $\sim 2\pi$ (Fig. 6.19(c)). The f/b differential phases ($\Delta\varphi^{f/b}$) obtained in the two enantiomers are almost exactly opposite (Fig. 6.19(d)). To a first approximation, the presence of this huge asymmetry is unexpected. The circularly polarized field acts during the continuum-continuum transitions, which should be affected mostly by the long-range (non-chiral) part of the molecular poten-

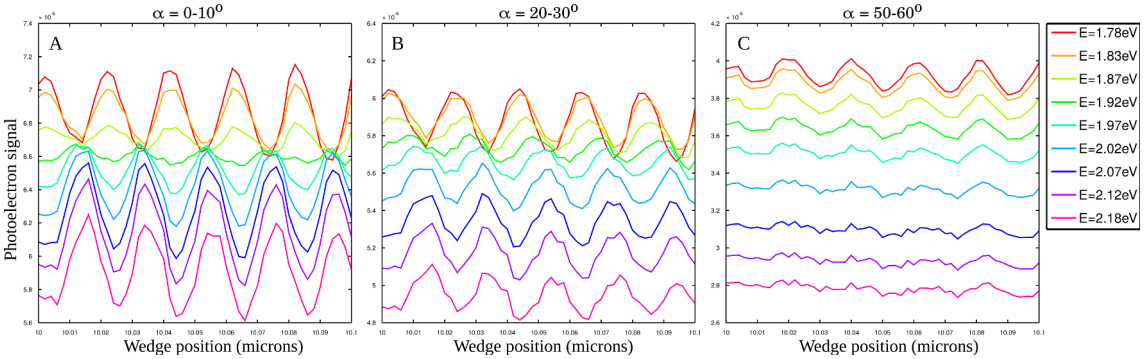

Figure 6.20: Raw oscillations of the SB1 signal as a function of photoelectron energy and ejection angle. The different colored lines represent different photoelectron energy. The electrons are ejected between 0-10° in (a), between 20-30° in (b) and between 50-60° in (c). These data were taken with linearly polarized UV and circularly polarized IR fields, in 1S-(-)-camphor.

tial and should, therefore, be f/b symmetric [Chacon et al. 2014]. Our measurement demonstrates that in the vicinity of a resonance, the f/b symmetry can also be broken during the continuum-continuum transitions. This finding is in agreement with a recent theoretical investigation of photoelectron interferometry, which demonstrated that the simple separation of the measured delay (τ_S) in a sum of the contributions from Wigner (τ_W) and continuum-continuum (τ_{cc}) delays did not hold anymore in the presence of a resonance [Argenti et al. 2017]. Indeed, Argenti *et al.* demonstrated that τ_W and τ_{cc} are entangled in resonant photoionization [Argenti et al. 2017]. The measured delay (τ_S) is representative of the two-color photoionization process, and our results show that the circular polarization of the weak IR field is sufficient to induce a major symmetry breaking, in the presence of a resonance.

The spectrally-resolved sideband oscillation phases presented in Fig. 6.19 were obtained by angularly-integrating the signal in the forward and in the backward quadrants, respectively. However, these phases can also depend on the electron ejection angle. Indeed, by looking at oscillation of the raw SB1 signal as a function of photoelectron energy and ejection angle, presented in Fig. 6.20, we clearly see a steep $\sim \pi$ phase-jump between 1.87 eV and 1.92 eV for electron ejected between 0-10° (Fig. 6.20 (a)). For electron ejected between 20-30° (Fig. 6.20 (b)), the magnitude of the phase jump across the resonance is still $\sim \pi$, but is much smoother. The phase jump disappear for ejection angle between 50-60° (Fig. 6.20 (c)). One can notice that the signal-to-noise ratio is very good for electron ejected closer to the laser polarization axis, where the photoelectron signal is maximum.

6.5.3 Temporal profile of the photoionized wavepackets

Using our spectrally- and angularly-resolved photoelectron interferometry technique, we have shown that we can measure the spectral amplitude and oscillation phase around the resonant SB1. Applying the 'Rainbow-RABBITT' idea developed by Gruson *et al.* [Gruson et al. 2016], we could thus retrieve the temporal profiles of the two-color forward and backward wavepackets by Fourier-transforming the measured spectral amplitudes and phases. Figure 6.21 shows the resulting angle-resolved photoelectron wavepackets, in the temporal domain. In both polarization configurations, the wavepacket shows a single temporal peak when the electrons are ejected close to the propagation axis of the light (90°), and a double peak structures when the electrons are ejected near the laser polarization plane (0°). The latter are signatures of the temporal interference between

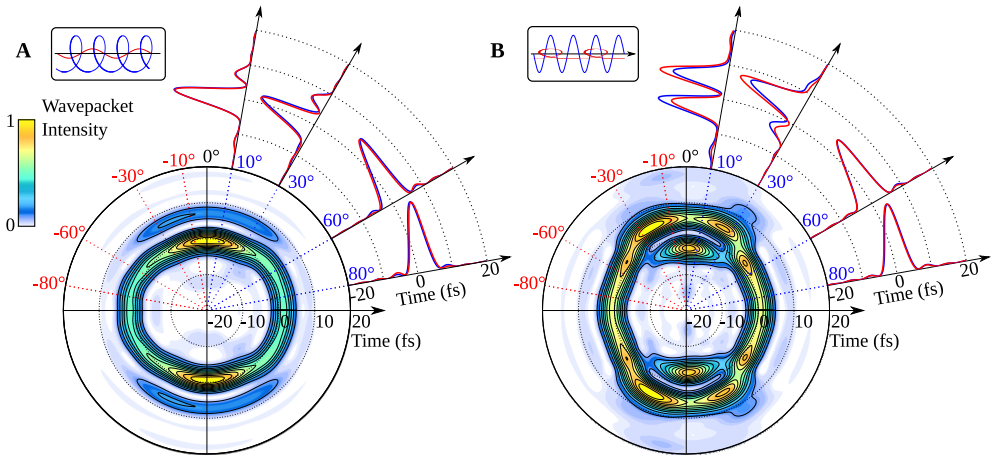

Figure 6.21: Angle-resolved temporal profile of the autoionizing photoelectron wavepacket. The contour plot depicts the temporal profile of the wavepacket as a function of the electron ejection angle. The upright external plots show forward (blue) and backward (red) cuts of the wavepackets along specific angles. (a): left-circularly polarized UV, linearly polarized IR. (b): linearly polarized UV, left-circularly polarized IR.

the direct non-resonant and the resonant components of the autoionizing wavepackets [Gruson et al. 2016]. The effect of the resonance appears more confined around the laser polarization direction when the UV field is linearly polarized (Fig. 6.21(b)), probably because of a stronger anisotropy of the resonant excitation compared to the circularly polarized case.

The chiral nature of the photoionization process can be investigated by comparing cuts of the temporal profile of electrons ejected at positive (forward, blue) and negative (backward, red) angles (α), with respect to the light polarization plane. In order to ease the visualization, and to demonstrate the quality of the enantiomeric mirroring, we present the cuts for each angular slice of 10 °, for both polarization configurations and in both enantiomers (see Fig. 6.22 and Fig. 6.23).

When the UV field is circularly polarized, the two bumps of the forward electron wavepacket emitted around 30° maximize $\sim$ 400 as after the backward wavepacket (Fig. 6.21(a) and Fig. 6.22). Interestingly, a similar delay is measured around 60°, where the wavepacket shows a single peak structure. As the ejection angle further increases, the ordering between forward and backward emission reverses, with a $\sim$ -250 as delay around 80°. These subtle features obey chiral inversion when switching from one enantiomer to the other, as shown in the Fig. 6.22.

In the other polarization configuration (Fig. 6.21(b) and Fig. 6.23), the two bumps from the forward and backward wavepackets are synchronized in time for electrons ejected close to the laser polarization plane ($\alpha = 0°$). However, their relative yield is strongly f/b asymmetric. This means that in the vicinity of resonances, where τ_W and τ_{cc} are strongly entangled [Argenti et al. 2017], the perturbative IR pulse can be used to break the f/b symmetry and to subsequently tailor asymmetric electronic wavepackets, both in time and space. This scheme is easily transposable to the situation where a single XUV photon could be used to photoionize a chiral molecule near a resonance, and a weak CPL IR pulses could be used to f/b asymmetrically shape the two-photon outgoing electron wavepacket. At larger emission angles, where the dynamics are governed by a single -non-

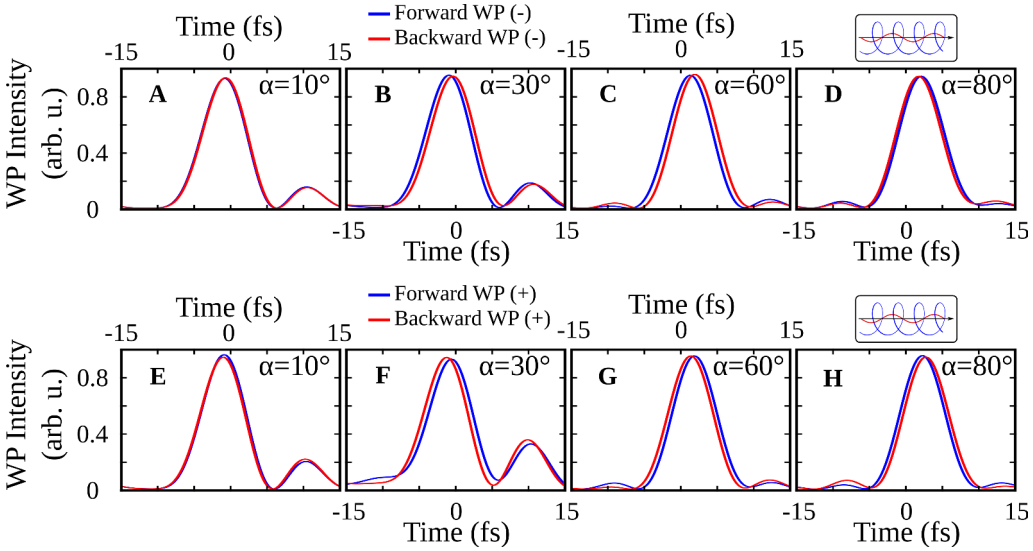

Figure 6.22: Temporal profile of the resonant electron wavepackets emitted in different directions in (1S)-(-)-camphor (top, a-d) and (1R)-(+)-camphor (bottom, e-h), using a circularly polarized UV and a linearly polarized IR field.

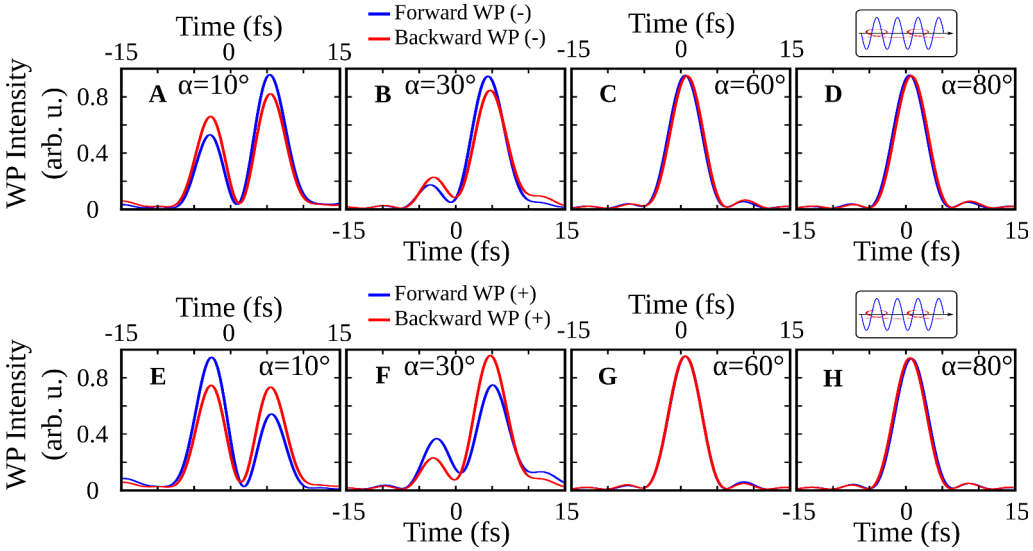

Figure 6.23: Temporal profile of the resonant electron wavepackets emitted in different directions in (1S)-(-)-camphor (top, a-d) and (1R)-(+)-camphor (bottom, e-h), using a circularly polarized UV and a linearly polarized IR field.

resonant- pathway, the single-peak wavepackets become forward-backward symmetric. This analysis provides deep insights into the angular-dependence of the multielectron dynamics governing autoionization.

Comparing the two polarization configurations used in the measurements (Fig. 6.21) shows that the wavepacket asymmetry is in fact much stronger when it is the weak IR field that is circularly polarized. We attribute this result to the sequential nature of the resonant photoionization process. The linearly polarized UV photons populate a quasi-bound state embedded in the continuum, which can be depleted by ionization, releasing electrons

at the energy of the first ATI peak. However, another process could lead to ionization of the quasi-bound state: the absorption of one IR photon releasing an electron with the energy of the first sideband. This can be seen as a classic PECD experiment, starting from a highly excited quasi-bound state. We have shown in the two previous chapters that PECD could be observed when bound states excited by linear photons were ionized by circularly polarized photons. The present scheme extends this scenario to quasi-bound states. On the other hand, when the UV photons are circularly polarized, they can induce an asymmetric wavepacket in the excited states, a phenomenon that we have presented in the previous chapter and which is called PhotoeXcitation Circular Dichroism (PXCD) [Beaulieu et al. 2016c]. The ionization of such a wavepacket by linearly polarized light produces f/b asymmetries, but they were observed to be weaker than the PECD from excited states. This could explain why we observe a weaker wavepacket asymmetry when the IR photons are linearly polarized.

6.5.4 Time-frequency analysis of the resonant photoelectron wavepacket

The temporal profile of the wavepackets only provides spectrally integrated information about the rich ongoing dynamics. The spectral origin of temporal asymmetries can be revealed using a time-frequency analysis [Busto et al. 2018]. Let us make an analogy with the time-frequency analysis that has been presented in the HHG chapter of this thesis. When we were investigating the possible origin of the new (resonant) spectral features that showed up in both the experiments and in the 1D-TDSE, we have seen that the time-frequency (Gabor) analysis of the 1D-TDSE dipole provided invaluable information about the temporal build-up of the HHG spectrum. It helped us to solve the mystery of the delayed emission mechanism of e-HHG (see Fig. 2.19). Here, we will use time-frequency analysis to get insight into the build-up of the resonant photoelectron wavepacket, in time and frequency domains simultaneously. A more general discussion about time-frequency analysis was introduced in the HHG chapter of this thesis manuscript.

The time-frequency analysis presented here was motivated by the analysis of resonant photoelectron wavepackets performed by the Lund and Saclay teams, using Wigner-Ville distributions [Busto et al. 2018]. The Wigner-Ville distribution (WVD) is particularly interesting because it encodes the quantum interference between different components of a wavepacket. For a wavefunction $\Psi(t)$, the WVD ($W(\Omega,t)$) is defined as:

$$W(\Omega,t) = \int \Psi(t-\tau/2)\Psi^*(t+\tau/2)e^{i\Omega\tau}d\tau \tag{6.28}$$

where Ω is the angular frequency, and t is the time. Figure 6.24 shows the WVD of the electron wavefunctions emitted around α = +10° (forward, $\Psi^f(t)$) and α = -10° (backward, $\Psi^b(t)$)) from the laser polarization plane. We choose to present these wavepackets because they were the one showing the strongest signature of the resonant character (double bump feature, in the time-domain). In order to increase the statistics, the distributions were calculated by averaging the wavepacket from (+)-camphor and the mirrored wavepacket from (-)-camphor.

The rather complex forward and backward WTD (Fig. 6.24 (a) and (b)) can be decomposed into different components, in order to ease their interpretation. First, a spectrally narrow and temporally long feature is seen around the resonant energy (1.9 eV). This is the contribution of the resonant pathway to the wavepacket. Around $t = 0$, a spectrally broad and temporally narrow strong component emerges, which is the signature of the non-resonant (direct) photoelectrons. A strong negative lobe is present around time $t = 0$

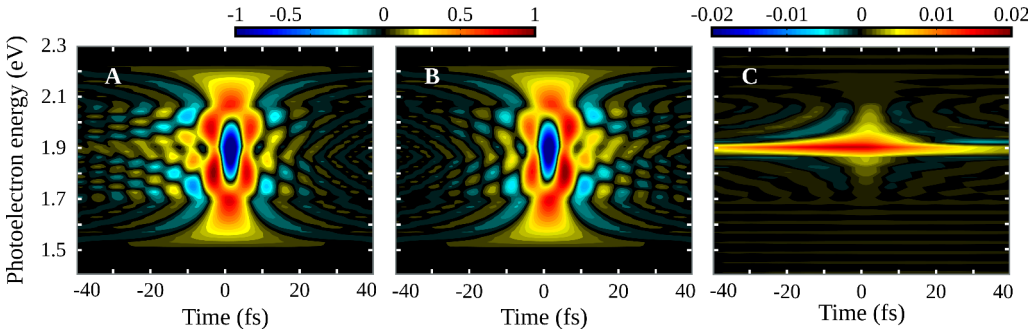

Figure 6.24: Wigner-Ville distributions of the autoionizing photoelectron wavepackets. The distributions were calculated on an average wavepacket obtained by summing the wavepacket from (1R)-(+)-camphor and the mirrored wavepacket from (1S)-(-)-camphor. (a) shows the WVD of a forward wavepacket emitted around α = 10° from the linearly polarized UV field, and (b) the WVD of a backward wavepacket emitted around α = -10° (c) is the WVD of the forward-backward differential wavepacket.

at the energy of the resonance (1.9 eV), revealing the quantum interference between the direct and indirect ionization components.

In order to isolate the asymmetric part of the wavefunction, we calculated the WVD of the differential wavefunction $\Delta\Psi^{fb}(t) = \Psi^{f}(t) - \Psi^{b}(t)$ (Fig. 6.24(c)). The WVD of the differential wavepacket turns out to be strikingly simple, with a temporally long and spectrally narrow signal at the energy of the resonance, and almost no negative components. We concluded that while the forward and backward wavepackets are each formed by the coherent superposition of a resonant and a non-resonant contribution, the chiral character of the wavepacket appears to be strongly dominated by a single - resonant - pathway, which leads to the disappearance of the signature of quantum mechanical interference in the WVD. The WVD thus provides unique insight into the origin of the asymmetric shaping of photoelectron wavepackets during resonant photoionization of chiral molecules.

The Wigner-Ville distributions provide invaluable information about the time-frequency dynamics of the resonant photoelectron wavepackets. In particular, it takes negative values when quantum mechanical interferences occur. It is thus well suited to study autoionizing photoelectron wavepackets, which are shaped by the quantum interference of a direct and an indirect pathways. However, such negative values in a quasiprobability distribution might be somehow counterintuitive, and other time-frequency distributions, that are also based on the WVD, can be used to avoid the occurrence of negative values. One way to get rid of negative values is to smooth the Wigner-Ville distribution with a phase-space Gaussian function (Weierstrass transform). Weierstrass transforming the Wigner-Ville distribution provides the so-called Husimi distribution, an all-positive coarse-grained quasiprobability representation of quantum wavefunctions. For a wavefunction $\Psi(t)$, the Husimi distribution ($Q(\Omega,t)$) is defined as:

$$Q(\Omega,t) = \int\int \left[\int \Psi(t-\tau/2)\Psi^{*}(t+\tau/2)e^{i\Omega\tau}d\tau \right] e^{-\Omega^2/(2\sigma_\Omega^2)} e^{-\tau^2/(2\sigma_\tau^2)} d\Omega d\tau, \quad (6.29)$$

where σ_Ω= 75 meV, σ_t= 4 fs are the RMS width of the Gaussian functions used for the convolution along the frequency and time axis, respectively. The size of the Gaussian

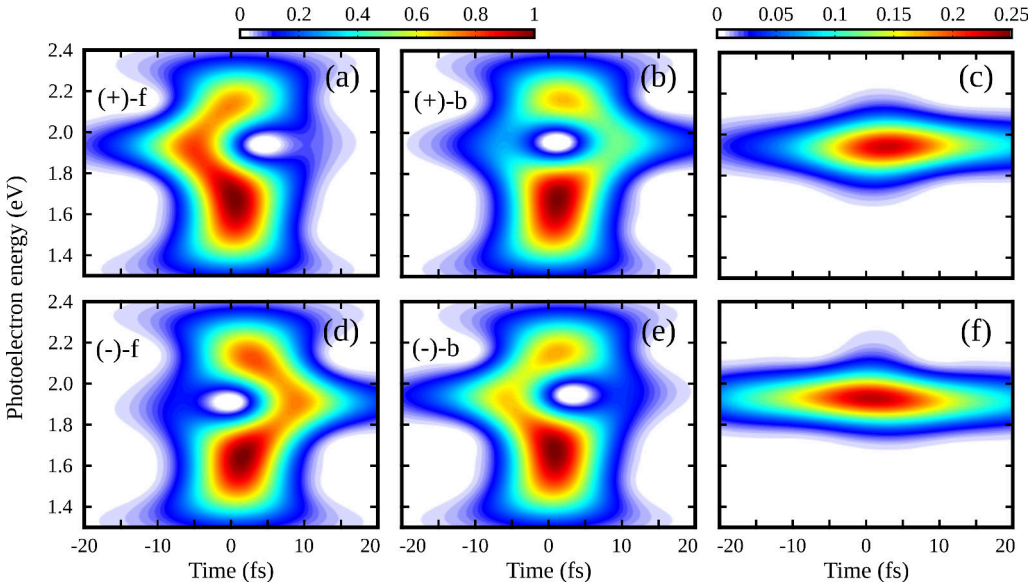

Figure 6.25: Husimi distribution of the autoionizing photoelectron wavepackets for (1R)-(+)-camphor (a)-(c) and (1S)-(-)-camphor (d)-(f) produced by absorption of linear UV and circular IR photons. (a) and (d) represent the forward wavepackets, (b) and (e) the backward wavepackets, and (c) and (f) the differential f/b wavepackets.

window functions used for the convolutions is chosen such that all the negative components of the distribution are washed out. Because the Husimi distribution is obtained by coarse-graining the WVD, it leads to the better signal-to-noise ratio. We will thus be able to present the forward, backward and differential Husimi distribution for both enantiomers, without having to average the (+)-camphor and the mirrored wavepacket from (-)-camphor, like in Fig. 6.24.

Figure 6.25(a)-(b) and (d)-(e) show the Husimi distributions of the forward and backward photoelectron wavepackets ($\Psi^F(t)$ and $\Psi^B(t)$), obtained in both enantiomers, in the case of resonant photoionization using linear-UV and circular-IR. In figure 6.25 (d), a hole around $t = 0$ fs followed by a long emission tail for positive time delays is observed, at the energy of the resonance. This hole is a consequence of the destructive interference between the direct and indirect ionization pathways. The temporal ordering of the hole and the tail reverses when changing the observation direction (forward/backward) or the enantiomer. In addition, a spectrally much broader and temporally confined emission is observed between $\sim$ -10 fs and 10 fs. This component comes from the non-resonant photoionization pathway.

In order to shed light on the asymmetric part of the wavepacket, induced by the chiral nature of the interaction, we have extracted the Husimi distribution for the differential wavepackets $\Psi^F(t) - \Psi^B(t)$ (Fig. 6.25(c) and (f)). Like in the case of the Wigner-Ville distributions, they are strikingly simple, with a temporally long and spectrally narrow signal, at the energy of the resonance: while the forward and backward wavepackets are each formed by the coherent superposition of a resonant and a non-resonant contribution, the chiral character of the wavepacket appears to be strongly dominated by the resonant pathway.

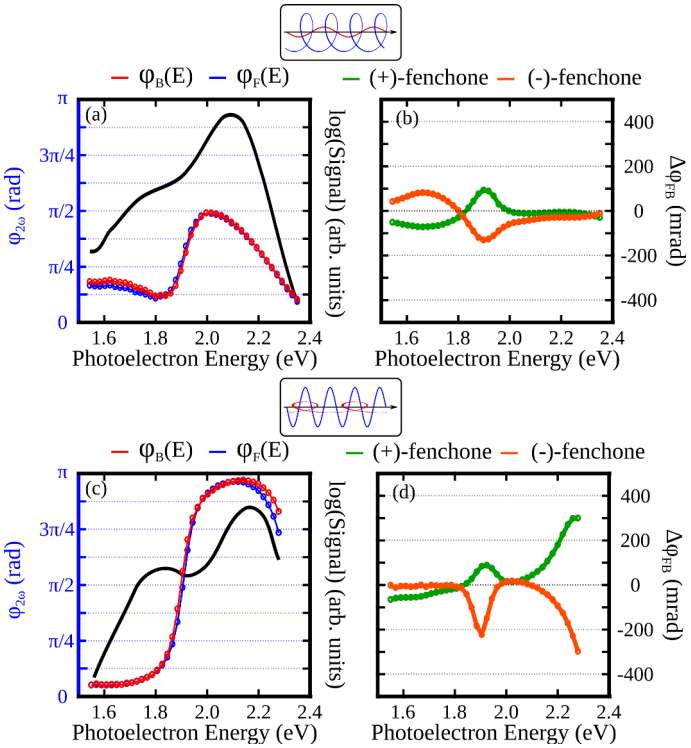

Figure 6.26: Phase-resolved resonant photoionization in fenchone. (a),(c) Spectral amplitudes (black) and forward and backward spectral phases ($\varphi^f(E)$, blue and $\varphi^b(E)$, red) of SB1 in (+)-fenchone, using left-circularly polarized UV - linearly polarized IR (a) and linearly polarized UV - left-circularly polarized IR (c). (b),(d) forward backward asymmetry of the spectral phase ($\Delta\varphi^{f/b}$) in fenchone, using left-circularly polarized UV - linearly polarized IR in (b) and linearly polarized UV - left-circularly polarized IR (d).

6.6 Conclusion and perspectives

The results presented in this chapter show that using circularly polarized photons to drive photoionization of chiral molecules not only produces a forward-backward asymmetry in the photoelectron angular distribution (PECD) but also induces forward-backward asymmetric delays in the photoemission, on both femtosecond and attosecond timescales. In direct non-resonant photoionization, the forward/backward asymmetry in the photoionization time delays is on the order of few attoseconds. Angularly resolving this physical quantity reveals that the asymmetry in the photoionization delays is strongly anisotropic: it is large for electrons emitted close the laser propagation direction and is vanishing for electrons emitted in the vicinity of the polarization plane of the laser.

In the vicinity of an autoionizing resonance, which is driven by electronic correlation, the temporal profile of the emitted two-color photoelectron wavepacket exhibits a double peak structure, as in the case of resonant photoionization of Helium [Gruson et al. 2016], which is the signature of the interplay between the direct and indirect pathways. We have found strong angularly anisotropic temporal profiles of the emitted two-color photoelectron wavepacket, as well as a strongly forward-backward asymmetric behavior, demonstrating the chiral character of this multielectronic effect. By using the synergies of molecular and light chirality in the vicinity of resonances, we have demonstrated a tailoring of the shape of the released electron wavepackets, both in time and space, which is a new scheme for multidimensional attosecond quantum control. The high accuracy of

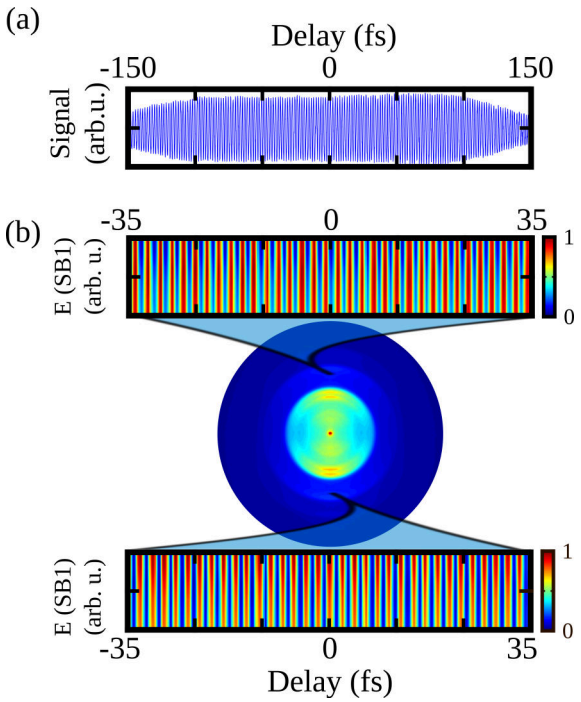

Figure 6.27: Photoelectron interferometry using the 2 MHz Yb laser. We took 10000 images, where each image correspond to a different delay between the ω (1030 nm, 13.7 W) and 2ω (515 nm, 2.3 W) fields and where each image is acquired for 50 ms camera opening time. It leads us to acquire more than 170 sideband oscillation periods, in 8 minutes. (a) The integrated signal in the upper hemisphere of the detector, as a function of the delay between the ω and 2ω fields. In (b), the upper (lower) graph is the photoelectron energy (PE) resolved signal of the first sideband (SB1), which have been integrated angularly in the upper (lower) hemisphere, as a function of the delay. A typical PES is also shown in (b).

the measurements can also be used as a powerful benchmarking tool for quantum theories of molecular photoionization.

These investigations open many different perspectives for future measurements. First, as we have seen throughout this manuscript, performing the same experiment in the structural isomer of camphor, namely the fenchone molecule, always provides useful insight about the sensitivity of the observable to the subtleties of the molecular species. We have thus repeated the experiment in both fenchone enantiomers, in the exact same experimental conditions. As in camphor, we have observed signature of resonance on the first sideband (SB1), originating from a near-threshold autoionizing resonance at the energy of the first ATI peak. The energy-resolved oscillation phases of the resonant SB1, for both polarization configuration, are shown in Fig. 6.26. We are currently working on the deep analysis of these data with the goal of comparing the angularly-resolved temporal profile of the resonant photoelectron wavepacket with the ones measured in camphor.

As we will see in greater details in the general conclusions and perspectives, a new high-repetition-rate (166 kHz - 2 MHz) high power (2 x 50 W) Ytterbium (Yb) fiber laser delivering 130 fs pulses is available at CELIA. Experiments which are very similar to the ones presented in this subsection are currently being performed using this new laser system. The very high-repetition-rate allows acquiring much larger, high-quality data sets, in very short time. It is thus possible to perform experiments that would have been

impossible at 1 kHz. For example, acquiring 5 oscillation periods using the kHz laser system, for the photoelectron interferometric data presented in Fig. 6.7, took us more than two hours for each enantiomer and each helicity. By performing a similar scan, using the 2 MHz Yb laser system, we recorded more than 170 sideband oscillation periods in roughly 8 minutes (see Fig. 6.27).

The high-quality of the data and the high speed at which it can be acquired is clearly a major game changer. The investigation of high-resolution and angularly-resolved asymmetry of the photoionization delays in a large number of different molecules would definitely provide unprecedentedly rich benchmark tests for quantum theories which are dealing with chiral molecular photoionization.

7. General conclusions and perspectives

The work presented in this manuscript shows that using a broad range of ultrashort light sources, from the mid-infrared to the extreme ultraviolet range, enables probing a wide variety of phenomena, from rare gases and diatomics to polyatomic chiral molecules, occurring on different timescales, from picoseconds down to a few attoseconds. To conclude this work, we briefly summarize the main results and discuss short and long-term perspectives they opened.

7.1 Strong-field and attosecond physics

Throughout the different chapters of the manuscript, we have demonstrated several advances from the point-of-view of strong-field and attosecond physics. These advances are mainly articulated around the development of cutting-edge light source [Cardin et al. 2015; Thiré et al. 2015] (Chapter 1), the role of Rydberg states in strong-field interaction with atoms [Beaulieu et al. 2017a; Beaulieu et al. 2016a] (Chapter 2) and the strong-field ionization of chiral molecules using chiral light pulse (Chapter 4). The latter led us to demonstrate the universality of Photoelectron Circular Dichroism, *i.e.* its emergence is all ionization regime [Beaulieu et al. 2016b]. This has ultimately enabled us to perform the measurement of chiral attosecond photoionization dynamics, using a photoelectron interferometric technique that relies on strong-field ionization [Beaulieu et al. 2017b] (Chapter 6).

7.1.1 HHG, Rydberg states, and bicircular bichromatic fields

In Chapter 2, we have found out that Rydberg states, which are usually assumed to be silent spectators of High-order Harmonic Generation (HHG) can, in fact, play a significant role in the process. They open new cross-channels for HHG when they are coherently populated during the laser pulse. We have observed new spectral features concomitant with standard odd harmonics, which are associated with delayed emission coming from the ionization from excited states and recombination onto the ground state [Beaulieu

et al. 2016a]. Moreover, we have shown that this HHG channel is not the only radiative doorway for these highly excited states. The XUV Free-Induction Decay emission of the electronic wavepacket created upon excitation of these Rydberg states can be used as a powerful time-resolved spectroscopic technique [Beaulieu et al. 2017a], providing very similar information as in certain types of Attosecond Transient Absorption Spectroscopy (ATAS) experiments.

We have seen several times during this work the importance of increasing the number of knobs in an experiment, *i.e.* the number of degrees of freedom of the laser-matter interaction. In particular, the polarization state of the light is a very important parameter for strong field physics, enabling the manipulation of electronic trajectories and giving access to chiral sensitivity. However, circularly polarized radiation does not enable the rescattering of the ionized electrons with their parent ion and does not produce high-order harmonics [Budil et al. 1993]. An elegant solution to this issue is to use counter-rotating bicircular bichromatic pulses. When combining a circularly polarized pulse (ω) with its counter-rotating second harmonic (2ω), the total electric field emerged as a chiral threefold clover-leaf shape (see Fig. 8.1 (a)). Reversing the helicity of the two fields leads to a switch in the handedness of the threefold clover-leaf.

Bicircular bichromatic pulses have become a 'hot topic' in our community, because the electrons which are strong-field ionized by this type of waveform can rescatter three times per laser cycle onto the parent ion, leading to the efficient emission of XUV radiation through HHG [Eichmann et al. 1995; Fleischer et al. 2014; Kfir et al. 2015]. The emerging HHG spectrum appears as a succession of harmonics at 3N+1 and 3N+2 multiples of the fundamental driving frequency, while the 3N lines are forbidden, because of conservation of spin angular momentum (see Fig. 8.1). Indeed, since each emitted XUV photon can only carry one unit of spin angular momentum, the difference in the number of photons absorbed from the fundamental and the second harmonic needs to be $\pm$ 1. Also due to the conservation of spin angular momentum, the 3N+1 and 3N+2 harmonics are circularly polarized and have the same helicity as the ω and 2ω fields, respectively. The fact that driving HHG using these waveforms produce ultrafast circularly polarized XUV harmonics make them pretty attracting to us, from the point-of-view of our interest for generating chiral light pulses, in order to study the photoionization of gas-phase chiral molecules.

When driving HHG using collinear counter-rotating bicircular bichromatic pulses, the adjacent harmonics with opposite helicity (3N+1 and 3N+2) are propagating in the same direction. This can potentially be a problem for future PECD experiments, because the two frequency combs will produce partially overlapping photoelectron spectra, canceling some of the PECD effects. This problem can be avoided by driving HHG using a non-collinear geometry [Bertrand et al. 2011; Hickstein et al. 2015]. Indeed, because the ω and 2ω fields do not propagate in the same direction, and because the 3N+1 and 3N+2 harmonics with opposite helicity are generated through a different combination of ω and 2ω photons, the generated harmonics with opposite helicity propagate at different angles (see Fig. 8.1 (a)). By spatially filtering the XUV emission in the far-field, this could potentially allow having a light source with purely right- or left- circularly polarized photons, which would be ideal for PECD experiments.

We carried out a first experimental campaign to investigate HHG by non-collinear counter-rotating bicircular bichromatic pulses. The HHG spectrum generated by combined 800 nm and 400 nm fields in Argon is shown in Fig. 8.1 (b). The 3N+1 and 3N+2 harmonics traveling in different directions can clearly be identified. The different number of photon absorbed from each field (ω,2ω) can be determined from the emission direction

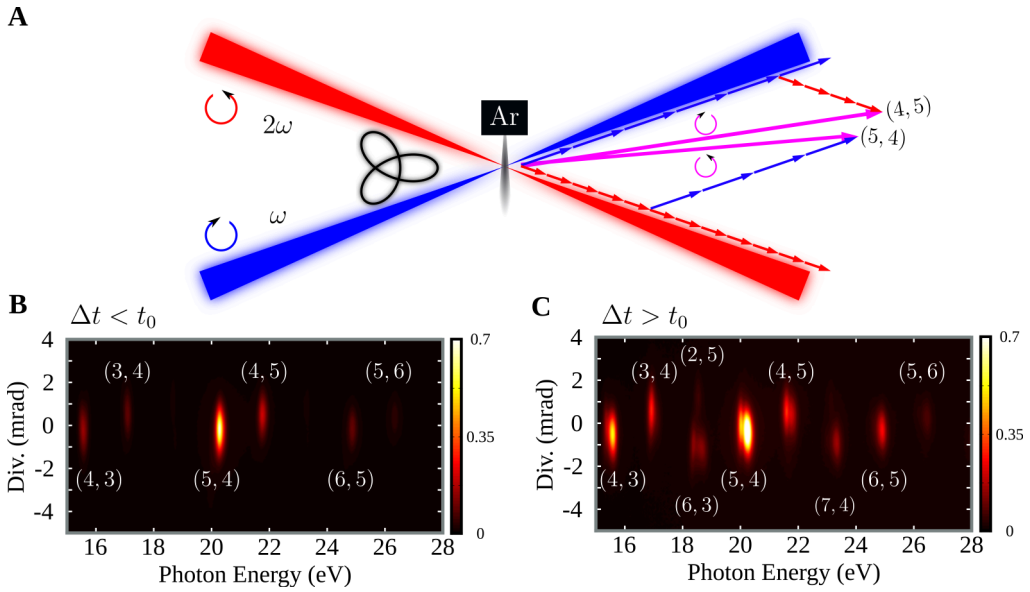

Figure 7.1: The role of Rydberg states in HHG driven by counter-rotating bicircular bichromatic pulses. In (a), schematic of the conservation of momentum and spin angular momentum in HHG driven by non-collinear counter-rotating bicircular bichromatic pulses. The propagation direction and the polarization state of each harmonic are given by the number of photons absorbed from ω and 2ω fields. In (b), a spectrally-resolved HHG spectrum driven when the 800 nm comes slightly before the 400 nm (Δt = -80 fs). The number of photons absorbed from each field is identify (ω,2ω) below or above each harmonic. We can clearly see that the forbidden 3N harmonics are missing, as expected from the conservation of spin angular momentum laws. When the two pulses do not overlap, the HHG signal vanishes. The FWHM cross-correlation of the total HHG signal is $\sim$ 110 fs ($\sim$ 200 fs tail-to-tail). In (c), a spectrally-resolved HHG spectrum driven when the 400 nm comes slightly before the 800 nm (Δt = 80 fs). The 400 nm is known to create a coherent electronic superposition between the ground and Rydberg states. We can clearly see the appearance of forbidden 3N harmonics, generated through photon combination that seems to violate the spin angular momentum conservation.

of the harmonics [Bertrand et al. 2011], and is labeled, in white, above or below each harmonic. As predicted by the spin angular momentum conservation laws, the forbidden 3N harmonics are missing (Fig. 8.1(b)). However, when slightly delaying the ω field with respect to the 2ω field (Fig. 8.1(c)), a strong signal appears at the forbidden 3N harmonics position, and all the harmonics are spectrally split into several components. What is the origin of these effects? The generation of forbidden 3N harmonics is the signature of a dynamical symmetry breaking in the generation process. A recent theoretical work from Jiménez -Galán *et al.* demonstrated that such a dynamical symmetry breaking occurs when Rydberg states are populated [Jiménez-Galán et al. 2017]. This is consistent with our experiment, in which the 400 nm field efficiently populates Rydberg states as we have seen in Chapter 2.

While the dynamical symmetry breaking argument enables understanding the emergence of forbidden harmonics from a time-domain perspective, there has to be a frequency-domain perspective interpretation as well: how many photons of each field are absorbed to produce these forbidden harmonics? This question can be answered by looking at the spatial position of the forbidden harmonics. Strikingly, we find that the forbidden harmonics seem to violate the spin angular momentum conservation laws. Indeed, focusing on the $\sim$ 19 eV region, for example, the forbidden harmonics are generated through channels characterized by a combination of (6 x ω, 3 x 2ω) and (2 x ω, 5 x 2ω). Moreover, the

spectral splitting between these two channels corresponds to energy differences between Rydberg states converging two different spin-orbit coupled ionic cores (170 meV). If, for example, 6 x ω + 3 x 2ω photons have been absorbed (imbalance of three unit of spin angular momentum), and if the emitted XUV photon can carry only one quantum of spin angular momentum, where are the two extra quanta missing? What is the polarization state of the forbidden 3N harmonics? These questions are currently investigated in a collaboration with theoreticians Alvaro Jiménez -Galán and Misha Ivanov, from MBI Berlin. This experiment links our investigation of the role of Rydberg states in HHG and our quest to produce chiral XUV pulses for fundamental studies of photoionization of chiral molecules.

The chiral nature of these fields can also be used to probe molecular chirality using High-order Harmonic Spectroscopy (HHG). In 2015, Cireasa *et al.* have demonstrated chiral discrimination using HHG driven by single-color elliptically polarized pulses [Cireasa et al. 2015]. In this first implementation of chiral-HHG, they reported a $\sim$ 2-3 % chiroptical signal, using drivers with only 1 % ellipticity. The origin of this signal is caused by a chirosensitive hole dynamics between ionization and recombination, involving the interplay of electric-dipole and the magnetic-dipole transitions. The drawback of this approach is that the recollision nature the process yields in a dramatic decay of the HHG total signal as the ellipticity (chirality) of the driver increases. The use of highly chiral single-color drivers is thus prohibitive for the efficient generation of HHG, and thus, for efficient chiral discrimination using HHS. Only a few months after the original publication of Cireasa *et al.*, it was realized that using counter-rotating bicircular bichromatic drivers could be a perfect alternative to performed chirosensitive HHS [Smirnova et al. 2015], since these drivers allow the efficient generation of harmonics using highly chiral pulses. Smirnova *et al.* originally predicted high enantiospecific response of chiral molecular ensemble (tens of %) to the helicity of the counter-rotating bicircular bichromatic drivers [Smirnova et al. 2015]. More recently, Ayuso *et al.* performed a theoretical investigation using accurate photorecombination matrix elements and showed that bi-elliptical pulse can induce strong chiral dichroism in the HHG of chiral molecules, for a broad range of harmonic numbers and ellipticities [Ayuso et al. 2018]. We are aware that few experimental groups around the world are currently working on this topic. Chiral HHS using counter-rotating bicircular bichromatic drivers, intrinsically coming with attosecond temporal and Ångstrom spatial resolution, is thus about to emerge as a new strong field sensitive probe of molecular chirality.

7.1.2 Photoelectron circular dichroism using bicircular bichromatic fields

Bicircular bichromatic fields are not only interesting for HHG experiments but also to investigate strong-field ionization, where they enable fine control of 2D electron trajectories. Recent experimental studies have shown that they produced characteristic clover-leaf shaped photoelectron angular distributions [Mancuso et al. 2016; Mancuso et al. 2015], and that they could be used to investigate electron-ion rescattering effects with high sensitivity [Eckart et al. 2017]. However, up to now, the chiral nature of these fields have not been used in photoionization experiments. Following our investigations of PECD, we naturally wondered if bicircular bichromatic fields were relevant tools to measure chiroptical effects in the photoionization of chiral molecules.

We used a combination of 800 nm and 400 nm circular fields with opposite helicities to photoionize fenchone and camphor molecules, and measured the projection of the photoelectron angular distribution with our velocity map imaging spectrometer. The threefold symmetry of the fields prevents retrieving the 3D angular distribution from a

single projection. Following the procedure introduced in [Mancuso et al. 2016; Mancuso et al. 2015], we recorded a set of projections corresponding to different orientations of the clover-leaf field, controlled simply by changing the relative (attosecond) delay between the two pulses. With this set of projections and using a tomographic reconstruction method, based on inverse Radon transform, we have fully reconstructed the 3D-PAD, without having to assume any symmetry of the interaction. The reconstructed 3D-PADs, as well as their anti-symmetric part (PECD), are presented in Fig. 8.2.

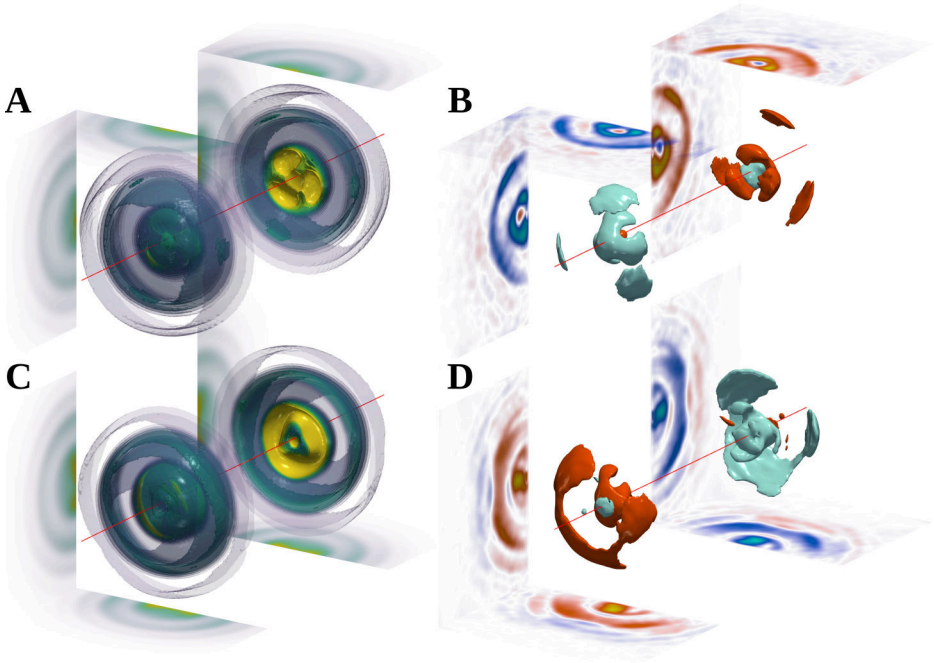

Figure 7.2: Strong-field ionization of chiral molecules using counter-rotating bicircular bichromatic pulses. In (a) and (c) the tomographically reconstructed 3D photoelectron angular distribution, in camphor and fenchone, respectively. The thin red lines represent the light propagation axis. In (b) and (d) the forward-backward asymmetry (PECD), associated with the tomographically reconstructed 3D photoelectron angular distribution, in camphor and fenchone, respectively.

In Fig. 8.2, we can see that both the PAD and the PECD possess the threefold symmetry imposed by the shape of the driving field. The subtleties behind photoionization of chiral molecules using these peculiar driving waveforms are still under analysis, with the help of classical and quantum simulations performed by Bernard Pons. The questions that we are currently investigating are the following: Can we use the angular shifts between the different above-threshold ionization peaks to extract the same kind of information as in an attoclock experiment [Eckle et al. 2008; Torlina et al. 2015]? Is the sign flip of the PECD for low-energy electrons (Fig. 8.2 (b)) a consequence of rescattering? Can we control the magnitude of the PECD by tuning the intensity ratio between the ω and 2ω fields, which is known to strongly affect the outgoing electron trajectories [Mancuso et al. 2016]? These results are pretty promising and continue to trigger our interest in linking strong-field physics with the study of chiral molecules.

7.2 Femtosecond dynamics in polyatomic and chiral molecules

Another pillar of the work presented in this thesis is the investigation of ultrafast dynamics in photoexcited molecules, using femtosecond pump-probe schemes. In Chapter 3, we

have demonstrated the fundamental role of coupled nuclear and electronic dynamics in the relaxation of photoexcited molecules. We have used time-resolved Coulomb Explosion Imaging (TR-CEI) to follow the photoisomerization of acetylene cation, by detecting the cationic photofragment in coincidence [Ibrahim et al. 2014]. This technique allows reconstructing the 3D momentum vector of each fragment, in the molecular (recoil) frame. However, since the photoelectrons are not detected, the information about the electronic state of the molecules undergoing Coulomb explosion cannot be directly accessed.

On the other hand, we have measured time-resolved photoelectron angular distributions in Chapter 5 to investigate the ultrafast dynamics of chiral molecules [Beaulieu et al. 2016c; Comby et al. 2016]. By photoexciting chiral molecules using a linearly polarized pump pulse and subsequently ionizing them using a delayed left- or right- circularly polarized probe pulse, we have measured, for the first time, the time-resolved photoelectron circular dichroism (TR-PECD) signal. Our systematic wavelength study has allowed us to show the extreme sensitivity of TR-PECD to the excitation anisotropy decay as well as to subtle vibronic dynamics within the excited states. Using the same pump-probe setup coupled with the same angularly-resolved photoelectron detection scheme (VMI), but using a circularly polarized pump and linearly polarized probe, we have discovered two new chiroptical effects, PXCD and PXECD [Beaulieu et al. 2018b]. PhotoeXcitation Circular Dichroism (PXCD) is characterized by the emergence of an enantiospecific oscillating dipole along the light propagation axis when multiple bound excited states are coherently populated using circular photons. The phase of the dipole oscillations reverses when switching the molecule or the pump pulse handedness, which is the hallmark of chiral observables. Photoionizing different bound states within the wavepacket to the same final (continuum) state, using linear (non-chiral) photon, leads to the emergence of a forward-backward asymmetry in the angular distribution of the photoelectrons (PhotoeXcitation induced Electron Circular Dichroism, PXECD).

TR-PECD and TR-PXECD are the first techniques which enable probing the ultrafast dynamics of chiral molecules in the gas-phase, with a femtosecond time-resolution. They thus promise to revolutionize our understanding of the fundamental aspects of chiral reactivity. We have up to now carried proof-of-principle experiments on the vibronic relaxation of highly excited molecules. Our schemes could be straightforwardly used to probe the influence of vibrations in the ground state on molecular chirality (through impulsive stimulated Raman scattering), or to investigate the death of chirality in the dissociation of a chiral molecule. One difficulty that may emerge in such studies is the interpretation of the data. Indeed, PECD and PXCD are extremely sensitive observables, and disentangling the contribution of different sources of signal variations in dynamical studies will be a real challenge. The interaction with theoreticians will be of prime importance here.

Several technical improvements can be envisaged in the future to investigate more complex dynamics of more complex chiral systems. Indeed, we have seen that measuring the photofragment in coincidence allows for extracting structural information in the molecular (or recoil) frame. This technique is however blind to the electronic structure of the molecules undergoing dynamics. We have also seen that looking at the photoelectron energies and angular distributions provide rich information about both the electronic state and the associated vibrational progression from which the electron is departing. Combining the detection of electron and ion in coincidence is a challenging but powerful tool to combine the information encoded in all the photoproducts of photoionization. Indeed, by looking at the angle-resolved photoelectron spectrum associated to a given ionic species (*e.g.* parent ion or fragment) allows to disentangle the contribution of different ionization

channel (*e.g.* molecular orbitals) to the total signal. Moreover, looking at the electron that is detected in coincidence with fragments produced through dissociative ionization or Coulomb explosion allows retrieving the photoelectron spectrum and angular-distribution in the molecular (recoil) frame. This has been used in pioneering experiments by Tia *et al.* who measured the PECD in the molecular-frame [Tia et al. 2017]. Moreover, since this technique allows for the identification of the species from which the electrons are ejected, performing experiments using a mixture of different chemical species become possible. It thus allows performing, under the exact same experimental conditions, simultaneous data acquisitions from different chiral molecules as well as with different cluster sizes of a given chiral monomer, for example.

The group at CELIA is currently building a COLTRIMS apparatus (from RoentDek GmbH) to detect the photoelectron in coincidence with photoion(s), allowing to unambiguously assign the channels and/or the species from which the photoelectron are originating. Moreover, since this apparatus measures both the time-of-flight and the (x,y) position of the charged particles onto the detector, the exact 3D-PAD will be retrieved without having to make any assumption about the symmetry of the laser-matter interaction. From an analytical point-of-view, this apparatus will be used to measure the composition and the enantiomeric excess of complex multi-component mixtures of chiral molecules. From a more fundamental scientific point-of-view, by increasing the dimensionality of the measurements, it will enable to extend our understanding of complex time-resolved PECD data as well as tackling fundamental question related to photodissociation of chiral clusters. Amongst the many open questions, one particularly important aspect is the chiral recognition process, the mechanism through which two chiral molecules identify themselves as left- or right-handed when they interact with each other. By photodissociating dimer of chiral molecules or chiral dimer formed by non-chiral monomers, one could investigate the opposite reaction pathway that leads to the birth of chirality from achiral precursors and the chiral recognition of gas-phase chiral precursors. Time-resolved PECD is an ideal probe of the birth and death of chirality in dimers and clusters. These kinds of experiments will be performed soon at CELIA.

For this detection scheme to work, only one molecule per laser shot (statistically even less than that) can be ionized. A lot of laser shots are thus necessary to have statistically relevant data when working in such 'counting mode'. Performing such experiments at 1 kHz is extremely challenging, if not impossible. To solve this issue, we are currently developing a beamline seeded by a high- and tunable-repetition rate (166 kHz to 2 MHz) and high-average-power (2 synchronized 50 W output) with 130 fs pulse duration Ytterbium (1030 nm) fiber laser (Amplitude, Tangerine short pulse). In one (pump) arm of this beamline will be installed a spectrally-tunable UV OPA, while in the other (probe) arm, we are currently building an HHG-based high-flux (bright and phase-matched) circular XUV source. An hollow-core fiber post-compression stage is currently being installed, in order to shorten the pulse duration used to drive HHG, to roughly sub-15 fs. We will have the flexibility to post-compress the fundamental 1030 nm beam or its second harmonic (515 nm).

In the XUV probe arm, which will be used to photoionized excited chiral molecules, we are currently exploring two different configurations. The first configuration consists of using multilayer mirrors to select only one low-order circular harmonic, which will produce a femtosecond XUV probe pulse, allowing to measure near-threshold PECD from the ionization of valence shells electrons, with a relatively high-spectral resolution. The second configuration consists of generating circular attosecond pulses around 70 eV to photoionize the inner-shell electrons from halogen atom of chiral molecules, for example.

To wrap up, coupling our versatile high-repetition-rate beamline with the COLTRIMS apparatus will definitely enable increasing the dimensionality of the measurements, which is often critical to understand rich and complex experimental data.

To conclude, we have investigated a broad variety of curiosity-driven scientific problems in the fields of strong-field and attosecond physics as well as femtochemistry. This reflects perfectly the range of expertise of scientists which I had to chance to work with at both CELIA and INRS. Using these expertise to study chiral molecules, which is a fascinating class of molecules from the point-of-view of physics, chemistry and even life sciences constitute a truly original program, which I am sure, will lead to elegant and important discoveries in the coming years.

8. Conclusions générales et perspectives

Le travail présenté dans ce manuscrit démontre que l'utilisation d'une large gamme de sources de lumière ultrabrèves, de l'infrarouge moyen à l'extrême ultraviolet, permet de sonder une grande variété de phénomènes dans différents systèmes, des gaz rares et diatomiques aux molécules polyatomiques et chirales, sur différentes échelles de temps, de quelques picosecondes jusqu'à quelques attosecondes. Pour conclure ces travaux, nous résumons brièvement les principaux résultats obtenus et discutons des perspectives à court et à long terme ouvertes par nos résultats.

8.1 Physique en champ fort et science attoseconde

Tout au long des différents chapitres de ce manuscrit, nous avons démontré plusieurs avancées du point de vue de la physique en champs forts et de la science attoseconde. Ces avancées s'articulent principalement autour du développement de sources de lumières de pointes [Cardin et al. 2015; Thiré et al. 2015] (Chapitre 1), de la prise en compte rôle des états de Rydberg dans l'interaction atomes - champ fort [Beaulieu et al. 2017a; Beaulieu et al. 2016a] (Chapitre 2) et de l'ionisation en champ fort de molécules chirales, en utilisant des impulsions lumineuses circulairement polarisées (Chapitre 4). Cette dernière application nous a conduit à démontrer l'universalité du Dichroïsme Circulaire de Photoélectron, *i.e.* son émergence dans tous les régimes d'ionisations [Beaulieu et al. 2016b]. Ceci nous a finalement permis d'effectuer la mesure de des dynamiques chirales de photoionisation, à l'échelle attoseconde, en utilisant une technique d'interférométrie de photoélectrons qui repose sur l'ionisation en champ fort [Beaulieu et al. 2017b] (Chapitre 6).

8.1.1 GHOE, états de Rydberg et champs bichromatiques bicirculaires

Au chapitre 2, nous avons découvert que les états de Rydberg, qui sont généralement considérés comme des spectateurs passifs de la génération d'harmoniques d'ordre élevé (GHOE), peuvent en fait jouer un rôle important dans ce processus. Ils ouvrent de nouveaux canaux croisés pour la GHOE, lorsqu'ils sont peuplés de manière cohérente

durant l'impulsion laser. Nous avons observé de nouvelles caractéristiques spectrales concomitantes aux harmoniques impaires standard, associées à un mécanisme d'émission retardée temporellement, provenant de l'ionisation des états excités et de la recombinaison sur l'état fondamental [Beaulieu et al. 2016a]. De plus, nous avons démontré que ce canal de GHOE n'est pas le seul mécanisme radiatif depuis ces états hautement excités. L'émission due à la décroissance libre de l'induction XUV par le paquet d'ondes électronique créé lors de l'excitation de ces états de Rydberg peut être utilisée comme une puissante technique spectroscopique résolue en temps [Beaulieu et al. 2017a], fournissant des informations très similaires à celles obtenues dans certains types d'expériences de spectroscopie d'absorption transitoire attoseconde.

Nous avons vu à plusieurs reprises au cours de cette thèse l'importance d'augmenter le nombre de paramètres libres dans une expérience, *c'est-à-dire le nombre de degrés de liberté nous permettant de contrôler l'interaction laser-matière*. En particulier, l'état de polarisation de la lumière est un paramètre très important pour la physique en champ fort, permettant la manipulation des trajectoires électroniques et donnant accès à des mesures sensibles à la chiralité moléculaire. Cependant, le rayonnement polarisé circulairement ne permet pas la recollision des électrons ionisés avec leur ion parent, menant à une suppression de la GHOE [Budil et al. 1993]. Une solution élégante à ce problème consiste à utiliser des impulsions bichromatiques bicirculaires contrarotatives. La combinaison d'une impulsion polarisée circulairement (ω) avec sa seconde harmonique contrarotative (2ω), génère un champ électrique total apparaissant sous la forme d'un trèfle irlandais (trèfle à trois feuilles) chiral (voir Fig. 8.1). L'inversion de l'hélicité des deux champs contrarotatifs conduit à une inversion de la chiralité du champ électrique total (du trèfle irlandais).

Ces dernières années, les impulsions bichromatiques bicirculaires sont devenues un sujet chaud dans notre communauté, puisque les électrons ionisés par ce type de champ électrique peuvent recollisionner trois fois par cycle optique sur l'ion parent, ce qui conduit à l'émission efficace de rayonnement XUV par GHOE [Eichmann et al. 1995; Fleischer et al. 2014; Kfir et al. 2015]. Le spectre de GHOE émergeant apparaît comme une succession d'harmoniques à tous les 3N+1 et 3N+2 multiples de la fréquence fondamentale, alors que les harmoniques d'ordre 3N sont interdites, en raison de la conservation du moment angulaire de spin (voir Fig. 8.1). En effet, puisque chaque photon XUV émis ne peut porter qu'un seul quanta de moment angulaire de spin, la différence entre le nombre de photons absorbés du champ fondamental et de sa seconde harmonique doit être $\pm$ 1. De plus, toujours en raison de la conservation du moment angulaire de spin, les harmoniques 3N+1 et 3N+2 sont polarisées circulairement et ont la même hélicité que les champs ω et 2ω, respectivement. Le fait que la GHOE avec ce type de champ électrique générateur produise des harmoniques polarisées circulairement rend cette technique très attractive pour nous, du point de vue de notre intérêt pour la génération d'impulsions lumineuses chirales afin d'étudier la photoionisation de molécules chirales en phase gazeuse.

Lorsqu'on génère des harmoniques avec des impulsions bichromatiques bicirculaires contrarotatives colinéaires, les harmoniques adjacentes (3N+1 et 3N+2), caractérisées par des hélicités opposées, se propagent dans la même direction. Cela peut être problématique pour de futures expériences de DCPE, puisque les deux peignes de fréquence contrarotatifs produiront des spectres de photoélectrons se chevauchant partiellement, ce que mène potentiellement à l'atténuation ou même l'annulation de certains des effets de DCPE. Ce problème peut être évité en générant les harmoniques en géométrie non-colinéaire [Bertrand et al. 2011; Hickstein et al. 2015]. En effet, puisque les champs ω et 2ω ne se propagent alors pas dans la même direction, et puisque les harmoniques 3N+1 et 3N+2 ayant une hélicité opposée sont générées par une combinaison différente de photons ω et

2ω, les harmoniques d'hélicités opposées se propagent dans directions différentes (voir Fig. 8.1 (a)). En filtrant spatialement l'émission XUV en champ lointain, cette technique pourrait potentiellement permettre d'avoir une source attoseconde de photons polarisés circulairement exclusivement droite ou gauche, ce qui serait idéal pour les expériences de DCPE.

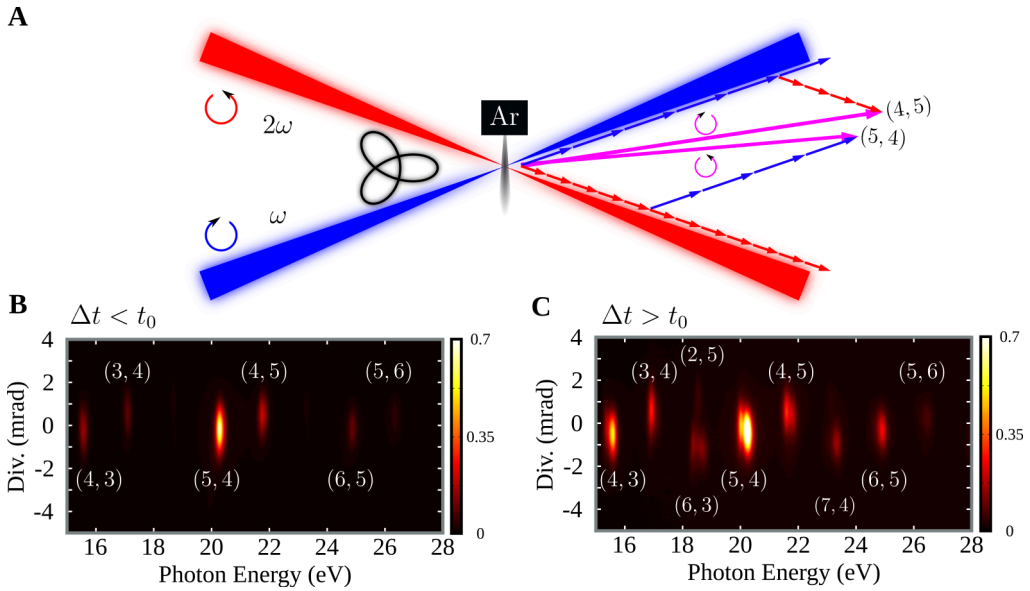

Figure 8.1: Le rôle des états de Rydberg dans la GHOE avec des impulsions bichromatiques bicirculaires contrarotatives. En (a), schéma de la conservation de la quantité de mouvement et du moment angulaire de spin dans la GHOE par des impulsions bichromatiques bicirculaires contrarotatives non-colinéaires. La direction de propagation et l'état de polarisation de chaque harmonique sont donnés par le nombre de photons absorbés par les champs ω et 2ω. En (b), un spectre de GHOE lorsque le 800 nm arrive sur cible légèrement avant le 400 nm (Δt = -80 fs). Le nombre de photons absorbés par chaque champ est identifié (ω, 2ω) en dessous ou au-dessus de chaque harmonique. Nous pouvons clairement voir que les harmoniques interdites 3N sont absentes. Lorsque les deux impulsions ne se chevauchent pas temporellement, le signal de GHOE est nul. La largeur à mi-hauteur de la corrélation croisée du signal total de GHOE est de $\sim$ 110 fs ($\sim$ 200 fs pied-à-pied). En (c), un spectre de GHOE lorsque le 400 nm arrive sur cible légèrement avant le 800 nm (Δt = 80 fs). Nous pouvons clairement voir l'apparition d'harmoniques interdites (3N), générées par une combinaison de photons qui semble violer la conservation du moment angulaire de spin.

Nous avons effectué une première campagne expérimentale pour étudier la GHOE avec des impulsions bichromatiques bicirculaires non-colinéaires. Un spectre de GHOE typique généré par ce type de champ électrique dans l'Argon est présenté sur la figure 8.1 (b). Les harmoniques 3N+1 et 3N+2, qui propagent dans des directions différentes, peuvent être clairement identifiées. Le nombre de photons absorbés par chaque champ (ω, 2ω) peut être déterminé à partir de la direction de propagation des harmoniques [Bertrand et al. 2011], et est indiqué en blanc au-dessus ou en dessous de chaque harmonique. Comme prédit par la loi de conservation du moment angulaire de spin, les harmoniques d'ordre 3N (interdites) sont absentes (Fig. 8.1 (b)). Cependant, en introduisant un léger retard temporel du champ ω par rapport au champ 2ω (Fig. 8.1 (c)), un fort signal apparaît aux positions attendues pour les harmoniques interdites (3N). De plus, toutes les harmoniques sont alors spectralement divisées en plusieurs composantes spectrales. Quelle est l'origine de ces effets? La génération d'harmoniques interdites (3N) est la signature d'une brisure de symétrie dynamique dans le processus de génération. Une récente étude théorique par

Jiménez -Galán *et al.* a démontrée qu'une telle brisure de symétrie dynamique se produisait lorsque des états de Rydberg sont peuplés [Jiménez-Galán et al. 2017]. Cependant, si cet argument de brisure de symétrie dynamique permet de comprendre l'émergence d'harmoniques interdites d'un point de vue du domaine temporel, il nous faut aussi élaborer une interprétation d'un point de vue du domaine fréquentiel: combien de photons de chaque champ sont absorbés pour produire ces harmoniques interdites? Cette question peut être résolue en regardant la position spatiale des harmoniques interdites sur le détecteur. Il est frappant de constater que les harmoniques interdites semblent violer la loi de conservation du moment angulaire du spin. En effet, en se concentrant sur la région spectral $\sim$ 19 eV, par exemple, on voit que les harmoniques interdites sont générées par des canaux caractérisés par une combinaison de (6xω, 3x(2ω)) et (2xω, 5x(2ω)). De plus, la séparation spectrale entre ces deux canaux correspond à la différence d'énergie entre des états de Rydberg convergeant vers deux ions de configuration spin-orbit différents ($\sim$ 170 meV). Si, par exemple, 6xω + 3x(2ω) photons ont été absorbés (déséquilibre de trois quanta de moment angulaire de spin), et si le photon XUV émis peut seulement porter un quantum de moment angulaire de spin, où sont les deux quanta supplémentaires? Quel est l'état de polarisation des harmoniques interdites 3N? Ces questions sont actuellement étudiées en collaboration avec les théoriciens Alvaro Jiménez-Galán et Misha Ivanov, du MBI Berlin. Cette étude lie notre travail sur le rôle des états de Rydberg dans la GHOE et notre quête pour produire des impulsions XUV chirales.

La nature chirale des champs bicirculaires bichromatiques peut également être utilisée pour sonder la chiralité moléculaire en utilisant la spectroscopie par génération d'harmonique d'ordre élevé (SGHOE). En 2015, Cireasa *et al.* ont démontré une discrimination chirale en générant des harmoniques avec des impulsions lasers polarisées elliptiquement [Cireasa et al. 2015]. Cette première implémentation de SGHOE chirale, a mesuré un signal chiroptique d'environ 2-3 %, en utilisant un champ laser avec seulement 1 % d'ellipticité. L'origine de ce signal chiroptique est liée à une dynamique de trou entre l'ionisation et la recombinaison, impliquant l'interférence de transitions dipolaires électrique et magnétique. L'inconvénient de cette approche est que la nature du mécanisme de GHOE mène à une décroissance dramatique du signal total lorsque l'ellipticité du champ électrique augmente. L'utilisation de champs hautement chiraux est donc prohibitive pour la génération efficace d'harmoniques, et ainsi, pour la discrimination chirale efficace en utilisant la GHOE. Quelques mois seulement après la publication des travaux de Cireasa *et al.*, l'équipe d'Olga Smirnova au MBI a établi que l'utilisation de champs bichromatiques bicirculaires contrarotatifs pourrait être une alternative parfaite pour la discrimination chirale par GHOE, car ces champs permettent la génération efficace d'harmoniques en utilisant des impulsions hautement chirales [Smirnova et al. 2015]. Ces travaux théoriques ont prédit une forte réponse énantiospécifique (des dizaines de %) à l'hélicité des champ bichromatiques bicirculaires contrarotatifs. Plus récemment, Ayuso *et al.* ont effectué une étude théorique en utilisant des éléments de matrices de photorecombinaison précis et ont montrés que des champs bi-elliptique pouvaient induire un fort dichroïsme dans la GHOE depuis des molécules chirales, sur une large gamme d'harmoniques et d'ellipticités [Ayuso et al. 2018]. Nous savons que plusieurs groupes expérimentaux à travers le monde travaillent actuellement sur ce sujet. La technique de GHOE dans des molécules chirales avec des champ bichromatiques bicirculaires contrarotatifs, présentant intrinsèquement une résolution temporelle attoseconde et une résolution spatiale de l'ordre de l'Ångström, est donc sur le point d'émerger comme une nouvelle sonde de la chiralité moléculaire.

8.1.2 Dichroïsme circulaire de photoélectron avec des champs bichromatiques bicirculaires

Les champs bichromatiques bicirculaires ne sont pas seulement intéressants pour les expériences de GHOE, mais aussi pour étudier l'ionisation en champ fort, où ils permettent un contrôle précis des trajectoires électroniques. De récentes études expérimentales ont montré que l'ionisation avec ces champs produisaient des distributions angulaires de photoélectrons en forme de trèfle irlandais [Mancuso et al. 2016; Mancuso et al. 2015], et qu'on pouvaient les utiliser pour étudier les effets de recollision électrons-ions, avec une très grande sensibilité [Eckart et al. 2017]. Cependant, jusqu'à présent, la nature chirale de ces champs n'a pas été utilisée dans des expériences de photoionisation. Suite à nos recherches sur le DCPE, nous nous sommes naturellement demandé si les champs bichromatiques bicirculaires étaient des outils pertinents pour mesurer certains effets chiroptiques lors de la photoionisation des molécules chirales.

Nous avons utilisé une combinaison de champs circulaires à 800 nm et à 400 nm avec des hélicités opposées pour photoioniser des molécules de fenchone et de camphre, et nous avons mesuré la projection de la distribution angulaire de photoélectrons avec notre spectromètre d'imagerie de vecteurs vitesse. La symétrie de ces champs nous empêche de retrouver la distribution angulaire des photoélectrons en 3D à partir d'une seule projection 2D. En suivant la procédure introduite dans [Mancuso et al. 2016; Mancuso et al. 2015], nous avons enregistré un ensemble de projections correspondant à différentes orientations du champ. La rotation du champ est contrôlée par le retard relatif entre les deux impulsions. Avec cet ensemble de projections et en utilisant une méthode de reconstruction tomographique, basée sur la transformation de Radon inverse, nous avons entièrement reconstruit la distribution angulaire 3D des photoélectrons, sans avoir à supposer une quelconque symétrie de l'interaction. Les distributions reconstruites, ainsi que leurs parties anti-symétriques (DCPE), sont présentés à la Fig. 8.2.

Sur la Fig. 8.1, nous pouvons voir que le DAP et le DCPE possèdent une symétrie C_3 imposée par la forme du champ ionisant. Les subtilités de la photoionisation des molécules chirales à l'aide de ces fameux champs sont encore en cours d'analyse, à l'aide de simulations classiques et quantiques réalisées par Bernard Pons. Les questions que nous étudions actuellement sont les suivantes: Pouvons-nous utiliser les décalages angulaires entre les différents pics d'ionisation au-dessus du seuil pour extraire le même type d'information que dans une expérience d'attoclock [Eckle et al. 2008; Torlina et al. 2015]? Le changement de signe du DCPE pour les électrons de faible énergie (Fig. 8.2 (b)) est-il une conséquence de la recollision électron-ion? Pouvons-nous contrôler l'amplitude du DCPE en ajustant le rapport d'intensité entre les champs ω et 2ω, dont il est établi qu'il affecte fortement les trajectoires électroniques [Mancuso et al. 2016]? Ces résultats sont assez prometteurs et continuent de susciter notre intérêt pour l'étude de molécules chirales en champ fort.

8.2 Dynamique femtoseconde dans les molécules polyatomiques et chirales

Un autre pilier du travail présenté dans cette thèse est l'étude de la dynamique ultrarapide dans les molécules photoexcitées, en utilisant des schémas pompe-sonde femtoseconde. Au chapitre 3, nous avons démontré le rôle fondamental du couplage entre les degrées de liberté nucléaire et électronique lors de la relaxation de molécules photoexcitées. Nous avons utilisé l'imagerie par explosion Coulombienne résolue en temps pour suivre la photoisomérisation du cation d'acétylène, en détectant tous les photofragments cationiques en coïncidence [Ibrahim et al. 2014]. Cette technique permet de reconstruire les vecteurs

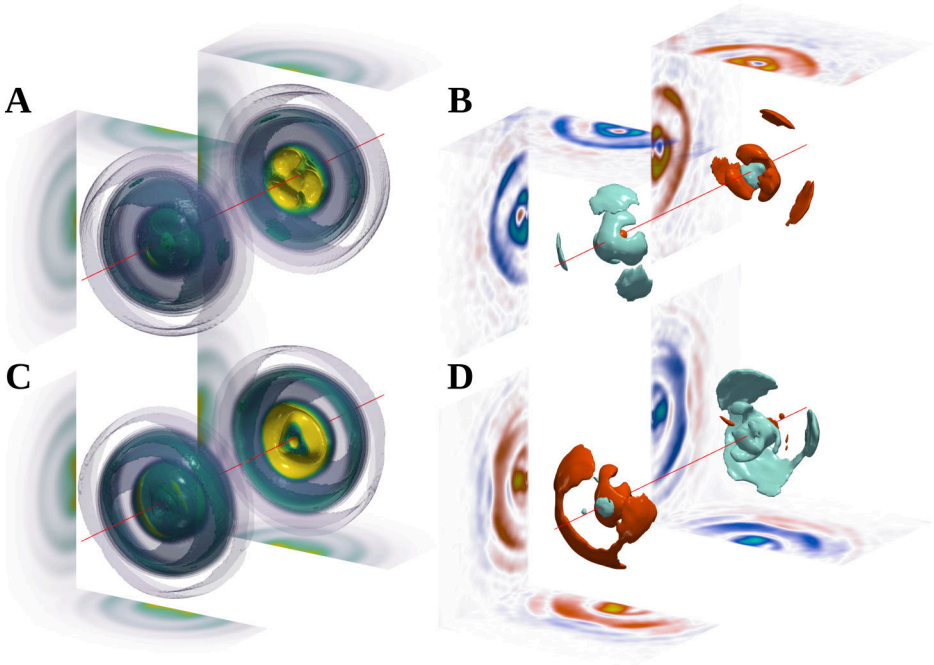

Figure 8.2: Ionisation en champ fort de molécules chirales en utilisant des impulsions bichromatiques bicirculaires contrarotatives. En (a) et (c), la distribution angulaire de photoélectrons 3D reconstruite par tomographie, dans le camphre et la fenchone, respectivement. Les fines lignes rouges représentent l'axe de propagation de la lumière. En (b) et (d) l'asymétrie avant-arrière (DCPE), associée à la distribution angulaire de photoélectrons 3D reconstruite par tomographie, dans le camphre et la fenchone, respectivement.

impulsion en 3D pour chaque fragment ionique. Cependant, puisque les photoélectrons ne sont pas détectés, les informations sur l'état électronique des molécules subissant l'explosion Coulombienne ne peuvent pas être connues de façon directe.

D'autre part, dans le chapitre 5, nous avons mesuré les distributions angulaires de photoélectrons résolues en temps pour étudier la dynamique ultrarapide de molécules chirales photoexcitées [Beaulieu et al. 2016c; Comby et al. 2016]. En photoexcitant des molécules chirales avec une impulsion pompe polarisée linéairement et en les ionisant ensuite avec une impulsion sonde polarisée circulairement gauche ou droite, nous avons mesuré, pour la première fois, le dichroïsme circulaire de photoélectrons résolu en temps. Nos études systématiques en fonction des longueurs d'ondes de pompe et de sonde nous ont permis de démontrer la forte sensibilité du dichroïsme circulaire de photoélectrons résolu en temps à la relaxation de l'anisotropie d'excitation ainsi qu'aux dynamiques vibroniques. En utilisant la même configuration pompe-sonde, couplée au même schéma de détection de photoélectrons résolus angulairement, mais en utilisant une pompe polarisée circulairement et une sonde polarisée linéairement, nous avons découvert deux nouveaux effets chiroptiques, le dichroïsme circulaire de photoexcitation (DCPX) et le dichroïsme circulaire d'électrons induit par photoexcitation (DCEPX) [Beaulieu et al. 2018b]. Le DCPX est caractérisé par l'émergence d'un dipôle énantiospécifique oscillant le long de l'axe de propagation de la lumière, lorsque plusieurs états liés sont peuplés de manière cohérente, en utilisant des photons circulairement polarisés. La phase des oscillations du dipôle s'inverse lorsqu'on qu'on inverse la chiralité de l'impulsion pompe ou des molécules, ce qui est un comportement caractéristique des observables chiroptiques. La photoionisation de différents états liés formant le paquet d'ondes vers le même état final (continuum), en

utilisant un photon linéaire (non-chiral), conduit à l'émergence d'une asymétrie avant-arrière dans la distribution angulaire des photoélectrons (dichroïsme circulaire d'électrons induit par photoexcitation (DCEPX)).

Le DCPE et le DCEPX résolus en temps sont les premières techniques qui permettent de sonder la dynamique ultrarapide des molécules chirales en phase gazeuse, avec une résolution temporelle femtoseconde. Ils promettent de révolutionner notre compréhension des aspects fondamentaux de la réactivité chirale. Ces schémas pourraient être directement utilisés pour sonder l'influence des vibrations dans l'état fondamental sur la chiralité moléculaire (par la diffusion Raman stimulée impulsionnelle), ou pour étudier la mort de la chiralité dans la dissociation d'une molécule chirale. Une des difficulté qui peut apparaître dans de telles études est l'interprétation des résultats expérimentaux. En effet, le DCPE, le DCPX et le DCEPX sont des observables extrêmement sensibles, et démêler la contribution des différentes sources de variations du signal dans les études dynamiques sera un véritable défi. Pour ce faire, l'interaction avec les théoriciens sera d'une importance primordiale.

Dans le futur, plusieurs améliorations techniques peuvent être envisagées pour étudier les dynamiques de systèmes chiraux plus complexes. En effet, nous avons vu que mesurer les photofragments cationiques en coïncidence permettait d'extraire des informations structurelles dans le référentielle moléculaire. Cette technique est cependant insensible à la structure électronique des molécules. Nous avons également vu que la mesure de l'énergie et de la distributions angulaire des photoélectrons donnait accès à des informations riches, à la fois sur l'état électronique et sur la progression vibrationnelle associée à l'état depuis lequel les électrons sont photoionisés. La détection simultanée d'électrons et d'ions en coïncidence est un outil assez difficile d'implémentation, mais extrêmement puissant, permettant l'accès à tous les informations encodées dans tous les photoproduits de photoionisation/dissociation. En effet, en considérant le spectre de photoélectrons résolu en angle associé à une espèce ionique donnée (*e.g.* fragments ou ion parent), il est possible de démêler la contribution de différents canaux d'ionisation (*e.g.* ionisation depuis différentes orbitales moléculaires) au signal total. De plus, la mesure d'électrons détectés en coïncidence avec des fragments, suivant l'ionisation dissociative ou l'explosion Coulombienne, permet de récupérer le spectre de photoélectrons ainsi que sa distribution angulaire dans le référentiel moléculaire. Cette technique a été récemment employée dans des expériences pionnières dans des molécules chirales par Tia *et al.* [Tia et al. 2017]. De plus, puisque cette technique permet l'identification des espèces à partir desquelles les électrons sont éjectés, il est possible de réaliser des expériences en utilisant un mélange de différentes espèces chimiques. Ceci permet ainsi de réaliser, dans les mêmes conditions expérimentales, des acquisitions de données simultanées pour différentes espèces moléculaire chirales, ainsi que pour différentes tailles d'agrégats d'un monomère chiral, par exemple.

Le groupe de recherche du CELIA assemble actuellement un spectromètre COLTRIMS (de RoentDek GmbH), permettant la détection des photoélectrons en coïncidence avec des photoions, ce qui permettra d'attribuer sans ambiguïté les canaux et/ou les espèces moléculaires d'où proviennent ces photoélectrons. De plus, puisque cet appareil mesure à la fois le temps de vol et la position (x,y) des particules chargées sur le détecteur, la distribution angulaire tridimensionnelle des photoélectrons pourra être reconstruite sans avoir à faire aucune hypothèse sur la symétrie de l'interaction lumière-matière. D'un point de vue analytique, cet appareil sera utilisé pour mesurer la composition et l'excès énantiomérique de mélanges complexes multicomposants de molécules chirales. D'un point de vue plus fondamental, en augmentant la dimensionnalité des mesures, il sera

possible d'étendre notre compréhension des données expérimentales complexes de DCPE résolues en temps et d'aborder des questions fondamentales liées à la photodissociation d'agrégats chiraux par exemple. En effet, parmi les nombreuses questions ouvertes, un aspect particulièrement important est le processus de reconnaissance chirale, le mécanisme par lequel deux molécules chirales s'identifient comme étant gauches ou droites lorsqu'elles interagissent entre elles. En utilisant la photodissociation de dimères de molécules chirales ou de dimères chiraaux formé par des monomères non-chiraux, on pourrait étudier le chemin de réaction inverse qui conduit à la naissance de la chiralité à partir de précurseurs achiraux et la reconnaissance chirale en phase gazeuse. Le DCPE résolu en temps est une sonde idéale pour étudier la naissance et de la mort de la chiralité dans les dimères et les agrégats. Ce genre d'expériences sera bientôt réalisés au CELIA.

Pour que ce type de schéma de détection fonctionne, une seule molécule par tir laser (voire en pratique une seule tous les 10 tirs lasers) peut être ionisée. Un très grand nombre de tirs laser est donc nécessaire pour recueillir des données statistiquement pertinentes lorsque l'on travaille dans un tel 'mode de comptage'. Effectuer de telles expériences à 1 kHz est extrêmement difficile. Pour résoudre ce problème, nous développons actuellement une ligne lumière caractérisée par un taux de répétition très élevé et ajustable (166 kHz à 2 MHz) et par une puissance moyenne très élevée (2 sorties de 50 W synchronisées), avec une durée d'impulsion de 130 fs. Ceci est possible grâce à l'émergence des laser Ytterbium (1030 nm) à fibre (Amplitude, Tangerine pulse court). Dans le bras (pompe) de cette ligne de lumière sera installé un amplificateur paramétrique optique UV accordable spectralement, tandis que dans l'autre bras (sonde), nous construisons actuellement une source XUV circulaire à très haut flux de photon basée sur la GHOE. Un étage de post-compression dans une fibre creuse remplie de gaz rare est actuellement en cours d'installation, afin de réduire la durée des impulsions à environ 15 fs. Nous aurons la flexibilité de post-comprimer le faisceau fondamental (1030 nm) ou sa seconde harmonique (515 nm).

Dans le bras de sonde (XUV), qui sera utilisé pour photoionisées des molécules chirales excitées, nous explorons actuellement deux configurations différentes. La première configuration consiste à utiliser des miroirs multicouches pour sélectionner une seule (relativement basse) harmonique circulaire, qui produira une impulsion femtoseconde XUV, permettant de mesurer le PECD proche du seuil d'ionisation, à partir de l'ionisation des électrons de valence. La deuxième configuration consiste à générer des impulsions attosecondes uniques et circulaires autour de 70 eV pour photoioniser des électrons de la couche interne d'atomes d'halogènes au sein de molécules chirales, par exemple. Le couplage de cette ligne de lumière polyvalente à haut taux de répétition avec le COLTRIMS va certainement permettre d'augmenter la dimensionnalité des mesures, ce qui est souvent essentiel pour comprendre des données expérimentales riches et complexes.

En conclusion, nous avons étudié une grande variété de problèmes scientifiques dans les domaines de la physique en champ fort, de la physique de «l'attoseconde» ainsi que de la femtochimie. Ces thématiques reflètent parfaitement l'éventail d'expertise des scientifiques avec lesquels j'ai eu la chance de travailler, à la fois au CELIA et à l'INRS. Utiliser cette expertise pour étudier les molécules chirales, qui constituent une classe fascinante de molécules du point de vue de la physique, de la chimie et même des sciences de la vie, constitue un programme de recherche vraiment original qui, j'en suis sûr, conduira à des découvertes élégantes et importantes, dans les années à venir.

Bibliography

Articles

Abe, Mayumi, Yukiyoshi Ohtsuki, Yuichi Fujimura, and Wolfgang Domcke (2005). "Optimal control of ultrafast cis-trans photoisomerization of retinal in rhodopsin via a conical intersection". In: *The Journal of Chemical Physics* 123.14, page 144508. ISSN: 0021-9606.

Abrines, R and I C Percival (1966). "Classical theory of charge transfer and ionization of hydrogen atoms by protons". In: *Proceedings of the Physical Society* 88.4, page 861.

Abu-samha, M. and L. B. Madsen (2010). "Single-active-electron potentials for molecules in intense laser fields". In: *Phys. Rev. A* 81 (3), page 033416.

Agostini, P., F. Fabre, G. Mainfray, G. Petite, and N. K. Rahman (1979). "Free-Free Transitions Following Six-Photon Ionization of Xenon Atoms". In: *Phys. Rev. Lett.* 42 (17), pages 1127–1130.

Akturk, Selcuk, Xun Gu, Pamela Bowlan, and Rick Trebino (2010). "Spatio-temporal couplings in ultrashort laser pulses". In: *Journal of Optics* 12.9, page 093001.

Alnaser, A. S., M. Kübel, R. Siemering, B. Bergues, Nora G. Kling, K. J. Betsch, Y. Deng, J. Schmidt, Z. A. Alahmed, A. M. Azzeer, J. Ullrich, I. Ben-Itzhak, R. Moshammer, U. Kleineberg, F. Krausz, R. de Vivie-Riedle, and M. F. Kling (2014). "Subfemtosecond steering of hydrocarbon deprotonation through superposition of vibrational modes". en. In: *Nature Communications* 5, page 3800. ISSN: 2041-1723.

Alnaser, A S, I Litvinyuk, T Osipov, B Ulrich, A Landers, E Wells, C M Maharjan, P Ranitovic, I Bochareva, D Ray, and C L Cocke (2006). "Momentum-imaging investigations of the dissociation of D 2 + and the isomerization of acetylene to vinylidene by intense short laser pulses". In: *Journal of Physics B: Atomic, Molecular and Optical Physics* 39.13, S485.

Alnaser, A. S., X. M. Tong, T. Osipov, S. Voss, C. M. Maharjan, B. Shan, Z. Chang, and C. L. Cocke (2004). "Laser-peak-intensity calibration using recoil-ion momentum imaging". In: *Phys. Rev. A* 70 (2), page 023413.

Amati, D. (1960). "M. E. Rose -Elementary Theory of Angular Momentum". In: *Il Nuovo Cimento (1955-1965)* 16.6, pages 1160–1160. ISSN: 1827-6121.

Ammosov, M. V., N. B. Delone, and V. P. Krainov (1986). "Tunnel ionization of complex atoms and of atomic ions in an alternating electromagnetic field." In: *Sov. Phys. JETP* 64, page 1191.

Anderson, D. and M. Lisak (1983). "Nonlinear asymmetric self-phase modulation and self-steepening of pulses in long optical waveguides". In: *Phys. Rev. A* 27 (3), pages 1393–1398.

Antoine, Philippe, Bertrand Carré, Anne L'Huillier, and Maciej Lewenstein (1997). "Polarization of high-order harmonics". In: *Phys. Rev. A* 55 (2), pages 1314–1324.

Argenti, L., Á. Jiménez-Galán, J. Caillat, R. Taıeb, A. Maquet, and F. Martın (2017). "Control of photoemission delay in resonant two-photon transitions". In: *Phys. Rev. A* 95 (4), page 043426.

Asami, Takahiro, Robert H. Cowie, and Kako Ohbayashi (1998). "Evolution of Mirror Images by Sexually Asymmetric Mating Behavior in Hermaphroditic Snails". In: *The American Naturalist* 152.2, pages 225–236. ISSN: 00030147, 15375323.

Aseyev, S., Y. Ni, L. Frasinski, H. Muller, and M. Vrakking (2003). "Attosecond Angle-Resolved Photoelectron Spectroscopy". In: *Physical Review Letters* 91.22. ISSN: 0031-9007, 1079-7114.

Attar, Andrew R., Aditi Bhattacherjee, C. D. Pemmaraju, Kirsten Schnorr, Kristina D. Closser, David Prendergast, and Stephen R. Leone (2017). "Femtosecond x-ray spectroscopy of an electrocyclic ring-opening reaction". en. In: *Science* 356.6333, pages 54–59. ISSN: 0036-8075, 1095-9203.

Ayuso, David, Piero Decleva, Serguei Patchkovskii, and Olga Smirnova (2018). "Chiral dichroism in bi-elliptical high-order harmonic generation". en. In: *Journal of Physics B: Atomic, Molecular and Optical Physics* 51.6, 06LT01. ISSN: 0953-4075.

Baker, S. (2006). "Probing Proton Dynamics in Molecules on an Attosecond Time Scale". In: *Science* 312.5772, pages 424–427. ISSN: 0036-8075, 1095-9203.

Balavoine, G., A. Moradpour, and H. B. Kagan (1974). "Preparation of chiral compounds with high optical purity by irradiation with circularly polarized light, a model reaction for the prebiotic generation of optical activity". In: *Journal of the American Chemical Society* 96.16, pages 5152–5158.

Balcou, Ph., Anne L'Huillier, and D. Escande (1996). "High-order harmonic generation processes in classical and quantum anharmonic oscillators". In: *Phys. Rev. A* 53 (5), pages 3456–3468.

Bandarage, Gunadya, Alfred Maquet, Thierry Ménis, Richard Taıeb, Valérie Véniard, and J. Cooper (1992). "Harmonic generation by laser-driven classical hydrogen atoms". In: *Phys. Rev. A* 46 (1), pages 380–390.

Baykusheva, Denitsa and Hans Jakob Wörner (2017). "Theory of attosecond delays in molecular photoionization". In: *The Journal of Chemical Physics* 146.12, page 124306.

Beaulieu, S., E. Bloch, L. Barreau, A. Comby, D. Descamps, R. Géneaux, F. Légaré, S. Petit, and Y. Mairesse (2017a). "Phase-resolved two-dimensional spectroscopy of electronic wave packets by laser-induced XUV free induction decay". In: *Phys. Rev. A* 95 (4), page 041401 (cited on pages 14, 21, 84, 86–89, 92–94, 251, 252, 259, 260).

Beaulieu, S., S. Camp, D. Descamps, A. Comby, V. Wanie, S. Petit, F. Légaré, K. J. Schafer, M. B. Gaarde, F. Catoire, and Y. Mairesse (2016a). "Role of Excited States In High-order Harmonic Generation". In: *Physical Review Letters* 117.20, page 203001 (cited on pages 14, 21, 61, 64, 67, 68, 70, 76, 83, 104, 107, 236, 251, 259, 260).

Beaulieu, S., A. Comby, A. Clergerie, J. Caillat, D. Descamps, N. Dudovich, B. Fabre, R. Géneaux, F. Légaré, S. Petit, B. Pons, G. Porat, T. Ruchon, R. Taïeb, V. Blanchet, and Y. Mairesse (2017b). "Attosecond-resolved photoionization of chiral molecules". en. In: *Science* 358.6368, pages 1288–1294. ISSN: 0036-8075, 1095-9203 (cited on pages 16, 23, 107, 251, 259).

Beaulieu, S., A. Comby, D. Descamps, B. Fabre, G. A. Garcia, R. Géneaux, A. G. Harvey, F. Légaré, Z. Mašín, L. Nahon, A. F. Ordonez, S. Petit, B. Pons, Y. Mairesse, O. Smirnova, and V. Blanchet (2018a). "Photoexcitation circular dichroism in chiral molecules". en. In: *Nature Physics*, page 1. ISSN: 1745-2481.

Beaulieu, S., A. Comby, D. Descamps, S. Petit, F. Légaré, B. Fabre, V. Blanchet, and Y. Mairesse (2018b). "Disentangling the Role of Bound-Bound and Bound-Continuum Transitions in Multiphoton Photoelectron Circular Dichroism of Limonene". In: *ArXiv e-prints* (cited on pages 15, 23, 191, 194, 195, 256, 264).

Beaulieu, S., A. Ferré, R. Géneaux, R. Canonge, D. Descamps, B. Fabre, N. Fedorov, F. Légaré, S. Petit, T. Ruchon, V Blanchet, Y. Mairesse, and B. Pons (2016b). "Universality of photoelectron circular dichroism in the photoionization of chiral molecules". en. In: *New Journal of Physics* 18.10, page 102002. ISSN: 1367-2630 (cited on pages 15, 23, 163, 166, 168, 171, 176, 251, 259).

Beaulieu, Samuel, Antoine Comby, Baptiste Fabre, Dominique Descamps, Amélie Ferré, Gustavo Garcia, Romain Géneaux, Francois Légaré, Laurent Nahon, Stéphane Petit, Thierry Ruchon, Bernard Pons, Valérie Blanchet, and Yann Mairesse (2016c). "Probing ultrafast dynamics of chiral molecules using time-resolved photoelectron circular dichroism". en. In: 194, pages 325–348. ISSN: 1364-5498 (cited on pages 15, 23, 157, 160, 187–189, 192, 194, 197, 244, 256, 264).

Beck, Annelise R., Birgitta Bernhardt, Erika R. Warrick, Mengxi Wu, Shaohao Chen, Mette B. Gaarde, Kenneth J. Schafer, Daniel M. Neumark, and Stephen R. Leone (2014). "Attosecond transient absorption probing of electronic superpositions of bound states in neon: detection of quantum beats". en. In: *New Journal of Physics* 16.11, page 113016. ISSN: 1367-2630.

Bellini, M., C. Lyngå, A. Tozzi, M. B. Gaarde, T. W. Hänsch, A. L'Huillier, and C.-G. Wahlström (1998). "Temporal Coherence of Ultrashort High-Order Harmonic Pulses". In: *Physical Review Letters* 81.2, pages 297–300.

Bengtsson, S., E.W. Larsen, D. Kroon, S. Camp, M. Miranda, C.L. Arnold, A. L'Huillier, K.J. Schafer, Gaarde M.B., L. Rippe, and J. Mauritsson (2017). "Space–time control of free induction decay in the extreme ultraviolet". In: *Nature Photonics* 11, pages 252–259.

Bengtsson, Samuel, Esben W. Larsen, David Kroon, Seth Camp, Miguel Miranda, Cord L. Arnold, Anne L'Huillier, Kenneth J. Schafer, Mette B. Gaarde, Lars Rippe, and Johan Mauritsson (2016). "Controlled free-induction decay in the extreme ultraviolet". In: *arXiv:1611.04836 [physics]*. arXiv: 1611.04836.

Bertrand, J. B., H. J. Wörner, H.-C. Bandulet, É. Bisson, M. Spanner, J.-C. Kieffer, D. M. Villeneuve, and P. B. Corkum (2011). "Ultrahigh-Order Wave Mixing in Noncollinear High Harmonic Generation". In: *Phys. Rev. Lett.* 106 (2), page 023001.

Besler, Brent H., Kenneth M. Merz, and Peter A. Kollman (1990). "Atomic charges derived from semiempirical methods". In: *Journal of Computational Chemistry* 11.4, pages 431–439. ISSN: 1096-987X.

Bhattacherjee, Aditi, Chaitanya Das Pemmaraju, Kirsten Schnorr, Andrew R. Attar, and Stephen R. Leone (2017). "Ultrafast Intersystem Crossing in Acetylacetone via Femtosecond X-ray Transient Absorption at the Carbon K-Edge". In: *Journal of the American Chemical Society* 139.46. PMID: 29083165, pages 16576–16583.

Bisgaard, Christer Z., Owen J. Clarkin, Guorong Wu, Anthony M. D. Lee, Oliver Geßner, Carl C. Hayden, and Albert Stolow (2009). "Time-Resolved Molecular Frame Dynamics of Fixed-in-Space CS2 Molecules". en. In: *Science* 323.5920, pages 1464–1468. ISSN: 0036-8075, 1095-9203.

Blaga, C.I., F. Catoire, P. Colosimo, G.G. Paulus, H.G. Muller, P. Agostini, and L.F. DiMauro (2009). "Strong-field photoionization revisited". In: *Nature Photonics* 5, pages 335–338.

Blanchet, Valérie, Marek Z. Zgierski, Tamar Seideman, and Albert Stolow (1999). "Discerning vibronic molecular dynamics using time-resolved photoelectron spectroscopy". en. In: *Nature* 401.6748, pages 52–54. ISSN: 1476-4687.

Blokhin, A. P., M. F. Gelin, E. V. Khoroshilov, I. V. Kryukov, and A. V. Sharkov (2003). "Dynamics of optically induced anisotropy in an ensemble of asymmetric top molecules in the gas phase". en. In: *Optics and Spectroscopy* 95.3, pages 346–352. ISSN: 0030-400X, 1562-6911.

Bodi, Andras, Patrick Hemberger, Thomas Gerber, and Bálint Sztáray (2012). "A new double imaging velocity focusing coincidence experiment: i2PEPICO". In: *Review of Scientific Instruments* 83.8, page 083105.

Bohman, Samuel, Akira Suda, Masanori Kaku, Muhammad Nurhuda, Takuya Kanai, Shigeru Yamaguchi, and Katsumi Midorikawa (2008). "Generation of 5 fs, 0.5 TW pulses focusable to relativistic intensities at 1 kHz". In: *Opt. Express* 16.14, pages 10684–10689.

Bohman, Samuel, Akira Suda, Tsuneto Kanai, Shigeru Yamaguchi, and Katsumi Midorikawa (2010). "Generation of 5.0 fs, 5.0 mJ pulses at 1kHz using hollow-fiber pulse compression". In: *Opt. Lett.* 35.11, pages 1887–1889.

Bonner, William A. (1995). "Chirality and life". In: *Origins of Life and Evolution of the Biosphere* 25.1, pages 175–190. ISSN: 1573-0875.

Botheron, P. and B. Pons (2009). "One-electron atom in a strong and short laser pulse: Comparison of classical and quantum descriptions". In: *Phys. Rev. A* 80 (2), page 023402.

Böwering, N., T. Lischke, B. Schmidtke, N. Müller, T. Khalil, and U. Heinzmann (2001). "Asymmetry in Photoelectron Emission from Chiral Molecules Induced by Circularly Polarized Light". In: *Physical Review Letters* 86.7, pages 1187–1190 (cited on pages 15, 22, 140, 146, 154, 156).

Boyé-Péronne, Séverine, Dolores Gauyacq, and Jacques Liévin (2006). "Vinylidene-acetylene cation isomerization investigated by large scale ab initio calculations". In: *The Journal of Chemical Physics* 124.21, page 214305.

Brumer, Paul and Moshe Shapiro (1986). "Control of unimolecular reactions using coherent light". In: *Chemical Physics Letters* 126.6, pages 541–546. ISSN: 0009-2614.

Bucksbaum, P. H., A. Zavriyev, H. G. Muller, and D. W. Schumacher (1990). "Softening of the H_2^+ molecular bond in intense laser fields". In: *Phys. Rev. Lett.* 64 (16), pages 1883–1886.

Budil, K. S., P. Salières, Anne L'Huillier, T. Ditmire, and M. D. Perry (1993). "Influence of ellipticity on harmonic generation". In: *Phys. Rev. A* 48 (5), R3437–R3440.

Busto, D., L. Barreau, M. Isinger, M. Turconi, C. Alexandridi, A. Harth, S. Zhong, R. J. Squibb, D. Kroon, S. Plogmaker, M Miranda, Á Jiménez-Galán, L. Argenti, C. L. Arnold, R. Feifel, F. Martín, M. Gisselbrecht, A. L'Huillier, and P Salières (2018). "Time–frequency representation of autoionization dynamics in helium". en. In: *Journal of Physics B: Atomic, Molecular and Optical Physics* 51.4, page 044002. ISSN: 0953-4075.

Cahn, R. S., Christopher Ingold, and V. Prelog (1966). "Specification of Molecular Chirality". In: *Angewandte Chemie International Edition in English* 5.4, pages 385–415. ISSN: 1521-3773.

Calegari, F., D. Ayuso, A. Trabattoni, L. Belshaw, S. De Camillis, S. Anumula, F. Frassetto, L. Poletto, A. Palacios, P. Decleva, J. B. Greenwood, F. Martín, and M. Nisoli (2014). "Ultrafast electron dynamics in phenylalanine initiated by attosecond pulses". en. In: *Science* 346.6207, pages 336–339. ISSN: 0036-8075, 1095-9203 (cited on pages 13, 20).

Camp, Seth, Samuel Beaulieu, Kenneth J Schafer, and Mette B Gaarde (2018). "Resonantly-initiated quantum trajectories and their role in the generation of near-threshold harmonics". In: *Journal of Physics B: Atomic, Molecular and Optical Physics* 51.6, page 064001.

Camp, Seth, Kenneth J. Schafer, and Mette B. Gaarde (2015). "Interplay between resonant enhancement and quantum path dynamics in harmonic generation in helium". In: *Physical Review A* 92.1, page 013404.

Camper, Antoine, Amélie Ferré, Nan Lin, Emmanouil Skantzakis, David Staedter, Elizabeth English, Bastian Manschwetus, Frédéric Burgy, Stéphane Petit, Dominique Descamps, Thierry Auguste, Olivier Gobert, Bertrand Carré, Pascal Salières, Yann Mairesse, and Thierry Ruchon (2015). "Transverse Electromagnetic Mode Conversion for High-Harmonic Self-Probing Spectroscopy". en. In: *Photonics* 2.1, pages 184–199.

Cao, Wei, Erika R. Warrick, Ashley Fidler, Stephen R. Leone, and Daniel M. Neumark (2016a). "Near-resonant four-wave mixing of attosecond extreme-ultraviolet pulses with near-infrared pulses in neon: Detection of electronic coherences". In: *Physical Review A* 94.2, page 021802.

Cao, Wei, Erika R. Warrick, Daniel M. Neumark, and Stephen R. Leone (2016b). "Attosecond transient absorption of argon atoms in the vacuum ultraviolet region: line energy shifts versus coherent population transfer". en. In: *New Journal of Physics* 18.1, page 013041. ISSN: 1367-2630.

Cardin, Vincent, Nicolas Thiré, Samuel Beaulieu, Vincent Wanie, François Légaré, and Bruno E. Schmidt (2015). "0.42TW 2-cycle pulses at 1.8m via hollow-core fiber compression". In: *Applied Physics Letters* 107.18, page 181101 (cited on pages 13, 21, 35, 36, 38, 251, 259).

Carlström, Stefanos, Jana Preclíková, Eleonora Lorek, Esben Witting Larsen, Christoph M Heyl, David Paleček, Donatas Zigmantas, Kenneth J Schafer, Mette B Gaarde, and Johan Mauritsson (2016). "Spatially and spectrally resolved quantum path interference with chirped driving pulses". In: *New Journal of Physics* 18.12, page 123032.

Catoire, F., A. Ferré, O. Hort, A. Dubrouil, L. Quintard, D. Descamps, S. Petit, F. Burgy, E. Mével, Y. Mairesse, and E. Constant (2016). "Complex structure of spatially resolved high-order-harmonic spectra". In: *Phys. Rev. A* 94 (6), page 063401.

Catone, D., M. Stener, P. Decleva, G. Contini, N. Zema, T. Prosperi, V. Feyer, K. C. Prince, and S. Turchini (2012). "Resonant Circular Dichroism of Chiral Metal-Organic Complex". In: *Phys. Rev. Lett.* 108 (8), page 083001.

Cavalieri, A. L., N. Müller, Th. Uphues, V. S. Yakovlev, A. Baltuška, B. Horvath, B. Schmidt, L. Blümel, R. Holzwarth, S. Hendel, M. Drescher, U. Kleineberg, P. M. Echenique, R. Kienberger, F. Krausz, and U. Heinzmann (2007). "Attosecond spectroscopy in condensed matter". In: *Nature* 449.7165, pages 1029–1032. ISSN: 0028-0836, 1476-4687 (cited on pages 13, 20, 215).

Chacon, Alexis, Manfred Lein, and Camilo Ruiz (2014). "Asymmetry of Wigner's time delay in a small molecule". en. In: *Physical Review A* 89.5. ISSN: 1050-2947, 1094-1622.

Chen, Ce, Yi-Yian Yin, and D. S. Elliott (1990). "Interference between optical transitions". In: *Phys. Rev. Lett.* 64 (5), pages 507–510.

Chen, M.-C., P. Arpin, T. Popmintchev, M. Gerrity, B. Zhang, M. Seaberg, D. Popmintchev, M. M. Murnane, and H. C. Kapteyn (2010). "Bright, Coherent, Ultrafast Soft X-Ray

Harmonics Spanning the Water Window from a Tabletop Light Source". In: *Phys. Rev. Lett.* 105 (17), page 173901.

Chen, Shaohao, M. Justine Bell, Annelise R. Beck, Hiroki Mashiko, Mengxi Wu, Adrian N. Pfeiffer, Mette B. Gaarde, Daniel M. Neumark, Stephen R. Leone, and Kenneth J. Schafer (2012). "Light-induced states in attosecond transient absorption spectra of laser-dressed helium". In: *Physical Review A* 86.6, page 063408.

Cherepkov, N. A. (1982). "Circular dichroism of molecules in the continuous absorption region". In: *Chemical Physics Letters* 87.4, pages 344–348. ISSN: 0009-2614.

Chini, M., K. Zhao, and Z. Chang (2014a). "The generation, characterization and applications of broadband isolated attosecond pulses". In: *Nature Photonics* 8, pages 178–186.

Chini, Michael, Xiaowei Wang, Yan Cheng, He Wang, Yi Wu, Eric Cunningham, Peng-Cheng Li, John Heslar, Dmitry A. Telnov, Shih-I. Chu, and Zenghu Chang (2014b). "Coherent phase-matched VUV generation by field-controlled bound states". en. In: *Nature Photonics* 8.6, pages 437–441. ISSN: 1749-4885.

Chini, Michael, Baozhen Zhao, He Wang, Yan Cheng, S. X. Hu, and Zenghu Chang (2012). "Subcycle ac Stark Shift of Helium Excited States Probed with Isolated Attosecond Pulses". In: *Physical Review Letters* 109.7, page 073601.

Cireasa, R., A. E. Boguslavskiy, B. Pons, M. C. H. Wong, D. Descamps, S. Petit, H. Ruf, N. Thiré, A. Ferré, J. Suarez, J. Higuet, B. E. Schmidt, A. F. Alharbi, F. Légaré, V. Blanchet, B. Fabre, S. Patchkovskii, O. Smirnova, Y. Mairesse, and V. R. Bhardwaj (2015). "Probing molecular chirality on a sub-femtosecond timescale". en. In: *Nature Physics* 11.8, pages 654–658. ISSN: 1745-2481.

Cirelli, Claudio, Carlos Marante, Sebastian Heuser, C. L. M. Petersson, Álvaro Jiménez Galán, Luca Argenti, Shiyang Zhong, David Busto, Marcus Isinger, Saikat Nandi, Sylvain Maclot, Linnea Rading, Per Johnsson, Mathieu Gisselbrecht, Matteo Lucchini, Lukas Gallmann, J. Marcus Dahlström, Eva Lindroth, Anne L'Huillier, Fernando Martín, and Ursula Keller (2018). "Anisotropic photoemission time delays close to a Fano resonance". en. In: *Nature Communications* 9.1, page 955. ISSN: 2041-1723.

Clerici, Matteo, Marco Peccianti, Bruno E. Schmidt, Lucia Caspani, Mostafa Shalaby, Mathieu Giguère, Antonio Lotti, Arnaud Couairon, Fran çois Légaré, Tsuneyuki Ozaki, Daniele Faccio, and Roberto Morandotti (2013). "Wavelength Scaling of Terahertz Generation by Gas Ionization". In: *Phys. Rev. Lett.* 110 (25), page 253901.

Cloux, F., B. Fabre, and B. Pons (2015). "Semiclassical description of high-order-harmonic spectroscopy of the Cooper minimum in krypton". In: *Physical Review A* 91.2, page 023415.

Comby, Antoine, Samuel Beaulieu, Martial Boggio-Pasqua, Dominique Descamps, Francois Légaré, Laurent Nahon, Stéphane Petit, Bernard Pons, Baptiste Fabre, Yann Mairesse, and Valérie Blanchet (2016). "Relaxation Dynamics in Photoexcited Chiral Molecules Studied by Time-Resolved Photoelectron Circular Dichroism: Toward Chiral Femtochemistry". In: *The Journal of Physical Chemistry Letters* 7.22, pages 4514–4519. ISSN: 1948-7185 (cited on pages 15, 23, 188, 191, 197, 198, 256, 264).

Cooper, J. W. (1962). "Photoionization from outer atomic subshells. A model study". In: *Phys. Rev.* 128, page 681.

Corkum, P. B. (1993). "Plasma perspective on strong field multiphoton ionization". In: *Physical Review Letters* 71.13, pages 1994–1997.

Cousin, S. L., F. Silva, S. Teichmann, M. Hemmer, B. Buades, and J. Biegert (2014). "High-flux table-top soft x-ray source driven by sub-2-cycle, CEP stable, 1.85-μm 1-kHz pulses for carbon K-edge spectroscopy". In: *Opt. Lett.* 39.18, pages 5383–5386.

Dahlström, J. M., A. L'Huillier, and A. Maquet (2012). "Introduction to attosecond delays in photoionization". en. In: *Journal of Physics B: Atomic, Molecular and Optical Physics* 45.18, page 183001. ISSN: 0953-4075.

Daly, Steven, Ivan Powis, Gustavo A. Garcia, Héloïse Soldi-Lose, and Laurent Nahon (2011). "Photoionization of epichlorohydrin enantiomers and clusters studied with circularly polarized vacuum ultraviolet radiation". In: *The Journal of Chemical Physics* 134.6, page 064306.

D'Ariano, G. M. and P. Lo Presti (2001). "Quantum Tomography for Measuring Experimentally the Matrix Elements of an Arbitrary Quantum Operation". In: *Phys. Rev. Lett.* 86 (19), pages 4195–4198.

Decleva, P, A Lisini, and M Venuti (1994). "Multichannel continuum states by a least-squares approach in a spline basis: application to He and H - photoionization". In: *Journal of Physics B: Atomic, Molecular and Optical Physics* 27.20, page 4867.

Dholakia, K., N. B. Simpson, M. J. Padgett, and L. Allen (1996). "Second-harmonic generation and the orbital angular momentum of light". In: *Phys. Rev. A* 54 (5), R3742–R3745.

Di Piazza, Antonino and Emilio Fiordilino (2001). "Why hyper-Raman lines are absent in high-order harmonic generation". In: *Phys. Rev. A* 64 (1), page 013802.

Dill, Dan and J. L. Dehmer (1974). "Electronmolecule scattering and molecular photoionization using the multiplescattering method". In: *The Journal of Chemical Physics* 61.2, pages 692–699.

Dörner, R., V. Mergel, O. Jagutzki, L. Spielberger, J. Ullrich, R. Moshammer, and H. Schmidt-Böcking (2000). "Cold Target Recoil Ion Momentum Spectroscopy: a 'momentum microscope' to view atomic collision dynamics". In: *Physics Reports* 330.2–3, pages 95–192. ISSN: 0370-1573.

Dreissigacker, Ingo and Manfred Lein (2014). "Photoelectron circular dichroism of chiral molecules studied with a continuum-state-corrected strong-field approximation". In: *Phys. Rev. A* 89 (5), page 053406.

Dribinski, Vladimir, Alexei Ossadtchi, Vladimir A. Mandelshtam, and Hanna Reisler (2002). "Reconstruction of Abel-transformable images: The Gaussian basis-set expansion Abel transform method". In: *Review of Scientific Instruments* 73.7, pages 2634–2642.

Dubietis, A., G. Jonušauskas, and A. Piskarskas (1992). "Powerful femtosecond pulse generation by chirped and stretched pulse parametric amplification in BBO crystal". In: *Optics Communications* 88.4, pages 437–440. ISSN: 0030-4018.

Dubs, Richard L., S. N. Dixit, and V. McKoy (1986). "Circular dichroism in photoelectron angular distributions as a probe of atomic and molecular alignment". In: *The Journal of Chemical Physics* 85.2, pages 656–663.

Dupont, E., P. B. Corkum, H. C. Liu, M. Buchanan, and Z. R. Wasilewski (1995). "Phase-Controlled Currents in Semiconductors". In: *Phys. Rev. Lett.* 74 (18), pages 3596–3599.

Eckart, S., M. Kunitski, I. Ivanov, M. Richter, K. Fehre, A. Hartung, J. Rist, K. Henrichs, D. Trabert, N. Schlott, L. Ph H. Schmidt, T. Jahnke, M. S. Schöffler, A. Kheifets, and R. Dörner (2017). "Sub-Cycle Interference upon Tunnel-Ionization by Counterrotating Two-Color Fields". In: *arXiv:1711.03880 [physics]*. arXiv: 1711.03880.

Eckle, P., A. N. Pfeiffer, C. Cirelli, A. Staudte, R. Dörner, H. G. Muller, M. Büttiker, and U. Keller (2008). "Attosecond Ionization and Tunneling Delay Time Measurements in Helium". en. In: *Science* 322.5907, pages 1525–1529. ISSN: 0036-8075, 1095-9203.

Eichmann, H., A. Egbert, S. Nolte, C. Momma, B. Wellegehausen, W. Becker, S. Long, and J. K. McIver (1995). "Polarization-dependent high-order two-color mixing". In: *Phys. Rev. A* 51 (5), R3414–R3417.

Endo, Tomoyuki, Hikaru Fujise, Yuuna Kawachi, Ayaka Ishihara, Akitaka Matsuda, Mizuho Fushitani, Hirohiko Kono, and Akiyoshi Hishikawa (2017). "Selective bond breaking of CO 2 in phase-locked two-color intense laser fields: laser field intensity dependence". en. In: *Physical Chemistry Chemical Physics* 19.5, pages 3550–3556.

Endo, Tomoyuki, Hikaru Fujise, Akitaka Matsuda, Mizuho Fushitani, Hirohiko Kono, and Akiyoshi Hishikawa (2016). "Coincidence momentum imaging of asymmetric Coulomb explosion of CO2 in phase-locked two-color intense laser fields". In: *Journal of Electron Spectroscopy and Related Phenomena* 207, pages 50–54. ISSN: 0368-2048.

Eriksson, Tommy, Sven Björkman, Bodil Roth, Årsa Fyge, and Peter Höuglund (1995). "Stereospecific determination, chiral inversion in vitro and pharmacokinetics in humans of the enantiomers of thalidomide". In: *Chirality* 7.1, pages 44–52. ISSN: 1520-636X.

Ervin, Kent M., Joe Ho, and W. C. Lineberger (1989). "A study of the singlet and triplet states of vinylidene by photoelectron spectroscopy of H2C=C, D2C=C, and HDC=C. Vinylidene–acetylene isomerization". In: *The Journal of Chemical Physics* 91.10, pages 5974–5992.

Even, U., J. Jortner, D. Noy, N. Lavie, and C. Cossart-Magos (2000). "Cooling of large molecules below 1 K and He clusters formation". en. In: *The Journal of Chemical Physics* 112.18, pages 8068–8071. ISSN: 0021-9606, 1089-7690.

Fano, U. (1961). "Effects of Configuration Interaction on Intensities and Phase Shifts". In: *Phys. Rev.* 124 (6), pages 1866–1878.

Fanood, Mohammad M Rafiee, N. Bhargava Ram, C. Stefan Lehmann, Ivan Powis, and Maurice H. M. Janssen (2015). "Enantiomer-specific analysis of multi-component mixtures by correlated electron imaging–ion mass spectrometry". In: *Nature Communications* 6, page 7511. ISSN: 2041-1723.

Ferrari, F., F. Calegari, M. Lucchini, C. Vozzi, S. Stagira, G. Sansone, and M. Nisoli (2010). "High-energy isolated attosecond pulses generated by above-saturation few-cycle fields". In: *Nature Photonics* 4, pages 875–879.

Ferray, M, A L'Huillier, X F Li, L A Lompre, G Mainfray, and C Manus (1988). "Multiple-harmonic conversion of 1064 nm radiation in rare gases". In: *Journal of Physics B: Atomic, Molecular and Optical Physics* 21.3, page L31 (cited on pages 12, 20, 25, 43, 45).

Ferré, A., A. E. Boguslavskiy, M. Dagan, V. Blanchet, B. D. Bruner, F. Burgy, A. Camper, D. Descamps, B. Fabre, N. Fedorov, J. Gaudin, G. Geoffroy, J. Mikosch, S. Patchkovskii, S. Petit, T. Ruchon, H. Soifer, D. Staedter, I. Wilkinson, A. Stolow, N. Dudovich, and Y. Mairesse (2015a). "Multi-channel electronic and vibrational dynamics in polyatomic resonant high-order harmonic generation". In: *Nature Communications* 6, page 5952.

Ferré, A., C. Handschin, M. Dumergue, F. Burgy, A. Comby, D. Descamps, B. Fabre, G. A. Garcia, R. Géneaux, L. Merceron, E. Mével, L. Nahon, S. Petit, B. Pons, D. Staedter, S. Weber, T. Ruchon, V. Blanchet, and Y. Mairesse (2015b). "A table-top ultrashort light source in the extreme ultraviolet for circular dichroism experiments". en. In: *Nature Photonics* 9.2, pages 93–98. ISSN: 1749-4885.

Fleischer, Avner, Ofer Kfir, Tzvi Diskin, Pavel Sidorenko, and Oren Cohen (2014). "Spin angular momentum and tunable polarization in high-harmonic generation". In: *Nat Photon* 8.7, pages 543–549. ISSN: 1749-4885.

Forbes, Ruaridh, Andrey E. Boguslavskiy, Iain Wilkinson, Jonathan G. Underwood, and Albert Stolow (2017). "Excited state wavepacket dynamics in NO2 probed by strong-field ionization". In: *The Journal of Chemical Physics* 147.5, page 054305.

Franken, P. A., A. E. Hill, C. W. Peters, and G. Weinreich (1961). "Generation of Optical Harmonics". In: *Phys. Rev. Lett.* 7 (4), pages 118–119.

Freeman, R. R., P. H. Bucksbaum, H. Milchberg, S. Darack, D. Schumacher, and M. E. Geusic (1987). "Above-threshold ionization with subpicosecond laser pulses". In: *Phys. Rev. Lett.* 59 (10), pages 1092–1095.

Froud, Christopher A., Edward T. Rogers, David C. Hanna, William S. Brocklesby, Matthew Praeger, Ana M. de Paula, Jeremy J. Baumberg, and Jeremy G. Frey (2006). "Soft-x-ray wavelength shift induced by ionization effects in a capillary". In: *Opt. Lett.* 31.3, pages 374–376.

Gaarde, Mette B, Jennifer L Tate, and Kenneth J Schafer (2008). "Macroscopic aspects of attosecond pulse generation". In: *Journal of Physics B: Atomic, Molecular and Optical Physics* 41.13, page 132001.

Gaarde, Mette and Kenneth Schafer (2002). "Quantum path distributions for high-order harmonics in rare gas atoms". In: *Physical Review A* 65.3. ISSN: 1050-2947, 1094-1622.

Gaillac, Romain, Morgane Vacher, Alfred Maquet, Richard Taıeb, and Jérémie Caillat (2016). "Attosecond photoemission dynamics encoded in real-valued continuum wave functions". In: *Phys. Rev. A* 93 (1), page 013410.

Gallagher, T. F. (1988). "Above-Threshold Ionization in Low-Frequency Limit". In: *Phys. Rev. Lett.* 61 (20), pages 2304–2307.

Garcia, G. A., B. K. Cunha de Miranda, M. Tia, S. Daly, and L. Nahon (2013a). "DELICIOUS III: A multipurpose double imaging particle coincidence spectrometer for gas phase vacuum ultraviolet photodynamics studies". In: *Review of Scientific Instruments* 84.5, page 053112.

Garcia, Gustavo A., Heloise Dossmann, Laurent Nahon, Steven Daly, and Ivan Powis (2014). "Photoelectron circular dichroism and spectroscopy of trifluoromethyl- and methyl-oxirane: a comparative study". In: *Phys. Chem. Chem. Phys.* 16 (30), pages 16214–16224.

Garcia, Gustavo A., Laurent Nahon, Steven Daly, and Ivan Powis (2013b). "Vibrationally induced inversion of photoelectron forward-backward asymmetry in chiral molecule photoionization by circularly polarized light". en. In: *Nature Communications* 4, page 2132. ISSN: 2041-1723.

Garcia, Gustavo A., Laurent Nahon, Chris J. Harding, and Ivan Powis (2008). "Chiral signatures in angle-resolved valence photoelectron spectroscopy of pure glycidol enantiomers". In: *Phys. Chem. Chem. Phys.* 10 (12), pages 1628–1639.

Garcia, Gustavo A., Laurent Nahon, Mogens Lebech, Jean-Christophe Houver, Danielle Dowek, and Ivan Powis (2003). "Circular dichroism in the photoelectron angular distribution from randomly oriented enantiomers of camphor". In: *The Journal of Chemical Physics* 119.17, pages 8781–8784.

Garcia, Gustavo A., Laurent Nahon, and Ivan Powis (2004). "Two-dimensional charged particle image inversion using a polar basis function expansion". In: *Review of Scientific Instruments* 75.11, pages 4989–4996.

Gariepy, Genevieve, Jonathan Leach, Kyung Taec Kim, T. J. Hammond, E. Frumker, Robert W. Boyd, and P. B. Corkum (2014). "Creating High-Harmonic Beams with Controlled Orbital Angular Momentum". In: *Phys. Rev. Lett.* 113 (15), page 153901.

Gaumnitz, Thomas, Arohi Jain, Yoann Pertot, Martin Huppert, Inga Jordan, Fernando Ardana-Lamas, and Hans Jakob Wörner (2017). "Streaking of 43-attosecond soft-X-ray pulses generated by a passively CEP-stable mid-infrared driver". In: *Opt. Express* 25.22, pages 27506–27518 (cited on pages 13, 20, 26).

Gauthier, D., P. Rebernik Ribič, G. Adhikary, A. Camper, C. Chappuis, R. Cucini, L. F. DiMauro, G. Dovillaire, F. Frassetto, R. Géneaux, P. Miotti, L. Poletto, B. Ressel, C. Spezzani, M. Stupar, T. Ruchon, and G. De Ninno (2017). "Tunable orbital angular momentum in high-harmonic generation". En. In: *Nature Communications* 8, page 14971. ISSN: 2041-1723.

Géneaux, Romain (2016). "Le moment angulaire de la lumière en génération d'harmoniques d'ordre élevé". In: 2016SACLS474.

Géneaux, Romain, Céline Chappuis, Thierry Auguste, Samuel Beaulieu, Timothy T. Gorman, Fabien Lepetit, Louis F. DiMauro, and Thierry Ruchon (2017). "Radial index of Laguerre-Gaussian modes in high-order-harmonic generation". In: *Phys. Rev. A* 95 (5), page 051801.

Giusti-Suzor, A., X. He, O. Atabek, and F. H. Mies (1990). "Above-threshold dissociation of H_2^+ in intense laser fields". In: *Phys. Rev. Lett.* 64 (5), pages 515–518.

Goetz, R.E., T.A. Isaev, B. Nikoobakht, R. Berger, and C.P. Koch (2017). "Theoretical description of circular dichroism in photoelectron angular distributions of randomly oriented chiral molecules after multi-photon photoionization". In: *The Journal of Chemical Physics* 146.2, page 024306. ISSN: 0021-9606.

Goldberger, Marvin L. and Kenneth M. Watson (1962). "Concerning the Notion of "Time Interval" in *S*-Matrix Theory". In: *Phys. Rev.* 127 (6), pages 2284–2286.

Gong, Xiaochun, Peilun He, Qiying Song, Qinying Ji, Haifeng Pan, Jingxin Ding, Feng He, Heping Zeng, and Jian Wu (2014). "Two-Dimensional Directional Proton Emission in Dissociative Ionization of H_2". In: *Phys. Rev. Lett.* 113 (20), page 203001.

Goulielmakis, E., M. Schultze, M. Hofstetter, V. S. Yakovlev, J. Gagnon, M. Uiberacker, A. L. Aquila, E. M. Gullikson, D. T. Attwood, R. Kienberger, F. Krausz, and U. Kleineberg (2008). "Single-Cycle Nonlinear Optics". In: *Science* 320.5883, pages 1614–1617. ISSN: 0036-8075, 1095-9203.

Goulielmakis, Eleftherios, Zhi-Heng Loh, Adrian Wirth, Robin Santra, Nina Rohringer, Vladislav S. Yakovlev, Sergey Zherebtsov, Thomas Pfeifer, Abdallah M. Azzeer, Matthias F. Kling, Stephen R. Leone, and Ferenc Krausz (2010). "Real-time observation of valence electron motion". en. In: *Nature* 466.7307, pages 739–743. ISSN: 0028-0836.

Gruson, V., L. Barreau, Á. Jiménez-Galan, F. Risoud, J. Caillat, A. Maquet, B. Carré, F. Lepetit, J.-F. Hergott, T. Ruchon, L. Argenti, R. Taıeb, F. Martın, and P. Salières (2016). "Attosecond dynamics through a Fano resonance: Monitoring the birth of a photoelectron". In: *Science* 354.6313, pages 734–738. ISSN: 0036-8075.

Guo, L., S. S. Han, X. Liu, Y. Cheng, Z. Z. Xu, J. Fan, J. Chen, S. G. Chen, W. Becker, C. I. Blaga, A. D. DiChiara, E. Sistrunk, P. Agostini, and L. F. DiMauro (2013). "Scaling of the Low-Energy Structure in Above-Threshold Ionization in the Tunneling Regime: Theory and Experiment". In: *Phys. Rev. Lett.* 110 (1), page 013001.

Haessler, S, J Caillat, and P Salières (2011). "Self-probing of molecules with high harmonic generation". In: *Journal of Physics B: Atomic, Molecular and Optical Physics* 44.20, page 203001 (cited on pages 13, 21).

Haessler, S., B. Fabre, J. Higuet, J. Caillat, T. Ruchon, P. Breger, B. Carré, E. Constant, A. Maquet, E. Mével, P. Salières, R. Taïeb, and Y. Mairesse (2009). "Phase-resolved attosecond near-threshold photoionization of molecular nitrogen". In: *Physical Review A* 80.1. ISSN: 1050-2947, 1094-1622 (cited on pages 13, 20, 215, 220).

Hammond, T.J., G.G. Brown, K.T. Kim, D.M. Villeneuve, and Corkum P.B. (2016). "Photonic streaking of attosecond pulse trains". In: *Nature Photonics* 10, pages 171–174.

Handschin, Charles (2013). "Spectroscopie EUV résolue temporellement à l'échelle femtoseconde par imagerie de vecteur vitesse et génération d'harmoniques d'ordres élevés". In: 2013BOR14814.

Harding, Chris J., Elisabeth Mikajlo, Ivan Powis, Silko Barth, Sanjeev Joshi, Volker Ulrich, and Uwe Hergenhahn (2005). "Circular dichroism in the angle-resolved C 1s photoemission spectra of gas-phase carvone enantiomers". In: *The Journal of Chemical Physics* 123.23, page 234310.

Harvey, Alex G., Zdeněk Mašín, and Olga Smirnova (2018). "General theory of photoexcitation induced photoelectron circular dichroism". In: *arXiv:1802.08662 [physics]*. arXiv: 1802.08662.

Hasson, K. C., Feng Gai, and Philip A. Anfinrud (1996). "The photoisomerization of retinal in bacteriorhodopsin: Experimental evidence for a three-state model". en. In: *Proceedings of the National Academy of Sciences* 93.26, pages 15124–15129. ISSN: 0027-8424, 1091-6490.

Hauri, C. P., A. Guandalini, P. Eckle, W. Kornelis, J. Biegert, and U. Keller (2005). "Generation of intense few-cycle laser pulses through filamentation – parameter dependence". In: *Opt. Express* 13.19, pages 7541–7547.

Heck, Albert J. R. and David W. Chandler (1995). "Imaging Techniques for the Study of Chemical Reaction Dynamics". In: *Annual Review of Physical Chemistry* 46.1. PMID: 24329711, pages 335–372.

Hell, Stefan W. and Jan Wichmann (1994). "Breaking the diffraction resolution limit by stimulated emission: stimulated-emission-depletion fluorescence microscopy". In: *Opt. Lett.* 19.11, pages 780–782.

Hentschel, M., R. Kienberger, Ch Spielmann, G. A. Reider, N. Milosevic, T. Brabec, P. Corkum, U. Heinzmann, M. Drescher, and F. Krausz (2001). "Attosecond metrology". en. In: *Nature* 414.6863, pages 509–513. ISSN: 1476-4687 (cited on pages 12, 20).

Hergenhahn, Uwe, Emma E. Rennie, Oliver Kugeler, Simon Marburger, Toralf Lischke, Ivan Powis, and Gustavo Garcia (2004). "Photoelectron circular dichroism in core level ionization of randomly oriented pure enantiomers of the chiral molecule camphor". In: *The Journal of Chemical Physics* 120.10, pages 4553–4556. ISSN: 0021-9606, 1089-7690.

Hernández-Garcıa, Carlos, Antonio Picón, Julio San Román, and Luis Plaja (2013). "Attosecond Extreme Ultraviolet Vortices from High-Order Harmonic Generation". In: *Phys. Rev. Lett.* 111 (8), page 083602.

Heuser, Sebastian, Álvaro Jiménez Galán, Claudio Cirelli, Carlos Marante, Mazyar Sabbar, Robert Boge, Matteo Lucchini, Lukas Gallmann, Igor Ivanov, Anatoli S. Kheifets, J. Marcus Dahlström, Eva Lindroth, Luca Argenti, Fernando Martín, and Ursula Keller (2016). "Angular dependence of photoemission time delay in helium". en. In: *Physical Review A* 94.6. ISSN: 2469-9926, 2469-9934.

Heyl, C M, C L Arnold, A Couairon, and A L'Huillier (2017). "Introduction to macroscopic power scaling principles for high-order harmonic generation". In: *Journal of Physics B: Atomic, Molecular and Optical Physics* 50.1, page 013001.

Hickstein, Daniel D., Franklin J. Dollar, Patrik Grychtol, Jennifer L. Ellis, Ronny Knut, Carlos Hernández-García, Dmitriy Zusin, Christian Gentry, Justin M. Shaw, Tingting Fan, Kevin M. Dorney, Andreas Becker, Agnieszka Jaroń-Becker, Henry C. Kapteyn, Margaret M. Murnane, and Charles G. Durfee (2015). "Non-collinear generation of angularly isolated circularly polarized high harmonics". In: *Nat Photon* 9.11, pages 743–750. ISSN: 1749-4885.

Higuet, J., H. Ruf, N. Thiré, R. Cireasa, E. Constant, E. Cormier, D. Descamps, E. Mével, S. Petit, B. Pons, Y. Mairesse, and B. Fabre (2011). "High-order harmonic spectroscopy

of the Cooper minimum in argon: Experimental and theoretical study". In: *Physical Review A* 83.5. ISSN: 1050-2947, 1094-1622.

Hishikawa, Akiyoshi, Akitaka Matsuda, Mizuho Fushitani, and Eiji J. Takahashi (2007). "Visualizing Recurrently Migrating Hydrogen in Acetylene Dication by Intense Ultrashort Laser Pulses". In: *Phys. Rev. Lett.* 99 (25), page 258302.

Hockett, P, E Frumker, D M Villeneuve, and P B Corkum (2016). "Time delay in molecular photoionization". In: *Journal of Physics B: Atomic, Molecular and Optical Physics* 49.9, page 095602.

Hockett, Paul (2017). "Angle-resolved RABBIT: theory and numerics". In: *arXiv:1703.08586 [physics, physics:quant-ph]*. arXiv: 1703.08586.

Holler, M., F. Schapper, L. Gallmann, and U. Keller (2011). "Attosecond Electron Wave-Packet Interference Observed by Transient Absorption". In: *Physical Review Letters* 106.12, page 123601.

Houston, Paul L., Xiaohong Wang, Aryya Ghosh, Joel M. Bowman, Mitchell S. Quinn, and Scott H. Kable (2017). "Formaldehyde roaming dynamics: Comparison of quasi-classical trajectory calculations and experiments". In: *The Journal of Chemical Physics* 147.1, page 013936. ISSN: 0021-9606.

Huppert, Martin, Inga Jordan, Denitsa Baykusheva, Aaron von Conta, and Hans Jakob Wörner (2016). "Attosecond Delays in Molecular Photoionization". In: *Phys. Rev. Lett.* 117 (9), page 093001 (cited on pages 13, 20).

Ibrahim, Heide, Catherine Lefebvre, André D Bandrauk, André Staudte, and François Légaré (2018). "H 2 : the benchmark molecule for ultrafast science and technologies". In: *Journal of Physics B: Atomic, Molecular and Optical Physics* 51.4, page 042002.

Ibrahim, Heide, Benji Wales, Samuel Beaulieu, Bruno E. Schmidt, Nicolas Thiré, Emmanuel P. Fowe, Éric Bisson, Christoph T. Hebeisen, Vincent Wanie, Mathieu Giguére, Jean-Claude Kieffer, Michael Spanner, André D. Bandrauk, Joseph Sanderson, Michael S. Schuurman, and François Légaré (2014). "Tabletop imaging of structural evolutions in chemical reactions demonstrated for the acetylene cation". en. In: *Nature Communications* 5, page 4422. ISSN: 2041-1723 (cited on pages 14, 22, 112, 120–123, 256, 263).

Isinger, M., R. J. Squibb, D. Busto, S. Zhong, A. Harth, D. Kroon, S. Nandi, C. L. Arnold, M. Miranda, J. M. Dahlström, E. Lindroth, R. Feifel, M. Gisselbrecht, and A. L'Huillier (2017). "Photoionization in the time and frequency domain". en. In: *Science*, eaao7043. ISSN: 0036-8075, 1095-9203.

Itatani, J., J. Levesque, D. Zeidler, H. Niikura, H. Pepin, J. C. Kieffer, P. B. Corkum, and D. M. Villeneuve (2004). "Tomographic imaging of molecular orbitals". In: *Nature* 432.7019, page 867 (cited on pages 13, 21).

Itatani, J., F. Quéré, G. L. Yudin, M. Yu. Ivanov, F. Krausz, and P. B. Corkum (2002). "Attosecond Streak Camera". In: *Phys. Rev. Lett.* 88 (17), page 173903.

Jacobson, Matthew P. and Robert W. Field (2000). "Acetylene at the Threshold of Isomerization". In: *The Journal of Physical Chemistry A* 104.14, pages 3073–3086.

Jiang, Y. H., A. Rudenko, O. Herrwerth, L. Foucar, M. Kurka, K. U. Kühnel, M. Lezius, M. F. Kling, J. van Tilborg, A. Belkacem, K. Ueda, S. Düsterer, R. Treusch, C. D. Schröter, R. Moshammer, and J. Ullrich (2010). "Ultrafast Extreme Ultraviolet Induced Isomerization of Acetylene Cations". In: *Phys. Rev. Lett.* 105 (26), page 263002.

Jiang, Y H, A Senftleben, M Kurka, A Rudenko, L Foucar, O Herrwerth, M F Kling, M Lezius, J V Tilborg, A Belkacem, K Ueda, D Rolles, R Treusch, Y Z Zhang, Y F Liu, C D Schröter, J Ullrich, and R Moshammer (2013). "Ultrafast dynamics in acetylene clocked in a femtosecond XUV stopwatch". In: *Journal of Physics B: Atomic, Molecular and Optical Physics* 46.16, page 164027.

Jiménez-Galán, Álvaro, Nickolai Zhavoronkov, Marcel Schloz, Felipe Morales, and Misha Ivanov (2017). "Time-resolved high harmonic spectroscopy of dynamical symmetry breaking in bi-circular laser fields: the role of Rydberg states". In: *Opt. Express* 25.19, pages 22880–22896.

Johnson, A. S., L. Miseikis, D. A. Wood, D. R. Austin, C. Brahms, S. Jarosch, C. S. Strüber, P. Ye, and J. P. Marangos (2016). "Measurement of sulfur L2,3 and carbon K edge XANES in a polythiophene film using a high harmonic supercontinuum". In: *Structural Dynamics* 3.6, page 062603.

Johnson, B. R. (1978). "The renormalized Numerov method applied to calculating bound states of the coupledchannel Schroedinger equation". In: *The Journal of Chemical Physics* 69.10, pages 4678–4688.

Kabachnik, N M and I P Sazhina (1976). "Angular distribution and polarization of photoelectrons in the region of resonances". In: *Journal of Physics B: Atomic and Molecular Physics* 9.10, page 1681.

Karimi, E., R. W. Boyd, P. de la Hoz, H. de Guise, J. Řehá ček, Z. Hradil, A. Aiello, G. Leuchs, and L. L. Sánchez-Soto (2014). "Radial quantum number of Laguerre-Gauss modes". In: *Phys. Rev. A* 89 (6), page 063813.

Kastner, Alexander, Tom Ring, Bastian C. Krüger, G. Barratt Park, Tim Schäfer, Arne Senftleben, and Thomas Baumert (2017). "Intermediate state dependence of the photoelectron circular dichroism of fenchone observed via femtosecond resonance-enhanced multi-photon ionization". In: *The Journal of Chemical Physics* 147.1, page 013926.

Kelkensberg, F., W. Siu, J. F. Pérez-Torres, F. Morales, G. Gademann, A. Rouzée, P. Johnsson, M. Lucchini, F. Calegari, J. L. Sanz-Vicario, F. Martın, and M. J. J. Vrakking (2011). "Attosecond Control in Photoionization of Hydrogen Molecules". In: *Phys. Rev. Lett.* 107 (4), page 043002.

Kfir, Ofer, Patrik Grychtol, Emrah Turgut, Ronny Knut, Dmitriy Zusin, Dimitar Popmintchev, Tenio Popmintchev, Hans Nembach, Justin M. Shaw, Avner Fleischer, Henry Kapteyn, Margaret Murnane, and Oren Cohen (2015). "Generation of bright phase-matched circularly-polarized extreme ultraviolet high harmonics". In: *Nat Photon* 9.2, pages 99–105. ISSN: 1749-4885.

Kim, Hong Lae and Richard Bersohn (1997). "Control of photofragment angular distribution by laser phase variation". In: *The Journal of Chemical Physics* 107.12, pages 4546–4550.

Kim, K.T., C. Chunmei Zhang, T. Ruchon, J.-F. Hergott, T. Auguste, D.M. Villeneuve, P.B. Corkum, and F. Quéré (2013). "Photonic streaking of attosecond pulse trains". In: *Nature Photonics* 7, pages 651–656.

Kleiman, Valeria D., Langchi Zhu, Xiaonong Li, and Robert J. Gordon (1995). "Coherent phase control of the photoionization of H2S". In: *The Journal of Chemical Physics* 102.14, pages 5863–5866.

Kling, M. F., Ch Siedschlag, A. J. Verhoef, J. I. Khan, M. Schultze, Th Uphues, Y. Ni, M. Uiberacker, M. Drescher, F. Krausz, and M. J. J. Vrakking (2006). "Control of Electron Localization in Molecular Dissociation". en. In: *Science* 312.5771, pages 246–248. ISSN: 0036-8075, 1095-9203.

Klünder, K., J. M. Dahlström, M. Gisselbrecht, T. Fordell, M. Swoboda, D. Guénot, P. Johnsson, J. Caillat, J. Mauritsson, A. Maquet, R. Taïeb, and A. L'Huillier (2011). "Probing Single-Photon Ionization on the Attosecond Time Scale". In: *Physical Review Letters* 106.14, page 143002 (cited on pages 13, 20, 215, 219, 220, 228).

Kobayashi, Takayoshi, Takashi Saito, and Hiroyuki Ohtani (2001). "Real-time spectroscopy of transition states in bacteriorhodopsin during retinal isomerization". en. In: *Nature* 414.6863, pages 531–534. ISSN: 1476-4687.

Kondepudi, Dilip K. and Daniel J. Durand (2001). "Chiral asymmetry in spiral galaxies?" In: *Chirality* 13.7, pages 351–356. ISSN: 1520-636X.

Kong, Fanqi, Chunmei Zhang, Frédéric Bouchard, Zhengyan Li, Graham G. Brown, Dong Hyuk Ko, T. J. Hammond, Ladan Arissian, Robert W. Boyd, Ebrahim Karimi, and P. B. Corkum (2017). "Controlling the orbital angular momentum of high harmonic vortices". En. In: *Nature Communications* 8, page 14970. ISSN: 2041-1723.

Koopmans, T (1934). "Uber die Zuordnung von Wellenfunktionen und Eigenwerten zu den Einzelnen Elektronen Eines Atoms". In: *Physica* 1.1, pages 104–113. ISSN: 0031-8914.

Kotur, M., D. Guénot, Á Jiménez-Galán, D. Kroon, E. W. Larsen, M. Louisy, S. Bengtsson, M. Miranda, J. Mauritsson, C. L. Arnold, S. E. Canton, M. Gisselbrecht, T. Carette, J. M. Dahlström, E. Lindroth, A. Maquet, L. Argenti, F. Martín, and A. L'Huillier (2016). "Spectral phase measurement of a Fano resonance using tunable attosecond pulses". en. In: *Nature Communications* 7, page 10566. ISSN: 2041-1723.

Kraus, P. M., Y. Arasaki, J. B. Bertrand, S. Patchkovskii, P. B. Corkum, D. M. Villeneuve, K. Takatsuka, and H. J. Wörner (2012). "Time-resolved high-harmonic spectroscopy of nonadiabatic dynamics in NO_2". In: *Phys. Rev. A* 85 (4), page 043409.

Krause, Jeffrey L., Kenneth J. Schafer, and Kenneth C. Kulander (1992). "High-order harmonic generation from atoms and ions in the high intensity regime". In: *Physical Review Letters* 68.24, pages 3535–3538.

Krausz, Ferenc and Misha Ivanov (2009). "Attosecond physics". In: *Rev. Mod. Phys.* 81 (1), pages 163–234 (cited on pages 13, 20).

Kremer, Manuel, Bettina Fischer, Bernold Feuerstein, Vitor L. B. de Jesus, Vandana Sharma, Christian Hofrichter, Artem Rudenko, Uwe Thumm, Claus Dieter Schröter, Robert Moshammer, and Joachim Ullrich (2009). "Electron Localization in Molecular Fragmentation of $\mathbf{H}_2$ by Carrier-Envelope Phase Stabilized Laser Pulses". In: *Phys. Rev. Lett.* 103 (21), page 213003.

Krishnan, R., J. S. Binkley, R. Seeger, and J. A. Pople (1980). "Selfconsistent molecular orbital methods. XX. A basis set for correlated wave functions". In: *The Journal of Chemical Physics* 72.1, pages 650–654.

Kübel, M., R. Siemering, C. Burger, Nora G. Kling, H. Li, A. S. Alnaser, B. Bergues, S. Zherebtsov, A. M. Azzeer, I. Ben-Itzhak, R. Moshammer, R. de Vivie-Riedle, and M. F. Kling (2016). "Steering Proton Migration in Hydrocarbons Using Intense Few-Cycle Laser Fields". In: *Physical Review Letters* 116.19, page 193001.

Kuchiev, M. Yu. (1987). "Atomic antenna". In: *JETP* 45, page 404.

Kuga, Takahiro, Yoshio Torii, Noritsugu Shiokawa, Takuya Hirano, Yukiko Shimizu, and Hiroyuki Sasada (1997). "Novel Optical Trap of Atoms with a Doughnut Beam". In: *Phys. Rev. Lett.* 78 (25), pages 4713–4716.

Lai, Chien-Jen, Kyung-Han Hong, Jonathas P Siqueira, Peter Krogen, Chun-Lin Chang, Gregory J Stein, Houkun Liang, Phillip D Keathley, Guillaume Laurent, Jeffrey Moses, Luis E Zapata, and Franz X Kärtner (2015). "Multi-mJ mid-infrared kHz OPCPA and Yb-doped pump lasers for tabletop coherent soft x-ray generation". In: *Journal of Optics* 17.9, page 094009.

Lavery, Martin P. J., Fiona C. Speirits, Stephen M. Barnett, and Miles J. Padgett (2013). "Detection of a Spinning Object Using Light's Orbital Angular Momentum". en. In: *Science* 341.6145, pages 537–540. ISSN: 0036-8075, 1095-9203.

Le, Anh-Thu, R. R. Lucchese, S. Tonzani, T. Morishita, and C. D. Lin (2009). "Quantitative rescattering theory for high-order harmonic generation from molecules". In: *Phys. Rev. A* 80 (1), page 013401.

Légaré, F., Kevin F. Lee, I. V. Litvinyuk, P. W. Dooley, S. S. Wesolowski, P. R. Bunker, P. Dombi, F. Krausz, A. D. Bandrauk, D. M. Villeneuve, and P. B. Corkum (2005). "Laser Coulomb-explosion imaging of small molecules". In: *Phys. Rev. A* 71 (1), page 013415.

Lehmann, C.S., N. Bhargava Ram, I. Powis, and M.H.M. Janssen (2013). "Imaging photoelectron circular dichroism of chiral molecules by femtosecond multiphoton coincidence detection". In: *The Journal of Chemical Physics* 139.23, page 234307. ISSN: 0021-9606 (cited on pages 15, 22, 155, 162, 174, 175, 177).

Lewenstein, M., Ph. Balcou, M. Yu. Ivanov, Anne L'Huillier, and P. B. Corkum (1994). "Theory of high-harmonic generation by low-frequency laser fields". In: *Physical Review A* 49.3, pages 2117–2132.

Liao, Chen-Ting, Arvinder Sandhu, Seth Camp, Kenneth J. Schafer, and Mette B. Gaarde (2015). "Beyond the Single-Atom Response in Absorption Line Shapes: Probing a Dense, Laser-Dressed Helium Gas with Attosecond Pulse Trains". In: *Physical Review Letters* 114.14, page 143002.

Liekhus-Schmaltz, Chelsea, Gregory A. McCracken, Andreas Kaldun, James P. Cryan, and Philip H. Bucksbaum (2016). "Coherent control using kinetic energy and the geometric phase of a conical intersection". In: *The Journal of Chemical Physics* 145.14, page 144304.

López-Martens, R. B., T. W. Schmidt, and G. Roberts (2000). "ac Stark shifts in Rydberg NO levels induced by intense laser pulses". In: *Physical Review A* 62.1, page 013414.

Lucchini, M., S. A. Sato, A. Ludwig, J. Herrmann, M. Volkov, L. Kasmi, Y. Shinohara, K. Yabana, L. Gallmann, and U. Keller (2016). "Attosecond dynamical Franz-Keldysh effect in polycrystalline diamond". en. In: *Science* 353.6302, pages 916–919. ISSN: 0036-8075, 1095-9203.

Lux, Christian, Arne Senftleben, Cristian Sarpe, Matthias Wollenhaupt, and Thomas Baumert (2016). "Photoelectron circular dichroism observed in the above-threshold ionization signal from chiral molecules with femtosecond laser pulses". en. In: *Journal of Physics B: Atomic, Molecular and Optical Physics* 49.2, 02LT01. ISSN: 0953-4075.

Lux, Christian, Matthias Wollenhaupt, Tom Bolze, Qingqing Liang, Jens Köhler, Cristian Sarpe, and Thomas Baumert (2012). "Circular Dichroism in the Photoelectron Angular Distributions of Camphor and Fenchone from Multiphoton Ionization with Femtosecond Laser Pulses". In: *Angewandte Chemie International Edition* 51.20, pages 5001–5005. ISSN: 1521-3773 (cited on pages 15, 22, 154–156, 174).

Lux, Christian, Matthias Wollenhaupt, Cristian Sarpe, and Thomas Baumert (2015). "Photoelectron Circular Dichroism of Bicyclic Ketones from Multiphoton Ionization with Femtosecond Laser Pulses". In: *ChemPhysChem* 16.1, pages 7–7. ISSN: 1439-7641.

MacDermott, A.J., L.D. Barron, A. Brack, T. Buhse, A.F. Drake, R. Emery, G. Gottarelli, J.M. Greenberg, R. Haberle, R.A. Hegstrom, K. Hobbs, D.K. Kondepudi, C. McKay, S. Moorbath, F. Raulin, M. Sandford, D.W. Schwartzman, W.H.-P. Thiemann, G.E. Tranter, and J.C. Zarnecki (1996). "Homochirality as the signature of life: the SETH Cigar". In: *Planetary and Space Science* 44.11, pages 1441–1446. ISSN: 0032-0633.

Madjet, Mohamed El-Amine, Zheng Li, and Oriol Vendrell (2013). "Ultrafast hydrogen migration in acetylene cation driven by non-adiabatic effects". In: *The Journal of Chemical Physics* 138.9, page 094311.

Madjet, Mohamed El-Amine, Oriol Vendrell, and Robin Santra (2011). "Ultrafast Dynamics of Photoionized Acetylene". In: *Phys. Rev. Lett.* 107 (26), page 263002.

Mahieu, Benoît, David Gauthier, Michel Perdrix, Xunyou Ge, Willem Boutu, Fabien Lepetit, Fan Wang, Bertrand Carré, Thierry Auguste, Hamed Merdji, David Garzella, and Olivier Gobert (2015). "Spatial quality improvement of a Ti:Sapphire laser beam by modal filtering". In: *Applied Physics B* 118.1, pages 47–60. ISSN: 1432-0649.

Maiman, T.H. (1960). "Stimulated Optical Radiation in Ruby". In: *Nature* 187, pages 493–494 (cited on pages 12, 20, 25).

Mair, Alois, Alipasha Vaziri, Gregor Weihs, and Anton Zeilinger (2001). "Entanglement of the orbital angular momentum states of photons". en. In: *Nature* 412.6844, pages 313–316. ISSN: 1476-4687.

Mairesse, Y., J. Higuet, N. Dudovich, D. Shafir, B. Fabre, E. Mével, E. Constant, S. Patchkovskii, Z. Walters, M. Yu. Ivanov, and O. Smirnova (2010). "High Harmonic Spectroscopy of Multichannel Dynamics in Strong-Field Ionization". In: *Physical Review Letters* 104.21. ISSN: 0031-9007, 1079-7114.

Mammana, Angela, Gregory T. Carroll, Jetsuda Areephong, and Ben L. Feringa (2011). "A Chiroptical Photoswitchable DNA Complex". In: *The Journal of Physical Chemistry B* 115.40. PMID: 21879715, pages 11581–11587.

Mancuso, Christopher A., Daniel D. Hickstein, Kevin M. Dorney, Jennifer L. Ellis, Elvedin Hasovi ć, Ronny Knut, Patrik Grychtol, Christian Gentry, Maithreyi Gopalakrishnan, Dmitriy Zusin, Franklin J. Dollar, Xiao-Min Tong, Dejan B. Milo ševi ć, Wilhelm Becker, Henry C. Kapteyn, and Margaret M. Murnane (2016). "Controlling electron-ion rescattering in two-color circularly polarized femtosecond laser fields". In: *Phys. Rev. A* 93 (5), page 053406.

Mancuso, Christopher A., Daniel D. Hickstein, Patrik Grychtol, Ronny Knut, Ofer Kfir, Xiao-Min Tong, Franklin Dollar, Dmitriy Zusin, Maithreyi Gopalakrishnan, Christian Gentry, Emrah Turgut, Jennifer L. Ellis, Ming-Chang Chen, Avner Fleischer, Oren Cohen, Hehaesnry C. Kapteyn, and Margaret M. Murnane (2015). "Strong-field ionization with two-color circularly polarized laser fields". In: *Phys. Rev. A* 91 (3), page 031402.

Marangos, J P (2016). "Development of high harmonic generation spectroscopy of organic molecules and biomolecules". In: *Journal of Physics B: Atomic, Molecular and Optical Physics* 49.13, page 132001 (cited on pages 13, 21).

Marcatili, E. A. J. and R. A. Schmeltzer (1964). "Hollow metallic and dielectric waveguides for long distance optical transmission and lasers". In: *The Bell System Technical Journal* 43.4, pages 1783–1809. ISSN: 0005-8580.

Marian, Adela, Matthew C. Stowe, John R. Lawall, Daniel Felinto, and Jun Ye (2004). "United Time-Frequency Spectroscopy for Dynamics and Global Structure". en. In: *Science* 306.5704, pages 2063–2068. ISSN: 0036-8075, 1095-9203.

Mashiko, Hiroki, Steve Gilbertson, Chengquan Li, Sabih D. Khan, Mahendra M. Shakya, Eric Moon, and Zenghu Chang (2008). "Double Optical Gating of High-Order Harmonic Generation with Carrier-Envelope Phase Stabilized Lasers". In: *Phys. Rev. Lett.* 100 (10), page 103906.

Massari, M., G. Ruffato, M. Gintoli, F. Ricci, and F. Romanato (2015). "Fabrication and characterization of high-quality spiral phase plates for optical applications". In: *Appl. Opt.* 54.13, pages 4077–4083.

Matsuda, Akitaka, Mizuho Fushitani, Eiji J. Takahashi, and Akiyoshi Hishikawa (2011). "Visualizing hydrogen atoms migrating in acetylene dication by time-resolved three-body and four-body Coulomb explosion imaging". en. In: *Physical Chemistry Chemical Physics* 13.19, pages 8697–8704.

Mauguière, Frédéric A. L., Peter Collins, Zeb C. Kramer, Barry K. Carpenter, Gregory S. Ezra, Stavros C. Farantos, and Stephen Wiggins (2015). "Phase Space Structures

Explain Hydrogen Atom Roaming in Formaldehyde Decomposition". In: *The Journal of Physical Chemistry Letters* 6.20, pages 4123–4128. ISSN: 1948-7185.

Maurer, Jochen, Darko Dimitrovski, Lauge Christensen, Lars Bojer Madsen, and Henrik Stapelfeldt (2012). "Molecular-Frame 3D Photoelectron Momentum Distributions by Tomographic Reconstruction". In: *Phys. Rev. Lett.* 109 (12), page 123001.

McFarland, Brian K., Joseph P. Farrell, Philip H. Bucksbaum, and Markus Gühr (2008). "High Harmonic Generation from Multiple Orbitals in N2". en. In: *Science* 322.5905, pages 1232–1235. ISSN: 0036-8075, 1095-9203.

McPherson, A., G. Gibson, H. Jara, U. Johann, T. S. Luk, I. A. McIntyre, K. Boyer, and C. K. Rhodes (1987). "Studies of multiphoton production of vacuum-ultraviolet radiation in the rare gases". In: *J. Opt. Soc. Am. B* 4.4, pages 595–601 (cited on pages 12, 20, 26, 43, 45).

Medcraft, Chris, Robert Wolf, and Melanie Schnell (2014). "High-Resolution Spectroscopy of the Chiral Metal Complex [CpRe(CH3)(CO)(NO)]: A Potential Candidate for Probing Parity Violation". en. In: *Angewandte Chemie International Edition* 53.43, pages 11656–11659. ISSN: 1521-3773.

Medisauskas, Lukas, Jack Wragg, Hugo van der Hart, and Misha Yu. Ivanov (2015). "Generating Isolated Elliptically Polarized Attosecond Pulses Using Bichromatic Counterrotating Circularly Polarized Laser Fields". In: *Phys. Rev. Lett.* 115 (15), page 153001.

Meinert, Cornelia and Uwe J. Meierhenrich (2012). "A New Dimension in Separation Science: Comprehensive Two-Dimensional Gas Chromatography". In: *Angewandte Chemie International Edition* 51.42, pages 10460–10470. ISSN: 1521-3773.

Mendoza-Hernández, Job, Maximino Luis Arroyo-Carrasco, Marcelo David Iturbe-Castillo, and Sabino Chávez-Cerda (2015). "Laguerre–Gauss beams versus Bessel beams showdown: peer comparison". In: *Opt. Lett.* 40.16, pages 3739–3742.

Miles, J., D. Fernandes, A. Young, C.M.M. Bond, S.W. Crane, O. Ghafur, D. Townsend, J. Sá, and J.B. Greenwood (2017). "A New Experimental Paradigm for Probing Chirality". In: *Submitted*.

Millack, Thomas and Alfred Maquet (1993). "Hyper-Raman Lines Produced During High Harmonic Generation". In: *Journal of Modern Optics* 40.11, pages 2161–2171.

Moore, L. R., M. A. Lysaght, J. S. Parker, H. W. van der Hart, and K. T. Taylor (2011). "Time delay between photoemission from the 2p and 2s subshells of neon". In: *Phys. Rev. A* 84 (6), page 061404.

Nafie, Laurence A. (1997). "INFRARED AND RAMAN VIBRATIONAL OPTICAL ACTIVITY: Theoretical and Experimental Aspects". In: *Annual Review of Physical Chemistry* 48.1, pages 357–386.

Nagy, Tamas, Michael Forster, and Peter Simon (2008). "Flexible hollow fiber for pulse compressors". In: *Appl. Opt.* 47.18, pages 3264–3268.

Nagy, Tamas, Vladimir Pervak, and Peter Simon (2011). "Optimal pulse compression in long hollow fibers". In: *Opt. Lett.* 36.22, pages 4422–4424.

Nahon, Laurent and Christian Alcaraz (2004). "SU5: a calibrated variable-polarization synchrotron radiation beam line in the vacuum-ultraviolet range". In: *Appl. Opt.* 43.5, pages 1024–1037.

Nahon, Laurent, Gustavo A. Garcia, Chris J. Harding, Elisabeth Mikajlo, and Ivan Powis (2006). "Determination of chiral asymmetries in the valence photoionization of camphor enantiomers by photoelectron imaging using tunable circularly polarized light". In: *The Journal of Chemical Physics* 125.11, page 114309.

Nahon, Laurent, Gustavo A. Garcia, and Ivan Powis (2015). "Valence shell one-photon photoelectron circular dichroism in chiral systems". In: *Journal of Electron Spectroscopy*

and Related Phenomena 204, Part B. Gas phase spectroscopic and dynamical studies at Free-Electron Lasers and other short wavelength sources, pages 322–334. ISSN: 0368-2048.

Nahon, Laurent, Gustavo A. Garcia, Héloıse Soldi-Lose, Steven Daly, and Ivan Powis (2010). "Effects of dimerization on the photoelectron angular distribution parameters from chiral camphor enantiomers obtained with circularly polarized vacuum-ultraviolet radiation". In: *Phys. Rev. A* 82 (3), page 032514.

Nahon, Laurent, Lipsa Nag, Gustavo A. Garcia, Iuliia Myrgorodska, Uwe Meierhenrich, Samuel Beaulieu, Vincent Wanie, Valérie Blanchet, Romain Géneaux, and Ivan Powis (2016). "Determination of accurate electron chiral asymmetries in fenchone and camphor in the VUV range: sensitivity to isomerism and enantiomeric purity". en. In: *Physical Chemistry Chemical Physics* 18.18, pages 12696–12706. ISSN: 1463-9084.

Nahon, Laurent, Nelson de Oliveira, Gustavo A. Garcia, Jean-François Gil, Bertrand Pilette, Olivier Marcouillé, Bruno Lagarde, and François Polack (2012). "DESIRS: a state-of-the-art VUV beamline featuring high resolution and variable polarization for spectroscopy and dichroism at SOLEIL". In: *Journal of Synchrotron Radiation* 19.4, pages 508–520.

Nambu, Y. and G. Jona-Lasinio (1961). "Dynamical Model of Elementary Particles Based on an Analogy with Superconductivity. I". In: *Phys. Rev.* 122 (1), pages 345–358.

Neidel, Ch., J. Klei, C.-H. Yang, A. Rouzée, M. J. J. Vrakking, K. Klünder, M. Miranda, C. L. Arnold, T. Fordell, A. L'Huillier, M. Gisselbrecht, P. Johnsson, M. P. Dinh, E. Suraud, P.-G. Reinhard, V. Despré, M. A. L. Marques, and F. Lépine (2013). "Probing Time-Dependent Molecular Dipoles on the Attosecond Time Scale". In: *Phys. Rev. Lett.* 111 (3), page 033001 (cited on pages 13, 20).

Nisoli, M., S. De Silvestri, and O. Svelto (1996). "Generation of high energy 10 fs pulses by a new pulse compression technique". In: *Applied Physics Letters* 68.20, pages 2793–2795.

Nisoli, M., S. De Silvestri, O. Svelto, R. Szipöcs, K. Ferencz, Ch. Spielmann, S. Sartania, and F. Krausz (1997). "Compression of high-energy laser pulses below 5 fs". In: *Opt. Lett.* 22.8, pages 522–524.

Nurhuda, Muhammad, Akira Suda, Katsumi Midorikawa, Masatoshi Hatayama, and Keigo Nagasaka (2003). "Propagation dynamics of femtosecond laser pulses in a hollow fiber filled with argon: constant gas pressure versus differential gas pressure". In: *J. Opt. Soc. Am. B* 20.9, pages 2002–2011.

Ordonez, Andres F. and Olga Smirnova (2018). "Generalized perspective on chiral measurements without magnetic interactions". In: *arXiv:1802.06540 [physics, physics:quant-ph]*. arXiv: 1802.06540.

Osipov, T, T N Rescigno, T Weber, S Miyabe, T Jahnke, A S Alnaser, M P Hertlein, O Jagutzki, L Ph H Schmidt, M Schöffler, L Foucar, S Schössler, T Havermeier, M Odenweller, S Voss, B Feinberg, A L Landers, M H Prior, R Dörner, C L Cocke, and A Belkacem (2008). "Fragmentation pathways for selected electronic states of the acetylene dication". In: *Journal of Physics B: Atomic, Molecular and Optical Physics* 41.9, page 091001.

Ott, Christian, Andreas Kaldun, Philipp Raith, Kristina Meyer, Martin Laux, Jörg Evers, Christoph H. Keitel, Chris H. Greene, and Thomas Pfeifer (2013). "Lorentz Meets Fano in Spectral Line Shapes: A Universal Phase and Its Laser Control". en. In: *Science* 340.6133, pages 716–720. ISSN: 0036-8075, 1095-9203.

Patterson, David and John M. Doyle (2013a). "Sensitive Chiral Analysis via Microwave Three-Wave Mixing". In: *Phys. Rev. Lett.* 111 (2), page 023008.

Patterson, David, Melanie Schnell, and John M. Doyle (2013b). "Enantiomer-specific detection of chiral molecules via microwave spectroscopy". En. In: *Nature* 497.7450, page 475. ISSN: 1476-4687.

Paul, P. M., E. S. Toma, P. Breger, G. Mullot, Ph. Balcou, H. G. Muller, and P. Agostini (2001). "Observation of a Train of Attosecond Pulses from High Harmonic Generation". In: *Science* 292, page 1689 (cited on pages 12, 20, 26, 46, 128).

Paulus, G G, W Becker, W Nicklich, and H Walther (1994). "Rescattering effects in above-threshold ionization: a classical model". In: *Journal of Physics B: Atomic, Molecular and Optical Physics* 27.21, page L703.

Pavicic, Domagoj, Kevin F. Lee, D. M. Rayner, P. B. Corkum, and D. M. Villeneuve (2007). "Direct Measurement of the Angular Dependence of Ionization for N_{2}, O_{2}, and CO_{2} in Intense Laser Fields". In: *Physical Review Letters* 98.24. ISSN: 0031-9007, 1079-7114.

Pertot, Yoann, Cédric Schmidt, Mary Matthews, Adrien Chauvet, Martin Huppert, Vit Svoboda, Aaron von Conta, Andres Tehlar, Denitsa Baykusheva, Jean-Pierre Wolf, and Hans Jakob Wörner (2017). "Time-resolved x-ray absorption spectroscopy with a water window high-harmonic source". In: *Science* 355.6322, pages 264–267. ISSN: 0036-8075.

Piancastelli, M.N (1999). "The neverending story of shape resonances". In: *Journal of Electron Spectroscopy and Related Phenomena* 100.1–3, pages 167–190. ISSN: 0368-2048.

Picón, A., J. Mompart, J. R. Vázquez de Aldana, L. Plaja, G. F. Calvo, and L. Roso (2010). "Photoionization with orbital angular momentum beams". In: *Opt. Express* 18.4, pages 3660–3671.

Plick, William N. and Mario Krenn (2015). "Physical meaning of the radial index of Laguerre-Gauss beams". In: *Phys. Rev. A* 92 (6), page 063841.

Pons, Maria Llusa, Richard Taieb, and Alfred Maquet (1996). "Importance of population transfers in high-order harmonic-generation spectra". In: *Phys. Rev. A* 54 (4), pages 3634–3641.

Popmintchev, Tenio, Ming-Chang Chen, Alon Bahabad, Michael Gerrity, Pavel Sidorenko, Oren Cohen, Ivan P Christov, Margaret M Murnane, and Henry C Kapteyn (2009). "Phase Matching of High Harmonic Generation in the Soft and Hard X-Ray Regions of the Spectrum". en. In: *Proceedings of the National Academy of Sciences* 106.26, pages 10516–10521. ISSN: 0027-8424, 1091-6490.

Popmintchev, Tenio, Ming-Chang Chen, Dimitar Popmintchev, Paul Arpin, Susannah Brown, Skirmantas Ališauskas, Giedrius Andriukaitis, Tadas Balčiunas, Oliver D. Mücke, Audrius Pugzlys, Andrius Baltuška, Bonggu Shim, Samuel E. Schrauth, Alexander Gaeta, Carlos Hernández-Garcıa, Luis Plaja, Andreas Becker, Agnieszka Jaron-Becker, Margaret M. Murnane, and Henry C. Kapteyn (2012). "Bright Coherent Ultrahigh Harmonics in the keV X-ray Regime from Mid-Infrared Femtosecond Lasers". In: *Science* 336.6086, pages 1287–1291. ISSN: 0036-8075.

Porter, G. (1950). "Flash photolysis and spectroscopy. A new method for the study of free radical reactions". en. In: *Proc. R. Soc. Lond. A* 200.1061, pages 284–300. ISSN: 0080-4630, 2053-9169 (cited on pages 12, 20).

Powis, Ivan (2000). "Photoelectron circular dichroism of the randomly oriented chiral molecules glyceraldehyde and lactic acid". In: *The Journal of Chemical Physics* 112.1, pages 301–310.

Powis, Ivan, Steven Daly, Maurice Tia, Barbara Cunha de Miranda, Gustavo A. Garcia, and Laurent Nahon (2014). "A photoionization investigation of small, homochiral clusters of glycidol using circularly polarized radiation and velocity map electron-ion coincidence imaging". In: *Phys. Chem. Chem. Phys.* 16 (2), pages 467–476.

Powis, Ivan, Steven Daly, Maurice Tia, Barbara Cunha de Miranda, Gustavo A. Garcia, and Laurent Nahon (2013). "A photoionization investigation of small, homochiral clusters of glycidol using circularly polarized radiation and velocity map electron–ion coincidence imaging". en. In: *Physical Chemistry Chemical Physics* 16.2, pages 467–476. ISSN: 1463-9084.

Powis, Ivan, Chris J. Harding, Gustavo A. Garcia, and Laurent Nahon (2008). "A Valence Photoelectron Imaging Investigation of Chiral Asymmetry in the Photoionization of Fenchone and Camphor". en. In: *Chem. Phys. Chem.* 9.3, pages 475–483. ISSN: 1439-7641.

Powis, Ivan, Minna Patanen, Egill Antonsson, Christophe Nicolas, Catalin Miron, and David M. P. Holland (2017). "Vibration-dependent photoelectron angular distributions and branching ratios observed across the Cooper-minimum region of bromobenzene". In: *Phys. Rev. A* 96 (1), page 013413.

Prokhorenko, Valentyn I., Andrea M. Nagy, Stephen A. Waschuk, Leonid S. Brown, Robert R. Birge, and R. J. Dwayne Miller (2006). "Coherent Control of Retinal Isomerization in Bacteriorhodopsin". en. In: *Science* 313.5791, pages 1257–1261. ISSN: 0036-8075, 1095-9203.

Pulm, Friedhelm, Jörg Schramm, Josef Hormes, Stefan Grimme, and Sigrid D. Peyerimhoff (1997). "Theoretical and experimental investigations of the electronic circular dichroism and absorption spectra of bicyclic ketones". In: *Chemical Physics* 224.2, pages 143–155. ISSN: 0301-0104.

Quéré, F., H. Vincenti, A. Borot, S. Monchocé, T. J. Hammond, Kyung Taec Kim, J. A. Wheeler, Chunmei Zhang, T. Ruchon, T. Auguste, J. F. Hergott, D. M. Villeneuve, P. B. Corkum, and R. Lopez-Martens (2014). "Applications of ultrafast wavefront rotation in highly nonlinear optics". en. In: *Journal of Physics B: Atomic, Molecular and Optical Physics* 47.12, page 124004. ISSN: 0953-4075.

Rafiee Fanood, M.M., M.H.M. Janssen, and I. Powis (2016). "Wavelength dependent photoelectron circular dichroism of limonene studied by femtosecond multiphoton laser ionization and electron-ion coincidence imaging". In: *The Journal of Chemical Physics* 145.12, page 124320. ISSN: 0021-9606.

Rafiee Fanood, Mohammad M, Hassan Ganjitabar, Gustavo A Garcia, Laurent Nahon, Stefano Turchini, and Ivan Powis (2017). "Intense Vibronic Modulation of the Chiral Photoelectron Angular Distribution Generated by Photoionization of Limonene Enantiomers with Circularly Polarized Synchrotron Radiation". en. In: *ChemPhysChem*. ISSN: 14394235.

Rafiee Fanood, Mohammad M., Maurice H. M. Janssen, and Ivan Powis (2015). "Enantioselective femtosecond laser photoionization spectrometry of limonene using photoelectron circular dichroism". In: *Phys. Chem. Chem. Phys.* 17 (14), pages 8614–8617.

Rafiee Fanood, Mohammad M., Ivan Powis, and Maurice H. M. Janssen (2014). "Chiral Asymmetry in the Multiphoton Ionization of Methyloxirane Using Femtosecond Electron–Ion Coincidence Imaging". In: *The Journal of Physical Chemistry A* 118.49. PMID: 25402546, pages 11541–11546.

Rausch, Stefan, Thomas Binhammer, Anne Harth, Franz X. Kärtner, and Uwe Morgner (2008). "Few-cycle femtosecond field synthesizer". In: *Opt. Express* 16.22, pages 17410–17419.

Ray, D., F. He, S. De, W. Cao, H. Mashiko, P. Ranitovic, K. P. Singh, I. Znakovskaya, U. Thumm, G. G. Paulus, M. F. Kling, I. V. Litvinyuk, and C. L. Cocke (2009). "Ion-Energy Dependence of Asymmetric Dissociation of $\mathbf{D}_2$ by a Two-Color Laser Field". In: *Phys. Rev. Lett.* 103 (22), page 223201.

Reduzzi, Maurizio, Johan Hummert, Antoine Dubrouil, Francesca Calegari, Mauro Nisoli, Fabio Frassetto, Luca Poletto, Shaohao Chen, Mengxi Wu, Mette B. Gaarde, Kenneth Schafer, and Giuseppe Sansone (2015). "Polarization control of absorption of virtual dressed states in helium". In: *Physical Review A* 92.3, page 033408.

Reed, Murray K., Michael K. Steiner-Shepard, and Daniel K. Negus (1994). "Widely tunable femtosecond optical parametric amplifier at 250 kHz with a Ti:sapphire regenerative amplifier". In: *Opt. Lett.* 19.22, pages 1855–1857.

Rego, Laura, Julio San Román, Antonio Picón, Luis Plaja, and Carlos Hernández-Garcıa (2016). "Nonperturbative Twist in the Generation of Extreme-Ultraviolet Vortex Beams". In: *Phys. Rev. Lett.* 117 (16), page 163202.

Rennie, Emma E, Ivan Powis, Uwe Hergenhahn, Oliver Kugeler, Gustavo Garcia, Toralf Lischke, and Simon Marburger (2002). "Valence and C 1s core level photoelectron spectra of camphor". In: *Journal of Electron Spectroscopy and Related Phenomena* 125.3, pages 197–203. ISSN: 0368-2048.

Ritchie, Burke (1976). "Theory of the angular distribution of photoelectrons ejected from optically active molecules and molecular negative ions". In: *Physical Review A* 13.4, pages 1411–1415 (cited on pages 15, 22, 140, 142, 146, 154, 236).

Rotermund, F, V Petrov, and F Noack (2000). "Difference-frequency generation of intense femtosecond pulses in the mid-IR (4–12 m) using HgGa2S4 and AgGaS2". In: *Optics Communications* 185.1, pages 177–183. ISSN: 0030-4018.

Roudnev, V. and B. D. Esry (2007). "General Theory of Carrier-Envelope Phase Effects". In: *Phys. Rev. Lett.* 99 (22), page 220406.

Rupenyan, A., P. M. Kraus, J. Schneider, and H. J. Wörner (2013). "Quantum interference and multielectron effects in high-harmonic spectra of polar molecules". In: *Physical Review A* 87.3, page 031401.

Salakhutdinov, V. D., E. R. Eliel, and W. Löffler (2012). "Full-Field Quantum Correlations of Spatially Entangled Photons". In: *Phys. Rev. Lett.* 108 (17), page 173604.

Sansone, G., E. Benedetti, F. Calegari, C. Vozzi, L. Avaldi, R. Flammini, L. Poletto, P. Villoresi, C. Altucci, R. Velotta, S. Stagira, S. De Silvestri, and M. Nisoli (2006). "Isolated Single-Cycle Attosecond Pulses". In: *Science* 314.5798, pages 443–446. ISSN: 0036-8075.

Sansone, G., F. Kelkensberg, J. F. Pérez-Torres, F. Morales, M. F. Kling, W. Siu, O. Ghafur, P. Johnsson, M. Swoboda, E. Benedetti, F. Ferrari, F. Lépine, J. L. Sanz-Vicario, S. Zherebtsov, I. Znakovskaya, A. L'Huillier, M. Yu Ivanov, M. Nisoli, F. Martín, and M. J. J. Vrakking (2010). "Electron localization following attosecond molecular photoionization". en. In: *Nature* 465.7299, pages 763–766. ISSN: 1476-4687.

Schafer, K. J., Baorui Yang, L. F. DiMauro, and K. C. Kulander (1993). "Above threshold ionization beyond the high harmonic cutoff". In: *Phys. Rev. Lett.* 70.11, pages 1599–1602.

Schaftenaar, G. and J.H. Noordik (2000). "Molden: a pre- and post-processing program for molecular and electronic structures*". In: *Journal of Computer-Aided Molecular Design* 14.2, pages 123–134. ISSN: 1573-4951.

Schmidt, Bruno E., Pierre Béjot, Mathieu Giguère, Andrew D. Shiner, Carlos Trallero-Herrero, Éric Bisson, Jérôme Kasparian, Jean-Pierre Wolf, David M. Villeneuve, Jean-Claude Kieffer, Paul B. Corkum, and François Légaré (2010). "Compression of 1.8m laser pulses to sub two optical cycles with bulk material". In: *Applied Physics Letters* 96.12, page 121109.

Schmidt, Bruno E., Andrew D. Shiner, Philippe Lassonde, Jean-Claude Kieffer, Paul B. Corkum, David M. Villeneuve, and François Légaré (2011). "CEP stable 1.6 cycle laser pulses at 1.8 μm". In: *Opt. Express* 19.7, pages 6858–6864.

Schmidt, Michael W., Kim K. Baldridge, Jerry A. Boatz, Steven T. Elbert, Mark S. Gordon, Jan H. Jensen, Shiro Koseki, Nikita Matsunaga, Kiet A. Nguyen, Shujun Su, Theresa L. Windus, Michel Dupuis, and John A. Montgomery (1993). "General atomic and molecular electronic structure system". In: *Journal of Computational Chemistry* 14.11, pages 1347–1363. ISSN: 1096-987X.

Schultze, M., M. Fiess, N. Karpowicz, J. Gagnon, M. Korbman, M. Hofstetter, S. Neppl, A. L. Cavalieri, Y. Komninos, T. Mercouris, C. A. Nicolaides, R. Pazourek, S. Nagele, J. Feist, J. Burgdorfer, A. M. Azzeer, R. Ernstorfer, R. Kienberger, U. Kleineberg, E. Goulielmakis, F. Krausz, and V. S. Yakovlev (2010). "Delay in Photoemission". In: *Science* 328.5986, pages 1658–1662. ISSN: 0036-8075, 1095-9203 (cited on pages 13, 20, 220).

Schultze, Martin, Krupa Ramasesha, C. D. Pemmaraju, S. A. Sato, D. Whitmore, A. Gandman, James S. Prell, L. J. Borja, D. Prendergast, K. Yabana, Daniel M. Neumark, and Stephen R. Leone (2014). "Attosecond band-gap dynamics in silicon". en. In: *Science* 346.6215, pages 1348–1352. ISSN: 0036-8075, 1095-9203 (cited on pages 13, 20, 80).

Sedlacek, M. and M. Krumpholc (2005). "Digital measurement of phase difference - a comparative study of DSP algoriths". In: *Metrology and Measurement Systems* 12 (4), s427–448.

Sen, Ananya, S. T. Pratt, and K. L. Reid (2017). "Circular dichroism in photoelectron images from aligned nitric oxide molecules". In: *The Journal of Chemical Physics* 147.1, page 013927.

Shafir, D., Y. Mairesse, D. M. Villeneuve, P. B. Corkum, and N. Dudovich (2009). "Atomic wavefunctions probed through strong-field light–matter interaction". en. In: *Nature Physics* 5.6, pages 412–416. ISSN: 1745-2473.

Shafir, Dror, Hadas Soifer, Barry D. Bruner, Michal Dagan, Yann Mairesse, Serguei Patchkovskii, Misha Yu Ivanov, Olga Smirnova, and Nirit Dudovich (2012). "Resolving the time when an electron exits a tunnelling barrier". en. In: *Nature* 485.7398, pages 343–346. ISSN: 1476-4687.

Shepp, L. A. and J. B. Kruskal (1978). "Computerized Tomography: The New Medical X-Ray Technology". In: *The American Mathematical Monthly* 85.6, pages 420–439. ISSN: 00029890, 19300972.

Shin, Hyun Joon, Dong Gun Lee, Yong Ho Cha, Kyung Han Hong, and Chang Hee Nam (1999). "Generation of Nonadiabatic Blueshift of High Harmonics in an Intense Femtosecond Laser Field". In: *Phys. Rev. Lett.* 83 (13), pages 2544–2547.

Shiner, A. D., C. Trallero-Herrero, N. Kajumba, H.-C. Bandulet, D. Comtois, F. Légaré, M. Giguère, J-C. Kieffer, P. B. Corkum, and D. M. Villeneuve (2009). "Wavelength Scaling of High Harmonic Generation Efficiency". In: *Phys. Rev. Lett.* 103 (7), page 073902.

Shubert, V. Alvin, David Schmitz, Cristóbal Pérez, Chris Medcraft, Anna Krin, Sérgio R. Domingos, David Patterson, and Melanie Schnell (2016). "Chiral Analysis Using Broadband Rotational Spectroscopy". In: *The Journal of Physical Chemistry Letters* 7.2. PMID: 26745342, pages 341–350.

Singh, K. P., F. He, P. Ranitovic, W. Cao, S. De, D. Ray, S. Chen, U. Thumm, A. Becker, M. M. Murnane, H. C. Kapteyn, I. V. Litvinyuk, and C. L. Cocke (2010). "Control of Electron Localization in Deuterium Molecular Ions using an Attosecond Pulse Train and a Many-Cycle Infrared Pulse". In: *Phys. Rev. Lett.* 104 (2), page 023001.

Skruszewicz, S., J. Tiggesbäumker, K.-H. Meiwes-Broer, M. Arbeiter, Th. Fennel, and D. Bauer (2015). "Two-Color Strong-Field Photoelectron Spectroscopy and the Phase of the Phase". In: *Physical Review Letters* 115.4, page 043001.

Smeenk, C, L Arissian, A Staudte, D M Villeneuve, and P B Corkum (2009). "Momentum space tomographic imaging of photoelectrons". In: *Journal of Physics B: Atomic, Molecular and Optical Physics* 42.18, page 185402.

Smialek, M. A., M.-J. Hubin-Franskin, J. Delwiche, D. Duflot, N. J. Mason, S. Vronning-Hoffmann, G. G. B. de Souza, A. M. Ferreira Rodrigues, F. N. Rodrigues, and P. Limao-Vieira (2012). "Limonene: electronic state spectroscopy by high-resolution vacuum ultraviolet photoabsorption, electron scattering, He(i) photoelectron spectroscopy and ab initio calculations". In: *Phys. Chem. Chem. Phys.* 14 (6), pages 2056–2064.

Smirnova, Olga, Yann Mairesse, and Serguei Patchkovskii (2015). "Opportunities for chiral discrimination using high harmonic generation in tailored laser fields". en. In: *Journal of Physics B: Atomic, Molecular and Optical Physics* 48.23, page 234005. ISSN: 0953-4075.

Smirnova, Olga, Yann Mairesse, Serguei Patchkovskii, Nirit Dudovich, David Villeneuve, Paul Corkum, and Misha Yu. Ivanov (2009). "High harmonic interferometry of multi-electron dynamics in molecules". In: *Nature* 460.7258, pages 972–977. ISSN: 0028-0836, 1476-4687.

Smith, L. Montgomery, Dennis R. Keefer, and S.I. Sudharsanan (1988). "Abel inversion using transform techniques". In: *Journal of Quantitative Spectroscopy and Radiative Transfer* 39.5, pages 367–373. ISSN: 0022-4073.

Soifer, H., P. Botheron, D. Shafir, A. Diner, O. Raz, B. D. Bruner, Y. Mairesse, B. Pons, and N. Dudovich (2010). "Near-Threshold High-Order Harmonic Spectroscopy with Aligned Molecules". In: *Phys. Rev. Lett.* 105 (14), page 143904.

Song, Qiying, Peifen Lu, Xiaochun Gong, Qinying Ji, Kang Lin, Wenbin Zhang, Junyang Ma, Heping Zeng, and Jian Wu (2017). "Dissociative double ionization of CO in orthogonal two-color laser fields". In: *Phys. Rev. A* 95 (1), page 013406.

Stener, M., G. Fronzoni, D. Di Tommaso, and P. Decleva (2004). "Density functional study on the circular dichroism of photoelectron angular distribution from chiral derivatives of oxirane". In: *The Journal of Chemical Physics* 120.7, pages 3284–3296.

Stibenz, Gero, Nickolai Zhavoronkov, and Günter Steinmeyer (2006). "Self-compression of millijoule pulses to 7.8 fs duration in a white-light filament". In: *Opt. Lett.* 31.2, pages 274–276.

Strelkov, V. (2010). "Role of Autoionizing State in Resonant High-Order Harmonic Generation and Attosecond Pulse Production". In: *Phys. Rev. Lett.* 104 (12), page 123901.

Strickland, Donna and Gerard Mourou (1985). "Compression of amplified chirped optical pulses". In: *Optics Communications* 56.3, pages 219–221. ISSN: 0030-4018.

Sueda, K., G. Miyaji, N. Miyanaga, and M. Nakatsuka (2004). "Laguerre-Gaussian beam generated with a multilevel spiral phase plate for high intensity laser pulses". In: *Opt. Express* 12.15, pages 3548–3553.

Takahashi, Eiji J., Tsuneto Kanai, Yasuo Nabekawa, and Katsumi Midorikawa (2008). "10mJ class femtosecond optical parametric amplifier for generating soft x-ray harmonics". In: *Applied Physics Letters* 93.4, page 041111.

Tang, Xiaofeng, Gustavo A. Garcia, Jean-François Gil, and Laurent Nahon (2015). "Vacuum upgrade and enhanced performances of the double imaging electron/ion coincidence end-station at the vacuum ultraviolet beamline DESIRS". In: *Review of Scientific Instruments* 86.12, page 123108.

Telnov, Dmitry A. and Shih-I Chu (2009). "Effects of electron structure and multielectron dynamical response on strong-field multiphoton ionization of diatomic molecules with arbitrary orientation: An all-electron time-dependent density-functional-theory approach". In: *Phys. Rev. A* 79 (4), page 041401.

Thiré, Nicolas, Samuel Beaulieu, Vincent Cardin, Antoine Laramée, Vincent Wanie, Bruno E. Schmidt, and Francois Légaré (2015). "10 mJ 5-cycle pulses at 1.8m through optical parametric amplification". In: *Applied Physics Letters* 106.9, page 091110 (cited on pages 13, 21, 29, 31, 32, 251, 259).

Tia, Maurice, Barbara Cunha de Miranda, Steven Daly, François Gaie-Levrel, Gustavo A. Garcia, Laurent Nahon, and Ivan Powis (2014). "VUV Photodynamics and Chiral Asymmetry in the Photoionization of Gas Phase Alanine Enantiomers". In: *The Journal of Physical Chemistry A* 118.15. PMID: 24654892, pages 2765–2779.

Tia, Maurice, Martin Pitzer, Gregor Kastirke, Janine Gatzke, Hong-Keun Kim, Florian Trinter, Jonas Rist, Alexander Hartung, Daniel Trabert, Juliane Siebert, Kevin Henrichs, Jasper Becht, Stefan Zeller, Helena Gassert, Florian Wiegandt, Robert Wallauer, Andreas Kuhlins, Carl Schober, Tobias Bauer, Natascha Wechselberger, Phillip Burzynski, Jonathan Neff, Miriam Weller, Daniel Metz, Max Kircher, Markus Waitz, Joshua B. Williams, Lothar Ph. H. Schmidt, Anne D. Müller, André Knie, Andreas Hans, Ltaief Ben Ltaief, Arno Ehresmann, Robert Berger, Hironobu Fukuzawa, Kiyoshi Ueda, Horst Schmidt-Böcking, Reinhard Dörner, Till Jahnke, Philipp V. Demekhin, and Markus Schöffler (2017). "Observation of Enhanced Chiral Asymmetries in the Inner-Shell Photoionization of Uniaxially Oriented Methyloxirane Enantiomers". In: *The Journal of Physical Chemistry Letters* 8.13. PMID: 28582620, pages 2780–2786.

Torlina, Lisa, Felipe Morales, Jivesh Kaushal, Igor Ivanov, Anatoli Kheifets, Alejandro Zielinski, Armin Scrinzi, Harm Geert Muller, Suren Sukiasyan, Misha Ivanov, and Olga Smirnova (2015). "Interpreting attoclock measurements of tunnelling times". en. In: *Nature Physics* 11.6, pages 503–508. ISSN: 1745-2481.

Townsend, D., S. A. Lahankar, S. K. Lee, S. D. Chambreau, A. G. Suits, X. Zhang, J. Rheinecker, L. B. Harding, and J. M. Bowman (2004). "The Roaming Atom: Straying from the Reaction Path in Formaldehyde Decomposition". en. In: *Science* 306.5699, pages 1158–1161. ISSN: 0036-8075, 1095-9203.

Trebino, Rick, Kenneth W. DeLong, David N. Fittinghoff, John N. Sweetser, Marco A. Krumbügel, Bruce A. Richman, and Daniel J. Kane (1997). "Measuring ultrashort laser pulses in the time-frequency domain using frequency-resolved optical gating". In: *Review of Scientific Instruments* 68.9, pages 3277–3295.

Turchini, Stefano, Daniele Catone, Giorgio Contini, Nicola Zema, Simona Irrera, Mauro Stener, Devis Di Tommaso, Piero Decleva, and Tommaso Prosperi (2009). "Conformational Effects in Photoelectron Circular Dichroism of Alaninol". en. In: *ChemPhysChem* 10.11, pages 1839–1846. ISSN: 1439-7641.

Vachon, Jerome, Gregory T. Carroll, Michael M. Pollard, Emile M. Mes, Albert M. Brouwer, and Ben L. Feringa (2014). "An ultrafast surface-bound photo-active molecular motor". In: *Photochem. Photobiol. Sci.* 13 (2), pages 241–246.

Varju, K., Y. Mairesse, B. Carré, M. B. Gaarde, P. Johnsson, S. Kazamias, R. Lopez-Martens, J. Mauritsson, K. J. Schafer, P. Balcou, A. L'Huillier, and P. Salières (2005). "Frequency chirp of harmonic and attosecond pulses". In: *Journal of Modern Optics* 52, page 379.

Vincenti, H. and F. Quéré (2012). "Attosecond Lighthouses: How To Use Spatiotemporally Coupled Light Fields To Generate Isolated Attosecond Pulses". In: *Physical Review Letters* 108.11, page 113904.

Vodungbo, Boris, Anna Barszczak Sardinha, Julien Gautier, Guillaume Lambert, Constance Valentin, Magali Lozano, Grégory Iaquaniello, Franck Delmotte, Stéphane Sebban, Jan Lüning, and Philippe Zeitoun (2011). "Polarization control of high order harmonics in the EUV photon energy range". In: *Opt. Express* 19.5, pages 4346–4356.

Wahlström, C.-G., J. Larsson, A. Persson, T. Starczewski, S. Svanberg, P. Salières, Ph. Balcou, and Anne L'Huillier (1993). "High-order harmonic generation in rare gases with an intense short-pulse laser". In: *Phys. Rev. A* 48 (6), pages 4709–4720.

Wales, Benji, Eric Bisson, Reza Karimi, Jean-Claude Kieffer, Francois Légaré, and Joseph Sanderson (2012). "A coincidence detection algorithm for improving detection rates in coulomb explosion imaging". In: *Nuclear Instruments and Methods in Physics Research Section A: Accelerators, Spectrometers, Detectors and Associated Equipment* 667, pages 11–15. ISSN: 0168-9002.

Wang, Charles C. and George W. Racette (1965). "MEASUREMENT OF PARAMETRIC GAIN ACCOMPANYING OPTICAL DIFFERENCE FREQUENCY GENERATION". In: *Applied Physics Letters* 6.8, pages 169–171.

Wang, Ding, Yuxin Leng, and Zhizhan Xu (2013). "Measurement of nonlinear refractive index coefficient of inert gases with hollow-core fiber". In: *Applied Physics B* 111.3, pages 447–452. ISSN: 1432-0649.

Wang, He, Michael Chini, Shouyuan Chen, Chang-Hua Zhang, Feng He, Yan Cheng, Yi Wu, Uwe Thumm, and Zenghu Chang (2010). "Attosecond Time-Resolved Autoionization of Argon". In: *Physical Review Letters* 105.14, page 143002.

Wanie, Vincent, Heide Ibrahim, Samuel Beaulieu, Nicolas Thiré, Bruno E Schmidt, Yunpei Deng, Ali S Alnaser, Igor V Litvinyuk, Xiao-Min Tong, and François Légaré (2016). "Coherent control of D 2 /H 2 dissociative ionization by a mid-infrared two-color laser field". In: *Journal of Physics B: Atomic, Molecular and Optical Physics* 49.2, page 025601 (cited on pages 14, 22, 130, 135, 136).

Warrick, Erika R., Wei Cao, Daniel M. Neumark, and Stephen R. Leone (2016). "Probing the Dynamics of Rydberg and Valence States of Molecular Nitrogen with Attosecond Transient Absorption Spectroscopy". In: *The Journal of Physical Chemistry A* 120.19, pages 3165–3174. ISSN: 1089-5639.

Wells, E., C. E. Rallis, M. Zohrabi, R. Siemering, Bethany Jochim, P. R. Andrews, U. Ablikim, B. Gaire, S. De, K. D. Carnes, B. Bergues, R. de Vivie-Riedle, M. F. Kling, and I. Ben-Itzhak (2013). "Adaptive strong-field control of chemical dynamics guided by three-dimensional momentum imaging". en. In: *Nature Communications* 4, page 2895. ISSN: 2041-1723.

West, J B, A C Parr, B E Cole, D L Ederer, R Stockbauer, and J L Dehmer (1980). "Shape-resonance-induced non-Franck-Condon vibrational intensities in 3 g photoionisation of N 2". In: *Journal of Physics B: Atomic and Molecular Physics* 13.3, page L105.

Wigner, Eugene (1955). "Lower Limit for the Energy Derivative of the Scattering Phase Shift". In: *Physical Review* 98.1, pages 145–147.

Wilkinson, Iain, Andrey E. Boguslavskiy, Jochen Mikosch, Julien B. Bertrand, Hans Jakob Wörner, David M. Villeneuve, Michael Spanner, Serguei Patchkovskii, and Albert Stolow (2014). "Excited state dynamics in SO2. I. Bound state relaxation studied by time-resolved photoelectron-photoion coincidence spectroscopy". In: *The Journal of Chemical Physics* 140.20, page 204301.

Willems, F., C. T. L. Smeenk, N. Zhavoronkov, O. Kornilov, I. Radu, M. Schmidbauer, M. Hanke, C. von Korff Schmising, M. J. J. Vrakking, and S. Eisebitt (2015). "Probing ultrafast spin dynamics with high-harmonic magnetic circular dichroism spectroscopy". In: *Phys. Rev. B* 92 (22), page 220405.

Wollenhaupt, M., M. Krug, J. Köhler, T. Bayer, C. Sarpe-Tudoran, and T. Baumert (2009). "Three-dimensional tomographic reconstruction of ultrashort free electron wave packets". In: *Applied Physics B* 95.4, pages 647–651. ISSN: 1432-0649.

Wörner, H. J., J. B. Bertrand, B. Fabre, J. Higuet, H. Ruf, A. Dubrouil, S. Patchkovskii, M. Spanner, Y. Mairesse, V. Blanchet, E. Mével, E. Constant, P. B. Corkum, and D. M. Villeneuve (2011). "Conical Intersection Dynamics in NO2 Probed by Homodyne High-Harmonic Spectroscopy". en. In: *Science* 334.6053, pages 208–212. ISSN: 0036-8075, 1095-9203.

Wu, Mengxi, Shaohao Chen, Seth Camp, Kenneth J Schafer, and Mette B Gaarde (2016). "Theory of strong-field attosecond transient absorption". In: *Journal of Physics B: Atomic, Molecular and Optical Physics* 49.6, page 062003.

Xu, Han, Hongtao Hu, Xiao-Min Tong, Peng Liu, Ruxin Li, Robert T. Sang, and Igor V. Litvinyuk (2016). "Coherent control of the dissociation probability of H_2^+ in ω-3ω two-color fields". In: *Phys. Rev. A* 93 (6), page 063416.

Xu, Han, J-P Maclean, D E Laban, W C Wallace, D Kielpinski, R T Sang, and I V Litvinyuk (2013). "Carrier-envelope-phase-dependent dissociation of hydrogen". In: *New Journal of Physics* 15.2, page 023034.

Yakovlev, Vladislav V., Bern Kohler, and Kent R. Wilson (1994). "Broadly tunable 30-fs pulses produced by optical parametric amplification". In: *Opt. Lett.* 19.23, pages 2000–2002.

Yanai, Takeshi, David P Tew, and Nicholas C Handy (2004). "A new hybrid exchange–correlation functional using the Coulomb-attenuating method (CAM-B3LYP)". In: *Chemical Physics Letters* 393.1, pages 51–57. ISSN: 0009-2614.

Yang, Baorui, K. J. Schafer, B. Walker, K. C. Kulander, P. Agostini, and L. F. DiMauro (1993). "Intensity-dependent scattering rings in high order above-threshold ionization". In: *Phys. Rev. Lett.* 71 (23), pages 3770–3773.

Yang, C. N. (1950). "Selection Rules for the Dematerialization of a Particle into Two Photons". In: *Phys. Rev.* 77 (2), pages 242–245.

Yin, Yi-Yian, Ce Chen, D. S. Elliott, and A. V. Smith (1992). "Asymmetric photoelectron angular distributions from interfering photoionization processes". In: *Phys. Rev. Lett.* 69 (16), pages 2353–2356.

Yin, Yi-Yian, D.S. Elliott, R. Shehadeh, and E.R. Grant (1995). "Two-pathway coherent control of photoelectron angular distributions in molecular NO". In: *Chemical Physics Letters* 241.5, pages 591–596. ISSN: 0009-2614.

Yoshino, Kouichi (1970). "Absorption Spectrum of the Argon Atom in the Vacuum-Ultraviolet Region". EN. In: *JOSA* 60.9, pages 1220–1229.

Young, L., D. A. Arms, E. M. Dufresne, R. W. Dunford, D. L. Ederer, C. Höhr, E. P. Kanter, B. Krässig, E. C. Landahl, E. R. Peterson, J. Rudati, R. Santra, and S. H. Southworth (2006). "X-Ray Microprobe of Orbital Alignment in Strong-Field Ionized Atoms". In: *Physical Review Letters* 97.8, page 083601.

Zewail, Ahmed H. (2000). "Femtochemistry: Atomic-Scale Dynamics of the Chemical Bond". In: *The Journal of Physical Chemistry A* 104.24, pages 5660–5694. ISSN: 1089-5639 (cited on pages 12, 20).

Zhao, Arthur, Péter Sándor, Tamás Rozgonyi, and Thomas Weinacht (2014). "Removing electrons from more than one orbital: direct and indirect pathways to excited states of molecular cations". In: *Journal of Physics B: Atomic, Molecular and Optical Physics* 47.20, page 204023.

Zipp, Lucas J., Adi Natan, and Philip H. Bucksbaum (2014). "Probing electron delays in above-threshold ionization". In: *Optica* 1.6, pages 361–364.

Znakovskaya, I., P. von den Hoff, G. Marcus, S. Zherebtsov, B. Bergues, X. Gu, Y. Deng, M. J. J. Vrakking, R. Kienberger, F. Krausz, R. de Vivie-Riedle, and M. F. Kling (2012).

"Subcycle Controlled Charge-Directed Reactivity with Few-Cycle Midinfrared Pulses". In: *Phys. Rev. Lett.* 108 (6), page 063002.

Znakovskaya, I., P. von den Hoff, S. Zherebtsov, A. Wirth, O. Herrwerth, M. J. J. Vrakking, R. de Vivie-Riedle, and M. F. Kling (2009). "Attosecond Control of Electron Dynamics in Carbon Monoxide". In: *Phys. Rev. Lett.* 103 (10), page 103002.

Zuo, T. and A. D. Bandrauk (1995). "Charge-resonance-enhanced ionization of diatomic molecular ions by intense lasers". In: *Phys. Rev. A* 52 (4), R2511–R2514.

Zurch, M., C. Kern, P. Hansinger, A. Dreischuh, and Ch. Spielmann (2012). "Strong-field physics with singular light beams". In: *Nature Physics* 8, pages 743–746.